


Spectral Functions of the Holstein Polaron: Exact and Approximate Solutions

Petar Mitrić¹, Veljko Janković¹, Nenad Vukmirović¹, and Darko Tanasković¹
Institute of Physics Belgrade, University of Belgrade, Pregrevica 118, 11080 Belgrade, Serbia

 (Received 10 January 2022; revised 2 May 2022; accepted 5 August 2022; published 22 August 2022)

It is generally accepted that the dynamical mean field theory gives a good solution of the Holstein model, but only in dimensions greater than two. Here, we show that this theory, which becomes exact in the weak coupling and in the atomic limit, provides an excellent, numerically cheap, approximate solution for the spectral function of the Holstein model in the whole range of parameters, even in one dimension. To establish this, we make a detailed comparison with the spectral functions that we obtain using the newly developed momentum-space numerically exact hierarchical equations of motion method, which yields electronic correlation functions directly in real time. We crosscheck these conclusions with our path integral quantum Monte Carlo and exact diagonalization results, as well as with the available numerically exact results from the literature.

DOI: [10.1103/PhysRevLett.129.096401](https://doi.org/10.1103/PhysRevLett.129.096401)

The Holstein model is the simplest model that describes an electron that propagates through the crystal and interacts with localized optical phonons [1]. On the example of this model, numerous many-body methods were developed and tested [2]. The Holstein molecular crystal model is also very important in order to understand the role of polarons (quasiparticles formed by an electron dressed by lattice vibrations) in real materials [3]. This is still a very active field of research fueled by new directions in theoretical studies [4–12] and advances in experimental techniques [13].

The Holstein model can be solved analytically only in the limits of weak and strong electron-phonon coupling [14–16]. Reliable numerical results for the ground state energy and quasiparticle effective mass were obtained in the late 1990s using the density matrix renormalization group (DMRG) [17,18] and path integral quantum Monte Carlo (QMC) methods [19], and also within variational approaches [20–22]. At the time, numerically exact spectral functions for one-dimensional (1D) systems were obtained only within the DMRG method [17,18]. The main drawback of the QMC method is that it gives correlation functions in imaginary time and obtaining spectral functions and dynamical response functions is often impossible since the analytical continuation to the real frequency is a numerically ill-defined procedure. Interestingly, at finite temperature the spectral functions were obtained only very recently using finite- T Lanczos (FTLM) [23] and finite- T DMRG [24] methods. All these methods have their strengths and weaknesses depending on the parameter regime and temperature. As usually happens in a strongly interacting many-body problem, a complete physical picture emerges only by taking into account the solutions obtained with different methods.

The hierarchical equations of motion (HEOM) method is a numerically exact technique that has recently gained

popularity in the chemical physics community [25–28]. It has been used to explore the dynamics of an electron (or exciton) linearly coupled to a Gaussian bosonic bath. Within HEOM, we calculate the correlation functions directly on the real time (real frequency) axis [29]. Nevertheless, the applications of the HEOM method to the Holstein model [30–34] have been, so far, scarce because of the numerical instabilities stemming from the discreteness of the phonon bath on a finite lattice.

Along with numerically exact methods, a number of approximate techniques have been developed and applied to the Holstein model [35–38]. The dynamical mean field theory (DMFT) is a simple nonperturbative technique that has emerged as a method of choice for the studies of the Mott physics within the Hubbard model [39,40]. It can also be applied to the Holstein model giving numerically cheap results directly on the real frequency axis [41]. This method fully takes into account local quantum fluctuations and it becomes exact in the limit of infinite coordination number when the correlations become completely local. It was soon recognized [42,43] that the DMFT gives qualitatively correct spectral functions and conductivity for the Holstein model in three dimensions. In low-dimensional systems the solution is approximate as it neglects the nonlocal correlations and one might expect that the DMFT solution would not be accurate, particularly in one dimension. Surprisingly, to our knowledge, only the DMFT solution for the Bethe lattice was used in comparisons with the numerically exact results for the ground state properties in one dimension [20,44]. The quantitative agreement was rather poor, suggesting that the DMFT cannot provide a realistic description of the low-dimensional Holstein model due to the importance of nonlocal correlations [16,20,44].

In this Letter, we present a comprehensive solution of the 1D Holstein model: (i) We solve the DMFT equations in all

parameter regimes. At zero temperature we find a remarkable agreement of the DMFT ground state energy and effective mass with the available results from the literature in one, two, and three dimensions. (ii) For intermediate electron-phonon coupling, we obtain numerically exact spectral functions using the recently developed momentum-space HEOM approach [45]. For strong coupling we calculate the spectral functions using exact diagonalization (ED). We find a very good agreement with DMFT results and therefore demonstrate that the DMFT is rather accurate, in sharp contrast to current belief in the literature. (iii) We crosscheck the results with our QMC calculations in imaginary time. Overall, we demonstrate that the DMFT emerges as a unique method that gives close to exact spectral functions in the whole parameter space of the Holstein model, both at zero and at finite temperature.

Model and methods.—We study the 1D Holstein model given by the Hamiltonian

$$H = -t_0 \sum_i (c_i^\dagger c_{i+1} + \text{H.c.}) - g \sum_i n_i (a_i^\dagger + a_i) + \omega_0 \sum_i a_i^\dagger a_i. \quad (1)$$

Here, c_i^\dagger (a_i^\dagger) are the electron (phonon) creation operators, t_0 is the hopping parameter, and $n_i = c_i^\dagger c_i$. We consider dispersionless optical phonons of frequency ω_0 , and g denotes the electron-phonon coupling parameter. t_0 , \hbar , k_B , and lattice constant are set to 1. We consider the dynamics of a single electron in the band. It is common to define several dimensionless parameters: adiabatic parameter $\gamma = \omega_0/2t_0$, electron-phonon coupling $\lambda = g^2/2t_0\omega_0$, and $\alpha = g/\omega_0$. These parameters correspond to different physical regimes of the Holstein model shown schematically in Fig. 1(a).

In order to obtain reliable solutions in the whole parameter space, we use two approximate methods and three methods that are numerically exact. In the Holstein model, the DMFT reduces to solving the polaron impurity problem in the conduction electron band supplemented by the self-consistency condition [41]. The impurity problem can be solved in terms of the continued fraction expansion, giving the local Green's function on the real frequency axis (see Ref. [41] and Supplemental Material (SM) [46], Sec. I, for details). A crucial advantage of the DMFT for the Holstein model is that it becomes exact in both the weak coupling and in the atomic limit, and that it can be easily applied in the whole parameter space both at zero and at finite temperature. The DMFT equations can be solved on a personal computer in just a few seconds to a few minutes depending on the parameters. On general grounds, the DMFT is expected to work particularly well at high temperatures when the correlations become more local due to the thermal fluctuations [47,48]. We will compare the DMFT with the well-known self-consistent Migdal

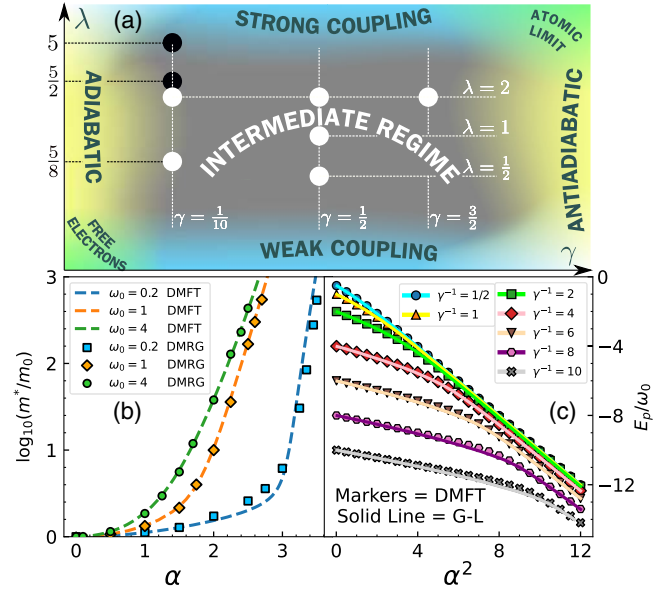


FIG. 1. (a) Schematic plot of different regimes in the (γ, λ) parameter space. The white (black) circles correspond to parameters for which both HEOM and QMC (just QMC) calculations were performed. The DMFT results are obtained in practically whole space of parameters. (b) Comparison of the DMFT and DMRG (taken from Refs. [17,20]) renormalized electron mass at $T = 0$. (c) Comparison of the ground state energy from the DMFT and the global-local variational approach (taken from Ref. [20]) at $T = 0$.

approximation (SCMA) [49], which becomes exact only in the weak coupling limit; see Sec. II of SM [46].

We have recently developed the momentum-space HEOM method [45] that overcomes the numerical instabilities originating from the discrete bosonic bath. Within this method we calculate the time-dependent greater Green's function $G^>(k, t)$, which presents the root of the hierarchy of the auxiliary Green's functions. The hierarchy is, in principle, infinite, and one actually solves the model by truncating the hierarchy at certain depth D . The HEOM are propagated independently for each allowed value of k up to long times ($\omega_0 t_{\max} \sim 500$). The propagation takes 5 to 10 hours on 16 cores per momentum k . The discrete Fourier transform is then used to obtain spectral functions without introducing any artificial broadening. Numerical error in the HEOM solution can originate from the finite-size effects since the method is applied on the lattice with N sites, and also from the finite depth D . We always use N and D , as given in SM [46], which correctly represent the thermodynamic limit. Generally, for larger g we need smaller N and larger D . This is why the ED method with a small number of sites could be a better option in the strong coupling regime. The ED method can be used more efficiently after the initial Hamiltonian is transformed by applying the Lang-Firsov transformation; see SM [46], Sec. III.

In the QMC method, we calculate the correlation function $C_k(\tau) = \langle c_k(\tau) c_k^\dagger \rangle_{T,0}$ in imaginary time. The thermal

expectation value is performed over the states with zero electrons and $c_k(\tau) = e^{\tau H} c_k e^{-\tau H}$. We use the path integral representation, the discretization of imaginary time, and analytical calculation of integrals over the phonon coordinates. We then evaluate a multidimensional sum over the electronic coordinates by a Monte Carlo method. This method is a natural extension of early works where such approach was applied just to thermodynamic quantities [50–52]. Details of the method are presented in Ref. [45].

Results at zero temperature.—In Fig. 1(b), we show the DMFT results for the electron effective mass at the bottom of the band, $m^*/m_0 = 1 - d\text{Re}\Sigma(\omega)/d\omega|_{E_p}$ (where $\Sigma(\omega)$ is the self-energy), over a broad range of parameters covering practically the whole parameter space in the (γ, λ) plane. We see that the mass renormalization is in striking agreement with the DMRG result [17,20] that presents the best available result from the literature. Small discrepancies are visible only for stronger interaction with small ω_0 . A similar level of agreement can be seen in the comparison of the ground state (polaron) energy E_p in Fig. 1(c). Here, the results obtained with variational global-local method [20,21] are taken as a reference. While the agreement in the weak coupling and in the atomic limit could be anticipated since the DMFT becomes exact in these limits, we find the quantitative agreement in the crossover regime between these two limits rather surprising, having in mind that the DMFT completely neglects nonlocal correlations. It is also interesting that this was not observed earlier. The only difference from the standard reference of Ciuchi *et al.* [41] is that we applied the DMFT to the 1D case, as opposed to the Bethe lattice. This is, however, a key difference. Otherwise the DMFT provides only a qualitative description of the Holstein model [3,16,20,44,53]. From the technical side, the only difference as compared to the case of the Bethe lattice is in the self-consistency equation. For obtaining a numerically stable and precise solution, it was crucial to use an analytical expression for the self-consistency relation (see Sec. IB in SM [46]). We have also calculated the effective mass for two- and three-dimensional lattices (see Sec. IC in SM [46]) and the agreement with the QMC calculation from Ref. [19] is excellent. This was now expected since the importance of nonlocal correlations decreases in higher dimensions. A comparison with the Bethe lattice effective mass is illustrated in SM [46], Sec. ID.

The next step is to check if the agreement with the numerically exact solution extends also to spectral functions. Typical results at $k = 0$ are illustrated in Fig. 2. We note that at $T = 0$ the DMFT quasiparticle peak is a delta function (broadened in Fig. 2), while satellite peaks are incoherent having intrinsic nonzero width. In HEOM, the peak broadening due to the finite lattice size N and finite propagation time t_{max} is generally much smaller than the Lorentzian broadening used in the insets of Figs. 2(a)–2(d). The weights of the DMFT and HEOM quasiparticle peaks

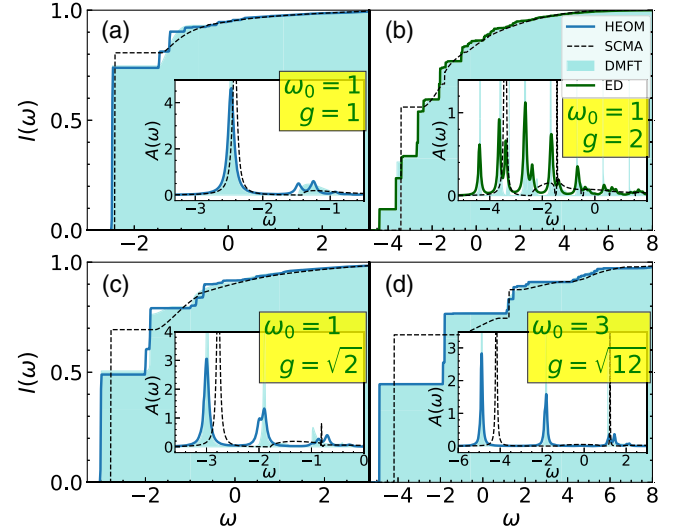


FIG. 2. (a)–(d) Integrated HEOM, DMFT, SCMA, and ED spectral weight, $I(\omega) = \int_{-\infty}^{\omega} d\nu A_k(\nu)$, for $k = 0$ and $T = 0$. The insets show comparisons of the spectral functions. $I(\omega)$ is obtained without broadening, whereas $A(\omega)$ is broadened by Lorentzians of half-width $\eta = 0.05$.

correspond to the m_0/m^* ratio. The satellite peaks are also very well captured by the DMFT solution in all parameter regimes. For $g = 1$ we can see two small peaks in the first satellite structure of the HEOM solution. We find very similar peaks also in the DMFT solution when applied on a lattice of the same size, which is here equal to 10 (see SM [46], Sec. IV). Hence, we conclude that these peaks are an artefact of the finite lattice size. In the strong coupling regime $\omega_0 = 1$, $g = 2$, the DMFT is compared with ED since the thermodynamic limit is practically reached for $N = 4$; see SM [46], Sec. IV. Here, we notice a pronounced excited quasiparticle peak [22,23] whose energy is below $E_p + \omega_0$. This peak, which consists of a polaron and a bound phonon, is also very well resolved within the DMFT solution. For parameters in Fig. 2(d) the lattice sites are nearly decoupled, approaching the atomic limit ($t_0 \ll g, \omega_0$), when the DMFT becomes exact (see Sec. V in SM [46]). For a comparison, we show also the SCMA spectral functions. As the interaction increases, the SCMA solution misses the position and the weight of the quasiparticle peak and the satellite peaks are not properly resolved. Further comparisons of zero temperature spectral functions are shown in Sec. VI of SM [46].

Results at finite temperature.—Reliable finite- T results for the spectral functions of the Holstein model have been obtained only very recently using the FTLM [23] and finite- T DMRG methods [24]. Here, we calculate the spectral functions using HEOM or ED and compare them extensively with the DMFT. The results are crosschecked using the QMC results in imaginary time.

Typical results for the spectral functions are shown in Fig. 3, while additional results for other momenta and other

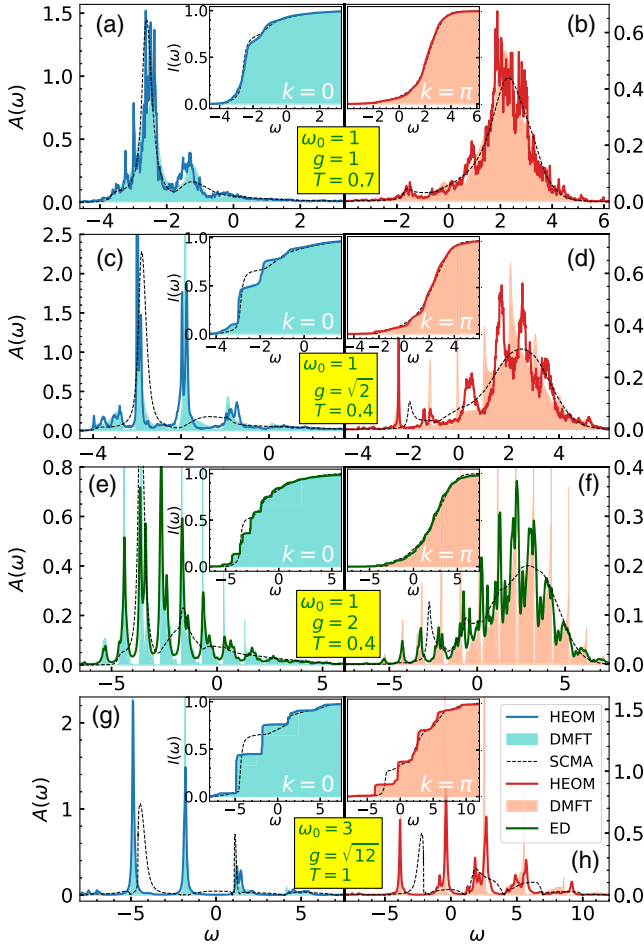


FIG. 3. (a)–(h) Spectral functions at $T > 0$ for $k = 0$ and $k = \pi$. In panels (e)–(f) only the ED results are broadened by Lorentzians of half-width $\eta = 0.05$, while all the curves are broadened in (g)–(h) with the same η . All insets are shown without broadening.

parameters are shown in Sec. VII of SM [46]. We see that for $T > 0$ the satellite peaks appear also below the quasiparticle peak. The agreement between the DMFT and the HEOM (ED) spectral functions is very good. The agreement remains excellent even for $g = 2$ where the electrons are strongly renormalized $m^*/m_0 \approx 10$, which is far away from both the atomic and weak coupling limits, where the DMFT is exact. A part of the difference between the DMFT and the HEOM (ED) results can be ascribed to the small finite-size effects in the HEOM and ED solutions, as detailed in SM [46], Sec. IV. In accordance with the presented results, it is not surprising that the self-energies are nearly k independent, as shown in SM [46], Sec. VIII. It is also instructive to examine the difference between the SCMA and DMFT (HEOM) solutions. For moderate interaction [Figs. 3(a) and 3(b)], the weight of the SCMA quasiparticle peak is nearly equal to the DMFT (HEOM) quasiparticle weight, and the overall agreement of spectral functions is rather good. This is not the case for stronger

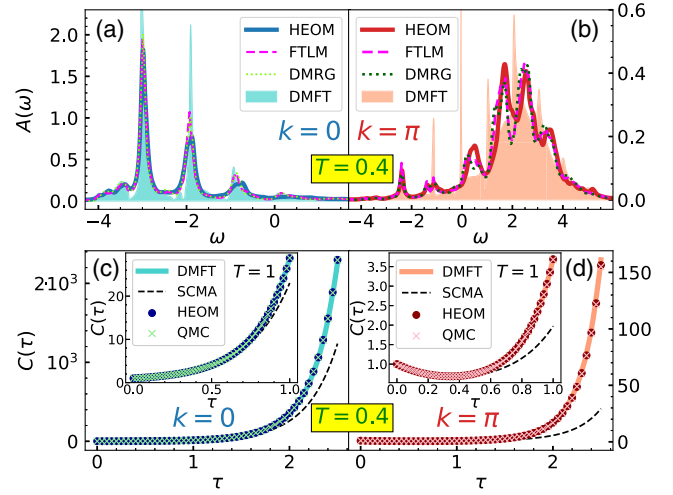


FIG. 4. (a), (b) Comparison of DMFT, HEOM, and finite- T DMRG and FTLM (taken from Ref. [24]) spectral functions at $T = 0.4$. All the lines are here broadened by Lorentzians of half-width $\eta = 0.05$. (c), (d) DMFT, QMC, HEOM, and SCMA imaginary time correlation functions at $T = 0.4$ ($T = 1$ in the insets). Here, $g = \sqrt{2}$, $\omega_0 = 1$.

electron-phonon coupling [Figs. 3(c)–3(h)] where the SCMA poorly approximates the true spectrum.

We observe that for $g = \sqrt{2}$ and $k = \pi$ the DMFT and HEOM satellite peaks are somewhat shifted with respect to one another; see Figs. 3(c) and 3(d). This is the most challenging regime for the DMFT, representing a crossover ($\lambda = 1$) between the small and large polaron. Nevertheless, the agreement remains very good near the quasiparticle peak for $k = 0$, which will be the most important for transport in weakly doped systems. In order to gain further confidence into the details of the HEOM spectral functions for $g = \sqrt{2}$, we compare them with the available results obtained within the finite- T DMRG and Lanczos methods. We find an excellent agreement, as shown in Figs. 4(a) and 4(b).

The DMFT and HEOM results are crosschecked with the path integral QMC calculations. The quantity that we obtain in QMC is the single electron correlation function in imaginary time, which can be expressed through the spectral function as $C_k(\tau) = \int_{-\infty}^{\infty} d\omega e^{-\omega\tau} A_k(\omega)$. Typical results are illustrated in Figs. 4(c) and 4(d), while extensive comparisons are presented in Sec. IX of SM [46]. At $T = 0.4$ we can see a small difference in $C_\pi(\tau)$ between the DMFT and QMC (HEOM) results. At $T = 1$, both for $k = 0$ and $k = \pi$, the difference in $C_k(\tau)$ is minuscule, well below the QMC error bar, which is smaller than the symbol size. This confirms that nonlocal correlations are weak. Similarly, as for the spectral functions, the SCMA correlation functions show clear deviation from other solutions. We, however, note that great care is needed when drawing conclusions from the imaginary axis data since a very small difference in the imaginary axis correlation functions can correspond to substantial differences in spectral functions.

Conclusions.—In summary, we have presented a comprehensive solution of the 1D Holstein polaron covering all parameter regimes. We showed that the DMFT is a remarkably good approximation in the whole parameter space. This approximation is simple, numerically efficient, and can also be easily applied in two and three dimensions. We successfully used momentum-space HEOM and ED methods for comparisons with the DMFT spectral functions both at zero and at finite temperature. The comparisons showed an excellent agreement between the spectral functions in most of the parameter space. For parameters that are most challenging for the DMFT, a very good agreement was found around $k = 0$ and a reasonably good agreement was obtained at larger values of k . All of the results are crosschecked with the imaginary axis QMC calculations and with the available results from the literature. Both the DMFT and HEOM methods are implemented directly in real frequency, without artificial broadening of the spectral functions. This will be crucial in order to calculate dynamical quantities and determine a potential role of the vertex corrections to conductivity by avoiding possible pitfalls of the analytical continuation, which we leave as a challenge for future work.

D. T. acknowledges useful discussions with V. Dobrosavljević. We thank J. Bonča for sharing with us the data from Ref. [23]. The authors acknowledge funding provided by the Institute of Physics Belgrade, through the grant by the Ministry of Education, Science, and Technological Development of the Republic of Serbia. Numerical simulations were performed on the PARADOX supercomputing facility at the Scientific Computing Laboratory, National Center of Excellence for the Study of Complex Systems, Institute of Physics Belgrade.

-
- [1] T. Holstein, *Ann. Phys. (N.Y.)* **8**, 325 (1959).
 [2] A. S. Alexandrov, *Polarons in Advanced Materials* (Springer, New York, 2007).
 [3] C. Franchini, M. Reticcioli, M. Setvin, and U. Diebold, *Nat. Rev. Mater.* **6**, 560 (2021).
 [4] L. Vidmar, J. Bonča, M. Mierzejewski, P. Prelovšek, and S. A. Trugman, *Phys. Rev. B* **83**, 134301 (2011).
 [5] B. Kloss, D. R. Reichman, and R. Tempelaar, *Phys. Rev. Lett.* **123**, 126601 (2019).
 [6] C. Brockett and E. Jeckelmann, *Phys. Rev. B* **95**, 064309 (2017).
 [7] N. Prodanović and N. Vukmirović, *Phys. Rev. B* **99**, 104304 (2019).
 [8] J. Stolpp, J. Herbrych, F. Dorfner, E. Dagotto, and F. Heidrich-Meisner, *Phys. Rev. B* **101**, 035134 (2020).
 [9] Y. Murakami, P. Werner, N. Tsuji, and H. Aoki, *Phys. Rev. B* **91**, 045128 (2015).
 [10] D. Jansen, J. Stolpp, L. Vidmar, and F. Heidrich-Meisner, *Phys. Rev. B* **99**, 155130 (2019).
 [11] J. H. Fetherolf, D. Golež, and T. C. Berkelbach, *Phys. Rev. X* **10**, 021062 (2020).
 [12] A. S. Mishchenko, N. Nagaosa, and N. Prokof'ev, *Phys. Rev. Lett.* **113**, 166402 (2014).
 [13] M. Kang, S. W. Jung, W. J. Shin, Y. Sohn, S. H. Ryu, T. K. Kim, M. Hoesch, and K. S. Kim, *Nat. Mater.* **17**, 676 (2018).
 [14] G. Mahan, *Many-Particle Physics* (Kluwer Academic, New York, 2000).
 [15] I. Lang and Y. A. Firsov, *Zh. Eksp. Teor. Fiz.* **43**, 1843 (1962) [*Sov. Phys. JETP* **16**, 1301 (1963)].
 [16] A. S. Alexandrov and J. T. Devreese, *Advances in Polaron Physics* (Springer, New York, 2010).
 [17] E. Jeckelmann and S. R. White, *Phys. Rev. B* **57**, 6376 (1998).
 [18] C. Zhang, E. Jeckelmann, and S. R. White, *Phys. Rev. B* **60**, 14092 (1999).
 [19] P. E. Kornilovitch, *Phys. Rev. Lett.* **81**, 5382 (1998).
 [20] A. H. Romero, D. W. Brown, and K. Lindenberg, *J. Chem. Phys.* **109**, 6540 (1998).
 [21] A. H. Romero, D. W. Brown, and K. Lindenberg, *Phys. Rev. B* **59**, 13728 (1999).
 [22] J. Bonča, S. A. Trugman, and I. Batistić, *Phys. Rev. B* **60**, 1633 (1999).
 [23] J. Bonča, S. A. Trugman, and M. Berciu, *Phys. Rev. B* **100**, 094307 (2019).
 [24] D. Jansen, J. Bonča, and F. Heidrich-Meisner, *Phys. Rev. B* **102**, 165155 (2020).
 [25] Y. Tanimura, *J. Chem. Phys.* **153**, 020901 (2020).
 [26] R.-X. Xu and Y. J. Yan, *Phys. Rev. E* **75**, 031107 (2007).
 [27] J. Jin, X. Zheng, and Y. J. Yan, *J. Chem. Phys.* **128**, 234703 (2008).
 [28] D. Hou, R. Wang, X. Zheng, N. H. Tong, J. H. Wei, and Y. J. Yan, *Phys. Rev. B* **90**, 045141 (2014).
 [29] Z. H. Li, N. H. Tong, X. Zheng, D. Hou, J. H. Wei, J. Hu, and Y. J. Yan, *Phys. Rev. Lett.* **109**, 266403 (2012).
 [30] L. Chen, Y. Zhao, and Y. Tanimura, *J. Phys. Chem. Lett.* **6**, 3110 (2015).
 [31] L. Song and Q. Shi, *J. Chem. Phys.* **142**, 174103 (2015).
 [32] L. Song and Q. Shi, *J. Chem. Phys.* **143**, 194106 (2015).
 [33] I. S. Dunn, R. Tempelaar, and D. R. Reichman, *J. Chem. Phys.* **150**, 184109 (2019).
 [34] Y. Yan, T. Xing, and Q. Shi, *J. Chem. Phys.* **153**, 204109 (2020).
 [35] M. Hohenadler, M. Aichhorn, and W. von der Linden, *Phys. Rev. B* **68**, 184304 (2003).
 [36] G. De Filippis, V. Cataudella, V. Marigliano Ramaglia, and C. A. Perroni, *Phys. Rev. B* **72**, 014307 (2005).
 [37] M. Berciu, *Phys. Rev. Lett.* **97**, 036402 (2006).
 [38] G. L. Goodvin, M. Berciu, and G. A. Sawatzky, *Phys. Rev. B* **74**, 245104 (2006).
 [39] A. Georges, G. Kotliar, W. Krauth, and M. J. Rozenberg, *Rev. Mod. Phys.* **68**, 13 (1996).
 [40] R. M. Martin, L. Reining, and D. M. Ceperley, *Interacting Electrons: Theory and Computational Approaches* (Cambridge University Press, Cambridge, England, 2016).
 [41] S. Ciuchi, F. de Pasquale, S. Fratini, and D. Feinberg, *Phys. Rev. B* **56**, 4494 (1997).
 [42] S. Fratini, F. de Pasquale, and S. Ciuchi, *Phys. Rev. B* **63**, 153101 (2001).
 [43] S. Fratini and S. Ciuchi, *Phys. Rev. Lett.* **91**, 256403 (2003).
 [44] L.-C. Ku, S. A. Trugman, and J. Bonča, *Phys. Rev. B* **65**, 174306 (2002).

- [45] V. Janković and N. Vukmirović, *Phys. Rev. B* **105**, 054311 (2022).
- [46] See Supplemental Material at <http://link.aps.org/supplemental/10.1103/PhysRevLett.129.096401> for detailed analysis and supporting data.
- [47] J. Vučičević, J. Kokalj, R. Žitko, N. Wentzell, D. Tanasković, and J. Mravlje, *Phys. Rev. Lett.* **123**, 036601 (2019).
- [48] A. Vranić, J. Vučičević, J. Kokalj, J. Skolimowski, R. Žitko, J. Mravlje, and D. Tanasković, *Phys. Rev. B* **102**, 115142 (2020).
- [49] A. Migdal, *Zh. Eksp. Teor. Fiz.* **34**, 1438 (1958) [*Sov. Phys. JETP* **7**, 996 (1958)].
- [50] H. De Raedt and A. Lagendijk, *Phys. Rev. Lett.* **49**, 1522 (1982).
- [51] H. De Raedt and A. Lagendijk, *Phys. Rev. B* **27**, 6097 (1983).
- [52] H. De Raedt and A. Lagendijk, *Phys. Rev. B* **30**, 1671 (1984).
- [53] O. S. Barišić, *Phys. Rev. B* **76**, 193106 (2007).

Nonequilibrium Thermodynamics of Charge Separation in Organic Solar Cells

Waldemar Kaiser, Veljko Janković, Nenad Vukmirović, and Alessio Gagliardi*



Cite This: *J. Phys. Chem. Lett.* 2021, 12, 6389–6397



Read Online

ACCESS |



Metrics & More

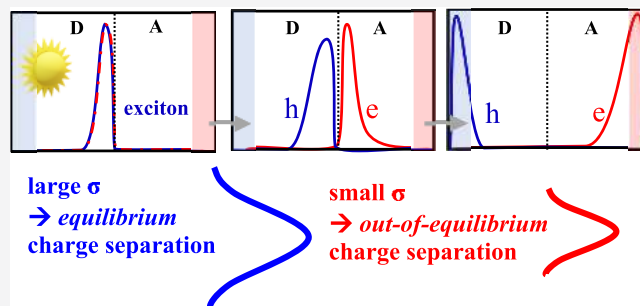


Article Recommendations



Supporting Information

ABSTRACT: This work presents a novel theoretical description of the nonequilibrium thermodynamics of charge separation in organic solar cells (OSCs). Using stochastic thermodynamics, we take realistic state populations derived from the phonon-assisted dynamics of electron–hole pairs within photoexcited organic bilayers to connect the kinetics with the free energy profile of charge separation. Hereby, we quantify for the first time the difference between nonequilibrium and equilibrium free energy profile. We analyze the impact of energetic disorder and delocalization on free energy, average energy, and entropy. For a high disorder, the free energy profile is well-described as equilibrated. We observe significant deviations from equilibrium for delocalized electron–hole pairs at a small disorder, implying that charge separation in efficient OSCs proceeds via a cold but nonequilibrated pathway. Both a large Gibbs entropy and large initial electron–hole distance provide an efficient charge separation, while a decrease in the free energy barrier does not necessarily enhance charge separation.



Despite years of research on the fundamental properties of organic solar cells (OSCs), one of the essential aspects of these materials is still under debate: what causes the efficient dissociation of charge transfer (CT) states into free charge carriers despite the presence of the strong Coulomb attraction? Various mechanisms have been proposed to promote the CT separation. On the one hand, “hot” CT states are considered to provide sufficient excess energy for the charges to overcome the binding energy before they relax and become trapped at the bottom of the CT manifold.^{1–4} On the other hand, the internal quantum efficiency that is independent of the excitation energy suggests an efficient separation of “cold” CT states.^{5,6} The precise mechanism of cold charge separation, however, is to be established.

Kinetic models of charge separation suggest that delocalized charges can efficiently escape their strong binding due to a reduced Coulomb interaction.^{7–13} Furthermore, a moderate disorder in combination with delocalization positively impacts charge separation,^{10,14} while a strong disorder hampers charge transport,^{15,16} traps charge carriers, and influences charge recombination.¹⁷ Thermodynamic considerations reassessed the widespread view that charges have to overcome large energy barriers to become fully separated.^{18–22} In materials of higher dimensionality, entropy, reflecting the number of available states, significantly reduces the free energy barrier.^{18,21,22} Hood and Kassal emphasized that relying only on dimensionality underestimates the contribution of the energetic disorder, σ , to the free energy for disordered organic semiconductors.¹⁹ Assuming the canonical distribution of CT

states in energy, they predict a reduction in free energy barrier with increased σ . For $\sigma \geq 100$ meV, equilibrium thermodynamic arguments suggest that charges are not bound and can be separated under favorable kinetic conditions. The extension of the formalism to include charge delocalization²³ revealed that the positive impact of delocalization on charge separation cannot be rationalized in terms of equilibrium thermodynamics alone, as it predicts an increase in the energy barrier for more delocalized carriers. The conclusions drawn from existing thermodynamic studies of charge separation in OSCs seem to contradict the intuitive picture emerging from kinetic models.

Some of the weaknesses of existing thermodynamic arguments and their possible solutions are as follows: (i) The population of CT states described by the canonical distribution is unrealistic. Nonequilibrated electron–hole pairs due to an incomplete thermalization were indeed observed in CT electroluminescence²⁴ and photoluminescence²⁵ measurements in bulk heterojunction OSCs. Giazitidis et al.²⁶ proposed to correct the equilibrium free energy with the probability distribution of finding a CT state at a certain distance. Shi et al. emphasize that the disorder-enhanced

Received: June 8, 2021

Accepted: July 2, 2021

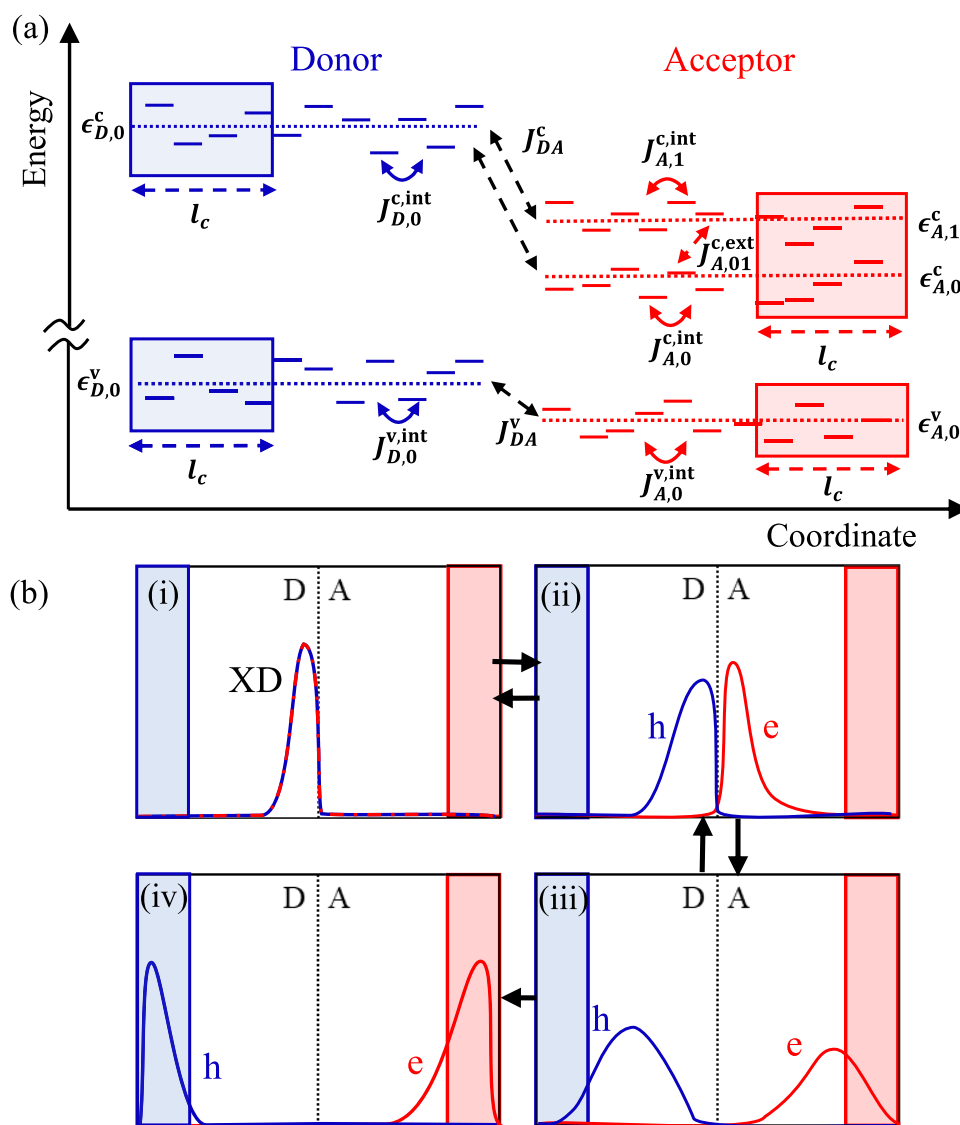


Figure 1. (a) Schematic representation of the organic bilayer model. Dotted lines give the different average on-site energies of the LUMO (superscript c) and of the HOMO (superscript v) in the donor (D) and in the acceptor (A); solid lines represent the actual on-site energies, which vary from the average on-site energies due to the Gaussian energetic disorder σ . The different transfer integrals within the donor ($J_{D,0}^{c,int}$) and the acceptor ($J_{A,0}^{c,int}$) as well as the coupling between the donor and acceptor (J_{DA}^c) are highlighted. In the acceptor region, LUMO (subscript 0) and LUMO+1 (subscript 1) are considered with the transfer integral $J_{A,01}^{c,ext}$ representing the coupling of the LUMO and LUMO+1 orbitals. Highlighted regions at the left and the right end of the donor and acceptor, respectively, with length l_c visualize contact regions. (b) Representative evolution of an electron–hole pair in the organic bilayer: (i) donor exciton (XD), (ii) CT state—electron in the acceptor and hole in the donor localized at the donor/acceptor interface, (iii) CT state featuring larger intrapair separation and more delocalized carriers, (iv) contact state—electron and hole located in the contact region.

dissociation is a nonequilibrium effect.¹⁴ They observed a deviation of the actual energy barrier from the equilibrium one by averaging Monte Carlo trajectories but neglected the weighting of the energies by their population probability. (ii) The finite lifetime of CT states, which may eliminate a large percentage of possible separation pathways, is completely neglected in previous thermodynamic studies.^{18,19,23} (iii) Most of the thermodynamic considerations do not include the coupling of electronic excitations to phonons. Such effects were partially included in previous equilibrium thermodynamic studies in refs 27 and 28.

Previous works gave clear suggestions that the equilibrium free energy profile might not be adequate to study the charge separation process. In this work, we make use of the nonequilibrium free energy rigorously derived from the theory

of stochastic thermodynamics^{29,30} to connect the kinetic and thermodynamic perspectives on charge separation and quantify for the first time the difference between nonequilibrium and equilibrium free energy. We perform the study for different values of energetic disorder and delocalization and find that this difference is strongest when charge separation efficiency is largest. Our results therefore imply that charge separation in efficient OSCs proceeds via cold, but nonequilibrium, pathways.

To establish the connection between kinetic and thermodynamic properties in the charge separation process in a photoexcited organic bilayer, representing the donor/acceptor interface in OSCs, we use the following procedure: (i) We model the organic bilayer using a minimal microscopic Hamiltonian that captures all important physical effects—

delocalization, disorder, electron–hole interaction, and electron–phonon coupling—in the system. We obtain the eigenstates of this Hamiltonian that we classify as states of excitons in the donor, CT states, and contact states; (ii) We compute the transition rates between pairs of states obtained in step (i) and solve the master equation to obtain the nonequilibrium steady-state populations of all non-contact states; (iii) We evaluate the nonequilibrium free energy profile of CT states.

(i) The organic bilayer model used in this step has been reported in previous publications.^{10,31} Here, we outline its most important ingredients, while we provide all details in the [Supporting Information](#) (section Model Hamiltonian therein). We consider a lattice model with N sites corresponding to the donor material and N sites corresponding to the acceptor material, schematically shown in [Figure 1a](#). The effects of delocalization are included through electronic couplings between neighboring sites, while the effects of disorder are included through random on-site electron and hole energies drawn from Gaussian distributions of standard deviation σ centered around the site energies. An attractive electron–hole interaction is approximated using the Ohno potential. The model parameters were chosen such that the band offsets, band gaps, bandwidths, and binding energies of the donor, acceptor, and CT excitons correspond to the values for the P3HT/PCBM interface. We then solve the eigenvalue problem of this Hamiltonian, which provides a set of excitonic states. On the basis of the spatial distribution of the electron and of the hole component of the excitonic state, we classify these states as (a) donor exciton states—states where both the electron and the hole are predominantly located in the donor, (b) CT states—states where the hole and the electron are located predominantly in the donor and in the acceptor, respectively, and (c) contact states—states where the electron is predominantly located in the region of length l_c far away from the interface in the acceptor, while the hole is predominantly located in such a region in the donor (see [Figure 1b](#)). Contact states can be considered as states of fully separated charges. A typical spatial distribution of donor, CT, and contact states is shown in [Figure 1b](#). All values of the model parameters are summarized in [Table S1, Supporting Information](#).

(ii) In this step we calculate the steady-state populations f_x^{st} of the excitonic states $|x\rangle$ by solving the master equation

$$0 = g_x - \tau_x^{-1} f_x^{\text{st}} - \sum_{x',x} w_{x'x} f_x^{\text{st}} + \sum_{x' \notin C} w_{xx'} f_{x'}^{\text{st}} \quad (1)$$

where $w_{x'x}$ is the transition rate from state $|x\rangle$ to state $|x'\rangle$, τ_x is the lifetime of the state $|x\rangle$, and g_x is the generation rate in state $|x\rangle$ that is chosen to mimic the excitation by incident sunlight. The last sum in [eq 1](#) does not include contact states C , because we impose that once a contact state is reached, the charges are fully separated and cannot return back to the system. The detailed models used for phonon-assisted transition rates $w_{x'x}$, lifetimes τ_x , and generation rates g_x are provided in [Supporting Information](#) (section Model Hamiltonian therein).

Electron–hole pairs evolve within a phase space of excitonic states with a large energetic disorder and variable mean distance between the wave function of the electron and the hole; see [Figure 1b](#). We assume that the charge separation starts from states of donor excitons ([Figure 1b\(i\)](#)) that are populated as a result of the absorption of natural sunlight. It proceeds via phonon-assisted transitions between space-

separated CT states ([Figure 1b\(ii,iii\)](#)) and finishes once the charges are collected at a contact state ([Figure 1b\(iv\)](#)) or recombine. The expression for the charge separation efficiency

$$\eta = \frac{\sum_{x' \in C} \sum_{x \notin C} w_{x'x} f_x^0}{\sum_{x \notin C} g_x} \quad (2)$$

contains phonon-assisted transition rates $w_{x'x}$ toward contact states $|x'\rangle \in C$, which are appreciable only when state $|x\rangle$ features the electron in the acceptor and the hole in the donor part of the bilayer. In the following, instead of considering the full distribution, we concentrate on the steady-state populations of CT states, in which the charges are spatially separated and reside in different regions of the bilayer, as contact states can only be reached when $|x\rangle$ ([eq 2](#)) is a CT state.

(iii) The theory of stochastic thermodynamics extends equilibrium thermodynamic concepts to describe thermodynamic quantities of out-of-equilibrium systems and processes that are governed by Markovian dynamics. The major advantages of stochastic thermodynamics are that it can be applied to small-scale systems to study the effect of fluctuations^{29,30,32,33} and that it is not restricted to near-equilibrium dynamics.^{29,30} Stochastic thermodynamics formulates the first and second laws of thermodynamics for a system that is described by discrete microstates m of energy E_m with probability $p_m(t)$ of the system being in state m . This allows us to define thermodynamic quantities such as the energy of the system, $E = \sum_m p_m E_m$, and the Gibbs entropy, $S = -k_B \sum_m p_m \ln p_m$, from the probability distributions as known from statistical mechanics, with the major difference being that p_m can be time-dependent and out-of-equilibrium. While classical thermodynamics provides fundamental boundaries for entropy production ($\Delta S \geq 0$, second law of thermodynamics), stochastic thermodynamics can quantify the amount of entropy that is produced and even the entropy contribution of each microscopic state transition.²⁹ Stochastic thermodynamics was used to derive thermodynamic efficiency limits of nanothermoelectric engines at the maximum power point³⁴ and to derive protocols to extract the maximum work from nanoscale processes,³⁵ to mention a few examples. An application of stochastic thermodynamics to existing few-level photovoltaic models^{36–38} may yield thermodynamic quantities from kinetics but cannot capture the broad CT manifold in terms of energy, delocalization, and electron–phonon coupling. Therefore, a combination of our model and stochastic thermodynamics provides a minimal, yet physically plausible, framework to study the nonequilibrium thermodynamics of charge separation.

Previous equilibrium studies^{19,23} assumed the Maxwell–Boltzmann distribution of CT states $|m\rangle$, $f_m^{\text{eq}} \propto e^{-\beta E_m}$, where E_m is the energy of CT state $|m\rangle$, while $\beta = (k_B T)^{-1}$, with T being the phonon-bath temperature. To study if, and to which extent, charge separation occurs out-of-equilibrium, we formulate the free energy F^{st} in the steady state as a function of the intrapair distance r using the free energy relation from stochastic thermodynamics^{29,39}

$$\begin{aligned} \beta(F^{\text{st}}(r) - F^{\text{eq}}(r)) &= D_{\text{KL}}(p^{\text{st}} \| p^{\text{eq}}) \\ &= \sum_m p_m^{\text{st}}(r) \ln \left(\frac{p_m^{\text{st}}(r)}{p_m^{\text{eq}}(r)} \right) \end{aligned} \quad (3)$$

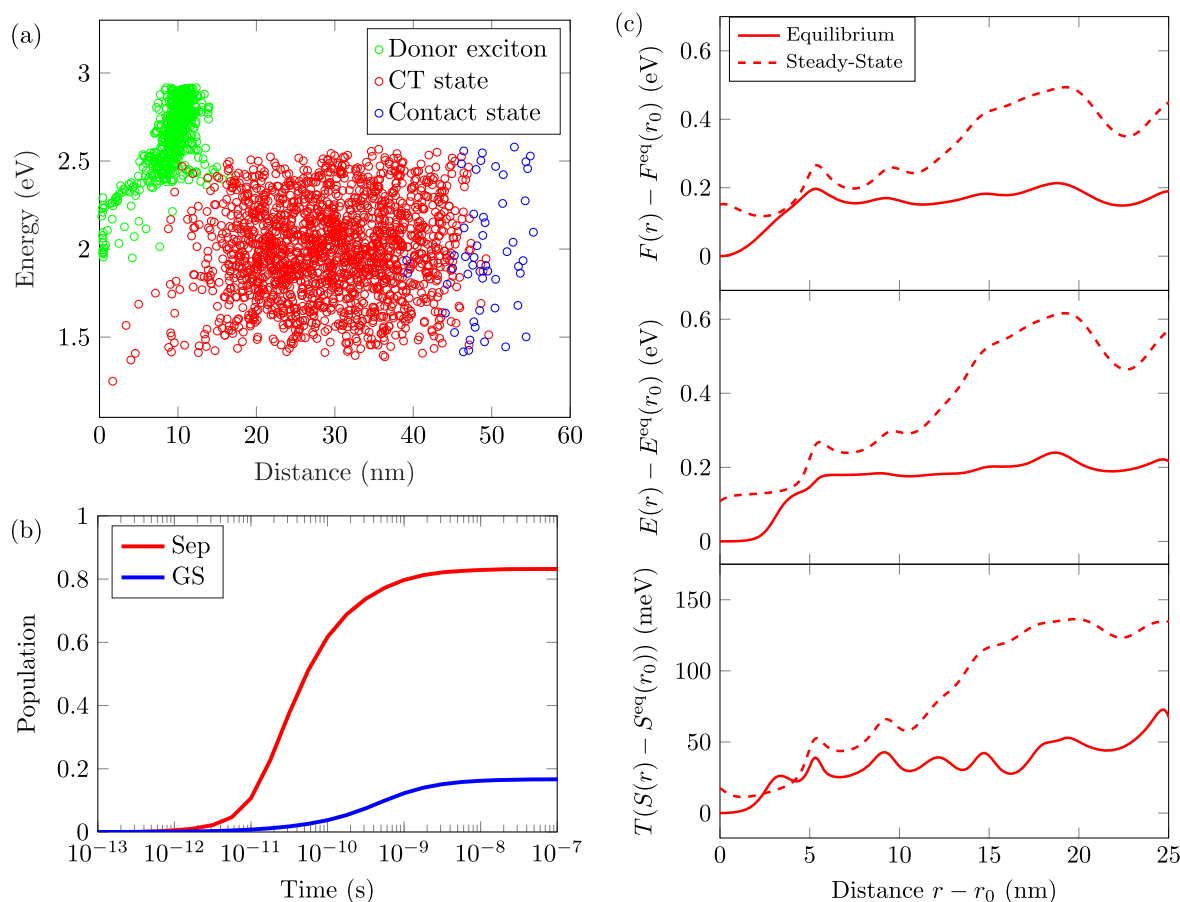


Figure 2. (a) Exemplary distribution of electron–hole pairs in the distance–energy phase space: donor excitons (green), CT states (red), and contact states (blue). (b) Time dependence of fully separated (Sep) and recombined states (GS) for the given network. (c) Distance dependence of the free energy $F(r)$, energy $E(r)$, and entropy contribution $TS(r)$. Solid lines represent the equilibrium values; dashed lines give the nonequilibrium results. All curves are normalized to the equilibrium value (subscript eq) at the distance r_0 .

with the Kullback–Leibler (KL) divergence $D_{\text{KL}}(p^{\text{st}}||p^{\text{eq}})$ between the steady-state probability distribution p^{st} and the equilibrium probability distribution p^{eq} of all CT states $|m\rangle$. For a given r value, the steady-state probability distribution p_m^{st} is obtained from the stationary populations f_m^{st} as follows

$$p_m^{\text{st}}(r) = f_m^{\text{st}} \times \exp\left(-\frac{(r_m - r)^2}{2\sigma_b^2}\right) \left[\sum_k f_k^{\text{st}} \times \exp\left(-\frac{(r_k - r)^2}{2\sigma_b^2}\right) \right]^{-1} \quad (4)$$

At the same time, the equilibrium distribution p_m^{eq} is obtained using the approach of Hood and Kassal.¹⁹

$$p_m^{\text{eq}}(r) = \exp(-\beta E_m) \times \exp\left(-\frac{(r_m - r)^2}{2\sigma_b^2}\right) \left[\sum_k \exp(-\beta E_k) \times \exp\left(-\frac{(r_k - r)^2}{2\sigma_b^2}\right) \right]^{-1} \quad (5)$$

The KL divergence in eq 3 defines a measure of the difference of a given probability distribution—in our case p^{st} —from a reference probability distribution—here p^{eq} . Note that $D_{\text{KL}} \geq 0$ and that D_{KL} takes zero if and only if $p_m^{\text{st}} = p_m^{\text{eq}}$ for each individual CT state $|m\rangle$. If $p_m^{\text{st}} \neq p_m^{\text{eq}}$, the CT state $|m\rangle$ is not equilibrated, and consequently $F^{\text{st}} > F^{\text{eq}}$. The difference

between F^{st} and F^{eq} gives us a measure of how close to equilibrium charge separation occurs. This allows us to connect the kinetics of charge separation, given by p^{st} , with thermodynamic quantities of the charge separation process.

Rearranging eq 3 gives the well-known expression of the free energy

$$F^{\text{st}}(r) = \sum_m p_m^{\text{st}}(r) E_m + \beta^{-1} p_m^{\text{st}}(r) \ln p_m^{\text{st}}(r) = E^{\text{st}}(r) - TS^{\text{st}}(r) \quad (6)$$

Using p^{st} , we calculate the average energy $E^{\text{st}}(r)$, which electron–hole pairs pass during separation, and the Gibbs entropy $S^{\text{st}}(r)$, which accounts for the accessible states.

Note that, in comparison to previous studies,^{18,19,23} we replaced the counting of the states within a shell of thickness b by a Gaussian multiplier with width σ_b , accounting for the proximity of CT state $|m\rangle$ to r , to avoid discontinuities in the thermodynamic quantities. In the following, we take $\sigma_b = 0.5$ nm. A sensitivity analysis of σ_b is provided in Figure S4, Supporting Information. We consider the system in the linear regime, where occupations of all states are proportional to the intensity of the incident radiation; the thermodynamic quantities do not depend in this regime on the intensity of incident radiation. This can be straightforwardly proved using eqs 2, 4, 5, and 6.

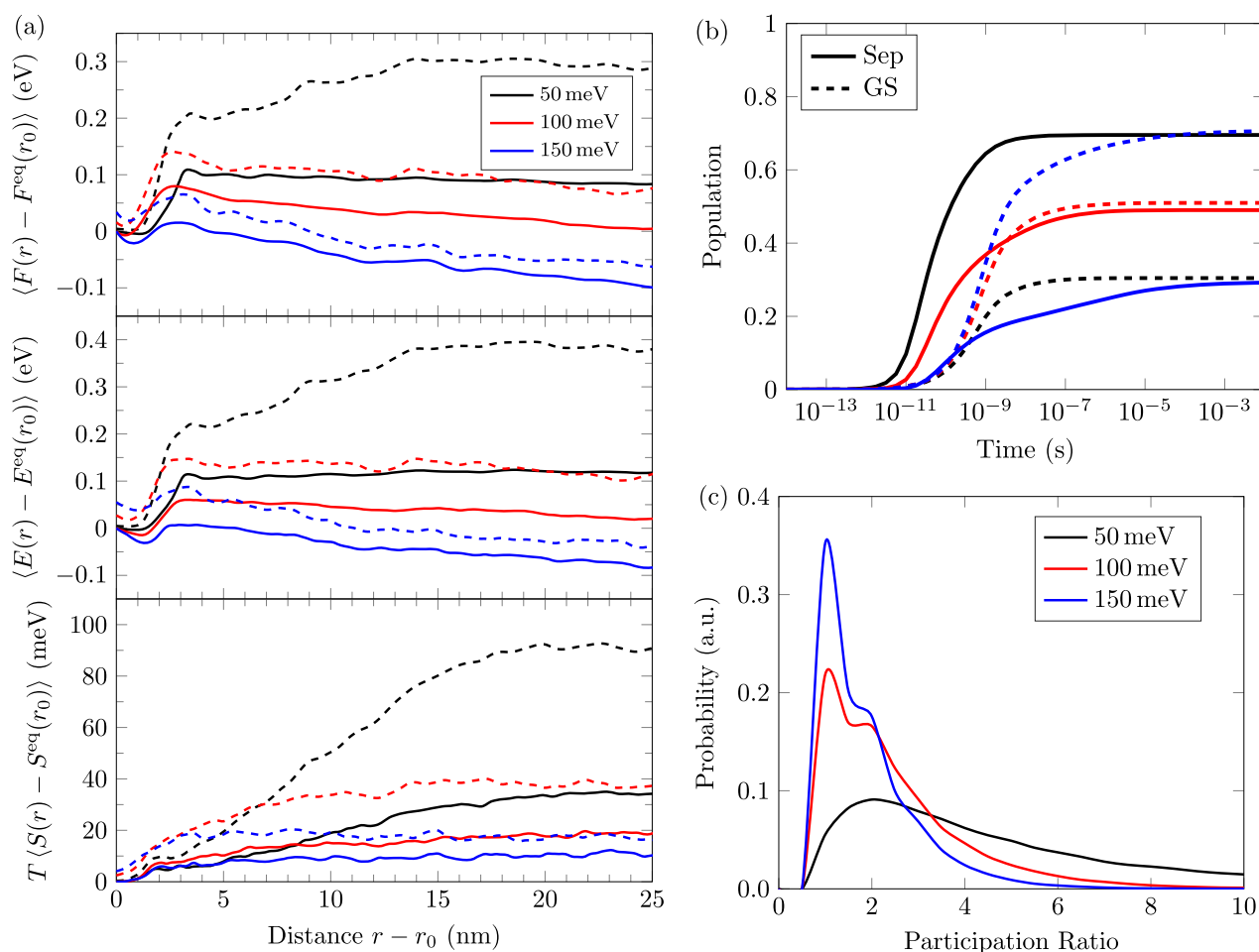


Figure 3. (a) Distance dependence of the free energy $F(r)$, energy $E(r)$, and entropic contribution $TS(r)$ for different disorder σ : 50 meV (black), 100 meV (red), and 150 meV (blue). The $\langle \cdot \rangle$ labels the ensemble average over 256 configurations. r_0 gives the smallest distance of CT states in each configuration. Solid and dashed curves present the equilibrium and stationary thermodynamic quantities, respectively. All curves are normalized to the equilibrium value (superscript eq) at the distance r_0 . (b) Time dependence of the separation yield (solid line) and the recombined states (dashed line). (c) Distribution of CT states as a function of their electron participation ratio. All curves in (a–c) show averages across 256 configurations.

First, we present the capabilities of the developed method by calculating the free energy for a particular network of exciton states at $\sigma = 50$ meV. Figure 2a shows the energy and the intrapair distance of each electron–hole pair (donor excitons, CT states, and contact states). The time evolution of fully separated and of recombined electron–hole pairs, see Figure 2b, shows a separation yield of 83.3%. The temporal evolution of the charge separation process and, in particular, hot and cold pathways were investigated in detail in ref 31. Here, our focus is on the thermodynamic quantities characterizing charge separation.

Figure 2c shows F^{st} and F^{eq} as a function of the intrapair distance relative to the smallest intrapair distance r_0 of all CT states. The free energy and the energy are smallest at close intrapair distances. The one-dimensional organic bilayer model only shows very few CT states at short distances of $r \leq 10$ nm, which are all strongly bound; see Figure 2a. The energy at equilibrium, E^{eq} , increases at short intrapair distances up to a value of 180 meV and only increases slightly up to 220 meV for distances beyond $r - r_0 \geq 10$ nm. F^{eq} shows a similar trend, while being up to 70 meV below E^{eq} . The difference is due to entropy contribution, which increases by 50–70 meV and shows minor fluctuations with the intrapair distance. At the

steady state, the thermodynamic quantities show significant deviations from equilibrium. F^{st} increases up to 450 meV at $r - r_0 \approx 20$ nm and remains roughly constant for larger distances. The energy of occupied states even reaches values of 600 meV. In addition, the Gibbs entropy S^{st} shows 2–3 times the value of S^{eq} . Especially, a large slope in S^{st} for intrapair distances below 20 nm can be observed, which was shown to be highly desirable for electron–hole pairs to overcome their mutual Coulomb attraction.¹⁸

By considering equilibrated electron–hole pairs, one imposes an instant thermalization of electron–hole pairs at each time and every position. This, however, is a strong assumption, as highlighted by the stationary distributions. Our model shows that the thermodynamic quantities are not well-captured by the equilibrium assumption, which further suggests that photogenerated electron–hole pairs propagate through nonequilibrated CT states of higher energy and reach contact states before an equilibration in the density of states (DOS) can occur. This explains the significantly higher value in Gibbs entropy, as more CT states are available at higher energies with respect to tail states, which consequently increases the chance for charge separation. In realistic three-

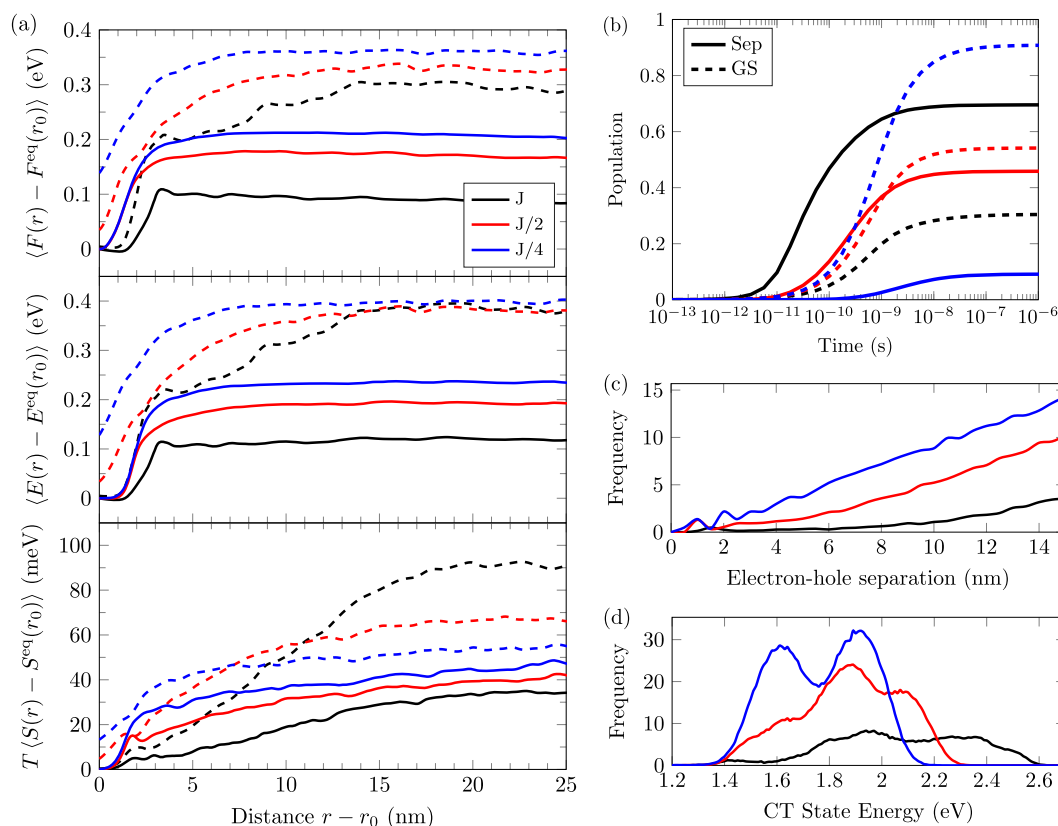


Figure 4. (a) Distance dependence of the free energy $F(r)$, energy $E(r)$, and entropy contribution $TS(r)$ for different coupling integrals: J (black), $J/2$ (red), and $J/4$ (blue). The $\langle \cdot \rangle$ labels the ensemble average over 256 configurations. r_0 gives the smallest distance of CT states in each configuration. Solid and dashed curves present the equilibrium and stationary quantities, respectively. All curves are normalized to the equilibrium value (superscript eq) at the distance r_0 . (b) Time dependence of the separation yield (solid line) and the recombined states (dashed line). (c) Frequency of electron–hole separation and (d) of state energy of CT states with electron participation ratio $\text{PR} \leq 3$ mimicking localized CT states. All curves in (a–d) show averages across 256 configurations.

dimensional (3D) systems, the entropy may reach even higher values and may dominate the energy contribution.^{18,21,22}

We now study the role of the energetic disorder σ on the thermodynamic quantities for $\sigma \in \{50 \text{ meV}, 100 \text{ meV}, 150 \text{ meV}\}$. For each σ , we take an ensemble average over 256 configurations to gain a reliable statistics. Figure 3a shows the thermodynamic quantities in the equilibrium and in the steady-state as a function of the intrapair distance $r - r_0$. First, we analyze the equilibrium quantities. F^{eq} decreases strongly with increased σ . For $\sigma \geq 100 \text{ meV}$, F^{eq} even decreases with increased intrapair distance r as reported by Hood and Kassal.¹⁹ The decrease in free energy with σ is mainly caused by a decrease in the average energy of populated states during charge separation, showing a similar distance dependence as the free energy. The entropy contribution shows significant differences for different σ . At $\sigma = 50 \text{ meV}$, TS^{eq} increases monotonously with intrapair distance and reaches 35 meV. For larger σ , TS^{eq} is significantly reduced and reaches values of only 20 meV (10 meV) at $\sigma = 100 \text{ meV}$ (150 meV). At a high disorder, the entropy contribution remains roughly constant for $r - r_0 \geq 5 \text{ nm}$.

For a low σ of 50 meV, significant differences between F^{eq} and F^{st} are observable. F^{st} , computed from realistic populations of CT states, increases up to 300 meV at $r - r_0 = 15 \text{ nm}$, while F^{eq} remains roughly constant for $r - r_0 \geq 3 \text{ nm}$. The entropy contribution shows a large increase up to 90 meV, which explains the difference between the free energy and energy. For $\sigma \geq 100 \text{ meV}$, E^{st} differs by less than 40 meV from F^{st} due to a

low entropy contribution. At $\sigma = 150 \text{ meV}$, the entropy stays constant ($\sim 20 \text{ meV}$) within the considered region. Entropy contributions that do not change with distance have been observed for 1D systems without disorder,¹⁸ but also for two-dimensional (2D) systems with large σ values.¹⁹

Figure 3b visualizes the time dependence of fully separated and of recombined states for different σ . With increased σ , the separation yield decreases from 69.5% ($\sigma = 50 \text{ meV}$) to 49.0% ($\sigma = 100 \text{ meV}$) and 29.3% ($\sigma = 150 \text{ meV}$). In addition, the time scale on which charge separation takes place increases by several orders of magnitude. At high σ , electron–hole pairs thermalize within the DOS and populate tail states. Equilibrated electron–hole pairs can only separate by propagation through low-energy states. The density of tail states, however, does not increase significantly with intrapair distance. A large σ value helps to initially separate charge carriers in space, while a low entropy slows further charge transport. The lack of available states leads to high recombination losses and can promote nongeminate recombination—which is neglected in this study—as a further limitation of charge separation.

To understand the efficient separation despite the large free energy barrier at a low σ , we analyze the delocalization of the CT states in terms of the participation ratio (PR, defined in eq S22, Supporting Information), which is a measure of the number of sites over which the electron (the hole) of the CT state delocalizes. Figure 3c visualizes the PR distribution for different σ . At $\sigma = 50 \text{ meV}$, a large spread in the PR with a high

amount of delocalized CT states is observed. With a rising σ , the amount of strongly localized CT states increases significantly, and delocalized CT states of $PR \geq 5$ vanish. All CT states with a low state energy show low PR values (see Figure S6, Supporting Information), that is, all energetically strongly bound CT states are strongly localized. The main difference between the configurations with different σ is that a large tail in the CT manifold of $\sim 200\text{--}300$ meV below the tail states at $\sigma = 50$ meV is observable (see Figure S7, Supporting Information). Several studies proposed that excitons can transform to delocalized CT states in the presence of a resonant coupling between donor excitons and delocalized CT states,^{40,41} which can be assisted in the presence of substantial vibronic couplings.^{42,43}

At $\sigma = 50$ meV, strongly bound electron–hole pairs with $r \leq 3$ nm face a large barrier in free energy (~ 300 meV), which makes it thermodynamically unfavorable to reach larger r values, while electron–hole pairs at distances larger than 3 nm see a strong reduction in the free energy barrier such that they need to overcome less than 100 meV in free energy to fully separate (see Figure 3a). Suppose the system starts in CT state with the smallest distance r_0 , that is, in a strongly bound CT state. In that case, all the thermodynamic quantities during charge separation are well-described by the equilibrium populations; see Figure S2, Supporting Information. The chance that donor excitons transform to CT states of a large PR ratio, however, is high due to a large amount of delocalized CT states and the energetic resonance of XD and CT states (see Figure S7, Supporting Information). Thus, considering the transformation of donor excitons into CT states with a significant intrapair separation is crucial to understand the efficiency of the charge separation process.

One of the main observations from Figure 3 is that charge separation within OSCs with a high energetic disorder occurs close to equilibrium. To achieve efficient OSCs, however, typically low σ values are required.^{44,45} High σ hinder the charge transport⁴⁶ and strongly reduce the attainable open-circuit voltage.^{47,48} For high σ , electron–hole pairs lose energy while moving toward the contact states, matching previous reports.⁴⁹ In contrast, the rather delocalized electron–hole pairs at $\sigma = 50$ meV do not equilibrate and lose less energy before reaching the contact states. Our previous analysis (ref 31) showed that the separation goes via a cold pathway. The significant deviation in free energy for a low disorder, however, tells us that the separation of cold charge carriers does not happen in equilibrium and that charge pairs sample a relatively wide energy window before they eventually separate. Thus, we emphasize that charge separation in efficient OSCs occurs out of equilibrium. Thermodynamically, charge separation is favored in systems of a large energetic disorder. The kinetics of the charge carriers, however, is too slow to compete with charge recombination. An efficient separation of delocalized CT states in systems of low energetic disorder seems thermodynamically not favored, while their kinetics show a sufficient separation.

Now, we study the role of delocalization on the free energy; see Figure 4a. We increase charge localization by scaling all transfer integrals $J_{A/D,0/1}^{E/V}$ (see Figure 1a) with 1/2 and 1/4. According to both descriptions, the free energy increases with localization. Again, the energy follows the free energy closely. For $J/2$ and $J/4$, reduced separation yields of 45.9% and 9.1%, respectively, are observed (see Figure 4b). This agrees with the increase in the free energy and energy barrier with a larger

localization. Interestingly, F^{st} deviates strongly from equilibrium for $J/2$ and $J/4$. At large distances, E^{st} approaches the same value of ~ 380 meV for different localization. In contrast, significant differences in E^{st} are observed for short distances; strongly localized electron–hole pairs occupy states with an energy of 130 meV (40 meV) above the equilibrium for $J/4$ ($J/2$).

The occupation of electron–hole states at the interface determines the measured emission spectra by electro- and photoluminescence studies of donor–acceptor blends, which are frequently related to the open-circuit voltage in OSCs.^{50,51} Our results show that, especially for a strong localization, nonequilibrium state occupations of electron–hole pairs at the interface need to be considered. For a large localization, the probability of donor excitons transforming to a CT state with a small intrapair distance is higher because the number of such CT states strongly increases (see Figure 4c). The state population at the interface, following exciton dissociation to a CT state, is strongly impacted by the competition between thermalization dynamics and recombination. The significant deviation from equilibrium indicates that electron–hole pairs with small intrapair distances do not fully thermalize before recombination occurs, being in line with recent electroluminescence²⁴ and photoluminescence studies.²⁵ Strictly assuming equilibrated states may lead to a misinterpretation of experimental photo/electroluminescence data.

With an increased localization, the Gibbs entropy contribution deviates at short distances by up to 20 meV from equilibrium. Weak coupling integrals result in many CT states with small intrapair distances. Figure 4c,d visualizes the distribution of localized CT states, defined by the electron participation ratio of $PR \leq 3$, in electron–hole separation and in CT state energy, respectively. For a large localization, the amount of localized CT states strongly increases for all intrapair distances. Especially at the interface, the amount of localized CT states is significantly higher than for the reference configuration. The distribution in energy (Figure 4d and Figure S10, Supporting Information, for individual states) of localized CT states shows a large spread, which can explain the deviation of F^{st} from equilibrium predictions. S^{st} differs from the equilibrium values as electron–hole pairs tend to recombine before thermalization is completed. Interestingly, S^{st} at short distances is roughly equal for different localizations (see Figure S3, Supporting Information). At a larger distance, the entropy increases more strongly with larger delocalizations. For $J/4$, the S^{st} value remains nearly constant, indicating that charge separation gets suppressed with an increased localization.

In contrast to previous theoretical studies,²³ our results emphasize that the free energy decreases with delocalization. In ref 23 the free energy was analyzed for electron–hole distances of less than 4 nm for a large energetic disorder of $\sigma \geq 100$ meV. An increase in coupling reduces the amount of electron–hole pairs with a small intrapair distance (cf. Figure 5 of ref 23), while only a few deep trap states remain. This may explain the predicted increase in free energy. However, efficient OSCs are characterized by long-range exciton separation, which can directly populate rather delocalized CT states of a large electron–hole distance and consequently reduce the relevance of strongly bound CT states, which comes closer to our model (see, e.g., Figure 4c).^{2,4,7,12} Gluchowski et al.²³ further hypothesize that a potential improvement of the delocalization for charge separation may occur through nonequilibrium

kinetic effects, which are particularly included within our model. This indicates that equilibrium thermodynamics results may provide potentially misleading conclusions and further underlines the relevance of our nonequilibrium thermodynamics analysis.

In conclusion, we have presented novel physical insights into the nonequilibrium thermodynamics of charge separation in OSCs by combining the phonon-assisted dynamics of electron–hole pairs within a 1D model Hamiltonian of an organic bilayer with the free energy based on the concept of stochastic thermodynamics. We derive thermodynamic quantities, in particular, the free energy, average energy, and entropy contributions of charge separation based on realistic steady-state populations for different energetic disorders and different localizations. In contrast to previous studies, the presented methodology accounts for the finite lifetime of CT states to provide more realistic thermodynamic quantities. Our analysis reveals significant deviations from equilibrium in the free energy and Gibbs entropy for delocalized electron–hole pairs at a small energetic disorder, representing efficient OSCs. While previous studies showed that charge separation occurs via cold pathways, our nonequilibrium thermodynamic analysis reveals that the separation of cold charge carriers in efficient OSCs proceeds out of the equilibrium. In systems of large energetic disorder, steady-state occupations of electron–hole pair states can be well-described as equilibrated. Furthermore, localized electron–hole pairs with small intrapair distances exhibit a significant nonequilibrium distribution, explaining previous observations from photoluminescence measurements. Our results emphasize that both a large Gibbs entropy and delocalized CT states at the interface can support efficient separation, while a decrease with distance in the free energy does not necessarily correlate with an enhanced charge separation. Overall, we believe that this work provides both an important contribution to understanding the physics of charge separation in organic semiconductors and a novel theoretical approach allowing access to nonequilibrium thermodynamic properties.

■ ASSOCIATED CONTENT

Supporting Information

The Supporting Information is available free of charge at <https://pubs.acs.org/doi/10.1021/acs.jpcllett.1c01817>.

Description of the model Hamiltonian and of the transition rate derivation of the organic bilayer; model parameters used in computations; numerical solution procedure of the Master equation; sensitivity analysis on hyperparameter σ_b ; analysis on state energies, electron–hole pair distances, and state delocalization (PDF)

■ AUTHOR INFORMATION

Corresponding Author

Alessio Gagliardi – Department of Electrical and Computer Engineering, Technical University of Munich, 80333 Munich, Germany; orcid.org/0000-0002-3322-2190;
Email: alessio.gagliardi@tum.de

Authors

Waldemar Kaiser – Department of Electrical and Computer Engineering, Technical University of Munich, 80333 Munich, Germany; orcid.org/0000-0001-9069-690X

Veljko Janković – Institute of Physics Belgrade, University of Belgrade, 11080 Belgrade, Serbia; orcid.org/0000-0002-0297-2167

Enad Vukmirović – Institute of Physics Belgrade, University of Belgrade, 11080 Belgrade, Serbia; orcid.org/0000-0002-4101-1713

Complete contact information is available at:
<https://pubs.acs.org/10.1021/acs.jpcllett.1c01817>

Notes

The authors declare no competing financial interest.

■ ACKNOWLEDGMENTS

W.K. and A.G. acknowledge the TUM International Graduate School of Science and Engineering and Germany's excellence cluster *e-conversion* by the German Research Foundation (Deutsche Forschungsgemeinschaft) for funding. N.V. and V.J. acknowledge funding by the Institute of Physics Belgrade, through the grant by the Ministry of Education, Science, and Technological Development of the Republic of Serbia. Numerical computations were partially performed on the PARADOX-IV supercomputing facility at the Scientific Computing Laboratory, National Center of Excellence for the Study of Complex Systems, Institute of Physics Belgrade.

■ REFERENCES

- (1) Bäessler, H.; Köhler, A. Hot or cold: how do charge transfer states at the donor–acceptor interface of an organic solar cell dissociate? *Phys. Chem. Chem. Phys.* **2015**, *17*, 28451–28462.
- (2) Grancini, G.; Maiuri, M.; Fazzi, D.; Petrozza, A.; Egelhaaf, H.; Brida, D.; Cerullo, G.; Lanzani, G. Hot exciton dissociation in polymer solar cells. *Nat. Mater.* **2013**, *12*, 29.
- (3) Jones, M. L.; Dyer, R.; Clarke, N.; Groves, C. Are hot charge transfer states the primary cause of efficient free-charge generation in polymer: fullerene organic photovoltaic devices? A kinetic Monte Carlo study. *Phys. Chem. Chem. Phys.* **2014**, *16*, 20310–20320.
- (4) Bakulin, A. A.; Rao, A.; Pavelyev, V. G.; van Loosdrecht, P. H.; Pshenichnikov, M. S.; Niedzialek, D.; Cornil, J.; Beljonne, D.; Friend, R. H. The role of driving energy and delocalized states for charge separation in organic semiconductors. *Science* **2012**, *335*, 1340–1344.
- (5) Vandewal, K.; et al. Efficient charge generation by relaxed charge-transfer states at organic interfaces. *Nat. Mater.* **2014**, *13*, 63–68.
- (6) Armin, A.; Kassel, I.; Shaw, P. E.; Hambsch, M.; Stolterfoht, M.; Lyons, D. M.; Li, J.; Shi, Z.; Burn, P. L.; Meredith, P. Spectral Dependence of the Internal Quantum Efficiency of Organic Solar Cells: Effect of Charge Generation Pathways. *J. Am. Chem. Soc.* **2014**, *136*, 11465–11472.
- (7) Kahle, F.-J.; Saller, C.; Olthof, S.; Li, C.; Lebert, J.; Weiß, S.; Herzig, E. M.; Hüttner, S.; Meerholz, K.; Strohriegel, P.; Köhler, A. Does Electron Delocalization Influence Charge Separation at Donor–Acceptor Interfaces in Organic Photovoltaic Cells? *J. Phys. Chem. C* **2018**, *122*, 21792–21802.
- (8) Deibel, C.; Strobel, T.; Dyakonov, V. Origin of the efficient polaron-pair dissociation in polymer–fullerene blends. *Phys. Rev. Lett.* **2009**, *103*, 036402.
- (9) Tscheuschner, S.; Bäessler, H.; Huber, K.; Köhler, A. A Combined Theoretical and Experimental Study of Dissociation of Charge Transfer States at the Donor–Acceptor Interface of Organic Solar Cells. *J. Phys. Chem. B* **2015**, *119*, 10359–10371.
- (10) Janković, V.; Vukmirović, N. Combination of Charge Delocalization and Disorder Enables Efficient Charge Separation at Photoexcited Organic Bilayers. *J. Phys. Chem. C* **2018**, *122*, 10343–10359.

- (11) Athanasopoulos, S.; Bäessler, H.; Köhler, A. Disorder vs Delocalization: Which Is More Advantageous for High-Efficiency Organic Solar Cells? *J. Phys. Chem. Lett.* **2019**, *10*, 7107–7112.
- (12) Felekidis, N.; Melianas, A.; Kemerink, M. The Role of Delocalization and Excess Energy in the Quantum Efficiency of Organic Solar Cells and the Validity of Optical Reciprocity Relations. *J. Phys. Chem. Lett.* **2020**, *11*, 3563–3570.
- (13) Athanasopoulos, S.; Schauer, F.; Nádaždy, V.; Weiß, M.; Kahle, F.-J.; Scherf, U.; Bäessler, H.; Köhler, A. What is the binding energy of a charge transfer state in an organic solar cell? *Adv. Energy Mater.* **2019**, *9*, 1900814.
- (14) Shi, L.; Lee, C. K.; Willard, A. P. The Enhancement of Interfacial Exciton Dissociation by Energetic Disorder Is a Non-equilibrium Effect. *ACS Cent. Sci.* **2017**, *3*, 1262–1270.
- (15) Köhler, A.; Bäessler, H. *Electronic processes in organic semiconductors: An introduction*; John Wiley & Sons, 2015.
- (16) Kaiser, W.; Albes, T.; Gagliardi, A. Charge carrier mobility of disordered organic semiconductors with correlated energetic and spatial disorder. *Phys. Chem. Chem. Phys.* **2018**, *20*, 8897–8908.
- (17) Albes, T.; Gagliardi, A. Influence of permittivity and energetic disorder on the spatial charge carrier distribution and recombination in organic bulk-heterojunctions. *Phys. Chem. Chem. Phys.* **2017**, *19*, 20974–20983.
- (18) Gregg, B. A. Entropy of charge separation in organic photovoltaic cells: the benefit of higher dimensionality. *J. Phys. Chem. Lett.* **2011**, *2*, 3013–3015.
- (19) Hood, S. N.; Kassal, I. Entropy and disorder enable charge separation in organic solar cells. *J. Phys. Chem. Lett.* **2016**, *7*, 4495–4500.
- (20) Gao, F.; Tress, W.; Wang, J.; Inganäs, O. Temperature Dependence of Charge Carrier Generation in Organic Photovoltaics. *Phys. Rev. Lett.* **2015**, *114*, 128701.
- (21) Clarke, T. M.; Durrant, J. R. Charge Photogeneration in Organic Solar Cells. *Chem. Rev.* **2010**, *110*, 6736–6767.
- (22) Nayak, P. K.; Narasimhan, K. L.; Cahen, D. Separating Charges at Organic Interfaces: Effects of Disorder, Hot States, and Electric Field. *J. Phys. Chem. Lett.* **2013**, *4*, 1707–1717.
- (23) Gluchowski, A.; Gray, K. L.; Hood, S. N.; Kassal, I. Increases in the Charge Separation Barrier in Organic Solar Cells Due to Delocalization. *J. Phys. Chem. Lett.* **2018**, *9*, 1359–1364.
- (24) Melianas, A.; Felekidis, N.; Puttison, Y.; Meskers, S. C.; Inganäs, O.; Chen, W. M.; Kemerink, M. Nonequilibrium site distribution governs charge-transfer electroluminescence at disordered organic heterointerfaces. *Proc. Natl. Acad. Sci. U. S. A.* **2019**, *116*, 23416–23425.
- (25) Brigeman, A.; Fusella, M.; Rand, B. P.; Giebink, N. Nonthermal site occupation at the donor-acceptor interface of organic solar cells. *Phys. Rev. Appl.* **2018**, *10*, 034034.
- (26) Giazitzidis, P.; Argyrakis, P.; Bisquert, J.; Vukobratović, V. S. Charge separation in organic photovoltaic cells. *Org. Electron.* **2014**, *15*, 1043–1049.
- (27) Lankevich, V.; Bittner, E. R. Relating free energy and open-circuit voltage to disorder in organic photovoltaic systems. *J. Chem. Phys.* **2018**, *149*, 244123.
- (28) Kawashima, E.; Fujii, M.; Yamashita, K. Entropy promotes charge separation in bulk heterojunction organic photovoltaics. *J. Photochem. Photobiol., A* **2019**, *382*, 111875.
- (29) Van den Broeck, C.; Esposito, M. Ensemble and trajectory thermodynamics: A brief introduction. *Phys. A* **2015**, *418*, 6–16.
- (30) Seifert, U. Stochastic thermodynamics, fluctuation theorems and molecular machines. *Rep. Prog. Phys.* **2012**, *75*, 126001.
- (31) Janković, V.; Vukmirović, N. Energy–Temporal Pathways of Free-Charge Formation at Organic Bilayers: Competition of Delocalization, Disorder, and Polaronic Effects. *J. Phys. Chem. C* **2020**, *124*, 4378–4392.
- (32) Rao, R.; Esposito, M. Nonequilibrium thermodynamics of chemical reaction networks: wisdom from stochastic thermodynamics. *Phys. Rev. X* **2016**, *6*, 041064.
- (33) Leonard, T.; Lander, B.; Seifert, U.; Speck, T. Stochastic thermodynamics of fluctuating density fields: non-equilibrium free energy differences under coarse-graining. *J. Chem. Phys.* **2013**, *139*, 204109.
- (34) Esposito, M.; Lindenberg, K.; Van den Broeck, C. Thermoelectric efficiency at maximum power in a quantum dot. *Europhys. Lett.* **2009**, *85*, 60010.
- (35) Esposito, M.; Kawai, R.; Lindenberg, K.; Van den Broeck, C. Finite-time thermodynamics for a single-level quantum dot. *Europhys. Lett.* **2010**, *89*, 20003.
- (36) Ajisaka, S.; Žunkovič, B.; Dubi, Y. The molecular photo-cell: Quantum transport and energy conversion at strong non-equilibrium. *Sci. Rep.* **2015**, *5*, 1–6.
- (37) Nemati Aram, T.; Anghel-Vasilescu, P.; Asgari, A.; Ernzerhof, M.; Mayou, D. Modeling of molecular photocells: Application to two-level photovoltaic system with electron-hole interaction. *J. Chem. Phys.* **2016**, *145*, 124116.
- (38) Aram, T. N.; Asgari, A.; Ernzerhof, M.; Quémérais, P.; Mayou, D. Quantum modeling of two-level photovoltaic systems. *EPJ Photovoltaics* **2017**, *8*, 85503.
- (39) Qian, H. Relative entropy: Free energy associated with equilibrium fluctuations and nonequilibrium deviations. *Phys. Rev. E: Stat. Phys., Plasmas, Fluids, Relat. Interdiscip. Top.* **2001**, *63*, 042103.
- (40) Savoie, B. M.; Rao, A.; Bakulin, A. A.; Gelinas, S.; Movaghar, B.; Friend, R. H.; Marks, T. J.; Ratner, M. A. Unequal partnership: Asymmetric roles of polymeric donor and fullerene acceptor in generating free charge. *J. Am. Chem. Soc.* **2014**, *136*, 2876–2884.
- (41) Caruso, D.; Troisi, A. Long-range exciton dissociation in organic solar cells. *Proc. Natl. Acad. Sci. U. S. A.* **2012**, *109*, 13498–13502.
- (42) Tamura, H.; Burghardt, I. Ultrafast charge separation in organic photovoltaics enhanced by charge delocalization and vibronically hot exciton dissociation. *J. Am. Chem. Soc.* **2013**, *135*, 16364–16367.
- (43) Yao, Y.; Xie, X.; Ma, H. Ultrafast long-range charge separation in organic photovoltaics: promotion by off-diagonal vibronic couplings and entropy increase. *J. Phys. Chem. Lett.* **2016**, *7*, 4830–4835.
- (44) Wu, J.; Lee, J.; Chin, Y.-C.; Yao, H.; Cha, H.; Luke, J.; Hou, J.; Kim, J.-S.; Durrant, J. R. Exceptionally low charge trapping enables highly efficient organic bulk heterojunction solar cells. *Energy Environ. Sci.* **2020**, *13*, 2422–2430.
- (45) Liu, S.; Yuan, J.; Deng, W.; Luo, M.; Xie, Y.; Liang, Q.; Zou, Y.; He, Z.; Wu, H.; Cao, Y. High-efficiency organic solar cells with low non-radiative recombination loss and low energetic disorder. *Nat. Photonics* **2020**, *14*, 300–305.
- (46) Pasveer, W.; Cottaar, J.; Tanase, C.; Coehoorn, R.; Bobbert, P.; Blom, P.; De Leeuw, D.; Michels, M. Unified description of charge-carrier mobilities in disordered semiconducting polymers. *Phys. Rev. Lett.* **2005**, *94*, 206601.
- (47) Blakesley, J. C.; Neher, D. Relationship between energetic disorder and open-circuit voltage in bulk heterojunction organic solar cells. *Phys. Rev. B: Condens. Matter Mater. Phys.* **2011**, *84*, 075210.
- (48) Kaiser, W.; Gagliardi, A. Kinetic Monte Carlo Study of the Role of the Energetic Disorder on the Open-Circuit Voltage in Polymer/Fullerene Solar Cells. *J. Phys. Chem. Lett.* **2019**, *10*, 6097–6104.
- (49) Melianas, A.; Etzold, F.; Savenije, T. J.; Laquai, F.; Inganäs, O.; Kemerink, M. Photo-generated carriers lose energy during extraction from polymer-fullerene solar cells. *Nat. Commun.* **2015**, *6*, 1–8.
- (50) Vandewal, K.; Tvingstedt, K.; Gadisa, A.; Inganäs, O.; Manca, J. V. Relating the open-circuit voltage to interface molecular properties of donor: acceptor bulk heterojunction solar cells. *Phys. Rev. B: Condens. Matter Mater. Phys.* **2010**, *81*, 125204.
- (51) Rau, U. Reciprocity relation between photovoltaic quantum efficiency and electroluminescent emission of solar cells. *Phys. Rev. B: Condens. Matter Mater. Phys.* **2007**, *76*, 085303.

Holstein polaron transport from numerically “exact” real-time quantum dynamics simulations

Cite as: J. Chem. Phys. 159, 094113 (2023); doi: 10.1063/5.0165532

Submitted: 29 June 2023 • Accepted: 14 August 2023 •

Published Online: 6 September 2023



View Online



Export Citation



CrossMark

Veljko Janković^{a)}

AFFILIATIONS

Institute of Physics Belgrade, University of Belgrade, Pregrevica 118, 11080 Belgrade, Serbia

Note: This paper is part of the 2023 JCP Emerging Investigators Special Collection.

^{a)} Author to whom correspondence should be addressed: veljko.jankovic@ipb.ac.rs

ABSTRACT

Numerically “exact” methods addressing the dynamics of coupled electron–phonon systems have been intensively developed. Nevertheless, the corresponding results for the electron mobility μ_{dc} are scarce, even for the one-dimensional (1d) Holstein model. Building on our recent progress on single-particle properties, here we develop the momentum-space hierarchical equations of motion (HEOM) method to evaluate real-time two-particle correlation functions of the 1d Holstein model at a finite temperature. We compute numerically “exact” dynamics of the current–current correlation function up to real times sufficiently long to capture the electron’s diffusive motion and provide reliable results for μ_{dc} in a wide range of model parameters. In contrast to the smooth ballistic-to-diffusive crossover in the weak-coupling regime, we observe a temporally limited slow-down of the electron on intermediate time scales already in the intermediate-coupling regime, which translates to a finite-frequency peak in the optical response. Our momentum-space formulation lowers the numerical effort with respect to existing HEOM-method implementations, while we remove the numerical instabilities inherent to the undamped-mode HEOM by devising an appropriate hierarchy closing scheme. Still, our HEOM remains unstable at too low temperatures, for too strong electron–phonon coupling, and for too fast phonons.

Published under an exclusive license by AIP Publishing. <https://doi.org/10.1063/5.0165532>

I. INTRODUCTION

The electron–phonon interaction governs the transport of charge (and energy) in systems ranging from semiconductors,^{1–6} organic molecular crystals, and polymers^{7–9} to molecular aggregates relevant for photosynthesis.^{10–14} The simplest model of such diverse systems is the Holstein model,¹⁵ in which an electron is locally and linearly coupled to phonons. Well-established transport theories are formulated as perturbative expansions from either the limit of vanishing coupling (Boltzmann-like^{4,5,16} or Redfield-like^{13,14,17} theories) or vanishing electronic bandwidth (small-polaron/Lang–Firsov,¹⁸ Marcus,^{13,14,19} or Förster^{13,14,20} theories). However, in many instances, the energy scales representative of electron motion, phonons, electron–phonon interaction, and thermal fluctuations are all comparable to one another.^{1,21–23} This circumstance calls for the development of methods beyond standard transport theories.

Such methods are typically formulated under physically motivated approximations. Examples include the cumulant expansion,^{24–28} dynamical mean-field theory,^{29–33} polaron

transformation-based approaches,^{34–43} momentum-average approximation,^{44–46} and kinetic Monte Carlo approaches.^{47,48} The approximate methods are generally computationally efficient and can thus be combined with electronic-structure methods to provide first-principles results on systems large enough that a direct comparison with experimental results is sensible.^{49–55} While the agreement between numerical and experimental results justifies the approximations introduced, it does not fully reveal their domain of validity. This can be unveiled by comparison to results produced by numerically “exact” methods, which do not lean on any approximation beyond those in the Hamiltonian. Since they are computationally intensive, numerically “exact” methods are usually applied to model Hamiltonians only.

The numerically “exact” approaches used to study interacting electron–phonon models may be roughly divided into the following: (i) quantum Monte Carlo (QMC) methods,^{56–63} (ii) wavefunction-based methods considering the electron and phonons as a closed system, such as exact diagonalization (ED)-based techniques,^{64–69} the density-matrix renormalization group (DMRG),^{70–77} thermo-field dynamics,^{78–80} and the hierarchy of Davydov’s

Ansätze,^{81–85} (iii) methods leaning on the theory of open quantum systems, such as the hierarchical equations of motion (HEOM),^{86–89} its generalizations,^{90,91} and hybridizations^{92,93} with the stochastic Schrödinger equation.^{94,95}

Many of the above-mentioned methods deliver practically exact results on the ground-state or equilibrium finite-temperature properties of the Holstein model.^{58,65,70,76} Some of them have recently been used to examine the model's single-particle properties (the electronic spectral function or linear absorption spectra),^{67–69,71,73,76,77,92,95,96} However, much more demanding numerically “exact” evaluations of two-particle correlation functions at finite temperatures, such as the ac and dc electrical conductivity, have started only recently.^{27,61–63,74,75,77,93,97–99} Each class of the above-mentioned numerically “exact” methods encounters certain issues in computations of two-particle quantities. (i) QMC methods are usually formulated directly in the thermodynamic limit but require numerical analytical continuation to reconstruct real-frequency spectra. A combination of statistical errors and uncertainties in the analytical continuation may lead to final results whose errors are comparable to the results themselves. Real-time QMC simulations witness a progressive development of the infamous sign (or phase) problem, which limits their applicability to relatively short-time dynamics. (ii) ED-based methods are applied to small clusters and typically require artificial broadening parameters to construct real-frequency spectra. The DMRG equations can be propagated only for relatively short times,^{76,77} which may not be long enough to reliably estimate the dc mobility.⁷⁷ (iii) The HEOM method treats small clusters but can, in principle, capture the full decay of correlation functions.^{97–100} Being based on a formally exact expression for the electronic reduced density matrix (RDM), the HEOM method is undoubtedly numerically “exact.” However, when employed on a finite system and truncated at a finite depth, the HEOM with undamped phonon modes suffers from numerical instabilities,¹⁰¹ which practically limit the maximum propagation time¹⁰² and whose overcoming requires further algorithmic developments.^{101,103}

In this study, we provide numerically “exact” results for the electron mobility within the 1d Holstein model. In contrast to the best currently available results, which are obtained by performing the numerical analytical continuation of imaginary-axis QMC data⁶¹ (possibly combined with real-time QMC data on rather short time scales⁶³), our results entirely follow from real-time computations. We extend the momentum-space HEOM we developed in Ref. 96 to follow the time evolution of finite-temperature two-particle correlation functions up to very long (practically infinite) real times. In addition, our momentum-space HEOM also enables us to obtain highly accurate results for imaginary-time correlation functions, which are the central quantities in QMC simulations. Our imaginary-axis results help us establish the minimum chain length and hierarchy depth needed to obtain results representative of the thermodynamic limit. The high quality of our real-time results is ensured by checking that different sum rules (e.g., the optical sum rule—OSR) are satisfied with high accuracy. We lower the numerical effort with respect to existing HEOM implementations by exploiting the translational symmetry, which reduces the number of independent dynamical variables in the formalism, and noting that the totally symmetric phonon mode does not contribute to the time evolution of correlation functions. We avoid numerical

instabilities in a wide range of parameter spaces by devising a specific closing of the hierarchy. Still, the numerical instabilities inherent to the undamped-mode HEOM prevent us from obtaining results at low temperatures, for strong electron–phonon coupling, and when electronic dynamics is much slower than phonon dynamics (the so-called antiadiabatic regime).

The paper is organized as follows. Section II specifies the model and introduces our momentum-space HEOM method for the current–current correlation function. Technical details are presented in Appendixes A–D. In Sec. III, we provide a number of numerical examples testing critical points of our methodology and present our main results concerning temperature-dependent dc mobility. Section IV is devoted to a summary and prospects for future work.

II. THEORETICAL FRAMEWORK

A. Model and definitions

We consider the Holstein model on the 1d lattice comprising N sites with periodic boundary conditions. In the momentum space, its Hamiltonian reads as

$$H = H_e + H_{ph} + H_{e-ph} \\ = \sum_k \varepsilon_k |k\rangle\langle k| + \sum_q \omega_q b_q^\dagger b_q + \sum_q V_q B_q. \quad (1)$$

The electronic and phononic wave numbers k and q may assume any of the N allowed values in the first Brillouin zone $-\pi < k, q \leq \pi$. The Hamiltonian H_e describes an electron in a free-electron band whose dispersion $\varepsilon_k = -2J \cos(k)$ originates from the nearest-neighbor electronic hopping of amplitude J . The Hamiltonian H_{ph} describes an optical-phonon branch with dispersion ω_q such that $\omega_{q=0} \neq 0$. The interaction term H_{e-ph} is characterized by its strength g and contains the purely electronic operator $V_q = \sum_k |k+q\rangle\langle k|$, which increases the electronic momentum by q , and the purely phononic operator $B_q = \frac{g}{\sqrt{N}}(b_q + b_{-q}^\dagger)$, which decreases the phononic momentum by q . In the following, we set the lattice constant a_l and the elementary charge e_0 , and the physical constants \hbar and k_B to unity.

We focus on the dynamics of the current–current correlation function

$$C_{jj}(t) = \frac{1}{Z} \text{Tr} \{ j(t) j(0) e^{-\beta H} \}, \quad (2)$$

where the current operator reads as

$$j = -2J \sum_k \sin(k) |k\rangle\langle k|, \quad (3)$$

where $j(t) = e^{iHt} j e^{-iHt}$, while $Z = \text{Tr} e^{-\beta H}$ is the partition sum at temperature $T = \beta^{-1}$. Its Fourier transform $C_{jj}(\omega) = \int_{-\infty}^{+\infty} dt e^{i\omega t} C_{jj}(t)$ [with $C_{jj}(-t) = C_{jj}(t)^*$] determines the frequency-dependent (or dynamical) mobility,

$$\text{Re} \mu_{ac}(\omega) = \frac{1 - e^{-\beta\omega}}{2\omega} C_{jj}(\omega) \\ = \frac{C_{jj}(\omega) - C_{jj}(-\omega)}{2\omega}, \quad (4)$$

where the second equality follows from the fluctuation–dissipation theorem for equilibrium correlation functions, $C_{jj}(-\omega) = e^{-\beta\omega} C_{jj}(\omega)$. The dc mobility is $\mu_{dc} = \lim_{\omega \rightarrow 0} \text{Re } \mu_{ac}(\omega)$ and may be computed using only the real or only the imaginary part of $C_{jj}(t)$,¹⁰⁴

$$\begin{aligned} \mu_{dc} &= \frac{1}{T} \int_0^{+\infty} dt \text{Re } C_{jj}(t) \\ &= -2 \int_0^{+\infty} dt t \text{Im } C_{jj}(t). \end{aligned} \quad (5)$$

$C_{jj}(t)$ (for $t > 0$) carries information on the carrier's dynamics resulting from a sudden (δ -like) perturbation of the electron–phonon equilibrium. Its real part is proportional to the velocity–velocity anticommutator correlation function, which is the quantum counterpart of the velocity–velocity correlation function used, e.g., to study Brownian motion. The mean-square displacement (MSD) of the carrier's position, $\Delta x^2(t) = \langle [x(t) - x(0)]^2 \rangle$, where $\langle \dots \rangle$ denotes averaging with respect to $e^{-\beta H}/Z$, grows at a rate determined by the time-dependent diffusion constant,¹⁰⁵

$$\mathcal{D}(t) = \frac{1}{2} \frac{d}{dt} \Delta x^2(t) = \int_0^t ds \text{Re } C_{jj}(s). \quad (6)$$

Within the model considered here, $\text{Re } C_{jj}(t)$ decays to zero in the long-time limit, so that $\mathcal{D}(t)$ varies from 0 at short times to $\mathcal{D}_\infty = \int_0^{+\infty} ds \text{Re } C_{jj}(s)$ at long times, where \mathcal{D}_∞ is the diffusion constant related to the dc mobility by the Einstein relation (in the units we use, $\mu_{dc} = \mathcal{D}_\infty/T$). The electron's dynamics then exhibits a crossover from short-time ballistic dynamics, when $\Delta x^2(t) = C_{jj}(0)t^2$ and $\mathcal{D}(t) = C_{jj}(0)t$, to long-time diffusive dynamics, when $\Delta x^2(t) = 2\mathcal{D}_\infty t$ and $\mathcal{D}(t) = \mathcal{D}_\infty$. In addition to $\mathcal{D}(t)$, another quantity useful to describe this crossover is the diffusion exponent $\alpha(t) \geq 0$ defined by assuming that the power-law scaling $\Delta x^2(t) \propto t^{\alpha(t)}$ holds locally around instant t ,¹⁰⁶ so that

$$\alpha(t) = \frac{2t\mathcal{D}(t)}{\Delta x^2(t)}. \quad (7)$$

At short times, $\alpha(t)$ is close to 2, while it reaches the value of unity in the long-time diffusive limit.

B. HEOM for the real-time current-current correlation function

We formulate the HEOM method for the purely electronic operator

$$i(t) = \frac{1}{Z} \text{Tr}_{\text{ph}} \left\{ e^{-iHt} j e^{-\beta H} e^{iHt} \right\}, \quad (8)$$

while $C_{jj}(t) = \text{Tr}_e \{ j t(t) \}$. Since the totally symmetric phonon mode ($q = 0$ mode) couples to the unit operator in the electronic subspace, it does not affect the dynamics of $i(t)$, while its contributions to Z and $e^{-\beta H}$ cancel out after performing the partial trace over phonons. This decoupling of the $q = 0$ phonon mode from the rest of the phonon modes and the electronic states¹⁰⁷ somewhat lowers the number of auxiliary density operators (ADOs) $i_{\mathbf{n}}^{(n)}(t)$, which are characterized by the vector $\mathbf{n} = \{n_{qm} | q \neq 0, m = 0, 1\}$ containing $2(N - 1)$ non-negative integers n_{qm} counting individual phonon

absorption and emission events whose total number is $n = \sum'_{qm} n_{qm}$. The prime on the sum indicates the omission of the $q = 0$ term. The momentum conservation implies that the ADO $i_{\mathbf{n}}^{(n)}(t)$ changes the electronic momentum by $k_{\mathbf{n}} = \sum'_{qm} q n_{qm}$, so that only N of its N^2 matrix elements are nonzero. The only nonzero matrix elements of $i_{\mathbf{n}}^{(n)}(t)$ are the ones connecting the states whose momenta differ by $k_{\mathbf{n}}$. This requirement leads to a drastic reduction in the number of equations with respect to existing real-space HEOM formulations.^{97,99,102} A more detailed discussion in this direction is deferred to the last paragraph of Sec. III B.

The dynamics of $i(t)$ follows from the real-time HEOM

$$\begin{aligned} \partial_t \langle k | i_{\mathbf{n}}^{(n)}(t) | k + k_{\mathbf{n}} \rangle &= -i(\varepsilon_k - \varepsilon_{k+k_{\mathbf{n}}} + \mu_{\mathbf{n}}) \langle k | i_{\mathbf{n}}^{(n)}(t) | k + k_{\mathbf{n}} \rangle \\ &+ i \sum'_{qm} \sqrt{(1 + n_{qm}) c_{qm}} \langle k - q | i_{\mathbf{n}_{qm}^+}^{(n+1)}(t) | k + k_{\mathbf{n}} \rangle \\ &- i \sum'_{qm} \sqrt{(1 + n_{qm}) c_{qm}} \langle k | i_{\mathbf{n}_{qm}^-}^{(n+1)}(t) | k + k_{\mathbf{n}} + q \rangle \\ &+ i \sum'_{qm} \sqrt{n_{qm} c_{qm}} \langle k + q | i_{\mathbf{n}_{qm}^-}^{(n-1)}(t) | k + k_{\mathbf{n}} \rangle \\ &- i \sum'_{qm} \sqrt{n_{qm}} \frac{c_{qm}}{\sqrt{c_{qm}}} \langle k | i_{\mathbf{n}_{qm}^-}^{(n-1)}(t) | k + k_{\mathbf{n}} - q \rangle, \end{aligned} \quad (9)$$

where $\mu_{\mathbf{n}} = \sum'_q \omega_q (n_{q0} - n_{q1})$. The ADO $i_{\mathbf{n}}^{(n)}(t)$ couples to ADOs at depths $n \pm 1$, which are characterized by vectors \mathbf{n}_{qm}^\pm whose components are $[\mathbf{n}_{qm}^\pm]_{q'm'} = n_{q'm'} \pm \delta_{q'q} \delta_{m'm}$. The coefficients c_{qm} and c_{qm}^{\pm} are defined in Eqs. (A2) and (A3) of Appendix A, where we provide a detailed derivation of Eq. (9).

The initial condition for Eq. (9) is set by the equilibrium state of the interacting electron–phonon system [see also Eq. (8)]. In our previous publication,⁹⁶ we derived that the hierarchical representation of that equilibrium state can be obtained from the following imaginary-time HEOM:

$$\begin{aligned} \partial_\tau \langle k | \sigma_{\mathbf{n}}^{(n)}(\tau) | k + k_{\mathbf{n}} \rangle &= -(\varepsilon_k + \mu_{\mathbf{n}}) \langle k | \sigma_{\mathbf{n}}^{(n)}(\tau) | k + k_{\mathbf{n}} \rangle \\ &+ \sum'_{qm} \sqrt{(1 + n_{qm}) c_{qm}} \langle k - q | \sigma_{\mathbf{n}_{qm}^+}^{(n+1)}(\tau) | k + k_{\mathbf{n}} \rangle \\ &+ \sum'_{qm} \sqrt{n_{qm} c_{qm}} \langle k + q | \sigma_{\mathbf{n}_{qm}^-}^{(n-1)}(\tau) | k + k_{\mathbf{n}} \rangle. \end{aligned} \quad (10)$$

Equation (10) is propagated in imaginary time τ from 0 to β with the infinite-temperature initial condition $\langle k | \sigma_{\mathbf{n}}^{(n)}(0) | k + k_{\mathbf{n}} \rangle = \delta_{n,0}$. The initial condition for Eq. (9) is finally

$$\langle k | i_{\mathbf{n}}^{(n)}(0) | k + k_{\mathbf{n}} \rangle = Z_e^{-1} (-2J) \sin(k) \langle k | \sigma_{\mathbf{n}}^{(n)}(\beta) | k + k_{\mathbf{n}} \rangle, \quad (11)$$

where the so-called electronic partition sum reads as

$$Z_e = \sum_p \langle p | \sigma_0^{(0)}(\beta) | p \rangle. \quad (12)$$

A more detailed derivation is provided in Appendix A. Here, let us emphasize that the structure of the imaginary-time HEOM in Eq. (10) is fully compatible with the structure of the real-time HEOM in Eq. (9). This is different from existing approaches, in which the

structures of the imaginary-time and real-time HEOMs are not manifestly identical^{99,108} and may require appropriate rearrangement steps to obtain the initial condition for the real-time HEOM.¹⁰⁸

C. Closing the HEOM for the real-time current-current correlation function

When truncated at a finite maximum depth D , the real-time HEOM in Eq. (9) suffers from numerical instabilities appearing at sufficiently long times, which are commonly ascribed to the discrete and undamped nature of phonons.¹⁰¹ Such instabilities have been observed even for not-too-strong couplings and at not-too-low temperatures. The instabilities are particularly detrimental to evaluations of μ_{dc} , for which we need $C_{jj}(t)$ up to times so long that it has decayed almost to zero [Eq. (5)]. They may be eliminated by projecting out the unstable eigenmodes of the truncated HEOM,¹⁰¹ which requires numerically complicated filtration algorithms, or by deriving a new hierarchy of equations,¹⁰³ whose generally nontrivial relation to the original hierarchy may complicate evaluations of physically relevant quantities. The numerical instabilities reported in Ref. 101 were observed under the so-called time-nonlocal (TNL) truncation scheme, which sets all ADOs at depths $n > D$ to zero. One may thus hope that an appropriate closing of the HEOM at the maximum depth could eliminate numerical instabilities. While a number of closing schemes have been proposed recently,^{91,109,110} we find that none of them stabilizes Eq. (9). A possible reason behind our observation is that these schemes were tried and tested for the electron coupled to a phonon bath, i.e., when the spectral density of the electron-phonon interaction is a continuous function of the energy exchanged. On the other hand, here we deal with a discrete spectral density consisting of a finite number δ peaks at $\pm\omega_q$. In Appendix B, we build on previous density-matrix studies^{111–113} and derive in detail a specific closing of Eq. (9) that permits us to overcome the instabilities in many (but not all) parameter regimes. Here, let us only mention that we eliminate the ADOs at depth $D + 1$ from the equations at the maximum depth D by (i) setting the ADOs with $n \geq D + 2$ to zero and (ii) solving the resulting equations at depth $D + 1$, which then contain only the ADOs at depth D in the Markov and adiabatic approximations. The structure of the resulting equations at depth D is, however, more involved than the structure of Eq. (9) because the ADOs at depth D become mutually coupled. We eliminate these equal-depth couplings by resorting to the random phase approximation, which neglects momentum-averaged matrix elements of the ADOs at depth D due to random phases at different momenta. The above-described procedure for closing the HEOM results in equations for maximum-depth ADOs ($n = D$) that feature exponential damping terms

$$\left[\partial_t \langle k | I_n^{(n)}(t) | k + k_n \rangle \right]_{\text{close}} = -\delta_{n,D} \frac{1}{2} (\tau_k^{-1} + \tau_{k+k_n}^{-1}) \times \langle k | I_n^{(n)}(t) | k + k_n \rangle, \quad (13)$$

where τ_k is the carrier scattering time in the second-order perturbation theory and the long-chain limit [see Eq. (B7) and Ref. 42].

In our numerical computations, we assume that phonons are dispersionless, $\omega_q \equiv \omega_0$. For $\omega_0/J \geq 2$, the closing scheme in Eq. (13) cannot fully remove the numerical instabilities inherent to the undamped-mode HEOM because the carrier scattering times then

become infinite for k states in the vicinity of $\pm\pi/2$.^{26,42} We thus obtain HEOM results for $\omega_0/J \geq 2$ only at sufficiently high temperatures and for sufficiently (but not excessively) strong interactions. For $\omega_0/J < 2$, our results summarized in Secs. III A and III E show that the closing scheme in Eq. (13) removes the instabilities of Eq. (9) for not too strong g or at not too low T . The instabilities remain for strong g and at low T , while their relatively early appearance prevents us from reliably computing μ_{dc} in such parameter regimes (see Sec. III F).

D. HEOM for the imaginary-time current-current correlation function

In order for $C_{jj}(t)$ to be representative of the long-chain limit and take all relevant phonon-assisted processes into account, both N and D should be sufficiently large. The first proxy for how large N and D should be follows from analyzing the current-current correlation function $C_{jj}(\tau)$ in imaginary time.

While $C_{jj}(\tau)$ is directly accessible in QMC simulations,^{61,63,100} its evaluation using the HEOM method has not been considered so far, to the best of our knowledge. The appropriate imaginary-time HEOM is obtained from Eq. (9) by performing Wick's rotation $t \rightarrow -i\tau$. We employ the TNL truncation of the HEOM thus obtained, i.e., we simply set all the ADOs with $n > D$ to zero. $C_{jj}(\tau)$ is to be determined on the interval $[0, \beta]$, on which it is symmetric with respect to $\beta/2$. To enable as accurate an evaluation of $C_{jj}(\tau)$ as possible, we find it useful to consider the symmetrized correlation function

$$C_{jj}^{\text{sym}}(\tau) = \frac{1}{Z} \text{Tr} \left\{ e^{-\beta H/2} e^{H\tau} j e^{-H\tau} e^{-\beta H/2} j \right\}, \quad (14)$$

on the interval $[-\beta/2, \beta/2]$, which is related to $C_{jj}(\tau)$ via $C_{jj}(\tau) = C_{jj}^{\text{sym}}(\tau - \beta/2)$ for $0 \leq \tau \leq \beta$. We note that the use of the symmetrized correlation function instead of the standard one is advantageous in real-time QMC simulations¹¹⁴ and is also reported to be useful in real-time HEOM computations.^{98,99} Nevertheless, we find that the numerical instabilities of the real-time HEOM [Eqs. (9) and (13)] are reflected on both $C_{jj}(t)$ and $C_{jj}^{\text{sym}}(t)$ in the same manner, which is the reason why we consider the non-symmetrized correlation function [Eq. (2)] in all our real-time computations.

We determine $C_{jj}^{\text{sym}}(\tau)$ by two independent imaginary-time propagations: one forward from 0 to $\beta/2$ and the other backward from 0 to $-\beta/2$. The initial condition (at $\tau = 0$) for both propagations is obtained from the imaginary-time HEOM for the equilibrium state of the coupled electron-phonon system [Eq. (10)], which we (i) propagate from 0 to $\beta/2$, (ii) multiply by j from the left, and (iii) propagate once again from 0 to $\beta/2$. Since $C_{jj}^{\text{sym}}(\tau)$ is symmetric around 0, the results of the forward and backward propagations in imaginary time should coincide. We use this fact to gain insight into the maximum hierarchy depth D that is needed to obtain converged results. In more detail, we find that the relative deviation ($-\beta/2 \leq \tau \leq \beta/2$)

$$\delta_{jj}^{\text{sym}}(\tau) = 2 \frac{|C_{jj}^{\text{sym}}(\tau) - C_{jj}^{\text{sym}}(-\tau)|}{C_{jj}^{\text{sym}}(\tau) + C_{jj}^{\text{sym}}(-\tau)}, \quad (15)$$

decreases with increasing D . Furthermore, following how $C_{jj}(\tau) = [C_{jj}^{\text{sym}}(\tau - \beta/2) + C_{jj}^{\text{sym}}(\beta/2 - \tau)]/2$ ($0 \leq \tau \leq \beta$) changes with the chain length N provides information about the minimum chain length N needed to obtain results representative of the thermodynamic limit. We, however, emphasize that the estimates for D and N that stem from imaginary-axis data may differ from the corresponding estimates originating from real-time data. Whenever possible, we also perform real-time simulations for multiple N and D to ensure that our real-time results are also representative of the thermodynamic limit.

E. Sum rules

To gain additional confidence in our HEOM results, we check that certain sum rules for frequency-resolved quantities are satisfied with sufficient accuracy.^{77,115} We compare the moments of frequency-dependent quantities evaluated by (i) numerical integration over frequency and (ii) averaging an appropriate operator in the equilibrium state of the coupled electron and phonon. We consider the OSR

$$\int_0^{+\infty} d\omega \operatorname{Re} \mu_{\text{ac}}(\omega) = -\frac{\pi}{2} \langle H_e \rangle, \quad (16)$$

and the sum rules

$$\int_{-\infty}^{+\infty} \frac{d\omega}{2\pi} \omega^n C_{jj}(\omega) = M_n, \quad (17)$$

for the first three moments ($n = 0, 1, 2$) of the real-frequency current–current correlation function. In Eq. (16), we use the dynamical mobility computed using the first equalities in Eqs. (4) (for $\omega \neq 0$) and (5) (for $\omega = 0$). The electron’s kinetic energy entering Eq. (16) is evaluated using the quantities defined in Eqs. (10) and (12),⁹⁶

$$\langle H_e \rangle = \frac{1}{Z_e} \sum_k \varepsilon_k \langle k | \sigma_0^{(0)}(\beta) | k \rangle. \quad (18)$$

We note that the initial conditions $i_n^{(n)}(t=0)$ [Eq. (11)] for the real-time HEOM [Eq. (9)] do not enter Eq. (18). On the other hand, the quantities M_n entering Eq. (17) are expressed in terms of the initial conditions $i_n^{(n)}(t=0)$ for the real-time HEOM, and we derive the corresponding relations in Appendix C. Strictly speaking, Eq. (16) holds only in the long-chain limit, and in Appendix D, we demonstrate that the corresponding finite-size corrections decrease with increasing N . On the contrary, for any given N and D , Eq. (17) (with the expressions obtained in Appendix C) is exact. Having all these things considered, we conclude that checking the sum rules in Eq. (17) provides an important self-consistency check that all the numerical procedures (e.g., the numerical Fourier transformation) are properly implemented while providing limited information on the adequacy of N and D employed. In addition to a test for numerical implementation procedures, checking the OSR constitutes a nontrivial test for the adequacy of both D and N employed,

which is in line with previous studies.¹¹⁵ It is for this reason that we focus our discussion in Sec. III on the OSR. As a general trend, we observe that the sum rules in Eq. (17) are satisfied with better relative accuracy than the OSR.

III. NUMERICAL RESULTS

We limit ourselves to dispersionless optical phonons, $\omega_q \equiv \omega_0$, and perform HEOM computations for three different values of ω_0/J spanning the range from the adiabatic regime of slow phonons ($\omega_0/J = 1/3$) to the extreme quantum regime ($\omega_0/J = 1$) and the antiadiabatic regime of fast phonons ($\omega_0/J = 3$). Since most of our results are obtained for $\omega_0/J \leq 1$, we use the dimensionless interaction parameter,

$$\lambda = \frac{g^2}{2J\omega_0}, \quad (19)$$

that is appropriate to describe the zero-temperature transition from free electrons ($\lambda < 1$) to polarons ($\lambda > 1$) at such phonon frequencies.

We devote Secs. III A–III C to discussing the performance of the closing strategy embodied in Eq. (13) (Sec. III A) and the effects of finite N and D on the HEOM results in imaginary and real time (Sec. III B), as well as the accuracy with which the OSR is satisfied (Sec. III C). Section III D summarizes the most representative HEOM results for the time evolution of C_{jj} and the dynamical-mobility profile. Our most significant results, which concern the temperature dependence of μ_{dc} for different values of ω_0/J , are presented in Sec. III E. To further illustrate the capabilities and limitations of our approach, we present HEOM results for $C_{jj}(t)$ for strong electron–phonon couplings and at different temperatures in Sec. III F.

We provide HEOM data on $C_{jj}(t)$, its Fourier transformation $C_{jj}(\omega)$ computed using the FFTW3 software package,¹¹⁶ as well as $\operatorname{Re} \mu_{\text{ac}}(\omega)$, in different parameter regimes, as a freely available dataset. For more details, see Ref. 117, which contains all our numerical data, and the supplementary material of this manuscript, which contains their detailed description. Here, let us only mention that the HEOM in Eq. (9) supplemented with the closing in Eq. (13) is propagated using the algorithm proposed in Ref. 118 with the time step $\omega_0 \Delta t = (1 - 2) \times 10^{-2}$. While the maximum propagation time t_{max} generally shortens with increasing g and/or T , it is a highly nontrivial task to give its *a priori* estimate based only on the values of model parameters. Fortunately, in contrast to some other numerically “exact” methods, such as the DMRG⁷⁷ or real-time QMC,⁶³ the computational demands of the HEOM method do not increase with time t and are completely determined by $N, D, \Delta t$, and the propagation algorithm. We thus propagate the HEOM up to real times that are sufficiently long so that the integral $\int_0^t ds \operatorname{Re} C_{jj}(s)/T$ [see Eq. (5)] as a function of t enters saturation [see, e.g., Figs. 3(b) and 3(c)]. The frequency resolution in the optical response is increased by continuing $C_{jj}(t)$ symmetrically for negative times $-t_{\text{max}} \leq t \leq 0$ using $C_{jj}(-t) = C_{jj}(t)^*$, which results in the frequency step $\Delta\omega/\omega_0 = \pi/(\omega_0 t_{\text{max}})$. Therefore, if one wants both a reliable result for μ_{dc} and a finely resolved optical response, the maximum propagation time should be sufficiently long. In practice, we used $\omega_0 t_{\text{max}} \gtrsim 500$

for small g and at relatively low T , $\omega_0 t_{\max} \approx 300$ at intermediate values of g and T , and $\omega_0 t_{\max} \lesssim 100$ for large g or at high T .

A. Effectiveness and reliability of our closing strategy

We offer numerical examples demonstrating that the closing in Eq. (13) actually stabilizes the real-time HEOM [Eq. (9)] without compromising the results for μ_{dc} .

Figure 1(a) (its inset) shows the evolution of $\text{Re } C_{jj}$ ($\text{Im } C_{jj}$) with the closing in Eq. (13) and the TNL truncation in the weak-coupling regime and at a relatively low temperature. The beneficial effects of our closing strategy on HEOM stability are apparent. Moreover, the HEOM [with closing in Eq. (13)] estimate for $\mu_{\text{dc}}^{\text{HEOM}} = 68.0$ using $Jt_{\max} = 800$ agrees well with the estimate $\mu_{\text{dc}}^{\text{wcl}} = 72.5$ emerging from the weak-coupling limit [see Eq. (49) in Ref. 42]. The relative difference between the two results is under 10%, which eventually emerges as the relative error that is to be associated with $\mu_{\text{dc}}^{\text{HEOM}}$ (see Sec. III B). With TNL truncation, it is much more difficult to obtain a reliable estimate of μ_{dc} . This is evident when μ_{dc} is computed using only $\text{Re } C_{jj}(t)$ [the first equality in Eq. (5)], which under TNL truncation develops a pronounced hump for $Jt \gtrsim 100$. The same applies to the computation using only $\text{Im } C_{jj}(t)$ [the

second equality in Eq. (5)], when the small-amplitude long-time oscillations of $\text{Im } C_{jj}$ around zero are amplified by multiplication with time.

One may still argue that at higher temperatures, when carrier scattering rates entering Eq. (13) become large, our hierarchy closing may underestimate μ_{dc} . Such an effect may be particularly pronounced for not too strong coupling when the maximum depth D is not very large so that the exponentially damping terms in Eq. (13) may appreciably affect the quantity at the hierarchy root, i.e., $C_{jj}(t)$. The inset of Fig. 1(b) shows that the estimate for μ_{dc} using the closing in Eq. (13) and propagating the HEOM to sufficiently long times (we took $Jt_{\max} = 100$) is approximately the same as the one using the TNL truncation and propagating the HEOM to times before the instabilities arise (up to $Jt \approx 20$). Both of these estimates ($\mu_{\text{dc}}^{\text{HEOM}} = 0.53$) agree reasonably well with the estimate $\mu_{\text{dc}}^{\text{wcl}} = 0.61$ emerging from the weak-coupling limit.

B. Effects of finite N and D on the current-current correlation function and dc mobility

We first analyze $C_{jj}(\tau)$. We fix $g/J = \omega_0/J = T/J = 1$ and discuss the importance of finite-size effects for maximum hierarchy depth $D = 6$. Figure 2(a) shows that $C_{jj}(\tau)$ steadily approaches its long-chain limit with increasing N . The approach to that limit is quite fast because the relative deviation with respect to the results for the longest chain studied ($N = 13$) decreases by almost three orders of magnitude upon increasing N from 7 to 10 [see the inset of Fig. 2(a)]. Therefore, already, $N = 10$ should be sufficiently large to obtain results representative of the long-chain limit. Figure 2(b) shows that the quality of our imaginary-time data, quantified by the relative difference $\delta_{jj}^{\text{sym}}(\tau)$ [Eq. (15)], steadily increases with increasing D .

While Figs. 2(a) and 2(b) demonstrate a steady convergence of the imaginary-time data toward the large- N and large- D limit as N and D are increased, the situation on the real axis is somewhat more complicated, which is summarized in Figs. 3(a)–3(c). Fixing D to 6, Fig. 3(a) [Fig. 3(b)] shows that $\text{Re } C_{jj}(t)$ [$\text{Im } C_{jj}(t)$] is virtually the same for $N = 10, 13$, and 15. For $N = 7, 10$, and 13, we propagated HEOM up to $Jt_{\max} = 400$, while we used $Jt_{\max} = 300$ for $N = 15$. At longer times (not shown here), both $\text{Re } C_{jj}(t)$ and $\text{Im } C_{jj}(t)$ exhibit small-amplitude oscillations around zero. The agreement between the results for different N in the real-time domain translates to the overall profile of $\text{Re } \mu_{\text{ac}}(\omega)$ [see the inset of Fig. 3(a)]. However, the dc mobility somewhat decreases upon increasing N from 7 to 10 and 13, while its values for $N = 13$ and 15 are virtually the same [see the full dots in the inset of Fig. 3(a) and Table I]. The relative differences between μ_{dc} for different values of N considered are of the order of percent, which is also evident from the inset of Fig. 3(b) displaying the convergence to the dc limit when only $\text{Im } C_{jj}(t)$ is used to evaluate μ_{dc} [the second equality in Eq. (5)]. The integral $-2 \int_0^t ds \text{Im } C_{jj}(s)$ is expected to display long-time oscillations originating from the corresponding oscillations of $\text{Im } C_{jj}(s)$ around zero. The inset of Fig. 3(b) thus shows the smoothed data obtained using the moving-average procedure, which is employed at sufficiently long times to reliably compute μ_{dc} . In more detail, the moving average of the quantity $-2 \int_0^t ds \text{Im } C_{jj}(s)$ at instant t is computed as the arithmetic average of its N_{move} values right after t and its N_{move}

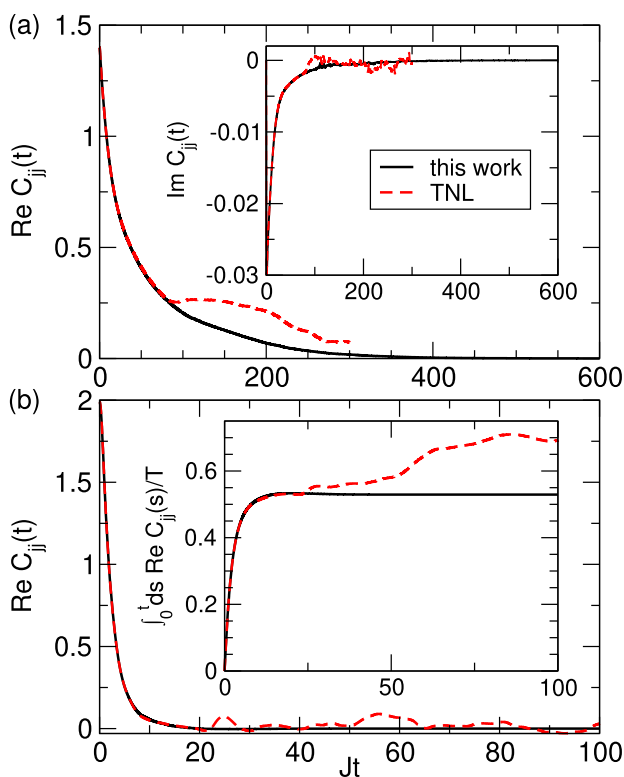


FIG. 1. Time dependence of $\text{Re } C_{jj}$ (in units of J^2) employing the closing in Eq. (13) (full black line, label “this work”) or the time-nonlocal truncation (dashed red line, label “TNL”). The values of model parameters are $\omega_0/J = 1$, $\lambda = 0.01$, and (a) $T/J = 1$, $N = 160$, $D = 2$ (in units of J^2), (b) $T/J = 10$, $N = 40$, $D = 3$. The insets show the time dependence of (a) $\text{Im } C_{jj}$, (in units of J^2) (b) the quantity $\int_0^t ds \text{Re } C_{jj}(s)/T$, which tends to μ_{dc} as $t \rightarrow +\infty$.

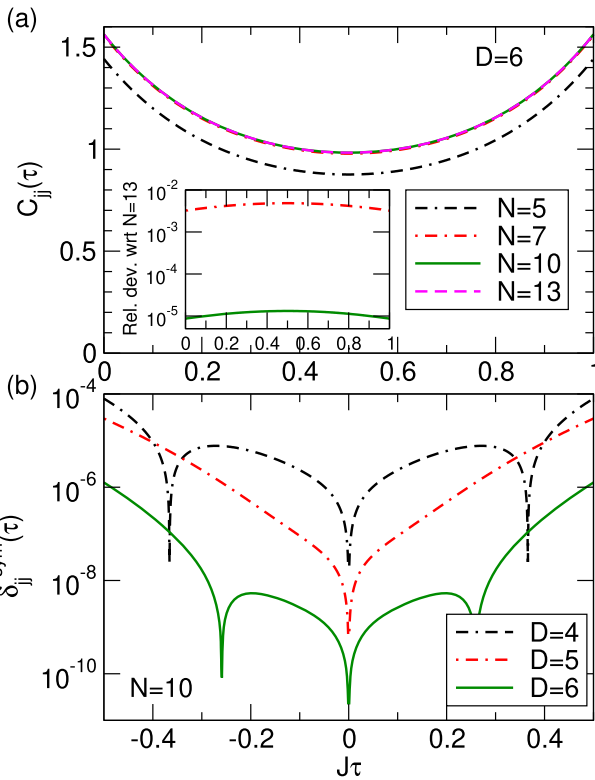


FIG. 2. (a) Current–current correlation function (in units of J^2) in imaginary time $J\tau \in [0, \beta J]$ for $D = 6$ and different chain lengths N . The inset shows the quantity $|C_{ij}^N(\tau) - C_{ij}^{N=13}(\tau)|/C_{ij}^{N=13}(\tau)$ for $N = 7$ and 10 . (b) The quantity $\delta_{ij}^{\text{sym}}(\tau)$ [Eq. (15)] as a function of imaginary time $J\tau \in [-\beta J/2, \beta J/2]$ for a 10-site chain and different maximum hierarchy depths D . Note the logarithmic scale on the vertical axis in the insets of (a) and (b). The model parameters are $g/J = \omega_0/J = T/J = 1$.

values right before t . We take N_{move} to be 10% of the total number of points for which we have HEOM data. Figure 4(a) shows that the moving-average procedure indeed smooths out the long-time oscillations of the quantity $-2\int_0^t ds \text{Im} C_{ij}(s)$, while the dependence of the final result for μ_{dc} on the averaging window is much less pronounced than, e.g., its dependence on the parity of D , *vide infra*. The μ_{dc} estimates using the two equalities in Eq. (5) agree up to a couple of percent (see Table I). The relative difference of the same order of magnitude is obtained when D is increased from 6 to 8 when $N = 10$, while decreasing D from 6 to 5 leads to a decrease in μ_{dc} of around 10% [see Fig. 3(c) and Table I]. For $N = 10$ and $D = 7$, $\text{Re} C_{ij}(t)$ becomes negative at long times, which may prevent us from reliably estimating μ_{dc} . Nevertheless, we see that following the time evolution up to $Jt_{\text{max}} = 70$ provides an estimate of μ_{dc} that differs from the estimate for $N = 10, D = 5$, by a couple of percent. We thus conclude that μ_{dc} estimates may depend on the parity of the maximum hierarchy depth D . For sufficiently large D , the estimates for D and $D + 2$ differ by a couple of percent, and those for D and $D + 1$ differ by around 10%. While we find that such a behavior of μ_{dc} as a function of D (for fixed N) is generic, the

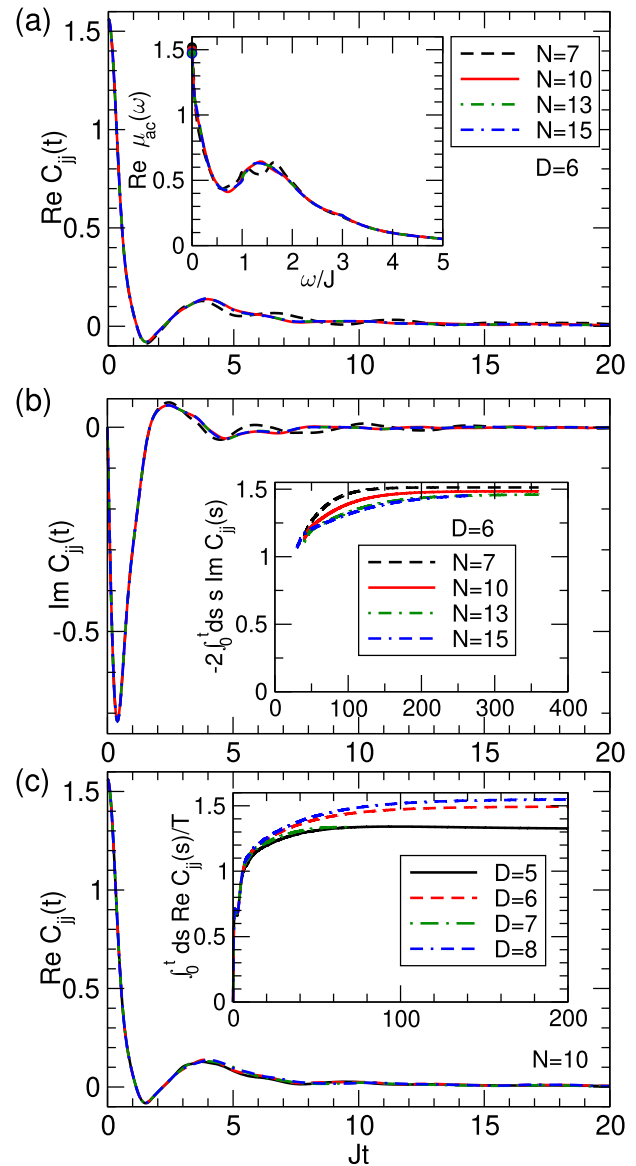


FIG. 3. Time dependence of (a) $\text{Re} C_{ij}$ and (b) $\text{Im} C_{ij}$ (both in units of J^2) for $D = 6$ and different chain lengths N . (c) Time dependence of $\text{Re} C_{ij}$ (in units of J^2) for $N = 10$ and different maximum hierarchy depths D . The inset in (a) shows the frequency profile of the dynamic mobility for $D = 6$ and different N . Full dots at $\omega = 0$ represent the results for μ_{dc} using the first equality in Eq. (5) (see also Table I). The inset in (b) shows how the result of the integration in Eq. (5) converges toward μ_{dc} as we increase the upper integration limit. To obtain smooth curves, we perform the moving average procedure described in the text. The inset in (c) shows how the result of the integration in Eq. (5) converges toward μ_{dc} as we increase the upper integration limit. The model parameters are $g/J = \omega_0/J = T/J = 1$.

magnitudes of the above-mentioned relative differences generally decrease with temperature. The preceding discussion implies that HEOM estimates for μ_{dc} should be taken with relative uncertainties not surpassing 10%.

TABLE I. Effects of finite N and D on HEOM results for the dc mobility. The HEOM is propagated up to time Jt_{\max} . Model parameters are $g/J = \omega_0/J = T/J = 1$.

(N, D)	μ_{dc} from Re $C_{jj}(t)$	μ_{dc} from Im $C_{jj}(t)$	Jt_{\max}
(10,5)	1.327	1.308	400
(10,6)	1.493	1.484	400
(10,7)	1.336	1.325	70
(10,8)	1.548	1.537	200
(7,6)	1.520	1.513	400
(13,6)	1.472	1.459	400
(15,6)	1.473	1.452	300

Without the specific HEOM closing [Eq. (13)], it would be nearly impossible to obtain meaningful results for the dc or ac mobility, which is apparent from Fig. 4(b) showing HEOM data for Re $C_{jj}(t)$ that use the TNL truncation. Model parameters are the same as in Fig. 3(c), to which the results in Fig. 4(b) are to be compared. Our closing smooths the local maximum in Re $C_{jj}(t)$ around $Jt \approx 4$ and stabilizes the subsequent time evolution, whose oscillatory features under TNL truncation become more pronounced with increasing D . In addition to Re $C_{jj}(t)$, in Fig. 4(c), we show the quantity $\int_0^t ds \text{Re } C_{jj}(s)/T$ [see Eq. (5)] under TNL truncation (dashed lines) and our closing scheme (solid lines). While the agreement between the dashed and solid lines in Fig. 4(c) is good for $Jt \lesssim 10$, the results obtained under TNL truncation do not show any sign of reaching a long-time limit with increasing t . One could use the HEOM data with TNL truncation up to $Jt_{\max} \approx 20$ (before the instabilities become more pronounced) to extract the dc mobility of around 1.25, and virtually the same estimate would be obtained using the HEOM data with our closing scheme up to $Jt_{\max} \approx 20$ [see Fig. 4(c)]. Nevertheless, if one is to obtain the optical response with a decent frequency resolution using the HEOM data in Fig. 4(b) up to $Jt_{\max} \approx 20$, one should probably perform additional numerical procedures, such as the zero-padding (to effectively increase t_{\max}), possibly combined with signal windowing.^{77,96} Such procedures,

however, may affect the intensities (and to some extent the positions) of the optical-response features, mainly in the low-frequency part that corresponds to the most challenging long-time dynamics. On the other hand, when we propagate our stabilized HEOM up to long real times, no additional numerical procedures on the HEOM data for $C_{jj}(t)$ are required to compute the optical response. While the observed dependence of our HEOM results on the parity of D could be attributed to our closing scheme, we believe that we handle this effect in an appropriate manner because we use it to estimate the relative error of our results for μ_{dc} . While a detailed explanation of our observations is beyond the scope of this investigation, we speculate about their possible origin as follows. In Eq. (9), $\mu_{\mathbf{n}}$ is the change in energy of the phononic subsystem due to the sequence of electron-phonon interaction events described by \mathbf{n} . At depth n , $\mu_{\mathbf{n}}/\omega_0$ can assume values $\pm n, \pm(n-2), \dots$, while at odd depths n , all $\mu_{\mathbf{n}}$ s are nonzero, even depths feature some vectors \mathbf{n} for which $\mu_{\mathbf{n}} = 0$. At even depths, there are thus ADOs having both $\mu_{\mathbf{n}} = 0$ and $k_{\mathbf{n}} = 0$, meaning that the resonance condition $\varepsilon_k - \varepsilon_{k+k_{\mathbf{n}}} + \mu_{\mathbf{n}} = 0$ emerging from the free-rotation term in Eq. (9) is perfectly satisfied. On the other hand, at odd depths, the resonance condition is almost never perfectly met: even if $k_{\mathbf{n}} = 0$ for a particular \mathbf{n} , $\mu_{\mathbf{n}}$ is certainly nonzero. When the closing scheme in Eq. (13) is applied, the behavior of all ADOs at an odd maximum depth can be described by damped oscillations (in the lowest approximation that neglects links to other ADOs). In the same approximation, at an even maximum depth, there are ADOs that are exponentially suppressed with time without displaying any oscillatory behavior. The influence of such ADOs on the overall HEOM dynamics might be less pronounced than the influence of ADOs exhibiting damped oscillations.

We finish this section by briefly discussing the decrease in the number of active variables in our momentum-space HEOM with respect to existing real-space formulations. Namely, for an N -site chain, the number of ADOs upon hierarchy truncation at depth D is $n_{\text{ADO}}^{\text{rs}} = \binom{2N+D}{D}$ when working in real space ($q = 0$ phonon mode is considered) and $n_{\text{ADO}}^{\text{ms}} = \binom{2(N-1)+D}{D}$ when working in momentum space ($q = 0$ phonon mode is not considered). As the number of entries in each ADO is at the same time reduced by a

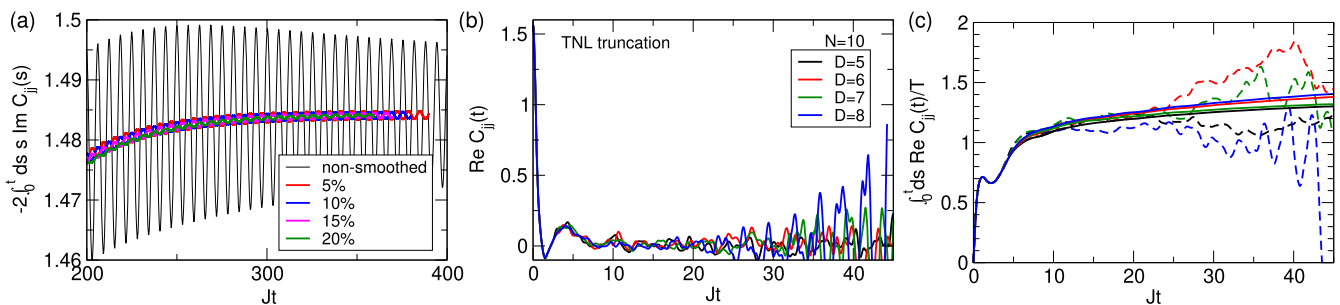


FIG. 4. (a) Long-time evolution of the quantity $-2 \int_0^t ds \text{Im } C_{jj}(s)$ [black solid line, label “non-smoothed,” see Eq. (5)] and its moving averages computed for different sizes (determined by N_{move} defined in the text) of the averaging window. Percentages are to be taken from the total number of points for which HEOM data are available. (b) Time dependence of Re C_{jj} (in units of J^2) under the TNL truncation for different values of D . (c) Time dependence of the quantity $\int_0^t ds \text{Re } C_{jj}(s)/T$ [see Eq. (5)] under the TNL truncation (dashed lines) and our closing in Eq. (13) (solid lines). The values of the model parameters and the color code are the same as in (b). The model parameters are $g/J = \omega_0/J = T/J = 1$, $N = 10$ in all three panels, and $D = 6$ in panel (a).

factor of N , the relative decrease in the number of variables that have to be propagated upon transferring from real to momentum space is

$$\frac{N^2 n_{\text{ADO}}^{\text{rs}} - N n_{\text{ADO}}^{\text{ms}}}{N^2 n_{\text{ADO}}^{\text{rs}}} = 1 - \frac{2(2N - 1)}{(2N + D)(2N + D - 1)}. \quad (20)$$

For a fixed N , the savings in computer memory increase with D . While the savings in computer memory for fixed D decrease with N , they can be substantial on relatively short chains that are still sufficiently long so that the corresponding results are representative of the long-chain limit. For example, for $N = 10$ and $D = 6$ (as in Fig. 3), the relative decrease in the number of active variables with respect to HEOM formulations in real space is around 40%.

C. Numerical examples concerning sum rules

Figure 5(a) summarizes how the relative accuracy

$$\delta_{\text{OSR}} = \frac{\left| \int_0^{+\infty} d\omega \text{Re} \mu_{\text{ac}}(\omega) - \frac{\pi}{2} |\langle H_e \rangle| \right|}{\frac{\pi}{2} |\langle H_e \rangle|}, \quad (21)$$

with which the OSR is satisfied depends on N and D for the same values of model parameters as in Figs. 2–4. We observe that, in the ranges of N and D considered, δ_{OSR} generally decreases with both N [assuming fixed D ; see black circles, right vertical and top horizontal axes in Fig. 5(a)] and D [assuming fixed N ; see red squares, left vertical and bottom horizontal axes in Fig. 5(a)].

Fixing D to 6 and varying N from 7 to 15, we observe the steepest decrease in δ_{OSR} upon increasing N from 7 to 10, while further increases in N from 10 to 13 and 15 result in a much milder decrease in δ_{OSR} . This observation is consistent with both the imaginary-axis data shown in Fig. 2(a) and the real-time data presented in Figs. 3(a) and 3(b) and Table I. Namely, the largest (and smallest) variation in $C_{ij}(\tau)$, $C_{ij}(t)$, and μ_{dc} upon increasing $N \in \{7, 10, 13, 15\}$ to the subsequent value from the sequence $\{7, 10, 13, 15\}$ is observed for $N = 7$ ($N = 13$). The decrease in δ_{OSR} with increasing N is, however, ultimately limited by the fact that δ_{OSR} depends on quantities that are themselves calculated numerically and thus bring their own numerical errors into the final expression. The integral over frequencies is computed using the trapezoidal rule, while $\langle H_e \rangle$ is computed for finite values of N and D (we do not use its “exact” value in the limit $N, D \rightarrow \infty$ that could be obtained using our⁹⁶ or some other⁷⁶ method). The error incurred when the integral $\int_0^{+\infty} d\omega \text{Re} \mu_{\text{ac}}(\omega)$ is evaluated using the trapezoidal rule is of the order of $(\Delta\omega/J)^3$,¹¹⁹ where the frequency step $\Delta\omega$ is related to the maximum propagation time t_{max} by $\Delta\omega/J = \pi/(Jt_{\text{max}})$. Fixing D and varying N , we use $Jt_{\text{max}} = 300$, meaning that the numerical error of the integral $\int_0^{+\infty} d\omega \text{Re} \mu_{\text{ac}}(\omega)$ is of the order of $(\pi/300)^3 \sim 10^{-6}$. In other words, $N = 15$ is sufficiently large that δ_{OSR} is most probably not dominated by finite-size effects in N but rather by the error of numerical integration. This is further corroborated by the fact that the kinetic energies for $N = 13$ and $N = 15$ differ on the seventh decimal place (see Table II), meaning that the error of the kinetic energy for $N = 15$ is at least an order of magnitude below the numerical integration error. On the other hand, for $N = 7$, δ_{OSR} is most probably limited by the finite-size effects in $\langle H_e \rangle$. The data in Table II suggest that the error of $|\langle H_e \rangle|_{N=7, D=6}$, which can be inferred from its deviation

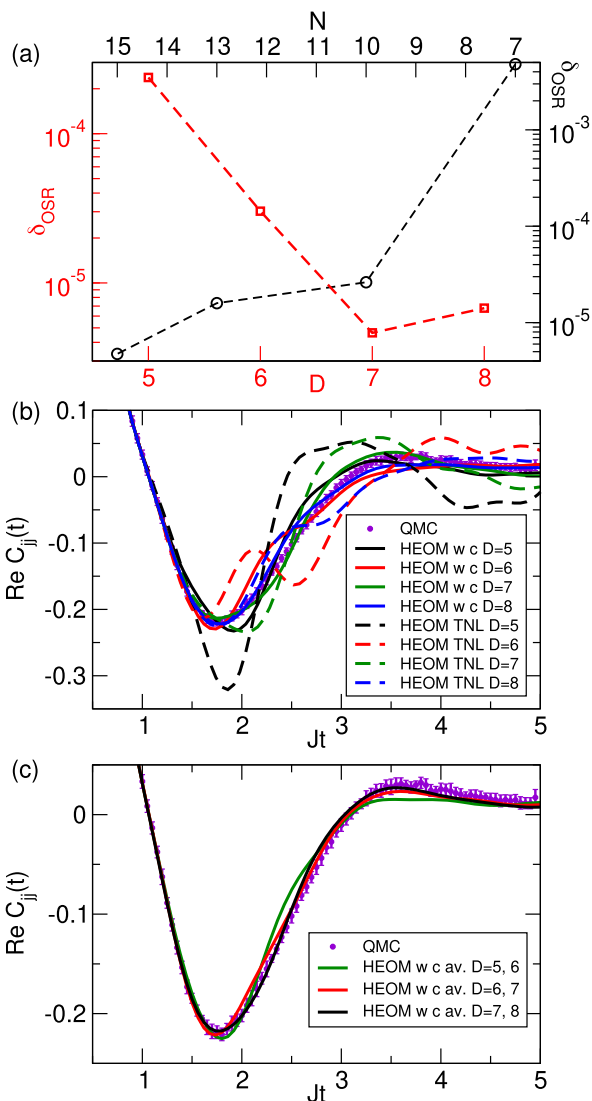


FIG. 5. (a) Relative accuracy δ_{OSR} [Eq. (21)] as a function of D for $N = 10$ (red squares, left vertical and bottom horizontal axes) and as a function of N for $D = 6$ (black circles, right vertical and top horizontal axes). The dashed lines connecting the symbols serve as guides for the eye. The model parameters are $g/J = \omega_0/J = T/J = 1$ ($\lambda = 0.5$). For $N = 10$, we use $C_{ij}(t)$ up to $Jt_{\text{max}} = 200$ for $D = 5, 6$, and 8, while for $D = 7$, we take $Jt_{\text{max}} = 70$ (see also Table I). For $D = 6$, we use $C_{ij}(t)$ up to $Jt_{\text{max}} = 300$ for $N = 7, 10, 13$, and 15. (b) Comparison of HEOM (lines) and QMC (symbols with error bars) results for $\text{Re} C_{ij}(t)$ (in units of J^2) for $N = 10$, $g/J = 1/\sqrt{3}$, $\omega_0/J = 1/3$, $T/J = 1$ ($\lambda = 0.5$), and different values of D . Solid lines (label “w c”) employ our closing [Eq. (13)], while dashed lines (label “TNL”) use the TNL truncation. (c) Comparison of HEOM results averaged over depths $D - 1$ and D (solid lines) with QMC results (symbols with error bars) for $D = 6, 7$, and 8, while other parameters assume the same values as in (b). QMC data are the courtesy of N. Vukmirović.

from $|\langle H_e \rangle|_{N=10, D=6}$, is of the order of 10^{-3} . This is consistent with the value of δ_{OSR} reported in Fig. 5(a).

A similar analysis can be repeated by fixing N and varying D . In practice, our criterion for choosing N and D is that $\delta_{\text{OSR}} \lesssim 10^{-4}$. As

TABLE II. Kinetic energy of the electron as a function of N and D for $g/J = \omega_0/J = T/J = 1$.

(N, D)	$ \langle H_e \rangle /J$
(7,6)	1.155 308 279 5
(10,6)	1.154 623 995 5
(13,6)	1.154 622 914 9
(15,6)	1.154 623 007 8

mentioned in Sec. II E and as can be seen from the supplementary material, the relative accuracy with which the sum rules in Eq. (17) are satisfied is generally better than δ_{OSR} .

At higher temperatures ($T/\omega_0 \gtrsim 3$), we find that HEOM data for fixed N and two sufficiently large consecutive depths $D - 1$ and D generally have almost the same δ_{OSR} [as in Fig. 5(a)], while there are some differences between them already at relatively short times. For example, for $g/J = 1/\sqrt{3}$, $\omega_0/J = 1/3$, and $T/J = 1$ ($\lambda = 0.5$), we find that the differences between HEOM results for different values of D (we fix $N = 10$) appear already for $Jt \simeq 2$ or $\omega_0 t \simeq 2/3$ [see Fig. 5(b)], in contrast to the situation in Figs. 3(c) and 4(c), where the differences appear at somewhat longer times. We perform HEOM computations with TNL truncation and our specific closing and find that the short-time differences observed in Fig. 5(b) cannot be exclusively attributed to our closing scheme as they are also present under the TNL truncation. Actually, our closing stabilizes the evolution of $\text{Re } C_{jj}(t)$ and lowers the differences between HEOM results for different values of D (with respect to the TNL truncation). To reveal whether our HEOM results are reliable, we compare them with QMC data obtained using the methodology developed in Ref. 63. QMC results are numerically “exact,” as their convergence with respect to all control parameters of the simulation has been carefully checked. In Figs. 5(b) and 5(c), we show QMC results with their statistical error bars. Figure 5(b) suggests that the difference between HEOM (with our closing) and QMC results decreases relatively slowly with increasing D , while HEOM dynamics for D s of the same parity ($D = 5, 7$ and $D = 6, 8$) deviate from the QMC results in a similar manner (both deviations are positive/negative). It is known that the convergence of a slowly converging sequence can be improved by performing an appropriate sequence transformation, such as the Shanks or Richardson transformation.¹²⁰ Here, inspired by the reasoning behind the Shanks transformation, we want to improve the convergence of the sequence $C_{jj}(D; t)$ in D (for fixed N and at each instant t) by handling the term whose decay (as a function of D) toward zero is the slowest. Based on Fig. 5(b), one may imagine that the dependence of $C_{jj}(D; t)$ on D can be represented as

$$C_{jj}(D; t) = C_{jj}^{D \rightarrow \infty}(t) + \alpha(t) \frac{(-1)^D}{D^a}, \quad (22)$$

where $a > 0$, $\alpha(t)$ is a complex number, $C_{jj}^{D \rightarrow \infty}(t)$ is the sought large- D limit, while the alternating term $(-1)^D$ mimics the observed alternation of HEOM results with respect to QMC results with the parity of D . We use Eq. (22) to arrive at

$$\frac{C_{jj}(D-1; t) - C_{jj}^{D \rightarrow \infty}(t)}{C_{jj}(D; t) - C_{jj}^{D \rightarrow \infty}(t)} = -\left(\frac{D-1}{D}\right)^a \approx -1, \quad (23)$$

where the last approximate equality holds for sufficiently large D (the smaller a , the smaller the minimum value of D for which the approximation is good). Equation (23) implies that

$$C_{jj}^{D \rightarrow \infty}(t) \approx \frac{C_{jj}(D; t) + C_{jj}(D-1; t)}{2}, \quad (24)$$

which suggests that the large- D limit of $C_{jj}(D; t)$ can be approached more rapidly by considering the transformed sequence $[C_{jj}(D; t) + C_{jj}(D-1; t)]/2$ instead of the original sequence $C_{jj}(D; t)$. While our arguments are not fully mathematically rigorous, they produce plausible results, as revealed in Fig. 5(c), showing how the HEOM data averaged over two consecutive depths (5 and 6, 6 and 7, 7 and 8) compare to the QMC data. We observe that the agreement with the QMC data improves with increasing the depths over which the averaging is performed. As a result, when averaging over depths 7 and 8, HEOM results are within the QMC error bars in the largest portion of the time window displayed. It then seems reasonable that our final HEOM result in this parameter regime be the average of the results for $D = 7$ and 8. Finally, whenever our dataset¹¹⁷ provides raw data for $C_{jj}(t)$ for two consecutive depths, we use the average $C_{jj}(t)$ when computing physical quantities.

D. Signatures of the electron-phonon interaction in time and frequency domains

Figures 6(a1)–6(c3) present selected results concerning the dynamics of the $j-j$ correlation function, diffusion constant, and diffusion exponent, together with the frequency profile of the dynamical mobility. Our analysis of the parameter regimes in which HEOM computations are free of numerical instabilities [see Figs. 7(a)–7(c)] identifies three typical behaviors of the aforementioned quantities.

In the weak-coupling regime ($\lambda = 0.01$) for $\omega_0/J = 1/3$ and 1, we find a smooth crossover from the ballistic electronic motion at short times toward the diffusive motion at long times. The representative results for $\omega_0/J = 1$ are shown in Figs. 1(a) and 1(b), while Figs. 6(a1)–6(a3) show representative results for $\omega_0/J = 1/3$. $\text{Re } C_{jj}(t)$, $\mathcal{D}(t)$, and $\alpha(t)$ are all monotonic functions of time, while the dynamical-mobility profile has only the Drude peak at $\omega = 0$ and bears an overall resemblance to the Drude model.

Already in the intermediate-coupling regime ($\lambda = 0.5$) for $\omega_0/J = 1/3$ and 1, the ballistic-to-diffusive crossover is not smooth. The representative results for $\omega_0/J = 1$ are presented in Figs. 3(a)–3(c), whereas Figs. 6(b1)–6(b3) show representative results for $\omega_0/J = 1/3$. $\text{Re } C_{jj}(t)$, $\mathcal{D}(t)$, and $\alpha(t)$ are non-monotonic functions of time. We observe that $\text{Re } C_{jj}(t) < 0$ on intermediate time scales, on which the diffusion constant decreases with time. This is clear from Eq. (6), which establishes a connection between the sign of $\text{Re } C_{jj}(t)$ and the intervals of monotonicity of $\mathcal{D}(t)$. $\alpha(t)$ reaches a pronounced local minimum on the very same time scale. In other words, intermediate time scales in the intermediate-interaction regime witness a temporally limited slow-down of the electronic motion. Depending on the parameter regime (typically for strong g and at high T), that slow-down may be so pronounced that the electronic motion changes its character from superdiffusive ($\alpha > 1$) to subdiffusive ($\alpha < 1$) over a limited time frame. While such a change occurs for model parameters studied in Figs. 6(b1)–6(b3),

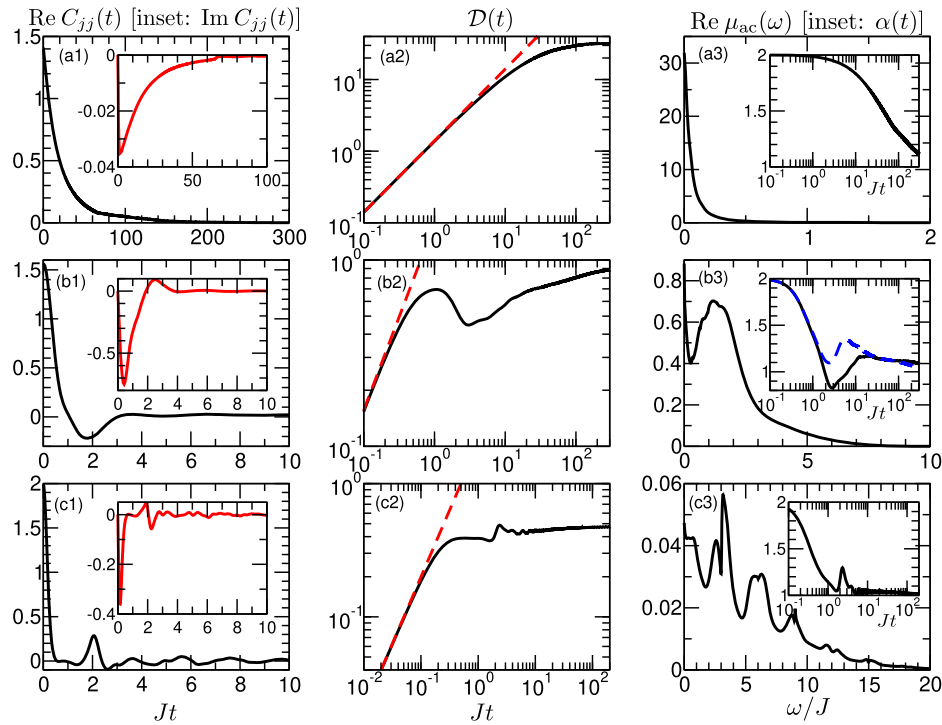


FIG. 6. Time dependence of $\text{Re } C_{jj}$ [in units of J^2 , (a1)–(c1)], \mathcal{D} [in units of J , (a2)–(c2)], and the frequency dependence of $\text{Re } \mu_{\text{dc}}(\omega)$ [(a3)–(c3)] for (a) $\omega_0/J = 1/3, \lambda = 0.01, T/J = 1$, (b) $\omega_0/J = 1/3, \lambda = 0.5, T/J = 1$, and (c) $\omega_0/J = 3, \lambda = 0.5, T/J = 10$. The insets of panels (a1)–(c1) [(a3)–(c3)] display the time dependence of $\text{Im } C_{jj}$ in units of J^2 (α). The dashed lines in (a2)–(c2) represent the short-time (ballistic) limit of the diffusion constant, $\mathcal{D}_{\text{bal}}(t) = C_{jj}(0)t$. The dashed line in the inset of (c2) represents $\alpha(t)$ for the parameter regime examined in Fig. 3. The results in (a1)–(a3) emerge from HEOM computations using $N = 128, D = 2$, while the remaining results are the arithmetic average of HEOM computations using: (b1)–(b3) $N = 10, D = 7$ and $N = 10, D = 8$; (c1)–(c3) $N = 5, D = 18$ and $N = 5, D = 19$.

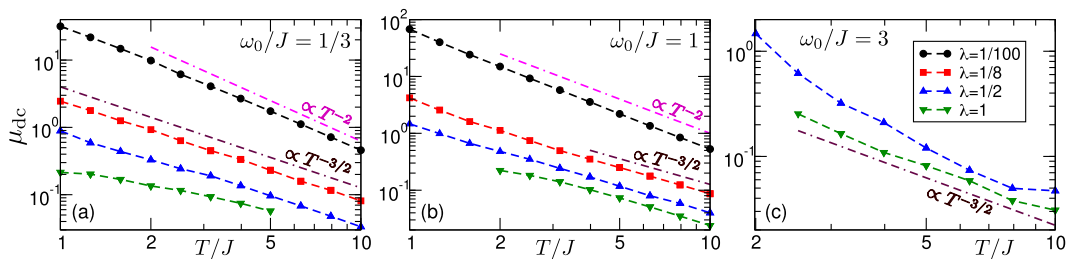


FIG. 7. HEOM-method results for the temperature-dependent dc mobility for different interaction strengths (different values of parameter λ) and (a) $\omega_0/J = 1/3$, (b) $\omega_0/J = 1$, and (c) $\omega_0/J = 3$. Full symbols are HEOM-method results, while dashed lines connecting them serve as guides to the eye. Double dashed–dotted lines show the theoretically predicted²⁶ power-law scaling $\mu_{\text{dc}} \propto T^{-2}$ or $\mu_{\text{dc}} \propto T^{-3/2}$ in appropriate limiting cases (no fitting procedures have been performed on the HEOM data).

it is absent for model parameters studied in Figs. 3(a)–3(c) [see the dashed line in the inset of Fig. 6(b3)]. Apart from the Drude peak at $\omega = 0$, the dynamical mobility features a prominent finite-frequency peak.

The available results for $\omega_0/J = 3$, which are obtained for sufficiently strong interactions and at sufficiently high temperatures, also display a non-monotonic behavior of $\text{Re } C_{jj}(t)$, $\mathcal{D}(t)$, and $\alpha(t)$. In contrast to the results for $\omega_0/J = 1/3$ and 1, $\mathcal{D}(t)$ increases in almost regular steps centered around integer multiples of $2\pi/\omega_0$. The first peak of $\text{Re } C_{jj}(t)$ is indeed centered at $2\pi/\omega_0$,

while subsequent peaks are somewhat displaced toward earlier times [see Fig. 6(c1)]. The dynamic-mobility profile is characterized by relatively broad peaks centered around integer multiples of ω_0 . These features suggest that we are close to the genuine small-polaron limit.^{18,32}

E. Temperature dependence of the dc mobility

Figures 7(a)–7(c) present the central result of our study, the HEOM-method results for the temperature dependence of μ_{dc} for three different values of ω_0/J . As discussed in Sec. III B, our results

for μ_{dc} should be assigned relative errors not surpassing 10%. The values reported in Figs. 7(a)–7(c) are obtained by averaging μ_{dc} computed using only $\text{Re } C_{jj}(t)$ or only $\text{Im } C_{jj}(t)$ [Eq. (5)]. The smoothing procedure described in Sec. III B is applied when considering only $\text{Im } C_{jj}(t)$. At elevated temperatures ($T/\omega_0 \gtrsim 3$), we additionally average HEOM results for two consecutive depths, as discussed in Sec. III C.

Section III F gives an example of numerical instabilities appearing for sufficiently strong g or at sufficiently low T , which prevent us from obtaining reliable HEOM results, e.g., when $\lambda > 1$ or when $T/J < 2$ and $\lambda = 1$ in Fig. 7(b). Our data for $\lambda = 1$ in Figs. 7(a) and 7(b) suggest that μ_{dc} enters saturation on the low-temperature side. If we could lower the temperature further, we would enter the regime of thermally activated transport, in which μ_{dc} grows with T , while we obtain HEOM results only in regimes where μ_{dc} decreases with T . Concerning the temperature dependence of μ_{dc} , we find that the HEOM mobilities at low g and for $\omega_0/J = 1/3$ and 1 are consistent with the recently found scaling $\mu_{dc} \propto T^{-2}$,²⁶ which is shown as a double dashed–dotted line. For stronger coupling and at sufficiently high temperatures, the HEOM mobilities are consistent with the scaling $\mu_{dc} \propto T^{-3/2}$, which is again shown as a double dashed–dotted line.

F. Numerical instabilities for strong electron-phonon interactions and at low temperatures

For stronger interactions, at lower temperatures, and for larger ω_0/J , the numerical instabilities appearing already at relatively short real times (despite employing our specific closing strategy) prevent us from computing the long-time dynamics of $C_{jj}(t)$ and thus μ_{dc} . As an example, in Figs. 8(a) and 8(b), we present our HEOM results in the strong-coupling regime ($\lambda = 2$) for $\omega_0/J = 1$ at a relatively low temperature $T/J = 1$ [Fig. 8(a)] and at an elevated temperature $T/J = 5$ [Fig. 8(b)].

For $T/J = 1$, numerical instabilities appear already for $Jt \gtrsim 3$ and become more pronounced at longer times. The maximum time up to which reliable HEOM results for $C_{jj}(t)$ can be obtained is thus of the same order of magnitude as the maximum time that can be reached in real-time QMC simulations, whose results are shown as full symbols (QMC error bars are omitted here for visual clarity). The inset of Fig. 8(a) shows how the integrals $\int_0^t ds \text{Re } C_{jj}(s)/T$ and $-2 \int_0^t ds \text{Im } C_{jj}(s)$, whose $t \rightarrow +\infty$ limit determines μ_{dc} , evolve as functions of their upper limit t . While the numerical instabilities become amplified when μ_{dc} is computed using only $\text{Im } C_{jj}(t)$, the data using only $\text{Re } C_{jj}(t)$ may suggest that the maximum time $Jt_{\text{max}} = 3$ is sufficiently long to capture the electron's diffusive motion [$\int_0^t ds \text{Re } C_{jj}(s)/T$ reaches a plateau for $2 \leq Jt \leq 3$]. Nevertheless, the corresponding mobility estimate may be unreliable. Namely, as discussed in Ref. 42, for strong interactions and at not too high temperatures, $\text{Re } C_{jj}(t)$ exhibits a series of peaks whose envelope decays over many phonon periods. Our HEOM computations do capture the most prominent peak centered at $t = 0$. Still, the numerical instabilities arise well before the completion of the first phonon period $2\pi/\omega_0$, meaning that the HEOM results fully miss the contributions to μ_{dc} from the peaks at later times. Such contributions may be appreciable because of the slowly decaying envelope, and one may thus expect that the HEOM result underestimates the dc mobility.

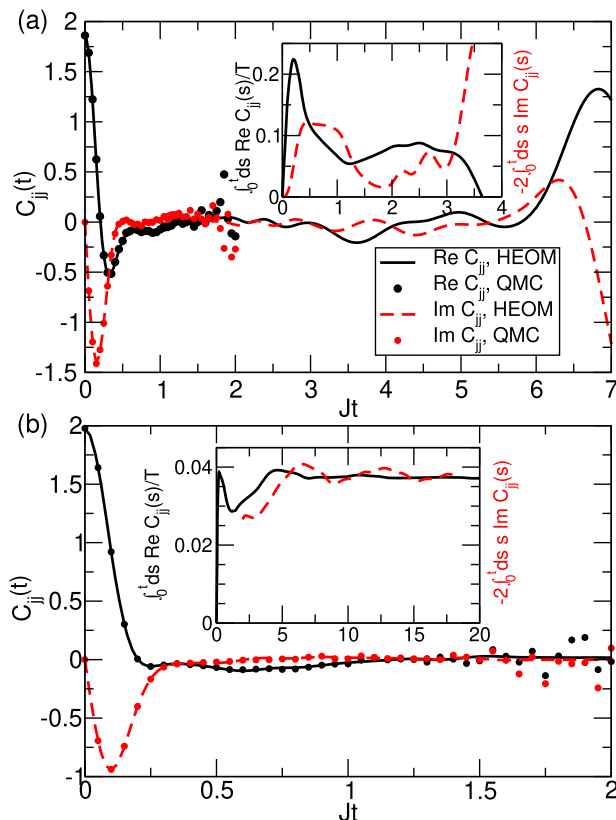


FIG. 8. Time dependence of C_{jj} (in units of J_2) computed using the HEOM method (lines) and the real-time QMC method developed in Ref. 63 (symbols) for $\omega_0/J = 1$, $\lambda = 2$, and (a) $T/J = 1$, (b) $T/J = 5$. Solid (dashed) lines display $\text{Re } C_{jj}(t)$ [$\text{Im } C_{jj}(t)$]. The insets display time evolution of $\int_0^t ds \text{Re } C_{jj}(s)/T$ (solid lines) and $-2 \int_0^t ds \text{Im } C_{jj}(s)$ (dashed lines). The HEOM computations in (a) use $N = 10$ and $D = 8$, while (b) shows the arithmetic average of HEOM results obtained for $N = 7, D = 10$ and $N = 7, D = 11$. QMC simulations in both (a) and (b) use $N = 10$, and the respective data are the courtesy of N. Vukmirović.

For strong interactions and at higher temperatures, we do not observe numerical instabilities [see Fig. 8(b)], and our HEOM method can again reach much longer times than real-time QMC methods. Higher temperatures, in combination with our closing strategy, generally stabilize the HEOM. Since the amplitude of the aforementioned later-time peaks is strongly suppressed at higher temperatures,⁴² the HEOM method may provide reliable results for μ_{dc} . The inset of Fig. 8(b) shows that mobility computations using either $\text{Re } C_{jj}(t)$ or $\text{Im } C_{jj}(t)$ [the latter in conjunction with the moving-average procedure, see the discussion of Fig. 3(b)] lead to virtually the same HEOM result, $\mu_{dc}^{\text{HEOM}} = 0.0375$.

Finally, the very good agreement between the HEOM and QMC results in Figs. 8(a) and 8(b) strongly suggests that the values of D employed in the corresponding HEOM computations are sufficiently large. One may ask themselves whether a larger value of D could mitigate the instabilities observed in Fig. 8(a). Unfortunately, the results of Ref. 101 show that the undamped-mode HEOM cannot be stabilized by further increasing D .

IV. CONCLUSION AND OUTLOOK

We develop the momentum-space HEOM method to compute the real-time current–current correlation function at finite temperature for the 1d Holstein model, which provides us with direct access to its transport properties. By exploiting the decoupling of the $q = 0$ phonon mode and formulating the HEOM in the momentum representation, we greatly reduce the number of variables with respect to existing real-space HEOM implementations. This circumstance has enabled us to obtain results that take into account all important phonon-assisted processes (i.e., D is sufficiently large) on chains that are sufficiently long (i.e., N is sufficiently large) so that the finite-size effects are minimized. Another distinctive feature of our formalism is its specific hierarchy closing strategy [Eq. (13)], which has enabled us to overcome the numerical instabilities inherent to the undamped-mode HEOM formulated on a finite chain and truncated at a finite maximum hierarchy depth. We are thus in a position to provide reliable results for the dc mobility by computing $C_{jj}(t)$ up to quite long real times by which it has almost decayed to zero, i.e., the electronic motion has become diffusive. A detailed analysis of how $C_{jj}(t)$ and, therefore, μ_{dc} depend on N and D suggests that our results for temperature-dependent mobility should be considered with uncertainties typically below 10%. Still, the instabilities remain for strong couplings, at low temperatures, and for large phonon frequencies. In such parameter regimes, we can obtain $C_{jj}(t)$ only up to relatively short real times.

Our momentum-space HEOM method, which has already achieved substantial memory savings with respect to existing real-space HEOM implementations (see Sec. III B), may be combined with advanced propagation techniques based on the tensor formalism^{80,103,121–123} or with on-the-fly filtering techniques¹²⁴ to treat longer chains or larger maximum depths. This could pave the way toward HEOM computations at lower temperatures or stronger interactions. In such parameter regimes, accurate results for electronic dynamics can be obtained using the hierarchy of Davydov's *Ansätze*.^{81,82} However, its current implementations assume that the initial state of the electron–phonon system is factorized and that phonons are in thermal equilibrium with the system with no electrons. While following the electron's dynamics from such a state can provide information on the dc mobility,^{40,83,97} it provides no information on the frequency-dependent mobility, which follows from the current–current correlation function (see Sec. II A). Its computation, in turn, necessitates an appropriate representation of the thermal equilibrium state of the interacting electrons and phonons (see Sec. II B), which has still not been addressed using the hierarchy of Davydov's *Ansätze*, to the best of our knowledge. Our study may motivate an extension of Davydov's *Ansätze* approach to compute equilibrium correlation functions in parameter regimes that are the most challenging for the HEOM method.

We also note that, at least in the limiting case of slow phonons, an interesting physical picture for the finite-frequency peak we observe in the optical response may be constructed based on the transient localization scenario.¹²⁵ While this approach was originally devised to study transport limited by intermolecular vibrations modulating the hopping amplitude, its more recent refinements¹²⁶ and applications¹²⁷ have considered the Holstein model in the limit of vanishing carrier density. A more detailed study in this direction might be the subject of future work. We finally note that the method

proposed in this manuscript cannot be directly applied to study carrier transport limited by the nonlocal electron–phonon interaction (e.g., the Peierls model).¹²⁸ The developments reported here crucially lean on the fact that the current operator j is a purely electronic operator [see Eq. (3)]. In other words, the current–current correlation function $C_{jj}(t)$ can be computed using only the electronic RDM (see Sec. II B). On the other hand, when the electron interacts linearly with intermolecular phonons modulating the hopping integral, the current operator is a mixed electron–phonon operator.^{37,100} This means that $C_{jj}(t)$ cannot be computed using only the electronic RDM. One should thus devise a procedure to retrieve correlation functions involving phonon operators from the HEOM formalism. While this complex issue is well beyond the scope of this study, the herein developed momentum-space representation of the HEOM will remain beneficial to the overall computational performance of such a procedure.

SUPPLEMENTARY MATERIAL

See the supplementary material for the details of HEOM computations [values of N and D employed, reference HEOM results for the electron's kinetic energy and moments of $C_{jj}(\omega)$, as well as the relative accuracy with which different sum rules are satisfied]. The supplementary material contains all the information needed to use our numerical data that are deposited on the Zenodo platform (see Ref. 117).

ACKNOWLEDGMENTS

The author acknowledges Nenad Vukmirović, Darko Tanasković, and Petar Mitrić for numerous insightful and stimulating discussions. The author acknowledges funding provided by the Institute of Physics Belgrade through a grant from the Ministry of Science, Technological Development, and Innovations of the Republic of Serbia. Computational time on the ARIS supercomputing facility (GRNET, Athens, Greece) was granted by the NI4OS-Europe network under the CoNTraSt project (Open Call 2022, Project No. ni4os002). Computations were also partially performed on the PARADOX-IV supercomputing facility at the Scientific Computing Laboratory, National Center of Excellence for the Study of Complex Systems, Institute of Physics Belgrade.

AUTHOR DECLARATIONS

Conflict of Interest

The author has no conflicts to disclose.

Author Contributions

Veljko Janković: Conceptualization (lead); Data curation (lead); Formal analysis (lead); Investigation (lead); Methodology (lead); Validation (lead); Visualization (lead); Writing – original draft (lead).

DATA AVAILABILITY

The data that support the findings of this study are openly available on the Zenodo platform at <http://doi.org/10.5281/zenodo.8068547>.¹¹⁷

APPENDIX A: DERIVATION OF THE HEOM FOR THE REAL-TIME CURRENT-CURRENT CORRELATION FUNCTION

The decoupling of the $q = 0$ phonon mode from the rest of the system permits us to consider Hamiltonians $H'_{\text{ph}} = \sum'_q \omega_q b_q^\dagger b_q$ and $H'_{\text{e-ph}} = \sum'_q V_q B_q$ without the $q = 0$ term, which is signaled by primes. The Feynman–Vernon influence functional theory¹²⁹ implies that the only phonon quantity that determines the dynamics of $\iota(t)$ is the equilibrium free-phonon correlation function (we assume $t > 0$ and $q_2, q_1 \neq 0$),

$$C_{q_2 q_1}(t) = \text{Tr}'_{\text{ph}} \left\{ B_{q_2}^{(I)}(t) B_{q_1} \frac{e^{-\beta H'_{\text{ph}}}}{Z'_{\text{ph}}} \right\} \\ = \delta_{q_1, -q_2} \sum_{m=0}^1 c_{q_2 m} e^{-\mu_{q_2} m t}. \quad (\text{A1})$$

The time dependence in Eq. (A1) is in the interaction picture [signaled by the superscript (I)], $B_q^{(I)}(t) = e^{iH'_{\text{ph}} t} B_q e^{-iH'_{\text{ph}} t}$, $Z'_{\text{ph}} = \text{Tr}'_{\text{ph}} e^{-\beta H'_{\text{ph}}}$ is the free-phonon partition sum, while

$$c_{q0} = \left(\frac{g}{\sqrt{N}} \right)^2 \frac{1}{1 - e^{-\beta \omega_q}}, \quad \mu_{q0} = +i\omega_q, \quad (\text{A2})$$

$$c_{q1} = \left(\frac{g}{\sqrt{N}} \right)^2 \frac{1}{e^{\beta \omega_q} - 1}, \quad \mu_{q1} = -i\omega_q. \quad (\text{A3})$$

The partial trace over phonons in Eq. (8) is performed in the same manner as in Refs. 96, 98, 99, and 108, and the final result for ι in the interaction picture reads as

$$\iota^{(I)}(t) = \mathcal{T} e^{-[\Phi_1(t) + \Phi_2(\beta) + \Phi_3(t, \beta)]} j \frac{e^{-\beta H_c}}{Z_e}. \quad (\text{A4})$$

Here, $Z_e = Z/Z'_{\text{ph}}$ is the electronic partition sum [Eq. (12)], while the influence phases are given as

$$\Phi_1(t) = \sum'_{qm} \int_0^t ds_2 \int_0^{s_2} ds_1 V_q^{(I)}(s_2)^\times e^{-\mu_{qm}(s_2 - s_1)} \\ \times \left[\frac{c_{qm} + c_{q\bar{m}}}{2} V_{-q}^{(I)}(s_1)^\times + \frac{c_{qm} - c_{q\bar{m}}}{2} V_{-q}^{(I)}(s_1)^\circ \right], \quad (\text{A5})$$

$$\Phi_2(\beta) = -\sum'_{qm} \int_0^\beta d\tau_2 \int_0^{\tau_2} d\tau_1 C \bar{V}_{-q}(\tau_1) \\ \times e^{i\mu_{qm}(\tau_2 - \tau_1)} c_{qm} C \bar{V}_{-q}(\tau_2), \quad (\text{A6})$$

$$\Phi_3(t, \beta) = -i \sum'_{qm} \int_0^t ds \int_0^\beta d\tau V_q^{(I)}(s)^\times \\ \times e^{-\mu_{qm}s} e^{i\mu_{qm}(\beta - \tau)} c_{qm} C \bar{V}_{-q}(\tau). \quad (\text{A7})$$

The influence phase $\Phi_1(t)$ describes the pure real-time evolution, and the hyperoperators V^\times and V° entering Eq. (A5) act on an arbitrary operator O as $V^\times O = [V, O]$ (commutator) and $V^\circ O = \{V, O\}$ (anticommutator), respectively. We define $\bar{m} = 1$ for $m = 0$ and vice versa. The influence phase $\Phi_2(\beta)$ represents the pure imaginary-time evolution, while $\Phi_3(t, \beta)$ takes into account the contributions

mixing the real-time and imaginary-time evolutions. The imaginary time-dependent operator in the interaction picture is defined as $\bar{V}(\tau) = e^{H_c \tau} V e^{-H_c \tau}$, while the hyperoperator $C V$ appearing in Eqs. (A6) and (A7) acts on an arbitrary operator O as $C V O = O V$. The time ordering symbol \mathcal{T} imposes the following hyperoperator ordering: the hyperoperators depending on real time act after the imaginary time-dependent hyperoperators; the arguments of real time-dependent hyperoperators are chronologically ordered, while the arguments of imaginary time-dependent hyperoperators are anti-chronologically ordered. This ensures that the general term in the expansion of Eq. (A4) is of the form

$$V_{q_n}^{(I)}(s_n)^{\pi_n} \dots V_{q_1}^{(I)}(s_1)^{\pi_1} j \frac{e^{-\beta H_c}}{Z_e} \bar{V}_{p_m}(\tau_m) \dots \bar{V}_{p_1}(\tau_1),$$

where $n + m$ is even, $\pi_1, \dots, \pi_n \in \{\times, \circ\}$, $t \geq s_n \geq \dots \geq s_1 \geq 0$, $\beta \geq \tau_m \geq \dots \geq \tau_1 \geq 0$, and $q_n + \dots + q_1 + p_m + \dots + p_1 = 0$.

Starting from Eq. (A4), the HEOM [Eq. (9)] is formulated in the standard manner.^{88,96} The ADO $\iota_n^{(n)}$ is defined (in the interaction picture) as

$$\iota_n^{(I, n)}(t) = f(\mathbf{n}) \mathcal{T} \prod'_{qm} \left\{ i \int_0^t ds e^{-\mu_{qm}(t-s)} \left[\frac{c_{qm} + c_{q\bar{m}}}{2} V_{-q}^{(I)}(s)^\times \right. \right. \\ \left. \left. + \frac{c_{qm} - c_{q\bar{m}}}{2} V_{-q}^{(I)}(s)^\circ \right] + e^{-\mu_{qm} t} \int_0^\beta d\tau e^{i\mu_{qm}(\beta - \tau)} \right. \\ \left. \times c_{qm} C \bar{V}_{-q}(\tau) \right\}^{n_{qm}} e^{-[\Phi_1(t) + \Phi_2(\beta) + \Phi_3(t, \beta)]} j \frac{e^{-\beta H_c}}{Z_e}. \quad (\text{A8})$$

The rescaling factor $f(\mathbf{n})$ reads as¹²⁴

$$f(\mathbf{n}) = \prod'_{qm} [c_{qm}^{n_{qm}} n_{qm}!]^{-1/2}. \quad (\text{A9})$$

Equation (A8) explicitly shows that $\iota_n^{(n)}$ decreases the momentum of the electronic subsystem by $k_n = \sum'_{qm} q n_{qm}$, meaning that only N matrix elements $\langle k | \iota_n^{(n)} | k + k_n \rangle$ connecting the free-electron states whose momenta differ by k_n assume nonzero values.

Setting $t = 0$ in Eq. (A8) gives the following initial condition for the real-time HEOM:

$$\iota_n^{(n)}(0) = j f(\mathbf{n}) \mathcal{T} \prod'_{qm} \left\{ \int_0^\beta d\tau e^{i\mu_{qm}(\beta - \tau)} c_{qm} C \bar{V}_{-q}(\tau) \right\}^{n_{qm}} \\ \times e^{-\Phi_2(\beta)} \frac{e^{-\beta H_c}}{Z_e}. \quad (\text{A10})$$

In Eq. (A10), we may move the current operator to the left-most position because all the hyperoperators act on the operator $j e^{-\beta H_c} / Z_e$ from the right. Similarly to Ref. 96, one may now recognize that $\iota_n^{(n)}(0)$ is the product of operator j and the ADO $\sigma_n^{(n)}(\beta)$, which is one of the components in the hierarchical representation of the (unnormalized) reduced density operator,

$$\sigma_0^{(0)}(\beta) = \mathcal{T} e^{-\Phi_2(\beta)} e^{-\beta H_c}. \quad (\text{A11})$$

To actually evaluate $\sigma_n^{(n)}(\beta)$ and the normalization constant $Z_e = \text{Tr}_e \sigma_0^{(0)}(\beta)$, we consider the imaginary time-dependent analog of Eq. (A11),

$$\sigma_0^{(0)}(\tau) = \mathcal{T} e^{-\Phi_2(\tau)} e^{-\tau H_e}, \quad (\text{A12})$$

where $0 \leq \tau \leq \beta$. As discussed in detail in Ref. 96, Eq. (A12) can be transformed into the imaginary-time HEOM given in Eq. (10).

APPENDIX B: DERIVATION OF THE CLOSING SCHEME IN EQ. (13)

Here, we provide a detailed derivation of our strategy for hierarchy closing that is embodied in Eq. (13).

Let us consider the equation for $\langle k | l_{\mathbf{D}}^{(D)}(t) | k + k_{\mathbf{D}} \rangle$ at the maximum depth D , which contains the ADOs $l_{\mathbf{D}}^{(D+1)}$ at depth $D + 1$. The equation of motion for $l_{\mathbf{D}}^{(D+1)}$ contains ADOs at depth $D + 2$, which will be set to zero. Moreover, its coupling with the ADOs at depth D will be restricted by assuming it couples back only to the original ADO $l_{\mathbf{D}}^{(D)}$ we are considering. With these assumptions, the equation at depth $D + 1$ reads as

$$\begin{aligned} \partial_t \langle k | l_{\mathbf{D}}^{(D+1)}(t) | k + k_{\mathbf{D}} + q \rangle &= -i(\varepsilon_k - \varepsilon_{k+k_{\mathbf{D}}+q} + \mu_{\mathbf{D}}) \langle k | l_{\mathbf{D}}^{(D+1)}(t) | k + k_{\mathbf{D}} + q \rangle \\ &+ i\sqrt{(1 + D_{qm})c_{qm}} \langle k + q | l_{\mathbf{D}}^{(D)}(t) | k + k_{\mathbf{D}} + q \rangle \\ &- i\sqrt{1 + D_{qm}} \frac{c_{q\bar{m}}}{\sqrt{c_{qm}}} \langle k | l_{\mathbf{D}}^{(D)}(t) | k + k_{\mathbf{D}} \rangle. \end{aligned} \quad (\text{B1})$$

Using the initial condition $\langle k | l_{\mathbf{D}}^{(D+1)}(0) | k + k_{\mathbf{D}} + q \rangle = 0$, which is appropriate because the imaginary-time HEOM in Eq. (10) is truncated at the maximum depth D , Eq. (B1) can be formally integrated to yield

$$\begin{aligned} \langle k | l_{\mathbf{D}}^{(D+1)}(t) | k + k_{\mathbf{D}} + q \rangle &= i\sqrt{1 + D_{qm}} \int_0^t dt_1 e^{-i(\varepsilon_k - \varepsilon_{k+k_{\mathbf{D}}+q} + \mu_{\mathbf{D}})(t-t_1)} \\ &\times \left[\sqrt{c_{qm}} e^{-i(\varepsilon_{k+q} - \varepsilon_{k+k_{\mathbf{D}}+q} + \mu_{\mathbf{D}})t_1} f_1(t_1) \right. \\ &\left. - \frac{c_{q\bar{m}}}{\sqrt{c_{qm}}} e^{-i(\varepsilon_k - \varepsilon_{k+k_{\mathbf{D}}+q} + \mu_{\mathbf{D}})t_1} f_2(t_1) \right]. \end{aligned} \quad (\text{B2})$$

We have introduced the auxiliary function $f_1(t)$ representing the slowly changing part of the ADO at depth D by factoring out the oscillating (rapidly changing) part as follows:

$$\langle k + q | l_{\mathbf{D}}^{(D)}(t) | k + k_{\mathbf{D}} + q \rangle = e^{-i(\varepsilon_{k+q} - \varepsilon_{k+k_{\mathbf{D}}+q} + \mu_{\mathbf{D}})t} f_1(t), \quad (\text{B3})$$

and similarly for $f_2(t)$. Under the integral entering Eq. (B2), we introduce the variable change $s = t - t_1$ and subsequently apply the Markovian approximation $f_{1/2}(t-s) \approx f_{1/2}(t)$ to the slowly changing part. As a result, we obtain

$$\begin{aligned} \langle k | l_{\mathbf{D}}^{(D+1)}(t) | k + k_{\mathbf{D}} + q \rangle &= i\sqrt{(1 + D_{qm})} \left\{ \sqrt{c_{qm}} \int_0^t ds e^{-i[\varepsilon_k - \varepsilon_{k+q} + (\delta_{m0} - \delta_{m1})\omega_q]s} \right. \\ &\times \langle k + q | l_{\mathbf{D}}^{(D)}(t) | k + k_{\mathbf{D}} + q \rangle - \frac{c_{q\bar{m}}}{\sqrt{c_{qm}}} \\ &\times \int_0^t ds e^{-i[\varepsilon_{k+k_{\mathbf{D}}} - \varepsilon_{k+k_{\mathbf{D}}+q} + (\delta_{m0} - \delta_{m1})\omega_q]s} \\ &\left. \times \langle k | l_{\mathbf{D}}^{(D)}(t) | k + k_{\mathbf{D}} \rangle \right\}. \end{aligned} \quad (\text{B4})$$

Using the last result, we write one of the terms that couple the equations at depths D and $D + 1$ [the third term on the RHS of Eq. (9)] as follows:

$$\begin{aligned} -i \sum'_{qm} \sqrt{(1 + D_{qm})c_{qm}} \langle k | l_{\mathbf{D}}^{(D+1)}(t) | k + k_{\mathbf{D}} + q \rangle &= \sum'_{qm} (1 + D_{qm})c_{qm} \int_0^t ds e^{-i[\varepsilon_k - \varepsilon_{k+q} + (\delta_{m0} - \delta_{m1})\omega_q]s} \\ &\times \langle k + q | l_{\mathbf{D}}^{(D)}(t) | k + k_{\mathbf{D}} + q \rangle \\ - \sum'_{qm} (1 + D_{qm})c_{q\bar{m}} \int_0^t ds e^{-i[\varepsilon_{k+k_{\mathbf{D}}} - \varepsilon_{k+k_{\mathbf{D}}+q} + (\delta_{m0} - \delta_{m1})\omega_q]s} &\times \langle k | l_{\mathbf{D}}^{(D)}(t) | k + k_{\mathbf{D}} \rangle. \end{aligned} \quad (\text{B5})$$

The second term on the RHS of Eq. (9) can be written and analyzed in an analogous manner.

To evaluate Eq. (B5), we have to know the detailed structure of the vector \mathbf{D} that characterizes the ADOs at the maximum depth D . We also observe that the second term on the RHS of Eq. (B5) depends only on the quantity $\langle k | l_{\mathbf{D}}^{(D)}(t) | k + k_{\mathbf{D}} \rangle$ whose differential equation we are considering. On the other hand, the matrix elements of $l_{\mathbf{D}}^{(D)}$ entering the first term on the RHS of Eq. (B5) depend on q . This term may be neglected by invoking a sort of random phase approximation: the matrix elements $\langle k + q | l_{\mathbf{D}}^{(D)}(t) | k + k_{\mathbf{D}} + q \rangle$ are typically oscillatory functions of q , and one may then argue that their average over all momenta q is close to zero. A similar approximation is also at the heart of the momentum-average approximation.^{44,45} In the remaining terms, we (i) exploit that for dispersionless optical phonons ($\omega_q \equiv \omega_0$), c_{qm} does not depend on q , (ii) neglect the contributions containing D_{qm} , and (iii) evaluate the remaining integral in Eq. (B5) by invoking the so-called adiabatic approximation, in which the upper limit t of the integral is replaced by $+\infty$. We furthermore keep only the real part of the integral evaluated so that

$$\int_0^t ds e^{-i\Omega s} \approx \int_0^{+\infty} ds e^{-i\Omega s} \approx \pi\delta(\Omega). \quad (\text{B6})$$

This way, we introduce physically motivated damping of the ADOs at the terminal level of the hierarchy. The damping effectively replaces higher-order phonon-assisted processes that are not explicitly taken into account, while phonon-assisted processes involving

at most D phonons are completely taken into account through the HEOM. In the resulting expressions, we recognize the second-order approximation for carrier scattering time out of the free-electron state $|k\rangle$,

$$\frac{1}{\tau_k} = 2\pi \frac{g^2}{N} \sum_q' \left[(1 - e^{-\beta\omega_0})^{-1} \delta(\varepsilon_k - \varepsilon_{k-q} - \omega_0) + (e^{\beta\omega_0} - 1)^{-1} \delta(\varepsilon_k - \varepsilon_{k-q} + \omega_0) \right], \quad (\text{B7})$$

for which an analytical expression in the limit of infinite N has been derived in Refs. 42 and 26. Even though we perform HEOM computations on finite chains, in Eq. (13) we use the value of τ_k obtained in the infinite-chain limit. We believe that such a procedure is appropriate because we invested great effort to perform computations with a sufficiently large N .

Instead of neglecting the term containing D_{qm} in Eq. (B5), we may have replaced D_{qm} by its average value $D/[2(N-1)]$ at depth D [the sum $\sum_{qm}' D_{qm}$, which is equal to D , contains $2(N-1)$ terms]. Such a replacement would lead to larger damping factors at depth D , which may have already been overestimated by using the value of τ_k in the infinite-chain limit. Since the substitution $D_{qm} \rightarrow D/[2(N-1)]$ does not improve the stability of the hierarchy at low temperatures, for strong interactions, and for fast phonons, we decided not to use it in our computations.

APPENDIX C: SUM RULES

The zeroth-moment sum rule states that

$$M_0 = \int_{-\infty}^{+\infty} \frac{d\omega}{2\pi} C_{ij}(\omega) = \langle j^2 \rangle. \quad (\text{C1})$$

Since j is a purely electronic operator, the evaluation of M_0 necessitates only the operator $i_0^{(0)}(t=0)$,

$$M_0 = -2J \sum_k \sin(k) \langle k | i_0^{(0)}(t=0) | k \rangle \equiv C_{ij}(t=0). \quad (\text{C2})$$

On the other hand, to evaluate M_n for $n \geq 1$, we need all ADOs $i_n^{(n)}(t=0)$ at depths starting from 0 and concluding with n . The first-moment sum rule is

$$M_1 = \int_{-\infty}^{+\infty} \frac{d\omega}{2\pi} \omega C_{ij}(\omega) = \langle [j, H] j \rangle. \quad (\text{C3})$$

It can be shown that

$$[j, H] = [j, H_{e-\text{ph}}] = -2J \sum_{q \neq 0, p} [\sin(p+q) - \sin(p)] |p+q\rangle \langle p| B_q. \quad (\text{C4})$$

Therefore,

$$M_1 = -2J \sum_{q \neq 0, p} [\sin(p+q) - \sin(p)] \times \left\langle p \left| \text{Tr}_{\text{ph}} \left\{ B_q j \frac{e^{-\beta H}}{Z} \right\} \right| p+q \right\rangle. \quad (\text{C5})$$

The second-moment sum rule is somewhat more cumbersome to evaluate

$$M_2 = \int_{-\infty}^{+\infty} \frac{d\omega}{2\pi} \omega^2 C_{ij}(\omega) = \langle [[j, H], H] j \rangle. \quad (\text{C6})$$

We separately evaluate the three contributions to the double commutator

$$[[j, H], H] = \underbrace{[[j, H], H_e]}_{K_1} + \underbrace{[[j, H], H_{\text{ph}}]}_{K_2} + \underbrace{[[j, H], H_{e-\text{ph}}]}_{K_3}, \quad (\text{C7})$$

starting from the result for $[j, H]$ embodied in Eq. (C4). We obtain

$$K_1 = -2J \sum_{q \neq 0, p} [\sin(p+q) - \sin(p)] (\varepsilon_p - \varepsilon_{p+q}) |p+q\rangle \langle p| B_q, \quad (\text{C8})$$

$$K_2 = -2J \sum_{q \neq 0, p} [\sin(p+q) - \sin(p)] \omega_q \frac{g}{\sqrt{N}} \times (|p+q\rangle \langle p| b_q - |p+q\rangle \langle p| b_{-q}^\dagger), \quad (\text{C9})$$

$$K_3 = -2J \sum_{\substack{q_1 \neq 0 \\ q_2 \neq 0}} \sum_p |p+q_1+q_2\rangle \langle p| B_{q_2} B_{q_1} \times [\sin(p+q_1+q_2) - \sin(p+q_1) - \sin(p+q_2) + \sin(p)]. \quad (\text{C10})$$

In addition to the single-phonon-assisted ADO $\text{Tr}_{\text{ph}} \{ B_q j \frac{e^{-\beta H}}{Z} \}$, the evaluation of $\langle K_1 j \rangle$, $\langle K_2 j \rangle$, and $\langle K_3 j \rangle$ necessitates their contributions describing phonon absorption and emission, which stem from the definition $B_q = \frac{g}{\sqrt{N}} (b_q + b_{-q}^\dagger)$, as well as the two-phonon-assisted ADO $\text{Tr}_{\text{ph}} \{ B_{q_2} B_{q_1} j \frac{e^{-\beta H}}{Z} \}$. In the following, we compute these (electronic) operators using the ideas developed in Refs. 130 and 131.

Denoting $\frac{e^{-\beta H}}{Z} = \rho_T^{\text{eq}}$, we can write

$$j \rho_T^{\text{eq}} = \mathcal{T} \exp \left[- \int_0^\beta d\tau \sum_q' C \bar{V}_q(\tau) C \bar{B}_q(\tau) \right] \times j \frac{e^{-\beta H_e}}{Z_e} \frac{e^{-\beta H_{\text{ph}}}}{Z_{\text{ph}}}. \quad (\text{C11})$$

To evaluate phonon-assisted contributions, we introduce auxiliary fields $f_q(\tau)$ and consider their functional

$$j \rho_{T,f}^{\text{eq}} = \mathcal{T} \exp \left[- \int_0^\beta d\tau \sum_q' C [\bar{V}_q(\tau) + f_q(\tau)] C \bar{B}_q(\tau) \right] \times j \frac{e^{-\beta H_e}}{Z_e} \frac{e^{-\beta H_{\text{ph}}}}{Z_{\text{ph}}}. \quad (\text{C12})$$

Defining

$$j \rho_f^{\text{eq}} = j \text{Tr}_{\text{ph}} \rho_{T,f}^{\text{eq}}, \quad (\text{C13})$$

one can show that

$$\left[j \frac{\delta \rho_f^{\text{eq}}}{\delta f_q(\beta)} \right]_{f=0} = -\text{Tr}_{\text{ph}} \{ B_q j \rho_T^{\text{eq}} \}, \quad (\text{C14})$$

$$\left[j \frac{\delta^2 \rho_f^{\text{eq}}}{\delta f_{q_2}(\beta) \delta f_{q_1}(\beta)} \right]_{f=0} = \text{Tr}_{\text{ph}} \{ B_{q_2} B_{q_1} j \rho_T^{\text{eq}} \}. \quad (\text{C15})$$

On the other hand,

$$\rho_f^{\text{eq}} = \mathcal{T} e^{-\Phi_{2,f}(\beta)} \frac{e^{-\beta H_c}}{Z_e}, \quad (\text{C16})$$

where the influence phase $\Phi_{2,f}(\beta)$ is a functional of auxiliary fields $f_q(\tau)$ [cf. Eq. (A6)],

$$\begin{aligned} \Phi_{2,f}(\beta) = & - \int_0^\beta d\tau_2 \int_0^{\tau_2} d\tau_1 \sum_{qm}^C [\bar{V}_{-q}(\tau_1) + f_{-q}(\tau_1)] \\ & \times e^{i\mu_{qm}(\tau_2-\tau_1)} c_{qm}^C [\bar{V}_q(\tau_2) + f_q(\tau_2)]. \end{aligned} \quad (\text{C17})$$

It then follows that

$$\frac{\delta \rho_f^{\text{eq}}}{\delta f_{q_1}(\beta)} = \mathcal{T} \left\{ - \frac{\delta \Phi_{2,f}(\beta)}{\delta f_{q_1}(\beta)} e^{-\Phi_{2,f}(\beta)} \right\} \frac{e^{-\beta H_c}}{Z_e}, \quad (\text{C18})$$

$$\begin{aligned} \frac{\delta^2 \rho_f^{\text{eq}}}{\delta f_{q_2}(\beta) \delta f_{q_1}(\beta)} & = \mathcal{T} \left\{ \left[- \frac{\delta^2 \Phi_{2,f}(\beta)}{\delta f_{q_2}(\beta) \delta f_{q_1}(\beta)} + \frac{\delta \Phi_{2,f}(\beta)}{\delta f_{q_2}(\beta)} \frac{\delta \Phi_{2,f}(\beta)}{\delta f_{q_1}(\beta)} \right] e^{-\Phi_{2,f}(\beta)} \right\} \\ & \times \frac{e^{-\beta H_c}}{Z_e}, \end{aligned} \quad (\text{C19})$$

The explicit evaluation of the functional derivatives produces

$$\frac{\delta \Phi_{2,f}(\beta)}{\delta f_{q_1}(\beta)} = - \int_0^\beta d\tau \sum_m c_{q_1 m} e^{i\mu_{q_1 m}(\beta-\tau)} C [\bar{V}_{-q_1}(\tau) + f_{-q_1}(\tau)], \quad (\text{C20})$$

$$\frac{\delta^2 \Phi_f(\beta)}{\delta f_{q_2}(\beta) \delta f_{q_1}(\beta)} = -\delta_{q_2, -q_1} \sum_m c_{q_1 m}. \quad (\text{C21})$$

Using the definition of ADOs $t_n^{(n)}$ at $t=0$ [Eq. (A8)] and rescaling factors $f(\mathbf{n})$ [Eq. (A9)], we finally obtain

$$\text{Tr}_{\text{ph}} \{ B_q j \rho_T^{\text{eq}} \} = - \sum_m \frac{1}{f(\mathbf{0}_{qm}^+)} t_{\mathbf{0}_{qm}^+}^{(1)}(t=0), \quad (\text{C22})$$

$$\begin{aligned} \text{Tr}_{\text{ph}} \{ B_{q_2} B_{q_1} \rho_T^{\text{eq}} \} & = \delta_{q_2, -q_1} \left(\sum_m c_{q_1 m} \right) t_{\mathbf{0}}^{(0)}(t=0) + \sum_{m_2 m_1} \\ & \times \frac{1}{f(\mathbf{0}_{(q_1 m_1), (q_2 m_2)}^{++})} t_{\mathbf{0}_{(q_1 m_1), (q_2 m_2)}^{++}}^{(2)}(t=0). \end{aligned} \quad (\text{C23})$$

The contributions that differentiate between absorption and emission of a single phonon are most straightforwardly obtained by explicitly setting up an equation of motion for such processes and comparing the kinetic term in the equation thus obtained with the kinetic term in Eq. (9). This procedure yields

$$\frac{g}{\sqrt{N}} \text{Tr}_{\text{ph}} \{ b_q j \rho_T^{\text{eq}} \} = - \frac{1}{f(\mathbf{0}_{q0}^+)} t_{\mathbf{0}_{q0}^+}^{(1)}(t=0), \quad (\text{C24})$$

$$\frac{g}{\sqrt{N}} \text{Tr}_{\text{ph}} \{ b_{-q}^\dagger j \rho_T^{\text{eq}} \} = - \frac{1}{f(\mathbf{0}_{q1}^+)} t_{\mathbf{0}_{q1}^+}^{(1)}(t=0). \quad (\text{C25})$$

The final result for the first-moment sum rule reads as

$$\begin{aligned} M_1 = & 2J \sum_{q \neq 0, p} \sum_m \frac{\sin(p+q) - \sin(p)}{f(\mathbf{0}_{qm}^+)} \\ & \times \langle p | t_{\mathbf{0}_{qm}^+}^{(1)}(t=0) | p+q \rangle. \end{aligned} \quad (\text{C26})$$

The final result for the second-moment sum rule reads as

$$M_2 = \langle K_{1j} \rangle + \langle K_{2j} \rangle + \langle K_{3j} \rangle, \quad (\text{C27})$$

where

$$\begin{aligned} \langle K_{1j} \rangle = & 2J \sum_{q \neq 0, p} \sum_m \frac{\sin(p+q) - \sin(p)}{f(\mathbf{0}_{qm}^+)} (\varepsilon_p - \varepsilon_{p+q}) \\ & \times \langle p | t_{\mathbf{0}_{qm}^+}^{(1)}(t=0) | p+q \rangle, \end{aligned} \quad (\text{C28})$$

$$\begin{aligned} \langle K_{2j} \rangle = & 2J \sum_{q \neq 0, p} \sum_m (-1)^m \frac{\sin(p+q) - \sin(p)}{f(\mathbf{0}_{qm}^+)} \omega_q \\ & \times \langle p | t_{\mathbf{0}_{qm}^+}^{(1)}(t=0) | p+q \rangle, \end{aligned} \quad (\text{C29})$$

and

$$\begin{aligned} \langle K_{3j} \rangle = & -2J \sum_{q \neq 0, p} \sum_m 4 \sin(p) \sin^2(q/2) c_{qm} \langle p | t_{\mathbf{0}}^{(0)}(t=0) | p \rangle \\ & - 2J \sum_{\substack{q_2, q_1 \neq 0 \\ p}} \sum_{m_2 m_1} \frac{\langle p | t_{\mathbf{0}_{(q_1 m_1), (q_2 m_2)}^{++}}^{(2)}(t=0) | p+q_1+q_2 \rangle}{f(\mathbf{0}_{(q_1 m_1), (q_2 m_2)}^{++})} \\ & \times [\sin(p+q_1+q_2) - \sin(p+q_1) - \sin(p+q_2) + \sin(p)]. \end{aligned} \quad (\text{C30})$$

APPENDIX D: OPTICAL SUM RULE AND FINITE-SIZE EFFECTS

We find that the relative accuracy with which the OSR is satisfied increases with increasing N , see Sec. III C. This observation suggests that the OSR formulated in Eq. (16) is strictly valid only in the long-chain limit, while on finite chains there are finite-size corrections that vanish as $N \rightarrow \infty$. In the following, we provide a derivation of the OSR for finite N , identify the finite-size corrections, and demonstrate that they vanish in the long-chain limit.

Let us start by noting that the current operator on an N -site chain, defined in Eq. (3), may be expressed in the site basis as

$$j = iJ \sum_{m=0}^{N-1} (|m\rangle \langle m \oplus 1| - |m \oplus 1\rangle \langle m|). \quad (\text{D1})$$

The cyclic addition $\oplus [a \oplus b = (a+b) \bmod N]$ takes into account that sites 0 and $N-1$ are first neighbors because of the periodic boundary conditions. Our derivation of the OSR makes use of the continuity equation

$$\tilde{j} = \frac{dP}{dt} = -i[P, H], \quad (\text{D2})$$

where the polarization operator (in the site basis) is given as

$$P = -\sum_{m=0}^{N-1} m|m\rangle\langle m|. \quad (\text{D3})$$

While the current operators \tilde{j} and j are identical in the infinite-chain limit, their difference on a finite chain reads as

$$\tilde{j} - j = -i\widehat{P}_{N-1,0}, \quad (\text{D4})$$

where

$$\widehat{P}_{N-1,0} = N(|N-1\rangle\langle 0| - |0\rangle\langle N-1|). \quad (\text{D5})$$

Our derivation starts from the integral $I = \int_{-\infty}^{+\infty} d\omega \text{Re}\mu_{ac}(\omega)$, whose integrand is expressed using the first equality in Eq. (4). Substituting $C_{jj}(\omega)$ in terms of $C_{jj}(t)$, writing the resulting expression in the eigenbasis $\{|\alpha\rangle\}$ of the full Hamiltonian H ($H|\alpha\rangle = E_\alpha|\alpha\rangle$), and performing the integrations over time and frequency, we obtain

$$I = \pi \sum_{\alpha'\alpha} \frac{\langle \alpha'|j|\alpha\rangle\langle \alpha|j|\alpha'\rangle}{E_\alpha - E_{\alpha'}} \frac{e^{-\beta E_{\alpha'}} - e^{-\beta E_\alpha}}{Z}. \quad (\text{D6})$$

We can eliminate the energy difference $E_\alpha - E_{\alpha'}$ in the denominator of each term by expressing one of the current operators using the continuity equation [Eq. (D2)]. We should, however, take into account the finite-size correction entering Eq. (D4). We then obtain

$$\begin{aligned} I &= -i\pi \sum_{\alpha'\alpha} \langle \alpha'|P|\alpha\rangle\langle \alpha|j|\alpha'\rangle \frac{e^{-\beta E_{\alpha'}} - e^{-\beta E_\alpha}}{Z} \\ &\quad + i\pi \int \sum_{\alpha'\alpha} \frac{\langle \alpha'|\widehat{P}_{N-1,0}|\alpha\rangle\langle \alpha|j|\alpha'\rangle}{E_\alpha - E_{\alpha'}} \frac{e^{-\beta E_{\alpha'}} - e^{-\beta E_\alpha}}{Z} \\ &= I_1 + I_2. \end{aligned} \quad (\text{D7})$$

The term I_1 can then be written as

$$I_1 = -i\pi \text{Tr} \left\{ [P, j] \frac{e^{-\beta H}}{Z} \right\}. \quad (\text{D8})$$

The commutator $[P, j]$, where both operators are defined on a finite chain, is equal to

$$[P, j] = -iH_e - i\widehat{P}_{N-1,0}, \quad (\text{D9})$$

so that

$$\begin{aligned} I_1 &= -\pi \text{Tr}_e \left\{ H_e \frac{\sigma_0^{(0)}(\beta)}{Z_e} \right\} - \pi \int \text{Tr}_e \left\{ \widehat{P}_{N-1,0} \frac{\sigma_0^{(0)}(\beta)}{Z_e} \right\} \\ &= I_{1,1} + I_{1,2}. \end{aligned} \quad (\text{D10})$$

While the term $I_{1,1}$ alone gives the desired result for the OSR ($I = -\pi\langle H_e \rangle$), the terms $I_{1,2}$ and I_2 are finite-size corrections. The

term I_2 can be transformed by applying the steps that led to Eq. (D6) in the reverse order, which gives

$$\begin{aligned} I_2 &= \int_{-\infty}^{+\infty} d\omega \frac{1 - e^{-\beta\omega}}{2\omega} \int_{-\infty}^{+\infty} dt e^{i\omega t} \\ &\quad \times \text{Tr} \left\{ e^{iHt} \widehat{P}_{N-1,0} e^{-iHt} j \frac{e^{-\beta H}}{Z} \right\} \\ &= \int_{-\infty}^{+\infty} d\omega \frac{1 - e^{-\beta\omega}}{2\omega} \int_{-\infty}^{+\infty} dt e^{i\omega t} \text{Tr}_e \{ \widehat{P}_{N-1,0} \iota(t) \}. \end{aligned} \quad (\text{D11})$$

Both $I_{1,2}$ and I_2 reduce to expectation values of the purely electronic operator $\widehat{P}_{N-1,0}$ with respect to the reduced (purely electronic) density matrix $\sigma_0^{(0)}(\beta)/Z_e$ (for $I_{1,2}$) or $\iota(t)$ (for I_2) that is diagonal in the momentum representation. For example,

$$\text{Tr}_e \{ \widehat{P}_{N-1,0} \iota(t) \} = -2i \sum_k \langle k|\iota(t)|k\rangle \sin\left(2\pi n_k \frac{N-1}{N}\right), \quad (\text{D12})$$

where the sum is over N allowed values of the wave number $k = 2\pi n_k/N$, with n_k being N consecutive integers. As $N \rightarrow +\infty$, $(N-1)/N \rightarrow 1$, and each term entering Eq. (D12) tends to zero. In other words, the finite-size correction I_2 vanishes in the infinite-chain limit. The same reasoning may be applied to show that $I_{1,2}$ vanishes in the infinite-chain limit.

REFERENCES





- C. Franchini, M. Reticcioli, M. Setvin, and U. Diebold, "Polarons in materials," *Nat. Rev. Mater.* **6**, 560–586 (2021).
- L. R. V. Buizza and L. M. Herz, "Polarons and charge localization in metal-halide semiconductors for photovoltaic and light-emitting devices," *Adv. Mater.* **33**, 2007057 (2021).
- C. Jacoboni, *Theory of Electron Transport in Semiconductors: A Pathway from Elementary Physics to Nonequilibrium Green Functions* (Springer-Verlag Berlin Heidelberg, 2010).
- F. Rossi, *Theory of Semiconductor Quantum Devices: Microscopic Modeling and Simulation Strategies* (Springer-Verlag Berlin Heidelberg, 2011).
- G. Mahan, *Many-Particle Physics* (Kluwer Academic, New York, 2000).
- A. S. Alexandrov and J. T. Devreese, *Advances in Polaron Physics* (Springer-Verlag Berlin Heidelberg, 2010).
- V. Coropceanu, J. Cornil, D. A. da Silva Filho, Y. Olivier, R. Silbey, and J.-L. Brédas, "Charge transport in organic semiconductors," *Chem. Rev.* **107**, 926–952 (2007).
- M. Mladenović and N. Vukmirović, "Charge carrier localization and transport in organic semiconductors: Insights from atomistic multiscale simulations," *Adv. Funct. Mater.* **25**, 1915–1932 (2015).
- A. Köhler and H. Bässler, *Electronic Processes in Organic Semiconductors* (Wiley-VCH Verlag GmbH & Co. KGaA, 2015).
- M. Schröter, S. Ivanov, J. Schulze, S. Polyutov, Y. Yan, T. Pullerits, and O. Kühn, "Exciton–vibrational coupling in the dynamics and spectroscopy of Frenkel excitons in molecular aggregates," *Phys. Rep.* **567**, 1–78 (2015).
- S. J. Jang and B. Mennucci, "Delocalized excitons in natural light-harvesting complexes," *Rev. Mod. Phys.* **90**, 035003 (2018).
- V. van Amerongen, L. Valkunas, and R. van Grondelle, *Photosynthetic Excitons* (World Scientific Publishing Co. Pte., Ltd., 2000).
- V. May and O. Kühn, *Charge and Energy Transfer Dynamics in Molecular Systems*, 3rd ed. (WILEY-VCH Verlag GmbH & Co. KGaA, Weinheim, 2011).
- L. Valkunas, D. Abramavicius, and T. Mančal, *Molecular Excitation Dynamics and Relaxation* (WILEY-VCH Verlag GmbH & Co. KGaA, 2013).
- T. Holstein, "Studies of polaron motion: Part I. The molecular-crystal model," *Ann. Phys.* **8**, 325–342 (1959).

- ¹⁶S. Poncé, W. Li, S. Reichardt, and F. Giustino, "First-principles calculations of charge carrier mobility and conductivity in bulk semiconductors and two-dimensional materials," *Rep. Prog. Phys.* **83**, 036501 (2020).
- ¹⁷A. G. Redfield, "The theory of relaxation processes," in *Advances in Magnetic Resonance, Advances in Magnetic and Optical Resonance Vol. 1*, edited by J. S. Waugh (Academic Press, 1965), pp. 1–32.
- ¹⁸I. Lang and Y. A. Firsov, "Kinetic theory of semiconductors with low mobility," *Sov. Phys. JETP* **16**, 1301–1312 (1963).
- ¹⁹R. A. Marcus, "Electron transfer reactions in chemistry. Theory and experiment," *Rev. Mod. Phys.* **65**, 599–610 (1993).
- ²⁰T. Förster, "Delocalized excitation and excitation transfer. Bulletin no. 18," Technical Report FSU-2690-18, Florida State University; Department of Chemistry, Tallahassee, 1964).
- ²¹A. Zhugayevych and S. Tretiak, "Theoretical description of structural and electronic properties of organic photovoltaic materials," *Annu. Rev. Phys. Chem.* **66**, 305–330 (2015).
- ²²A. Ishizaki and G. R. Fleming, "Quantum coherence in photosynthetic light harvesting," *Annu. Rev. Condens. Matter Phys.* **3**, 333–361 (2012).
- ²³A. Chenu and G. D. Scholes, "Coherence in energy transfer and photosynthesis," *Annu. Rev. Phys. Chem.* **66**, 69–96 (2015).
- ²⁴P. J. Robinson, I. S. Dunn, and D. R. Reichman, "Cumulant methods for electron-phonon problems. I. Perturbative expansions," *Phys. Rev. B* **105**, 224304 (2022).
- ²⁵P. J. Robinson, I. S. Dunn, and D. R. Reichman, "Cumulant methods for electron-phonon problems. II. The self-consistent cumulant expansion," *Phys. Rev. B* **105**, 224305 (2022).
- ²⁶P. Mitrić, V. Janković, N. Vukmirović, and D. Tanasković, "Cumulant expansion in the Holstein model: Spectral functions and mobility," *Phys. Rev. B* **107**, 125165 (2023).
- ²⁷J. Ma and J. Cao, "Förster resonance energy transfer, absorption and emission spectra in multichromophoric systems. I. Full cumulant expansions and system-bath entanglement," *J. Chem. Phys.* **142**, 094106 (2015).
- ²⁸J. A. Nöthling, T. Mančal, and T. P. J. Krüger, "Accuracy of approximate methods for the calculation of absorption-type linear spectra with a complex system-bath coupling," *J. Chem. Phys.* **157**, 095103 (2022).
- ²⁹S. Ciuchi, F. de Pasquale, S. Fratini, and D. Feinberg, "Dynamical mean-field theory of the small polaron," *Phys. Rev. B* **56**, 4494–4512 (1997).
- ³⁰S. Fratini, F. de Pasquale, and S. Ciuchi, "Optical absorption from a nondegenerate polaron gas," *Phys. Rev. B* **63**, 153101 (2001).
- ³¹S. Fratini and S. Ciuchi, "Dynamical mean-field theory of transport of small polarons," *Phys. Rev. Lett.* **91**, 256403 (2003).
- ³²S. Fratini and S. Ciuchi, "Optical properties of small polarons from dynamical mean-field theory," *Phys. Rev. B* **74**, 075101 (2006).
- ³³P. Mitrić, V. Janković, N. Vukmirović, and D. Tanasković, "Spectral functions of the Holstein polaron: Exact and approximate solutions," *Phys. Rev. Lett.* **129**, 096401 (2022).
- ³⁴M. Grover and R. Silbey, "Exciton migration in molecular crystals," *J. Chem. Phys.* **54**, 4843–4851 (1971).
- ³⁵D. R. Yarkony and R. Silbey, "Variational approach to exciton transport in molecular crystals," *J. Chem. Phys.* **67**, 5818–5827 (1977).
- ³⁶R. Silbey and R. W. Munn, "General theory of electronic transport in molecular crystals. I. Local linear electron-phonon coupling," *J. Chem. Phys.* **72**, 2763–2773 (1980).
- ³⁷K. Hannewald and P. A. Bobbert, "Anisotropy effects in phonon-assisted charge-carrier transport in organic molecular crystals," *Phys. Rev. B* **69**, 075212 (2004).
- ³⁸Y.-C. Cheng and R. J. Silbey, "A unified theory for charge-carrier transport in organic crystals," *J. Chem. Phys.* **128**, 114713 (2008).
- ³⁹F. Ortmann, F. Bechstedt, and K. Hannewald, "Theory of charge transport in organic crystals: Beyond Holstein's small-polaron model," *Phys. Rev. B* **79**, 235206 (2009).
- ⁴⁰D. Chen, J. Ye, H. Zhang, and Y. Zhao, "On the Munn-Silbey approach to polaron transport with off-diagonal coupling and temperature-dependent canonical transformations," *J. Phys. Chem. B* **115**, 5312–5321 (2011).
- ⁴¹M. Kornjača and N. Vukmirović, "Polaron mobility obtained by a variational approach for lattice Fröhlich models," *Ann. Phys.* **391**, 183–202 (2018).
- ⁴²N. Prodanović and N. Vukmirović, "Charge carrier mobility in systems with local electron-phonon interaction," *Phys. Rev. B* **99**, 104304 (2019).
- ⁴³J. H. Fetherolf, D. Golež, and T. C. Berkelbach, "A unification of the Holstein polaron and dynamic disorder pictures of charge transport in organic crystals," *Phys. Rev. X* **10**, 021062 (2020).
- ⁴⁴M. Berciu, "Green's function of a dressed particle," *Phys. Rev. Lett.* **97**, 036402 (2006).
- ⁴⁵G. L. Goodvin, M. Berciu, and G. A. Sawatzky, "Green's function of the Holstein polaron," *Phys. Rev. B* **74**, 245104 (2006).
- ⁴⁶G. L. Goodvin, A. S. Mishchenko, and M. Berciu, "Optical conductivity of the Holstein polaron," *Phys. Rev. Lett.* **107**, 076403 (2011).
- ⁴⁷D. Balzer, T. J. Smolders, D. Blyth, S. N. Hood, and I. Kassal, "Delocalised kinetic Monte Carlo for simulating delocalisation-enhanced charge and exciton transport in disordered materials," *Chem. Sci.* **12**, 2276 (2021).
- ⁴⁸J. T. Willson, W. Liu, D. Balzer, and I. Kassal, "Jumping kinetic Monte Carlo: Fast and accurate simulations of partially delocalized charge transport in organic semiconductors," *J. Phys. Chem. Lett.* **14**, 3757–3764 (2023).
- ⁴⁹K. Hannewald and P. A. Bobbert, "Ab initio theory of charge-carrier conduction in ultrapure organic crystals," *Appl. Phys. Lett.* **85**, 1535–1537 (2004).
- ⁵⁰F. Ortmann, F. Bechstedt, and K. Hannewald, "Charge transport in organic crystals: Interplay of band transport, hopping and electron-phonon scattering," *New J. Phys.* **12**, 023011 (2010).
- ⁵¹J.-J. Zhou and M. Bernardi, "Predicting charge transport in the presence of polarons: The beyond-quasiparticle regime in SrTiO₃," *Phys. Rev. Res.* **1**, 033138 (2019).
- ⁵²L. Cupellini, F. Lipparini, and J. Cao, "Absorption and circular dichroism spectra of molecular aggregates with the full cumulant expansion," *J. Phys. Chem. B* **124**, 8610–8617 (2020).
- ⁵³N. Vukmirović, "Calculations of electron mobility in II-VI semiconductors," *Phys. Rev. B* **104**, 085203 (2021).
- ⁵⁴B. K. Chang, J.-J. Zhou, N.-E. Lee, and M. Bernardi, "Intermediate polaronic charge transport in organic crystals from a many-body first-principles approach," *npj Comput. Mater.* **8**, 63 (2022).
- ⁵⁵S. Hutsch, M. Panhans, and F. Ortmann, "Charge carrier mobilities of organic semiconductors: Ab initio simulations with mode-specific treatment of molecular vibrations," *npj Comput. Mater.* **8**, 228 (2022).
- ⁵⁶H. De Raedt and A. Lagendijk, "Numerical calculation of path integrals: The small-polaron model," *Phys. Rev. B* **27**, 6097–6109 (1983).
- ⁵⁷H. De Raedt and A. Lagendijk, "Numerical study of Holstein's molecular-crystal model: Adiabatic limit and influence of phonon dispersion," *Phys. Rev. B* **30**, 1671–1678 (1984).
- ⁵⁸N. V. Prokofev and B. V. Svistunov, "Polaron problem by diagrammatic quantum Monte Carlo," *Phys. Rev. Lett.* **81**, 2514–2517 (1998).
- ⁵⁹A. S. Mishchenko, N. V. Prokofev, A. Sakamoto, and B. V. Svistunov, "Diagrammatic quantum Monte Carlo study of the Fröhlich polaron," *Phys. Rev. B* **62**, 6317–6336 (2000).
- ⁶⁰A. S. Mishchenko, "Diagrammatic Monte Carlo method as applied to the polaron problems," *Phys.-Usp.* **48**, 887 (2005).
- ⁶¹A. S. Mishchenko, N. Nagaosa, G. De Filippis, A. de Candia, and V. Cataudella, "Mobility of Holstein polaron at finite temperature: An unbiased approach," *Phys. Rev. Lett.* **114**, 146401 (2015).
- ⁶²Y.-C. Wang and Y. Zhao, "Diagrammatic quantum Monte Carlo toward the calculation of transport properties in disordered semiconductors," *J. Chem. Phys.* **156**, 204116 (2022).
- ⁶³S. Miladić and N. Vukmirović, "Method for obtaining polaron mobility using real and imaginary time path-integral quantum Monte Carlo," *Phys. Rev. B* **107**, 184315 (2023).
- ⁶⁴P. Prelovšek and J. Bonča, "Ground state and finite temperature Lanczos methods," in *Strongly Correlated Systems: Numerical Methods*, edited by A. Avella and F. Mancini (Springer Berlin Heidelberg, Berlin, Heidelberg, 2013), pp. 1–30.
- ⁶⁵J. Bonča, S. A. Trugman, and I. Batistić, "Holstein polaron," *Phys. Rev. B* **60**, 1633–1642 (1999).


- ⁶⁶O. S. Barišić, “Calculation of excited polaron states in the Holstein model,” *Phys. Rev. B* **69**, 064302 (2004).
- ⁶⁷J. Bonča, S. A. Trugman, and M. Berciu, “Spectral function of the Holstein polaron at finite temperature,” *Phys. Rev. B* **100**, 094307 (2019).
- ⁶⁸J. Bonča and S. A. Trugman, “Dynamic properties of a polaron coupled to dispersive optical phonons,” *Phys. Rev. B* **103**, 054304 (2021).
- ⁶⁹J. Bonča and S. A. Trugman, “Electron removal spectral function of a polaron coupled to dispersive optical phonons,” *Phys. Rev. B* **106**, 174303 (2022).
- ⁷⁰E. Jeckelmann and S. R. White, “Density-matrix renormalization-group study of the polaron problem in the Holstein model,” *Phys. Rev. B* **57**, 6376–6385 (1998).
- ⁷¹C. Zhang, E. Jeckelmann, and S. R. White, “Dynamical properties of the one-dimensional Holstein model,” *Phys. Rev. B* **60**, 14092–14104 (1999).
- ⁷²J. Ren, W. Li, T. Jiang, Y. Wang, and Z. Shuai, “Time-dependent density matrix renormalization group method for quantum dynamics in complex systems,” *Wiley Interdiscip. Rev.: Comput. Mol. Sci.* **12**, e1614 (2022).
- ⁷³J. Ren, Z. Shuai, and G. Kin-Lic Chan, “Time-dependent density matrix renormalization group algorithms for nearly exact absorption and fluorescence spectra of molecular aggregates at both zero and finite temperature,” *J. Chem. Theory Comput.* **14**, 5027–5039 (2018).
- ⁷⁴W. Li, J. Ren, and Z. Shuai, “Finite-temperature TD-DMRG for the carrier mobility of organic semiconductors,” *J. Phys. Chem. Lett.* **11**, 4930–4936 (2020).
- ⁷⁵Y. Ge, W. Li, J. Ren, and Z. Shuai, “Computational method for evaluating the thermoelectric power factor for organic materials modeled by the Holstein model: A time-dependent density matrix renormalization group formalism,” *J. Chem. Theory Comput.* **18**, 6437–6446 (2022).
- ⁷⁶D. Jansen, J. Bonča, and F. Heidrich-Meisner, “Finite-temperature density-matrix renormalization group method for electron-phonon systems: Thermodynamics and Holstein-polaron spectral functions,” *Phys. Rev. B* **102**, 165155 (2020).
- ⁷⁷D. Jansen, J. Bonča, and F. Heidrich-Meisner, “Finite-temperature optical conductivity with density-matrix renormalization group methods for the Holstein polaron and bipolaron with dispersive phonons,” *Phys. Rev. B* **106**, 155129 (2022).
- ⁷⁸R. Borrelli and M. F. Gelin, “Quantum electron-vibrational dynamics at finite temperature: Thermo field dynamics approach,” *J. Chem. Phys.* **145**, 224101 (2016).
- ⁷⁹R. Borrelli and M. F. Gelin, “Simulation of quantum dynamics of excitonic systems at finite temperature: An efficient method based on thermo field dynamics,” *Sci. Rep.* **7**, 9127 (2017).
- ⁸⁰R. Borrelli and M. F. Gelin, “Finite temperature quantum dynamics of complex systems: Integrating thermo-field theories and tensor-train methods,” *Wiley Interdiscip. Rev.: Comput. Mol. Sci.* **11**, e1539 (2021).
- ⁸¹Y. Zhao, “The hierarchy of Davydov’s Ansatz: From guesswork to numerically ‘exact’ many-body wave functions,” *J. Chem. Phys.* **158**, 080901 (2023).
- ⁸²Y. Zhao, K. Sun, L. Chen, and M. Gelin, “The hierarchy of Davydov’s Ansatz and its applications,” *Wiley Interdiscip. Rev.: Comput. Mol. Sci.* **12**, e1589 (2022).
- ⁸³L. Chen and Y. Zhao, “Finite temperature dynamics of a Holstein polaron: The thermo-field dynamics approach,” *J. Chem. Phys.* **147**, 214102 (2017).
- ⁸⁴Z. Huang, L. Chen, N. Zhou, and Y. Zhao, “Transient dynamics of a one-dimensional Holstein polaron under the influence of an external electric field,” *Ann. Phys.* **529**, 1600367 (2017).
- ⁸⁵A. D. Somoza, K.-W. Sun, R. A. Molina, and Y. Zhao, “Dynamics of coherence, localization and excitation transfer in disordered nanorings,” *Phys. Chem. Chem. Phys.* **19**, 25996–26013 (2017).
- ⁸⁶Y. Tanimura, “Stochastic Liouville, Langevin, Fokker–Planck, and master equation approaches to quantum dissipative systems,” *J. Phys. Soc. Jpn.* **75**, 082001 (2006).
- ⁸⁷R.-X. Xu and Y. J. Yan, “Dynamics of quantum dissipation systems interacting with bosonic canonical bath: Hierarchical equations of motion approach,” *Phys. Rev. E* **75**, 031107 (2007).
- ⁸⁸A. Ishizaki and G. R. Fleming, “Unified treatment of quantum coherent and incoherent hopping dynamics in electronic energy transfer: Reduced hierarchy equation approach,” *J. Chem. Phys.* **130**, 234111 (2009).
- ⁸⁹Y. Tanimura, “Numerically ‘exact’ approach to open quantum dynamics: The hierarchical equations of motion (HEOM),” *J. Chem. Phys.* **153**, 020901 (2020).
- ⁹⁰C.-Y. Hsieh and J. Cao, “A unified stochastic formulation of dissipative quantum dynamics. I. Generalized hierarchical equations,” *J. Chem. Phys.* **148**, 014103 (2018).
- ⁹¹H.-D. Zhang, R.-X. Xu, X. Zheng, and Y. Yan, “Statistical quasi-particle theory for open quantum systems,” *Mol. Phys.* **116**, 780–812 (2018).
- ⁹²Y. Ke and Y. Zhao, “Hierarchy of stochastic Schrödinger equation towards the calculation of absorption and circular dichroism spectra,” *J. Chem. Phys.* **146**, 174105 (2017).
- ⁹³Y. Ke and Y. Zhao, “An extension of stochastic hierarchy equations of motion for the equilibrium correlation functions,” *J. Chem. Phys.* **146**, 214105 (2017).
- ⁹⁴L. Diósi and W. T. Strunz, “The non-Markovian stochastic Schrödinger equation for open systems,” *Phys. Lett. A* **235**, 569–573 (1997).
- ⁹⁵J. Roden, W. T. Strunz, and A. Eisfeld, “Non-Markovian quantum state diffusion for absorption spectra of molecular aggregates,” *J. Chem. Phys.* **134**, 034902 (2011).
- ⁹⁶V. Janković and N. Vukmirović, “Spectral and thermodynamic properties of the Holstein polaron: Hierarchical equations of motion approach,” *Phys. Rev. B* **105**, 054311 (2022).
- ⁹⁷D. Wang, L. Chen, R. Zheng, L. Wang, and Q. Shi, “Communications: A non-perturbative quantum master equation approach to charge carrier transport in organic molecular crystals,” *J. Chem. Phys.* **132**, 081101 (2010).
- ⁹⁸L. Song and Q. Shi, “Calculation of correlated initial state in the hierarchical equations of motion method using an imaginary time path integral approach,” *J. Chem. Phys.* **143**, 194106 (2015).
- ⁹⁹T. Xing, T. Li, Y. Yan, S. Bai, and Q. Shi, “Application of the imaginary time hierarchical equations of motion method to calculate real time correlation functions,” *J. Chem. Phys.* **156**, 244102 (2022).
- ¹⁰⁰L. Song and Q. Shi, “A new approach to calculate charge carrier transport mobility in organic molecular crystals from imaginary time path integral simulations,” *J. Chem. Phys.* **142**, 174103 (2015).
- ¹⁰¹I. S. Dunn, R. Tempelaar, and D. R. Reichman, “Removing instabilities in the hierarchical equations of motion: Exact and approximate projection approaches,” *J. Chem. Phys.* **150**, 184109 (2019).
- ¹⁰²L. Chen, Y. Zhao, and Y. Tanimura, “Dynamics of a one-dimensional Holstein polaron with the hierarchical equations of motion approach,” *J. Phys. Chem. Lett.* **6**, 3110–3115 (2015).
- ¹⁰³Y. Yan, T. Xing, and Q. Shi, “A new method to improve the numerical stability of the hierarchical equations of motion for discrete harmonic oscillator modes,” *J. Chem. Phys.* **153**, 204109 (2020).
- ¹⁰⁴C. Karrasch, D. M. Kennes, and J. E. Moore, “Transport properties of the one-dimensional Hubbard model at finite temperature,” *Phys. Rev. B* **90**, 155104 (2014).
- ¹⁰⁵B. Bertini, F. Heidrich-Meisner, C. Karrasch, T. Prosen, R. Steinigeweg, and M. Žnidarič, “Finite-temperature transport in one-dimensional quantum lattice models,” *Rev. Mod. Phys.* **93**, 025003 (2021).
- ¹⁰⁶G. De Filippis, V. Cataudella, A. S. Mishchenko, N. Nagaosa, A. Fierro, and A. de Candia, “Crossover from super- to subdiffusive motion and memory effects in crystalline organic semiconductors,” *Phys. Rev. Lett.* **114**, 086601 (2015).
- ¹⁰⁷N. Lu and S. Mukamel, “Polaron and size effects in optical line shapes of molecular aggregates,” *J. Chem. Phys.* **95**, 1588–1607 (1991).
- ¹⁰⁸Y. Tanimura, “Reduced hierarchical equations of motion in real and imaginary time: Correlated initial states and thermodynamic quantities,” *J. Chem. Phys.* **141**, 044114 (2014).
- ¹⁰⁹D. Hou, S. Wang, R. Wang, L. Z. Ye, R. X. Xu, X. Zheng, and Y. J. Yan, “Improving the efficiency of hierarchical equations of motion approach and application to coherent dynamics in Aharonov–Bohm interferometers,” *J. Chem. Phys.* **142**, 104112 (2015).
- ¹¹⁰T. P. Fay, “A simple improved low temperature correction for the hierarchical equations of motion,” *J. Chem. Phys.* **157**, 054108 (2022).
- ¹¹¹V. M. Axt and S. Mukamel, “Nonlinear optics of semiconductor and molecular nanostructures; a common perspective,” *Rev. Mod. Phys.* **70**, 145–174 (1998).
- ¹¹²F. Rossi and T. Kuhn, “Theory of ultrafast phenomena in photoexcited semiconductors,” *Rev. Mod. Phys.* **74**, 895–950 (2002).
- ¹¹³V. Janković and N. Vukmirović, “Dynamics of exciton formation and relaxation in photoexcited semiconductors,” *Phys. Rev. B* **92**, 235208 (2015).

- ¹¹⁴D. Thirumalai and B. Berne, “Methods for simulating time correlation functions in quantum systems,” *Comput. Phys. Commun.* **63**, 415–426 (1991).
- ¹¹⁵G. Schubert, G. Wellein, A. Weisse, A. Alvermann, and H. Fehske, “Optical absorption and activated transport in polaronic systems,” *Phys. Rev. B* **72**, 104304 (2005).
- ¹¹⁶M. Frigo and S. G. Johnson, “The design and implementation of FFTW3,” *Proc. IEEE* **93**, 216–231 (2005).
- ¹¹⁷V. Janković (2023), “Numerical study of the one-dimensional Holstein model using the momentum-space hierarchical equations of motion method,” Zenodo.
- ¹¹⁸D. M. Wilkins and N. S. Dattani, “Why quantum coherence is not important in the Fenna-Matthews-Olsen complex,” *J. Chem. Theory Comput.* **11**, 3411–3419 (2015).
- ¹¹⁹W. H. Press, S. A. Teukolsky, W. T. Vetterling, and B. P. Flannery, *Numerical Recipes in C*, 2nd ed. (Cambridge University Press, Cambridge, 1992).
- ¹²⁰C. M. Bender and S. A. Orszag, *Advanced Mathematical Methods for Scientists and Engineers* (McGraw-Hill Book Company, 1978).
- ¹²¹Q. Shi, Y. Xu, Y. Yan, and M. Xu, “Efficient propagation of the hierarchical equations of motion using the matrix product state method,” *J. Chem. Phys.* **148**, 174102 (2018).
- ¹²²Y. Yan, M. Xu, T. Li, and Q. Shi, “Efficient propagation of the hierarchical equations of motion using the Tucker and hierarchical Tucker tensors,” *J. Chem. Phys.* **154**, 194104 (2021).
- ¹²³E. Mangaud, A. Jaouadi, A. Chin, and M. Desouter-Lecomte, “Survey of the hierarchical equations of motion in tensor-train format for non-Markovian quantum dynamics,” *Eur. Phys. J.: Spec. Top.* (published online 2023). <https://doi.org/10.1140/epjs/s11734-023-00919-0>
- ¹²⁴Q. Shi, L. Chen, G. Nan, R.-X. Xu, and Y. Yan, “Efficient hierarchical Liouville space propagator to quantum dissipative dynamics,” *J. Chem. Phys.* **130**, 084105 (2009).
- ¹²⁵S. Fratini, D. Mayou, and S. Ciuchi, “The transient localization scenario for charge transport in crystalline organic materials,” *Adv. Funct. Mater.* **26**, 2292–2315 (2016).
- ¹²⁶S. Fratini and S. Ciuchi, “Dynamical localization corrections to band transport,” *Phys. Rev. Res.* **2**, 013001 (2020).
- ¹²⁷S. Fratini and S. Ciuchi, “Displaced Drude peak and bad metal from the interaction with slow fluctuations,” *SciPost Phys.* **11**, 039 (2021).
- ¹²⁸Y. Zhao, D. W. Brown, and K. Lindenberg, “On the Munn–Silbey approach to nonlocal exciton–phonon coupling,” *J. Chem. Phys.* **100**, 2335–2345 (1994).
- ¹²⁹R. Feynman and F. Vernon, “The theory of a general quantum system interacting with a linear dissipative system,” *Ann. Phys.* **24**, 118–173 (1963).
- ¹³⁰L. Zhu, H. Liu, W. Xie, and Q. Shi, “Explicit system-bath correlation calculated using the hierarchical equations of motion method,” *J. Chem. Phys.* **137**, 194106 (2012).
- ¹³¹A. Kato and Y. Tanimura, “Quantum heat current under non-perturbative and non-Markovian conditions: Applications to heat machines,” *J. Chem. Phys.* **145**, 224105 (2016).

Cumulant expansion in the Holstein model: Spectral functions and mobility

Petar Mitrić , Veljko Janković , Nenad Vukmirović , and Darko Tanasković 

Institute of Physics Belgrade, University of Belgrade, Pregrevica 118, 11080 Belgrade, Serbia

 (Received 29 December 2022; revised 6 March 2023; accepted 17 March 2023; published 30 March 2023)

We examine the range of validity of the second-order cumulant expansion (CE) for the calculation of spectral functions, quasiparticle properties, and mobility of the Holstein polaron. We devise an efficient numerical implementation that allows us to make comparisons in a broad interval of temperature, electron-phonon coupling, and phonon frequency. For a benchmark, we use the dynamical mean-field theory which gives, as we have recently shown, rather accurate spectral functions in the whole parameter space, even in low dimensions. We find that in one dimension, the CE resolves well both the quasiparticle and the first satellite peak in a regime of intermediate coupling. At high temperatures, the charge mobility assumes a power law $\mu \propto T^{-2}$ in the limit of weak coupling and $\mu \propto T^{-3/2}$ for stronger coupling. We find that, for stronger coupling, the CE gives slightly better results than the self-consistent Migdal approximation (SCMA), while the one-shot Migdal approximation is appropriate only for a very weak electron-phonon interaction. We also analyze the atomic limit and the spectral sum rules. We derive an analytical expression for the moments in CE and find that they are exact up to the fourth order, as opposed to the SCMA where they are exact to the third order. Finally, we analyze the results in higher dimensions.

DOI: [10.1103/PhysRevB.107.125165](https://doi.org/10.1103/PhysRevB.107.125165)

I. INTRODUCTION

The cumulant expansion (CE) method presents an alternative to the usual Dyson equation approach in the calculation of spectral functions of interacting quantum many-particle systems [1]. In this method, we express the Green's function in real time as an exponential function of an auxiliary quantity $C(t)$, called the cumulant, which can be calculated perturbatively [2]. In the late 1960s, it was established that the lowest order CE gives the exact solution of the problem of a core hole coupled to bosonic excitations (plasmons or phonons) [3,4]. While there were early papers that emphasized the potential role of CE as an approximate method to treat the electronic correlations in metals beyond the GW approximation [5–8] and the electron-phonon interaction in semiconductors and narrow band metals beyond the Migdal approximation (MA) [9–11], a surge of studies of CE has appeared only recently.

Renewed interest has emerged due to the possibility of combining CE with *ab initio* band-structure calculations. The CE for the electron-phonon interaction was used to obtain the spectral functions of several doped transition-metal oxides [12,13], showing a favorable comparison with angle-resolved photoemission spectroscopy [14]. A particularly appealing feature of the CE approach is that it describes the quasiparticle part of the spectrum as well as the satellite structure (sidebands). Combining the CE with the Kubo formula for charge transport gives an attractive route to calculate mobility in semiconductors beyond the Boltzmann approach, which is applicable only for weak electron-phonon coupling [15]. This was very recently demonstrated for SrTiO₃ [16] and naphthalene [17]. CE was also applied to elemental metals where a correction to the standard MA is discussed [18]. Similarly, the CE is successfully used to treat the electronic correlations beyond the GW approximation [19–25]. Further-

more, CE was used to study absorption spectra in molecular aggregates representative of photosynthetic pigment-protein complexes [26–28].

Despite the wide use of the lowest order CE, there seems to be a lack of studies establishing its range of validity, which represents the central motivation for this paper. To achieve this, we turn to simplified models of the electron-phonon interaction. CE for the Fröhlich model [29,30] gives the ground-state energy and the effective mass similar to the exact quantum Monte Carlo calculations for moderate interaction [31]. This is in contrast to the Dyson-Migdal approach, which severely underestimates mass renormalization. A comparison of the corresponding spectral functions is, however, missing, since reliable quantum Monte Carlo results are not available due to the well-known problems with analytical continuation. The Holstein polaron model gives a unique opportunity to explore the applicability of the CE since various numerically exact methods are developed and applied to this model covering different parameter regimes [32–49]. This was the approach of a very recent work by Reichman and collaborators [50,51]. Still, there are several questions that remained unresolved. Most importantly, a comparison of spectral functions was made just for a small set of parameters on a finite-size lattice, where the benchmark spectral functions were available from the finite-temperature Lanczos results, while the charge transport was not examined.

In our recent work [52], we established that the dynamical mean-field theory (DMFT) [53] gives close to exact spectral functions of the Holstein polaron for different phonon frequencies, electron-phonon couplings, and temperatures even in low dimensions, covering practically the whole parameter space. This method is computationally very fast and precise, which makes us ideally positioned to perform comprehensive comparisons with the CE method, which is the goal of

this paper. Within the CE, we calculate the spectral functions and charge mobility for a broad set of parameters and make detailed comparisons with DMFT and (self-consistent) MA. We find that the one-shot MA is appropriate only for very weak electron-phonon coupling. The validity of the CE and self-consistent Migdal approximation (SCMA) is much broader and for intermediate interaction CE even outperforms SCMA. We also derive analytical CE expressions for the ground-state energy, renormalized mass, and scattering rate as well as the spectral sum rules, and make comparisons between the methods. We establish a power-law behavior for the charge mobility at high temperatures. We also compare the performance of different methods as the bandwidth is reduced toward the atomic limit.

The remaining part of the paper is organized as follows. In Sec. II, we introduce the CE method and present details of its implementation on the Holstein model. DMFT and SCMA are here introduced as benchmark methods. Representative spectral functions are shown in Sec. III from weak toward the strong coupling. The high-temperature and atomic limits are analyzed in detail, as well as the spectral sum rules. In Sec. IV, we present the results for the effective mass and ground-state energy. The temperature dependence of the electron mobility is analyzed in Sec. V, and Sec. VI contains our conclusions. Some details concerning numerical implementations and additional figures for various parameters are shown in the Appendix and in the Supplemental Material (SM) [54].

II. MODEL AND METHODS

The Holstein model is the simplest model of the lattice electrons interacting with the phonons. It assumes a local electron-phonon interaction and dispersionless phonons. The Hamiltonian is given by

$$H = -t_0 \sum_{\langle ij \rangle} (c_i^\dagger c_j + \text{H.c.}) - g \sum_i n_i (a_i^\dagger + a_i) + \omega_0 \sum_i a_i^\dagger a_i. \quad (1)$$

Here, t_0 is the hopping parameter between the nearest neighbors and ω_0 is the phonon frequency. c_i and a_i are the electron and the phonon annihilation operators, $n_i = c_i^\dagger c_i$, and g denotes the electron-phonon coupling strength. We set \hbar, k_B , elementary charge e , and lattice constant to 1. We also often use a parameter $\alpha = g/\omega_0$. We study the model in the thermodynamic limit (number of sites $N \rightarrow \infty$). Furthermore, we consider a dynamics of a single electron in the conduction band and treat the electrons as spinless, since we are interested only in weakly doped semiconductors. This is equivalent to setting the chemical potential far below the conduction band, i.e., considering the limit $\tilde{\mu} \rightarrow -\infty$. This case is often referred to as the Holstein polaron problem. We mostly focus on the one-dimensional (1D) system, but we also consider the system in 2D and 3D.

A. Cumulant expansion

1. General theory

The central quantity of this paper is the electron spectral function $A_{\mathbf{k}}(\omega) = (-1/\pi)\text{Im}G_{\mathbf{k}}(\omega)$, where \mathbf{k} is the momen-

tum and $G_{\mathbf{k}}(\omega)$ is the retarded Green's function in frequency domain [1]. Its exact evaluation is often a formidable task, which is why approximate techniques are usually employed. One needs to be careful with such approaches not to violate some analytic properties, such as the pole structure of the Green's function, the positivity of the spectral function, or the spectral sum rules. At least some of these properties can be easily satisfied if the Green's function is not calculated directly but instead through some auxiliary quantity, such as the self-energy $\Sigma_{\mathbf{k}}(\omega)$. In the latter case, the connection with the Green's function is established via the Dyson equation

$$G_{\mathbf{k}}(\omega) = \frac{1}{G_{\mathbf{k},0}(\omega)^{-1} - \Sigma_{\mathbf{k}}(\omega)} = \frac{1}{\omega - \varepsilon_{\mathbf{k}} - \Sigma_{\mathbf{k}}(\omega)}, \quad (2)$$

where $G_{\mathbf{k},0}(\omega)$ is the noninteracting Green's function and $\varepsilon_{\mathbf{k}}$ is the noninteracting dispersion relation.

An alternative to the Dyson equation based approaches is the so-called cumulant expansion method [19], in which the exponential ansatz is chosen for the Green's function in the time domain:

$$G_{\mathbf{k}}(t) = G_{\mathbf{k},0}(t)e^{C_{\mathbf{k}}(t)} = -i\theta(t)e^{-i\varepsilon_{\mathbf{k}}t}e^{C_{\mathbf{k}}(t)}. \quad (3)$$

Here, $\theta(t)$ is the Heaviside step function and $C_{\mathbf{k}}(t)$ plays the role of an auxiliary quantity which is called the cumulant. Both Eqs. (2) and (3) would correspond to the same Green's function in frequency and time domain if the cumulant $C_{\mathbf{k}}(t)$ and the self-energy $\Sigma_{\mathbf{k}}(\omega)$ could be evaluated exactly [1]. In practice, however, one of these approaches is expected to perform better. The spectral function within the CE can be obtained as follows:

$$A_{\mathbf{k}}(\omega + \varepsilon_{\mathbf{k}}) = \frac{1}{\pi} \text{Re} \int_0^\infty dt e^{i\omega t} e^{C_{\mathbf{k}}(t)}. \quad (4)$$

Equation (4) circumvents the Fourier transform of the whole Green's function $A_{\mathbf{k}}(\omega) = -\frac{1}{\pi}\text{Im}G_{\mathbf{k}}(\omega)$, which is useful in practice, as the free electron part $e^{-i\varepsilon_{\mathbf{k}}t}$ typically oscillates much more quickly than $e^{C_{\mathbf{k}}(t)}$.

The expression for $C_{\mathbf{k}}(t)$ in the lowest order perturbation expansion can be obtained by taking the leading terms in the Taylor expansion of the Dyson equation $G_{\mathbf{k}}(\omega) = (G_{\mathbf{k},0}(\omega)^{-1} - \Sigma_{\mathbf{k}}(\omega))^{-1} \approx G_{\mathbf{k},0}(\omega) + G_{\mathbf{k},0}(\omega)\Sigma_{\mathbf{k}}(\omega)G_{\mathbf{k},0}(\omega)$, taking its inverse Fourier transform and equating it to Eq. (3), where the cumulant in the exponent is replaced with its linear approximation $e^{C_{\mathbf{k}}(t)} \approx 1 + C_{\mathbf{k}}(t)$:

$$C_{\mathbf{k}}(t) = ie^{i\varepsilon_{\mathbf{k}}t} \int_{-\infty}^\infty \frac{d\omega}{2\pi} \frac{e^{-i\omega t} \Sigma_{\mathbf{k}}(\omega)}{(\omega - \varepsilon_{\mathbf{k}} + i0^+)^2}. \quad (5)$$

Using the spectral representation of the self-energy

$$\Sigma_{\mathbf{k}}(\omega) = \int \frac{d\nu}{\pi} \frac{|\text{Im}\Sigma_{\mathbf{k}}(\nu)|}{\omega - \nu + i0^+}, \quad (6)$$

and the contour integration over ω , Eq. (5) simplifies to [19]

$$C_{\mathbf{k}}(t) = \frac{1}{\pi} \int_{-\infty}^\infty d\omega \frac{|\text{Im}\Sigma_{\mathbf{k}}(\omega + \varepsilon_{\mathbf{k}})|}{\omega^2} (e^{-i\omega t} + i\omega t - 1). \quad (7)$$

The corresponding spectral function satisfies the first two sum rules, irrespective of $\Sigma_{\mathbf{k}}(\omega)$. This is a consequence of the behavior of $C_{\mathbf{k}}(t)$ for small t ; see Sec. III C. In general, $C_{\mathbf{k}}(t=0) = 0$ is sufficient for the first spectral sum rule $\int A_{\mathbf{k}}(\omega)d\omega = 1$ to be satisfied. The second sum rule

$\int A_{\mathbf{k}}(\omega)\omega d\omega = \varepsilon_{\mathbf{k}}$ can also be satisfied if we additionally impose that the cumulant's first derivative at $t = 0$ is vanishing, $\frac{dC_{\mathbf{k}}}{dt}(0) = 0$. Both of these conditions are satisfied by the cumulant function in Eq. (7), as it is a quadratic function of time for small arguments $e^{-i\omega t} + i\omega t - 1 \approx -\omega^2 t^2/2$ for $t \rightarrow 0$.

The application of Eq. (7) is facilitated by the fact that it does not contain any iterative self-consistent calculations. However, one needs to overcome the numerical challenges caused by the removable singularity at $\omega = 0$ and by the rapidly oscillating trigonometric factor $e^{-i\omega t}$ for large t . The latter is important for the weak electron-phonon couplings, where it is necessary to propagate $C_{\mathbf{k}}(t)$ up to long times until the Green's function is sufficiently damped out. The same problem occurs in other regimes as well (e.g., close to the atomic limit), where the Green's function does not attenuate at all; see Sec. II A 4.

The numerical singularity at $\omega = 0$ can be completely avoided if we consider the cumulant's second derivative

$$\frac{d^2 C_{\mathbf{k}}(t)}{dt^2} = \int_{-\infty}^{\infty} \frac{d\omega}{\pi} \text{Im} \Sigma_{\mathbf{k}}(\omega + \varepsilon_{\mathbf{k}}) e^{-i\omega t} \equiv 2e^{i\varepsilon_{\mathbf{k}} t} \tilde{\sigma}_{\mathbf{k}}(t), \quad (8)$$

where we used $\text{Im} \Sigma_{\mathbf{k}}(\omega) < 0$ and introduced $\tilde{\sigma}_{\mathbf{k}}(t) \equiv \int_{-\infty}^{\infty} \text{Im} \Sigma_{\mathbf{k}}(\omega) e^{-i\omega t} \frac{d\omega}{2\pi}$. Then, $C_{\mathbf{k}}(t)$ is obtained as a double integral over time of Eq. (8),

$$C_{\mathbf{k}}(t) = 2 \int_0^t dt' \int_0^{t'} dt'' e^{i\varepsilon_{\mathbf{k}} t''} \tilde{\sigma}_{\mathbf{k}}(t''), \quad (9)$$

where the lower boundaries of both integrals have to be zero, as guaranteed by the initial conditions $C_{\mathbf{k}}(0) = \frac{dC_{\mathbf{k}}}{dt}(0) = 0$. Using the Cauchy formula for repeated integration, this can also be written as a single integral:

$$C_{\mathbf{k}}(t) = 2 \int_0^t (t-x) e^{i\varepsilon_{\mathbf{k}} x} \tilde{\sigma}_{\mathbf{k}}(x) dx. \quad (10)$$

This completely removed the problem of numerical singularities. Still, the problem of rapid oscillations of the subintegral function remains due to the presence of $e^{i\varepsilon_{\mathbf{k}} x}$ term. In Sec. II A 3, we provide an elegant solution for this issue, focusing on the case of the Holstein model.

2. Asymptotic expansion for cumulant when $t \rightarrow \infty$

The asymptotic expansion of $C_{\mathbf{k}}(t)$ for large times, as we now demonstrate, completely determines the quasiparticle properties within this method. This is one of the main motivations for studying the $t \rightarrow \infty$ limit. From Eq. (8), we see that

$$\begin{aligned} i \frac{dC_{\mathbf{k}}}{dt}(t \rightarrow \infty) &= i \int_0^{\infty} \frac{d^2 C_{\mathbf{k}}(t)}{dt^2} dt \\ &= -\frac{i}{\pi} \int_{-\infty}^{\infty} d\omega |\text{Im} \Sigma_{\mathbf{k}}(\omega + \varepsilon_{\mathbf{k}})| \int_0^{\infty} dt e^{-i\omega t} \\ &= \Sigma_{\mathbf{k}}(\varepsilon_{\mathbf{k}}), \end{aligned} \quad (11)$$

where we used the identity $\int_0^{\infty} dt e^{-i\omega t} = \pi \delta(\omega) - i\mathcal{P} \frac{1}{\omega}$ and the Kramers-Kronig relations for the self-energy. Hence, the cumulant function $C_{\mathbf{k}}(t)$, and also the whole exponent in Eq. (3) is a linear function of time $C_{\mathbf{k}}(t) - i\varepsilon_{\mathbf{k}} t \approx -i\tilde{E}_{\mathbf{k}} t +$

const for $t \rightarrow \infty$, where

$$\tilde{E}_{\mathbf{k}} = \varepsilon_{\mathbf{k}} + \Sigma_{\mathbf{k}}(\varepsilon_{\mathbf{k}}). \quad (12)$$

As a consequence, the Green's function in Fourier space has a simple pole situated at $\tilde{E}_{\mathbf{k}}$, as seen from the following expression:

$$G_{\mathbf{k}}(\omega) = -i \int_0^{\infty} e^{it(\omega - \varepsilon_{\mathbf{k}} - \frac{iC_{\mathbf{k}}(t)}{t})} dt. \quad (13)$$

Therefore, quasiparticle properties are encoded in $\tilde{E}_{\mathbf{k}}$: its real and imaginary parts correspond to the quasiparticle energy and scattering rate, respectively. We note that, in our present analysis, we implicitly assumed that $\frac{dC_{\mathbf{k}}}{dt}(t \rightarrow \infty)$ exists and is finite. Although this is generally true, there are a few exceptions. In the Holstein model, the first assumption is violated at the atomic limit [$t_0 = 0$; see Eq. (28)], while the second assumption is violated at the adiabatic limit ($\omega_0 = 0$) for $k = 0$ or $k = \pm\pi$; see Eqs. (18) or (19).

The knowledge that we gained about the analytic properties of the $C_{\mathbf{k}}(t)$ provides us with an intuitive understanding of how the shape of the cumulant determines the shape of the spectral function. The asymptotic limits $t \rightarrow \infty$ [where $C_{\mathbf{k}}(t)$ is linear] and $t \rightarrow 0$ [where $C_{\mathbf{k}}(t)$ is quadratic] by themselves, to a large extent, describe only the simple one-peak spectral functions, while the crossover between these limits is responsible for the emergence of satellite peaks. This can be explained as follows: If the cumulant was quadratic over the whole t domain $C_{\mathbf{k}}(t) = ct^2$, the spectral function would have a simple Gaussian shape. Similarly, the Lorentzian shape would be obtained from the linear cumulant $C_{\mathbf{k}}(t) = ct$. This suggests that the simple crossover between quadratic (at small t) and linear (at large t) behaviors would also give a simple one-peak shape of the spectral function. The information about phonon satellites is thus completely encoded in the $C_{\mathbf{k}}(t)$ for intermediate times t , which depends on the system and approximation in which the cumulant function is calculated.

3. Second-order cumulant expansion for the Holstein model

Let us now concentrate on a specific example, the Holstein model on a hypercubic lattice in n dimensions. The second-order cumulant is given by Eq. (7), where the self-energy is taken to be in the MA $\Sigma_{\mathbf{k}}(\omega) = \Sigma^{\text{MA}}(\omega)$, i.e., of the second (lowest) order with respect to the electron-phonon coupling g . This is in accordance with the derivation from Sec. II A 1, since we restricted ourselves to the lowest order terms in the Taylor expansion of the Dyson equation and of $e^{C_{\mathbf{k}}(t)}$. An alternative derivation of this expression is given in Sec. I of the SM [54]. MA is briefly discussed in Sec. II B 1. For our present purpose, we only need the expression for the imaginary part of the self-energy

$$\text{Im} \Sigma^{\text{MA}}(\omega) = -\pi g^2 [(n_{\text{ph}} + 1)\rho(\omega - \omega_0) + n_{\text{ph}}\rho(\omega + \omega_0)], \quad (14)$$

where $n_{\text{ph}} = 1/(e^{\omega_0/T} - 1)$ is the Bose factor, $\rho(\omega) = \frac{1}{N} \sum_{\mathbf{k}} \delta(\omega - \varepsilon_{\mathbf{k}})$ is the density of electron states for the system of size N , which we take in the thermodynamic limit $N \rightarrow \infty$, and $\varepsilon_{\mathbf{k}} = -2t_0 \sum_{j=1}^n \cos k_j$ is the noninteracting dispersion relation.

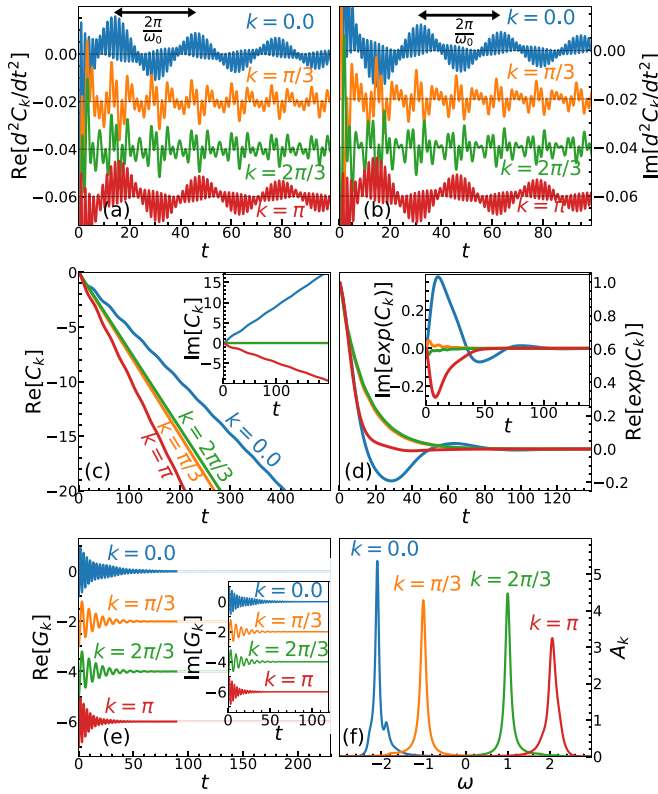


FIG. 1. (a)–(f) The cumulant, Green’s, and spectral function on the example of the one-dimensional Holstein model with the following values of the model parameters: $\omega_0 = 0.2$, $g = 0.2$, $T = 0.3$, and $t_0 = 1$.

The expression for the cumulant function, as seen from Eq. (10), is related to the inverse Fourier transform of $\text{Im}\Sigma^{\text{MA}}(\omega)$, which in turn is completely determined by the inverse Fourier transform of the density of states $\tilde{\rho}(t)$. The latter admits a closed-form solution

$$\begin{aligned} \tilde{\rho}(t) &= \int_{-\infty}^{\infty} \frac{d\omega e^{-i\omega t}}{(2\pi)^{n+1}} \int_{|0, 2\pi)^n} d^n \mathbf{k} \delta\left(\omega + 2t_0 \sum_{j=1}^n \cos k_j\right) \\ &= \frac{1}{2\pi} \left(\frac{1}{2\pi} \int_0^{2\pi} dk e^{2it_0t \cos k} \right)^n = \frac{J_0(2t_0t)^n}{2\pi}, \end{aligned} \quad (15)$$

where J_0 is the Bessel function of the first kind of order zero. Hence, Eqs. (10), (14), and (15) imply that the cumulant function can be written as

$$C_k(t) = -g^2 \int_0^t dx(t-x) iD(x) e^{ix\varepsilon_k} J_0(2t_0x)^n, \quad (16)$$

where $iD(t) = (n_{\text{ph}} + 1)e^{-i\omega_0 t} + n_{\text{ph}}e^{i\omega_0 t}$ is the phonon propagator in real time (for $t > 0$). In Fig. 1, we illustrate the cumulant function, as well as the corresponding Green’s function and spectral function. Figures 1(a) and 1(b) show the second derivative of the cumulant

$$\frac{d^2 C_k(t)}{dt^2} = -g^2 iD(t) e^{it\varepsilon_k} J_0(2t_0t)^n \quad (17)$$

to demonstrate the rapid oscillations that are also present in the cumulant itself. These are not easily observed by inspect-

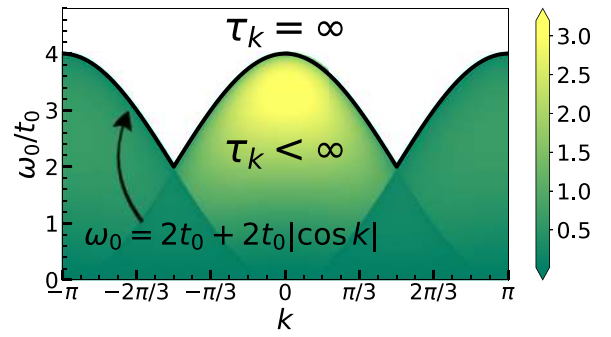


FIG. 2. Quasiparticle lifetime τ_k in the CE method for $T/t_0 = 2$ and $g/t_0 = 1$.

ing $C_k(t)$ directly, as the linear behavior dominates for large times. We observe that the $k = 0$ and $k = \pi$ results possess an oscillating envelope with period $2\pi/\omega_0$, while intermediate momenta have a much less regular structure. This can have direct consequences on the spectral functions, as the satellite peaks are expected to be at a distance ω_0 from each other. To be more explicit, oscillating envelopes suggest that there is a much higher chance for the occurrence of satellite peaks near the bottom ($k \approx 0$) and the top ($k \approx \pi$) of the band, than otherwise. However, that does not guarantee that the satellite peaks will in fact occur. Figure 1(c) shows that $\text{Re}C_k(t)$ is declining faster for $k > 0$ than for $k = 0$. As a consequence, $e^{C_k(t)}$ in Fig. 1(d) attenuates slower for $k = 0$, having enough time to complete a full period, while $k = \pi$ results are reminiscent of an overdamped oscillator. A similar, although much less evident, effect can be seen in the Green’s function itself; see Fig. 1(e). This is why the $k = \pi$ spectral function in Fig. 1(f) has a simple one-peak shape, while only the $k = 0$ result captures one small satellite peak.

From a numerical point of view, Eq. (16) is treated using Levin’s collocation method [55], which is reviewed in Appendix A. It provides a controlled, accurate, and numerically efficient way to integrate the product of trigonometric, Bessel, and some slowly varying function. This approach avoids using a dense t grid, which would otherwise be required, as the subintegral function in Eq. (16) has the same type of rapid oscillations present in $d^2 C_k(t)/dt^2$.

4. Lifetime

Another question of practical importance is how long we should propagate the cumulant function in real time until the corresponding Green’s function attenuates. A rough estimate of such quantity is given by the quasiparticle lifetime τ_k . The lifetime is given by $\tau_k = 1/(2|\text{Im}\tilde{E}_k|)$, where \tilde{E}_k is given by Eq. (12) and the self-energy is taken in the MA [see Eq. (14)]:

$$\begin{aligned} \tau_k^{-1} &= 2|\text{Im}\tilde{E}_k| = 2g^2 \frac{\theta(4t_0^2 - (\varepsilon_k - \omega_0)^2)}{\sqrt{4t_0^2 - (\varepsilon_k - \omega_0)^2}} (n_{\text{ph}} + 1) \\ &\quad + 2g^2 \frac{\theta(4t_0^2 - (\varepsilon_k + \omega_0)^2)}{\sqrt{4t_0^2 - (\varepsilon_k + \omega_0)^2}} n_{\text{ph}}. \end{aligned} \quad (18)$$

This is illustrated in Fig. 2. We observe that there is a considerable part of the parameter space where the lifetime is

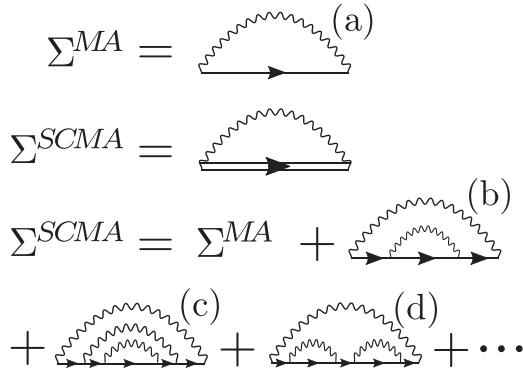


FIG. 3. Feynman diagrams in the Migdal approximation and the self-consistent Migdal approximation.

infinite, which means that the corresponding Green's function never attenuates. This occurs for $\omega_0 > 2t_0 + 2t_0|\cos k|$ in the case of finite temperatures, and for $\omega_0 > 4t_0 \sin^2 k/2$ in the $T = 0$ case. In these regimes, one could presume that this is reflected in the spectral functions through the appearance of Dirac delta peaks, which is not expected at finite temperatures. This illustrates one of the limitations of this method.

B. Benchmark methods

1. Migdal and self-consistent Migdal approximation

The Migdal approximation [56] is the simplest perturbation approach, whose self-energy is represented with a single, lowest order Feynman diagram, as shown in Fig. 3(a). The imaginary part of the self-energy is given by Eq. (14) in the case when there is just a single electron in the band, regardless of the dispersion relation or the number of dimensions of the system. The corresponding real part is obtained using the Kramers-Kronig relations, and in 1D reads as

$$\begin{aligned} \text{Re}\Sigma^{\text{MA}}(\omega) = & g^2(n_{\text{ph}} + 1) \frac{\theta((\omega - \omega_0)^2 - 4t_0^2)\text{sgn}(\omega - \omega_0)}{\sqrt{(\omega - \omega_0)^2 - 4t_0^2}} \\ & + g^2n_{\text{ph}} \frac{\theta((\omega + \omega_0)^2 - 4t_0^2)\text{sgn}(\omega + \omega_0)}{\sqrt{(\omega + \omega_0)^2 - 4t_0^2}}. \end{aligned} \quad (19)$$

The range of validity of the MA can be extended if we substitute the noninteracting electron propagator in Fig. 3(a) with an interacting one. At the same time, the interacting propagator itself is expressed through the self-energy via the Dyson equation. These relations constitute the SCMA. Figure 3 illustrates that the SCMA self-energy consists of a series of noncrossing diagrams, whose lowest order coincides with the MA. Figure 3(b) shows the second-order contribution, while the third-order contributions are shown in Figs. 3(c) and 3(d).

Mathematically, the self-consistency relations are straightforwardly derived and, in our case, read as

$$\Sigma^{\text{SCMA}}(\omega) = g^2(n_{\text{ph}} + 1)G(\omega - \omega_0) + g^2n_{\text{ph}}G(\omega + \omega_0), \quad (20a)$$

$$G(\omega) = \frac{1}{(2\pi)^n} \int_{-\pi}^{\pi} d^n\mathbf{k} \frac{1}{\omega - \varepsilon_{\mathbf{k}} - \Sigma^{\text{SCMA}}(\omega)}, \quad (20b)$$

where $G(\omega)$ is the local Green's function. We see that in the case of the Holstein model, the SCMA self-energy is \mathbf{k} independent.

2. Dynamical mean-field theory

Dynamical mean-field theory is a nonperturbative approximate method, that represents a natural generalization of the traditional mean-field theory [57]. It simplifies the original lattice problem by mapping it to a single site impurity problem, embedded into an external bath that is described with a frequency-dependent (i.e., dynamical) field $G_0(\omega)$, which needs to be determined self-consistently. This simplification is reflected on the self-energy, which is assumed to be \mathbf{k} -independent $\Sigma_{\mathbf{k}}(\omega) = \Sigma(\omega)$. The DMFT becomes exact in the limit of infinite dimensions or, equivalently, infinite coordination number.

In practice, $G_0(\omega)$ and $\Sigma(\omega)$ are determined self-consistently, by imposing that the local Green's function of the lattice problem

$$G(\omega) = \int_{-\infty}^{\infty} \frac{\rho(\epsilon)d\epsilon}{\omega - \Sigma(\omega) - \epsilon}, \quad (21)$$

and the self-energy $\Sigma(\omega)$ coincide with the corresponding quantities of the impurity problem. Here, $\rho(\epsilon)$ is the noninteracting density of states. The self-consistent loop is closed using the Dyson equation $G_0(\omega) = (G^{-1}(\omega) + \Sigma(\omega))^{-1}$. In the case of the Holstein model, the (polaron) impurity problem can be solved exactly, directly on the real-frequency axis, in terms of the continued fraction expansion [53]. Furthermore, in the one-dimensional case, Eq. (21) assumes a closed-form solution and reads as

$$G(\omega) = \text{Re} \frac{1}{2t_0B(\omega)\sqrt{1 - \frac{1}{B(\omega)^2}}} + i\text{Im} \frac{-i}{2t_0\sqrt{1 - B(\omega)^2}}, \quad (22)$$

where $B(\omega) = (\omega - \Sigma(\omega))/(2t_0)$; see Supplemental Material of Ref. [52]. We note that Eq. (22) can also be used for the SCMA in Eq. (20).

We have very recently shown [52], by using extensive comparisons with several numerically exact methods covering various parameter regimes, that the DMFT can provide a rather accurate solution for the Holstein polaron even in low dimension. Hence, the DMFT has emerged as a unique numerical method that gives close to exact spectral functions in practically the whole space of parameters, irrespective of the number of dimensions. This makes the DMFT an ideal benchmark method for comparisons with the CE results for the Holstein model.

III. SPECTRAL FUNCTIONS

In this section, we present the CE spectral functions of the 1D Holstein model. The DMFT is used as a benchmark, while MA and SCMA represent the main competitors and alternatives to the CE method. Section III A shows the results for $k = 0$, whereas heat plots and the $k = \pi$ results are shown in Sec. III B. High-temperature spectral functions and spectral sum rules are presented in Sec. III C. The behavior near the atomic limit is discussed in Sec. III D. We present only

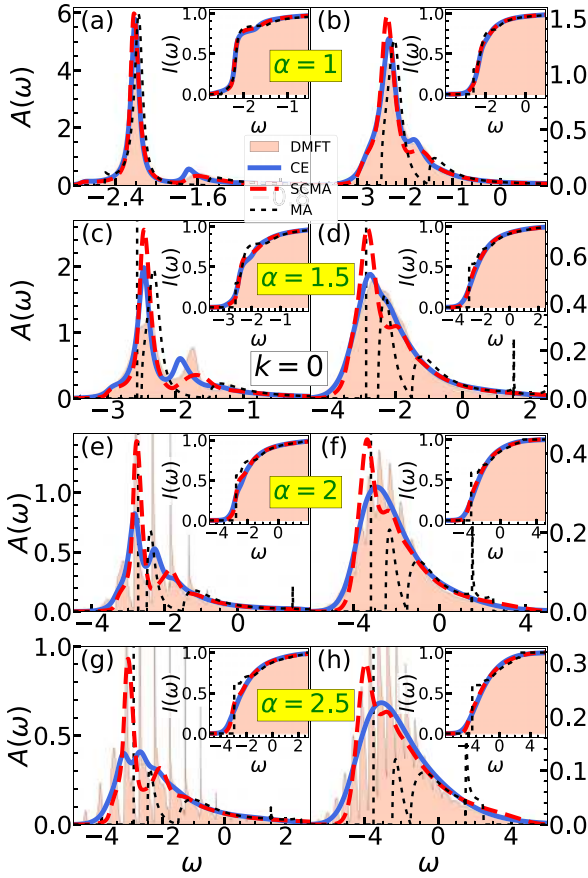


FIG. 4. (a)–(h) Spectral functions for $t_0 = 1$, $\omega_0 = 0.5$ and $k = 0$. In the left panels $T = 0.3$, while $T = 0.7$ in the right panels. Insets show the integrated spectral weights $I_k(\omega) = \int_{-\infty}^{\omega} A_k(v) dv$.

the results for $\omega_0 = 0.5$, while the results for other phonon frequencies and various momenta are shown in Sec. II of SM [54]. The 2D spectral functions are presented in Appendix B.

A. Low and intermediate temperatures for $k = 0$

In the weak-coupling limit $\alpha \rightarrow 0$, all these approximate methods (DMFT, CE, SCMA, MA) provide accurate results. In Fig. 4, we investigate how far from this strict limit each of our methods continues to give reasonably accurate spectral functions. In Fig. 4(a), we see that for $\alpha = 1$ all methods correctly capture the quasiparticle peak, which dominates in the structure of the spectrum. The MA satellite peak is slightly shifted towards higher frequencies, which becomes significantly more pronounced at higher temperatures; see Fig. 4(b). The limitations of the MA become more obvious for stronger couplings, where even the position and weight of the quasiparticle peak are inaccurate; see Figs. 4(c)–4(h).

While the quasiparticle properties of the CE and SCMA seem to be quite similar if α is not too large, some difference in satellite peaks is already visible in Figs. 4(b) and 4(c). Figure 4(c) shows that SCMA gives broader satellites than the DMFT benchmark, whereas CE slightly underestimates the position of the satellite. Neither CE nor SCMA can be characterized as distinctly better in this regime. On the other hand, Figs. 4(e) and 4(g) display a clear advantage of the CE.

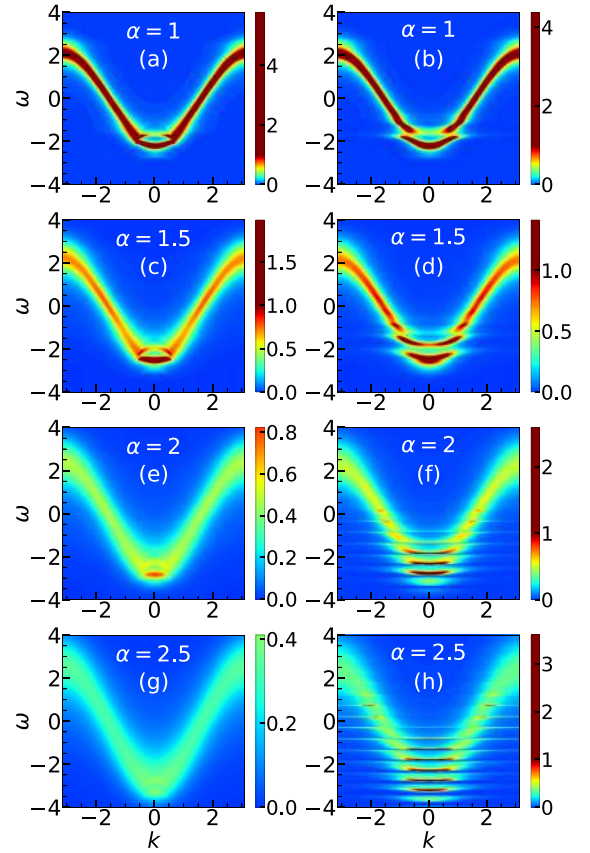


FIG. 5. (a)–(h) Heat maps of $A_k(\omega)$ for $t_0 = 1$, $\omega_0 = 0.5$, and $T = 0.3$. In the left panels, we present CE results, while the DMFT benchmark is presented in the right panel. All plots use the same color coding.

We see that it captures rather well the most distinctive features of the solutions, which are the first few satellites. This is not the case for SCMA.

Figures 4(f) and 4(h) demonstrate that the CE gives a rather quick crossover toward the high-temperature limit, as it predicts a simple broad one-peak structure for the spectral function already for $T = 0.7$. This large difference between the spectral functions for $T_1 = 0.3$ and $T_2 = 0.7$ can be understood by examining the ratio of their corresponding lifetimes $\tau(T_1)/\tau(T_2) = n_{\text{ph}}(T_2)/n_{\text{ph}}(T_1) \approx 8.5$. This implies that $\text{Re}C_k(t)$ for $T = 0.7$ has a much steeper slope as a function time, which suppresses the appearance of satellites, as explained in Sec. II A 3.

B. Low and intermediate temperatures for $k \neq 0$

To proceed with the analysis of the CE, we want to answer: (i) Whether the conclusions that we reached for $k = 0$ can be carried over to other momenta as well? (ii) Does CE continue to be better than SCMA at much higher temperatures? The first question is answered in Fig. 5, where we compare CE and DMFT heat plots. Figures 5(a) and 5(b) demonstrate that CE results are quite reminiscent of the DMFT results for $\alpha = 1$, even at nonzero momenta. The same conclusion holds for weaker couplings as well. On the other hand, there are differences between the results for somewhat stronger

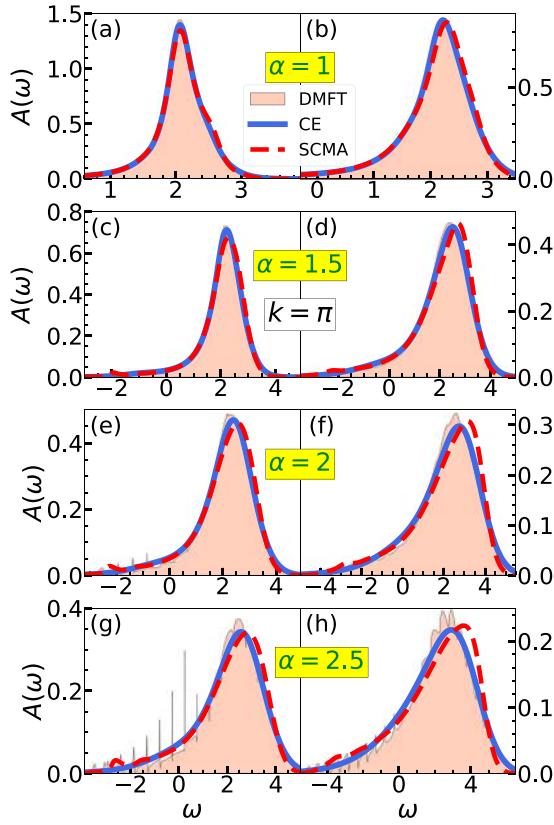


FIG. 6. (a)–(h) Spectral functions for $t_0 = 1$, $\omega_0 = 0.5$, and $k = \pi$. In the left panels $T = 0.3$, while $T = 0.7$ in the right panels.

coupling $\alpha = 1.5$, as shown in Figs. 5(c) and 5(d). While the polaron bands in both of these figures are convex, the CE predicts the first satellite to be concave, unlike the DMFT. In other words, CE predicts that the distance between the polaron peak and the satellites decreases as we increase the momentum. This is counterintuitive, as the satellites are perceived as the quasiparticle that absorbed or emitted a phonon, which should consequently be just at energy distance ω_0 apart. These limitations of the CE are much more pronounced for stronger electron-phonon couplings. While the DMFT solution in Figs. 5(f) and 5(h) exhibits a series of distinct bands, Figs. 5(e) and 5(g) demonstrate that the polaron and satellite bands of the CE merge into a single band at higher momenta. However, the most noticeable feature here is the fact that the CE is too smeared, as if the temperature is too high. This is a consequence of the fact that the lifetime in Eq. (18) scales as $\tau_{\mathbf{k}} \sim 1/g^2$. While the heat maps reveal noticeable discrepancies between the DMFT and CE for $k \neq 0$, it seems that these differences are much less pronounced around $k = \pi$. A more detailed comparison is presented in Fig. 6 that shows the results for the same regimes as in Fig. 4. The DMFT solution in Figs. 6(a)–6(d) shows that the main feature of the spectral function is a single broad peak for $\alpha \lesssim 1.5$, which is in agreement with the CE results. This is also the case for the SCMA, although we observe a slight tendency of the main peak to lean toward higher frequencies at higher temperatures. For larger interaction strengths, CE cannot fully reproduce the sharp peaks at lower frequencies of the low-temperature spectral function or the fine structure of the main peak at higher

temperatures; see Figs. 4(e)–4(h). Similarly, CE misses the quasiparticle peak as well, situated at low energy, although it is typically tiny and not (clearly) visible in Figs. 6(a)–6(h) (see Appendix C). A detailed comparison of the spectral functions for other momenta and phonon frequencies is presented in Sec. II of the SM [54].

Overall, we find that the CE gives the most accurate results for $k = 0$ and $k = \pi$ and that it is less accurate for other momenta. Although it cannot fully reproduce a tiny quasiparticle peak for $k = \pi$, it describes well a wide single-peak structure, which is the most prominent feature of the spectrum. A much larger discrepancy for $k = \pi$, between the CE and a reliable benchmark, was reported in Ref. [50] by examining the system on a finite lattice system with $N = 6$. In Appendix C, we examine the same parameter regime as in Ref. [50] and show that these discrepancies are significantly reduced in the thermodynamic limit.

C. Spectral functions at high temperatures and spectral sum rules

In Fig. 7, we show CE, SCMA, and DMFT spectral functions at high temperatures for the same electron-phonon couplings as in Figs. 4 and 6. We see that CE performs very well both for $k = 0$ and $k = \pi$. There are only small discrepancies at stronger interactions [see, e.g., Fig. 7(c)]. In contrast, the SCMA solution gets tilted relative to the DMFT and CE. In addition, it poorly reproduces the low-frequency part of the spectrum. It is not obvious whether the CE method is exact in the high-temperature limit $T \rightarrow \infty$. As we now demonstrate, this can be answered by examining the spectral sum rules:

$$\mathcal{M}_n(\mathbf{k}) = \int_{-\infty}^{\infty} A_{\mathbf{k}}(\omega) \omega^n d\omega. \quad (23)$$

These can be calculated both exactly,

$$\mathcal{M}_n^{\text{exact}}(\mathbf{k}) = \left\langle \underbrace{[\dots [c_{\mathbf{k}}, H], H] \dots, H]}_{n \text{ times}} c_{\mathbf{k}}^\dagger \right\rangle_T, \quad (24)$$

and within the CE approximation, where by combining Eqs. (4) and (23) we find

$$\begin{aligned} \mathcal{M}_n^{\text{CE}}(\mathbf{k}) &= \text{Re} \left[i^n \left(\frac{d}{dt} \right)^n e^{c_{\mathbf{k}}(t)} \right] \Big|_{t=0} \\ &\quad - \sum_{p=1}^n \binom{n}{p} (-\varepsilon_{\mathbf{k}})^p \mathcal{M}_{n-p}^{\text{CE}}(\mathbf{k}). \end{aligned} \quad (25)$$

The difference between these quantities $\mathcal{M}_n^{\text{CE}}(\mathbf{k}) - \mathcal{M}_n^{\text{exact}}(\mathbf{k})$ is zero for $n = 0$ and $n = 1$, as noted in Sec. II A 1. Higher order sum rules for the CE method are easily calculated, while the evaluation of the exact sum rules quickly becomes cumbersome for increasing n . The first five ($0 \leq n \leq 4$) sum rules were already calculated by Kornilovitch [58]

$$\mathcal{M}_2(\mathbf{k}) = \varepsilon_{\mathbf{k}}^2 + (2n_{\text{ph}} + 1)g^2, \quad (26a)$$

$$\mathcal{M}_3(\mathbf{k}) = \varepsilon_{\mathbf{k}}^3 + g^2\omega_0 + 2g^2(2n_{\text{ph}} + 1)\varepsilon_{\mathbf{k}}, \quad (26b)$$

$$\begin{aligned} \mathcal{M}_4(\mathbf{k}) &= \varepsilon_{\mathbf{k}}^4 + 2g^2\varepsilon_{\mathbf{k}}\omega_0 + g^2(2n_{\text{ph}} + 1) \\ &\quad \times (2t_0^2 + 3\varepsilon_{\mathbf{k}}^2 + \omega_0^2) + 3g^4(2n_{\text{ph}} + 1)^2. \end{aligned} \quad (26c)$$

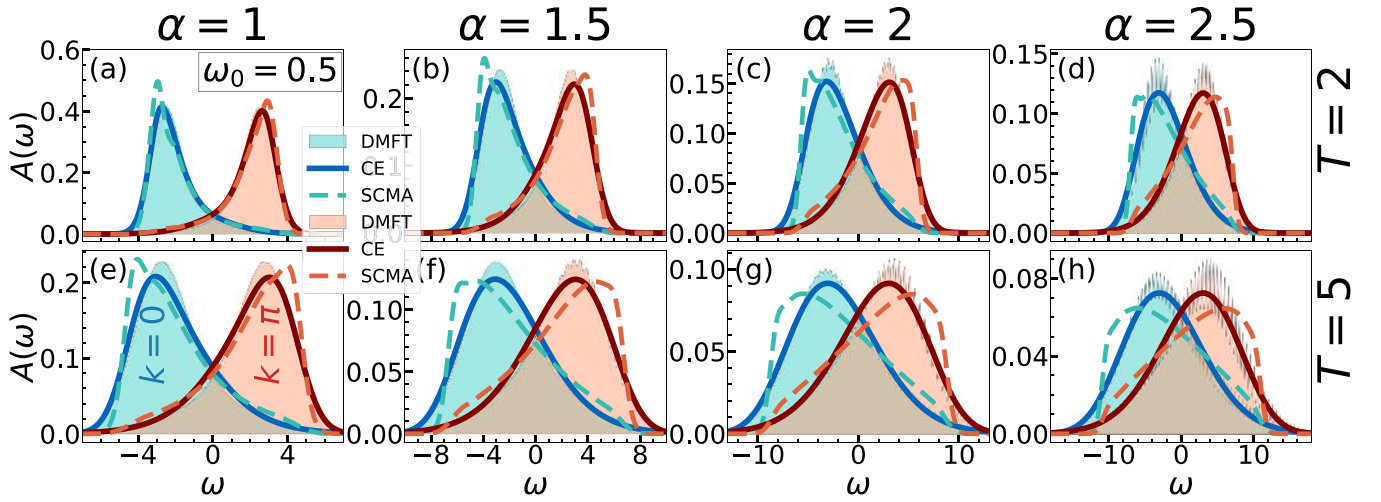


FIG. 7. (a)–(h) CE, DMFT, and SCMA spectral functions in 1D for $t_0 = 1$, $\omega_0 = 0.5$, and $k = 0, \pi$.

All of these are correctly predicted by the CE. However, the disagreement between $\mathcal{M}_n^{\text{exact}}$ and $\mathcal{M}_n^{\text{CE}}$ appears for $n = 5$, where we find

$$\begin{aligned} \mathcal{M}_5^{\text{exact}}(\mathbf{k}) &= \varepsilon_{\mathbf{k}}^5 + 3g^2\omega_0(2t_0^2 + \varepsilon_{\mathbf{k}}^2) + g^2\omega_0^3 \\ &\quad + 2g^2(2\varepsilon_{\mathbf{k}}^3 + 5g^2\omega_0 + \varepsilon_{\mathbf{k}}\omega_0^2 + 2t_0^2\varepsilon_{\mathbf{k}})(2n_{\text{ph}} + 1) \\ &\quad + 7g^4\varepsilon_{\mathbf{k}}(2n_{\text{ph}} + 1)^2, \end{aligned} \quad (27a)$$

$$\mathcal{M}_5^{\text{CE}}(\mathbf{k}) = \mathcal{M}_5^{\text{exact}}(\mathbf{k}) - 2g^4\varepsilon_{\mathbf{k}}(2n_{\text{ph}} + 1)^2. \quad (27b)$$

Hence, CE cannot be exact in the limit $T \rightarrow \infty$. However, we see that there are two limits where CE can potentially be exact: the weak-coupling limit $g \rightarrow 0$ and the atomic limit $\varepsilon_{\mathbf{k}} \rightarrow 0$. It turns out that CE is actually exact in both of these limits, as seen from Eqs. (3), (7), and (14) for the weak-coupling and Sec. III D for the atomic limit. We note that the SCMA gives correct sum rules only for $n \leq 3$ [42]. This is a consequence of the fact that SCMA ignores one of the fourth-order diagrams ($\sim g^4$) since it includes only the noncrossing diagrams. Also, we numerically checked that the DMFT results are in agreement with all of the sum rules that we listed above.

D. Atomic limit

In the atomic limit ($t_0 = 0$), the cumulant function can be evaluated exactly:

$$C(t) = \alpha^2(-2n_{\text{ph}} - 1 + it\omega_0 + iD(t)). \quad (28)$$

This follows from Eq. (16), using $J_0(0) = 1$. If we express the phonon propagator as $iD(t) = 2\sqrt{n_{\text{ph}}(n_{\text{ph}} + 1)} \cos[\omega_0(t + \frac{i}{2T})]$ and use the modified Jacobi-Anger identity

$$\begin{aligned} &e^{2\alpha^2\sqrt{n_{\text{ph}}(n_{\text{ph}}+1)}\cos[\omega_0(t+\frac{i}{2T})]} \\ &= \sum_{l=-\infty}^{\infty} I_l(2\alpha^2\sqrt{n_{\text{ph}}(n_{\text{ph}}+1)})e^{-il\omega_0 t} e^{\frac{l\omega_0}{2T}}, \end{aligned} \quad (29)$$

where I_l are the modified Bessel functions of the first kind, the spectral function [see Eqs. (3) and (4)] can be calculated

analytically and reads as

$$\begin{aligned} A(\omega) &= e^{-\alpha^2(2n_{\text{ph}}+1)} \\ &\quad \times \sum_{l=-\infty}^{\infty} I_l(2\alpha^2\sqrt{n_{\text{ph}}(n_{\text{ph}}+1)})e^{\frac{l\omega_0}{2T}} \delta(\omega + \alpha^2\omega_0 - l\omega_0). \end{aligned} \quad (30)$$

In the limit $T \rightarrow 0$, the previous expression reduces to

$$A(\omega) = e^{-\alpha^2} \sum_{l=0}^{\infty} \frac{\alpha^{2l}}{l!} \delta(\omega + \omega_0(\alpha^2 - l)). \quad (31)$$

This proves that CE gives correct results in the atomic limit, as Eqs. (30) and (31) coincide with the known exact results [1,44].

In contrast, the SCMA (let alone the MA) does not share this property, which is easy to show at zero temperature. In this case, Eq. (20a) and the Dyson equation imply that

$$G(\omega) = \frac{1}{\omega - g^2 G(\omega - \omega_0)}. \quad (32)$$

The previous equation can be solved by the iterative application of itself in terms of the continued fraction

$$G(\omega) = \frac{1}{\omega - \frac{g^2}{\omega - \omega_0 - \frac{g^2}{\omega - 2\omega_0 - \frac{g^2}{\omega - 3\omega_0 - \dots}}}}. \quad (33)$$

This does not coincide with Eq. (35) from Ref. [53], which represents the exact solution. Thus, SCMA cannot reproduce the correct result in the atomic limit.

While the CE is exact in the atomic limit ($t_0 = 0$), it is not immediately obvious how far from this limit it continues to give reliable results. This is why we now examine the regimes with small hopping parameter t_0 . Since the lifetime is infinitely large in some of these regimes (see Fig. 2), we introduce artificial attenuation η for the Green's function in real time by making a replacement $G(t) \rightarrow G(t)e^{-\eta t}$. The results are presented in Fig. 8. Here, the dotted line is the analytic solution in the atomic limit ($t_0 = 0$), determined by Eq. (30), where the Dirac delta functions have been replaced by Lorentzians of half-width η . It is used as a measure to see

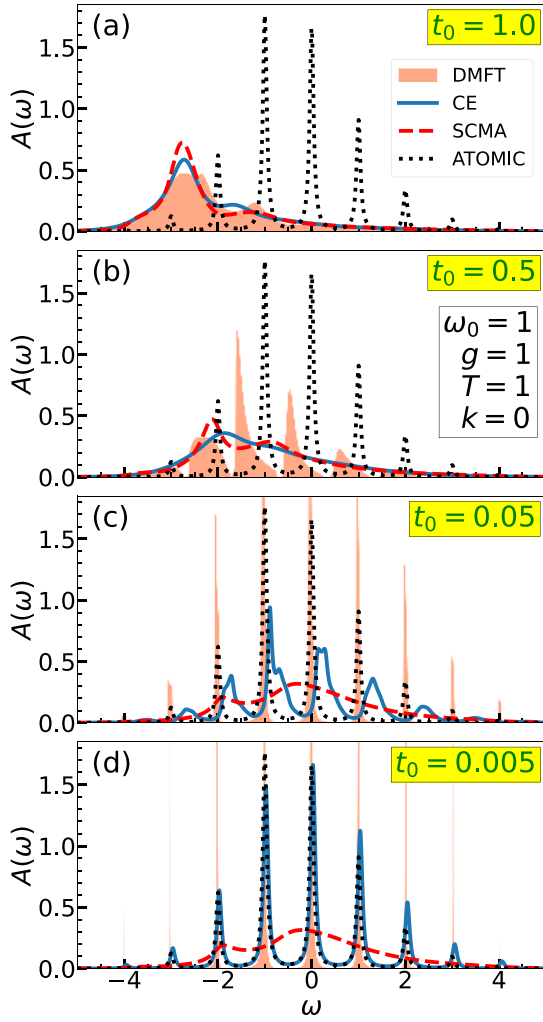


FIG. 8. (a)–(f) CE, DMFT, and SCMA spectral functions close to the atomic limit. Here, we use artificial Lorentzian broadening with half width set to $\eta = 0.05$.

how far the regime we are examining is from the exact atomic limit. In Fig. 8(a), we see that DMFT, SCMA, and CE spectral functions are in agreement. This regime is quite far from the atomic limit, as indicated by the dotted line. Figure 8(b) shows that the DMFT spectral function already consists of a series of peaks for $t_0 = 0.5$, while the CE and SCMA spectral functions are too flattened out. While the CE solution significantly improved in Fig. 8(c), it is still not giving satisfactory results, even though the DMFT suggests that we are already close to the atomic limit. Only for $t_0 \lesssim 0.005$ does the CE solution give accurate results; see Fig. 8(d). However, this is practically already at the atomic limit. It is interesting to note that while both the DMFT and the CE are exact in the weak-coupling and in the atomic limit, their behavior in other regimes can be quite different.

IV. QUASIPARTICLE PROPERTIES

We now investigate the quasiparticle properties obtained from the CE method and compare them extensively to the results obtained from the DMFT and SCMA. We note that

the lifetime within the CE was already studied in Sec. II A 4, so we supplement that study here with the results for the ground-state energy and the effective mass. Here we show the results in one, two, and three dimensions. Comparison with the MA ground-state energy, in the 1D case, is presented in Sec. III of the SM [54].

A. Ground-state energy

The polaron band dispersion $E_{p,\mathbf{k}}$ within the CE is given by the real part of Eq. (12), where the self-energy is taken in the MA:

$$E_{p,\mathbf{k}} = \varepsilon_{\mathbf{k}} + \text{Re}\Sigma^{\text{MA}}(\varepsilon_{\mathbf{k}}). \quad (34)$$

Since we deal with a single electron in the band, the ground-state energy E_p is given by $E_{p,\mathbf{k}=0}$ evaluated at zero temperature. In the 1D case, E_p is straightforwardly evaluated using Eq. (19) and reads as follows:

$$E_p^{1\text{D}} = -2t_0 - \frac{\alpha^2 \omega_0^2}{\sqrt{\omega_0^2 + 4\omega_0 t_0}}. \quad (35)$$

For the expression in higher dimensions, we need to go back to Eq. (14) that holds in any number of dimensions. At $T = 0$, it reads as

$$\text{Im}\Sigma^{\text{MA}}(\omega) = -\pi \alpha^2 \omega_0^2 \rho(\omega - \omega_0). \quad (36)$$

The real part of $\Sigma^{\text{MA}}(\omega)$ is obtained using the Kramers-Kronig relation

$$\text{Re}\Sigma^{\text{MA}}(\omega) = \pi \alpha^2 \omega_0^2 \mathcal{H}[\rho](\omega - \omega_0), \quad (37)$$

where $\mathcal{H}[\rho](\omega) = \mathcal{P} \int_{-\infty}^{\infty} \frac{dv}{\pi} \frac{\rho(v)}{\omega - v}$ is the Hilbert transform of the density of states $\rho(\omega)$ and \mathcal{P} is the Cauchy principle value. The evaluation of the Hilbert transform may be reduced to the evaluation of the Fourier transform \mathcal{F} , using the following identity:

$$\mathcal{F}^{-1}\mathcal{H}[\rho](t) = -i \text{sgn}(t) \mathcal{F}^{-1}[\rho](t). \quad (38)$$

The inverse Fourier transform of the density of states on the right-hand side was already calculated in Eq. (15) for the case of the hypercubic lattice with the nearest-neighbor hopping. Hence, $\mathcal{H}[\rho](\omega)$ is obtained by applying \mathcal{F} on both sides of Eq. (38),

$$\mathcal{H}[\rho](\omega) = \frac{1}{\pi} \int_0^{\infty} dx J_0(2t_0 x)^n \sin(x\omega), \quad (39)$$

where n is the number of dimensions. The polaron band dispersion then reads as

$$E_{p,\mathbf{k}} = \varepsilon_{\mathbf{k}} + \alpha^2 \omega_0^2 \int_0^{\infty} dx J_0(2t_0 x)^n \sin(x(\varepsilon_{\mathbf{k}} - \omega_0)). \quad (40)$$

E_p is thus a linear function with respect to α^2 , whose intercept is $\varepsilon_{\mathbf{k}}$, while its slope can be calculated accurately using the numerical scheme described in Appendix A. In the 2D case, it admits an analytical solution

$$E_p^{2\text{D}} = -4t_0 - \frac{2\alpha^2 \omega_0^2}{\pi(4t_0 + \omega_0)} K\left(\frac{4t_0}{4t_0 + \omega_0}\right), \quad (41)$$

where $K(k) = \int_0^{\pi/2} d\theta / \sqrt{1 - k^2 \sin^2 \theta}$ is the complete elliptic integral of the first kind. In the case $n = 3$, the integral

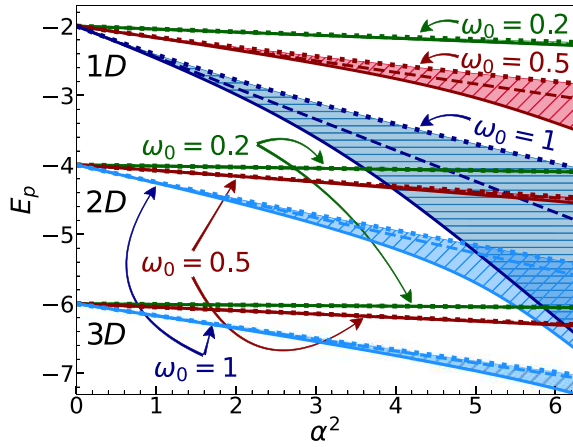


FIG. 9. Ground-state energy within the DMFT (solid line), CE (dashed line), and SCMA (dotted line). Here, $t_0 = 1$ and $T = 0$.

in Eq. (40) does not admit a closed-form solution and thus requires numerical calculation.

The polaron band dispersion $E_{p,\mathbf{k}}$ (and thus the ground state E_p) within the DMFT and SCMA is obtained numerically, as the smallest solution of the following equation:

$$E_{p,\mathbf{k}} = \varepsilon_{\mathbf{k}} + \text{Re}\Sigma(E_{p,\mathbf{k}}). \quad (42)$$

Results for the 1D, 2D, and 3D case are presented in Fig. 9. The DMFT benchmark, which is known to be very accurate [52], always gives the lowest ground-state energy predictions in comparison to the CE and SCMA. We see that CE always outperforms the SCMA, despite the fact that its predictions of the energy are always a linear function of α^2 . In the 1D case, we see that CE results for $\omega_0 = 0.5$ start to deviate more significantly from the DMFT just around $\alpha = 2.5$. Hence, the range of validity for the CE is similar as for the spectral functions in Fig. 4. The analogous conclusions can also be drawn from $\omega_0 = 1$ data as well. In contrast, all three methods seem to be in agreement for $\omega_0 = 0.2$ in the whole range of presented values of α . This is a consequence of the fact that the ground-state energy correction is small, as seen from Eqs. (35), (40), and (41) by fixing α and decreasing ω_0 . However, if we fix $g = \omega_0\alpha$ and then decrease ω_0 , the ground-state energy would change substantially [see, e.g., Eq. (35)], and the CE would certainly give poorer results.

Similar trends are observed in higher dimensions as well. Seemingly, the range of validity of the CE is increased in higher dimensions. However, one should keep in mind that the hopping parameter is always taken to be unity, which means that the bandwidth of the 2D and 3D systems are, respectively, two and three times larger than their 1D counterpart. Therefore, the correlation is weaker for a given coupling α .

B. Effective mass

Around the bottom ($|\mathbf{k}| \approx 0$) of the conduction band, the dispersion $E_{p,\mathbf{k}}$ assumes the following parabolic form:

$$E_{p,\mathbf{k}} \approx \text{const} + \frac{\mathbf{k}^2}{2m^*}, \quad (43)$$

where m^* is the effective mass, which we now calculate.

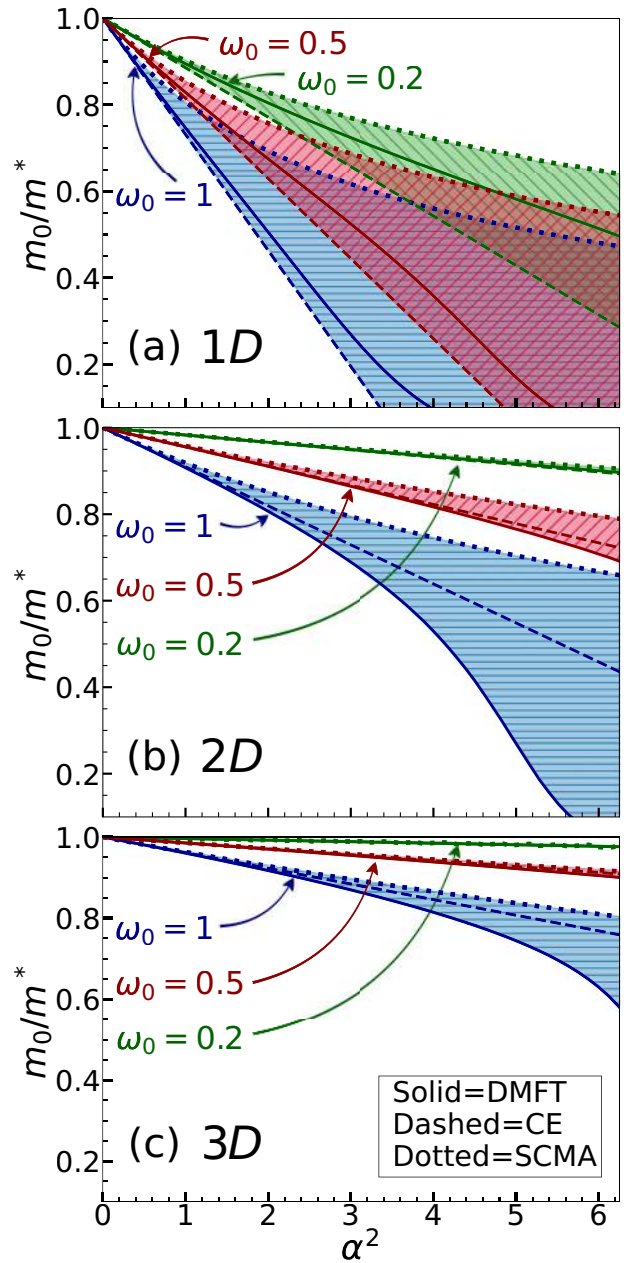


FIG. 10. Effective mass results within the DMFT, CE, and SCMA for $t_0 = 1$ and $T = 0$.

In the 1D case, one obtains the analytical result for the effective mass using Eqs. (19) and (34),

$$\left. \frac{m^*}{m_0} \right|_{1D, T=0} = \frac{1}{1 - \frac{(2t_0 + \omega_0)\alpha^2 \sqrt{\omega_0}}{(4t_0 + \omega_0)^{3/2}}}, \quad (44)$$

where $m_0 = 1/(2t_0)$ is the band mass which remains the same irrespective of the number of dimensions. Results for the higher number of dimensions are evaluated using Eq. (40). As for the ground-state energy, the 2D case admits an analytic solution

$$\left. \frac{m^*}{m_0} \right|_{2D, T=0} = \frac{1}{1 - \frac{2\alpha^2 \omega_0}{\pi(8t_0 + \omega_0)} E\left(\frac{4t_0}{4t_0 + \omega_0}\right)}, \quad (45)$$

where $E(k) = \int_0^{\pi/2} d\theta \sqrt{1 - k^2 \sin^2 \theta}$ is the complete elliptic integral of the second kind. Results in the n -dimensional case are given by

$$\left. \frac{m^*}{m_0} \right|_{T=0} = \frac{1}{1 + \pi \alpha^2 \omega_0^2 \left. \frac{d\mathcal{H}[\rho]}{d\omega} \right|_{\omega=-2m_0-\omega_0}}, \quad (46)$$

and require numerical calculation in the general case. From Eq. (46) we see that m_0/m^* is a linear function of α^2 . This linear behavior has to break down at one point, as m_0/m^* cannot be negative. This happens for strong interaction, where the CE is certainly not expected to be reliable. The mass renormalization within the DMFT and SCMA is calculated numerically as

$$\left. \frac{m^*}{m_0} \right|_{T=0} = 1 - \left. \frac{d\Sigma(\omega)}{d\omega} \right|_{\omega=E_p}, \quad (47)$$

where E_p is the ground-state energy. Results for the DMFT, CE, and SCMA effective mass in different parameter regimes and for different number of dimensions are presented in Fig. 10. In the 1D case, we see that the CE always underestimates, while the SCMA overestimates the results from the DMFT benchmark. Still, CE clearly outperforms the SCMA for $\omega_0 = 1$ and $\omega_0 = 0.5$, while the results in the vicinity of the adiabatic limit ($\omega_0 = 0.2$) seem to be equally well (poor) represented by both methods.

In the higher-dimensional case, we see that the CE is always a clearly better approximation than the SCMA, while both of them overestimate the DMFT predictions. As for the ground-state energy, we emphasize again that the hopping parameter was set to 1. As a consequence, the system has a larger bandwidth in the higher-dimensional case and, therefore, the correlations are weaker.

V. MOBILITY

The mobility is defined as the DC conductivity, normalized to the concentration of charge carriers n_e (and their unit charge which we set to $e = 1$), i.e., $\mu = \sigma^{\text{DC}}/n_e$. It can be calculated using the Kubo formalism, which relates μ to the current-current correlation function [1]. The latter can be written as a sum of the so-called bubble part, which is completely determined by the spectral functions $A_{\mathbf{k}}(\omega)$ and the vertex corrections. Within the DMFT, the vertex corrections vanish [57,59], while estimating their contribution in the general case is beyond the scope of this paper. In the following, we calculate the mobility solely from the bubble part.

In the case of a 1D system with a single spinless electron in the band, the mobility in the bubble approximation can be written as [1,60]

$$\mu = \frac{4\pi t_0^2}{T} \frac{\sum_{\mathbf{k}} \int_{-\infty}^{\infty} dv A_{\mathbf{k}}(v)^2 e^{-v/T} \sin^2 k}{\sum_{\mathbf{k}} \int_{-\infty}^{\infty} dv A_{\mathbf{k}}(v) e^{-v/T}}. \quad (48)$$

The processing time required for the calculation of μ within the CE method rises linearly with the number of k points we sum over. This is not the case for the DMFT and SCMA, as their self-energies are k independent and thus need to be calculated only once for a given parameter set. In every parameter regime the CE was applied to, we checked that 64 sampling points in the Brillouin zone are enough to be representative of

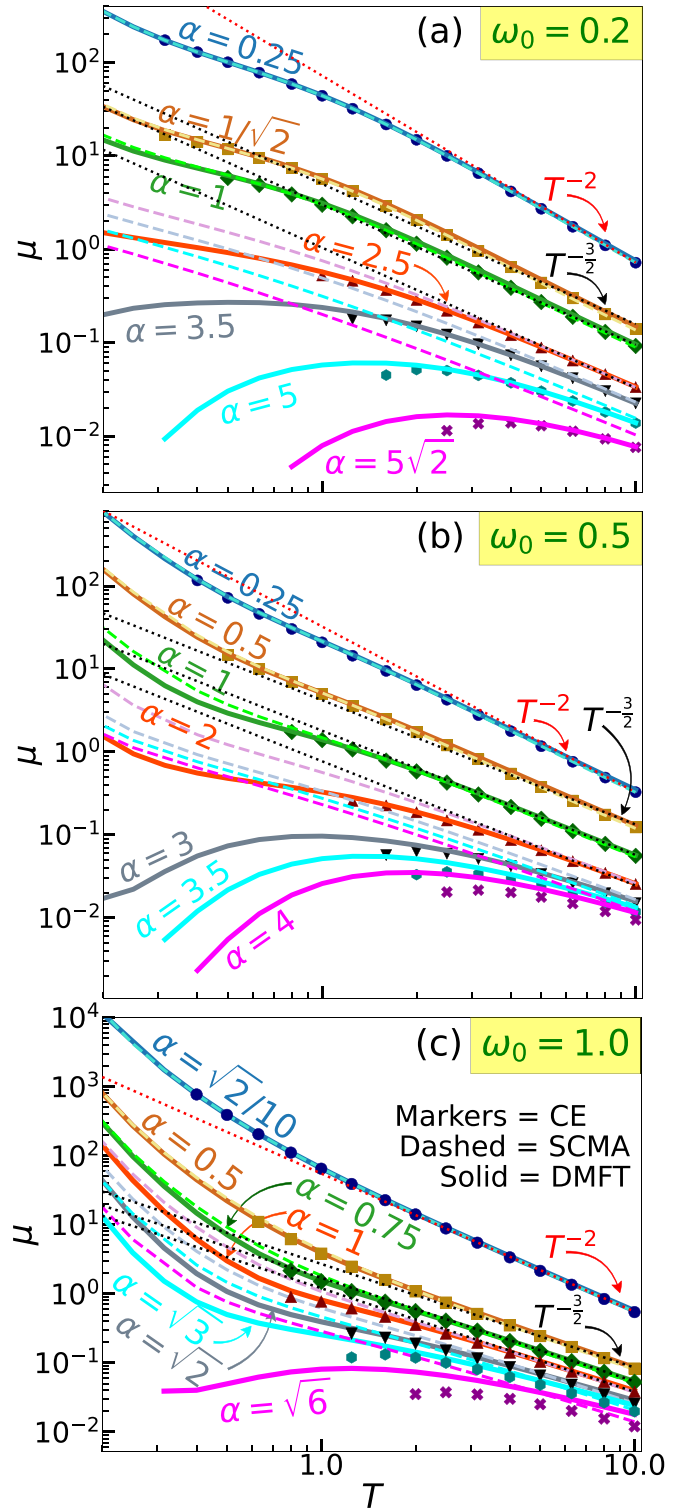


FIG. 11. Temperature dependence of the mobility for the CE, DMFT, and SCMA. The dotted red (black) lines are auxiliary lines with the power law behavior $\mu \propto T^{-2}$ ($\mu \propto T^{-3/2}$). Here $t_0 = 1$.

the thermodynamic limit. This was also crosschecked using the DMFT.

The exponential term $e^{-v/T}$ in Eq. (48) has some important implications. Despite the factor $\sin^2 k$, it implies that the largest contribution to the mobility most commonly comes

from the spectral functions around the bottom of the band ($k \approx 0$), as they are typically situated at lower frequencies with respect to their higher momentum counterparts. This is actually helpful, as we have seen that the CE is more reliable for $k \approx 0$ than for $0 < k < \pi$. However, $e^{-\nu/T}$ also introduces numerical instabilities, as even a small numerical noise of $A_k(\nu)$ at $\nu \ll -1$ will be inflated and give an enormous overall error in the mobility. This is why the integrals in Eq. (48) require introducing some kind of negative frequency cutoff $\int_{-\infty}^{\infty} \rightarrow \int_{-\Lambda}^{\infty}$. We always check that the mobility results converge with respect to Λ . This is easily done in both the DMFT and SCMA due to the high numerical accuracy of our numerical implementations. The convergence with respect to Λ is much harder to achieve within the CE, as the Green's functions are initially calculated in the time domain and require the use of numerical Fourier transform. We have implemented a well-known interpolation scheme [61] to increase the precision of the Fourier transform. Still, the numerical noise at low temperatures and strong interactions prevented us from precisely calculating the mobility in these regimes. We show only the data where an accurate calculation was possible.

In Fig. 11, we present numerical results for the temperature dependence of the electron mobility. For weak electron-phonon coupling, all methods are in agreement; see Fig. 11(a) for $\alpha \leq 1$ and Figs. 11(b) and 11(c) for $\alpha \leq 0.5$. Electron-phonon scattering is weak in these regimes, which is why the quasiparticle lifetime τ_k is long, and the linear time dependence dominates in the cumulant function. The spectral function and its square can thus be approximated as $A_k(\omega) \approx \delta(\omega - E_{p,k})$ and $A_k^2(\omega) \approx \frac{\tau_k}{\pi} \delta(\omega - E_{p,k})$, where δ is the Dirac delta function and $E_{p,k}$ is given by Eq. (34). The mobility from Eq. (48) thus simplifies to

$$\mu_{\text{weak}} \approx \frac{4t_0^2}{T} \frac{\sum_k \tau_k e^{-E_{p,k}/T} \sin^2 k}{\sum_k e^{-E_{p,k}/T}}. \quad (49)$$

At high temperatures, Eq. (49) further simplifies as $e^{-E_{p,k}/T} \approx 1$. In this case, the lifetime is inversely proportional to the temperature $\tau_k \propto 1/T$, as seen from Eq. (18), which implies the power-law behavior of the mobility $\mu_{\text{weak}} \propto 1/T^2$. This conclusion holds only for very weak electron-phonon couplings, where the assumption of weak scattering is still satisfied despite the high temperatures; see Figs. 11(a) and 11(b) for $\alpha = 0.25$ and Fig. 11(c) for $\alpha = \sqrt{2}/10$. This assumption is also violated at extremely high temperatures $T \rightarrow \infty$.

For stronger couplings, in the limit of high-temperatures $T \gg t_0, \omega_0$, the Green's function in the time domain is quickly damped, which is why $C_k(t)$ can be approximated with just the lowest order (quadratic) Taylor expansion around $t = 0$. Hence, Eqs. (3) and (17) imply that the Green's function can be written as

$$G_k(t) = -i\theta(t)e^{-i\varepsilon_k t} e^{-\frac{g^2}{2}(2n_{\text{ph}}+1)t^2}, \quad (50)$$

while the corresponding spectral function is given by the Gaussian:

$$A_k(\omega) = \frac{e^{-\frac{(\omega-\varepsilon_k)^2}{2g^2(2n_{\text{ph}}+1)}}}{\sqrt{2\pi g^2(2n_{\text{ph}}+1)}}. \quad (51)$$

Plugging this back into Eq. (48) and changing the sum over momenta to integral, we obtain

$$\mu_{\text{high-}T} = \frac{t_0}{g} \sqrt{\frac{\pi}{2n_{\text{ph}}+1}} \exp\left(-\frac{g^2(2n_{\text{ph}}+1)}{4T^2}\right) \frac{I_1\left(\frac{2t_0}{T}\right)}{I_0\left(\frac{2t_0}{T}\right)}, \quad (52)$$

where I_0 and I_1 are modified Bessel functions of the first kind, of zeroth and first orders, respectively. Equation (52) can be simplified by using the following approximations: $2n_{\text{ph}}+1 \approx 2T/\omega_0$ and $I_1(2t_0/T)/I_0(2t_0/T) \approx t_0/T$, that are valid for large T . Such a simplified formula coincides with the mobility obtained by combining the Einstein relation, between the mobility and diffusion coefficient, with the Marcus formula [45,62]. Furthermore, Eq. (52) implies the power-law behavior for the mobility $\mu_{\text{high-}T} \propto T^{-3/2}$, in the limit $T \gg t_0, \omega_0$. This is confirmed by our numerical results for a wide range of the electron-phonon coupling strengths, where all three methods are in agreement; see Fig. 11(a) for $1/\sqrt{2} \leq \alpha \leq 2.5$, Fig. 11(b) for $0.5 \leq \alpha \leq 2$, and Fig. 11(c) for $0.5 \leq \alpha \leq 1$.

While the SCMA gives satisfactory results for high temperatures and intermediate electron-phonon couplings, it deviates from the DMFT at lower temperatures [see, e.g., Fig. 11(a) for $\alpha = 2.5$ and Fig. 11(b) for $\alpha = 2$] and also for stronger coupling strengths [see, e.g., Fig. 11(a) for $\alpha > 2.5$ and Fig. 11(b) for $\alpha > 2$]. At these stronger couplings, the DMFT predicts the nonmonotonic mobility, where a region of decreasing mobility with decreasing temperature is ascribed to the hopping transport in phenomenological theories [38,62]. The strong coupling mobility is better described by the CE than SCMA, although low-temperature results are missing due to our inability to converge the results with respect to the cutoff Λ . In Appendix D, we also give mobility predictions of the MA.

VI. CONCLUSIONS AND OUTLOOK

In summary, we have presented a comprehensive analysis of the CE method in the context of the Holstein model. The second-order cumulant $C(t)$ is calculated in a broad temperature range for three vibrational frequencies $\omega_0/t_0 = 0.2, 0.5$, and 1, covering a regime from a weak to strong electron-phonon coupling. We mostly focused on the 1D system in the thermodynamic limit but some of the results are shown also in 2D and 3D. To avoid numerical instabilities and to reach high numerical precision, we derived a number of analytical expressions and we used the collocation method in calculations of the cumulant, as well as an interpolation scheme for the Fourier transform in corresponding calculations of the spectral functions. The quasiparticle properties, spectral functions, and charge mobility are shown in comparison to the DMFT and SCMA results. The DMFT, which gives close to the exact solution for the Holstein polaron throughout the parameter space [52], gave a valuable benchmark and facilitated a detailed analysis of the validity of the CE method.

At weak coupling (roughly corresponding to $m_0/m^* \gtrsim 0.9$) CE, DMFT, and SCMA give very similar spectral functions. Most of the spectral weight for $k = 0$ is in the quasiparticle peak, while even a small sideband (satellite) spectral weight is rather well reproduced in all three methods. As the interaction increases, a clear difference in the spectral functions

emerges. Nevertheless, the positions of the CE and DMFT quasiparticle and the first satellite peak at low temperatures are in rather good agreement. Furthermore, the overall spectral weight distribution is in a decent agreement even though the satellite peaks are more pronounced in DMFT for stronger electron-phonon coupling. Roughly speaking, there is a decent agreement in 1D up to the interactions corresponding to $m_0/m^* \sim 0.5$. Interestingly, the agreement between the CE and DMFT spectral functions persists also for $k = \pi$, although CE does not capture a tiny quasiparticle peak. In this case, the DMFT spectral weight almost merges to a single broad peak. We note that the difference for $k = \pi$ observed in Ref. [50] is solely due to considering a lattice of finite $N = 6$ size. The deviation of CE from the exact solution is most obvious for intermediate momenta where the CE solution merges to a single peak, while the satellite structure is seen in DMFT. At high temperatures, one might suspect that the CE would give the exact spectral functions. However, this is not the case, as we showed that the CE gives the exact spectral moments only up to the order $n = 4$. We note that in all these regimes, the CE gives slightly better results than the SCMA, while a single-shot MA is adequate only for very weak interactions.

The spectral functions were used to calculate the charge mobility from the Kubo formula without the vertex corrections. The agreement between DMFT and CE is quite good. This is the case even for stronger electron-phonon coupling where the CE even indicates nonmonotonic behavior of $\mu(T)$, with a region of increasing mobility with temperature which is usually assigned to hopping conduction in phenomenological theories. For strong electron-phonon coupling, the CE mobility results are shown only for $T \gtrsim t_0$ since a very small numerical noise at frequencies $\omega \ll E_p$ affects a precise calculation of mobility at lower temperatures. For high temperatures, the mobility assumes a universal form: For weak electron-phonon coupling $\mu \propto T^{-2}$, while for stronger coupling $\mu \propto T^{-3/2}$. These high-temperature limits can be obtained also analytically from the CE.

The CE method can be easily applied to different Hamiltonians, which makes it a particularly attractive method for the calculation of electronic properties beyond the weak-coupling limit in various systems. In particular, we argue that it will be most useful in calculations of charge mobility, as has already been done in *ab initio* calculations for SrTiO₃ [16] and naphthalene [17]. While our analysis may suggest that the DMFT appears computationally superior to CE, we note that the numerical efficiency that we achieved with DMFT is restricted to the Holstein model by virtue of the analytic solution for the impurity problem [53] and the local Green's function [52]. For predicting the properties of real materials, the numerical resources within the DMFT are vastly increased and also the issue of nonlocal correlations may emerge, while the CE remains simple and relatively inexpensive. Of course, for a definitive answer on the range of validity of CE in connection with *ab initio* calculations, one needs to perform a similar analysis for the Fröhlich model and for other models which can be used for realistic description of the electronic spectra and charge transport in real materials. A useful hint in this direction is provided by Ref. [51], which shows that the CE, around the bottom of the band, gives promising results for the spectral function even in the case when the phonons

have a dispersion [63]. Another very interesting question that we leave for further work is a possible contribution of vertex corrections to conductivity. Based on the weak coupling result [64], one might assume that their contribution is small for optical phonons, but this remains to be determined in the case of stronger coupling. Our high-temperature results for mobility may also be quite useful when analyzing a dominant type of electron-phonon coupling in real materials. Still, one needs to be cautious in such analyses since we see that at lower temperatures $\mu(T)$ does not assume a simple universal form.

ACKNOWLEDGMENTS

The authors acknowledge funding provided by the Institute of Physics Belgrade, through a grant by the Ministry of Science, Technological Development and Innovation of the Republic of Serbia. Numerical simulations were performed on the PARADOX supercomputing facility at the Scientific Computing Laboratory, National Center of Excellence for the Study of Complex Systems, Institute of Physics Belgrade.

APPENDIX A: NUMERICAL INTEGRATION SCHEME FOR THE HIGHLY OSCILLATING FUNCTIONS IN THE CE METHOD

We present a numerical integration scheme for the calculation of the cumulant function from Eq. (16). Since $C_k(t)$ will be expressed numerically on some t -grid [$t_0 = 0, t_1 \dots t_{G-1}$], it is much better to divide the integral \int_0^t from Eq. (16) into a sum of integrals of the form $\int_{t_{i-1}}^{t_i}$, where t_i are times from the previously defined t grid. In this manner, we do not integrate over the same interval multiple times. To shorten the notation, from now on, we denote $a \equiv t_{i-1}$ and $b \equiv t_i$. There are two different types of integrals in Eq. (16), and both of them have the following form:

$$I = \int_a^b dx g(x) e^{ir_1 x} J_0(r_2 x)^n, \quad (\text{A1})$$

where $g(x)$ is either a linear or a constant function, $r_1 = \varepsilon_{\mathbf{k}} \pm \omega_0$, and $r_2 = 2t_0$. Numerical integration of Eq. (A1) has already been studied by Levin for arbitrary r_1 and r_2 and slowly varying $g(x)$ [55]. In the rest of this Appendix, we review this method in the 1D ($n = 1$), 2D ($n = 2$), and 3D ($n = 3$) cases. The main idea is to rewrite the subintegral function as a scalar product of two columns $|\tilde{g}(x)\rangle$ and $|\tilde{J}(x)\rangle$, whose elements are functions:

$$I = \int_a^b dx \langle \tilde{g}(x) | \tilde{J}(x) \rangle. \quad (\text{A2})$$

Column $|\tilde{g}(x)\rangle$ consists exclusively of slowly varying functions, while $|\tilde{J}(x)\rangle$ contains highly oscillating functions, with the property that

$$\frac{d|\tilde{J}(x)\rangle}{dx} = \hat{A}(x)|\tilde{J}(x)\rangle, \quad (\text{A3})$$

where $\hat{A}(x)$ is a matrix of slowly varying functions. Then, the integral from Eq. (A2) can be written as

$$I = \int_a^b dx \frac{d}{dx} \langle \tilde{f}(x) | \tilde{J}(x) \rangle = \langle \tilde{f}(b) | \tilde{J}(b) \rangle - \langle \tilde{f}(a) | \tilde{J}(a) \rangle, \quad (\text{A4})$$

where $|\tilde{f}(x)\rangle$ satisfies

$$\left(\frac{d}{dx} + \hat{A}^\dagger(x) \right) |\tilde{f}(x)\rangle = |\tilde{g}(x)\rangle. \quad (\text{A5})$$

This is then, following Levin [55], solved by formally expanding $|\tilde{f}(x)\rangle = \sum_{k=1}^M u_k(x) [c_k \ d_k \ \dots]^T$ into a basis set of polynomials $u_k(x) = (x - \frac{a+b}{2})^{k-1}$ and determining the unknown polynomial coefficients $c_k, d_k \dots$ by imposing that Eq. (A5) is exactly satisfied at M uniformly distributed collocation points $x_j = a + \frac{(j-1)(b-a)}{M-1}$, $j = 1 \dots M$. The initial problem is thus reduced to a simple linear algebra problem.

1. 1D case

In the 1D case ($n = 1$), columns $|\tilde{g}(x)\rangle$ and $|\tilde{J}(x)\rangle$ assume the following form:

$$|\tilde{g}(x)\rangle = [g(x) \ 0]^T, \quad (\text{A6a})$$

$$|\tilde{J}(x)\rangle = e^{ir_1 x} [J_0(r_2 x) \ J_1(r_2 x)]^T, \quad (\text{A6b})$$

where $J_0(x)$ and $J_1(x)$ are the Bessel functions of the first kind, of zeroth and first order. The matrix $\hat{A}(x)$, such that Eq. (A3) holds, is given by

$$\hat{A}(x) = \begin{bmatrix} ir_1 & -r_2 \\ r_2 & ir_1 - \frac{1}{x} \end{bmatrix}. \quad (\text{A7})$$

The unknown coefficients c_k and d_k , which determine the column function

$$|\tilde{f}(x)\rangle = \sum_{k=1}^M u_k(x) [c_k \ d_k]^T, \quad (\text{A8})$$

are obtained from the following set of $2M$ linear equations:

$$\begin{bmatrix} \mathcal{C} & \mathcal{C}^d \\ \mathcal{D}^c & \mathcal{D} \end{bmatrix} \begin{bmatrix} c_1 \\ \vdots \\ c_M \\ d_1 \\ \vdots \\ d_M \end{bmatrix} = \begin{bmatrix} g(x_1) \\ \vdots \\ g(x_M) \\ 0 \\ \vdots \\ 0 \end{bmatrix}. \quad (\text{A9})$$

Here, $\mathcal{C}, \mathcal{C}^d, \mathcal{D}^c, \mathcal{D}$ are $M \times M$ matrices that read as

$$\mathcal{C}_{ij} = u'_j(x_i) - ir_1 u_j(x_i); \quad \mathcal{C}_{ij}^d = r_2 u_j(x_i), \quad (\text{A10a})$$

$$\mathcal{D}_{ij} = u'_j(x_i) - \left(ir_1 + \frac{1}{x_i} \right) u_j(x_i); \quad \mathcal{D}_{ij}^c = -r_2 u_j(x_i). \quad (\text{A10b})$$

2. 2D case

In the 2D case, the relevant quantities are given by

$$\begin{aligned} |\tilde{g}(x)\rangle &= [g(x) \ 0 \ 0]^T, \\ |\tilde{J}(x)\rangle &= e^{ir_1 x} [J_0(r_2 x)^2 \ J_0(r_2 x) J_1(r_2 x) \ J_1(r_2 x)^2]^T, \\ \hat{A}(x) &= \begin{bmatrix} ir_1 & -2r_2 & 0 \\ r_2 & ir_1 - \frac{1}{x} & -r_2 \\ 0 & 2r_2 & ir_1 - \frac{2}{x} \end{bmatrix}. \end{aligned} \quad (\text{A11})$$

The column $|\tilde{f}(x)\rangle = \sum_{k=1}^M u_k(x) [c_k \ d_k \ e_k]^T$ is determined by c_k, d_k , and e_k , which are obtained as a solution of the following system of $3M$ linear equations:

$$\begin{bmatrix} \mathcal{C} & \mathcal{C}^d & \mathcal{C}^e \\ \mathcal{D}^c & \mathcal{D} & \mathcal{D}^e \\ \mathcal{E}^c & \mathcal{E}^d & \mathcal{E} \end{bmatrix} \begin{bmatrix} c_1 \\ \vdots \\ c_M \\ d_1 \\ \vdots \\ d_M \\ e_1 \\ \vdots \\ e_M \end{bmatrix} = \begin{bmatrix} g(x_1) \\ \vdots \\ g(x_M) \\ 0 \\ \vdots \\ 0 \\ \vdots \end{bmatrix}. \quad (\text{A12})$$

Here, $\mathcal{C}, \mathcal{C}^d \dots \mathcal{E}$ are $M \times M$ matrices. Elements of \mathcal{C}_{ij} and \mathcal{C}_{ij}^d are the same as in Eq. (A10), while $\mathcal{C}_{ij}^e = \mathcal{E}_{ij}^c = 0$. All the other elements are given by

$$\begin{aligned} \mathcal{D}_{ij} &= u'_j(x_i) - \left(ir_1 + \frac{1}{x_i} \right) u_j(x_i), \\ \mathcal{E}_{ij} &= u'_j(x_i) - \left(ir_1 + \frac{2}{x_i} \right) u_j(x_i), \\ \mathcal{D}_{ij}^c &= -2r_2 u_j(x_i); \quad \mathcal{D}_{ij}^e = 2r_2 u_j(x_i); \quad \mathcal{E}_{ij}^d = -r_2 u_j(x_i). \end{aligned} \quad (\text{A13})$$

3. 3D case

The procedure that was presented so far is actually quite easily generalized to the 3D case as well. Here, the quantities of interest are easily derived and read as

$$\begin{aligned} |\tilde{g}(x)\rangle &= [g(x) \ 0 \ 0 \ 0]^T, \\ |\tilde{J}(x)\rangle &= e^{ir_1 x} [J_0(r_2 x)^3 \ J_0(r_2 x)^2 J_1(r_2 x) \\ &\quad J_0(r_2 x) J_1(r_2 x)^2 \ J_1(r_2 x)^3]^T, \\ \hat{A}(x) &= \begin{bmatrix} ir_1 & -3r_2 & 0 & 0 \\ r_2 & ir_1 - \frac{1}{x} & -2r_2 & 0 \\ 0 & 2r_2 & ir_1 - \frac{2}{x} & -r_2 \\ 0 & 0 & 3r_2 & ir_1 - \frac{3}{x} \end{bmatrix}, \\ \tilde{f}(x) &= \sum_{k=1}^M u_k(x) [c_k \ d_k \ e_k \ f_k]^T, \end{aligned} \quad (\text{A14})$$

where the coefficients c_k , d_k , e_k , and f_k satisfy

$$\begin{bmatrix} \mathcal{C} & \mathcal{C}^d & \mathcal{C}^e & \mathcal{C}^f \\ \mathcal{D}^c & \mathcal{D} & \mathcal{D}^e & \mathcal{D}^f \\ \mathcal{E}^c & \mathcal{E}^d & \mathcal{E} & \mathcal{E}^f \\ \mathcal{F}^c & \mathcal{F}^d & \mathcal{F}^e & \mathcal{F} \end{bmatrix} \begin{bmatrix} c_1 \\ \vdots \\ c_M \\ d_1 \\ \vdots \\ e_1 \\ \vdots \\ f_1 \\ \vdots \end{bmatrix} = \begin{bmatrix} g(x_1) \\ \vdots \\ g(x_M) \\ 0 \\ \vdots \\ 0 \\ \vdots \\ 0 \\ \vdots \end{bmatrix}. \quad (\text{A15})$$

Here \mathcal{C}_{ij} , \mathcal{C}_{ij}^d , \mathcal{C}_{ij}^e , \mathcal{D}_{ij} , \mathcal{D}_{ij}^e , \mathcal{E}_{ij}^c , and \mathcal{E}_{ij} are the same as in Eqs. (A10) and (A13), while $\mathcal{C}_{ij}^f = \mathcal{F}_{ij}^c = \mathcal{D}_{ij}^f = \mathcal{F}_{ij}^d = 0$. All other elements are given by

$$\begin{aligned} \mathcal{E}_{ij}^d &= -2r_2u_j(x_i); & \mathcal{E}_{ij}^f &= 3r_2u_j(x_i), \\ \mathcal{D}_{ij}^c &= -3r_2u_j(x_i); & \mathcal{F}_{ij}^e &= -r_2u_j(x_i), \\ \mathcal{F}_{ij} &= u'_j(x_i) - \left(ir_1 + \frac{3}{x_i}\right)u_j(x_i). \end{aligned} \quad (\text{A16})$$

Thus, our numerical scheme has been completely specified. We note that Eqs. (A10), (A13), and (A16) explicitly demonstrate that our numerical scheme is singular at $x = 0$. This does not pose any problems, as the subintegral function in our initial expression Eq. (A1) is not highly oscillatory around $x = 0$. Therefore, the trapezoid scheme can be applied there.

APPENDIX B: 2D SPECTRAL FUNCTIONS

We now examine the CE spectral functions in two dimensions and compare them to the results from DMFT and SCMA. We investigate the Hamiltonian from Eq. (1) on a square lattice and set \hbar , k_B and lattice constant to 1.

In the 2D case, the cumulant function is calculated from Eq. (16) by setting $n = 2$, and by exploiting the numerical integration scheme from Appendix A. The procedure for the implementation of the DMFT and SCMA is the same as explained in Sec. II B, with the only difference being that Eq. (22) no longer represents the solution for the local Green's function from Eqs. (20b) and (21). The local Green's function for the square lattice is obtained as follows. Let us introduce $B(\omega) \equiv (\omega - \Sigma(\omega))/(2t_0)$ and rewrite Eq. (21) as

$$G(\omega) = - \int_{-\infty}^{\infty} dx \tilde{\rho}(x) \int_{-\infty}^{\infty} d\varepsilon \frac{e^{ix\varepsilon}}{\varepsilon - 2t_0B(\omega)}. \quad (\text{B1})$$

The integral over ε can be solved using the residue theorem. It is thus important to note that the subintegral function has only a single pole at $\varepsilon_{\text{pole}} = 2t_0B(\omega)$ that is situated at the upper half-plane, i.e., $\text{Im}B(\omega) > 0$ (since $\text{Im}\Sigma(\omega) < 0$). Hence

$$G(\omega) = -2\pi i \int_{-\infty}^{\infty} dx \tilde{\rho}(x) e^{2ixt_0B(\omega)} \theta(x). \quad (\text{B2})$$

Here $\tilde{\rho}(x)$ is given by Eq. (15) for $n = 2$. Substituting this into Eq. (B2) and solving the integral gives

$$G(\omega) = \frac{K\left(\frac{2}{B(\omega)}\right)}{B(\omega)\pi t_0}, \quad (\text{B3})$$

where $K(k) \equiv \int_0^{\pi/2} d\theta / \sqrt{1 - k^2 \sin^2 \theta}$ is the complete elliptic integral of the first kind.

Results are presented in Fig. 12. We note that in Figs. 12(a)–12(d) [Figs. 12(i)–12(l)] the phonon frequency $\omega_0 = 0.2$ ($\omega_0 = 1$) is smaller (larger) than both of the temperatures $T_1 = 0.3$ and $T_2 = 0.7$ that we are considering. Therefore, we focus on Figs. 12(e)–12(h) where $T_1 < \omega_0 < T_2$, while other regimes can be analyzed analogously. We see that most of the spectral weight is concentrated in a smaller range of frequencies than in the 1D case; see Figs. 4 and 12(e)–12(h). This is a consequence of the fact that the hopping parameter is always set to unity, while the 2D bandwidth is twice as large in comparison with the bandwidth in the 1D system. Spectral functions from Figs. 12(e)–12(g) exhibit qualitatively similar behavior as results for the 1D system in Figs. 4(a)–4(d). Here, all methods are in agreement and predict that the quasiparticle peak dominates, while there is only a single tiny satellite structure that is more pronounced at higher temperatures. However, it seems that the satellites are more pronounced in the 1D spectral functions. A much more complicated multipeak structure is predicted by the DMFT in Fig. 10(h), where a large discrepancy can be observed in comparison to the CE and SCMA results. A better agreement is observed for higher temperatures.

It is interesting to note that while the DMFT frequently gave sharper peaks than other methods in 1D (see Fig. 4), here the roles are reversed. This is a consequence of the strong Van Hove singularity at the bottom of the band of a 1D system, which is highly relevant in our case when the concentration of electrons is very low, while the singularity in the 2D system is weaker and shifted to the center of the band.

APPENDIX C: A DETAILED STUDY OF THE SPECTRAL FUNCTION FOR $t_0 = \omega_0 = g = 1$ and $k = \pi$

In Sec. III, we concluded that the CE successfully captures the main features of the spectral functions both at the bottom of the band ($k \approx 0$) and at top of the band ($k \approx \pm\pi$) if the electron-phonon coupling is not too strong. Less promising results were reported in Ref. [50], where CE was examined on a finite lattice with $N = 6$ sites in the regime $t_0 = \omega_0 = g = 1$ and $k = \pi$, using the finite-temperature Lanczos method (FTLM) [44] as a benchmark. They found that the CE, in addition to the fact that it does not correctly reproduce a quasiparticle peak, predicts that the most prominent feature of the spectrum consists of only a single broad peak, whereas two distinct peaks are present in the FTLM solution. Here we show that this discrepancy between the CE and FTLM is significantly reduced in the thermodynamic limit.

Reference [50] emphasized that previous conclusions are valid only for low-temperature solutions, while CE becomes accurate for $T \geq \omega_0$. This was confirmed by the FTLM, whose spectral functions in this case look like a single broad

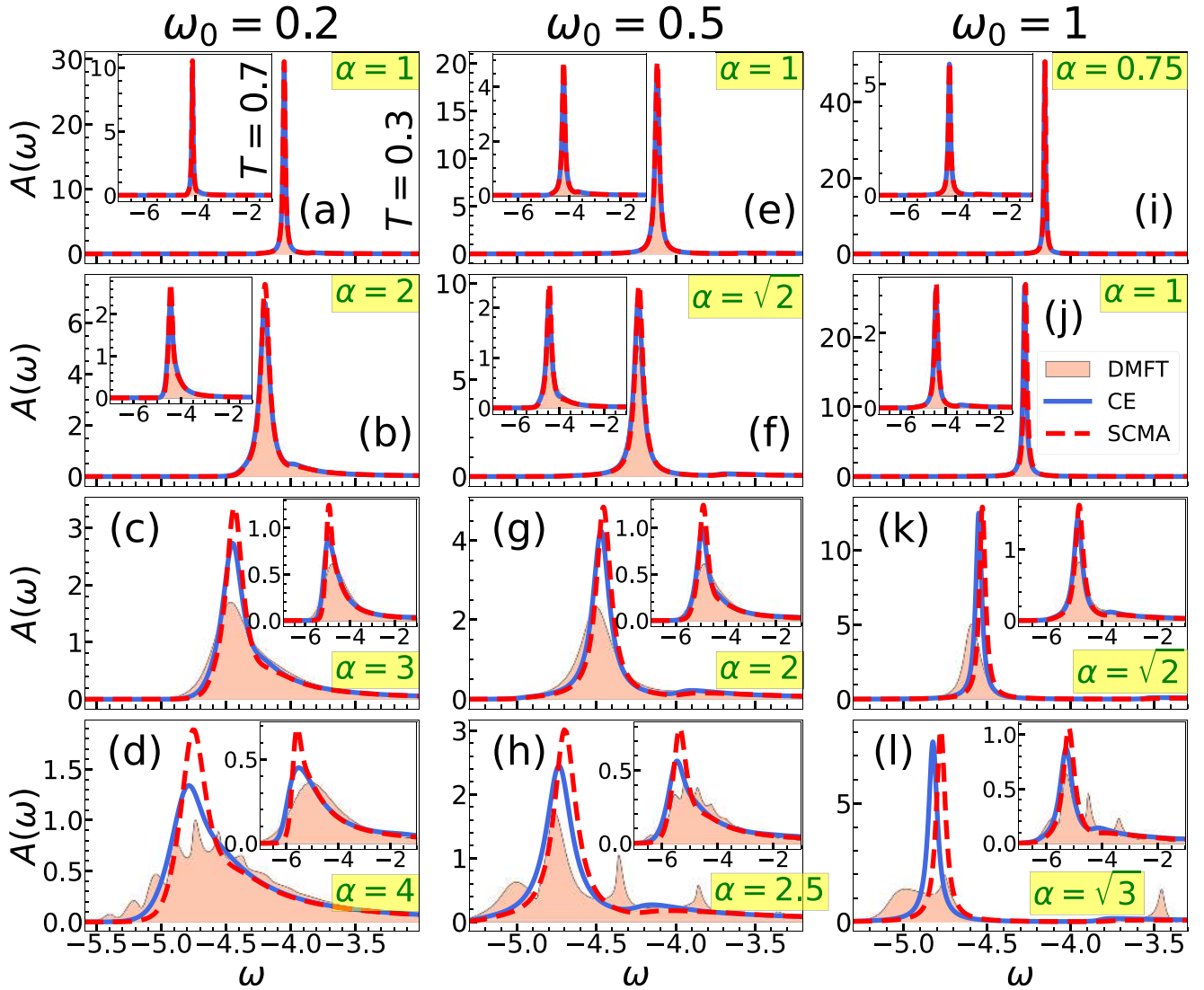


FIG. 12. (a)–(h) Comparison of the CE, DMFT, and SCMA spectral functions in 2D for $k = 0$ and $t_0 = 1$. The main panels show the results for $T_1 = 0.3$, while $T_2 = 0.7$ results are shown in the insets.

peak; see Fig. 1(c) from Ref. [50]. However, Fig. S9 in the Supplemental Material of Ref. [52] demonstrates that the spectral function in the thermodynamic limit for $t_0 = \omega_0 = g = 1$, $k = \pi$ consists of a broad single-peak structure even at $T = 0$. This conclusion was reached by carefully examining the finite-size effects using the numerically exact hierarchical equations of motion method (HEOM). It was established that the system with $N = 10$ lattice sites is representative of the thermodynamic limit, although much smaller systems are required for the $k = 0$ results. Furthermore, the same figure shows that two distinct peaks emerge for $N = 6$ and $k = \pi$, in accordance with the FTLM results. Hence, CE will provide much better results in the thermodynamic limit than previously expected. We note that for $t_0 = \omega_0 = g = 1$ and finite temperatures, one might expect that the required lattice size, representative of the thermodynamic limit, does not exceed $N = 10$, as the electron experiences much more scattering compared to the $T = 0$ case. This will be cross-checked independently (using the DMFT) in the rest of this Appendix for finite T , which satisfies the $T < \omega_0$ condi-

tion. In that case, we analyze the overall performance of the CE.

In Fig. 13(a), we show the FTLM data, (originally from Ref. [44]) used in Ref. [50], and compare them to the DMFT applied on a system of finite lattice size. We exploit the fact that the corresponding spectral functions (although certainly not as accurate in comparison with the exact solution) provide a rough estimate of how large N should be to faithfully represent the thermodynamic limit; see Sec. IV from the Supplemental Material of Ref. [52] for more details. In accordance with the FTLM results, we see that the DMFT spectral function for $N = 6$ also predicts distinct peaks around $\omega \approx 1.5$ and $\omega \approx 2.5$, although there is an additional peak around $\omega \approx 2$. Nevertheless, these results change drastically with increasing N and practically converge for $N = 10$. This is the same N as predicted by HEOM at $T = 0$. Therefore, the presented FTLM results are not representative of the thermodynamic limit. Additionally, Fig. 13(a) also shows that FTLM results for $T = 0.6$ and $T = 0.8$ are quite similar. Hence, our further analysis will be conducted for $T = 0.7$ case.

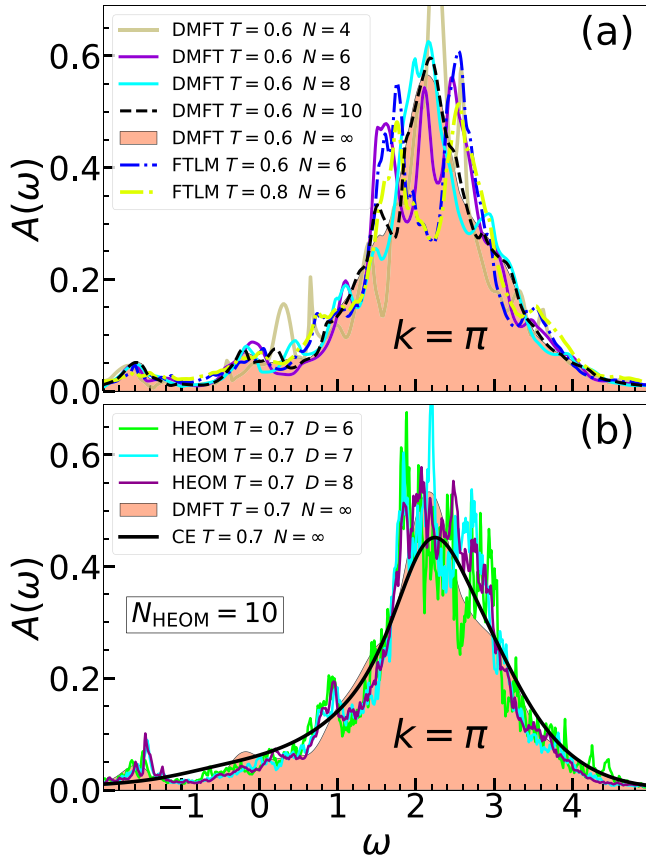


FIG. 13. CE, DMFT, FTLM, and HEOM spectral functions for $t_0 = \omega_0 = g = 1$. (a) Analysis of the finite-size effects. (b) Inspecting the convergence of HEOM data with respect to hierarchy depth D .

In Fig. 13(b), we present HEOM results for $N = 10$ and compare them to CE and DMFT. We note that HEOM has one additional parameter, the so-called hierarchy depth D . For details, we refer the reader to Ref. [47], but we only briefly mention that the numerically exact results are formally obtained in the limit $D \rightarrow \infty$. In practice, we always check whether the results converge with respect to D , which cannot be increased indefinitely, as finite computer memory presents a limiting factor. We see that the HEOM results have practically converged for $N = 10$ and $D = 8$. Here, the HEOM solution does not possess the two-peak structure predicted by the FTLM on a smaller lattice size ($N = 6$). It actually gives only a single, broad peak around $\omega \approx 2$, which is correctly reproduced by both the CE and the DMFT. Although the CE misses the quasiparticle peak around $\omega \approx -1.5$, we conclude that CE gives much more accurate results for the thermodynamic limit than for a finite system.

APPENDIX D: MOBILITY RESULTS FROM THE ONE-SHOT MIGDAL APPROXIMATION

In Sec. V, we presented and analyzed the mobility predictions from the CE, DMFT, and SCMA methods. Here, we supplement that study with the data from the one-shot MA (i.e., SCMA without self-consistency). The results are shown in Fig. 14. Since the mobility results have already been

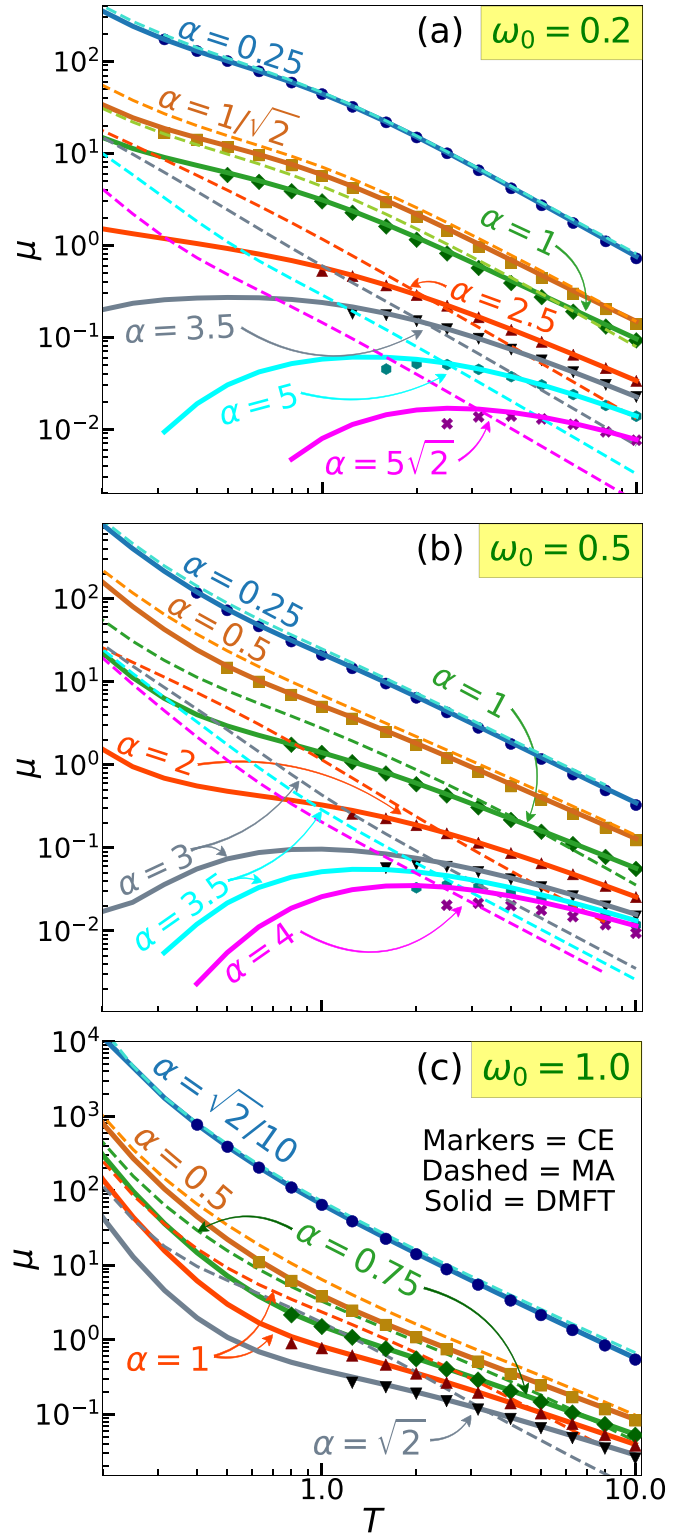


FIG. 14. Temperature dependence of the mobility within CE, DMFT, and MA. Here $t_0 = 1$.

thoroughly analyzed in Sec. V, we will here give only brief comments about the performance of the MA. Figure 14(a) shows that MA is practically useless for $\alpha \gtrsim 2.5$. Here, the results are not even qualitatively correct, regardless of the temperature. Even for $\alpha = 1$, the results are still not satisfactory:

the predictions for $T < 4$ ($T > 9$) overestimate (underestimate) the DMFT benchmark. MA proves to be reliable only for very weak interactions $\alpha \lesssim 1/\sqrt{2}$. Here, the results are better for higher temperatures. This is expected as the MA

takes into account only the lowest-order Feynman diagram, while the relevance of higher-order diagrams decreases as the temperature is increased. Similar analysis can be repeated for other phonon frequencies in Figs. 14(b) and 14(c).

-
- [1] G. Mahan, *Many-Particle Physics* (Kluwer Academic, New York, 2000).
- [2] R. Kubo, Generalized cumulant expansion method, *J. Phys. Soc. Jpn.* **17**, 1100 (1962).
- [3] B. I. Lundqvist, Characteristic structure in core electron spectra of metals due to the electron-plasmon coupling, *Phys. Kondens. Mater.* **9**, 236 (1969).
- [4] D. C. Langreth, Singularities in the x-ray spectra of metals, *Phys. Rev. B* **1**, 471 (1970).
- [5] L. Hedin, Effects of recoil on shake-up spectra in metals, *Phys. Scr.* **21**, 477 (1980).
- [6] L. Hedin, On correlation effects in electron spectroscopies and the *GW* approximation, *J. Phys.: Condens. Matter* **11**, R489 (1999).
- [7] F. Aryasetiawan, L. Hedin, and K. Karlsson, Multiple Plasmon Satellites in Na and Al Spectral Functions from *Ab Initio* Cumulant Expansion, *Phys. Rev. Lett.* **77**, 2268 (1996).
- [8] B. Holm and F. Aryasetiawan, Self-consistent cumulant expansion for the electron gas, *Phys. Rev. B* **56**, 12825 (1997).
- [9] G. D. Mahan, Phonon-broadened optical spectra: Urbach's rule, *Phys. Rev.* **145**, 602 (1966).
- [10] D. Dunn, Electron-Phonon Interactions in an insulator, *Can. J. Phys.* **53**, 321 (1975).
- [11] O. Gunnarsson, V. Meden, and K. Schönhammer, Corrections to Migdal's theorem for spectral functions: A cumulant treatment of the time-dependent Green's function, *Phys. Rev. B* **50**, 10462 (1994).
- [12] C. Verdi, F. Caruso, and F. Giustino, Origin of the crossover from polarons to Fermi liquids in transition metal oxides, *Nat. Commun.* **8**, 15769 (2017).
- [13] G. Antonius, Y.-H. Chan, and S. G. Louie, Polaron spectral properties in doped ZnO and SrTiO₃ from first principles, *Phys. Rev. Res.* **2**, 043296 (2020).
- [14] S. Moser, L. Moreschini, J. Jačimović, O. S. Barišić, H. Berger, A. Magrez, Y. J. Chang, K. S. Kim, A. Bostwick, E. Rotenberg, L. Forró, and M. Gironi, Tunable Polaronic Conduction in Anatase TiO₂, *Phys. Rev. Lett.* **110**, 196403 (2013).
- [15] F. Giustino, Electron-phonon interactions from first principles, *Rev. Mod. Phys.* **89**, 015003 (2017).
- [16] J.-J. Zhou and M. Bernardi, Predicting charge transport in the presence of polarons: The beyond-quasiparticle regime in SrTiO₃, *Phys. Rev. Res.* **1**, 033138 (2019).
- [17] B. K. Chang, J.-J. Zhou, N.-E. Lee, and M. Bernardi, Intermediate polaronic charge transport in organic crystals from a many-body first-principles approach, *npj Comput. Mater.* **8**, 63 (2022).
- [18] S. M. Story, J. J. Kas, F. D. Vila, M. J. Verstraete, and J. J. Rehr, Cumulant expansion for phonon contributions to the electron spectral function, *Phys. Rev. B* **90**, 195135 (2014).
- [19] J. J. Kas, J. J. Rehr, and L. Reining, Cumulant expansion of the retarded one-electron Green function, *Phys. Rev. B* **90**, 085112 (2014).
- [20] J. Lischner, D. Vigil-Fowler, and S. G. Louie, Satellite structures in the spectral functions of the two-dimensional electron gas in semiconductor quantum wells: A *GW* plus cumulant study, *Phys. Rev. B* **89**, 125430 (2014).
- [21] F. Caruso and F. Giustino, Spectral fingerprints of electron-plasmon coupling, *Phys. Rev. B* **92**, 045123 (2015).
- [22] J. S. Zhou, J. Kas, L. Sponza, I. Reshetnyak, M. Guzzo, C. Giorgetti, M. Gatti, F. Sottile, J. Rehr, and L. Reining, Dynamical effects in electron spectroscopy, *J. Chem. Phys.* **143**, 184109 (2015).
- [23] B. Gumhalter, V. Kovač, F. Caruso, H. Lambert, and F. Giustino, On the combined use of *GW* approximation and cumulant expansion in the calculations of quasiparticle spectra: The paradigm of Si valence bands, *Phys. Rev. B* **94**, 035103 (2016).
- [24] D. Vigil-Fowler, S. G. Louie, and J. Lischner, Dispersion and line shape of plasmon satellites in one, two, and three dimensions, *Phys. Rev. B* **93**, 235446 (2016).
- [25] J. S. Zhou, M. Gatti, J. J. Kas, J. J. Rehr, and L. Reining, Cumulant Green's function calculations of plasmon satellites in bulk sodium: Influence of screening and the crystal environment, *Phys. Rev. B* **97**, 035137 (2018).
- [26] J. Ma and J. Cao, Förster resonance energy transfer, absorption and emission spectra in multichromophoric systems. I. Full cumulant expansions and system-bath entanglement, *J. Chem. Phys.* **142**, 094106 (2015).
- [27] L. Cupellini, F. Lipparini, and J. Cao, Absorption and circular dichroism spectra of molecular aggregates with the full cumulant expansion, *J. Phys. Chem. B* **124**, 8610 (2020).
- [28] J. A. Nöthling, T. Mančal, and T. Krüger, Accuracy of approximate methods for the calculation of absorption-type linear spectra with a complex system-bath coupling, *J. Chem. Phys.* **157**, 095103 (2022).
- [29] J. P. Nery, P. B. Allen, G. Antonius, L. Reining, A. Miglio, and X. Gonze, Quasiparticles and phonon satellites in spectral functions of semiconductors and insulators: Cumulants applied to the full first-principles theory and the Fröhlich polaron, *Phys. Rev. B* **97**, 115145 (2018).
- [30] N. Kandolf, C. Verdi, and F. Giustino, Many-body Green's function approaches to the doped Fröhlich solid: Exact solutions and anomalous mass enhancement, *Phys. Rev. B* **105**, 085148 (2022).
- [31] A. S. Mishchenko, N. V. Prokof'ev, A. Sakamoto, and B. V. Svistunov, Diagrammatic quantum Monte Carlo study of the Fröhlich polaron, *Phys. Rev. B* **62**, 6317 (2000).
- [32] T. Holstein, Studies of polaron motion: Part I. The molecular-crystal model, *Ann. Phys.* **8**, 325 (1959).
- [33] I. Lang and Y. A. Firsov, Kinetic theory of semiconductors with low mobility, *Zh. Eksp. Teor. Fiz.* **43**, 1843 (1962) [*Sov. Phys. JETP* **16**, 1301 (1963)].
- [34] A. S. Alexandrov, *Polarons in Advanced Materials*, Springer Series in Materials Science, Vol. 103 (Springer, Dordrecht, 2007).

- [35] E. Jeckelmann and S. R. White, Density-matrix renormalization-group study of the polaron problem in the Holstein model, *Phys. Rev. B* **57**, 6376 (1998).
- [36] P. E. Kornilovitch, Continuous-Time Quantum Monte Carlo Algorithm for the Lattice Polaron, *Phys. Rev. Lett.* **81**, 5382 (1998).
- [37] A. H. Romero, D. W. Brown, and K. Lindenberg, Converging toward a practical solution of the Holstein molecular crystal model, *J. Chem. Phys.* **109**, 6540 (1998).
- [38] S. Fratini and S. Ciuchi, Dynamical Mean-Field Theory of Transport of Small Polarons, *Phys. Rev. Lett.* **91**, 256403 (2003).
- [39] S. Fratini and S. Ciuchi, Optical properties of small polarons from dynamical mean-field theory, *Phys. Rev. B* **74**, 075101 (2006).
- [40] C. Zhang, E. Jeckelmann, and S. R. White, Dynamical properties of the one-dimensional Holstein model, *Phys. Rev. B* **60**, 14092 (1999).
- [41] G. L. Goodvin, M. Berciu, and G. A. Sawatzky, Green's function of the Holstein polaron, *Phys. Rev. B* **74**, 245104 (2006).
- [42] M. Berciu, Green's Function of a Dressed Particle, *Phys. Rev. Lett.* **97**, 036402 (2006).
- [43] S. Ciuchi, E. Cappelluti, and S. Fratini, Optical properties of lattice/magnetic small polarons from DMFT, *J. Phys. Chem. Solids* **69**, 2164 (2008).
- [44] J. Bonča, S. A. Trugman, and M. Berciu, Spectral function of the Holstein polaron at finite temperature, *Phys. Rev. B* **100**, 094307 (2019).
- [45] N. Prodanović and N. Vukmirović, Charge carrier mobility in systems with local electron-phonon interaction, *Phys. Rev. B* **99**, 104304 (2019).
- [46] D. Jansen, J. Bonča, and F. Heidrich-Meisner, Finite-temperature density-matrix renormalization group method for electron-phonon systems: Thermodynamics and Holstein-polaron spectral functions, *Phys. Rev. B* **102**, 165155 (2020).
- [47] V. Janković and N. Vukmirović, Spectral and thermodynamic properties of the Holstein polaron: Hierarchical equations of motion approach, *Phys. Rev. B* **105**, 054311 (2022).
- [48] J. Bonča and S. A. Trugman, Electron removal spectral function of a polaron coupled to dispersive optical phonons, *Phys. Rev. B* **106**, 174303 (2022).
- [49] A. S. Mishchenko, N. Nagaosa, and N. Prokof'ev, Diagrammatic Monte Carlo Method for Many-Polaron Problems, *Phys. Rev. Lett.* **113**, 166402 (2014).
- [50] P. J. Robinson, I. S. Dunn, and D. R. Reichman, Cumulant methods for electron-phonon problems. I. Perturbative expansions, *Phys. Rev. B* **105**, 224304 (2022).
- [51] P. J. Robinson, I. S. Dunn, and D. R. Reichman, Cumulant methods for electron-phonon problems. II. The self-consistent cumulant expansion, *Phys. Rev. B* **105**, 224305 (2022).
- [52] P. Mitrić, V. Janković, N. Vukmirović, and D. Tanasković, Spectral Functions of the Holstein Polaron: Exact and Approximate Solutions, *Phys. Rev. Lett.* **129**, 096401 (2022).
- [53] S. Ciuchi, F. de Pasquale, S. Fratini, and D. Feinberg, Dynamical mean-field theory of the small polaron, *Phys. Rev. B* **56**, 4494 (1997).
- [54] See Supplemental Material at <http://link.aps.org/supplemental/10.1103/PhysRevB.107.125165> for additional figures and derivations.
- [55] D. Levin, Fast integration of rapidly oscillatory functions, *J. Comput. Appl. Math.* **67**, 95 (1996).
- [56] A. Migdal, Interaction between electrons and lattice vibrations in a normal metal, *Zh. Eksp. Teor. Fiz.* **34**, 1438 (1958) [*Sov. Phys. JETP* **7**, 996 (1958)].
- [57] A. Georges, G. Kotliar, W. Krauth, and M. J. Rozenberg, Dynamical mean-field theory of strongly correlated fermion systems and the limit of infinite dimensions, *Rev. Mod. Phys.* **68**, 13 (1996).
- [58] P. E. Kornilovitch, Photoemission spectroscopy and sum rules in dilute electron-phonon systems, *Europhys. Lett.* **59**, 735 (2002).
- [59] A. Khurana, Electrical Conductivity in the Infinite-Dimensional Hubbard Model, *Phys. Rev. Lett.* **64**, 1990 (1990).
- [60] S. Fratini, F. de Pasquale, and S. Ciuchi, Optical absorption from a nondegenerate polaron gas, *Phys. Rev. B* **63**, 153101 (2001).
- [61] W. H. Press, S. A. Teukolsky, W. T. Vetterling, and B. P. Flannery, *Numerical Recipes: The Art of Scientific Computing*, 3rd ed. (Cambridge University Press, Cambridge, 2007).
- [62] S. Fratini, D. Mayou, and S. Ciuchi, The transient localization scenario for charge transport in crystalline organic materials, *Adv. Funct. Mater.* **26**, 2292 (2016).
- [63] J. Bonča and S. A. Trugman, Dynamic properties of a polaron coupled to dispersive optical phonons, *Phys. Rev. B* **103**, 054304 (2021).
- [64] G. D. Mahan, Mobility of polarons, *Phys. Rev.* **142**, 366 (1966).

Fermionic-propagator and alternating-basis quantum Monte Carlo methods for correlated electrons on a lattice

Cite as: J. Chem. Phys. 158, 044108 (2023); doi: 10.1063/5.0133597

Submitted: 4 November 2022 • Accepted: 2 January 2023 •

Published Online: 24 January 2023



View Online



Export Citation



CrossMark

Veljko Janković^{a)}  and Jakša Vučičević^{b)} 

AFFILIATIONS

Institute of Physics Belgrade, University of Belgrade, Pregrevica 118, 11080 Belgrade, Serbia

^{a)} Author to whom correspondence should be addressed: veljko.jankovic@ipb.ac.rs

^{b)} jaksa.vucicevic@ipb.ac.rs

ABSTRACT

Ultracold-atom simulations of the Hubbard model provide insights into the character of charge and spin correlations in and out of equilibrium. The corresponding numerical simulations, on the other hand, remain a significant challenge. We build on recent progress in the quantum Monte Carlo (QMC) simulation of electrons in continuous space and apply similar ideas to the square-lattice Hubbard model. We devise and benchmark two discrete-time QMC methods, namely the fermionic-propagator QMC (FPQMC) and the alternating-basis QMC (ABQMC). In FPQMC, the time evolution is represented by snapshots in real space, whereas the snapshots in ABQMC alternate between real and reciprocal space. The methods may be applied to study equilibrium properties within the grand-canonical or canonical ensemble, external field quenches, and even the evolution of pure states. Various real-space/reciprocal-space correlation functions are also within their reach. Both methods deal with matrices of size equal to the number of particles (thus independent of the number of orbitals or time slices), which allows for cheap updates. We benchmark the methods in relevant setups. In equilibrium, the FPQMC method is found to have an excellent average sign and, in some cases, yields correct results even with poor imaginary-time discretization. ABQMC has a significantly worse average sign, but also produces good results. Out of equilibrium, FPQMC suffers from a strong dynamical sign problem. On the contrary, in ABQMC, the sign problem is not time-dependent. Using ABQMC, we compute survival probabilities for several experimentally relevant pure states.

Published under an exclusive license by AIP Publishing. <https://doi.org/10.1063/5.0133597>

I. INTRODUCTION

The last two decades have witnessed remarkable developments in laser and ultracold-atom technologies that have enabled experimental studies of strongly correlated electrons in and out of equilibrium.^{1,2} Ultracold atoms in optical lattices^{2,3} and optical tweezers arrays^{4–6} have been used as quantum simulators for paradigmatic models of condensed-matter physics, such as the Hubbard model.^{7,8} Recent experiments with fermionic ultracold atoms have probed the equation of state,⁹ charge, and spin correlation functions,^{10–13} as well as transport properties (by monitoring charge and spin diffusion^{14–17}).

These experimental achievements pose a significant challenge for the theory. The level of difficulty, however, greatly depends on whether one computes instantaneous (equal-time) correlations

or the full time/frequency dependence of dynamical correlators. The other factor is whether one considers thermal equilibrium or out-of-equilibrium setups.

Instantaneous correlators in equilibrium are the best-case scenario. The average density, double occupancy, and correlations between particle or spin densities on adjacent sites are still very important. They serve as a thermometer: the temperature in cold-atom experiments cannot be measured directly and is often gauged in comparison with numerical simulations.^{11,14} For this kind of application, current state-of-the-art methods^{18–43} are often sufficient. Equal-time multipoint density correlations are also of interest, as they hold information, e.g., about the emergence of string patterns^{13,44,45} or the effect of holes on antiferromagnetic correlations.^{46–48} However, measuring density at a larger number of points simultaneously is more difficult in many algorithms. For

example, in the Hirsch–Fye (HF) algorithm,^{24,49} one cannot do this straight-forwardly, as the auxiliary Ising spins only distinguish between singly occupied and doubly occupied/empty sites.

Of even greater interest and much greater difficulty are the time-dependent correlations in equilibrium. These pertain to studies of transport and hydrodynamics at the level of linear response theory.^{50–52} The limitations of current state-of-the-art methods here become starkly apparent. If one is interested in long-wavelength behavior (as is precisely the case in the study of hydrodynamic properties⁵²), the lattices treated in the simulation need to be sufficiently large. The finite-temperature Lanczos method^{53,54} can only treat up to 20 lattice sites^{50,55} and is unsuitable for such applications. Quantum Monte Carlo (QMC) methods can treat up to 300 sites,^{29,30} but only under certain conditions: doping away from half-filling leads to a significant sign problem, which becomes more severe as the lattice size, inverse temperature, and coupling constant are increased. Moreover, QMC methods are formulated in imaginary time and require ill-defined analytical continuation to reconstruct optical conductivity or any other real-frequency spectrum.⁵¹

Direct real-time calculations, regardless of proximity to the equilibrium, are the most difficult.^{31,56–69} These present an alternative to analytical continuation in equilibrium calculations but are necessary to describe non-equilibrium regimes, e.g., in external field quenches.¹⁶ In the corresponding Kadanoff–Baym–Keldysh three- or two-piece contour formalism, QMC computations are plagued by the dynamical sign problem, which has so far been overcome in only the smallest systems.⁶¹ The time-dependent density matrix renormalization group^{70–72} produces practically exact results, however, only in one-dimensional^{63,64} or ladder systems.⁷³ Simulations based on the nonequilibrium Green’s functions formalism⁷⁴ are also possible but not numerically exact. They can, however, treat much larger systems over much longer time scales than other real-time approaches.^{64,75–77}

The main goal of this work is to construct a numerically exact way to compute spatially resolved densities in setups relevant for optical lattice experiments. This includes general multipoint correlators in real space and momentum space, and we focus on densities of charge and spin. We are interested in both the equilibrium expectation values and their time dependence in transient regimes. (The latter can formally be used to access temporal correlations in equilibrium as well.)

We take a largely unexplored QMC route^{78–80} toward the computation of correlation functions in the square-lattice Hubbard model. Current state-of-the-art methods, such as the continuous-time interaction-expansion (CT-INT),^{31–33} the continuous-time auxiliary field (CT-AUX),^{31,34} and HF,^{24,49} rely on the computation of large matrix determinants, which, in many cases, presents the bottleneck of the algorithm. In CT-INT and CT-AUX, the size of the matrices generally grows with coupling, inverse temperature, and lattice size. In the HF, which is based on the Suzuki–Trotter decomposition (STD), the matrix size is fixed, yet presents a measure of the systematic error: the size of the matrix scales with both the number of time slices and the number of lattice sites. A rather separate approach is possible, where the size of the matrices scales only with the total number of electrons. This approach builds on the path-integral MC (PIMC).^{81,82} In PIMC, the trajectories of individual electrons are tracked. In continuous-space models,

PIMC was used successfully even in the calculation of dynamical response functions.^{83,84} The downside is that the antisymmetry of electrons feeds into the overall sign of a given configuration, thus contributing to the sign problem. A more sophisticated idea was put forward in Refs. 85–87. Namely, the propagation between two time slices can be described by a single many-fermion propagator, which groups (blocks) all possible ways the electrons can go from one set of positions to another—including all possible exchanges. The many-fermion propagator is evaluated as a determinant of a matrix of size equal to the total number of electrons. This scheme automatically eliminates one important source of the sign problem and improves the average sign drastically. Such *permutation blocking* algorithms have been utilized with great success to compute thermodynamic quantities in continuous-space fermionic models.^{88–96} Here, we investigate and test analogous formulations in the *lattice models* of interest and try generalizing the approach to real-time dynamics.

We develop and test two slightly different QMC methods. The Fermionic-propagator QMC (FPQMC) is a real-space method similar to the permutation-blocking and fermionic-propagator PIMC, respectively, developed by Dornheim *et al.*⁹⁰ and Filinov *et al.*⁹⁶ for continuous models. On the other hand, the alternating-basis QMC (ABQMC) method is formulated simultaneously in both real and reciprocal space, which makes measuring distance- and momentum-resolved quantities equally simple. The motion of electrons and their interactions are treated on an equal footing. Both methods are based on the STD and are straight-forwardly formulated along any part of or the entire Kadanoff–Baym–Keldysh three-piece contour. This allows access to both real- and imaginary-time correlation functions in and out of equilibrium. Unlike CT-INT, CT-AUX, and HF, our methods can also be used to treat canonical ensembles as well as the time evolution of pure states. Our formulation ensures that the measurement of an arbitrary multipoint charge or spin correlation function is algorithmically trivial and cheap.

We perform benchmarks on several examples where numerically exact results are available.

In calculations of instantaneous correlators for the 2D Hubbard model in equilibrium, our main finding is that the FPQMC method has a rather manageable sign problem. The average sign is anti-correlated with coupling strength, which is in sharp contrast with some of the standard QMC methods. More importantly, we find that the average sign drops off relatively slowly with the lattice size and the number of time slices—we have been able to converge results with as many as eight time slices, or as many as 80 lattice sites. At strong coupling and at half-filling, we find the average sign to be very close to 1. In the temperature range relevant for optical-lattice experiments, we find that the average occupancy can be computed to a high accuracy with as few as two time slices; the double occupancy and the instantaneous spin–spin correlations require somewhat finer time discretization, but often not more than six time-slices in total. We also document that FPQMC appears to be sign-problem-free for Hubbard chains.

However, in calculations of the time-evolving and spatially resolved density, we find that the FPQMC sign problem is mostly prohibitive of obtaining results. Nevertheless, employing the ABQMC algorithm, we are able to compute survival probabilities of various pure states on 4×4 clusters—in the ABQMC formulation, the sign-problem is manifestly independent of time and interaction

strength, and one can scan the entire time evolution for multiple strengths of interaction in a single run. The numerical results reveal several interesting trends. Similarly to observations made in Ref. 97, we find in general that the survival probability decays over longer times when interactions are stronger. At shorter times, we observe that the behavior depends strongly on the type of the initial state, likely related to the average density.

The paper is organized as follows: The FPQMC and ABQMC methods are developed in Sec. II and applied to equilibrium and out-of-equilibrium setups in Sec. III. Section IV discusses the FPQMC and ABQMC methods in light of other widely used QMC algorithms. Section V summarizes our main findings and their implications, and discusses prospects for further work.

II. MODEL AND METHOD

A. Hubbard Hamiltonian

We study the Hubbard model on a square-lattice cluster containing $N_c = N_x N_y$ sites under periodic boundary conditions (PBC). The Hamiltonian reads as

$$H = H_0 + H_{\text{int}}. \quad (1)$$

The noninteracting (single-particle) part H_0 of the Hamiltonian describes a band of itinerant electrons

$$H_0 = -J \sum_{\langle \mathbf{r}, \mathbf{r}' \rangle \sigma} c_{\mathbf{r}\sigma}^\dagger c_{\mathbf{r}'\sigma} = \sum_{\mathbf{k}\sigma} \varepsilon_{\mathbf{k}} n_{\mathbf{k}\sigma}, \quad (2)$$

where J is the hopping amplitude between the nearest-neighbor lattice sites \mathbf{r} and \mathbf{r}' , while the operators $c_{\mathbf{r}\sigma}^\dagger$ ($c_{\mathbf{r}\sigma}$) create (destroy) an electron of spin σ on lattice site \mathbf{r} . Under PBC, H_0 is diagonal in the momentum representation; the wave vector \mathbf{k} may assume any of the N_c allowed values in the first Brillouin zone of the lattice. The free-electron dispersion is given by $\varepsilon_{\mathbf{k}} = -2J(\cos k_x + \cos k_y)$. The density operator is $n_{\mathbf{k}\sigma} = c_{\mathbf{k}\sigma}^\dagger c_{\mathbf{k}\sigma}$ with $c_{\mathbf{k}\sigma} = \sum_{\mathbf{r}} \langle \mathbf{k} | \mathbf{r} \rangle c_{\mathbf{r}\sigma}$. The Hamiltonian of the on-site Hubbard interaction (two-particle part) reads as

$$H_{\text{int}} = U \sum_{\mathbf{r}} n_{\mathbf{r}\uparrow} n_{\mathbf{r}\downarrow}, \quad (3)$$

where U is the interaction strength, while $n_{\mathbf{r}\sigma} = c_{\mathbf{r}\sigma}^\dagger c_{\mathbf{r}\sigma}$.

If the number of particles is not fixed, Eq. (1) additionally features the chemical-potential term $-\mu \sum_{\mathbf{r}\sigma} n_{\mathbf{r}\sigma} = -\mu \sum_{\mathbf{k}\sigma} n_{\mathbf{k}\sigma}$ that can be added to either H_0 or H_{int} . Here, since we develop a coordinate-space QMC method, we add it to H_{int} .

B. FPQMC method

Finding viable approximations to the exponential of the form $e^{-\alpha H}$ is crucial to many QMC methods. With $\alpha = 1/T$ (T denotes temperature), this is the Boltzmann operator, which will play a role whenever the system is in thermal equilibrium. In the formulation of dynamical responses, the time-evolution operator will also have this form, with $\alpha = it$, where t is the (real) time. One possible way to deal with these is the lowest-order STD⁹⁸

$$e^{-\alpha H} \approx \left(e^{-\Delta\alpha H_0} e^{-\Delta\alpha H_{\text{int}}} \right)^{N_\alpha}, \quad (4)$$

where the interval of length $|\alpha|$ is divided into N_α subintervals of length $|\Delta\alpha|$ each, where $\Delta\alpha = \alpha/N_\alpha$. The error of the approximation is of the order of $|\Delta\alpha|^2 \| [H_0, H_{\text{int}}] \|$, where the norm $\| [H_0, H_{\text{int}}] \|$ may be defined as the largest (in modulus) eigenvalue of the commutator $[H_0, H_{\text{int}}]$.⁸⁰ The error can in principle be made arbitrarily small by choosing N_α large enough. However, the situation is complicated by the fact that the RHS of Eq. (4) contains both single-particle and two-particle contributions. The latter are diagonal in the coordinate representation, so that the spectral decomposition of $e^{-\Delta\alpha H_{\text{int}}}$ is performed in terms of totally antisymmetric states in the coordinate representation, aka the Fock states,

$$|\Psi_i\rangle = \prod_{\sigma} \prod_{j=1}^{N_\sigma} c_{\mathbf{r}_{j\sigma}^\sigma}^\dagger |\emptyset\rangle \quad (5)$$

that contain N_σ electrons of spin σ whose positions $\mathbf{r}_1^\sigma, \dots, \mathbf{r}_{N_\sigma}^\sigma$ are ordered according to a certain rule. We define $\varepsilon_{\text{int}}(\Psi_i) \equiv \langle \Psi_i | H_{\text{int}} | \Psi_i \rangle$. On the other hand, the matrix element of $e^{-\Delta\alpha H_0}$ between many-body states $|\Psi_i'\rangle$ and $|\Psi_i\rangle$ can be expressed in terms of determinants of single-electron propagators

$$\langle \Psi_i' | e^{-\Delta\alpha H_0} | \Psi_i \rangle = \prod_{\sigma} \det S(\Psi_i', \Psi_i, \Delta\alpha, \sigma), \quad (6)$$

$$[S(\Psi_i', \Psi_i, \Delta\alpha, \sigma)]_{j_1 j_2} = \langle \mathbf{r}_{j_1}^{\sigma'} | e^{-\Delta\alpha H_0} | \mathbf{r}_{j_2}^\sigma \rangle. \quad (7)$$

We provide a formal proof of Eqs. (6) and (7) in Appendix A. The same equations lie at the crux of conceptually similar permutation-blocking⁹⁰ and fermionic-propagator⁹⁶ PIMC methods, which are formulated for continuous-space models. When $\Delta\alpha$ is purely real (purely imaginary), the quantity on the right-hand side of Eq. (7) is the imaginary-time (real-time) lattice propagator of a free particle in the coordinate representation.⁸⁰ Its explicit expressions are given in Appendix B.

Further developments of the method somewhat depend on the physical situation of interest. We formulate the method first in equilibrium and then in out-of-equilibrium situations. To facilitate discussion, in Figs. 1(a)–1(d), we summarize the contours appropriate for the different situations we consider.

1. FPQMC method for thermodynamic quantities

The equilibrium properties at temperature $T = \beta^{-1}$ follow from the partition function $Z \equiv \text{Tr} e^{-\beta H}$, which may be computed by dividing the imaginary-time interval $[0, \beta]$ into N_τ slices of length $\Delta\tau \equiv \beta/N_\tau$, employing Eq. (4), and inserting the spectral decompositions of $e^{-\Delta\tau H_{\text{int}}}$. The corresponding approximant for Z reads as

$$Z \approx \sum_{\mathcal{C}} \mathcal{D}_{\beta}(\mathcal{C}, \Delta\tau) e^{-\Delta\tau \varepsilon_{\text{int}}(\mathcal{C})}. \quad (8)$$

The configuration

$$\mathcal{C} = \{ |\Psi_{i_1}\rangle, \dots, |\Psi_{i_{N_\tau}}\rangle \} \quad (9)$$

resides on the contour depicted in Fig. 1(a) and consists of N_τ Fock states $|\Psi_{i_l}\rangle$ in the coordinate representation. $\mathcal{D}_{\beta}(\mathcal{C}, \Delta\tau)$ depends

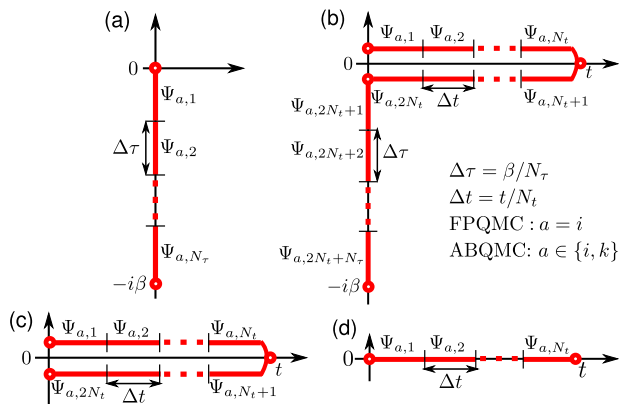


FIG. 1. Contours appropriate for computing (a) thermodynamic quantities at temperature $T = 1/\beta$, (b) time-dependent quantities after quantum quench in which the Hamiltonian is suddenly changed from $H(0)$ at $t < 0$ to H at $t > 0$, (c) time-dependent quantities during evolution from a pure state $|\psi(0)\rangle \equiv |\Psi_{i,1}\rangle$, (d) the survival probability of the initial pure state $|\psi(0)\rangle \equiv |\Psi_{i,1}\rangle$. In (a) and (b), the vertical part is divided into N_τ identical slices of length $\Delta\tau$. In (b)–(d), each horizontal line is divided into N_t identical slices of length Δt . Within the FPQMC method, a many-body state in the coordinate representation $|\Psi_{i,l}\rangle$ [Eq. (5)] is associated with each slice l . Within the ABQMC method, in addition to $|\Psi_{i,l}\rangle$, each slice l features a many-body state in the momentum representation $|\Psi_{k,l}\rangle$ [Eq. (29)].

on the temperature and imaginary-time discretization through the imaginary-time step $\Delta\tau$

$$\begin{aligned} \mathcal{D}_\beta(\mathcal{C}, \Delta\tau) &\equiv \prod_{l=1}^{N_\tau} \langle \Psi_{i,l|\oplus 1} | e^{-\Delta\tau H_0} | \Psi_{i,l} \rangle \\ &= \prod_{l=1}^{N_\tau} \prod_{\sigma} \det S(\Psi_{i,l|\oplus 1}, \Psi_{i,l}, \Delta\tau, \sigma) \end{aligned} \quad (10)$$

and is a product of $2N_\tau$ determinants of imaginary-time single-particle propagators on a lattice (this is emphasized by adding the subscript β). The cyclic addition in Eq. (10) is the standard addition for $l = 1, \dots, N_\tau - 1$, while $N_\tau \oplus 1 = 1$. The symbol $\varepsilon_{\text{int}}(\mathcal{C})$ stands for

$$\varepsilon_{\text{int}}(\mathcal{C}) \equiv \sum_{l=1}^{N_\tau} \varepsilon_{\text{int}}(\Psi_{i,l}). \quad (11)$$

By virtue of the cyclic invariance under trace, the thermodynamic expectation value of an observable A can be expressed as

$$\langle A \rangle = \frac{1}{N_\tau} \sum_{l=0}^{N_\tau-1} \frac{1}{Z} \text{Tr} \left\{ (e^{-\Delta\tau H})^l A (e^{-\Delta\tau H})^{N_\tau-l} \right\}. \quad (12)$$

The FPQMC method is particularly suitable for observables diagonal in the coordinate representation (e.g., the interaction energy H_{int} or the real-space charge density $n_{r\sigma}$). Such observables will be distinguished by adding the subscript i . Equation (12), combined with the lowest-order STD [Eq. (4)], produces the following approximant for $\langle A_i \rangle$:

$$\langle A_i \rangle \approx \frac{\sum_{\mathcal{C}} \mathcal{D}_\beta(\mathcal{C}, \Delta\tau) e^{-\Delta\tau \varepsilon_{\text{int}}(\mathcal{C})} \frac{1}{N_\tau} \sum_{l=1}^{N_\tau} \mathcal{A}_i(\Psi_{i,l})}{\sum_{\mathcal{C}} \mathcal{D}_\beta(\mathcal{C}, \Delta\tau) e^{-\Delta\tau \varepsilon_{\text{int}}(\mathcal{C})}}, \quad (13)$$

where

$$\mathcal{A}_i(\Psi_{i,l}) \equiv \langle \Psi_{i,l} | A_i | \Psi_{i,l} \rangle. \quad (14)$$

Defining the weight $w(\mathcal{C}, \Delta\tau)$ of configuration \mathcal{C} as

$$w(\mathcal{C}, \Delta\tau) \equiv |\mathcal{D}_\beta(\mathcal{C}, \Delta\tau)| e^{-\Delta\tau \varepsilon_{\text{int}}(\mathcal{C})}, \quad (15)$$

Eq. (13) is rewritten as

$$\langle A_i \rangle \approx \frac{\langle \text{sgn}(\mathcal{C}) \frac{1}{N_\tau} \sum_{l=1}^{N_\tau} \mathcal{A}_i(\Psi_{i,l}) \rangle_w}{\langle \text{sgn}(\mathcal{C}) \rangle_w}, \quad (16)$$

where $\langle \dots \rangle_w$ denotes the weighted average over all \mathcal{C} with respect to the weight $w(\mathcal{C})$; $\text{sgn}(\mathcal{C}) \equiv \mathcal{D}_\beta(\mathcal{C}, \Delta\tau) / |\mathcal{D}_\beta(\mathcal{C}, \Delta\tau)|$ is the sign of configuration \mathcal{C} , while $|\langle \text{sgn} \rangle| \equiv |\langle \text{sgn}(\mathcal{C}) \rangle_w|$ is the average sign of the QMC simulation.

By construction, our FPQMC approach yields exact results for the noninteracting electrons (ideal gas, $U = 0$) and in the atomic limit ($J = 0$). In both limits, due to $[H_0, H_{\text{int}}] = 0$, the FPQMC method with arbitrary N_τ should recover the exact results. However, the performance of the method, quantified through the average sign of the simulation, deteriorates with increasing N_τ . For $N_\tau = 1$, the FPQMC algorithm is sign-problem-free because it sums only diagonal elements $\langle \Psi_{i,1} | e^{-\beta H_0} | \Psi_{i,1} \rangle$ of the positive operator $e^{-\beta H_0}$. The sign problem is absent also for $N_\tau = 2$ because $\mathcal{D}_\beta(\mathcal{C}, \beta/2)$ is a square of a real number.

An important feature of the above-presented methodology is its direct applicability in both the grand-canonical and canonical ensemble. The grand-canonical formulation is essential to current state-of-the-art approaches³¹ (e.g., CT-INT or CT-AUX) relying on the thermal Wick's theorem, which is not valid in the canonical ensemble.⁹⁹ In the auxiliary-field QMC,^{22,23,25,27,28} the Hubbard–Stratonovich transformation¹⁰⁰ decouples many-body propagators into sums (or integrals) over one-body operators whether the particle number is fixed or not. Working in the grand-canonical ensemble is then analytically and computationally more convenient because the traces over *all possible* fermion occupations result in determinants.^{23,101} In the canonical ensemble, the computation of traces over constrained fermion occupations is facilitated by observing that the Hubbard–Stratonovich decoupling produces an ensemble of noninteracting systems¹⁰¹ to which theories developed for noninteracting systems in the canonical ensemble, such as particle projection^{102,103} or recursive methods,^{104,105} can be applied. While such procedures may be numerically costly and/or unstable,¹⁰¹ a very recent combination of the auxiliary-field QMC with the recursive auxiliary partition function formalism¹⁰⁵ is reported to be stable and scale favorably with the numbers of particles and available orbitals.¹⁰⁶ In contrast to all these approaches, the formulation of the FPQMC method does not depend on whether the electron number is fixed or not. However, the selection of MC updates does depend on the ensemble we work with. In the canonical ensemble, the updates should conserve the number of electrons; in the grand-canonical ensemble, we also need to include the updates that insert/remove electrons. Our MC updates, together with the

procedure used to extract MC results and estimate their statistical error, are presented in great detail in Sec. SI of the [supplementary material](#).

2. FPQMC method for time-dependent quantities

Ideally, numerical simulations of quench experiments such as those from Refs. 14, 16, and 17 should provide the time-dependent expectation value $\langle A(t) \rangle$ of an observable A at times $t > 0$ after the Hamiltonian undergoes a sudden change from $H(0)$ for $t < 0$ to H for $t > 0$. Again, in many instances,^{14,17} the experimentally measurable observable A is diagonal in the coordinate representation, which will be emphasized by the subscript i . The computation proceeds along the three-piece Kadanoff–Baym–Keldysh contour¹

$$\langle A_i(t) \rangle = \frac{\text{Tr}\left(e^{-\beta H(0)} e^{iHt} A_i e^{-iHt}\right)}{\text{Tr}\left(e^{-\beta H(0)} e^{iHt} e^{-iHt}\right)}, \quad (17)$$

where one may employ the above-outlined fermionic-propagator approach after dividing the whole contour into a number of slices, see Fig. 1(b). While H is the Hubbard Hamiltonian given in Eqs. (1)–(3), $H(0)$ describes correlated electrons whose charge (or spin) density is spatially modulated by external fields.

The immediate complication (compared to the equilibrium case) is that there are now three operators (instead of one) that need to be decomposed via the STD. A preset accuracy determined by the size of both $\Delta\tau$ and Δt will, therefore, require a larger number of time-slices. In turn, this will enlarge the configuration space to be sampled and potentially worsen the sign problem in the MC summation. Even worse, the individual terms in the denominator depend on time, so that the sign problem becomes time-dependent (dynamical). The problem is expected to become worse at long times t , yet vanishes in the $t \rightarrow 0$ limit.

To simplify the task and yet keep it relevant, we consider the evolution from a pure state $|\psi(0)\rangle$ that is an eigenstate of real-space density operators $n_{r\sigma}$, so that its most general form is given by Eq. (5). Such a setup has been experimentally realized.^{5,6,14,17} Replacing $e^{-\beta H(0)} \rightarrow |\psi(0)\rangle\langle\psi(0)|$ in Eq. (17) leads to the expression for the time-dependent expectation value of the observable A_i

$$\langle A_i(t) \rangle = \frac{\langle\psi(0)|e^{iHt} A_i e^{-iHt}|\psi(0)\rangle}{\langle\psi(0)|e^{iHt} e^{-iHt}|\psi(0)\rangle}. \quad (18)$$

Here, the STD should be applied to both the forward and backward evolution operators, see Fig. 1(c), which requires a larger number of time-slices to reach the desired accuracy (in terms of the systematic error). Nevertheless, Eq. (18) is the simplest example in which the applicability of the real-time FPQMC method to follow the evolution of real-space observables may be examined.

Generally speaking, the symmetries of the model should be exploited to enable as efficient as possible MC evaluation of Eq. (18). Recent experimental¹⁵ and theoretical¹⁰⁷ studies have discussed the dynamical symmetry of the Hubbard model, according to which the temporal evolution of certain observables is identical for repulsive and attractive interactions of the same magnitude. The symmetry relies on specific transformation laws of the Hamiltonian H , the

initial state $|\psi(0)\rangle$, and the observable of interest A_i under the combined action of two symmetry operations. The first is the bipartite lattice symmetry, or the π -boost¹⁵ operation, which exploits the symmetry $\epsilon_{\mathbf{k}} = -\epsilon_{\mathbf{k}+(\pi,\pi)}$ of the free-electron dispersion and is represented by the unitary operator B . The second is the time reversal symmetry represented by the antiunitary operator T ($TiT = -i$) that reverses electron spin and momentum according to $Tc_{r\sigma}^{(\dagger)}T = (-1)^{\delta_{\sigma,i}}c_{r\bar{\sigma}}^{(\dagger)}$ and $Tc_{k\sigma}^{(\dagger)}T = (-1)^{\delta_{\sigma,i}}c_{-k,\bar{\sigma}}^{(\dagger)}$. In Appendix C, we formulate our FPQMC method to evaluate Eq. (18) in a way that manifestly respects the dynamical symmetry of the model (each contribution to the MC sums respects the symmetry). Here, we only cite the final expression for the time-dependent expectation value of an observable A_i that satisfies $TBA_iBT = A_i$ when the evolution starts from a state $|\psi(0)\rangle$ satisfying $TB|\psi(0)\rangle = e^{i\chi}|\psi(0)\rangle$

$$\langle A_i(t) \rangle \approx \frac{\sum_{\mathcal{C}} \mathcal{A}_i(\Psi_{i,N_t+1}) \text{Re}\{\mathcal{D}_{2t}(\mathcal{C}, \Delta t)\} \cos[\Delta\epsilon_{\text{int}}(\mathcal{C})\Delta t]}{\sum_{\mathcal{C}} \text{Re}\{\mathcal{D}_{2t}(\mathcal{C}, \Delta t)\} \cos[\Delta\epsilon_{\text{int}}(\mathcal{C})\Delta t]}. \quad (19)$$

Here, the configuration resides on the contour depicted in Fig. 1(c), which is divided into $2N_t$ slices in total, and contains $2N_t - 1$ independent states. We assume that states $|\Psi_{i,l}\rangle$ for $l = 1, \dots, N_t$ ($l = N_t + 1, \dots, 2N_t$) lie on the forward (backward) branch of the contour, while $|\Psi_{i,1}\rangle \equiv |\psi(0)\rangle$. $\mathcal{A}_i(\Psi_{i,N_t+1})$ is defined as in Eq. (14), while

$$\Delta\epsilon_{\text{int}}(\mathcal{C}) \equiv \sum_{l=1}^{N_t} [\epsilon_{\text{int}}(\Psi_{i,l+N_t}) - \epsilon_{\text{int}}(\Psi_{i,l})]. \quad (20)$$

The symbol $\mathcal{D}_{2t}(\mathcal{C}, \Delta t)$ stands for the following combination of forward and backward fermionic propagators (which is also emphasized by the subscript $2t$):

$$\mathcal{D}_{2t}(\mathcal{C}, \Delta t) = \prod_{l=N_t+1}^{2N_t} \langle\Psi_{i,l\oplus 1}|e^{iH_0\Delta t}|\Psi_{i,l}\rangle \prod_{l=1}^{N_t} \langle\Psi_{i,l\oplus 1}|e^{-iH_0\Delta t}|\Psi_{i,l}\rangle. \quad (21)$$

The bipartite lattice symmetry guarantees that $\mathcal{D}_{2t}(\mathcal{C}, \Delta t) = \mathcal{D}_{2t}(\mathcal{C}, -\Delta t)$, see Eq. (C9). The numerator and denominator of the RHS of Eq. (19) are term-by-term invariant under the transformations $\Delta t \rightarrow -\Delta t$ and $\Delta\epsilon_{\text{int}}(\mathcal{C}) \rightarrow -\Delta\epsilon_{\text{int}}(\mathcal{C})$ that respectively reflect the transformation properties under the time reversal symmetry and the fact that the dynamics of $\langle A_i(t) \rangle$ are identical in the repulsive and the attractive model. Defining $w(\mathcal{C}) \equiv |\text{Re}\{\mathcal{D}_{2t}(\mathcal{C}, \Delta t)\}|$ and $\text{sgn}(\mathcal{C}) \equiv \text{Re}\{\mathcal{D}_{2t}(\mathcal{C}, \Delta t)\}/|\text{Re}\{\mathcal{D}_{2t}(\mathcal{C}, \Delta t)\}|$, Eq. (19) is recast as

$$\langle A_i(t) \rangle \approx \frac{\mathcal{A}_i(\Psi_{i,N_t+1}) \text{sgn}(\mathcal{C}) \cos[\Delta\epsilon_{\text{int}}(\mathcal{C})\Delta t] w}{\langle\text{sgn}(\mathcal{C}) \cos[\Delta\epsilon_{\text{int}}(\mathcal{C})\Delta t]\rangle_w}. \quad (22)$$

The sign problem in the MC evaluation of Eq. (22) is dynamical. It generally becomes more serious with increasing time t and interaction strength $|U|$. Moreover, $w(\mathcal{C})$ also depends on both t and U , meaning that MC evaluations for different t s and U s should be performed separately, using different Markov chains. It is thus highly desirable to employ further symmetries in order to improve the performance of the method. Particularly relevant initial states

$|\psi(0)\rangle$, from both an experimental^{14,17} and theoretical¹⁰⁸ viewpoint, are pure density-wave-like states. Such states correspond to extreme spin-density wave (SDW) and charge-density wave (CDW) patterns, which one obtains by applying strong external density-modulating fields. The SDW-like state can be written as

$$|\psi_{\text{SDW}}(\mathcal{G})\rangle = \prod_{\mathbf{r}_1 \in \mathcal{G}} c_{\mathbf{r}_1 \uparrow}^\dagger \prod_{\mathbf{r}_2 \in \mathcal{U} \setminus \mathcal{G}} c_{\mathbf{r}_2 \downarrow}^\dagger |\emptyset\rangle, \quad (23)$$

where \mathcal{G} denotes the multitude of sites on which the electron spins are polarized up, while set \mathcal{U} contains all sites of the cluster studied. The electron spins on sites belonging to $\mathcal{U} \setminus \mathcal{G}$ are thus polarized down. Such states have been experimentally realized in Ref. 17. The CDW-like states have also been realized in experiment,¹⁴ and they read as

$$|\psi_{\text{CDW}}(\mathcal{G})\rangle = \prod_{\mathbf{r} \in \mathcal{G}} c_{\mathbf{r} \uparrow}^\dagger c_{\mathbf{r} \downarrow}^\dagger |\emptyset\rangle. \quad (24)$$

The sites belonging to \mathcal{G} are doubly occupied, while the remaining sites are empty. The state $|\psi_{\text{CDW}}(\mathcal{G})\rangle$ can be obtained from the corresponding $|\psi_{\text{SDW}}(\mathcal{G})\rangle$ state by applying the partial particle-hole transformation that acts on spin-down electrons only

$$|\psi_{\text{SDW}}(\mathcal{G})\rangle = \prod_{\mathbf{r} \in \mathcal{U}} \left(c_{\mathbf{r} \downarrow}^\dagger (1 - n_{\mathbf{r} \downarrow}) + c_{\mathbf{r} \downarrow} n_{\mathbf{r} \downarrow} \right) |\psi_{\text{CDW}}(\mathcal{G})\rangle, \quad (25)$$

see also Refs. 109 and 110. By combining the partial particle-hole, time-reversal, and bipartite lattice symmetries, the authors of Ref. 108 have shown that the time evolution of spatially resolved charge and spin densities starting from states $|\psi_{\text{CDW}}(\mathcal{G})\rangle$ and $|\psi_{\text{SDW}}(\mathcal{G})\rangle$, respectively, obey

$$\begin{aligned} \langle \psi_{\text{CDW}}(\mathcal{G}) | e^{iHt} (n_{\mathbf{r} \uparrow} + n_{\mathbf{r} \downarrow} - 1) e^{-iHt} | \psi_{\text{CDW}}(\mathcal{G}) \rangle \\ = \langle \psi_{\text{SDW}}(\mathcal{G}) | e^{iHt} (n_{\mathbf{r} \uparrow} - n_{\mathbf{r} \downarrow}) e^{-iHt} | \psi_{\text{SDW}}(\mathcal{G}) \rangle. \end{aligned} \quad (26)$$

Equation (26) may be used to acquire additional statistics by combining the Markov chains for the two symmetry-related evolutions. The procedure is briefly described in Appendix C and applied to all corresponding computations presented in Sec. III B.

3. ABQMC method for time-dependent quantities

In this section, we develop the so-called alternating-basis QMC method, which is aimed at removing the dynamical character of the sign problem in real-time FPQMC simulations. Moreover, using the ABQMC method, the results for different real times t and different interactions U may be obtained using just a single Markov chain, in contrast to the FPQMC method, which employs separate chains for each t and U .

Possible advantages of the ABQMC over the FPQMC method are most easily appreciated on the example of the survival probability of the initial state $|\psi(0)\rangle$

$$P(t) = |\langle \psi(0) | e^{-iHt} | \psi(0) \rangle|^2, \quad (27)$$

which is the probability of finding the system in its initial state after a time t has passed. Evaluating Eq. (27) by any discrete-time QMC

method necessitates only one STD, see Fig. 1(d). The survival probability is thus the simplest example on which the applicability of any QMC method to out-of-equilibrium setups can be systematically studied.

The FPQMC computation of $P(t)$ may proceed via the ratio

$$\mathcal{R}(t) = \frac{\langle \psi(0) | e^{-iHt} | \psi(0) \rangle}{\langle \psi(0) | e^{-iH_0 t} | \psi(0) \rangle} \quad (28)$$

of the survival-probability amplitudes in the presence and absence of electron–electron interactions. However, the average sign of the MC simulation of Eq. (28) is proportional to the survival-probability amplitude of the noninteracting system, which generally decays very quickly to zero, especially for large clusters.⁶² This means that the dynamical sign problem in the FPQMC evaluation of Eq. (28) may become very severe already at relatively short times t .

Instead of expressing the many-body free propagator $\langle \Psi_i^\dagger | e^{-iH_0 \Delta t} | \Psi_i \rangle$ as a determinant of single-particle free propagators [Eqs. (6) and (7)], we could have introduced the spectral decomposition of $e^{-iH_0 \Delta t}$ in terms of Fock states $|\Psi_k\rangle$ in the momentum representation. In analogy with Eq. (5), such states are defined as

$$|\Psi_k\rangle = \prod_{\sigma} \prod_{j=1}^{N_{\sigma}} c_{\mathbf{k}_j^{\sigma}}^\dagger |\emptyset\rangle. \quad (29)$$

The state $|\Psi_k\rangle$ contains N_{σ} electrons of spin σ whose momenta $\mathbf{k}_1^{\sigma}, \dots, \mathbf{k}_{N_{\sigma}}^{\sigma}$ are ordered according to a certain rule and we define $\varepsilon_0(\Psi_k) \equiv \langle \Psi_k | H_0 | \Psi_k \rangle$. In this case, the final expression for the survival probability of state $|\psi(0)\rangle$ that satisfies $TB|\psi(0)\rangle = e^{\lambda} |\psi(0)\rangle$ reads as

$$P(t) \approx \left| \frac{\sum_{\mathcal{C}} \text{Re}\{\mathcal{D}(\mathcal{C})\} \cos[\varepsilon_0(\mathcal{C})\Delta t] \cos[\varepsilon_{\text{int}}(\mathcal{C})\Delta t]}{\sum_{\mathcal{C}} \text{Re}\{\mathcal{D}(\mathcal{C})\}} \right|^2. \quad (30)$$

A derivation of Eq. (30) is provided in Appendix D. The MC evaluation of Eq. (30) should sample a much larger configuration space than the MC evaluation of Eq. (28). The configuration \mathcal{C} in Eq. (30) also resides on the contour depicted in Fig. 1(d), but comprises $2N_t - 1$ states in total: N_t Fock states $|\Psi_{k,l}\rangle$ ($l = 1, \dots, N_t$) and $N_t - 1$ Fock states $|\Psi_{i,l}\rangle$ ($l = 2, \dots, N_t$) (again, $|\Psi_{i,1}\rangle \equiv |\psi(0)\rangle$). $\mathcal{D}(\mathcal{C})$ is the product of $2N_t$ Slater determinants

$$\mathcal{D}(\mathcal{C}) = \prod_{l=1}^{N_t} \langle \Psi_{i,l} | \Psi_{k,l} \rangle \langle \Psi_{k,l} | \Psi_{i,l} \rangle \quad (31)$$

that stem from the sequence of basis alternations between the momentum and coordinate eigenbasis. Using the notation of Eqs. (5) and (29), the most general Slater determinant $\langle \Psi_i | \Psi_k \rangle$ entering Eq. (10) is given as

$$\langle \Psi_i | \Psi_k \rangle = \prod_{\sigma} \det \tilde{\mathcal{S}}(\Psi_i, \Psi_k, \sigma), \quad (32)$$

$$[\tilde{\mathcal{S}}(\Psi_i, \Psi_k, \sigma)]_{j_1 j_2} = \langle \mathbf{r}_{j_1}^{\sigma} | \mathbf{k}_{j_2}^{\sigma} \rangle = \frac{\exp(i\mathbf{k}_{j_2}^{\sigma} \cdot \mathbf{r}_{j_1}^{\sigma})}{\sqrt{N_c}}, \quad (33)$$

where $1 \leq j_1, j_2 \leq N_{\sigma}$. The symbol $\varepsilon_0(\mathcal{C})$ stands for [cf. Eq. (11)]

$$\varepsilon_0(\mathcal{C}) \equiv \sum_{l=1}^{N_\tau} \varepsilon_0(\Psi_{k,l}). \quad (34)$$

We note that each term in Eq. (30) is invariant under transformations $\varepsilon_0(\mathcal{C}) \rightarrow -\varepsilon_0(\mathcal{C})$ and $\Delta t \rightarrow -\Delta t$, which reflect the action of the bipartite lattice symmetry and the time reversal symmetry, respectively. Being term-by-term invariant under the transformation $\varepsilon_{\text{int}}(\mathcal{C}) \rightarrow -\varepsilon_{\text{int}}(\mathcal{C})$, Eq. (30) explicitly satisfies the requirement that the dynamics of $P(t)$ for repulsive and attractive interactions of the same magnitude are identical. Defining $w(\mathcal{C}) \equiv |\text{Re}\{\mathcal{D}(\mathcal{C})\}|$ and $\text{sgn}(\mathcal{C}) \equiv \text{Re}\{\mathcal{D}(\mathcal{C})\}/|\text{Re}\{\mathcal{D}(\mathcal{C})\}|$, Eq. (30) is recast as

$$P(t) \approx \left| \frac{\langle \text{sgn}(\mathcal{C}) \cos[\varepsilon_0(\mathcal{C})\Delta t] \cos[\varepsilon_{\text{int}}(\mathcal{C})\Delta t] \rangle_w}{\langle \text{sgn}(\mathcal{C}) \rangle_w} \right|^2. \quad (35)$$

This choice for w is optimal in the sense that it minimizes the variance of $\langle \text{sgn}(\mathcal{C}) \rangle_w$,¹¹¹ whose modulus is the average sign of the ABQMC simulation. The sign problem encountered in the MC evaluation of Eq. (35) does not depend on either time t or interaction strength U , i.e., it is not dynamical. The weight $w(\mathcal{C})$ in Eq. (35) does not depend on either Δt or any other property of configuration \mathcal{C} ($\varepsilon_0, \varepsilon_{\text{int}}$). Therefore, the MC evaluation of Eq. (35) may be performed simultaneously (using a single Markov chain) for any U and any t . This presents a technical advantage over the FPQMC method, which may be outweighed by the huge increase in configuration space when going from FPQMC to ABQMC. To somewhat reduce the dimension of the ABQMC configuration space and improve the sampling efficiency, we design the MC updates so as to respect the momentum conservation law throughout the real-time evolution. The momentum conservation poses the restriction that all the momentum-space states $|\Psi_{k,l}\rangle$ have the same total electron momentum $\mathbf{K} \equiv \sum_{k\sigma} \mathbf{k} \langle \Psi_{k,l} | n_{k\sigma} | \Psi_{k,l} \rangle$ [modulo $(2\pi, 2\pi)$]. The MC updates in the ABQMC method for the evaluation of the survival probability are presented in great detail in Sec. SII of the [supplementary material](#).

By relying on the partial particle-hole and bipartite lattice symmetries, in [Appendix D](#) we demonstrate that the dynamics of the survival probabilities of states $|\psi_{\text{SDW}}(\mathcal{G})\rangle$ and $|\psi_{\text{CDW}}(\mathcal{G})\rangle$ are identical, i.e.,

$$|\langle \psi_{\text{SDW}}(\mathcal{G}) | e^{-iHt} | \psi_{\text{SDW}}(\mathcal{G}) \rangle|^2 = |\langle \psi_{\text{CDW}}(\mathcal{G}) | e^{-iHt} | \psi_{\text{CDW}}(\mathcal{G}) \rangle|^2. \quad (36)$$

Evaluating Eq. (35), additional statistics can be acquired by combining the Markov chains for the $P(t)$ calculations starting from the two symmetry-related states $|\psi_{\text{CDW}}(\mathcal{G})\rangle$ and $|\psi_{\text{SDW}}(\mathcal{G})\rangle$. The procedure is similar to that described in [Appendix C](#), and we apply it to all corresponding computations presented in Sec. III C.

III. NUMERICAL RESULTS

We first apply the FPQMC method to equilibrium situations (the particle number is not fixed), see Sec. III A, and then to time-dependent local densities during the evolution of pure states, see Sec. III B. Section III C presents our ABQMC results for the survival probability of pure states. Our implementation of the ABQMC method on the full Kadanoff-Baym-Keldysh contour [Eq. (17)] is benchmarked in Sec. SVII of the [supplementary material](#).

A. Equilibrium results: Equation of state

We start by considering the Hubbard dimer, the minimal model capturing the subtle interplay between electron delocalization and electron-electron interaction.¹¹² We opt for moderate temperature $T/J = 1$ and interaction $U/J = 4$, so that the expected number of imaginary-time slices needed to obtain convergent FPQMC results is not very large. [Figure 2](#) presents the equation of state (i.e., the dependence of the electron density $\rho_e = \langle \hat{N}_\uparrow + \hat{N}_\downarrow \rangle / N_c$ on the chemical potential μ) for a range of μ below the half-filling. Here, \hat{N}_\uparrow and \hat{N}_\downarrow are the operators of the total number of spin-up and spin-down electrons, respectively. [Figure 2](#) suggests that already $N_\tau = 2$ imaginary-time slices suffice to obtain very good results in the considered range of μ , while increasing N_τ from 2 to 4 somewhat improves the accuracy of the FPQMC results. It is interesting that, irrespective of the value of N_τ , FPQMC simulations on the dimer are manifestly sign-problem-free. First, the one-dimensional imaginary-time propagator defined in Eq. (B2) is positive, $\mathcal{I}(J\Delta\tau, l) = [e^{J\Delta\tau} + (-1)^l e^{-J\Delta\tau}] / 2$ for both $l = 0$ and 1. Second, the configuration containing two electrons of the same spin is of weight $\cosh^2(J\Delta\tau) - \sinh^2(J\Delta\tau) \equiv 1$, implying that the weights of all configurations are positive. Furthermore, our results on longer chains suggest that FPQMC simulations of one-dimensional lattice fermions do not display a sign problem. While similar statements have been repeated for continuum one-dimensional models of both noninteracting^{85,86} and interacting fermions,⁸⁷ there is, to the best of our knowledge, no rigorous proof that the sign problem is absent from coordinate-space QMC simulations of one-dimensional fermionic systems. While we do not provide such a proof either, [Fig. 3](#) is an illustrative example showing how the FPQMC results for the double occupancy $\sum_\tau \langle n_{\uparrow\tau} n_{\downarrow\tau} \rangle / N_c$ of the Hubbard chain at half-filling approach the reference result (taken from Ref. 113) as the imaginary-time discretization becomes finer. For all N_τ s considered, the average sign of FPQMC simulations is $|\langle \text{sgn} \rangle| = 1$.

We now apply the FPQMC method to evaluate the equation of state on larger clusters. We focus on a 4×4 cluster, which may already be representative of the thermodynamic limit at $T/J \gtrsim 1$.⁵⁰ We compare our $\rho_e(\mu)$ results with the results of the numerical linked-cluster expansion (NLCE) method.⁴⁰⁻⁴² The NLCE results are numerically exact and converged with respect to the control parameter, i.e., the maximal cluster-size used. NLCE is commonly

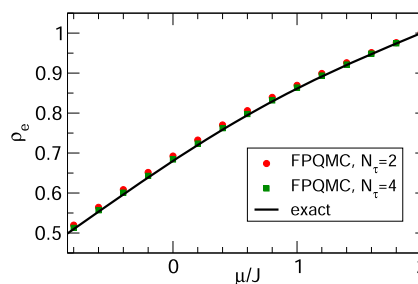


FIG. 2. Equation of state $\rho_e(\mu)$ for the Hubbard dimer with $T/J = 1$, $U/J = 4$. Full red circles (green squares) are the results of FPQMC simulations employing $N_\tau = 2$ ($N_\tau = 4$) imaginary-time slices, while the solid black line is computed using the exact diagonalization. The estimated statistical error of the FPQMC data is in all cases smaller than the symbol size.

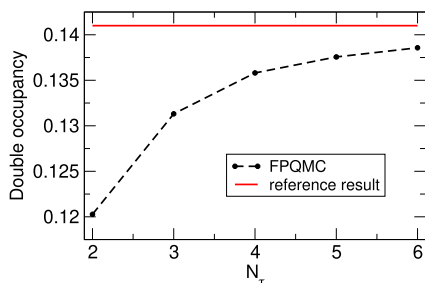


FIG. 3. Double occupancy of the $N_c = 20$ -site Hubbard chain at half-filling ($\mu = U/2$, $\rho_e = 1$) as a function of the number N_τ of imaginary-time slices. The remaining parameters are $U/J = 3$ and $T/J = 1$. The dotted line connecting full symbols (FPQMC results) serves as a guide to the eye. The reference result is taken from Ref. 113. The relative deviation of the FPQMC result with $N_\tau = 6$ from the reference result is around 2%. The statistical error bars of the FPQMC results are smaller than the symbol size.

used to benchmark methods and understand experimental data.^{9,10} Again, we keep $U/J = 4$, but we take $T/J = 1.0408$ to be able to compare results to the data of Ref. 41. Figure 4(a) reveals that the FPQMC results with only $N_\tau = 2$ imaginary-time slices agree very well (within a couple of percent) with the NLCE results over a wide range of chemical potentials. This is a highly striking observation, especially keeping in mind that the FPQMC method with $N_\tau = 2$ is sign-problem-free, see Fig. 4(b). It is unclear whether other STD-based methods would reach here the same level of accuracy with only two imaginary-time slices (and without the sign problem). This may be a specific property of the FPQMC method. Finer imaginary-time discretization introduces the sign problem, see Fig. 4(b), which becomes more pronounced as the density is increased and reaches a plateau for $\rho_e \gtrsim 0.8$. Still, the sign problem remains manageable. Increasing N_τ for 2 to 6 somewhat improves the agreement of the density ρ_e [the inset of Fig. 4(a)] and considerably improves the agreement of the double occupancy [Fig. 4(c)] with the referent NLCE results. Still, comparing the insets of Figs. 4(a) and 4(c), we observe that the agreement between FPQMC ($N_\tau = 6$) and NLCE results for ρ_e is significantly better than for the double occupancy. The systematic error in FPQMC comes from the time-discretization and the finite size of the system. At $N_\tau = 6$, it is not *a priori* clear which error contributes more, but it appears most likely that the time-discretization error is dominant. In any case, the reason why systematic error is greater for the double occupancy than for the average density could be that the double occupancy contains more detailed information about the correlations in the system. This might be an indication that measurement of multipoint density correlations will generally be more difficult—it may require a finer time resolution and/or greater lattice size.

The average sign above the half-filling, $\rho_e = 1$, mirrors that below the half-filling. The particle–hole symmetry ensures that $\rho_e(\mu) = 2 - \rho_e(U - \mu)$, but that it also governs the average sign is not immediately obvious from the construction of the method. A formal demonstration of the electron-doping–hole-doping symmetry of the average sign is, however, possible (see Appendix E). Note that we restrict our density calculations to $\rho_e < 1$ because, in this case, the numerical effort to manipulate the determinants [Eqs. (7) and (10)]

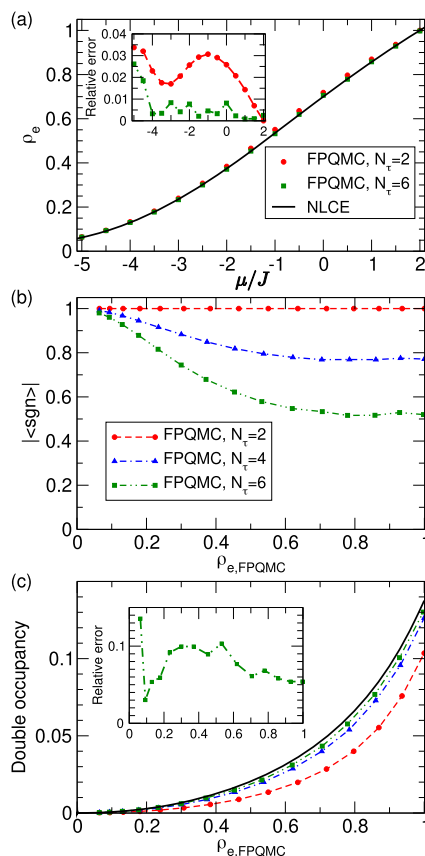


FIG. 4. (a) Equation of state $\rho_e(\mu)$ for the Hubbard model on a 4×4 cluster with the following values of model parameters: $U/J = 4$, $T/J = 1.0408$. (b) The average sign as a function of the FPQMC estimate $\rho_{e,\text{FPQMC}}$ of the electron density for different values of N_τ . The dashed lines are guides for the eye. (c) The double occupancy $\sum_\tau \langle n_{r\uparrow} n_{r\downarrow} \rangle / N_c$ as a function of the FPQMC estimate $\rho_{e,\text{FPQMC}}$ of the electron density for different values of N_τ . In (a) and (c), full symbols represent FPQMC results, the solid line shows the NLCE data taken from Ref. 41, while the insets show the relative deviation of FPQMC results from the reference NLCE results. The estimated statistical error of the FPQMC data is in all cases smaller than the symbol size.

is lower (size of the corresponding matrices is given by the number of particles of a given spin). The performance of the FPQMC algorithm to compute $\rho_e(\mu)$ (average time needed to propose/accept an MC update and acceptance rates of individual MC updates) is discussed in Sec. SIII of the [supplementary material](#).

We further benchmark our method in the case of very strong coupling, $U/J = 24$ and, again, $T/J = 1.0408$. Figure 5(a) compares the FPQMC results on a 4×4 cluster using $N_\tau = 2, 4$, and 6 imaginary-time slices with the NLCE results. At extremely low fillings $\rho_e \lesssim 0.1$, the relative importance of the interaction term with respect to the kinetic term is quite small, and taking only $N_\tau = 2$ suffices to reach a very good agreement between the FPQMC and NLCE results, see the inset of Fig. 5(a). As the filling is increased, the interaction effects become increasingly important, and it is necessary to increase N_τ in order to accurately describe the competition between

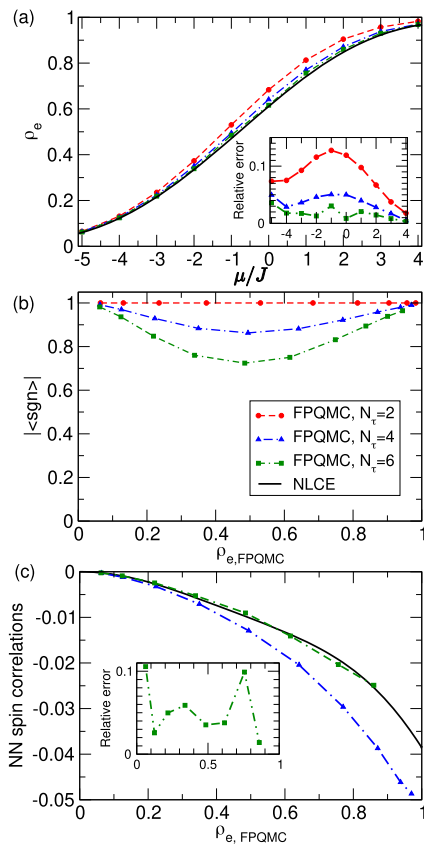


FIG. 5. (a) Equation of state $\rho_e(\mu)$ for the Hubbard model on a 4×4 cluster with the following values of model parameters: $U/J = 24$, $T/J = 1.0408$. (b) The average sign as a function of the FPQMC estimate $\rho_{e, \text{FPQMC}}$ of the electron density for different values of N_τ . (c) Nearest-neighbor spin correlations $\sum_{\mathbf{r}\delta} \langle S_{\mathbf{r}}^z S_{\mathbf{r}+\delta}^z \rangle / N_c$ as a function of the FPQMC estimate $\rho_{e, \text{FPQMC}}$ of the electron density for $N_\tau = 4$ and 6. In (a) and (c), full symbols represent FPQMC results, the solid line shows the NLCE data taken from Ref. 41, while the insets show the relative deviation of FPQMC results from the reference NLCE results. The dashed or dashed-dotted lines connecting the symbols serve as guides to the eye. The estimated statistical error of the FPQMC data are in all cases smaller than the symbol size.

the kinetic and interaction terms. In the inset of Fig. 5(a), we see that $N_\tau = 6$ is sufficient to reach an excellent (within a couple of percent) agreement between FPQMC and NLCE results over a broad range of fillings. At very high fillings $\rho_e \gtrsim 0.9$ and for $N_\tau = 6$, our MC updates that insert/remove particles have very low acceptance rates, which may lead to a slow sampling of the configuration space. It is for this reason that FPQMC results with $N_\tau = 6$ do not significantly improve over $N_\tau = 4$ in this parameter regime. For $N_\tau = 6$, an inefficient sampling near the half-filling also renders the corresponding results for the nearest-neighbor spin correlations $\sum_{\mathbf{r}\delta} \langle S_{\mathbf{r}}^z S_{\mathbf{r}+\delta}^z \rangle / N_c$ inaccurate, so that they are not displayed in Fig. 5(c). Here, vector δ connects nearest-neighboring sites, while $S_{\mathbf{r}}^z = (n_{\mathbf{r}\uparrow} - n_{\mathbf{r}\downarrow})/2$ is the operator of z projection of the local spin. At lower fillings, $\rho_e \lesssim 0.8$, the agreement between our FPQMC results with $N_\tau = 6$ and the NLCE results is good, while decreasing N_τ from 6 to 4 severely deteriorates the quality of the FPQMC results.

At this strong coupling, the dependence of the average sign on the density is somewhat modified, see Fig. 5(b). The minimal sign is no longer reached around half-filling but at quarter-filling, $\rho_e \sim 0.5$, around which $|\langle \text{sgn} \rangle|$ appears to be symmetric. Comparing Fig. 5(b) to Fig. 4(b), we see that the average sign does not become smaller with increasing interaction, in sharp contrast with interaction-expansion-based methods, such as CT-INT^{32,33} or configuration PIMC.⁸⁹

To better understand the relation between the average sign and the interaction, in Fig. 6(a) we plot $|\langle \text{sgn} \rangle|$ as a function of the ratio $U/(4J)$ of the typical interaction and kinetic energy. We take $N_\tau = 6$ and adjust the chemical potential using the data from Ref. 41 so that $\rho_e \approx 0.5$. We see that $|\langle \text{sgn} \rangle|$ monotonically increases with the interaction and reaches a plateau at very strong interactions. This is different from interaction-expansion-based QMC methods, whose sign problem becomes more pronounced as the interaction is

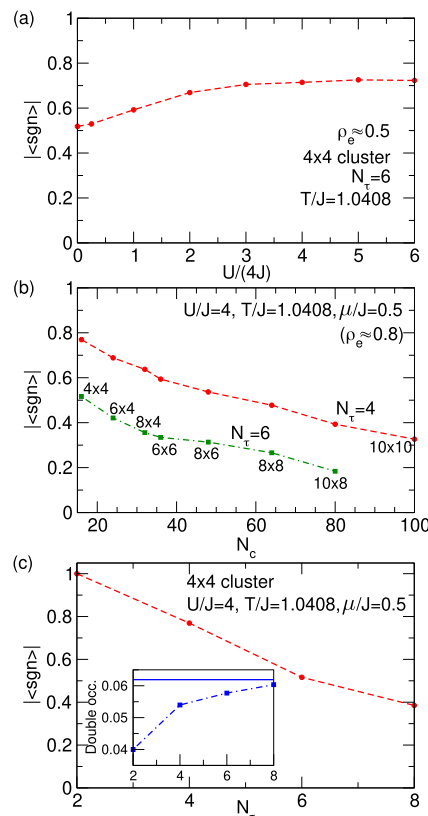


FIG. 6. (a) The average sign as a function of the ratio between the typical interaction and kinetic energies. Full symbols are results of FPQMC computations on a 4×4 cluster with $N_\tau = 6$, the temperature is fixed to $T/J = 1.0408$, and the chemical potential at each U is chosen such that $\rho_e \approx 0.5$. (b) The average sign as a function of the cluster size N_c for the values of model parameters summarized in the figure. The FPQMC results (full symbols) are obtained using $N_\tau = 4$ and 6. (c) Average sign as a function of N_τ . The FPQMC results (full symbols) are obtained on a 4×4 cluster for the values of model parameters summarized in the main part of the figure. The inset shows how the FPQMC result for double occupancy approaches the referent NLCE result as the imaginary-time discretization becomes finer.

increased. Moreover, for weak interactions, the performance of the FPQMC method deteriorates at high densities, see Fig. 4(b), while methods such as CT-INT become problematic at low densities. The FPQMC method could thus become a method of choice to study the regimes of moderate coupling and temperature, which are highly relevant for optical lattice experiments. Figure 6(b) shows the decrease of the average sign with the cluster size N_c in the weak-coupling and moderate-temperature regime at filling $\rho_e \approx 0.8$. We observe that for both $N_\tau = 4$ and $N_\tau = 6$, the average sign decreases linearly with N_c . For $N_\tau = 6$, we observe that the decrease for $N_c \lesssim 40$ is somewhat faster than the decrease for $N_c \gtrsim 40$. We, however, note that the acceptance rates of our MC updates strongly decrease with N_c and that this decrease is more pronounced for finer imaginary-time discretizations. That is why we were not able to obtain any meaningful result for the 10×10 cluster with $N_\tau = 6$. At fixed cluster size and filling, the average sign decreases linearly with N_τ , see the main part of Fig. 6(c), while the double occupancy tends to the referent NLCE value, see the inset of Fig. 6(c).

In Sec. SIV of the supplementary material, we provide an implementation of the ABQMC method in the equilibrium setup. Figures 7(a) and 7(b), which deal with the same parameter regimes as Figs. 4 and 5, respectively, clearly illustrate the advantages of the fermionic-propagator approach with respect to the alternating-basis approach in equilibrium. The average sign of ABQMC simulations with only two imaginary-time slices is orders of magnitude smaller than the sign of FPQMC simulations with three times finer imaginary-time discretization. Since the FPQMC and ABQMC methods are related by an exact transformation, they should produce

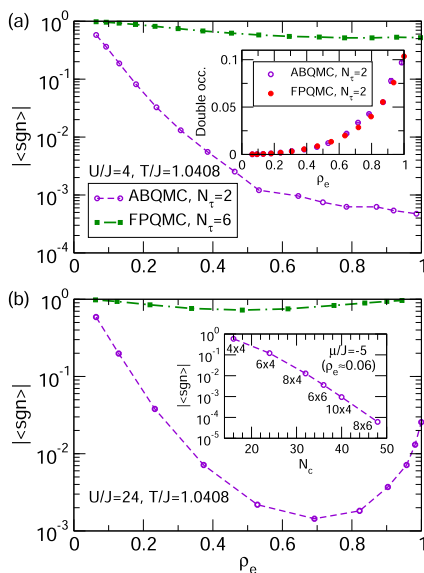


FIG. 7. Average sign as a function of the electron density in ABQMC simulations with $N_\tau = 2$ (open circles) and FPQMC simulations with $N_\tau = 6$ (full squares) for $T/J = 1.0408$ and (a) $U/J = 4$ and (b) $U/J = 24$. The inset in panel (a) compares ABQMC (open circles) and FPQMC (full circles) results for the double occupancy as a function of ρ_e (both methods employ $N_\tau = 2$). The inset in panel (b) shows the average sign of ABQMC simulations with $N_\tau = 2$ as a function of cluster size N_c at low density ($\rho_e \approx 0.06$, $\mu/J = -5$).

the same results for thermodynamic quantities (assuming that N_τ is the same in both methods). This is shown in the inset of Fig. 7(a) on the example of the double occupancy. The inset of Fig. 7(b) suggests that the average sign decreases exponentially with the cluster size N_c . Overall, our current implementation of the ABQMC method in equilibrium cannot be used to simulate larger clusters with a finer imaginary-time discretization.

B. Time-dependent results using FPQMC method: Local charge and spin densities

1. Benchmarks on small clusters

In Figs. 8(a) and 8(b), we benchmark our FPQMC method for time-dependent local densities on the example of the CDW state of the Hubbard tetramer, see the inset of Fig. 8(b). We follow the evolution of local charge densities on initially occupied sites for different ratios U/D , where D is the half-bandwidth of the free-electron band ($D = 2J$ for the tetramer). For all the interaction strengths considered, taking $N_t = 2$ real-time slices on each branch (four slices in total) is sufficient to accurately describe the evolution of local densities up to times $Dt \sim 2$, see full symbols in Fig. 8(a). At longer times, $2 < Dt \leq 4$, taking $N_t = 3$ improves results obtained using $N_t = 2$, compare empty to full symbols in Fig. 8(a). Nevertheless, for the strongest interaction considered ($U/D = 1$), 6 real-time slices are not sufficient to bring the FPQMC result closer to the exact result at times $3 \leq Dt \leq 4$. The average sign strongly depends on time, and it drops by an order of magnitude upon increasing N_t from 2 to 3, see Fig. 8(b). Despite this, the discrepancy between the $N_t = 3$ result

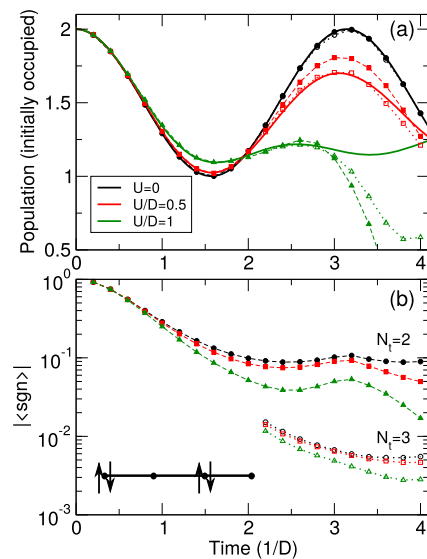


FIG. 8. (a) Time-dependent population of sites occupied in the initial CDW state of a tetramer for different interaction strengths. Solid lines represent exact results, full symbols connected by dashed lines are FPQMC results using $N_t = 2$ real-time slices, while empty symbols connected by dotted lines are FPQMC results using $N_t = 3$ real-time slices. The initial CDW state is schematically depicted in panel (b). (b) Time-dependent average sign of the FPQMC simulation using $N_t = 2$ (full symbols connected by dashed lines) and $N_t = 3$ (empty symbols connected by dotted lines) for different interaction strengths. In (a) and (b), FPQMC simulations using $N_t = 3$ real-time slices are carried out only for $2 < Dt \leq 4$.





and the exact result for $U/D = 1$ cannot be ascribed to statistical errors but rather to the systematic error of the FPQMC method (the minimum N_t needed to obtain results with certain systematic error increases with both time and interaction strength).

2. Results on larger clusters

Figure 9(a) summarizes the evolution of local charge densities on initially occupied sites of a half-filled 4×4 cluster, on which the electrons are initially arranged as depicted in the inset of Fig. 9(b). This state is representative of a CDW pattern formed by applying strong external density-modulating fields with wave vector $\mathbf{q} = (\pi, 0)$. The FPQMC method employs four real-time slices in total, i.e., the forward and backward branches are divided into $N_t = 2$ identical slices each. On the basis of the $N_t = 2$ results in Fig. 8(a), we present the FPQMC dynamics up to the maximum time $Dt_{\max} = 2$. The extent of the dynamical sign problem is shown in Fig. 9(b).

At the shortest times, $Dt \lesssim 1$, the results for all the interactions considered do not significantly differ from the noninteracting result. The same also holds for the average sign. As expected, the decrease of $|\langle \text{sgn} \rangle|$ with time becomes more rapid as the interaction U and time discretization $\Delta t = t/N_t$ are increased. The oscillatory nature of $\langle \text{sgn} \rangle$ as a function of time [see Eq. (22)] is correlated with the discontinuities in time-dependent populations observed in Fig. 9(a) for $U/D \geq 0.5$. Namely, at the shortest times and for all the interactions considered, $\langle \text{sgn} \rangle$ is positive, while for sufficiently strong interactions, it becomes negative at longer times. This change is indicated in Fig. 9(b) by placing the symbols “+” and “−” next to each relevant point. We now see that the discontinuities in populations occur precisely around instants at which $\langle \text{sgn} \rangle$ turns from positive to negative values. Focusing on $U/D = 1$, in Figs. 9(c1)–9(c3) we show the MC series for the population of initially occupied sites at instants before

TABLE I. Schematic representations of the initial states of small systems on which the ABQMC method for $P(t)$ is benchmarked.

system	$ \psi_{\text{CDW}}\rangle$	$ \psi_{\text{SDW}}\rangle$
Dimer		
Tetramer		

[(c1)] and after [(c2), (c3)] $\langle \text{sgn} \rangle$ passes through zero. The corresponding series for $\langle \text{sgn} \rangle$ are presented in Figs. 9(d1)–9(d3). Well before [Figs. 9(c1) and 9(d1)] and after [Figs. 9(c3) and 9(d3)] $\langle \text{sgn} \rangle$ changes sign, the convergence with the number of MC steps is excellent, while it is somewhat slower close to the positive-to-negative transition point, see Figs. 9(c2) and 9(d2). Still, the convergence at $Dt = 1.4$ cannot be denied, albeit the statistical error of the population is larger than at $Dt = 1.2$ and 1.6. At longer times $Dt \geq 1.5$, when $\langle \text{sgn} \rangle$ is negative and of appreciable magnitude, the population again falls in the physical range $[0, 2]$. Nevertheless, at such long times, the systematic error may be large due to the coarse real-time discretization.

In Sec. SV of the [supplementary material](#), we discuss FPQMC results for the dynamics of local charge densities starting from some other initial states.

C. Time-dependent results using ABQMC method: Survival probability

1. Benchmarks on small clusters

We first benchmark our ABQMC method for the survival probability on Hubbard dimers and tetramers. The initial states

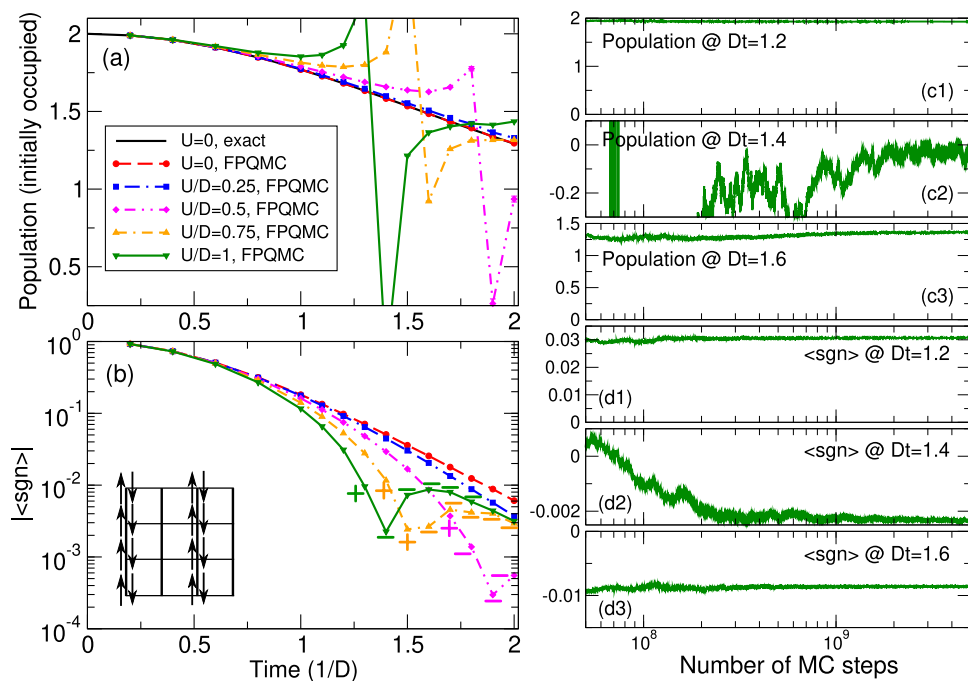


FIG. 9. (a) Time-dependent population of sites occupied in the initial CDW state of a 4×4 cluster, which is schematically depicted in the inset of panel (b). FPQMC results using $N_t = 2$ real-time slices (four slices in total) are shown for five different interaction strengths (symbols) and compared with the noninteracting result (solid line). (b) Magnitude of the average sign as a function of time for different interaction strengths. The color code is the same as in panel (a). For $U/D = 0.5, 0.75$, and 1 and $Dt \geq 1.2$, symbols “+” and “−” next to each point specify whether $\langle \text{sgn} \rangle$ is positive or negative. (c) MC series for the population of initially occupied sites for $U/D = 1$ and (c1) $Dt = 1.2$, (c2) $Dt = 1.4$, and (c3) $Dt = 1.6$. (d) MC series for $\langle \text{sgn} \rangle$ for $U/D = 1$ and (d1) $Dt = 1.2$, (d2) $Dt = 1.4$, and (d3) $Dt = 1.6$. Note the logarithmic scale on the abscissa in (c) and (d).

are schematically summarized in Table I. In both cases, we are at half-filling.

Figures 10(a1)–10(e2) present the time evolution of the survival probability of the initial CDW-like and SDW-like states depicted in Table I for the dimer (left panels, $D = J$) and tetramer (right panels, $D = 2J$) for different values of U/D starting from the limit of a weakly nonideal gas ($U/D = 0.05$) and approaching the atomic limit ($U/D = 20$). The results are obtained using $N_t = 2$ (full red circles) and $N_t = 4$ (blue stars) real-time slices and contrasted with the exact result (solid black lines). The ABQMC results with $N_t = 2$ agree both qualitatively (oscillatory behavior) and quantitatively with the exact result up to $t_{\max} \sim 1/U$. Increasing N_t from 2 to 4 may help decrease the deviation of the ABQMC data from the exact result at later times. Even when finer real-time discretization does not lead to better quantitative agreement, it may still help the ABQMC method qualitatively reproduce the gross features of the exact result. The converged values of $|\langle \text{sgn} \rangle|$ for the dimer and tetramer

TABLE II. Modulus of the average sign for ABQMC simulations of $P(t)$ on dimer and tetramer with $N_t = 2, 3$, and 4.

System	$N_t = 2$	$N_t = 3$	$N_t = 4$
Dimer	1/2	1/4	1/8
Tetramer	1/8	2.4×10^{-2}	3×10^{-3}

for $N_t = 2, 3$, and 4 are summarized in Table II. For the dimer, increasing N_t by one reduces $|\langle \text{sgn} \rangle|$ by a factor of 2. In contrast, in the case of the tetramer, increasing N_t by one reduces $|\langle \text{sgn} \rangle|$ by almost an order of magnitude.

2. Results on larger clusters

We move on to discuss the survival probability dynamics of different 16-electron and eight-electron states on a 4×4

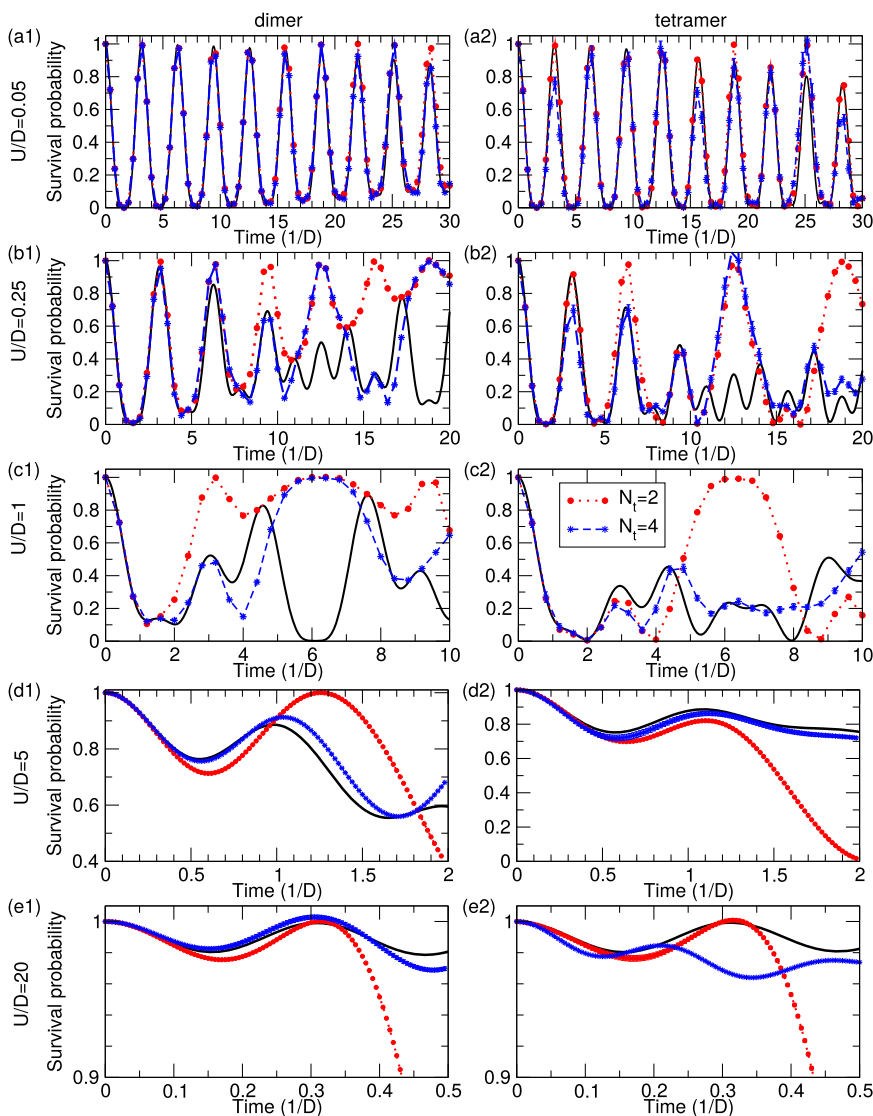


FIG. 10. Time dependence of the survival probability of the initial state $|\psi_{\text{CDW}}\rangle$ or $|\psi_{\text{SDW}}\rangle$ (see Table I) for the dimer [(a1)–(e1)] and tetramer [(a2)–(e2)] for five different interaction strengths starting from the noninteracting limit and approaching the atomic limit: $U/D = 0.05$ [(a1) and (a2)], $U/D = 0.25$ [(b1) and (b2)], $U/D = 1$ [(c1) and (c2)], $U/D = 5$ [(d1) and (d2)], and $U/D = 20$ [(e1) and (e2)]. The ABQMC results with $N_t = 2$ (red full circles) and $N_t = 4$ (blue stars) are compared with the exact result (black solid lines). The dotted/dashed lines connecting subsequent circles/stars are guides to the eye. In most cases, the MC error bars are smaller than the linear size of the symbols.

cluster. Figures 11(a) and 11(b) present $P(t)$ for 16-electron states schematically depicted in their respective insets. These states are representative of CDW patterns formed by applying strong external density-modulating fields with wave vectors $\mathbf{q} = (\pi, 0)$ in Figs. 11(a) and $\mathbf{q} = (\pi, \pi)$ in Fig. 11(b). Figures 11(c) and 11(d) present $P(t)$ for eight-electron states schematically depicted in their respective insets. The ABQMC method employs $N_t = 2$ real-time slices. The results are shown up to the maximum time $Dt_{\max} = 2.5$, which we chose on the basis of the results presented in Fig. 10(c2).

As a sensibility check of our ABQMC results, we first compare the exact result in the noninteracting limit, see solid lines in Figs. 11(a)–11(d), with the corresponding ABQMC prediction, see full circles in Figs. 11(a)–11(d). While the exact and ABQMC results agree quite well in Figs. 11(b) and 11(c), the agreement in Figs. 11(a) and 11(d) is not perfect. Since no systematic errors are expected in ABQMC at $U = 0$, the discrepancy must be due to statistical error. We confirm this expectation in Fig. 12 where we see that the obtained curve tends to the exact one with the increasing number of MC steps. The average sign cited in Fig. 11(d) suggests that more MC steps are needed to obtain fully converged results. Even though the converged average sign in Figs. 11(a)–11(c) is of the same order of magnitude, we find that the rate of convergence depends on both the number and the initial configuration of electrons.

In Figs. 11(a)–11(d), we observe that weak interactions ($U/D \lesssim 0.5$) do not cause any significant departure of $P(t)$ from the corresponding noninteracting result. On the other hand, the effect of somewhat stronger interactions on $P(t)$ depends crucially on the filling. In the 16-electron case, the increasing interactions speed up the initial decay of P , see Figs. 11(a) and 11(b), while in the eight-electron case interactions have little effect at $Dt < 1$, see Figs. 11(c) and 11(d). This we attribute to the essential difference in the overall electron density and the relative role of the interaction term in the Hamiltonian. In the 16-electron case, starting from the moderate coupling $U/D \sim 1$, there is a clear revival of the initial

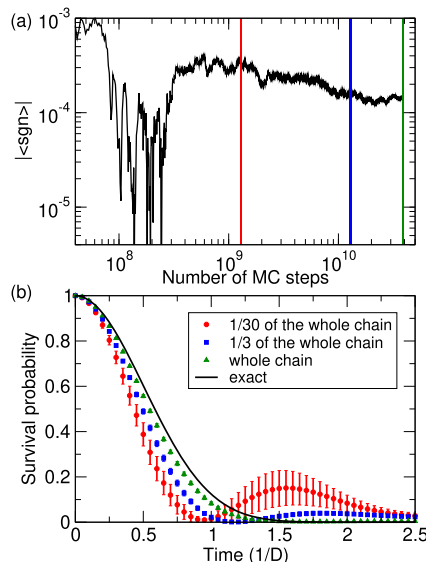


FIG. 12. (a) Average sign as a function of the number of MC steps in the ABQMC simulation of $P(t)$ for the 16-electron initial state schematically depicted in Fig. 11(a). (b) Time dependence of the survival probability for $U = 0$ extracted using the first 1/30 of the total number of MC steps completed (1.29×10^9 steps, full red circles), the first 1/3 of the total number of MC steps completed (1.29×10^{10} steps, full blue squares), and all the MC steps completed (3.87×10^{10} steps, full green up-triangles). These results are compared to the exact result in the noninteracting limit, which is represented by the solid line. The vertical lines in (a), whose colors match the colors of the symbols in (b), denote the ending points of the simulations.

state in Fig. 11(a), while no such a revival is observed in Fig. 11(b). Furthermore, the memory loss of the initial density-wave pattern is more rapid in Fig. 11(a) than in Fig. 11(b), even at $U = 0$. The revival of the initial state is observed in the eight-electron case as well: at

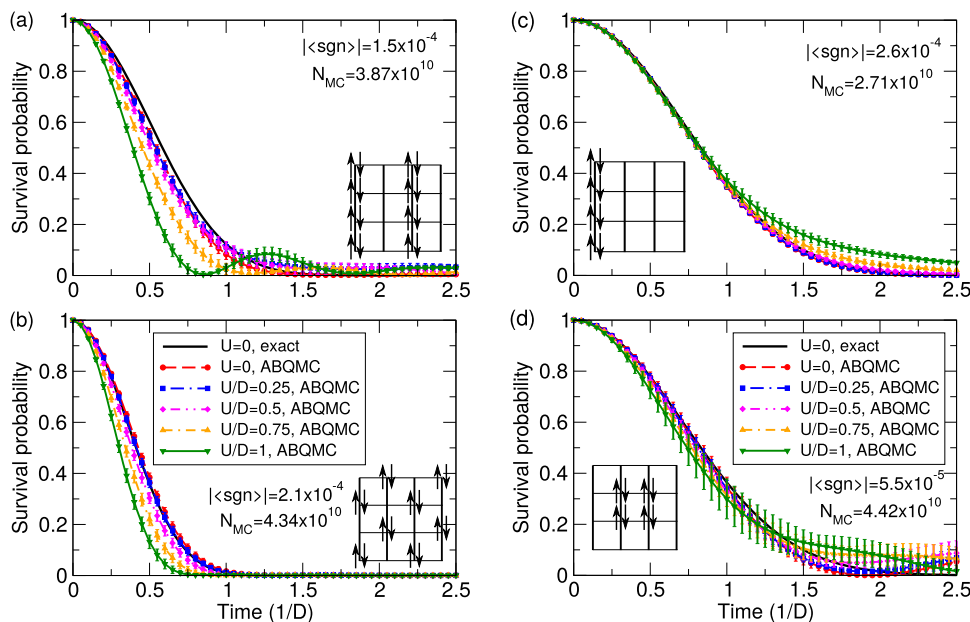


FIG. 11. Survival-probability dynamics of the 16-electron states [in (a) and (b)] and 8-electron states [in (c) and (d)] that are schematically depicted in the respective insets. The ABQMC results are shown for five different interaction strengths (symbols) and compared with the noninteracting result (solid line). We cite the converged value of the average sign $|\langle \text{sgn} \rangle|$, as well as the total number N_{MC} of MC steps completed.

$t < 1/D$ there is barely any effect of the interaction, yet at longer times it boosts P . However, in contrast to the 16-electron case, the results in Figs. 11(c) and 11(d) exhibit a weaker dependence of the survival-probability dynamics on the initial density-wave pattern. Indeed, the exact results in the noninteracting case are identical for both patterns in Figs. 11(c) and 11(d). Except in the case of the (π, π) wave, the interactions lead to a persistence of the initial pattern at longer times, $t > 1/D$. The precise form of temporal correlations that develop due to interactions apparently depends on the initial spatial arrangement of the electrons.

Section SVI of the [supplementary material](#) presents additional ABQMC results for the time-dependent survival probability.

IV. RELATION TO OTHER ALGORITHMS

As mentioned in the introduction, a variant of the FPQMC method was first proposed by De Raedt and Lagendijk in the 1980s.^{78–80} They, however, explicitly retain permutation operators appearing in Eq. (A5) in their final expression for Z , see, e.g., Eq. (3) in Ref. 78 or Eqs. (4.13) and (4.14) in Ref. 80. On the other hand, we analytically perform summation over permutation operators, thus grouping individual contributions into determinants. This is much more efficient [as the factorial number of terms is captured in only $O(N^3)$ steps, or even faster] and greatly improves the average sign (cancellations between different permutations are already contained in the determinant, see Fig. 7). The approach followed by De Raedt and Lagendijk later became known as permutation-sampling QMC, and the route followed by us is known as antisymmetric-propagator QMC,^{85,86} permutation-blocking QMC,⁹⁰ or fermionic-propagator QMC.⁹⁶ The analytical summation over permutation operators entering Eq. (A5) was first performed by Takahashi and Imada.⁸⁵

Our FPQMC method employs the lowest-order STD [Eq. (4)], which was also used in the permutation-sampling QMC method of De Raedt and Lagendijk.^{78–80} The maximum number of imaginary-time slices N_τ they could use was limited by the acceptance rates of MC updates, which decrease quickly with increasing N_τ and the cluster size N_c . In our present implementation of FPQMC, we encounter the same issue, and our sampling becomes prohibitively inefficient when the total number of time slices is greater than 6–8, depending on the cluster size. To circumvent this issue, the fermionic-propagator idea was combined with higher-order STDs^{98,114–116} and more advanced sampling techniques^{117,118} to simulate the equilibrium properties of continuum models of interacting fermions in the canonical^{90,92} and grand-canonical⁹⁶ ensembles. More recent algorithmic developments enabled simulations with as much as 2000 imaginary-time slices,¹¹⁹ which is a great improvement. Whether similar ideas can be applied to lattice systems to improve the efficiency of sampling is currently unclear. Generally, more sophisticated STD schemes have been regarded as not useful in lattice-model applications.¹²⁰ It is important to note that the success of the antisymmetric-propagator algorithms in continuous systems relies on weak degeneracy. This corresponds to an extremely low occupancy regime in lattice models, and it is precisely in this regime that our FPQMC method has an average sign close to 1 [see Figs. 4(b) and 5(b)], and the sampling is most efficient [see Sec. SIII of the [supplementary material](#)]. Near half-filling, lattice models present a fundamentally different physics,

which may ultimately require a substantially different algorithmic approach.

We further emphasize that the low acceptance rates and the resulting inefficiency of sampling that we encounter are directly related to the discrete nature of space in our model. Some strategies for treating the analogous problem in continuous-space models may not be applicable here. For example, in continuous-space models, acceptance rates of individual updates can be adjusted by moving electrons over shorter distances, so that the new configuration weight is less likely to be substantially different from the old one. In contrast, in lattice models, electronic coordinates are discrete, and the minimum distance the electrons may cover is set by the lattice constant; in most cases, moving a single electron by a single lattice spacing in a single time slice is sufficient to drastically reduce the configuration weight. There is no general rule on how electrons should be moved to ensure that the new configuration weight is close to the original one. This is particularly true for the updates that insert/remove a particle, and the problem becomes more pronounced with increasing N_τ . When each of the N_τ states $|\Psi_{i,l}\rangle$ [see Eq. (9)] is changed to $|\Psi'_{i,l}\rangle$, the chances that at least one of $\langle \Psi'_{i,l} | e^{-\Delta\tau H_0} | \Psi_{i,l} \rangle$ is much smaller than $\langle \Psi_{i,l} | e^{-\Delta\tau H_0} | \Psi_{i,l} \rangle$ [see Eq. (10)] increase with N_τ . Our configuration weight is appreciable only in small, mutually disconnected regions of the configuration space, the movement between which is difficult. In Sec. V, we touch upon possible strategies to improve sampling of such a structured configuration space.

It is also important to compare our methods to the HF QMC method,^{24,49} which is a well-established STD-based method for the treatment of the Hubbard model. The HF method is manifestly sign-problem-free but only at particle-hole symmetry. The sign problem can become severe away from half-filling, or on lattices other than the simple square lattice with no longer-range hoppings. On the other hand, our FPQMC method is nearly sign-problem-free at low occupancy, but also near half-filling, albeit only at strong coupling [see Figs. 4(b) and 5(b)]. The other important difference is that matrices manipulated in HF are of the size $N_c N_\tau$, while in FPQMC, the matrices are of the size $< 2N_c$, i.e., given by the number of particles. Algorithmic complexity of the individual MC step in FPQMC scales only linearly with N_τ , while in HF, the MC step may go as $O(N_\tau^2)$ [determinant is $O(N^3)$], but fast updates $O(N^2)$ are possible when the determinant is not calculated from scratch⁴⁹. Low cost of individual steps in FPQMC has allowed us to perform as many as $\sim 10^{10}$ MC steps in some calculations. This advantage, however, weighs against an increased configuration space to be sampled. In HF the number of possible configurations is $2^{N_c N_\tau}$ (space is spanned by $N_c N_\tau$ auxiliary Ising spins), while in FPQMC it is $4^{N_c N_\tau}$ (although, symmetries can be used to significantly reduce the number of possible configurations). The ABQMC method manipulates matrices of the same size as does FPQMC, but with twice the number, and the configuration space is *a priori* even bigger ($16^{N_c N_\tau}$). Our methods also have the technical advantage that the measurements of multipoint charge and spin correlation functions are algorithmically trivial and cheap. Especially in ABQMC, the densities in both coordinate and momentum space can be simply read off the configuration. This is not possible in HF, where the auxiliary Ising spin only distinguishes between singly occupied and doubly-occupied/empty sites. Most importantly, the ABQMC/FPQMC methods can be readily applied to canonical ensembles and pure states, which may

not be possible with the HF method. However, the HF is commonly used with tens of time slices for lattice sizes of order $N_c = 100\text{--}200$; in FPQMC, algorithmic developments related to configuration updates are necessary before it can become a viable alternative to the HF in a wide range of applications.

Finally, we are unaware of any numerically exact method for large lattice systems, which can treat the full Kadanoff–Baym–Keldysh contour, and yield real-time correlation functions. Our ABQMC method represents an interesting example of a real-time QMC method with manifestly no dynamical sign problem. However, the average sign is generally poor. To push ABQMC to larger number of time slices (as needed for calculation of the time-dependence of observables) and lattices larger than 4×4 will require further work, and most likely, conceptually new ideas.

V. SUMMARY AND OUTLOOK

We revisit one of the earliest proposals for a QMC treatment of the Hubbard model, namely the permutation-sampling QMC method developed in Refs. 78–80. Motivated by recent progress in the analogous approach to continuous space models, we group all permutations into a determinant, which is known as the antisymmetric-propagator,⁸⁵ permutation-blocking,⁹⁰ or fermionic-propagator⁹⁶ idea. We devise and implement two slightly different QMC methods. Depending on the details of the STD scheme, we distinguish between (1) the FPQMC method, where snapshots are given by real-space Fock states and determinants represent antisymmetric propagators between those states, and (2) the ABQMC method, where slices alternate between real and reciprocal space representation and determinants are simple Slater determinants. We thoroughly benchmark both methods against the available numerically exact data and then use ABQMC to obtain some new results in the real-time domain.

The FPQMC method exhibits several promising properties. The average sign can be close to 1 and does not drop off rapidly with either the size of the system or the number of time slices. In 1D, the method appears to be sign-problem-free. At present, the limiting factor is not the average sign but rather the ability to sample the large configuration space. At discretizations finer than $N_\tau = 6\text{--}8$, further algorithmic developments are necessary. Nevertheless, our calculations show that excellent results for instantaneous correlators can be obtained with very few time slices and efficiently. Average density, double occupancy, and antiferromagnetic correlations can already be computed with high accuracy at temperatures and coupling strengths relevant for optical-lattice experiments. The FPQMC method is promising for further applications in equilibrium setups. In real-time applications, however, the sign problem in FPQMC is severe.

On the other hand, the ABQMC method has a significant sign problem in equilibrium applications but has some advantages in real-time applications. In ABQMC, the sign problem is manifestly time-independent, and calculations can be performed for multiple times and coupling strengths with a single Markov chain. We use this method to compute time-dependent survival probabilities of different density-modulated states and identify several trends. The relevant transient regime is short, and based on benchmarks, we estimate the systematic error due to the time discretization here to be small. Our results reveal that interactions speed up the initial decay

of the survival probability but facilitate the persistence of the initial charge pattern at longer times. Additionally, we observe a characteristic value of the coupling constant, $U \sim 0.5D$, below which the interaction has no visible effect on time evolution. These findings bare qualitative predictions for future ultracold-atom experiments, but are limited to dynamics at the shortest wave-lengths, as dictated by the maximal size of the lattice that we can treat. We finally note that, within the ABQMC method, uniform currents, which are diagonal in the momentum representation, may be straightforwardly treated.

There is room for improvement in both the ABQMC and FPQMC methods. We already utilize several symmetries of the Hubbard model to improve efficiency and enforce some physical properties of solutions, but more symmetries can certainly be uncovered in the configuration spaces. Further grouping of configurations connected by symmetries can be used to alleviate some of the sign problem or improve efficiency. Also, sampling schemes may be improved along the lines of the recently proposed many-configuration Markov chain MC, which visits an arbitrary number of configurations at every MC step.¹²¹ Moreover, a better insight into the symmetries of the configuration space may make deterministic, structured sampling (along the lines of quasi-MC methods^{122–124}) superior to the standard pseudo-random sampling.

SUPPLEMENTARY MATERIAL

See the [supplementary material](#) for (i) a detailed description of MC updates within the FPQMC method, (ii) a detailed description of MC updates within the ABQMC method for time-dependent survival probability, (iii) details on the performance of the FPQMC method in equilibrium calculations, (iv) discussion on the applicability of the ABQMC method in equilibrium calculations, (v) additional FPQMC calculations of time-dependent local densities, (vi) additional ABQMC calculations of time-dependent survival probability, and (vii) formulation and benchmarks of ABQMC method in quench setups (on the full three-piece Kadanoff–Baym–Keldysh contour).

ACKNOWLEDGMENTS

We acknowledge funding provided by the Institute of Physics Belgrade through a grant from the Ministry of Education, Science, and Technological Development of the Republic of Serbia as well as by the Science Fund of the Republic of Serbia under the Key2SM project (PROMIS program, Grant No. 6066160). Numerical simulations were performed on the PARADOX-IV supercomputing facility at the Scientific Computing Laboratory, National Center of Excellence for the Study of Complex Systems, Institute of Physics Belgrade.

AUTHOR DECLARATIONS

Conflict of Interest

The authors have no conflicts to disclose.

Author Contributions

J.V. conceived the research. V.J. developed the formalism and computational codes under the guidance of J.V., conducted all numerical

simulations, analyzed their results, and prepared the initial version of the manuscript. Both authors contributed to the submitted version of the manuscript.

Veljko Janković: Conceptualization (supporting); Data curation (lead); Formal analysis (lead); Investigation (lead); Methodology (lead); Software (lead); Validation (lead); Visualization (lead); Writing – original draft (lead); Writing – review & editing (equal).
Jakša Vučićević: Conceptualization (lead); Funding acquisition (lead); Project administration (lead); Resources (lead); Software (supporting); Supervision (lead); Writing – review & editing (equal).

DATA AVAILABILITY

The data that support the findings of this study are available from the corresponding author upon reasonable request.

APPENDIX A: MANY-BODY PROPAGATOR AS A DETERMINANT OF SINGLE-PARTICLE PROPAGATORS

The demonstration of Eqs. (6) and (7) can be conducted for each spin component separately. We thus fix the spin index σ and further omit it from the definition of the many-fermion state $|\Psi_i\rangle$ [Eq. (5)]. Since H_0 is diagonal in the momentum representation, we express the state $|\Psi_i\rangle$ in the momentum representation

$$|\Psi_i\rangle = \sum_{\{\mathbf{k}_j\}} \left(\prod_{l=1}^N \langle \mathbf{k}_l | \mathbf{r}_l \rangle c_{\mathbf{k}_l}^\dagger \right) |\emptyset\rangle \quad (\text{A1})$$

and similarly for $|\Psi'_i\rangle$. While the positions $\mathbf{r}_1, \dots, \mathbf{r}_N$ are ordered according to a certain rule, the wave vectors $\mathbf{k}_1, \dots, \mathbf{k}_N$ entering Eq. (A1) are not ordered, and there is no restriction on the sum over them. We have

$$\begin{aligned} \langle \Psi'_i | e^{-\Delta\alpha H_0} | \Psi_i \rangle &= \sum_{\{\mathbf{k}'_j\}} \sum_{\{\mathbf{k}_j\}} e^{-\Delta\alpha \epsilon_{\mathbf{k}'_1}} \dots e^{-\Delta\alpha \epsilon_{\mathbf{k}'_N}} \\ &\times \langle \mathbf{r}'_N | \mathbf{k}'_N \rangle \dots \langle \mathbf{r}'_1 | \mathbf{k}'_1 \rangle \langle \mathbf{k}_1 | \mathbf{r}_1 \rangle \langle \mathbf{k}_N | \mathbf{r}_N \rangle \\ &\times \langle \emptyset | c_{\mathbf{k}'_N} \dots c_{\mathbf{k}'_1} c_{\mathbf{k}_1}^\dagger \dots c_{\mathbf{k}_N}^\dagger | \emptyset \rangle. \end{aligned} \quad (\text{A2})$$

The sums over $\{\mathbf{k}'_j\}$ are eliminated by employing the identity⁸⁰

$$\begin{aligned} \langle \emptyset | c_{\mathbf{k}'_N} \dots c_{\mathbf{k}'_1} c_{\mathbf{k}_1}^\dagger \dots c_{\mathbf{k}_N}^\dagger | \emptyset \rangle \\ = \sum_{\mathcal{P}} \text{sgn}(\mathcal{P}) \delta(\mathbf{k}'_1, \mathbf{k}_{\mathcal{P}(1)}) \dots \delta(\mathbf{k}'_N, \mathbf{k}_{\mathcal{P}(N)}), \end{aligned} \quad (\text{A3})$$

where the permutation operator \mathcal{P} acts on the set of indices $\{1, \dots, N\}$, while $\text{sgn}(\mathcal{P}) = \pm 1$ is the permutation parity. We then observe that

$$\prod_{l=1}^N \langle \mathbf{r}'_l | \mathbf{k}_{\mathcal{P}(l)} \rangle = \prod_{l=1}^N \langle \mathbf{r}'_{\mathcal{P}^{-1}(l)} | \mathbf{k}_l \rangle, \quad (\text{A4})$$

which permits us to perform the sums over individual \mathbf{k}_j s independently. Combining Eqs. (A2)–(A4) and changing the permutation variable $\mathcal{P}' = \mathcal{P}^{-1}$ we eventually obtain

$$\begin{aligned} \langle \Psi'_i | e^{-\Delta\alpha H_0} | \Psi_i \rangle &= \sum_{\mathcal{P}'} \text{sgn}(\mathcal{P}') \prod_{l=1}^N \langle \mathbf{r}'_{\mathcal{P}'(l)} | \mathbf{r}_l \rangle e^{-\Delta\alpha H_0 | \mathbf{r}_l} \\ &= \det S(\Psi'_i, \Psi_i, \Delta\alpha), \end{aligned} \quad (\text{A5})$$

where matrix $S(\Psi'_i, \Psi_i, \Delta\alpha)$ (here without the spin index) is defined in Eq. (7).

APPENDIX B: PROPAGATOR OF A FREE PARTICLE ON THE SQUARE LATTICE

Here, we provide the expressions for the propagator of a free particle on the square lattice in imaginary [$\Delta\alpha = \Delta\tau$ in Eq. (7)] and real [$\Delta\alpha = i\Delta t$ in Eq. (7)] time. In imaginary time,

$$\langle \mathbf{r}' | e^{-\Delta\tau H_0} | \mathbf{r} \rangle = \mathcal{I}(2J\Delta\tau, r'_x - r_x) \mathcal{I}(2J\Delta\tau, r'_y - r_y), \quad (\text{B1})$$

where the one-dimensional imaginary-time propagator (l is an integer)

$$\mathcal{I}(z, l) = \frac{1}{N} \sum_{j=0}^{N-1} \cos\left(\frac{2\pi j l}{N}\right) \exp\left(z \cos\left(\frac{2\pi j}{N}\right)\right) \quad (\text{B2})$$

is related to the modified Bessel function of the first kind $I_l(z)$ via

$$\lim_{N \rightarrow \infty} \mathcal{I}(z, l) = \frac{1}{\pi} \int_0^\pi d\theta \cos(l\theta) e^{z \cos \theta} = I_l(z). \quad (\text{B3})$$

In real time,

$$\langle \mathbf{r}' | e^{-i\Delta t H_0} | \mathbf{r} \rangle = \mathcal{J}(2J\Delta t, r'_x - r_x) \mathcal{J}(2J\Delta t, r'_y - r_y), \quad (\text{B4})$$

where the one-dimensional real-time propagator (l is an integer)

$$\mathcal{J}(z, l) = \frac{1}{N} \sum_{j=0}^{N-1} \cos\left(\frac{2\pi j l}{N}\right) \exp\left(iz \cos\left(\frac{2\pi j}{N}\right)\right) \quad (\text{B5})$$

is related to the Bessel function of the first kind $J_l(z)$ via

$$\lim_{N \rightarrow \infty} \mathcal{J}(z, l) = \frac{1}{\pi} \int_0^\pi d\theta \cos(l\theta) e^{iz \cos \theta} = i^l J_l(z). \quad (\text{B6})$$

For finite N , $\mathcal{J}(z, 2l)$ is purely real, while $\mathcal{J}(z, 2l+1)$ is purely imaginary.

APPENDIX C: DERIVATION OF THE FPQMC FORMULAE THAT MANIFESTLY RESPECT THE DYNAMICAL SYMMETRY OF THE HUBBARD MODEL

Here, we derive the FPQMC expression for the time-dependent expectation value of a local observable [Eq. (18)] that manifestly respects the dynamical symmetry of the Hubbard model.

We start by defining the operation of the bipartite lattice symmetry, which is represented by a unitary, hermitean, and involutive operator B ($B^\dagger = B = B^{-1}$) whose action on electron creation and annihilation operators in the real space is given as

$$Bc_{r\sigma}^{(\dagger)}B = (-1)^{r_x+r_y}c_{r\sigma}^{(\dagger)}. \quad (\text{C1})$$

In the momentum space, B is actually the so-called π -boost¹⁵

$$Bc_{\mathbf{k}\sigma}^{(\dagger)}B = c_{\mathbf{k}+\mathbf{Q},\sigma}^{(\dagger)} \quad (\text{C2})$$

that increases the electronic momentum by $\mathbf{Q} = (\pi, \pi)$. The time reversal operator T is an antiunitary (unitary and antilinear), involutive, and hermitean operator whose action on electron creation and annihilation operators in the real space is given as

$$Tc_{\mathbf{r}\uparrow}^{(\dagger)}T = c_{\mathbf{r}\downarrow}^{(\dagger)}, \quad Tc_{\mathbf{r}\downarrow}^{(\dagger)}T = -c_{\mathbf{r}\uparrow}^{(\dagger)}, \quad (\text{C3})$$

while the corresponding relations in the momentum space read as

$$Tc_{\mathbf{k}\uparrow}^{(\dagger)}T = c_{-\mathbf{k}\downarrow}^{(\dagger)}, \quad Tc_{\mathbf{k}\downarrow}^{(\dagger)}T = -c_{-\mathbf{k}\uparrow}^{(\dagger)}. \quad (\text{C4})$$

Using Eqs. (C1)–(C4), consequently

$$BH_0B = -H_0, \quad BH_{\text{int}}B = H_{\text{int}}, \quad TH_0T = H_0, \quad (\text{C5})$$

$$TH_{\text{int}}T = H_{\text{int}}.$$

In Sec. II B 2, we assumed that the initial state $|\psi(0)\rangle$ is an eigenstate of local density operators $n_{r\sigma}$, which means that $B|\psi(0)\rangle = e^{i\chi_B}|\psi(0)\rangle$, see Eq. (C1).

The denominator of Eq. (18)

$$A_{\text{den}}(t) = \langle \psi(0) | e^{iHt} e^{-iHt} | \psi(0) \rangle \quad (\text{C6})$$

is purely real, $A_{\text{den}}(t) = A_{\text{den}}(t)^*$, so that

$$A_{\text{den}}(t) \approx \frac{1}{2} \left\langle \psi(0) \left| \left(e^{iH_0\Delta t} e^{iH_{\text{int}}\Delta t} \right)^{N_t} \left(e^{-iH_0\Delta t} e^{-iH_{\text{int}}\Delta t} \right)^{N_t} \right| \psi(0) \right\rangle$$

$$+ \frac{1}{2} \left\langle \psi(0) \left| \left(e^{iH_{\text{int}}\Delta t} e^{iH_0\Delta t} \right)^{N_t} \left(e^{-iH_{\text{int}}\Delta t} e^{-iH_0\Delta t} \right)^{N_t} \right| \psi(0) \right\rangle. \quad (\text{C7})$$

We thus obtain

$$A_{\text{den}}(t) \approx \sum_{\mathcal{C}} \{ \text{Re} \{ \mathcal{D}_{2t}(\mathcal{C}, \Delta t) \} \cos[\Delta\varepsilon_{\text{int}}(\mathcal{C})\Delta t] - \text{Im} \{ \mathcal{D}_{2t}(\mathcal{C}, \Delta t) \} \sin[\Delta\varepsilon_{\text{int}}(\mathcal{C})\Delta t] \}, \quad (\text{C8})$$

where configuration \mathcal{C} consists of $2N_t - 1$ independent states $|\Psi_{i,2}\rangle, \dots, |\Psi_{i,2N_t}\rangle, |\Psi_{i,1}\rangle \equiv |\psi(0)\rangle$, while $\mathcal{D}_{2t}(\mathcal{C}, \Delta t)$ and $\Delta\varepsilon_{\text{int}}(\mathcal{C})$ are defined in Eqs. (21) and (20), respectively. The denominator is also invariant under time reversal, $A_{\text{den}}(t) = A_{\text{den}}(-t)$, which is not a consequence of a specific behavior of the initial state under time reversal but rather follows from $A_{\text{den}}(t) \equiv \langle \psi(0) | \psi(0) \rangle$. In other words, Eq. (C8) should contain only contributions invariant under the transformation $\Delta t \rightarrow -\Delta t$. Using the bipartite lattice symmetry, under which $B|\Psi_{i,l}\rangle = e^{i\chi_l}|\Psi_{i,l}\rangle$, we obtain

$$\mathcal{D}_{2t}(\mathcal{C}, -\Delta t) = \prod_{l=N_t+1}^{2N_t} \langle \Psi_{i,l\oplus 1} | BB e^{-iH_0\Delta t} BB | \Psi_{i,l} \rangle$$

$$\times \prod_{l=1}^{N_t} \langle \Psi_{i,l\oplus 1} | BB e^{iH_0\Delta t} BB | \Psi_{i,l} \rangle$$

$$= \prod_{l=N_t+1}^{2N_t} \langle \Psi_{i,l\oplus 1} | e^{iH_0\Delta t} | \Psi_{i,l} \rangle \prod_{l=1}^{N_t} \langle \Psi_{i,l\oplus 1} | e^{-iH_0\Delta t} | \Psi_{i,l} \rangle$$

$$= \mathcal{D}_{2t}(\mathcal{C}, \Delta t). \quad (\text{C9})$$

Equation (C8) then reduces to

$$A_{\text{den}}(t) = \sum_{\mathcal{C}} \text{Re} \{ \mathcal{D}_{2t}(\mathcal{C}, \Delta t) \} \cos[\Delta\varepsilon_{\text{int}}(\mathcal{C})\Delta t]. \quad (\text{C10})$$

We now turn to the numerator of Eq. (18)

$$A_{\text{num}}(t) = \langle \psi(0) | e^{iHt} A_i e^{-iHt} | \psi(0) \rangle, \quad (\text{C11})$$

which is also purely real, $A_{\text{num}}(t) = A_{\text{num}}(t)^*$, so that

$$A_{\text{num}}(t) \approx \sum_{\mathcal{C}} \mathcal{A}_i(\Psi_{i,N_t+1}) \{ \text{Re} \{ \mathcal{D}_{2t}(\mathcal{C}, \Delta t) \} \cos[\Delta\varepsilon_{\text{int}}(\mathcal{C})\Delta t] - \text{Im} \{ \mathcal{D}_{2t}(\mathcal{C}, \Delta t) \} \sin[\Delta\varepsilon_{\text{int}}(\mathcal{C})\Delta t] \}. \quad (\text{C12})$$

In the following discussion, we assume that the time reversal operation changes $|\psi(0)\rangle$ by a phase factor, $T|\psi(0)\rangle = e^{i\chi_T}|\psi(0)\rangle$. This, combined with $B|\psi(0)\rangle = e^{i\chi_B}|\psi(0)\rangle$, gives the assumption on $|\psi(0)\rangle$ that is mentioned before Eq. (19). We further assume that $TBA_iBT = A_i$. Under these assumptions, the numerator is invariant under time reversal, $A_{\text{num}}(-t) = A_{\text{num}}(t)$, meaning that Eq. (C12) should contain only contributions invariant under the transformation $\Delta t \rightarrow -\Delta t$. Using Eq. (C9), Eq. (C12) reduces to

$$A_{\text{num}}(t) \approx \sum_{\mathcal{C}} \mathcal{A}_i(\Psi_{i,N_t+1}) \text{Re} \{ \mathcal{D}_{2t}(\mathcal{C}, \Delta t) \} \cos[\Delta\varepsilon_{\text{int}}(\mathcal{C})\Delta t], \quad (\text{C13})$$

and Eq. (22) follows immediately.

An example of the initial state $|\psi(0)\rangle$ and the observable A_i that satisfy $TB|\psi(0)\rangle = e^{i\chi}|\psi(0)\rangle$ and $TBA_iBT = A_i$ are the CDW state $|\psi_{\text{CDW}}\rangle$ [Eq. (24)] and the local charge density $A_i = \sum_{\sigma} n_{r\sigma}$. While the time-reversal operation may change a general SDW state [Eq. (23)] by more than a phase factor, Eq. (C13) is still applicable when the observable of interest is the local spin density $A_i = n_{r\uparrow} - n_{r\downarrow}$. This follows from the transformation law $T(n_{r\uparrow} - n_{r\downarrow})T = n_{r\downarrow} - n_{r\uparrow}$ and the fact that the roles of spin-up and spin-down electrons in the state $T|\psi_{\text{SDW}}\rangle$ are exchanged with respect to the state $|\psi_{\text{SDW}}\rangle$.

We now explain how we use Eq. (26) to enlarge statistics in computations of time-dependent local spin (charge) densities when the evolution starts from state $|\psi_{\text{SDW}}\rangle$ in Eq. (23) [$|\psi_{\text{CDW}}\rangle$ in Eq. (24)]. Let us limit the discussion to the spin (charge) density at fixed position \mathbf{r} . Suppose that we obtained Markov chains (of length N_{CDW}) $\{ \mathcal{N}_1^{\text{CDW}}(t), \dots, \mathcal{N}_{N_{\text{CDW}}}^{\text{CDW}}(t) \}$ and $\{ \mathcal{D}_1^{\text{CDW}}, \dots, \mathcal{D}_{N_{\text{CDW}}}^{\text{CDW}} \}$ for the numerator and denominator. Suppose also that we obtained Markov chains (of length N_{SDW}) $\{ \mathcal{N}_1^{\text{SDW}}(t), \dots, \mathcal{N}_{N_{\text{SDW}}}^{\text{SDW}}(t) \}$ and $\{ \mathcal{D}_1^{\text{SDW}}, \dots, \mathcal{D}_{N_{\text{SDW}}}^{\text{SDW}} \}$ for the numerator and denominator. Using these Markov chains, we found that the best result for the time-dependent local spin (charge) density is obtained by joining them into one Markov chain $\{ \mathcal{N}_1^{\text{SDW}}(t), \dots, \mathcal{N}_{N_{\text{SDW}}}^{\text{SDW}}(t), \mathcal{N}_1^{\text{CDW}}(t), \dots, \mathcal{N}_{N_{\text{CDW}}}^{\text{CDW}}(t) \}$ of length $N_{\text{SDW}} + N_{\text{CDW}}$ for the numerator, and another Markov chain

$\{\mathcal{D}_1^{\text{SDW}}, \dots, \mathcal{D}_{N_{\text{SDW}}}^{\text{SDW}}, \mathcal{D}_1^{\text{CDW}}, \dots, \mathcal{D}_{N_{\text{CDW}}}^{\text{CDW}}\}$ of length $N_{\text{SDW}} + N_{\text{CDW}}$ for the denominator. If individual chain lengths N_{CDW} and N_{SDW} are sufficiently large, the manner in which the chains are joined is immaterial; here, we append the CDW chain to the SDW chain, and we note that other joining possibilities lead to the same final result (within the statistical error bars). To further reduce statistical error bars, we also combine SDW + CDW chains at all positions \mathbf{r} that have the same spin (charge) density by the symmetry of the initial state.

APPENDIX D: DERIVATION OF THE ABQMC FORMULA FOR THE SURVIVAL PROBABILITY

We start from the survival-probability amplitude

$$A_P(t) = \frac{\langle \psi(0) | e^{-iHt} | \psi(0) \rangle}{\langle \psi(0) | \psi(0) \rangle}, \quad (\text{D1})$$

whose numerator can be expressed as

$$\begin{aligned} \langle \psi(0) | e^{-iHt} | \psi(0) \rangle &\approx \frac{1}{2} \langle \psi(0) | \left(e^{-iH_0 \Delta t} e^{-iH_{\text{int}} \Delta t} \right)^{N_t} | \psi(0) \rangle + \frac{1}{2} \langle \psi(0) | \left(e^{-iH_{\text{int}} \Delta t} e^{-iH_0 \Delta t} \right)^{N_t} | \psi(0) \rangle \\ &= \sum_{\Psi_{i,2} \dots \Psi_{i,N_t}} \text{Re} \left\{ \prod_{l=1}^{N_t} \langle \Psi_{i,l \oplus 1} | e^{-iH_0 \Delta t} | \Psi_{i,l} \rangle \right\} e^{-i\varepsilon_{\text{int}}(C) \Delta t} \\ &= \sum_{\Psi_{i,2} \dots \Psi_{i,N_t}} \sum_{\Psi_{k,1} \dots \Psi_{k,N_t}} \text{Re} \left\{ \prod_{l=1}^{N_t} \langle \Psi_{i,l \oplus 1} | \Psi_{k,l} \rangle \langle \Psi_{k,l} | \Psi_{i,l} \rangle e^{-i\varepsilon_0(C) \Delta t} \right\} e^{-i\varepsilon_{\text{int}}(C) \Delta t} \\ &= \sum_C \{ \text{Re}\{\mathcal{D}(C)\} \cos[\varepsilon_0(C) \Delta t] + \text{Im}\{\mathcal{D}(C)\} \sin[\varepsilon_0(C) \Delta t] \} e^{-i\varepsilon_{\text{int}}(C) \Delta t}. \end{aligned} \quad (\text{D2})$$

In going from the second to the third line of Eq. (D2), we introduced spectral decompositions of N_t factors $e^{-iH_0 \Delta t}$. The configuration C entering the last line of Eq. (D2) consists of $N_t - 1$ independent states $|\Psi_{i,2}\rangle, \dots, |\Psi_{i,N_t}\rangle$ in the coordinate representation and N_t independent states $|\Psi_{k,1}\rangle, \dots, |\Psi_{k,N_t}\rangle$ in the momentum representation, while $|\Psi_{i,1}\rangle \equiv |\psi(0)\rangle$. $\mathcal{D}(C)$ and $\varepsilon_0(C)$ are defined in Eqs. (31) and (34), respectively. By virtue of the bipartite lattice symmetry, under which $\mathcal{D}(C)$ remains invariant, while $\varepsilon_0(C)$ changes sign, the summand containing $\sin[\varepsilon_0(C) \Delta t]$ in Eq. (D2) vanishes, so that

$$\langle \psi(0) | e^{-iHt} | \psi(0) \rangle \approx \sum_C \text{Re}\{\mathcal{D}(C)\} \cos[\varepsilon_0(C) \Delta t] e^{-i\varepsilon_{\text{int}}(C) \Delta t}. \quad (\text{D3})$$

This form should be used, e.g., when $|\psi(0)\rangle$ is the SDW state defined in Eq. (23). When the initial state is the CDW state defined in Eq. (24), $T|\psi(0)\rangle = e^{i\mathbf{x}\cdot\mathbf{r}}|\psi(0)\rangle$, $\langle \psi(0) | e^{-iHt} | \psi(0) \rangle$ is purely real, so that

$$\langle \psi(0) | e^{-iHt} | \psi(0) \rangle \approx \sum_C \text{Re}\{\mathcal{D}(C)\} \cos[\varepsilon_0(C) \Delta t] \cos[\varepsilon_{\text{int}}(C) \Delta t]. \quad (\text{D4})$$

Equation (30) then follows by combining Eq. (D4) with $\langle \psi(0) | \psi(0) \rangle = \sum_C \text{Re}\{\mathcal{D}(C)\}$.

We now provide a formal demonstration of Eq. (36). The partial particle-hole transformation is represented by a unitary, hermitian, and involutive operator P ($P^\dagger = P = P^{-1}$), whose action on electron creation and annihilation operators in real space is given as^{109,110}

$$P c_{\mathbf{r}\uparrow} P = c_{\mathbf{r}\uparrow}, \quad P c_{\mathbf{r}\uparrow}^\dagger P = c_{\mathbf{r}\uparrow}^\dagger, \quad (\text{D5})$$

$$P c_{\mathbf{r}\downarrow} P = (-1)^{r_x+r_y} c_{\mathbf{r}\downarrow}^\dagger, \quad P c_{\mathbf{r}\downarrow}^\dagger P = (-1)^{r_x+r_y} c_{\mathbf{r}\downarrow}. \quad (\text{D6})$$

The interaction Hamiltonian H_{int} thus transforms under the partial particle-hole transformation as $PH_{\text{int}}P = U\widehat{N}_\uparrow - H_{\text{int}}$. The action of the partial particle-hole transformation in the momentum space reads as $[\mathbf{Q} = (\pi, \pi)]$

$$P c_{\mathbf{k}\uparrow} P = c_{\mathbf{k}\uparrow}, \quad P c_{\mathbf{k}\uparrow}^\dagger P = c_{\mathbf{k}\uparrow}^\dagger, \quad (\text{D7})$$

$$P c_{\mathbf{k}\downarrow} P = c_{\mathbf{Q}-\mathbf{k},\downarrow}^\dagger, \quad P c_{\mathbf{k}\downarrow}^\dagger P = c_{\mathbf{Q}-\mathbf{k},\downarrow}. \quad (\text{D8})$$

The kinetic energy, therefore, remains invariant under the partial particle-hole transformation, i.e., $PH_0P = H_0$. Equations (D5) and (D6) imply that $P|\emptyset\rangle = \prod_{\mathbf{r} \in \mathcal{U}} c_{\mathbf{r}\downarrow}^\dagger |\emptyset\rangle$. We then find that $P|\psi_{\text{CDW}}\rangle = |\psi_{\text{SDW}}\rangle$, i.e., the partial particle-hole transformation transforms the CDW state defined in Eq. (24) into the SDW state defined in Eq. (23) and vice versa.¹⁰⁸ The states $|\psi_{\text{CDW}}\rangle$ and $|\psi_{\text{SDW}}\rangle$ have the same number of spin-up electrons, while their numbers of spin-down electrons add to N_c . Using the combination of the partial particle-hole transformation P and the bipartite lattice transformation B defined in Appendix C, one obtains

$$\langle \psi_{\text{CDW}} | e^{-iHt} | \psi_{\text{CDW}} \rangle = e^{-iN_\uparrow(\psi)Ut} \langle \psi_{\text{SDW}} | e^{-iHt} | \psi_{\text{SDW}} \rangle^*, \quad (\text{D9})$$

where $N_\uparrow(\psi) = \langle \psi_{\text{CDW}} | \widehat{N}_\uparrow | \psi_{\text{CDW}} \rangle = \langle \psi_{\text{SDW}} | \widehat{N}_\uparrow | \psi_{\text{SDW}} \rangle$ is the total number of spin-up electrons in CDW and SDW states. Equation (36) then follows immediately from Eq. (D9).

A similar procedure to that described in Appendix C is used to combine Markov chains for the survival probabilities of the CDW and SDW states related by the dynamical symmetry in Eq. (D9).

APPENDIX E: USING THE PARTICLE-HOLE SYMMETRY TO DISCUSS THE AVERAGE SIGN OF THE FPQMC METHOD FOR CHEMICAL POTENTIALS μ AND $U - \mu$

The (full) particle-hole transformation is represented by a unitary, hermitean, and involutive operator P_f ($P_f^\dagger = P_f = P_f^{-1}$) whose action on electron creation and annihilation operators in real space is defined as^{109,110}

$$P_f c_{r\sigma} P_f = (-1)^{r_x+r_y} c_{r\sigma}^\dagger \quad (\text{E1})$$

The corresponding formula in the momentum space reads as

$$P_f c_{k\sigma} P_f = c_{\mathbf{Q}-k,\sigma}^\dagger \quad (\text{E2})$$

Let us fix J, U, T , and N_τ and compute the equation of state $\rho_e(\mu)$ using Eq. (13) in which $A_i(\Psi_{i,l}) = [N_\uparrow(C) + N_\downarrow(C)]/N_c$. It is convenient to make the μ -dependence in $\varepsilon_{\text{int}}(C, \mu)$ explicit. In the sums entering Eq. (13) we make the substitution

$$C \rightarrow C' = \{|\Phi_{i,l}\rangle = P_f |\Psi_{i,l}\rangle | l = 1, \dots, N_\tau\} \quad (\text{E3})$$

under which

$$\mathcal{D}_\beta(C, \Delta\tau) = \mathcal{D}_\beta(C', \Delta\tau), \quad (\text{E4})$$

$$\varepsilon_{\text{int}}(C, \mu) = \varepsilon_{\text{int}}(C', U - \mu) + (U - 2\mu)N_\tau N_c, \quad (\text{E5})$$

$$N_\sigma(C') = N_c - N_\sigma(C). \quad (\text{E6})$$

It then follows that

$$\begin{aligned} & \frac{\sum_C \mathcal{D}_\beta(C, \Delta\tau) e^{-\Delta\tau \varepsilon_{\text{int}}(C, \mu)} [N_\uparrow(C) + N_\downarrow(C)]/N_c}{\sum_C \mathcal{D}_\beta(C, \Delta\tau) e^{-\Delta\tau \varepsilon_{\text{int}}(C, \mu)}} \\ &= 2 - \frac{\sum_{C'} \mathcal{D}_\beta(C', \Delta\tau) e^{-\Delta\tau \varepsilon_{\text{int}}(C', U - \mu)} [N_\uparrow(C') + N_\downarrow(C')]/N_c}{\sum_{C'} \mathcal{D}_\beta(C', \Delta\tau) e^{-\Delta\tau \varepsilon_{\text{int}}(C', U - \mu)}}. \end{aligned} \quad (\text{E7})$$

The FPQMC simulations of the ratios in the last equation are performed for chemical potentials μ and $U - \mu$, which are symmetric with respect to the chemical potential $U/2$ at the half-filling. Since $\varepsilon_{\text{int}}(C, \mu)$ and $\varepsilon_{\text{int}}(C', U - \mu)$ differ by a constant additive factor, the corresponding configuration weights differ by a constant multiplicative factor, and the average signs of the two FPQMC simulations are thus mutually equal.

REFERENCES

- ¹H. Aoki, N. Tsuji, M. Eckstein, M. Kollar, T. Oka, and P. Werner, "Nonequilibrium dynamical mean-field theory and its applications," *Rev. Mod. Phys.* **86**, 779–837 (2014).
- ²L. Tarruell and L. Sanchez-Palencia, "Quantum simulation of the Hubbard model with ultracold fermions in optical lattices," *C. R. Phys.* **19**, 365–393 (2018).
- ³I. Bloch, J. Dalibard, and W. Zwerger, "Many-body physics with ultracold gases," *Rev. Mod. Phys.* **80**, 885–964 (2008).
- ⁴S. Murmann, A. Bergschneider, V. M. Klinkhamer, G. Zürn, T. Lompe, and S. Jochim, "Two fermions in a double well: Exploring a fundamental building block of the Hubbard model," *Phys. Rev. Lett.* **114**, 080402 (2015).

- ⁵B. M. Spar, E. Guardado-Sanchez, S. Chi, Z. Z. Yan, and W. S. Bakr, "Realization of a Fermi-Hubbard optical tweezer array," *Phys. Rev. Lett.* **128**, 223202 (2022).
- ⁶Z. Z. Yan, B. M. Spar, M. L. Prichard, S. Chi, H.-T. Wei, E. Ibarra-García-Padilla, K. R. A. Hazzard, and W. S. Bakr, "Two-dimensional programmable tweezer arrays of fermions," *Phys. Rev. Lett.* **129**, 123201 (2022).
- ⁷J. Hubbard, "Electron correlations in narrow energy bands," *Proc. R. Soc. London, Ser. A* **276**, 238–257 (1963).
- ⁸"The Hubbard model at half a century," *Nat. Phys.* **9**, 523 (2013).
- ⁹E. Cocchi, L. A. Miller, J. H. Drewes, M. Koschorreck, D. Pertot, F. Brennecke, and M. Köhl, "Equation of state of the two-dimensional Hubbard model," *Phys. Rev. Lett.* **116**, 175301 (2016).
- ¹⁰E. Cocchi, L. A. Miller, J. H. Drewes, C. F. Chan, D. Pertot, F. Brennecke, and M. Köhl, "Measuring entropy and short-range correlations in the two-dimensional Hubbard model," *Phys. Rev. X* **7**, 031025 (2017).
- ¹¹M. F. Parsons, A. Mazurenko, C. S. Chiu, G. Ji, D. Greif, and M. Greiner, "Site-resolved measurement of the spin-correlation function in the Fermi-Hubbard model," *Science* **353**, 1253–1256 (2016).
- ¹²L. W. Cheuk, M. A. Nichols, K. R. Lawrence, M. Okan, H. Zhang, E. Khatami, N. Trivedi, T. Paiva, M. Rigol, and M. W. Zwierlein, "Observation of spatial charge and spin correlations in the 2D Fermi-Hubbard model," *Science* **353**, 1260–1264 (2016).
- ¹³C. S. Chiu, G. Ji, A. Bohardt, M. Xu, M. Knap, E. Demler, F. Grusdt, M. Greiner, and D. Greif, "String patterns in the doped Hubbard model," *Science* **365**, 251–256 (2019).
- ¹⁴P. T. Brown, D. Mitra, E. Guardado-Sanchez, R. Nourafkan, A. Reymbaut, C.-D. Hébert, S. Bergeron, A.-M. S. Tremblay, J. Kokalj, D. A. Huse, P. Schauss, and W. S. Bakr, "Bad metallic transport in a cold atom Fermi-Hubbard system," *Science* **363**, 379–382 (2019).
- ¹⁵U. Schneider, L. Hackermüller, J. P. Ronzheimer, S. Will, S. Braun, T. Best, I. Bloch, E. Demler, S. Mandt, D. Rasch, and A. Rosch, "Fermionic transport and out-of-equilibrium dynamics in a homogeneous Hubbard model with ultracold atoms," *Nat. Phys.* **8**, 213–218 (2012).
- ¹⁶W. Xu, W. R. McGehee, W. N. Morong, and B. DeMarco, "Bad-metal relaxation dynamics in a Fermi lattice gas," *Nat. Commun.* **10**, 1588 (2019).
- ¹⁷M. A. Nichols, L. W. Cheuk, M. Okan, T. R. Hartke, E. Mendez, T. Senthil, E. Khatami, H. Zhang, and M. W. Zwierlein, "Spin transport in a Mott insulator of ultracold fermions," *Science* **363**, 383–387 (2019).
- ¹⁸J. E. Hirsch, D. J. Scalapino, R. L. Sugar, and R. Blankenbecler, "Efficient Monte Carlo procedure for systems with fermions," *Phys. Rev. Lett.* **47**, 1628–1631 (1981).
- ¹⁹J. E. Hirsch, R. L. Sugar, D. J. Scalapino, and R. Blankenbecler, "Monte Carlo simulations of one-dimensional fermion systems," *Phys. Rev. B* **26**, 5033–5055 (1982).
- ²⁰R. Blankenbecler, D. J. Scalapino, and R. L. Sugar, "Monte Carlo calculations of coupled boson-fermion systems. I," *Phys. Rev. D* **24**, 2278–2286 (1981).
- ²¹D. J. Scalapino and R. L. Sugar, "Monte Carlo calculations of coupled Boson-Fermion systems. II," *Phys. Rev. B* **24**, 4295–4308 (1981).
- ²²J. E. Hirsch, "Monte Carlo study of the two-dimensional Hubbard model," *Phys. Rev. Lett.* **51**, 1900–1903 (1983).
- ²³J. E. Hirsch, "Two-dimensional Hubbard model: Numerical simulation study," *Phys. Rev. B* **31**, 4403–4419 (1985).
- ²⁴J. E. Hirsch and R. M. Fye, "Monte Carlo method for magnetic impurities in metals," *Phys. Rev. Lett.* **56**, 2521–2524 (1986).
- ²⁵S. R. White, D. J. Scalapino, R. L. Sugar, E. Y. Loh, J. E. Gubernatis, and R. T. Scalettar, "Numerical study of the two-dimensional Hubbard model," *Phys. Rev. B* **40**, 506–516 (1989).
- ²⁶S. Zhang, J. Carlson, and J. E. Gubernatis, "Constrained path quantum Monte Carlo method for fermion ground states," *Phys. Rev. Lett.* **74**, 3652–3655 (1995).
- ²⁷S. Zhang, "Finite-temperature Monte Carlo calculations for systems with fermions," *Phys. Rev. Lett.* **83**, 2777–2780 (1999).
- ²⁸S. Zhang and H. Krakauer, "Quantum Monte Carlo method using phase-free random walks with Slater determinants," *Phys. Rev. Lett.* **90**, 136401 (2003).
- ²⁹C. N. Varney, C.-R. Lee, Z. J. Bai, S. Chiesa, M. Jarrell, and R. T. Scalettar, "Quantum Monte Carlo study of the two-dimensional fermion Hubbard model," *Phys. Rev. B* **80**, 075116 (2009).

- ³⁰J. P. F. LeBlanc, A. E. Antipov, F. Becca, I. W. Bulik, G. K.-L. Chan, C.-M. Chung, Y. Deng, M. Ferrero, T. M. Henderson, C. A. Jiménez-Hoyos, E. Kozik, X.-W. Liu, A. J. Millis, N. V. Prokofev, M. Qin, G. E. Scuseria, H. Shi, B. V. Svistunov, L. F. Tocchio, I. S. Tupitsyn, S. R. White, S. Zhang, B.-X. Zheng, Z. Zhu, E. Gull Simons Collaboration on the Many-Electron Problem, “Solutions of the two-dimensional Hubbard model: Benchmarks and results from a wide range of numerical algorithms,” *Phys. Rev. X* **5**, 041041 (2015).
- ³¹E. Gull, A. J. Millis, A. I. Lichtenstein, A. N. Rubtsov, M. Troyer, and P. Werner, “Continuous-time Monte Carlo methods for quantum impurity models,” *Rev. Mod. Phys.* **83**, 349–404 (2011).
- ³²A. N. Rubtsov and A. I. Lichtenstein, “Continuous-time quantum Monte Carlo method for fermions: Beyond auxiliary field framework,” *JETP Lett.* **80**, 61–65 (2004).
- ³³A. N. Rubtsov, V. V. Savkin, and A. I. Lichtenstein, “Continuous-time quantum Monte Carlo method for fermions,” *Phys. Rev. B* **72**, 035122 (2005).
- ³⁴E. Gull, P. Werner, O. Parcollet, and M. Troyer, “Continuous-time auxiliary-field Monte Carlo for quantum impurity models,” *Europhys. Lett.* **82**, 57003 (2008).
- ³⁵N. V. Prokofev and B. V. Svistunov, “Polaron problem by diagrammatic quantum Monte Carlo,” *Phys. Rev. Lett.* **81**, 2514–2517 (1998).
- ³⁶N. Prokofev and B. Svistunov, “Bold diagrammatic Monte Carlo technique: When the sign problem is welcome,” *Phys. Rev. Lett.* **99**, 250201 (2007).
- ³⁷E. Kozik, K. Van Houcke, E. Gull, L. Pollet, N. Prokofev, B. Svistunov, and M. Troyer, “Diagrammatic Monte Carlo for correlated fermions,” *Europhys. Lett.* **90**, 10004 (2010).
- ³⁸K. Van Houcke, E. Kozik, N. Prokofev, and B. Svistunov, “Diagrammatic Monte Carlo,” *Phys. Procedia* **6**, 95–105 (2010).
- ³⁹W. Wu, M. Ferrero, A. Georges, and E. Kozik, “Controlling Feynman diagrammatic expansions: Physical nature of the pseudogap in the two-dimensional Hubbard model,” *Phys. Rev. B* **96**, 041105 (2017).
- ⁴⁰M. Rigol, T. Bryant, and R. R. P. Singh, “Numerical linked-cluster approach to quantum lattice models,” *Phys. Rev. Lett.* **97**, 187202 (2006).
- ⁴¹E. Khatami and M. Rigol, “Thermodynamics of strongly interacting fermions in two-dimensional optical lattices,” *Phys. Rev. A* **84**, 053611 (2011).
- ⁴²B. Tang, E. Khatami, and M. Rigol, “A short introduction to numerical linked-cluster expansions,” *Comput. Phys. Commun.* **184**, 557–564 (2013).
- ⁴³F. Šimković IV, R. Rossi, and M. Ferrero, “Two-dimensional Hubbard model at finite temperature: Weak, strong, and long correlation regimes,” *Phys. Rev. Res.* **4**, 043201 (2022).
- ⁴⁴J. Yang, L. Liu, J. Mongkolkiattichai, and P. Schauss, “Site-resolved imaging of ultracold fermions in a triangular-lattice quantum gas microscope,” *PRX Quantum* **2**, 020344 (2021).
- ⁴⁵S. Humeniuk and Y. Wan, “Numerically exact mimicking of quantum gas microscopy for interacting lattice fermions,” *Phys. Rev. B* **104**, 075155 (2021).
- ⁴⁶J. Koepsell, D. Bourgund, P. Sompet, S. Hirthe, A. Bohrdt, Y. Wang, F. Grusdt, E. Demler, G. Salomon, C. Gross, and I. Bloch, “Microscopic evolution of doped Mott insulators from polaronic metal to Fermi liquid,” *Science* **374**, 82–86 (2021).
- ⁴⁷Y. Wang, A. Bohrdt, S. Ding, J. Koepsell, E. Demler, and F. Grusdt, “Higher-order spin-hole correlations around a localized charge impurity,” *Phys. Rev. Res.* **3**, 033204 (2021).
- ⁴⁸D. Garwood, J. Mongkolkiattichai, L. Liu, J. Yang, and P. Schauss, “Site-resolved observables in the doped spin-imbalanced triangular Hubbard model,” *Phys. Rev. A* **106**, 013310 (2022).
- ⁴⁹K. Mikelsons, “Extensions of numerical methods for strongly correlated electron systems,” Ph.D. thesis, University of Cincinnati, 2009.
- ⁵⁰J. Vučićević, J. Kokalj, R. Žitko, N. Wentzell, D. Tanasković, and J. Mravlje, “Conductivity in the square lattice Hubbard model at high temperatures: Importance of vertex corrections,” *Phys. Rev. Lett.* **123**, 036601 (2019).
- ⁵¹E. W. Huang, R. Sheppard, B. Moritz, and T. P. Devereaux, “Strange metallicity in the doped Hubbard model,” *Science* **366**, 987–990 (2019).
- ⁵²J. Vučićević, S. Preditin, and M. Ferrero, “Charge fluctuations, hydrodynamics and transport in the square-lattice Hubbard model,” [arXiv:2208.04047](https://arxiv.org/abs/2208.04047) (2022).
- ⁵³J. Jaklič and P. Prelovšek, “Finite-temperature properties of doped antiferromagnets,” *Adv. Phys.* **49**, 1–92 (2000).
- ⁵⁴P. Prelovšek and J. Bonča, “Ground state and finite temperature Lanczos methods,” in *Strongly Correlated Systems: Numerical Methods*, edited by A. Avella and F. Mancini (Springer, Berlin, Heidelberg, 2013), pp. 1–30.
- ⁵⁵A. Vranić, J. Vučićević, J. Kokalj, J. Skolimowski, R. Žitko, J. Mravlje, and D. Tanasković, “Charge transport in the Hubbard model at high temperatures: Triangular versus square lattice,” *Phys. Rev. B* **102**, 115142 (2020).
- ⁵⁶P. Werner, T. Oka, and A. J. Millis, “Diagrammatic Monte Carlo simulation of nonequilibrium systems,” *Phys. Rev. B* **79**, 035320 (2009).
- ⁵⁷M. Schiró and M. Fabrizio, “Real-time diagrammatic Monte Carlo for nonequilibrium quantum transport,” *Phys. Rev. B* **79**, 153302 (2009).
- ⁵⁸M. Schiró, “Real-time dynamics in quantum impurity models with diagrammatic Monte Carlo,” *Phys. Rev. B* **81**, 085126 (2010).
- ⁵⁹E. Gull, D. R. Reichman, and A. J. Millis, “Numerically exact long-time behavior of nonequilibrium quantum impurity models,” *Phys. Rev. B* **84**, 085134 (2011).
- ⁶⁰G. Cohen, D. R. Reichman, A. J. Millis, and E. Gull, “Green’s functions from real-time bold-line Monte Carlo,” *Phys. Rev. B* **89**, 115139 (2014).
- ⁶¹G. Cohen, E. Gull, D. R. Reichman, and A. J. Millis, “Taming the dynamical sign problem in real-time evolution of quantum many-body problems,” *Phys. Rev. Lett.* **115**, 266802 (2015).
- ⁶²M. S. Church and B. M. Rubenstein, “Real-time dynamics of strongly correlated fermions using auxiliary field quantum Monte Carlo,” *J. Chem. Phys.* **154**, 184103 (2021).
- ⁶³C. Karrasch, D. M. Kennes, and J. E. Moore, “Transport properties of the one-dimensional Hubbard model at finite temperature,” *Phys. Rev. B* **90**, 155104 (2014).
- ⁶⁴N. Schlünzen, J.-P. Joost, F. Heidrich-Meisner, and M. Bonitz, “Nonequilibrium dynamics in the one-dimensional Fermi-Hubbard model: Comparison of the nonequilibrium Green-functions approach and the density matrix renormalization group method,” *Phys. Rev. B* **95**, 165139 (2017).
- ⁶⁵A. Akbari, M. J. Hashemi, A. Rubio, R. M. Nieminen, and R. van Leeuwen, “Challenges in truncating the hierarchy of time-dependent reduced density matrices equations,” *Phys. Rev. B* **85**, 235121 (2012).
- ⁶⁶D. Lacroix, S. Hermanns, C. M. Hinz, and M. Bonitz, “Ultrafast dynamics of finite Hubbard clusters: A stochastic mean-field approach,” *Phys. Rev. B* **90**, 125112 (2014).
- ⁶⁷Z. Li, N. Tong, X. Zheng, D. Hou, J. Wei, J. Hu, and Y. Yan, “Hierarchical Liouville-space approach for accurate and universal characterization of quantum impurity systems,” *Phys. Rev. Lett.* **109**, 266403 (2012).
- ⁶⁸S. Wang, X. Zheng, J. Jin, and Y. J. Yan, “Hierarchical Liouville-space approach to nonequilibrium dynamical properties of quantum impurity systems,” *Phys. Rev. B* **88**, 035129 (2013).
- ⁶⁹R. E. V. Profumo, C. Groth, L. Messio, O. Parcollet, and X. Waintal, “Quantum Monte Carlo for correlated out-of-equilibrium nanoelectronic devices,” *Phys. Rev. B* **91**, 245154 (2015).
- ⁷⁰M. A. Cazalilla and J. B. Marston, “Time-dependent density-matrix renormalization group: A systematic method for the study of quantum many-body out-of-equilibrium systems,” *Phys. Rev. Lett.* **88**, 256403 (2002).
- ⁷¹S. R. White and A. E. Feiguin, “Real-time evolution using the density matrix renormalization group,” *Phys. Rev. Lett.* **93**, 076401 (2004).
- ⁷²U. Schollwöck, “Time-dependent density-matrix renormalization-group methods,” *J. Phys. Soc. Jpn.* **74**, 246–255 (2005).
- ⁷³C. Yang and A. E. Feiguin, “Spectral function of the two-dimensional Hubbard model: A density matrix renormalization group plus cluster perturbation theory study,” *Phys. Rev. B* **93**, 081107 (2016).
- ⁷⁴G. Stefanucci and R. van Leeuwen, *Nonequilibrium Many-Body Theory of Quantum Systems: A Modern Introduction* (Cambridge University Press, New York, 2013).
- ⁷⁵N. Schlünzen, S. Hermanns, M. Scharnke, and M. Bonitz, “Ultrafast dynamics of strongly correlated fermions—Nonequilibrium Green functions and selfenergy approximations,” *J. Phys.: Condens. Matter* **32**, 103001 (2019).
- ⁷⁶N. Schlünzen, J. P. Joost, and M. Bonitz, “Achieving the scaling limit for nonequilibrium Green functions simulations,” *Phys. Rev. Lett.* **124**, 076601 (2020).

- ⁷⁷J.-P. Joost, N. Schlünzen, H. Ohldag, M. Bonitz, F. Lackner, and I. Březinová, “Dynamically screened ladder approximation: Simultaneous treatment of strong electronic correlations and dynamical screening out of equilibrium,” *Phys. Rev. B* **105**, 165155 (2022).
- ⁷⁸H. De Raedt and A. Lagendijk, “Monte Carlo calculation of the thermodynamic properties of a quantum model: A one-dimensional fermion lattice model,” *Phys. Rev. Lett.* **46**, 77–80 (1981).
- ⁷⁹H. De Raedt and A. Lagendijk, “Monte Carlo calculation of the thermodynamic properties of a one-dimensional fermion lattice model,” *J. Stat. Phys.* **27**, 731–744 (1982).
- ⁸⁰H. De Raedt and A. Lagendijk, “Monte Carlo simulation of quantum statistical lattice models,” *Phys. Rep.* **127**, 233–307 (1985).
- ⁸¹D. M. Ceperley, “Path integrals in the theory of condensed helium,” *Rev. Mod. Phys.* **67**, 279–355 (1995).
- ⁸²D. Thirumalai and B. J. Berne, “Methods for simulating time correlation functions in quantum systems,” *Comput. Phys. Commun.* **63**, 415–426 (1991).
- ⁸³T. Dornheim, S. Groth, J. Vorberger, and M. Bonitz, “*Ab initio* path integral Monte Carlo results for the dynamic structure factor of correlated electrons: From the electron liquid to warm dense matter,” *Phys. Rev. Lett.* **121**, 255001 (2018).
- ⁸⁴P. Hamann, T. Dornheim, J. Vorberger, Z. A. Moldabekov, and M. Bonitz, “Dynamic properties of the warm dense electron gas based on *ab initio* path integral Monte Carlo simulations,” *Phys. Rev. B* **102**, 125150 (2020).
- ⁸⁵M. Takahashi and M. Imada, “Monte Carlo calculation of quantum systems,” *J. Phys. Soc. Jpn.* **53**, 963–974 (1984).
- ⁸⁶A. P. Lyubartsev, “Simulation of excited states and the sign problem in the path integral Monte Carlo method,” *J. Phys. A: Math. Gen.* **38**, 6659–6674 (2005).
- ⁸⁷A. P. Lyubartsev, “Interacting electrons in one dimension: A path integral Monte Carlo study,” *J. Phys. A: Math. Theor.* **40**, 7151–7157 (2007).
- ⁸⁸V. S. Filinov, M. Bonitz, W. Ebeling, and V. E. Fortov, “Thermodynamics of hot dense H-plasmas: Path integral Monte Carlo simulations and analytical approximations,” *Plasma Phys. Control. Fusion* **43**, 743–759 (2001).
- ⁸⁹T. Schoof, M. Bonitz, A. Filinov, D. Hochstuhl, and J. W. Dufty, “Configuration path integral Monte Carlo,” *Contrib. Plasma Phys.* **51**, 687–697 (2011).
- ⁹⁰T. Dornheim, S. Groth, A. Filinov, and M. Bonitz, “Permutation blocking path integral Monte Carlo: A highly efficient approach to the simulation of strongly degenerate non-ideal fermions,” *New J. Phys.* **17**, 073017 (2015).
- ⁹¹T. Dornheim, T. Schoof, S. Groth, A. Filinov, and M. Bonitz, “Permutation blocking path integral Monte Carlo approach to the uniform electron gas at finite temperature,” *J. Chem. Phys.* **143**, 204101 (2015).
- ⁹²S. Groth, T. Schoof, T. Dornheim, and M. Bonitz, “*Ab initio* quantum Monte Carlo simulations of the uniform electron gas without fixed nodes,” *Phys. Rev. B* **93**, 085102 (2016).
- ⁹³T. Dornheim, S. Groth, and M. Bonitz, “The uniform electron gas at warm dense matter conditions,” *Phys. Rep.* **744**, 1–86 (2018).
- ⁹⁴T. Dornheim, “Fermion sign problem in path integral Monte Carlo simulations: Quantum dots, ultracold atoms, and warm dense matter,” *Phys. Rev. E* **100**, 023307 (2019).
- ⁹⁵T. Dornheim, “Fermion sign problem in path integral Monte Carlo simulations: Grand-canonical ensemble,” *J. Phys. A: Math. Theor.* **54**, 335001 (2021).
- ⁹⁶A. Filinov, P. R. Levashov, and M. Bonitz, “Thermodynamics of the uniform electron gas: Fermionic path integral Monte Carlo simulations in the restricted grand canonical ensemble,” *Contrib. Plasma Phys.* **61**, e202100112 (2021).
- ⁹⁷C. Watzböck, M. Fellingner, K. Held, and A. Toschi, “Long-term memory magnetic correlations in the Hubbard model: A dynamical mean-field theory analysis,” *SciPost Phys.* **12**, 184 (2022).
- ⁹⁸M. Suzuki, “Generalized Trotter’s formula and systematic approximants of exponential operators and inner derivations with applications to many-body problems,” *Commun. Math. Phys.* **51**, 183–190 (1976).
- ⁹⁹A. L. Fetter and J. D. Walecka, *Quantum Theory of Many-Particle Systems* (McGraw-Hill, Boston, 1971).
- ¹⁰⁰J. E. Hirsch, “Discrete Hubbard-Stratonovich transformation for Fermion lattice models,” *Phys. Rev. B* **28**, 4059–4061 (1983).
- ¹⁰¹T. Shen, Y. Liu, Y. Yu, and B. M. Rubenstein, “Finite temperature auxiliary field quantum Monte Carlo in the canonical ensemble,” *J. Chem. Phys.* **153**, 204108 (2020).
- ¹⁰²R. D. Sedgewick, D. J. Scalapino, R. L. Sugar, and L. Capriotti, “Canonical and grand canonical ensemble expectation values from quantum Monte Carlo simulations,” *Phys. Rev. B* **68**, 045120 (2003).
- ¹⁰³C. N. Gilbreth, S. Jensen, and Y. Alhassid, “Reducing the complexity of finite-temperature auxiliary-field quantum Monte Carlo,” *Comput. Phys. Commun.* **264**, 107952 (2021).
- ¹⁰⁴P. Borrmann and G. Franke, “Recursion formulas for quantum statistical partition functions,” *J. Chem. Phys.* **98**, 2484–2485 (1993).
- ¹⁰⁵H. Barghathi, J. Yu, and A. Del Maestro, “Theory of noninteracting fermions and bosons in the canonical ensemble,” *Phys. Rev. Res.* **2**, 043206 (2020).
- ¹⁰⁶T. Shen, H. Barghathi, J. Yu, A. Del Maestro, and B. Rubenstein, “A stable, recursive auxiliary field quantum Monte Carlo algorithm in the canonical ensemble: Applications to thermometry and the Hubbard model,” *arXiv:2212.08654* (2022).
- ¹⁰⁷J. Yu, N. Sun, and H. Zhai, “Symmetry protected dynamical symmetry in the generalized Hubbard models,” *Phys. Rev. Lett.* **119**, 225302 (2017).
- ¹⁰⁸H. Zhai, N. Sun, J. Yu, and P. Zhang, “New relations between spin and charge dynamics of the Fermi Hubbard model,” *New J. Phys.* **21**, 015003 (2019).
- ¹⁰⁹C. N. Yang and S. C. Zhang, “SO₄ symmetry in a Hubbard model,” *Mod. Phys. Lett. B* **04**, 759–766 (1990).
- ¹¹⁰G.-S. Tian, “Particle-hole transformations and sum rules for the Hubbard model,” *Phys. Lett. A* **228**, 383–390 (1997).
- ¹¹¹T. D. Kieu and C. J. Griffin, “Monte Carlo simulations with indefinite and complex-valued measures,” *Phys. Rev. E* **49**, 3855–3859 (1994).
- ¹¹²A. Avella, F. Mancini, and T. Saikawa, “The 2-site Hubbard and *t-J* models,” *Eur. Phys. J. B* **36**, 445–473 (2003).
- ¹¹³O. I. Pătu, A. Klümper, and A. Foerster, “Quantum critical behavior and thermodynamics of the repulsive one-dimensional Hubbard model in a magnetic field,” *Phys. Rev. B* **101**, 035149 (2020).
- ¹¹⁴M. Takahashi and M. Imada, “Monte Carlo calculation of quantum systems. II. Higher order correction,” *J. Phys. Soc. Jpn.* **53**, 3765–3769 (1984).
- ¹¹⁵M. Suzuki, “Fractal decomposition of exponential operators with applications to many-body theories and Monte Carlo simulations,” *Phys. Lett. A* **146**, 319–323 (1990).
- ¹¹⁶K. Sakkos, J. Casulleras, and J. Boronat, “High order Chin actions in path integral Monte Carlo,” *J. Chem. Phys.* **130**, 204109 (2009).
- ¹¹⁷N. Prokofev, B. Svistunov, and I. Tupitsyn, “‘Worm’ algorithm in quantum Monte Carlo simulations,” *Phys. Lett. A* **238**, 253–257 (1998).
- ¹¹⁸M. Boninsegni, N. Prokofev, and B. V. Svistunov, “Worm algorithm for continuous-space path integral Monte Carlo simulations,” *Phys. Rev. Lett.* **96**, 070601 (2006).
- ¹¹⁹T. Dornheim, S. Groth, and M. Bonitz, “Permutation blocking path integral Monte Carlo simulations of degenerate electrons at finite temperature,” *Contrib. Plasma Phys.* **59**, e201800157 (2019).
- ¹²⁰W. von der Linden, “A quantum Monte Carlo approach to many-body physics,” *Phys. Rep.* **220**, 53–162 (1992).
- ¹²¹F. Šimković and R. Rossi, “Many-configuration Markov-chain Monte Carlo,” *arXiv:2102.05613* [physics.comp-ph] (2021).
- ¹²²H. Niederreiter, “Quasi-Monte Carlo methods and pseudo-random numbers,” *Bull. Am. Math. Soc.* **84**, 957–1041 (1978).
- ¹²³M. Maček, P. T. Dumitrescu, C. Bertrand, B. Triggs, O. Parcollet, and X. Waintal, “Quantum quasi-Monte Carlo technique for many-body perturbative expansions,” *Phys. Rev. Lett.* **125**, 047702 (2020).
- ¹²⁴C. Bertrand, D. Bauernfeind, P. T. Dumitrescu, M. Maček, X. Waintal, and O. Parcollet, “Quantum quasi Monte Carlo algorithm for out-of-equilibrium Green functions at long times,” *Phys. Rev. B* **103**, 155104 (2021).

Spectral and thermodynamic properties of the Holstein polaron: Hierarchical equations of motion approach

Veljko Janković^{*} and Nenad Vukmirović[†]

Institute of Physics Belgrade, University of Belgrade, Pregrevica 118, 11080 Belgrade, Serbia



(Received 22 November 2021; accepted 7 February 2022; published 18 February 2022)

We develop a hierarchical equations of motion (HEOM) approach to compute real-time single-particle correlation functions and thermodynamic properties of the Holstein model at finite temperature. We exploit the conservation of the total momentum of the system to formulate the momentum-space HEOM whose dynamical variables explicitly keep track of momentum exchanges between the electron and phonons. Our symmetry-adapted HEOM enable us to overcome the numerical instabilities inherent to the commonly used real-space HEOM. The HEOM method is then used to study the spectral function and thermodynamic quantities of chains containing up to ten sites. The HEOM results compare favorably to existing literature. To provide an independent assessment of the HEOM approach and to gain insight into the importance of finite-size effects, we devise a quantum Monte Carlo (QMC) procedure to evaluate finite-temperature single-particle correlation functions in imaginary time and apply it to chains containing up to twenty sites. QMC results reveal that finite-size effects are quite weak, so that the results on 5 to 10-site chains, depending on the parameter regime, are representative of larger systems. A detailed comparison between the HEOM and QMC data place our HEOM method among reliable methods to compute real-time finite-temperature correlation functions in parameter regimes ranging from low- to high-temperature, and weak- to strong-coupling regime.

DOI: [10.1103/PhysRevB.105.054311](https://doi.org/10.1103/PhysRevB.105.054311)

I. INTRODUCTION

The coupling of electronic excitations (electrons or excitons) to quantum lattice vibrations fundamentally determines physical properties of a wide variety of systems. The examples include organic semiconductors [1–3] and photosynthetic pigment–protein complexes [4–6]. In such systems, the density of excitations, which are typically excited by light or introduced by doping, is low. An electronic excitation in the field of phonons is most simply modeled within the Holstein molecular-crystal model [7], in which the excitation is locally and linearly coupled to intramolecular vibrations. The distinctive feature of organic semiconductors and photosynthetic complexes is that the energy scales of the electronic (excitonic) bandwidth, phonon energy, and electron (exciton)–phonon couplings are all comparable to one another and to the thermal energy. In other words, there is no obvious small parameter in which a perturbation expansion can be performed, and the standard weak-coupling (Redfield-like [8]) and strong-coupling (Förster-like [9] or Marcus-like [10]) theories do not properly describe excitation dynamics [11]. Numerical studies are thus indispensable in tackling the most interesting intermediate-coupling regime.

Thermodynamic and dynamic properties of the Holstein model have been investigated using a host of numerical methods. The most popular ones are the exact diagonalization on finite lattices [12–18], quantum Monte Carlo

(QMC) methods [19–26], the density matrix renormalization group [27–29], variational techniques [30–34], and the momentum-average approximation [35,36]. The majority of these approaches were restricted to ground-state considerations, while the evaluation of finite-temperature (real-time) correlation functions has received limited attention. Early approaches to the finite-temperature single-particle spectral properties of the Holstein model were restricted to analytical [37] and numerical [12,38] studies on two-site systems. These were followed by the dynamical mean-field theory [39]. Recently, Bonča and collaborators have examined the Holstein polaron’s spectral function using the finite-temperature Lanczos method [40,41]. They have also investigated the thermodynamics and spectral functions of the Holstein polaron employing a finite-temperature time-dependent density-matrix renormalization group method [42]. Two-particle correlation functions, such as the conductivity, resistivity, mobility, or diffusion constant, were computed by performing different types of unitary transformations [43–50], or by resorting to the dynamical mean field theory [51,52], the momentum-average approximation [53], QMC [54], or finite-temperature time-dependent density matrix renormalization group [55].

On the other hand, within the chemical-physics community, the method of choice to investigate the dynamical properties of the Holstein model is the hierarchical equations of motion (HEOM) method [56–59]. The HEOM method is a numerically exact density-matrix technique to calculate the dynamics of a quantum system of interest (here, electronic excitations) that is linearly coupled to a Gaussian bath (here, phonons). Starting from the exact result of

^{*}veljko.jankovic@ipb.ac.rs

[†]nenad.vukmirovic@ipb.ac.rs

the Feynman–Vernon influence functional theory [60], the problem is formulated as an infinite hierarchy of dynamical equations for the reduced density matrix (RDM), which completely describes the system of interest, and the so-called auxiliary density matrices (ADMs). While the systematic hierarchy truncation schemes do exist [61,62], the number of ADMs that are necessary to obtain converged results can be quite high, which severely limits the applicability of the HEOM method. The HEOM method has been employed to examine the excitonic dynamics and absorption and emission spectra in Holstein-like models of photosynthetic molecular aggregates [63–68], as well as to study the equilibrium (e.g., the exciton–polaron size) and dynamical (e.g., mobility) properties of the canonical Holstein model [69–72]. Nevertheless, two aspects have received limited attention in the HEOM-method investigations of the Holstein model. (i) The translational symmetry, which reduces the numerical complexity of standard density-matrix techniques [73,74], has not been combined with the HEOM method. (ii) The HEOM method is usually applied to situations in which nuclear degrees of freedom constitute a genuine thermodynamic bath, i.e., the spectral density of the electron–phonon interaction is a continuous function. Its applications to the canonical Holstein model, for which the spectral density consists of delta-like peaks, may face serious numerical problems [75] and have treated relatively small systems [76,77] and/or relatively short time scales [71]. Developing novel techniques to improve the numerical stability of the HEOM method for discrete oscillator modes is thus an active line of research [75,78].

In this paper, we devise a momentum-space HEOM method suitable to compute real-time single-particle correlation functions and thermodynamic properties of the Holstein Hamiltonian at finite temperature. Our momentum-space formulation enhances the numerical stability of the HEOM method with respect to its real-space formulation. We then compute the spectral function and various thermodynamic quantities of the one-dimensional Holstein model containing up to ten sites and find quite good agreement with literature results in a wide range of model parameters. To provide an independent check of our HEOM results and to understand the importance of finite-size effects, we also present QMC results for imaginary-time single-particle correlation functions at finite temperature, which are obtained on chains containing up to 20 sites. We conclude that finite-size effects are not pronounced, while the HEOM and QMC results in imaginary time agree exceptionally well.

The paper is organized as follows. Having specified the model (Sec. II A) and the correlation functions we evaluate (Sec. II B), in Sec. II C we develop the HEOM approach, while in Sec. II D we develop the QMC approach. Section III discusses our HEOM method in light of the well-known weak-coupling (Sec. III A) and strong-coupling (Sec. III B) theories, whereas Sec. III C provides an interesting perspective on the artificial broadening of spectral lines, which is widely used in graphic representations of spectral functions. Section IV is devoted to a detailed presentation of the numerical results for the one-dimensional Holstein model. We first present the results of the HEOM method in different parameter regimes (Secs. IV C–IV E), and then transform them to imaginary time to enable a direct comparison with the QMC data and

to discuss finite-size effects (Sec. IV G). Section V provides further discussion of the methodologies used in this work, while Sec. VI summarizes our main results.

II. MODEL AND METHOD

A. Holstein model

We study the Holstein Hamiltonian on a one-dimensional lattice containing N sites with periodic boundary conditions (PBC). We work in the limit of low excitation (electron or exciton) density, in which it is enough to consider only the subspaces containing no excitations and a single excitation. The zero-excitation subspace is spanned by the collective state $|\text{vac}\rangle$, in which all units are unexcited. For the time being, we assume that the energy of the collective unexcited state sets the zero of our energy scale. An orthonormal basis in the single-excitation subspace is the so-called local basis $\{|j\rangle|j\rangle\}$, whose basis state $|j\rangle$ contains a single excitation localized on site j . We develop the theory in the momentum representation, in which the Holstein Hamiltonian reads as

$$H = H_e + H_{\text{ph}} + H_{e-\text{ph}}. \quad (1)$$

H_e is the tight-binding Hamiltonian of free electronic excitations that can hop between nearest-neighboring sites with hopping amplitude J

$$H_e = \sum_k \varepsilon_k |k\rangle \langle k|. \quad (2)$$

In Eq. (2), the dimensionless wave number k (expressed in units of inverse lattice spacing) may assume any of the N allowed values in the first Brillouin zone (IBZ) $-\pi < k \leq \pi$, while the free-electron dispersion is $\varepsilon_k = \varepsilon_e - 2J \cos(k)$, where ε_e is the on-site vertical excitation energy. The free-phonon Hamiltonian is

$$H_{\text{ph}} = \sum_q \hbar \omega_q b_q^\dagger b_q, \quad (3)$$

where ω_q denotes the dispersion relation of optical phonons, for which $\omega_0 \neq 0$ (in the center of the Brillouin zone), while b_q and b_q^\dagger are the phonon annihilation and creation operators. The electron–phonon interaction is conveniently written as

$$H_{e-\text{ph}} = \sum_q V_q B_q. \quad (4)$$

The purely electronic operator V_q increases the momentum of the electronic subsystem by q ,

$$V_q = \sum_k |k+q\rangle \langle k|, \quad (5)$$

while the purely phononic operator B_q decreases the momentum of phonons by q ,

$$B_q = \frac{\gamma}{\sqrt{N}} (b_q + b_{-q}^\dagger), \quad (6)$$

where γ is the constant of the local electron–phonon coupling. The operator V_q satisfies $V_{-q} = V_q^\dagger$, and the same holds for B_q .

B. Single-particle correlation functions

The single-particle spectral function, which contains complete information about the single-particle spectrum, is

proportional to the imaginary part of the retarded (causal) Green's function in the real-frequency domain. The corresponding expression in the real-time domain reads as [79]

$$G^R(k, t) = -i\theta(t)\langle\{c_k(t), c_k^\dagger\}\rangle. \quad (7)$$

Here, c_k and c_k^\dagger are electron annihilation and creation operators, which in the low-density limit should be replaced by

$$c_k \rightarrow |\text{vac}\rangle\langle k|, \quad c_k^\dagger \rightarrow |k\rangle\langle \text{vac}|, \quad (8)$$

while $\theta(t)$ is the step function. Temporal evolution of the annihilation operator $c_k(t) = e^{iHt/\hbar}c_k e^{-iHt/\hbar}$ entering Eq. (7) is governed by the total Hamiltonian H . The averaging is performed in the thermal equilibrium of the coupled electron–phonon system at temperature $T = (k_B\beta)^{-1}$

$$\langle \cdot \rangle = \text{Tr} \left(\cdot \frac{e^{-\beta H}}{Z} \right), \quad Z = \text{Tr} e^{-\beta H}. \quad (9)$$

In HEOM computations, we will separately compute the time-dependent greater

$$G^>(k, t) = -i\langle c_k(t)c_k^\dagger \rangle \quad (10)$$

and lesser

$$G^<(k, t) = i\langle c_k^\dagger c_k(t) \rangle \quad (11)$$

Green's functions for $t > 0$. In QMC computations, we compute the imaginary-time counterpart of the greater Green's function

$$C(k, \tau) = \langle c_k(\tau)c_k^\dagger \rangle_p, \quad (12)$$

where $0 \leq \tau \leq \beta\hbar$ is the imaginary time, while $c_k(\tau) = e^{H\tau/\hbar}c_k e^{-H\tau/\hbar}$ is the imaginary time-dependent operator. The subscript p denotes that the average is taken over the space of purely phononic states $\langle \cdot \rangle_p = \frac{\text{Tr}_p(Oe^{-\beta H})}{\text{Tr}_p(e^{-\beta H})}$.

Knowing $G^>$, the single-particle spectral function $A(k, \omega)$ is obtained using the fluctuation–dissipation theorem [79]. In the following, we shift the zero of the energy scale to the on-site vertical excitation energy ε_e , as is commonly done in the literature. It is physically plausible to assume that $\beta\varepsilon_e \gg 1$, i.e., that thermal fluctuations alone cannot bridge the gap between the unexcited and singly-excited states. The fluctuation–dissipation theorem then reduces to

$$A(k, \omega) = -\frac{1}{2\pi} \text{Im} G^>(k, \omega). \quad (13)$$

A more detailed discussion is provided in Sec. I of the Supplemental Material (SM) [80]. While $A(k, \omega)$ describes the addition of an electron to the system with initially no electrons, the following quantity

$$A^+(k, \omega) = \frac{1}{2\pi} \text{Im} G^<(k, \omega) \quad (14)$$

describes the removal of an electron from the system. The electron-addition and electron-removal spectral functions are not mutually independent, which is discussed in Sec. I of SM [80] and Sec. IV F.

The comparison between HEOM and QMC results is most conveniently done by transforming HEOM results to the

imaginary-time domain

$$C_{\text{HEOM}}(k, \tau) = \int_{-\infty}^{+\infty} d\omega e^{-\omega\tau} A(k, \omega) \quad (15)$$

and comparing $C_{\text{HEOM}}(k, \tau)$ with $C(k, \tau)$.

C. HEOM method for single-particle correlation functions

I. Preliminaries

Employing the low-density replacements [Eq. (8)] in Eqs. (10) and (11), we obtain

$$G^>(k, t) = -i\langle k|\rho_k^>(t)|\text{vac}\rangle \quad (16)$$

$$\rho_k^{(I, >)}(t) = \text{Tr}_{\text{ph}} \left(U_{e-\text{ph}}^{(I)}(t) |k\rangle\langle \text{vac}| \frac{e^{-\beta H_{\text{ph}}}}{Z_{\text{ph}}} \right) \quad (17)$$

$$G^<(k, t) = i\langle k|\rho_k^<(t)|\text{vac}\rangle \quad (18)$$

$$\rho_k^{(<, I)}(t) = \text{Tr}_{\text{ph}} \left(U_{e-\text{ph}}^{(I)}(t) \frac{e^{-\beta H}}{Z} |k\rangle\langle \text{vac}| \right) \quad (19)$$

While Eqs. (16) and (18) are formulated in the Schrödinger picture, Eqs. (17) and (19) are written in the interaction picture with respect to the noninteracting part $H_e + H_{\text{ph}}$ of the total Hamiltonian and the evolution operator $U_{e-\text{ph}}^{(I)}(t)$ reads as (T is the chronological time-ordering sign)

$$U_{e-\text{ph}}^{(I)}(t) = T \exp \left[-\frac{i}{\hbar} \int_0^t ds H_{e-\text{ph}}^{(I)}(s) \right]. \quad (20)$$

In Eq. (17), $Z_{\text{ph}} = \text{Tr}_{\text{ph}} e^{-\beta H_{\text{ph}}}$, while Tr_{ph} denotes the partial trace over phonons. The computation of $G^>$ proceeds in the zero-excitation subspace, as signaled by the free-phonon thermal distribution that is characteristic for the unexcited system. On the other hand, the computation of $G^<$ requires a precomputation of the thermal-equilibrium state of the coupled electron–phonon system, and it thus proceeds in the single-excitation subspace. While the computation of $G^>$ is analogous to the computation of the absorption spectrum of a molecular aggregate, the computation of $G^<$ is analogous to the computation of the emission spectrum. In both cases, the HEOM computations are less demanding than they usually are because the objects propagated in time are not two-sided (density matrix-like), but one-sided (wave function-like). This is reflected in Eqs. (17) and (19) by the absence of the backward evolution operator $U_{e-\text{ph}}^{(I)\dagger}(t)$. Equation (17) represents temporal evolution starting from the initial state that is factorized, and the manipulations that are necessary to rewrite it as HEOM should be similar to the ones employed in the standard HEOM derivation [58,60]. Recasting Eq. (19) in form of HEOM is more complicated because the initial condition for time evolution cannot be factorized.

2. HEOM method to compute $G^>(k, t)$

According to the Feynman–Vernon influence functional theory [60], the only phonon quantity that enters the reduced electronic description is the thermal free-phonon correlation function

$$C_{q_2 q_1}(t) = \text{Tr}_{\text{ph}} \left\{ B_{q_2}^{(I)}(t) B_{q_1}^{(I)}(0) \frac{e^{-\beta H_{\text{ph}}}}{Z_{\text{ph}}} \right\}. \quad (21)$$

The time dependence of phonon operators is with respect to the free-phonon Hamiltonian H_{ph} , which is emphasized by the superscript (I). The correlation function $C_{q_2q_1}(t)$ is a sum of two complex exponential (oscillating) terms ($t > 0$)

$$C_{q_2q_1}(t) = \delta_{q_2, -q_1} (\hbar\omega_0)^2 \sum_{m=0}^1 c_{q_2m} e^{-\mu_{q_2m} t}, \quad (22)$$

where

$$c_{q0} = \left(\frac{\gamma}{\hbar\omega_0\sqrt{N}} \right)^2 [1 + n_{\text{BE}}(\omega_q, T)], \quad \mu_{q0} = +i\omega_q, \quad (23)$$

$$c_{q1} = \left(\frac{\gamma}{\hbar\omega_0\sqrt{N}} \right)^2 n_{\text{BE}}(\omega_q, T), \quad \mu_{q1} = -i\omega_q, \quad (24)$$

while $n_{\text{BE}}(\omega_q, T) = (e^{\beta\hbar\omega_q} - 1)^{-1}$ is the number of phonons excited in mode q at temperature T .

Integrating out phonons on the right-hand side of Eq. (17), we obtain

$$\rho_k^{(I, >)}(t) = \mathcal{U}^{(I, >)}(t) |k\rangle \langle \text{vac}|, \quad (25)$$

where the reduced evolution superoperator $\mathcal{U}^{(I, >)}(t)$ is given by

$$\begin{aligned} \mathcal{U}^{(I, >)}(t) = T \exp \left[-\omega_0^2 \sum_{qm} \int_0^t ds_2 \right. \\ \left. \times \int_0^{s_2} ds_1 V_q^{(I)}(s_2)^C c_{qm} e^{-\mu_{qm}(s_2-s_1)} V_{-q}^{(I)}(s_1)^C \right]. \end{aligned} \quad (26)$$

The action of the hyperoperator V^C on an arbitrary operator O is defined as $V^C O = V O$. The hyperoperator notation is similar to that used in Ref. [67]. The time-ordering sign T enforces the chronological order of the arguments of hyperoperators V^C (later times are moved to the left). The structure of $\mathcal{U}^{(I, >)}(t)$ suggests that this superoperator conserves the momentum of the electronic subsystem. In other words, the only nontrivial matrix element of $\rho_k^{(I, >)}(t)$ is $\langle k | \rho_k^{(I, >)}(t) | \text{vac} \rangle$, which is in agreement with Eq. (16).

Starting from Eq. (25), the HEOM is derived in the standard manner [58]. The ADMs are characterized by the vector $\mathbf{n} = \{n_{qm} | q \in \text{IBZ}, m = 0, 1\}$ of nonnegative integers $n_{qm} \geq 0$ that count the order of phonon assistance. The ADM $\sigma_{k, \mathbf{n}}^{(I, >, n)}(t)$, which appears on the depth $n = \sum_{qm} n_{qm}$ of the hierarchy, is defined as

$$\begin{aligned} \sigma_{k, \mathbf{n}}^{(I, >, n)}(t) = T \left\{ \prod_{qm} \left[i\omega_0^2 c_{qm} \int_0^t ds e^{-\mu_{qm}(t-s)} V_{-q}^{(I)}(s) \right] \right\}^{n_{qm}} \\ \times \mathcal{U}^{(I, >)}(t) |k\rangle \langle \text{vac}|. \end{aligned} \quad (27)$$

By virtue of the conservation of the electronic momentum, the only nontrivial matrix element of $\sigma_{k, \mathbf{n}}^{(I, >, n)}(t)$ will be $\langle k - k_{\mathbf{n}} | \sigma_{k, \mathbf{n}}^{(I, >, n)}(t) | \text{vac} \rangle$, where

$$k_{\mathbf{n}} = \sum_{qm} q n_{qm} \quad (28)$$

is the electronic momentum carried by $\sigma_{k, \mathbf{n}}^{(I, >, n)}$. Defining the auxiliary Green's function (AGF) at depth n characterized by vector \mathbf{n}

$$G_{\mathbf{n}}^{(>, n)}(k - k_{\mathbf{n}}, t) = -i \langle k - k_{\mathbf{n}} | \sigma_{k, \mathbf{n}}^{(>, n)}(t) | \text{vac} \rangle, \quad (29)$$

we obtain the following HEOM for Green's functions

$$\begin{aligned} \partial_t G_{\mathbf{n}}^{(>, n)}(k - k_{\mathbf{n}}, t) \\ = -i(\Omega_{k-k_{\mathbf{n}}} + \mu_{\mathbf{n}}) G_{\mathbf{n}}^{(>, n)}(k - k_{\mathbf{n}}, t) \\ + i \sum_{qm} G_{\mathbf{n}_{qm}^+}^{(>, n+1)}(k - k_{\mathbf{n}} - q, t) \\ + i\omega_0^2 \sum_{qm} n_{qm} c_{qm} G_{\mathbf{n}_{qm}^-}^{(>, n-1)}(k - k_{\mathbf{n}} + q, t). \end{aligned} \quad (30)$$

In the last equation, we introduce

$$\mu_{\mathbf{n}} = -i \sum_{qm} \mu_{qm} n_{qm} = \sum_q \omega_q (n_{q0} - n_{q1}), \quad (31)$$

while $\Omega_k = \varepsilon_k / \hbar$ is the angular frequency of the free-electron state $|k\rangle$. The greater Green's function is then obtained as the root of the hierarchy, $G^{>}(k, t) = G_{\mathbf{0}}^{(>, 0)}(k, t)$. The hierarchy presented in Eq. (30) is propagated separately for each allowed value of k (there are N mutually independent hierarchies) with the initial condition

$$G_{\mathbf{n}}^{(>, n)}(k, t=0) = -i\delta_{n,0}, \quad (32)$$

which follows from Eqs. (27) and (29).

In the zero-temperature limit, the hierarchy in Eq. (30) reduces to the hierarchy presented in Refs. [35,36]. Our HEOM may thus be regarded as an extension of the hierarchy in Refs. [35,36] to nonzero temperatures. Due to the zero-temperature assumption, the hierarchy in Refs. [35,36] has only a single branch (our $m = 0$ branch). Since the thermal (or incoherent) phonon occupations are identically equal to zero, phonon-assisted processes proceed via virtual (or coherent) phonons, that are first created from the phonon vacuum and subsequently destroyed. On the other hand, our hierarchy has two branches describing phonon-assisted processes that proceed via thermal phonons and in which the order of phonon absorption and emission events is immaterial. One may attempt to solve Eq. (30) by Fourier or Laplace transform, as was done in Refs. [35,36]. This would transform the hierarchy of first-order linear differential equations into a (sparse) system of linear algebraic equations. While such a route is certainly possible, here, we opt for solving Eq. (30) directly in the time domain, after which the spectral properties are computed using the discrete Fourier transform.

3. HEOM method to compute $G^<(k, t)$

The main obstacle in the derivation of HEOM for the lesser Green's function is the fact that the density matrix $\rho_k^<(0)$ at the initial instant is not factorizable, see Eq. (19). Nevertheless, one may always write

$$\frac{e^{-\beta H}}{Z} = \frac{e^{-\beta H_e}}{Z_e} \frac{e^{-\beta H_{\text{ph}}}}{Z_{\text{ph}}} \times T \exp \left[-\frac{1}{\hbar} \int_0^{\beta\hbar} d\tau \bar{H}_{e-\text{ph}}(\tau) \right], \quad (33)$$

where Z_{ph} is the free-phonon partition sum, $Z_e = Z/Z_{\text{ph}}$ is still unknown electronic partition sum (it contains all the effects due to the electron–phonon interaction), while $\overline{H}_{e\text{-ph}}(\tau)$ denotes the electron–phonon coupling in the imaginary-time interaction picture

$$\overline{H}_{e\text{-ph}}(\tau) = e^{(H_e + H_{\text{ph}})\tau/\hbar} H_{e\text{-ph}} e^{-(H_e + H_{\text{ph}})\tau/\hbar}. \quad (34)$$

Inserting Eq. (33) in Eq. (19), the partial trace over phonons can be straightforwardly computed to obtain

$$\rho_k^{(l, <)}(t) = \left(\mathcal{U}^{(l, <)}(t, \beta\hbar) \frac{e^{-\beta H_e}}{Z_e} \right) |k\rangle \langle \text{vac}|. \quad (35)$$

The exact evolution superoperator $\mathcal{U}^{(l, <)}(t, \beta\hbar)$ is the time-ordered exponential of the sum of three influence phases

$$\mathcal{U}^{(l, <)}(t, \beta\hbar) = \mathcal{T} \exp\{-[\Phi_1(t) + \Phi_2(\beta\hbar) + \Phi_3(t, \beta\hbar)]\}, \quad (36)$$

$$\begin{aligned} \Phi_1(t) &= \omega_0^2 \sum_{qm} \int_0^t ds_2 \int_0^{s_2} ds_1 V_q^{(l)}(s_2)^C \\ &\quad \times c_{qm} e^{-\mu_{qm}(s_2 - s_1)} V_{-q}^{(l)}(s_1)^C, \end{aligned} \quad (37)$$

$$\begin{aligned} \Phi_2(\beta\hbar) &= -\omega_0^2 \sum_{qm} \int_0^{\beta\hbar} d\tau_2 \int_0^{\tau_2} d\tau_1 {}^C \overline{V}_{-q}(\tau_1) \\ &\quad \times c_{qm} e^{i\mu_{qm}(\tau_2 - \tau_1)} {}^C \overline{V}_q(\tau_2), \end{aligned} \quad (38)$$

$$\begin{aligned} \Phi_3(t, \beta\hbar) &= -i\omega_0^2 \sum_{qm} \int_0^t ds \int_0^{\beta\hbar} d\tau V_q^{(l)}(s)^C \\ &\quad \times c_{qm} e^{-\mu_{qm}s} e^{i\mu_{qm}(\beta\hbar - \tau)} {}^C \overline{V}_{-q}(\tau). \end{aligned} \quad (39)$$

The influence phase $\Phi_1(t)$ has already appeared in the derivation of HEOM for $G^>$ [see Eq. (26)] and it represents the pure real-time evolution. The influence phase $\Phi_2(\beta\hbar)$ is representative of the pure imaginary-time evolution, while $\Phi_3(t, \beta\hbar)$ contains cross contributions among real- and imaginary-time evolutions. We note that similar expressions have been obtained in the course of the derivation of the HEOM for the initial states that cannot be factorized into a purely electronic and purely phononic part [72,81]. In contrast to Refs. [72,81], here, the backward evolution operator is missing from Eqs. (17) and (19), so that the hyperoperators V^C and ${}^C V$ act only from one side. The action of the hyperoperator ${}^C V$ on an arbitrary operator O is defined as ${}^C V O = O V$. The parentheses on the right-hand side of Eq. (35) stress that all the hyperoperators ${}^C \overline{V}_{-q}(\tau)$ that act from the right should be applied before operator $|k\rangle \langle \text{vac}|$. The time-ordering sign \mathcal{T} in Eq. (36) enforces the chronological order of the real-time arguments s of hyperoperators V^C (later times are moved to the left) and the anti-chronological order of the imaginary-time arguments τ of hyperoperators ${}^C V$ (later times are moved to the right). There is no specific ordering of the real-time instants with respect to the imaginary-time instants because the hyperoperators V^C and ${}^C V$ act on operator $e^{-\beta H_e}/Z_e$ from opposite sides. The anti-chronological ordering of the imaginary-time arguments of operators ${}^C V$ is necessary in order to maintain the correct chronological order in the general term of the expansion of Eq. (35) [see also

Eqs. (19), (20), and (33)], whose operators are ordered as follows: $V_{q_n}^{(l)}(s_n) \dots V_{q_1}^{(l)}(s_1) [e^{-\beta H_e}/Z_e] \overline{V}_{p_m}(\tau_m) \dots \overline{V}_{p_1}(\tau_1)$, where $t \geq s_n \geq \dots \geq s_1 \geq 0$ and $\beta\hbar \geq \tau_m \geq \dots \geq \tau_1 \geq 0$, $n + m$ is even, and $q_n + \dots + q_1 + p_m + \dots + p_1 = 0$. The ADM $\sigma_{k, \mathbf{n}}^{(l, <, n)}(t)$ at depth n is defined as

$$\begin{aligned} \sigma_{k, \mathbf{n}}^{(l, <, n)}(t, \beta\hbar) &= \left\{ \mathcal{T} \prod_{qm} \left[i\omega_0^2 \int_0^t ds c_{qm} e^{-\mu_{qm}(t-s)} V_{-q}^{(l)}(s)^C \right. \right. \\ &\quad \left. \left. + \omega_0^2 e^{-\mu_{qm}t} \int_0^{\beta\hbar} d\tau c_{qm} e^{i\mu_{qm}(\beta\hbar - \tau)} {}^C \overline{V}_{-q}(\tau) \right] \right\}^{n_{qm}} \\ &\quad \times \mathcal{U}^{(l, <)}(t, \beta\hbar) \frac{e^{-\beta H_e}}{Z_e} \left\} |k\rangle \langle \text{vac}|. \end{aligned} \quad (40)$$

The AGF on level n that is characterized by vector \mathbf{n} is then defined analogously to Eq. (29)

$$G_{\mathbf{n}}^{(<, n)}(k - k_{\mathbf{n}}, t) = i \langle k - k_{\mathbf{n}} | \sigma_{k, \mathbf{n}}^{(<, n)}(t, \beta\hbar) | \text{vac} \rangle \quad (41)$$

and the HEOM for lesser Green's functions assume the form of Eq. (30). The initial condition under which the hierarchy for $G^<$ is solved is obtained by setting $t = 0$ in Eq. (40), which results in

$$\begin{aligned} \sigma_{k, \mathbf{n}}^{(n, <)}(0, \beta\hbar) &= \left\{ \mathcal{T} \prod_{qm} \left[\omega_0^2 \int_0^{\beta\hbar} d\tau c_{qm} e^{i\mu_{qm}(\beta\hbar - \tau)} {}^C \overline{V}_{-q}(\tau) \right] \right\}^{n_{qm}} \\ &\quad \times e^{-\Phi_2(\beta\hbar)} \frac{e^{-\beta H_e}}{Z_e} \left\} |k\rangle \langle \text{vac}|. \end{aligned} \quad (42)$$

Setting $n = 0$ and $\mathbf{n} = \mathbf{0}$ in Eq. (42), we recognize that $\sigma_{k, \mathbf{0}}^{(0, <)}(0, \beta\hbar)$ is, up to the factor $|k\rangle \langle \text{vac}|$, identical to the expression for the electronic RDM, see Eqs. (35) and (40). The equilibrium state of the coupled electron–phonon system has been computed in different ways. The imaginary-time HEOM was formulated only for a specific spectral density of the electron–phonon coupling and its structure was not compatible with the structure of the real-time HEOM [81]. The correlated equilibrium state was also computed by the technique of stochastic unraveling [72,82] or by finding the steady state of the real-time HEOM [83]. In the following section, we derive the imaginary-time HEOM for the correlated electron–phonon equilibrium that is specifically suited for the single-mode Holstein model and whose form is fully compatible with the real-time HEOM derived in this section.

4. HEOM method to compute the thermal equilibrium of coupled electrons and phonons

Taking the partial trace of Eq. (33) over phonons we obtain the following expression for the (normalized) thermal-equilibrium RDM for an electron that is coupled to phonons

$$\rho^{\text{eq}}(\beta\hbar) = \mathcal{T} e^{-\Phi_2(\beta\hbar)} \frac{e^{-\beta H_e}}{Z_e}. \quad (43)$$

However, the normalization constant Z_e is not known. To compute Z_e , let us consider the unnormalized and imaginary time-dependent analog of Eq. (43)

$$\rho_{\mathbf{n}}^{\text{un,eq}}(\tau) = \mathcal{T} e^{-\Phi_2(\tau)} e^{-H_e \tau / \hbar} \quad (44)$$

where $0 \leq \tau \leq \beta \hbar$. The imaginary-time HEOM is then obtained as usually, while the definition of the unnormalized ADM at level n reads as

$$\sigma_{\mathbf{n}}^{(n,\text{un,eq})}(\tau) = \mathcal{T} \prod_{qm} \left[\omega_0^2 \int_0^\tau d\tau' c_{qm} e^{i\mu_{qm}(\tau-\tau')} C \bar{V}_{-q}(\tau') \right]^{n_{qm}} \times e^{-\Phi_2(\tau)} e^{-H_e \tau / \hbar}. \quad (45)$$

Because of the momentum conservation, the ADM $\sigma_{\mathbf{n}}^{(n,\text{un,eq})}(\tau)$ has only N nonzero matrix elements, $\langle k - k_{\mathbf{n}} | \sigma_{\mathbf{n}}^{(n,\text{un,eq})}(\tau) | k \rangle$, and it turns out that the imaginary-time HEOM can be solved independently for each of N allowed values of k . The imaginary-time HEOM

$$\begin{aligned} \partial_\tau \langle k - k_{\mathbf{n}} | \sigma_{\mathbf{n}}^{(n,\text{un,eq})}(\tau) | k \rangle &= -(\Omega_{k-k_{\mathbf{n}}} + \mu_{\mathbf{n}}) \langle k - k_{\mathbf{n}} | \sigma_{\mathbf{n}}^{(n,\text{un,eq})}(\tau) | k \rangle \\ &+ \sum_{qm} \langle k - k_{\mathbf{n}} - q | \sigma_{\mathbf{n}_{qm}}^{(n+1,\text{un,eq})}(\tau) | k \rangle \\ &+ \omega_0^2 \sum_{qm} n_{qm} c_{qm} \langle k - k_{\mathbf{n}} + q | \sigma_{\mathbf{n}_{qm}}^{(n-1,\text{un,eq})}(\tau) | k \rangle \end{aligned} \quad (46)$$

is then solved with the initial condition that can be inferred from Eq. (45) and that reads as [81]

$$\langle k - k_{\mathbf{n}} | \sigma_{\mathbf{n}}^{(n,\text{un,eq})}(0) | k \rangle = \delta_{n,0}. \quad (47)$$

This initial condition assumes that all free-electron levels are equally populated, which is in agreement with the fact that point $\tau = 0$ corresponds to the infinite-temperature limit. Furthermore, thermal fluctuations are so strong that they completely suppress the effects due to the electron-phonon interaction, so that all ADMs are initially equal to zero. Once the imaginary-time propagation of Eq. (45) is done, the normalization constant Z_e is obtained as

$$Z_e = \sum_k \langle k | \sigma_{\mathbf{0}}^{(0,\text{un,eq})}(\beta \hbar) | k \rangle, \quad (48)$$

so that the normalized ADMs in thermal equilibrium read as

$$\sigma_{\mathbf{n}}^{(n,\text{eq})} = Z_e^{-1} \sigma_{\mathbf{n}}^{(n,\text{un,eq})}(\beta \hbar). \quad (49)$$

Finally, the initial condition for the real-time propagation of HEOM for $G^<$ reads as

$$G_{\mathbf{n}}^{(<,n)}(k - k_{\mathbf{n}}, 0) = i \langle k - k_{\mathbf{n}} | \sigma_{\mathbf{n}}^{(n,\text{eq})} | k \rangle. \quad (50)$$

5. Thermodynamic properties

Thermodynamic properties of the Holstein model have been extensively investigated using the QMC method in combination with the Feynman's path-integral theory [20–22] or the canonical Lang–Firsov transformation of the electron-phonon Hamiltonian [25] or the density-matrix renormalization group [42]. The algorithm presented in Refs. [20–22], in which the purely electronic model resulting from the analytical elimination of the nuclear degrees of freedom is simulated using the QMC, is very close in spirit to the method developed

here. It is mainly for this reason that we here compute the same thermodynamic quantities as in Refs. [20–22].

The kinetic energy of the electron is a purely electronic quantity and it thus depends only on the electronic RDM $\sigma_{\mathbf{0}}^{(0,\text{eq})}$

$$E_{\text{kin}} = \sum_k \varepsilon_k f_k = \sum_k \varepsilon_k \langle k | \sigma_{\mathbf{0}}^{(0,\text{eq})} | k \rangle, \quad (51)$$

where $f_k = \langle k | \sigma_{\mathbf{0}}^{(0,\text{eq})} | k \rangle \in [0, 1]$ is the population of electronic state with momentum k . The electron-phonon interaction energy is a mixed quantity that is linear in phonon coordinates. Even though our approach mainly deals with reduced, i.e., purely electronic quantities, the results of Ref. [84] suggest that the interaction energy should be extracted from ADMs at depth 1 as follows:

$$\begin{aligned} E_{e\text{-ph}} &= \frac{\gamma}{\sqrt{N}} \sum_{kq} \langle |k+q\rangle \langle k | (b_q + b_{-q}^\dagger) \\ &= \hbar \omega_0 \sum_q \sum_{m=0}^1 \sqrt{c_{qm}} \sum_k \langle k - q | \sigma_{\mathbf{0}_{qm}^+}^{(1,\text{eq})} | k \rangle. \end{aligned} \quad (52)$$

The fermion-boson correlation function contains information on how the electron distorts its surroundings by following how the presence of an electron on a site affects the nuclear motion on sites that are r lattice constants away

$$\begin{aligned} \varphi_r &= \frac{\gamma}{E_{e\text{-ph}}} \sum_j \langle |j\rangle \langle j | (b_{j+r} + b_{j+r}^\dagger) \\ &= \frac{\hbar \omega_0}{E_{e\text{-ph}}} \sum_q e^{iqr} \sum_{m=0}^1 \sqrt{c_{qm}} \sum_k \langle k - q | \sigma_{\mathbf{0}_{qm}^+}^{(1,\text{eq})} | k \rangle. \end{aligned} \quad (53)$$

This quantity has been used to gain insight into the spatial extent of the polaron [21,22,70].

D. QMC method for single-particle correlation function

We used a QMC method to calculate the single-particle correlation function in imaginary time. The method is based on the path-integral representation of the correlation function. In this representation, it is possible to integrate out the phononic degrees of freedom. For this reason, one ends up with the sum over electronic coordinates that is performed using the Monte Carlo method. Our approach essentially follows the path of early studies in Refs. [20–22] with a difference that we extend these studies (where only thermodynamic quantities were calculated) to calculate the imaginary-time correlation function. In addition, we formulate the method in such a way that phase space of electronic coordinates can be directly sampled. This is significantly more convenient than the sampling based on the Metropolis algorithm, which needs initial equilibration of the system and which suffers from the possibility of trapping the system in local minima. The QMC method that we used is also similar to the stochastic path integral method developed in the chemical physics community [82]. Within that method, phonon degrees of freedom are integrated out and the problem is eventually reduced to the problem of dynamics of the electronic subsystem in the presence of noise.

In more detail, to evaluate the imaginary time correlation function

$$C(k, \tau) = \frac{\text{Tr}_p(e^{-(\beta-\frac{\tau}{\hbar})H_{\text{ph}}} c_k e^{-\frac{\tau}{\hbar}H} c_k^\dagger)}{\text{Tr}_p e^{-\beta H_{\text{ph}}}} \quad (54)$$

we calculate it in the site basis

$$C_{ab}(\tau) = \frac{\text{Tr}_p(e^{-(\beta-\frac{\tau}{\hbar})H_{\text{ph}}} c_a e^{-\frac{\tau}{\hbar}H} c_b^\dagger)}{\text{Tr}_p e^{-\beta H_{\text{ph}}}} \quad (55)$$

and then we perform the transformation

$$C(k, \tau) = \frac{1}{N} \sum_{a=0}^{N-1} \sum_{b=0}^{N-1} e^{ik(b-a)} C_{ab}(\tau). \quad (56)$$

We calculate $C_{ab}(\tau)$ starting from

$$C_{ab}(\tau) = \frac{\int d\{x\}d\{y\} \langle \{x\} | e^{-(\beta-\frac{\tau}{\hbar})H_{\text{ph}}} | \{y\} \rangle \langle a\{y\} | e^{-\frac{\tau}{\hbar}H} | b\{x\} \rangle}{\int d\{x\}d\{y\} \langle \{x\} | e^{-(\beta-\frac{\tau}{\hbar})H_{\text{ph}}} | \{y\} \rangle \langle \{y\} | e^{-\frac{\tau}{\hbar}H_{\text{ph}}} | \{x\} \rangle} \quad (57)$$

where $\{x\}$ and $\{y\}$ denote the vectors containing the coordinates of all phonon modes. The term $\langle \{x\} | e^{-(\beta-\frac{\tau}{\hbar})H_{\text{ph}}} | \{y\} \rangle$ is expressed in an analytical form, since the following identity holds for a single phonon mode

$$\langle x | e^{-\alpha H_{\text{ph}}} | y \rangle = \sqrt{\frac{m\omega_0}{2\pi\hbar \sinh(\alpha\hbar\omega_0)}} \times e^{-\frac{m\omega_0}{2\hbar \sinh(\alpha\hbar\omega_0)} [(x^2+y^2) \cosh(\alpha\hbar\omega_0) - 2xy]}, \quad (58)$$

while the analogous term for multiple phonon modes is a simple product of the terms for each mode (m denotes the mass of the oscillator that can be set to 1 without the loss of generality). To evaluate the matrix elements $\langle a\{y\} | e^{-\frac{\tau}{\hbar}H} | b\{x\} \rangle$ and $\langle \{y\} | e^{-\frac{\tau}{\hbar}H_{\text{ph}}} | \{x\} \rangle$ we discretize the imaginary time τ by dividing it into K steps of duration $\Delta\tau = \frac{\tau}{K}$. We make use of the Suzuki-Trotter expansion of first order, which has a small controllable error of order $(\Delta\tau)^2$

$$e^{-\frac{\Delta\tau}{\hbar}H} \approx e^{-\frac{\Delta\tau}{\hbar}H_{\text{ph}}} e^{-\frac{\Delta\tau}{\hbar}H_e} e^{-\frac{\Delta\tau}{\hbar}H_c}. \quad (59)$$

We then have

$$\begin{aligned} \langle a\{y\} | e^{-\frac{\Delta\tau}{\hbar}H} | b\{x\} \rangle &= \int d\{z\} \sum_c \langle \{y\} | e^{-\frac{\Delta\tau}{\hbar}H_{\text{ph}}} | \{z\} \rangle \\ &\times \langle a\{z\} | e^{-\frac{\Delta\tau}{\hbar}H_e} | c\{x\} \rangle \langle c | e^{-\frac{\Delta\tau}{\hbar}H_c} | b \rangle. \end{aligned} \quad (60)$$

The term involving the electron-phonon interaction can be evaluated as

$$\langle a\{z\} | e^{-\frac{\Delta\tau}{\hbar}H_e} | c\{x\} \rangle = \delta_{ac} e^{-\frac{\Delta\tau}{\hbar}C x_a} \delta(\{z\} - \{x\}), \quad (61)$$

where $C = \frac{\gamma}{\hbar\omega_0} \sqrt{2\hbar m\omega_0^3}$ and x_a denotes the coordinate of the phonon at site a . The term containing H_c reads

$$\langle c | e^{-\frac{\Delta\tau}{\hbar}H_c} | b \rangle = \frac{1}{N} \sum_k e^{-\Delta\tau\epsilon_k} e^{ik(c-b)} \equiv f(c-b) \quad (62)$$

and we denote it as $f(c-b)$ in what follows. We thus obtain

$$\begin{aligned} \langle a\{y\} | e^{-\frac{\tau}{\hbar}H} | b\{x\} \rangle &= \sum_{i_1 \dots i_{K-1}} f(a-i_1) f(i_1-i_2) \dots f(i_{K-1}-b) \\ &\times \int d\{x\}^{(1)} \dots d\{x\}^{(K-1)} \langle \{y\} | e^{-\frac{\Delta\tau}{\hbar}H_{\text{ph}}} | \{x\}^{(1)} \rangle \\ &\times \langle \{x\}^{(1)} | e^{-\frac{\Delta\tau}{\hbar}H_{\text{ph}}} | \{x\}^{(2)} \rangle \dots \langle \{x\}^{(K-1)} | e^{-\frac{\Delta\tau}{\hbar}H_{\text{ph}}} | \{x\} \rangle \\ &\times e^{-\frac{\Delta\tau}{\hbar}C(x_a^{(1)}+x_{i_1}^{(2)}+\dots+x_{i_{K-2}}^{(K-1)}+x_{i_{K-1}})} \end{aligned} \quad (63)$$

and

$$\begin{aligned} \langle \{y\} | e^{-\frac{\tau}{\hbar}H_{\text{ph}}} | \{x\} \rangle &= \int d\{x\}^{(1)} \dots d\{x\}^{(K-1)} \langle \{y\} | e^{-\frac{\Delta\tau}{\hbar}H_{\text{ph}}} | \{x\}^{(1)} \rangle \\ &\times \langle \{x\}^{(1)} | e^{-\frac{\Delta\tau}{\hbar}H_{\text{ph}}} | \{x\}^{(2)} \rangle \dots \langle \{x\}^{(K-1)} | e^{-\frac{\Delta\tau}{\hbar}H_{\text{ph}}} | \{x\} \rangle. \end{aligned} \quad (64)$$

After substitution of expressions (58), (63), and (64) into Eq. (57) we obtain

$$C_{ab}(\tau) = \frac{\mathcal{N}}{\mathcal{D}}, \quad (65)$$

with

$$\begin{aligned} \mathcal{N} &= \sum_{i_1 \dots i_{K-1}} f(a-i_1) f(i_1-i_2) \dots f(i_{K-1}-b) \\ &\times \int d\{x\}d\{y\}d\{x\}^{(1)} \dots d\{x\}^{(K-1)} \\ &\times e^{-Q(\{x\}, \{y\}, \{x\}^{(1)}, \dots, \{x\}^{(K-1)})} e^{-L(\{x\}, \{y\}, \{x\}^{(1)}, \dots, \{x\}^{(K-1)})} \end{aligned} \quad (66)$$

and

$$\mathcal{D} = \int d\{x\}d\{y\}d\{x\}^{(1)} \dots d\{x\}^{(K-1)} e^{-Q(\{x\}, \{y\}, \{x\}^{(1)}, \dots, \{x\}^{(K-1)})}. \quad (67)$$

The term $Q(\{x\}, \{y\}, \{x\}^{(1)}, \dots, \{x\}^{(K-1)})$ in Eqs. (66) and (67) denotes the quadratic form of phonon coordinates, that contains the terms of second order only (i.e., the square of a phonon coordinate or the product of two phonon coordinates), while the term $L(\{x\}, \{y\}, \{x\}^{(1)}, \dots, \{x\}^{(K-1)})$ denotes the linear term that contains a linear combination of phonon coordinates. The integrals in Eqs. (66) and (67) are the Gaussian integrals that can be evaluated analytically using the formula for the Gaussian integral

$$\int d^n \mathbf{z} e^{-\frac{1}{2} \mathbf{z} \cdot \mathbf{A} \cdot \mathbf{z}} e^{\mathbf{b} \cdot \mathbf{z}} = (2\pi)^{n/2} (\det \mathbf{A})^{-1/2} e^{\frac{1}{2} \mathbf{b} \cdot \mathbf{A}^{-1} \cdot \mathbf{b}}, \quad (68)$$

where \mathbf{z} is a real vector of dimension n , \mathbf{A} is a real symmetric positive definite matrix of dimension $n \times n$, \mathbf{b} is a vector of dimension n , $\det \mathbf{A}$ is the determinant of matrix \mathbf{A} and \mathbf{A}^{-1} is its inverse. We then obtain

$$C_{ab}(\tau) = \sum_{i_1 \dots i_{K-1}} f(a-i_1) f(i_1-i_2) \dots f(i_{K-1}-b) e^{\frac{1}{2} \mathbf{b} \cdot \mathbf{A}^{-1} \cdot \mathbf{b}}, \quad (69)$$

where \mathbf{A} is the matrix representing the quadratic form Q and \mathbf{b} is the vector representing the linear form L . To evaluate the

last sum, we introduce the replacement of variables

$$a - i_1 = j_1, \quad i_1 - i_2 = j_2, \dots, i_{K-2} - i_{K-1} = j_{K-1}. \quad (70)$$

The sum then takes the form

$$C_{ab}(\tau) = \sum_{j_1 \dots j_{K-1}} f(j_1) f(j_2) \dots f(j_{K-1}) \times f\left(a - b - \sum_{i=1}^{K-1} j_i\right) e^{\frac{1}{2} \mathbf{b} \cdot \mathbf{A}^{-1} \cdot \mathbf{b}}. \quad (71)$$

To evaluate the last sum, we treat the non-negative function

$$g(j_1, \dots, j_{K-1}) = f(j_1) f(j_2) \dots f(j_{K-1}) \quad (72)$$

as the probability density. We perform Monte Carlo summation by choosing random integers j_1, j_2, \dots, j_{K-1} that follow the distribution $h(j) = \frac{f(j)}{\sum_j f(j)}$ and perform the summation of the term $f(a - b - \sum_{i=1}^{K-1} j_i) e^{\frac{1}{2} \mathbf{b} \cdot \mathbf{A}^{-1} \cdot \mathbf{b}}$. The replacement of variables introduced in Eq. (70) enabled us to directly sample the phase space of electronic coordinates rather than to perform sampling based on the Metropolis algorithm. The results presented in this work were obtained from 10^5 samples of electronic coordinates, unless otherwise stated. The integer K that defines the discretization of imaginary time was chosen so that $\Delta\tau \approx 0.05 \frac{\hbar}{J}$.

We used the same ideas to calculate the thermodynamic expectation values using the QMC method. The details of the method for these cases are given in Sec. II of SM [80].

III. RELATION OF THE HEOM METHOD TO EXISTING RESULTS

A. Weak-coupling limit

In the weak-coupling limit, the electron–phonon interaction constant is the smallest energy scale in the problem. It is then reasonable to treat the interaction within the second-order perturbation theory. In the HEOM approach, the second-order approximation is performed by truncating the hierarchy at depth 1 and solving the resulting equations for ADMs at depth 1 in the Markov and adiabatic approximations [58,85]. One eventually obtains the Rayleigh–Schrodinger perturbation theory expression for the self energy [79]. More details are provided in Sec. III of SM [80].

B. Strong-coupling limit

In the opposite, strong-coupling limit, the electronic coupling J is the smallest energy in the problem. The Holstein Hamiltonian then reduces to N independent single-site problems (the so-called independent-boson models), whose analytic solution is known [79]. In the following discussion, we assume for simplicity that phonons are dispersionless, i.e., $\omega_q = \omega_0$ for all q . In Sec. IV of SM [80], we demonstrate how the exact solution presented here is recast as the Lang–Firsov formula [86] for the single-site Green’s function. The crux of the derivation is to note that, in the single-site limit, the hyperoperators appearing in the evolution superoperator become time independent, which renders the time-ordering sign ineffective [67]. Here, we repeat the zero-temperature

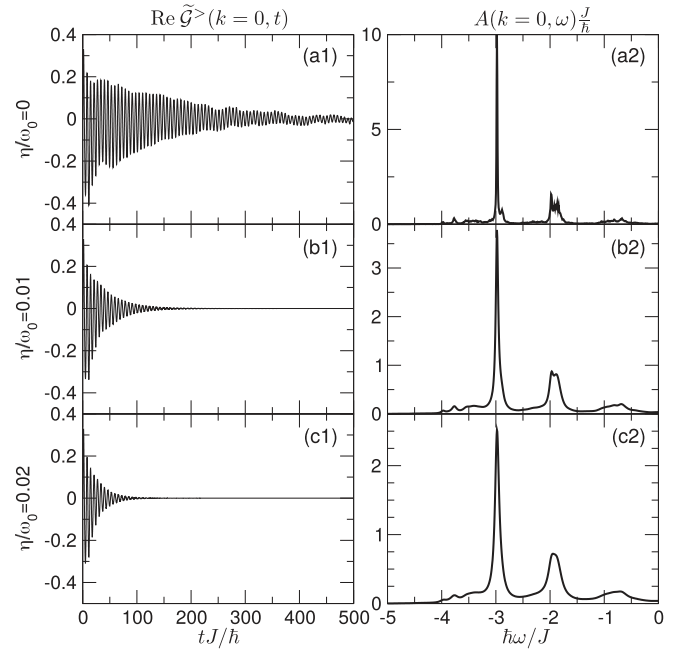


FIG. 1. [(a1),(b1),(c1)] Time dependence of the real part of the envelope $\tilde{G}^>(k=0, t)$ of the greater Green’s function in the zone center for three different values of the broadening parameter η . For a precise definition of $\tilde{G}^>(k, t)$, see Eq. (80). [(a2),(b2),(c2)] Spectral function $A(k=0, \omega)$ in the zone center for three different values of the broadening parameter η . The computation is performed on a $N = 8$ -site chain with $k_B T/J = 0.4$, $\hbar\omega_0/J = 1$, and $\gamma/J = \sqrt{2}$, while the maximum hierarchy depth is set to $D = 7$.

result

$$G^>(\omega) = -2\pi i e^{-\gamma^2/(\hbar\omega_0)^2} \times \sum_{n=0}^{+\infty} \frac{1}{n!} \left(\frac{\gamma}{\hbar\omega_0}\right)^{2n} \delta\left(\omega + \frac{\gamma^2}{\hbar^2\omega_0} - n\omega_0\right). \quad (73)$$

C. Artificial broadening of spectral lines

For graphic representations of the spectral function [Eq. (13)], the δ functions entering Eq. (73) are commonly replaced by their Lorentzian representation, $\delta(x) \rightarrow \eta/[\pi(x^2 + \eta^2)]$, where the small parameter η is the artificial broadening of the peaks. The discussion in Sec. IV of SM [80] suggests that the artificial broadening can be introduced in the exact result embodied in Eq. (26) by simply replacing $\mu_{qm} \rightarrow \mu_{qm} + \eta$. On the level of the HEOM, this replacement is reflected as an artificial damping at rate $n\eta$ of the AGFs at depth n , see Eqs. (30) and (31). The excellent agreement between the analytical and numerical results in the single-site limit with different levels of artificial broadening is demonstrated in Figs. 1 and 2 in Sec. IV of SM [80]. The replacement $\mu_{qm} \rightarrow \mu_{qm} + \eta$, however, changes the physical situation we are dealing with by effectively replacing the discrete phonon spectrum by a continuous one.

To elaborate on the last point, we recall that the thermal free-phonon correlation function $C_{q_2 q_1}(t)$ [Eq. (21)] can be

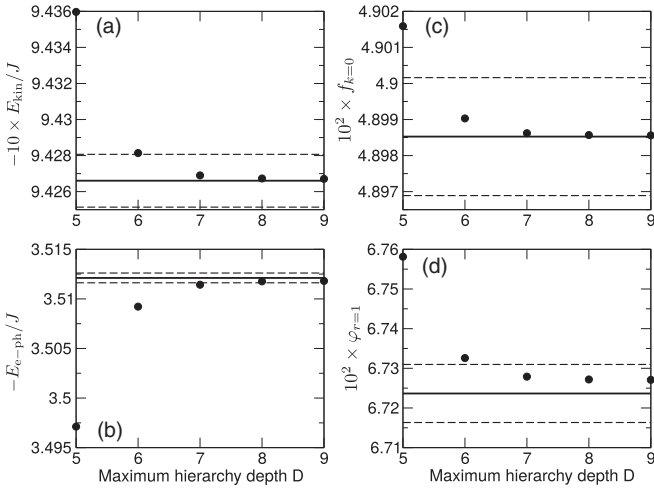


FIG. 2. Dependence of various thermodynamic quantities on the maximum hierarchy depth D (full dots) and comparison with QMC results (solid line). Vertical distance between the solid line and dashed lines is equal to the standard deviation of the sample containing 10 different realizations of the QMC algorithm. The model parameters assume the following values: $k_B T/J = 1$, $\hbar\omega_0/J = 1$, $\gamma/J = \sqrt{2}$, $N = 8$, $N_\theta = 6$. (a) Negative kinetic energy of the electron [Eq. (51)] in units of J multiplied by a factor of 10 (averaging over TBC is performed). (b) Negative electron–phonon interaction energy [Eq. (52)] in units of J (averaging over TBC is performed). (c) Population of the zero-momentum electronic state multiplied by a factor of 100. TBC are used to generate f_k for $NN_\theta = 48$ values of k in the IBZ and the overall normalization is such that the sum of these NN_θ values of f_k is equal to 1. (d) Fermion–boson correlation function [Eq. (53)] at distance of a single lattice spacing multiplied by a factor of 100 (PBC are used).

written as follows [87]:

$$C_{q_2 q_1}(t) = \delta_{q_2, -q_1} \frac{\hbar}{\pi} \int_{-\infty}^{+\infty} d\omega \mathcal{J}(\omega) \frac{e^{i\omega t}}{e^{\beta\hbar\omega} - 1}, \quad (74)$$

where the spectral density of the electron–phonon interaction for the (single-mode) Holstein model

$$\mathcal{J}(\omega) = \frac{\pi}{\hbar} \left(\frac{\gamma}{\sqrt{N}} \right)^2 [\delta(\omega - \omega_0) - \delta(\omega + \omega_0)] \quad (75)$$

has two discrete peaks at $\pm\omega_0$. In Sec. V of SM [80], we demonstrate that the replacement $\mu_{qm} \rightarrow \mu_{qm} + \eta$ means that, on the level of the spectral density, delta peaks should be replaced by Lorentzians characterized by the full width at half maximum η . Equation (75) is then replaced by the so-called underdamped Brownian oscillator spectral density [88]

$$\mathcal{J}(\omega) = \Lambda \left[\frac{\omega\eta}{(\omega - \omega_0)^2 + \eta^2} + \frac{\omega\eta}{(\omega + \omega_0)^2 + \eta^2} \right], \quad (76)$$

where $\Lambda = \gamma^2/(N\hbar\omega_0)$ is the appropriate polaron binding energy. The demonstration in Sec. V of SM [80] leans on the fact that the artificial broadening is the smallest energy scale in the problem, i.e., $\eta \ll \omega_0$ and $\hbar\eta \ll k_B T$. These assumptions

are commonly satisfied whenever spectral lines are artificially broadened [36,40].

As a numerical example beyond the single-site limit, in Fig. 1 we discuss how different levels of artificial broadening η affect the Green’s function in real time [panels (a1)–(c1)] and the spectral function [panels (a2)–(c2)] in the intermediate-coupling regime and at relatively low temperature. The broadening renders our HEOM method more numerically stable by ensuring that all dynamical quantities decay to zero on a time scale $\sim\eta^{-1}$, compare Figs. 1(b1) and 1(c1) to Fig. 1(a1), in which the Green’s function at long times oscillates around zero. However, we see that already $\eta/\omega_0 = 0.01$ greatly underestimates the decay time of the Green’s function, which means that the width of the quasiparticle peak and its first phonon replica is greatly overestimated, compare Figs. 1(b2) and 1(c2) to Fig. 1(a2). In the following, we will not introduce any artificial broadening to our HEOM.

IV. NUMERICAL RESULTS

We assume that the phonons are dispersionless, $\omega_q = \omega_0$, and focus on the so-called extreme quantum regime, $\hbar\omega_0/J = 1$, in which the approximate treatments specifically developed for the adiabatic and antiadiabatic regimes are not appropriate. Furthermore, we limit our investigations to the most challenging crossover regime $\gamma/J = \sqrt{2}$, in which the dimensionless electron–phonon coupling constant is $\lambda = \gamma^2/(2J\hbar\omega_0) = 1$. As the default value of the temperature, we choose $k_B T/J = 1$. All of these dimensionless ratios ($\hbar\omega_0/J$, γ/J , and $k_B T/J$) will be changed, one at a time, to examine the applicability of the HEOM method in various parameter regimes (low-/high-temperature, weak-/strong-coupling, adiabatic/antiadiabatic regime).

A. Hierarchy rescaling, rotating-wave system, and twisted boundary conditions

The HEOM for $G^>$ and $G^<$ are both of the same form, see Eq. (30). It is known that propagating such a form of HEOM produces numerical instabilities, especially for very strong electron–phonon couplings [61]. Equation (27) suggests that the ADM at depth n scales as the $(2n)$ th power of the interaction strength, meaning that, for sufficiently strong interaction, the magnitude of ADMs increases with n . However, it is desirable that the magnitude of ADMs at deeper hierarchy levels be smaller than at shallower levels. This is accomplished by performing the hierarchy rescaling introduced in Ref. [61]. We define the dimensionless time $\tilde{t} = \omega_0 t$ and rescale the AGFs as follows:

$$\tilde{G}_{\mathbf{n}}^{(n)}(k - k_{\mathbf{n}}, \tilde{t}) = \omega_0^{-n} f(\mathbf{n}) G_{\mathbf{n}}^{(n)}(k - k_{\mathbf{n}}, \omega_0^{-1} \tilde{t}), \quad (77)$$

where the rescaling factor $f(\mathbf{n})$ reads as

$$f(\mathbf{n}) = \prod_{qm} [c_{qm}^{n_{qm}} n_{qm}!]^{-1/2}, \quad (78)$$

while the factor ω_0^{-n} renders $\tilde{G}_{\mathbf{n}}^{(n)}$ dimensionless. The dimensionless and rescaled HEOM then reads as

$$\begin{aligned} \partial_{\tilde{t}} \tilde{G}_{\mathbf{n}}^{(n)}(k - k_{\mathbf{n}}, \tilde{t}) &= -i \frac{\Omega_{k-k_{\mathbf{n}}} + \mu_{\mathbf{n}}}{\omega_0} \tilde{G}_{\mathbf{n}}^{(n)}(k - k_{\mathbf{n}}, \tilde{t}) \\ &+ i \sum_{qm} \sqrt{1 + n_{qm}} \sqrt{c_{qm}} \tilde{G}_{\mathbf{n}_{qm}}^{(n+1)}(k - k_{\mathbf{n}} - q, \tilde{t}) \\ &+ i \sum_{qm} \sqrt{n_{qm}} \sqrt{c_{qm}} \tilde{G}_{\mathbf{n}_{qm}}^{(n-1)}(k - k_{\mathbf{n}} + q, \tilde{t}). \end{aligned} \quad (79)$$

The numerical stability of the HEOM method is further enhanced by performing the transition to the so-called rotating-wave system by separating out the rapidly oscillating from the slowly changing component (the envelope) of $\tilde{G}_{\mathbf{n}}^{(n)}$ as follows:

$$\begin{aligned} \tilde{G}_{\mathbf{n}}^{(n)}(k - k_{\mathbf{n}}, \tilde{t}) &= \exp\left(-i \frac{\Omega_{k-k_{\mathbf{n}}} + \mu_{\mathbf{n}}}{\omega_0} \tilde{t}\right) \\ &\times \tilde{\tilde{G}}_{\mathbf{n}}^{(n)}(k - k_{\mathbf{n}}, \tilde{t}). \end{aligned} \quad (80)$$

We propagate the HEOM for the envelope $\tilde{\tilde{G}}_{\mathbf{n}}^{(n)}(k - k_{\mathbf{n}}, \tilde{t})$ using the fourth-order Runge–Kutta method. We use the time step $\Delta\tilde{t} = \omega_0 \Delta t = 0.02$ in all the computations to be presented.

Having computed $G^{>/<}(k, \tilde{t})$ for $0 \leq \tilde{t} \leq \tilde{t}_{\max}$, the spectral analysis is performed by first continuing the Green's function symmetrically for $-\tilde{t}_{\max} \leq \tilde{t} \leq 0$ according to $G^{>/<}(k, -\tilde{t}) = -G^{>/<}(k, \tilde{t})^*$ and then multiplying it with the Hann window function

$$w(\tilde{t}) = \cos^2\left(\frac{\pi\tilde{t}}{2\tilde{t}_{\max}}\right), \quad -\tilde{t}_{\max} \leq \tilde{t} \leq \tilde{t}_{\max}. \quad (81)$$

The maximum time \tilde{t}_{\max} is always long enough so that the signal windowing accurately captures the spectral content of the short-time dynamics and yet eliminates the long-time oscillations of $G^{>/<}$ around zero, which originate from finite-size effects. In most cases, we take $\tilde{t}_{\max} = 500$.

The imaginary-time HEOM [Eq. (46)] is rescaled in a similar manner. Its propagation in dimensionless imaginary time $\tilde{\tau} = \omega_0 \tau$ is performed from 0 to $\beta\hbar\omega_0$. Typical number of imaginary-time steps that is sufficient to obtain converged results for the electron–phonon equilibrium is of the order of 100.

The number of dynamical variables $G_{\mathbf{n}}^{(n)}(k - k_{\mathbf{n}}, t)$ entering the HEOM is in principle infinite. Nevertheless, converged results are obtained by truncating the hierarchy at certain maximum depth D . The number of active variables at depth n , $0 \leq n \leq D$, is $\binom{n+2N-1}{n}$, while their total number in the hierarchy is

$$n_{\text{active}} = \sum_{n=0}^D \binom{n+2N-1}{n} = \binom{2N+D}{D}. \quad (82)$$

The dimensionality of the hierarchy grows very fast with increasing the maximum depth D and even faster with increasing the system size N . This limits the applicability of the HEOM method to relatively small systems and moderate maximum depths.

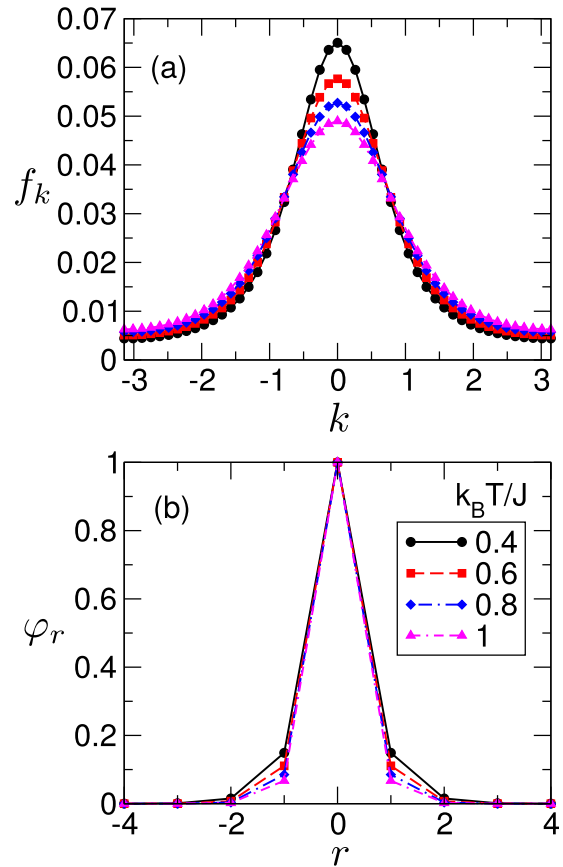


FIG. 3. (a) Electronic distribution over momenta f_k for different temperatures. TBC are used to generate f_k in NN_θ points in the IBZ and the overall normalization is such that the sum of these NN_θ values of f_k is equal to 1. (b) Fermion–boson correlation function φ_r for different temperatures (PBC are observed). Other model parameters assume the following values: $\hbar\omega_0/J = 1$, $\gamma/J = \sqrt{2}$, $N = 8$, $N_\theta = 6$, $D = 7$.

To reduce the influence of the finite-size effects on the thermodynamic quantities and to obtain $A(k, \omega)$ with a decent k -space resolution, we employ the twisted boundary conditions (TBC) [89], which are widely used to minimize one-body finite-size effects both at vanishing [40,41] and finite [90,91] electron densities. In practice, the free-electron dispersion relation ε_k appearing in Eq. (2) is replaced by $\varepsilon_{k\theta} = \varepsilon_e - 2J \cos(k + \theta)$, where θ is the twist angle. Even though the computations are performed on a finite chain of length N , the N allowed k points can be continuously connected by varying the twist angle through the range $[0, 2\pi/N]$. A typical choice for the values of the twist angle is $\theta_m = 2\pi m/(NN_\theta)$, where $m = 0, \dots, N_\theta - 1$.

B. Estimate of the maximum hierarchy depth

In computations based on HEOM it is always necessary to study if the depth D is sufficiently large so that the relevant quantities do not significantly change when D is increased further.

We show an example of such study for different thermodynamic quantities in Figs. 2(a)–2(d). Their dependence on D is shown in full dots in these figures. The computations are

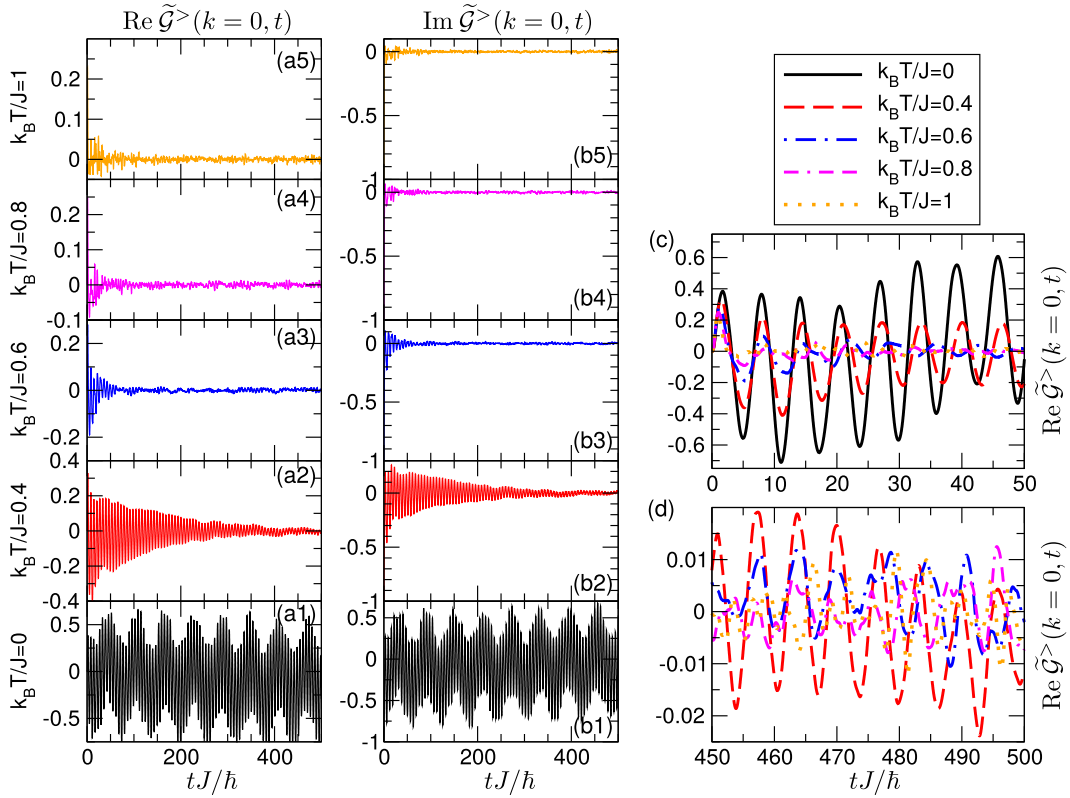


FIG. 4. Time dependence of the real [(a1)–(a5)] and imaginary part [(b1)–(b5)] of the envelope $\tilde{\mathcal{G}}^>(k=0, t)$ of the greater Green's function at $k=0$ for temperatures ranging from $k_B T/J=0$ [in (a1) and (b1)] to $k_B T/J=1$ [in (a5) and (b5)]. [(c), (d)] Time dependence of the envelope $\tilde{\mathcal{G}}^>(k=0, t)$ during the initial (c) and later (d) stages of temporal evolution for different temperatures. Other model parameters assume the following values: $\hbar\omega_0/J=1$, $\gamma/J=\sqrt{2}$, $N=8$, $N_\theta=6$, $D=7$.

performed on a lattice with $N=8$ sites, the twist angle θ may assume $N_\theta=6$ different values, while D is varied between 5 and 9. The results of the HEOM method are compared with QMC results represented by solid lines in Figs. 2(a)–2(d), while the width of the interval delimited by dashed lines is a measure of the statistical noise in QMC data. It is estimated by performing 10 different realizations of the QMC algorithm and computing the standard deviation of thus generated sample. The agreement between the HEOM and QMC results is remarkable. As a good compromise between the numerical effort and accuracy, we opt in this case for the maximum depth $D=7$, so that the number of active variables is $n_{\text{active}}=245157$.

An example of the estimate of D when the results for $G^>(k, t)$ and $A(k, \omega)$ are concerned is presented in Figs. 3 and 4 in Sec. VI of SM [80]. The figures demonstrate that the results in both time and frequency domains do not change significantly when D is increased from 7 to 8. At the same time, the late-time revival of oscillations in $\text{Re } \tilde{\mathcal{G}}^>(k=0, t)$ for $D=6$ indicates that $D=6$ may not be sufficient to obtain convergent results. These observations suggest that taking $D=7$ produces meaningful results for both $G^>(k, t)$ and $A(k, \omega)$ in this case.

C. Variations in temperature

The effects of the temperature variations on the electronic momentum distribution and the fermion–boson correlation

function are studied in Figs. 3(a) and 3(b), respectively. The TBC are employed to obtain the electronic momentum distribution on a relatively dense grid in the IBZ, as specified in greater detail in the caption of Fig. 3. As the temperature is increased, the momentum distribution flattens. At the same time, the corresponding real-space distribution $f_r = \frac{1}{N} \sum_k e^{ikr} f_k$ shrinks and develops a more pronounced peak at $r=0$, which suggests that the spatial extent of the polaron is decreased. This is also apparent from Fig. 3(b). These observations are in agreement with earlier results [47]. The results presented in Fig. 3(a) are further supported by their remarkable agreement with the corresponding QMC results, see Fig. 5 in Sec. VII of SM [80].

In Fig. 4 we present how temperature variations affect the time dependence of the envelope $\tilde{\mathcal{G}}^>(k=0, t)$ of the greater Green's function in the zone center. At zero temperature, the phonon-assisted processes proceed via virtual (coherent) phonons. There is no net energy exchange between the electron and the phonon subsystem, which is seen as the persistent oscillations in both the real and imaginary parts of $\tilde{\mathcal{G}}^>(k=0, t)$, see Figs. 4(a1) and 4(b1). As the temperature is increased, the oscillations in $\tilde{\mathcal{G}}^>(k=0, t)$ become damped, see Figs. 4(a2)–4(b5), which is a direct consequence of the energy exchange between the electron and thermally excited (incoherent) phonons. The higher the temperature, the more pronounced the damping of $\tilde{\mathcal{G}}^>(k=0, t)$. According to Fig. 4(c), the damping sets in already at the very initial stages of time evolution. Because of the finite-size effects,

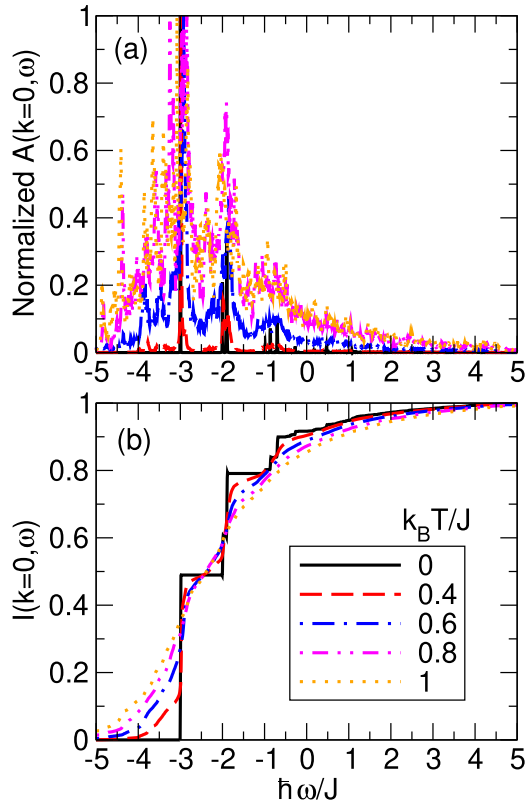


FIG. 5. (a) Spectral functions $A(k=0, \omega)$ for different temperatures. For the sake of graphical presentation, the spectral functions are renormalized so that the intensity of the QP peak at $\hbar\omega_{\text{QP}}/J \approx -3$ is equal to unity for all the temperatures examined. (b) Integrated spectral weight $I(k=0, \omega)$ [Eq. (83)] at different temperatures. The sum rule $\lim_{\omega \rightarrow +\infty} I(k=0, \omega) = 1$ is satisfied. Other model parameters assume the following values: $\hbar\omega_0/J = 1$, $\gamma/J = \sqrt{2}$, $N = 8$, $N_\theta = 6$, $D = 7$.

the envelopes at higher T do not decay to zero, but rather oscillate around it, see Fig. 4(d). At the latest instants we examine, the oscillation amplitude of $\text{Re } \tilde{G}^>(k=0, t)$ drops to less than 10% of its value around $t = 0$, compare the vertical-axis scales of Figs. 4(a2)–4(a5) and 4(d). At the same time, the amplitude of the imaginary part drops to less than 1% of its initial value, which is equal to unity, see also Eq. (32). Transforming the data in Fig. 4 to the frequency domain, the corresponding spectral functions for $k=0$ at different temperatures are shown in Fig. 5(a). For the sake of graphical presentation, the spectral functions in Fig. 5(a) are normalized so that the quasiparticle (QP) peak, which is located around $\hbar\omega_{\text{QP}}/J \approx -3$, is of unit intensity. The position of the QP peak agrees very well with the results from the variational ground-state study [33], the cluster perturbation theory [92], and the momentum average approximation [36]. Figure 5(b) presents the integrated spectral weight

$$I(k, \omega) = \int_{-\infty}^{\omega} d\omega' A(k, \omega') \quad (83)$$

at $k=0$ for different temperatures. At zero temperature, the peaks of $A(k=0, \omega)$ are quite narrow and their structure closely resembles the single-site vibronic progression, see the

narrowest peaks in Fig. 5(a) and the step-like increments in $I(k=0, \omega)$ in Fig. 5(b). The small, but finite, peak width is the consequence of performing time propagation on a finite chain and up to finite maximum time t_{max} and employing the Hann windowing procedure [Eq. (81)]. As the temperature is increased, the peaks become broadened, and the intensity of the QP peak is redistributed towards lower energies, see the bottom left parts of Figs. 5(a) and 5(b). The peak broadening is determined by the decay time of the envelope $\tilde{G}^>(k=0, t)$, see Fig. 4, and is larger at higher temperature. The spectral-intensity shift originates from the process in which the electron destroys one or more thermally excited phonons. The higher is the temperature, the larger is the number of thermal phonons and the more pronounced is the shift, compare $I(k=0, \omega)$ curves for different temperatures in the region $\omega < \omega_{\text{QP}}$ in Fig. 5(b). The integrated spectral density satisfies the sum rule for the spectral function $\int d\omega A(k, \omega) = 1$, see the upper right part of Fig. 5(b).

The momentum- and energy-resolved spectral functions $A(k, \omega)$ for three different temperatures are compared in Figs. 6(a)–6(c). At zero temperature, our result for $A(k, \omega)$, see Fig. 6(a), agrees quite well with the zero-temperature results of the cluster perturbation theory [92] and the momentum average approximation [36], as well as with the low-temperature results of the finite-temperature Lanczos method [40]. For a single electron on an infinite chain, the QP peak at $\omega_{\text{QP}}(k)$ is a delta function, while satellite peaks are of nonzero width. In that case, the lowest-energy polaronic band, which is energetically narrow enough so that it is entirely below the minimum energy for inelastic scattering $\hbar\omega_{\text{QP}}(k=0) + \hbar\omega_0$, is perfectly coherent, while higher-energy bands formed by satellite peaks are incoherent [39]. On finite chains studied here, the width of the QP peak is essentially determined by the frequency resolution π/t_{max} [we continue $G^>(k, t)$ to negative times $-t_{\text{max}} \leq t \leq 0$], so that the lowest-lying band in Fig. 6(a) may be regarded as perfectly coherent. The satellite peaks at each k display some structure, mainly due to the finite chain length N , and are thus somewhat wider, see the band whose minimum lies at $\hbar\omega/J \approx -2$ in Fig. 6(a). This band may be regarded as incoherent. As the temperature is increased, in addition to the broadening of the bands, the spectral intensity redistributes towards the region $\omega < \omega_{\text{QP}}(k)$. This intensity redistribution is most pronounced in the vicinity of the zone center, where the QP weight is appreciable. At $k_B T/J = 0.6$, due to the moderate spectral-intensity redistribution, the (broadened) polaronic band together with the associated one-phonon replica can still be recognized, see Fig. 6(b). On the other hand, at $k_B T/J = 1$, the spectral-intensity redistribution and the broadening are so pronounced that all the features of the zero-temperature spectrum merge into a continuum-like structure, see Fig. 6(c).

D. Variations in the electron–phonon coupling constant

The stronger the electron–phonon coupling, the larger the maximum depth of the hierarchy needed to obtain meaningful results. To keep the numerical effort within reasonable limits, varying the electron–phonon coupling we varied both the maximum depth D and the number of sites N . The precise

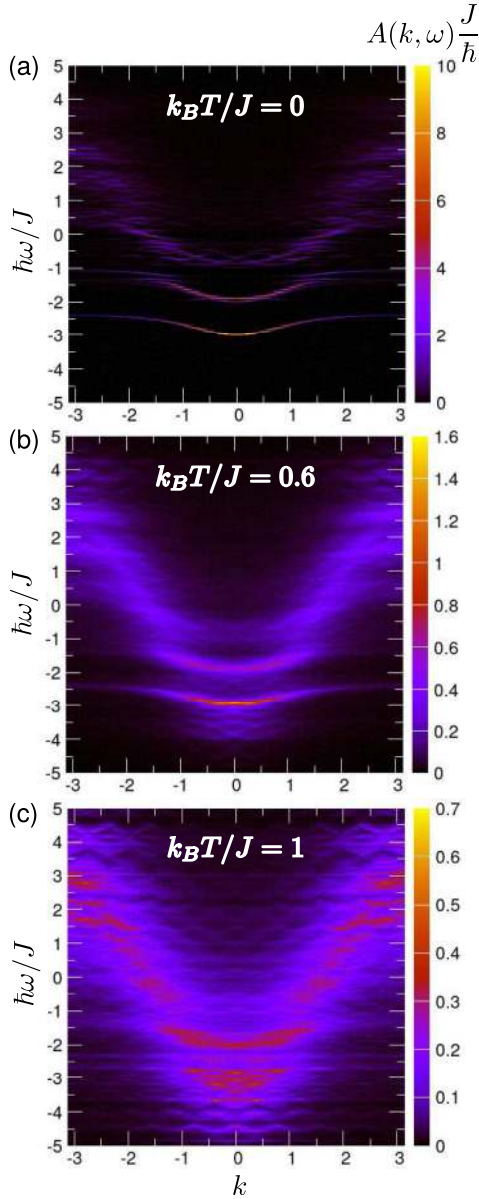


FIG. 6. Spectral function $A(k, \omega)$ at temperatures (a) $T = 0$, (b) $k_B T/J = 0.6$, and (c) $k_B T/J = 1$. Other model parameters assume the following values: $\hbar\omega_0/J = 1$, $\gamma/J = \sqrt{2}$, $N = 8$, $N_\theta = 6$, $D = 7$.

values of the model parameters that are changed together with the electron–phonon coupling are summarized in Table I.

As the dimensionless electron–phonon coupling constant λ is increased from 0.5 to 1 and 2 (γ/J is increased from 1 to $\sqrt{2}$ and 2), the electronic momentum distribution flattens, see

TABLE I. Values of model parameters that are changed together with the electron–phonon coupling constant.

Regime	γ/J	λ	N	N_θ	D	n_{active}
Weak-coupling	1	0.5	10	5	6	230 230
Intermediate-coupling	$\sqrt{2}$	1	8	6	7	245 157
Strong-coupling	2	2	6	8	9	293 930

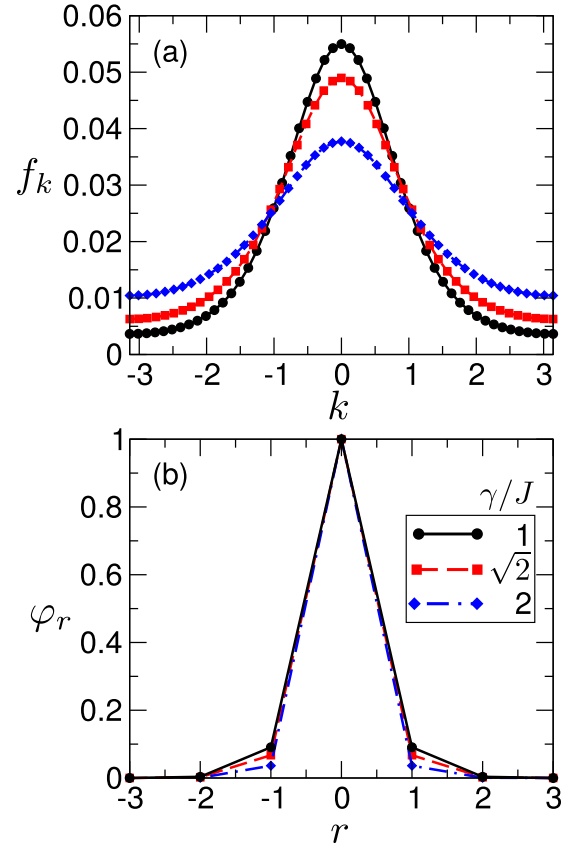


FIG. 7. (a) Electronic distribution in the momentum space for different values of the electron–phonon coupling constant γ (or λ). TBC are used to generate f_k in NN_θ points in the IBZ and the overall normalization is such that the sum of these NN_θ values of f_k is equal to 1. (b) Fermion–boson correlation function (PBC are observed) for different values of the electron–phonon coupling constant γ (or λ). Other model parameters assume the following values: $k_B T/J = 1$, $\hbar\omega_0/J = 1$, while the values of N , N_θ , and D are summarized in Table I.

Fig. 7(a), which together with the narrowing of the peak of the fermion–boson correlation function displayed in Fig. 7(b) suggests that the polaron becomes more localized. Increasing the electron–phonon coupling strength thus has similar effects on the equilibrium polaron properties as increasing the temperature, compare Figs. 3 and 7, which is in line with existing studies [47]. The results presented in Fig. 7(a) are further supported by their remarkable agreement with the corresponding QMC results, see Fig. 6 in Sec. VII of SM [80].

Spectral properties for different interaction strengths and temperatures are summarized in Figs. 8(a1)–8(c2). The zero-temperature results presented in Figs. 8(a1) and 8(c1) compare favorably to available zero-temperature [36,92] and low-temperature [40,42] results for $A(k, \omega)$. Moreover, our result for the polaronic band $\omega_{\text{QP}}(k)$ (under TBC) in the weak-coupling regime, see Fig. 8(a1), is in good agreement with the ground-state polaronic dispersion relation obtained in Ref. [33]. In the strong-coupling regime and at $T = 0$, see Fig. 8(c1), a clearly observable peak appears above the QP peak $\hbar\omega_{\text{QP}}/J \sim -4.4$ and below its one-phonon replica, in our case at around $\hbar\omega_{\text{BP}}/J \sim -3.55$. This peak corresponds

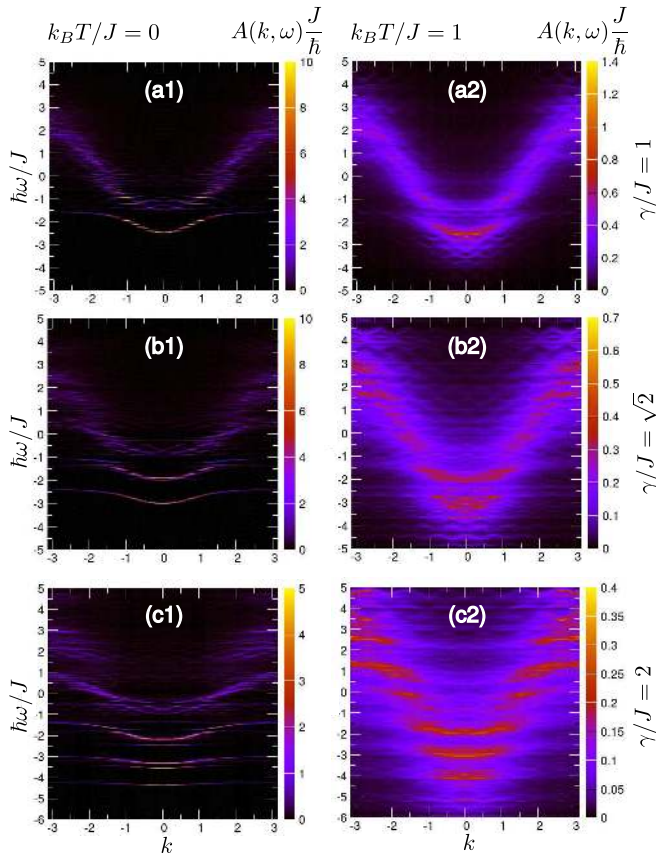


FIG. 8. Spectral function $A(k, \omega)$ (measured in units \hbar/J) for different electron–phonon interaction strengths [$\gamma/J = 1$ in (a1) and (a2), $\gamma/J = \sqrt{2}$ in (b1) and (b2), $\gamma/J = 2$ in (c1) and (c2)] and different temperatures [$k_B T/J = 0$ in (a1)–(c1) and $k_B T/J = 1$ in (a2)–(c2)]. The optical-phonon energy is $\hbar\omega_0/J = 1$, while the values of N , N_θ , and D are summarized in Table I.

to the so-called bound polaron state, in which a phonon is bound to the polaron [33,40]. At $k_B T/J = 1$, our data presented in Fig. 8(b2) overall agree with the results of the finite-temperature Lanczos method, see Fig. 2(d) of Ref. [40]. The spectral-intensity shift below the polaronic band becomes both larger and more intensive as the electron–phonon coupling is increased. In the weak- and intermediate-coupling regimes, the smearing of the (shifted) polaronic band makes it barely recognizable at finite temperature, see Figs. 8(a2) and 8(b2). On the other hand, in the strong-coupling regime, see Fig. 8(c2), the peaks at finite T are clearly recognizable, mutually separated by $\hbar\omega_0/J$, and resemble the vibronic progression in the single-site limit. Previous studies [92] suggested that the physical effects in the strong-coupling regime are predominantly local, which is also reflected in the very narrow polaronic band observed in Fig. 8(c1).

E. Variations in the optical phonon frequency

Here, we vary both the phonon energy $\hbar\omega_0/J$ and the coupling constant γ/J in such a way that we remain in the strong-coupling regime $\lambda = 2$, which limits our investigations to $N = 6$ -site chains. The temperature is fixed to its default

TABLE II. Values of model parameters that are changed together with the optical phonon frequency.

Regime	$\hbar\omega_0/J$	γ/J	N	N_θ	D	n_{active}
Adiabatic	0.2	$\sqrt{0.8}$	6	8	11	1 352 078
Extreme quantum	1	2	6	8	9	293 930
Antiadiabatic	3	$\sqrt{12}$	6	8	9	293 930

value $k_B T/J = 1$, while the precise values of the model parameters varied are summarized in Table II.

The adiabatic regime, $\hbar\omega_0/J = 0.2$, is numerically most challenging for the HEOM method. At the temperature we consider, $k_B T/J = 1$, the number of thermally excited phonons is large [$k_B T/(\hbar\omega_0) = 5$], and the hierarchical couplings are strong because they are determined by the product of the large electron–phonon coupling constant and the large number of thermally excited phonons. Therefore, one should study in more detail how the results for $G^>(k, t)$ and $A(k, \omega)$ change with the maximum hierarchy depth D . In Figs. 7 and 8 in Sec. VIII of SM [80] we compare the real-time and real-frequency data in the adiabatic regime for maximum hierarchy depths $D = 9, 10$, and 11. While the real-time data for $D = 10$ and 11 are to some extent similar, their spectral content seems to be very different. A comparison between the QMC and HEOM results, which is performed in Fig. 9 in Sec. VIII of SM [80], reveals that, as D is increased from 9 to 11, the agreement between the QMC and HEOM results in imaginary time becomes better. This favorable comparison suggests that the HEOM results for $A(k, \omega)$ obtained using $D = 11$, which

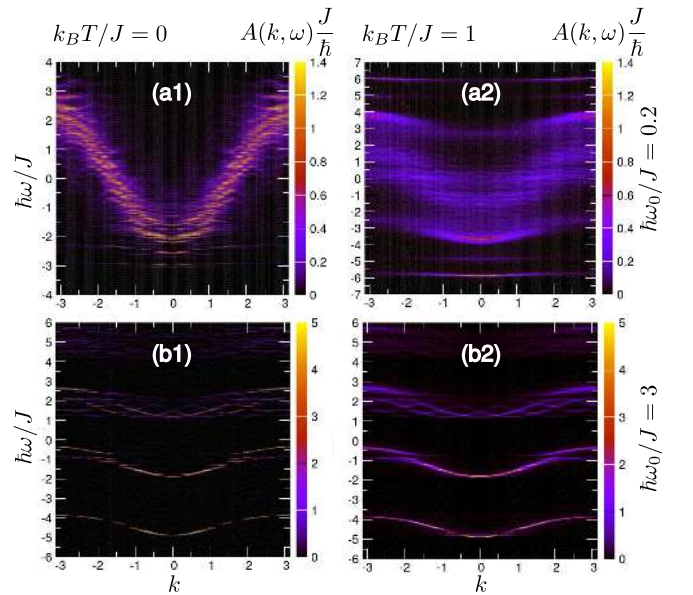


FIG. 9. Spectral function $A(k, \omega)$ (measured in units \hbar/J) for different values of the adiabaticity ratio [$\hbar\omega_0/J = 0.2$ in (a1) and (a2), $\hbar\omega_0/J = 3$ in (b1) and (b2)] and temperature [$T = 0$ in (a1) and (b1), $k_B T/J = 1$ in (a2) and (b2)]. The changes in the electron–phonon interaction strength that are necessary to remain in the strong-coupling regime ($\lambda = 2$) are summarized in Table II. The vertical-axis ranges in (a1) and (a2) are different.

are shown in Figs. 9(a1) (at $T = 0$) and 9(a2) (at $k_B T/J = 1$), may be representative of the true result.

In the antiadiabatic regime, $\hbar\omega_0/J = 3$, the temperature we study is relatively low, $k_B T/(\hbar\omega_0) = 1/3$, so that the zero-temperature spectrum in Fig. 9(b1) is quite similar to the finite-temperature spectrum in Fig. 9(b2). The spectrum consists of the polaronic band, the QP peak being located at $\hbar\omega_{\text{QP}}/J \sim -4.9$, which is accompanied by its single-phonon and two-phonon replicas, whose minima lie at approximately $\hbar(\omega_{\text{QP}} + \omega_0)/J$ and $\hbar(\omega_{\text{QP}} + 2\omega_0)/J$, respectively. In contrast to the zero-temperature bands in Fig. 9(b1), the finite-temperature bands in Fig. 9(b2) are somewhat broadened. The bandwidth $W_{\text{pol}}(T=0)$ of the polaronic band at $T = 0$ agrees reasonably well with the Lang–Firsov prediction $W_{\text{pol}}(T=0)/W_0 = \exp(-\gamma^2/(\hbar\omega_0)^2)$ ($W_0 = 4J$ is the bare bandwidth), while the corresponding finite-temperature expression $W_{\text{pol}}(T)/W_0 = \exp(-\gamma^2 \coth(\beta\hbar\omega_0/2)/(\hbar\omega_0)^2)$ underestimates the width of the lowest-lying band in Fig. 9(b2).

F. Electron-removal spectral function

Figure 10(a) presents the electron-removal spectral function $A^+(k, \omega)$ defined in Eq. (14) for $\gamma/J = \sqrt{2}$, $\hbar\omega_0/J = 1$, and $k_B T/J = 0.4$. We observe a prominent band whose minimum is situated at the quasiparticle peak $\hbar\omega_{\text{QP}}/J \sim -3$ along with its single-phonon replica, which is much less intense and starts at $\hbar(\omega_{\text{QP}} + \omega_0)/J$. The bands at frequencies $\omega < \omega_{\text{QP}}$ are not well resolved, but one can still glimpse certain wide structures whose minima lie at $\hbar(\omega_{\text{QP}} - n\omega_0)/J$, $n = 1, 2, 3$, and whose intensity diminishes as n is increased. The results summarized in Fig. 10(a) overall agree with the results for $A^+(k, \omega)$ presented in Ref. [42] for the same parameter regime. $A^+(k, \omega)$ satisfies the sum rule

$$\int_{-\infty}^{+\infty} d\omega A^+(k, \omega) = f_k \quad (84)$$

where f_k is the population of electronic state with momentum k .

According to the fluctuation–dissipation theorem [79], $A(k, \omega)$ and $A^+(k, \omega)$ are not mutually independent and are related by

$$A(k, \omega) = \mathcal{N} e^{\beta\hbar\omega} A^+(k, \omega). \quad (85)$$

The normalization constant \mathcal{N} enters Eq. (85) because A and A^+ satisfy different sum rules, while its value

$$\mathcal{N} = \sum_k \int_{-\infty}^{+\infty} d\omega A(k, \omega) e^{-\beta\hbar\omega} \quad (86)$$

is determined by the requirement that the number of electrons is equal to unity. To numerically check the validity of Eq. (85), in Fig. 10(b) we plot the spectral function $A(k=0, \omega)$ in the zone center computed using $G^>(k=0, t)$ [Eq. (13), solid line] and $G^<(k=0, t)$ [Eqs. (14), (85), and (86), dashed line]. Figure 10(c) presents the relative deviation between the results obtained in these two manners. While already Fig. 10(a) indicates that the agreement is good, Fig. 10(c) reveals that the relative difference between the data originating from $G^>$ and

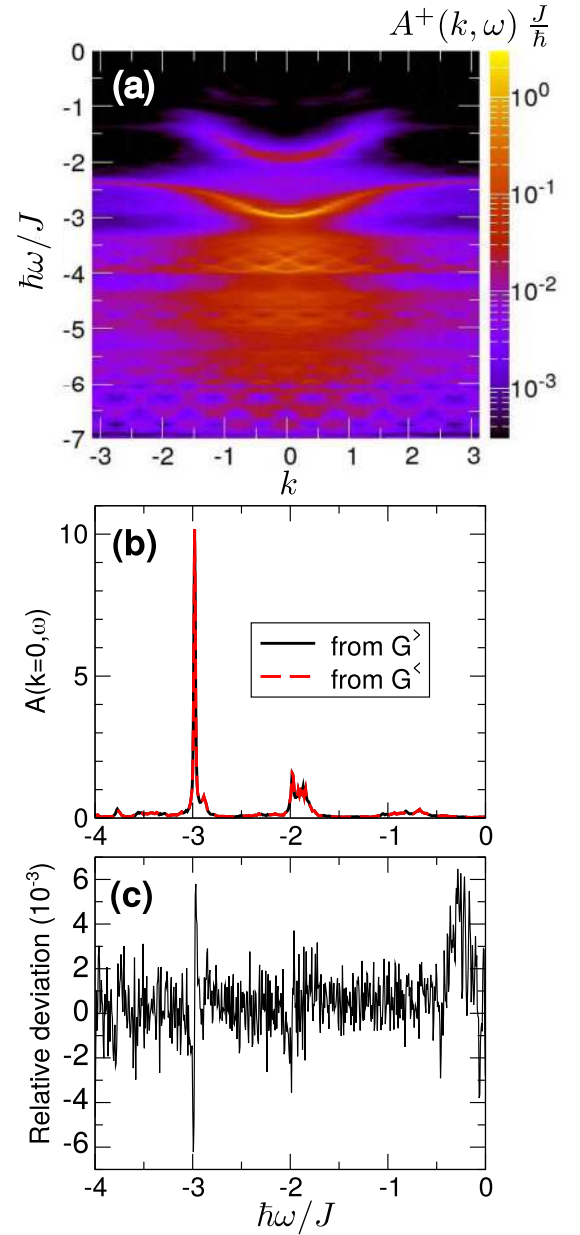


FIG. 10. (a) Momentum- and energy-resolved electron-removal spectral function $A^+(k, \omega)$ for $\gamma/J = \sqrt{2}$, $\hbar\omega_0/J = 1$, and $k_B T/J = 0.4$. Note the logarithmic scale of the color bar. [(b),(c)] Numerical verification of the fluctuation–dissipation theorem for A and A^+ . (b) Spectral function $A(k=0, \omega)$ in the zone center obtained using Eq. (13) (solid line, labeled “from $G^>$ ”) and using Eqs. (14), (85), and (86) (dashed line, labeled “from $G^<$ ”). (c) Relative deviation (in 10^{-3}) of $A(k=0, \omega)$ obtained from $G^>$ with respect to $A(k=0, \omega)$ obtained from $G^<$.

$G^<$ oscillates around zero and is smaller than 1%. These results offer further support for the correctness of our numerical implementation of the HEOM method.

G. Finite-size effects

The numerical cost of the HEOM method significantly increases with the chain length N , see Eq. (82). In all previous computations, N was restricted to relatively small values

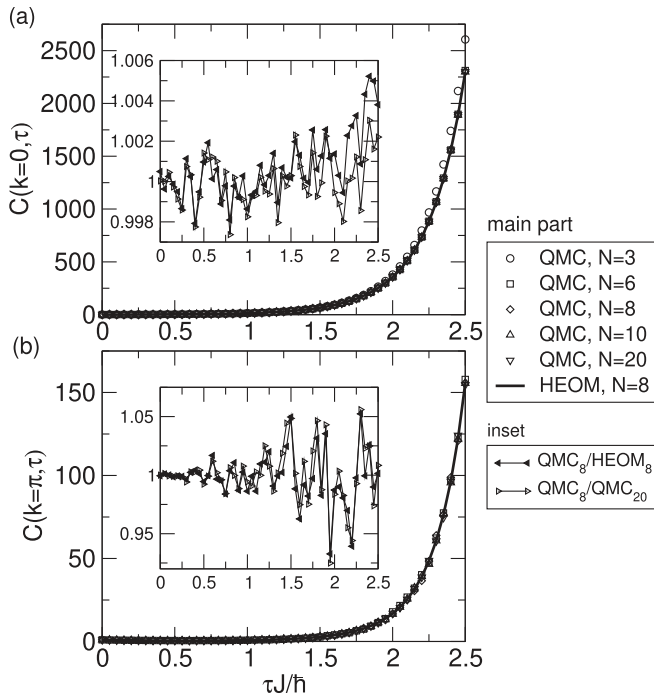


FIG. 11. Imaginary-time correlation function $C(k, \tau)$ [Eqs. (12) and (15)] (a) in the zone center $k = 0$ and (b) at the zone edge $k = \pi$ computed using QMC with different chain lengths (empty symbols) and HEOM (solid line). Insets present the ratio of QMC and HEOM results for $N = 8$ (full left-triangles) and the ratio of QMC results for $N = 8$ and $N = 20$ (empty right-triangles). The model parameters assume the following values: $k_B T/J = 0.4$, $\hbar\omega_0/J = 1$, and $\gamma/J = \sqrt{2}$.

(between 6 and 10). It is therefore highly important to understand how the finite-size effects influence the results presented so far. To that end, we compare the imaginary-time correlation functions obtained from the HEOM spectral function [Eq. (15)] and the QMC computations [Eq. (12)]. In addition to examining finite-size effects, the comparison of the HEOM and QMC results provides an independent check of the HEOM results, which makes this study self-contained.

In Figs. 11(a) and 11(b) we compare the QMC results for different chain lengths (empty symbols) with the HEOM result (solid line) for $k_B T/J = 0.4$, $\hbar\omega_0/J = 1$, and $\gamma/J = \sqrt{2}$. A more detailed comparison between the QMC and HEOM results for the fixed chain length is performed by calculating their mutual ratio, see the full left-triangles in the insets. The influence of the chain length on the imaginary-time results can be inferred from the ratio of QMC results for two very different chain lengths, see the empty right-triangles in the insets. The QMC results in Fig. 11(a) are virtually independent of N as long as $N \geq 8$, and the agreement between the QMC results for an 8-site and a 20-site chain is up to 0.3%, see the empty right-triangles in the inset of Fig. 11(a). The oscillations of the ratio $\text{QMC}_8/\text{QMC}_{20}$ reflect the statistical noise in the QMC data. The HEOM result (for $N = 8$) agrees with the corresponding QMC result up to 0.6%, see the full left-triangles in the inset of Fig. 11(a). Apart from the oscillations that reflect QMC statistical noise, there is also a systematic deviation of the QMC from the HEOM data that increases with τ . Keeping

in mind that $C(k, \beta J)$ is proportional to the equilibrium population of state $|k\rangle$, we may conclude that the aforementioned systematic deviation reflects small differences between the momentum distribution function obtained within QMC and HEOM methods, see also Fig. 5(b) in Sec. VII of SM [80]. At the zone edge, the QMC and HEOM results exhibit somewhat worse agreement, see the full left-triangles in the inset of Fig. 11(b), yet their relative difference is smaller than 5% for all τ . The systematic deviation between the HEOM and QMC data is hidden by the very strong noise in the QMC data. The statistical noise is much stronger at the zone boundary than in the zone center, compare the ranges of the vertical axes in the insets of Figs. 11(a) and 11(b), and, in principle, it could be eliminated by increasing the statistical sample of the QMC computation. We have checked that this is indeed the case by performing QMC calculations for $N = 8$ sites with the statistical sample that is 10 and 100 times larger than the one used in Figs. 11(a) and 11(b). The results of these calculations are presented in Figs. 10(a)–10(d) in Sec. IX of SM [80]. There, we observe that increasing sample size reduces the statistical noise in the QMC data and ultimately reveals a small systematic deviation between the HEOM and QMC data whose magnitude is consistent with the small differences between the HEOM and QMC momentum distribution functions, see also Fig. 11(a) and Fig. 5 of SM [80]. This relatively low-temperature regime is challenging for both the QMC and HEOM methods. While QMC necessitates finer discretization of the quite long imaginary-time interval over which the algorithm is performed, the HEOM may encounter problems with the long-time weakly damped oscillations in the Green's functions, see Figs. 4(a2) and 4(b2).

As the temperature is increased, the finite-size effects become less pronounced, even for reduced interaction strengths. This may be concluded from Figs. 12(a) and 12(b), which is obtained for $k_B T/J = 1$, $\hbar\omega_0/J = 1$, and $\gamma/J = 1$. There, both in the zone center [Fig. 12(a)] and at the zone edges [Fig. 12(b)], QMC results depend very weakly on N (empty right-triangles in the insets) and agree quite well (up to 1%) with the HEOM results (full left-triangles in the insets).

For strong electron–phonon coupling and at elevated temperatures, the finite-size effects are also not very pronounced and the HEOM results agree very well with the QMC results, see Figs. 13(a) and 13(b) that are plotted for $k_B T/J = 1$, $\hbar\omega_0/J = 1$, and $\gamma/J = 2$. Similar conclusions may be drawn in the adiabatic and antiadiabatic regime, see Figs. 11 and 12 in Sec. X of SM [80], which display quite a good agreement between the QMC and HEOM imaginary-time correlation functions and suggest that the results obtained on $N = 6$ -site chains are representative of larger systems.

The imaginary-time results presented in this section do establish that the HEOM-method results on short chains are representative of larger systems and strongly suggest that the spectral functions presented in Secs. IV C–IV E are close to the true result. We put some caution on this claim by noting that the operator that transforms the real-frequency spectral function to imaginary-time correlation function has a non-trivial null-space. For this reason, several different spectral functions may yield the same correlation function in imaginary time within the given small uncertainty. Therefore the agreement of imaginary-time correlation functions obtained

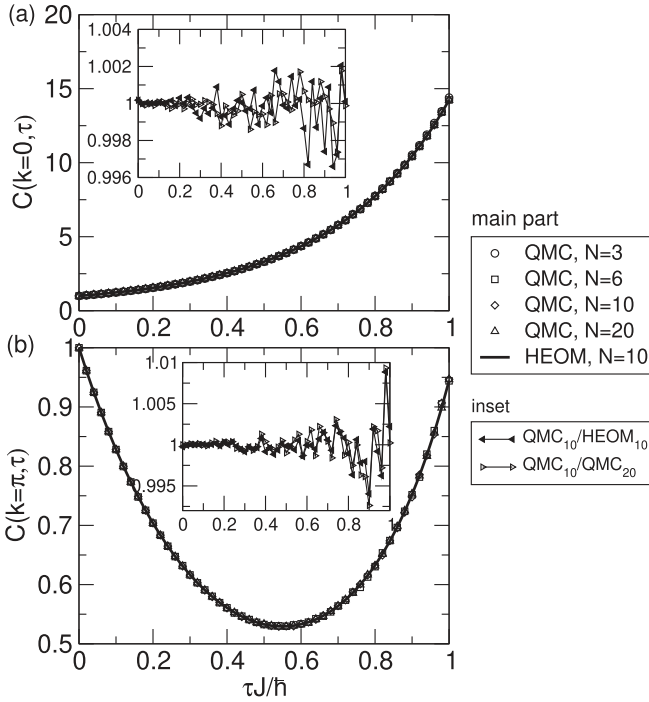


FIG. 12. Imaginary-time correlation function $C(k, \tau)$ [Eqs. (12) and (15)] (a) in the zone center $k = 0$ and (b) at the zone edge $k = \pi$ computed using QMC with different chain lengths (empty symbols) and HEOM (solid line). Insets present the ratio of QMC and HEOM results for $N = 10$ (full left-triangles) and the ratio of QMC results for $N = 10$ and $N = 20$ (empty right-triangles). The model parameters assume the following values: $k_B T/J = 1$, $\hbar\omega_0/J = 1$, and $\gamma/J = 1$.

by QMC and by transforming the HEOM spectral function does not provide a definite proof that HEOM spectral functions are accurate but it does provide a strong evidence. In our most recent paper [93], we compared the HEOM spectral functions with literature results for spectral functions obtained using the real-time/frequency numerically exact methods such as the finite-temperature Lanczos method [40,41] and the density-matrix renormalization group method [42]. Excellent agreement between our results and the literature results gives a definite proof of accuracy of HEOM for parameter values where literature results were available.

We note however that the number of sites when finite-size effects become negligible depends both on the parameters of the model and the physical quantity of interest. For example, in our previous work on the mobility in the Holstein model [49] we found that for small electron-phonon interaction when the mean free path is large, several tens of sites are required to obtain the converged result. Large number of sites is also necessary to obtain the long-time result if one is interested in the transport at finite bias [94].

V. DISCUSSION

Despite the unfavorable scaling of the amount of computational resources with system size [Eq. (82)], our HEOM approach to evaluate real-time correlation functions at finite

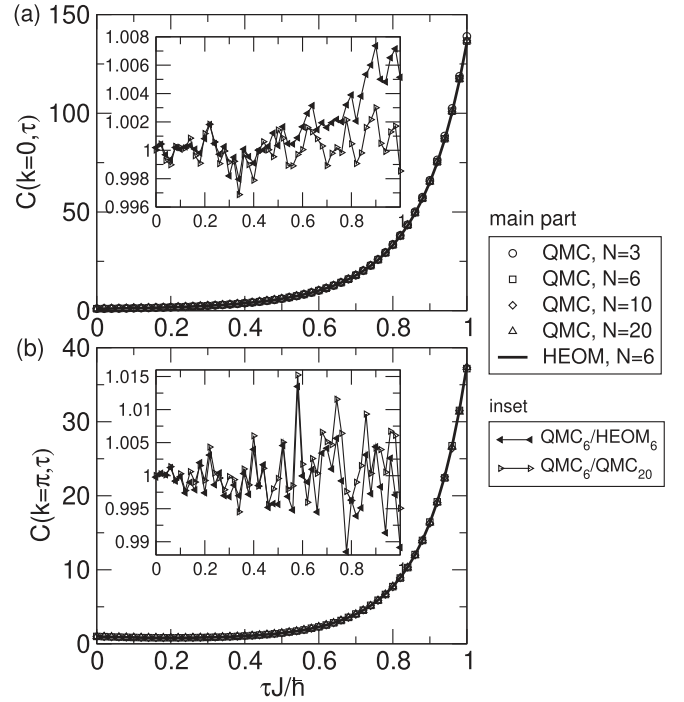


FIG. 13. Imaginary-time correlation function $C(k, \tau)$ [Eqs. (12) and (15)] (a) in the zone center $k = 0$ and (b) at the zone edge $k = \pi$ computed using QMC with different chain lengths (empty symbols) and HEOM (solid line). Insets present the ratio of QMC and HEOM results for $N = 6$ (full left-triangles) and the ratio of QMC results for $N = 6$ and $N = 20$ (empty right-triangles). The model parameters assume the following values: $k_B T/J = 1$, $\hbar\omega_0/J = 1$, and $\gamma/J = 2$.

temperatures occupies a special place in the gamut of numerical tools for interacting electron-phonon systems.

The exact diagonalization is a method of choice to accurately compute ground-state and finite-temperature spectral properties of relatively small clusters. However, obtaining real-time correlation functions is quite challenging. Furthermore, strictly speaking, the spectral function is a set of delta peaks on the frequency axis, and to get smooth spectra, one has to introduce artificial broadening. As discussed in Sec. III C, this artificial broadening actually changes the physical system we are dealing with by replacing a finite number of phonon modes by a thermodynamic reservoir consisting of infinitely many phonon modes. Even though the spectra become representative of the thermodynamic limit, the value of the broadening is to be chosen carefully [95]. On the one hand, it should be sufficiently large to remove finite-size effects, i.e., to damp the long-time oscillations in $G^>(k, t)$, see Fig. 4, to zero. On the other hand, it should be sufficiently small not to overbroaden the genuine features of spectra, i.e., not to affect the short-time decay of $G^>(k, t)$, see Fig. 4. In other words, even though the results are exact, the arbitrariness in the broadening casts doubts on the exactness of the physical quantities that may be obtained from the broadened data (e.g., the conductivity in the so-called bubble or independent-particle approximation [96], in which the current-current (two-particle) correlation function is approximated as the product of two single-particle correlation functions). QMC may treat larger clusters, as we

demonstrated, and thus minimize finite-size effects without introducing artificial broadenings. However, QMC methods to evaluate dynamic correlation functions may face severe problems. On the one hand, to obtain correlation functions on the real-frequency axis, one may perform the analytic continuation from the imaginary-frequency axis, which is in principle an ill-posed problem. On the other hand, one may attempt to directly evaluate correlation functions on the real-time axis, in which case the infamous sign problem is encountered. The difficulties in extracting real-time or real-frequency data from the results on the imaginary axis may be appreciated by contrasting Fig. 13 of the main text and Figs. 11 and 12 in Sec. X of SM [80], which are obtained in very different parameter regimes. The imaginary-time data in these cases are both qualitatively (the overall shape of the curves) and quantitatively (the vertical-axis ranges) similar to one another. Nevertheless, the spectral functions presented in Figs. 8(c2), 9(a2), and 9(b2) are considerably different from one another. In contrast to the above-discussed approaches, the HEOM method presented here deals directly with the real-time correlation functions and provides numerically exact results for the cluster of given size. HEOM data can be safely used to further compute physical quantities of interest, and the results will be numerically exact for the given system size. Even though we employed HEOM on relatively short chains, artificial broadening parameters are not necessary to obtain results representative of larger systems, which is demonstrated by the very good agreement between the imaginary-time correlation functions emerging from HEOM and QMC computations.

Another quantity relevant for the single-polaron problem is the phonon spectral function, which can be obtained from the greater Green's function in the phonon sector $D^>(q, t) = -i\langle [b_q(t) + b_{-q}^\dagger(t)][b_{-q} + b_q^\dagger] \rangle$. Its computation using the HEOM formalism developed here is complicated by at least two factors. Firstly, the partial trace over phonons lies at the heart of the HEOM formalism, meaning that correlation functions of mixed electron-phonon operators are not straightforwardly accessible from the purely electronic ADMs. Some other formalisms, such as the dissipaton equations of motion [62] or the generalized hierarchical equations [97,98], provide prescriptions to evaluate correlation functions of mixed electron-phonon operators using the ADMs. Secondly, while the hierarchy for $G^{>/<}(k, t)$ is single-sided [there is no backward evolution operator in Eqs. (16)–(19)], the hierarchy for $D^>(q, t)$ would be double-sided. The numerical effort to obtain $D^>(q, t)$ would thus be greater than in the case of $G^{>/<}(k, t)$.

Strictly speaking, the phonon spectral function in the zero-density limit, i.e., for one electron on an infinite chain, would be equal to the free-phonon spectral function directly accessible from Eq. (22) [99]. Even though our formulation is restricted to the single-electron case, the numerical results, which would be obtained on finite chains, would actually correspond to finite electron densities [99]. At low temperatures, the phonon spectra of the Holstein model on a finite chain feature the free-phonon line (bare, unrenormalized phonon line) at $\omega = \omega_0$ and a band that replicates the polaron band and whose minimum is at $(q, \omega) = (0, 0)$ [42,99,100]. The

minimum of the polaron band is at $\omega = 0$ because the zero-momentum phonon couples to the (constant) electron density, see Eq. (5). These features may be identified already in the single-site limit, when the phonon spectral function may be directly evaluated

$$iD^>(t) = [1 + n_{\text{BE}}(\omega_0, T)]e^{-i\omega_0 t} + 4\left(\frac{\gamma}{\hbar\omega_0}\right)^2 + n_{\text{BE}}(\omega_0, T)e^{i\omega_0 t}.$$

As the temperature is increased, the free-phonon line at negative frequency $\omega = -\omega_0$ acquires appreciable intensity, the reflected polaron band appears at $\omega < 0$, while the polaron band broadens at larger momenta [42].

Generally speaking, the extension of the developed method beyond the single-excitation case is not straightforward. This is most directly seen on the example of the equilibrium RDM (Sec. II C 4) within the Holstein model of mutually noninteracting spinless fermions (the many-fermion version of the present model). The expression for the RDM [Eq. (43)] and the definition of the ADM $\sigma_n^{(n, \text{un}, \text{eq})}(\tau)$ [Eq. (45)] remain the same as in the single-electron case, the only difference being that $V_q = \sum_k c_{k+q}^\dagger c_k$, cf. Eq. (5). However, the number of their nonzero matrix elements is significantly increased so that $\text{Tr}(c_{q_1}^\dagger \dots c_{q_l}^\dagger c_{p_1} \dots c_{p_m} \sigma_n^{(n, \text{un}, \text{eq})}) \neq 0$ only if $l = m$ and $q_1 + \dots + q_l - (p_1 + \dots + p_m) = k_n$. The evolution of single-particle quantities (singlets) depends on the evolution of two-particle quantities (doublets) etc., and one has to truncate the hierarchy induced by many-body effects and yet keep the hierarchy stemming from the electron-phonon interaction. One possibility is to employ the cluster-expansion method, see e.g., Ref. [74]. Another possibility, particularly appealing when studying time-dependent (exciton-)polaron formation triggered by a laser excitation [101], is the dynamics controlled truncation scheme, see Refs. [67,102]. For the Holstein-Hubbard model, an extension of the present approach is even more complicated, and the HEOM formalism has been successfully applied only to the Holstein-Hubbard dimer [103,104], where a direct enumeration of many-body states and the separation of different spin sectors are feasible.

Another aspect of our HEOM approach that is worth discussing is its symmetry-adapted formulation in the momentum space. While the application of the HEOM method to single-mode situations is not new [70,71,77], previous studies implemented the method in the real space, without exploiting its translational symmetry. In contrast to perturbative theories, which lean on approximations that have to be carried out in a specific basis (e.g., the momentum eigenbasis for the Redfield theory or the coordinate eigenbasis for the Marcus/Förster theory), the HEOM permits us to calculate the properties of interest in any basis. Furthermore, the equilibrium RDM of the electronic subsystem [Eq. (43)], as well as the Green's functions [Eq. (10)], can also be represented in any basis. However, the most convenient representation is the one in which the electronic RDM is diagonal. In that representation, the effects of the electron-phonon interaction on the reduced

electronic properties (i.e., the polaronic effects) are taken into account in the simplest possible way. The corresponding basis is known as the global basis [105], or pointer/preferred basis [68] in the framework of decoherence theory [106,107]. According to the momentum-conservation law, the electronic single-particle density matrix is diagonal in the eigenbasis $\{|k\rangle\}$ of the electronic momentum. We thus conclude that our momentum-space HEOM is indeed formulated in the preferred basis for the Holstein Hamiltonian.

Our optimal formulation of the problem comes with another advantage. The authors of Ref. [75] pointed out that the temporal propagation of the real-space HEOM method developed in Ref. [71] exhibits an exponential-instability wall. Having hit that wall, the observables diverge, and advanced techniques have to be employed to extract long-time dynamics of the single-mode Holstein model. All the results presented here unambiguously demonstrate that exploiting the translational symmetry of the model, i.e., transferring to the preferred basis of the problem, renders the equations numerically stable and thus obviates the need for advanced tools to mitigate potential instabilities. We propagated our symmetry-adapted HEOM in various parameter regimes up to quite long times $\omega_0 t_{\max} \sim 500$ with a moderate time step $\omega_0 \Delta t = 0.02$, see Fig. 4, and observed no sign of numerical instabilities in our data.

VI. CONCLUSIONS

We develop a novel HEOM-based approach that is specifically suited for evaluation of real-time single-particle correlation functions and thermodynamic properties of the Holstein Hamiltonian at finite temperature. The conservation of the total momentum enables us to formulate the hierarchy in the momentum space, so that its dynamical variables describe multiphonon absorption and emission processes in which the momentum is exchanged between the electron and quantum vibrations. Our momentum-space formulation is superior to the commonly used real-space formulation because it circumvents known numerical problems that arise during the propagation of the real-space HEOM.

We use our HEOM approach to compute the spectral function and thermodynamic quantities of the one-dimensional

Holstein model containing up to 10 sites. Our results agree quite well with the available results of the finite-temperature Lanczos method, the coupled-cluster theory, and the momentum average approximation. A further support to the HEOM approach comes from the comparison with imaginary-time data obtained using our QMC approach that provides access to the properties of larger chains. QMC results demonstrate that finite size effects are not pronounced and that relatively short chains, containing 5–10 sites, capture the behavior characteristic for longer chains.

All these results suggest that our HEOM approach may greatly contribute to future studies of finite-temperature Holstein polaron dynamics. Using advanced propagation techniques [108], our approach may become viable for larger or higher-dimensional systems and in multimode situations. It is interesting to note that our study is concurrent with other works aiming at extending the methods commonly applied to molecular systems (chemical-physics realm) to band-like situations (condensed-matter realm) [109]. Our method may contribute to revealing the (exciton-)polaron formation dynamics, which is highly relevant for a proper interpretation of ultrafast experimental signals in molecular aggregates [105], organic semiconductors [110], and photosynthetic pigment-protein complexes [101]. Finally, the HEOM developed here may be readily used to study finite-temperature transport properties of the Holstein model by approximating a two-particle correlation function as the product of two single-particle correlation functions [96].

ACKNOWLEDGMENTS

We acknowledge funding provided by the Institute of Physics Belgrade, through the Grant by the Ministry of Education, Science, and Technological Development of the Republic of Serbia. Numerical computations were performed on the PARADOX-IV supercomputing facility at the Scientific Computing Laboratory, National Center of Excellence for the Study of Complex Systems, Institute of Physics Belgrade. We thank Darko Tanasković and Petar Mitrić for insightful and stimulating discussions.

-
- [1] A. Köhler and H. Bässler, *Electronic Processes in Organic Semiconductors* (Wiley-VCH, Weinheim, 2015).
 - [2] V. Coropceanu, J. Cornil, D. A. da Silva Filho, Y. Olivier, R. Silbey, and J.-L. Brédas, Charge transport in organic semiconductors, *Chem. Rev.* **107**, 926 (2007).
 - [3] M. Mladenović and N. Vukmirović, Charge carrier localization and transport in organic semiconductors: Insights from atomistic multiscale simulations, *Adv. Funct. Mater.* **25**, 1915 (2015).
 - [4] S. J. Jang and B. Mennucci, Delocalized excitons in natural light-harvesting complexes, *Rev. Mod. Phys.* **90**, 035003 (2018).
 - [5] M. Schröter, S.D. Ivanov, J. Schulze, S.P. Polyutov, Y. Yan, T. Pullerits, and O. Kühn, Exciton–vibrational coupling in the dynamics and spectroscopy of Frenkel excitons in molecular aggregates, *Phys. Rep.* **567**, 1 (2015).
 - [6] V. van Amerongen, L. Valkunas, and R. van Grondelle, *Photosynthetic Excitons* (World Scientific, Singapore, 2000).
 - [7] T. Holstein, Studies of polaron motion: Part I. The molecular-crystal model, *Ann. Phys. (NY)* **8**, 325 (1959).
 - [8] A. G. Redfield, The theory of relaxation processes, in *Advances in Magnetic Resonance*, Advances in Magnetic and Optical Resonance, Vol. 1, edited by J. S. Waugh (Academic Press, New York, 1965), pp. 1–32.
 - [9] Th. Förster, *Delocalized Excitation and Excitation Transfer. Bulletin No. 18*, Tech. Rep. FSU-2690-18 (Florida State Univ., Tallahassee. Dept. of Chemistry, 1964).
 - [10] R. A. Marcus, Electron transfer reactions in chemistry. Theory and experiment, *Rev. Mod. Phys.* **65**, 599 (1993).

- [11] A. Ishizaki and G. R. Fleming, On the adequacy of the Redfield equation and related approaches to the study of quantum dynamics in electronic energy transfer, *J. Chem. Phys.* **130**, 234110 (2009).
- [12] J. Ranninger and U. Thibblin, Two-site polaron problem: Electronic and vibrational properties, *Phys. Rev. B* **45**, 7730 (1992).
- [13] F. Marsiglio, The spectral function of a one-dimensional Holstein polaron, *Phys. Lett. A* **180**, 280 (1993).
- [14] G. Wellein, H. Röder, and H. Fehske, Polarons and bipolarons in strongly interacting electron-phonon systems, *Phys. Rev. B* **53**, 9666 (1996).
- [15] M. Capone, W. Stephan, and M. Grilli, Small-polaron formation and optical absorption in Su-Schrieffer-Heeger and Holstein models, *Phys. Rev. B* **56**, 4484 (1997).
- [16] G. Wellein and H. Fehske, Polaron band formation in the Holstein model, *Phys. Rev. B* **56**, 4513 (1997).
- [17] J. M. Robin, Spectral properties of the small polaron, *Phys. Rev. B* **56**, 13634 (1997).
- [18] C. Zhang, E. Jeckelmann, and S. R. White, Dynamical properties of the one-dimensional Holstein model, *Phys. Rev. B* **60**, 14092 (1999).
- [19] J. E. Hirsch, R. L. Sugar, D. J. Scalapino, and R. Blankenbecler, Monte Carlo simulations of one-dimensional fermion systems, *Phys. Rev. B* **26**, 5033 (1982).
- [20] H. De Raedt and A. Lagendijk, Critical Quantum Fluctuations and Localization of the Small Polaron, *Phys. Rev. Lett.* **49**, 1522 (1982).
- [21] H. De Raedt and A. Lagendijk, Numerical calculation of path integrals: The small-polaron model, *Phys. Rev. B* **27**, 6097 (1983).
- [22] H. De Raedt and A. Lagendijk, Numerical study of Holstein's molecular-crystal model: Adiabatic limit and influence of phonon dispersion, *Phys. Rev. B* **30**, 1671 (1984).
- [23] N. V. Prokof'ev and B. V. Svistunov, Polaron Problem by Diagrammatic Quantum Monte Carlo, *Phys. Rev. Lett.* **81**, 2514 (1998).
- [24] P. E. Kornilovitch, Continuous-Time Quantum Monte Carlo Algorithm for the Lattice Polaron, *Phys. Rev. Lett.* **81**, 5382 (1998).
- [25] M. Hohenadler, H. G. Evertz, and W. von der Linden, Quantum Monte Carlo and variational approaches to the Holstein model, *Phys. Rev. B* **69**, 024301 (2004).
- [26] P. E. Spencer, J. H. Samson, P. E. Kornilovitch, and A. S. Alexandrov, Effect of electron-phonon interaction range on lattice polaron dynamics: A continuous-time quantum Monte Carlo study, *Phys. Rev. B* **71**, 184310 (2005).
- [27] E. Jeckelmann and S. R. White, Density-matrix renormalization-group study of the polaron problem in the Holstein model, *Phys. Rev. B* **57**, 6376 (1998).
- [28] C. Zhang, E. Jeckelmann, and S. R. White, Density Matrix Approach to Local Hilbert Space Reduction, *Phys. Rev. Lett.* **80**, 2661 (1998).
- [29] R. J. Bursill, R. H. McKenzie, and C. J. Hamer, Phase Diagram of the One-Dimensional Holstein Model of Spinless Fermions, *Phys. Rev. Lett.* **80**, 5607 (1998).
- [30] Z. Ivić, D. Kapor, M. Škrinjar, and Z. Popović, Self-trapping in quasi-one-dimensional electron- and exciton-phonon systems, *Phys. Rev. B* **48**, 3721 (1993).
- [31] A. H. Romero, D. W. Brown, and K. Lindenberg, Converging toward a practical solution of the Holstein molecular crystal model, *J. Chem. Phys.* **109**, 6540 (1998).
- [32] G. Wellein and H. Fehske, Self-trapping problem of electrons or excitons in one dimension, *Phys. Rev. B* **58**, 6208 (1998).
- [33] J. Bonča, S. A. Trugman, and I. Batistić, Holstein polaron, *Phys. Rev. B* **60**, 1633 (1999).
- [34] L.-C. Ku, S. A. Trugman, and J. Bonča, Dimensionality effects on the Holstein polaron, *Phys. Rev. B* **65**, 174306 (2002).
- [35] M. Berciu, Green's Function of a Dressed Particle, *Phys. Rev. Lett.* **97**, 036402 (2006).
- [36] G. L. Goodvin, M. Berciu, and G. A. Sawatzky, Green's function of the Holstein polaron, *Phys. Rev. B* **74**, 245104 (2006).
- [37] S. Paganelli and S. Ciuchi, Tunnelling system coupled to a harmonic oscillator: An analytical treatment, *J. Phys.: Condens. Matter* **18**, 7669 (2006).
- [38] E. V. L. de Mello and J. Ranninger, Dynamical properties of small polarons, *Phys. Rev. B* **55**, 14872 (1997).
- [39] S. Ciuchi, F. de Pasquale, S. Fratini, and D. Feinberg, Dynamical mean-field theory of the small polaron, *Phys. Rev. B* **56**, 4494 (1997).
- [40] J. Bonča, S. A. Trugman, and M. Berciu, Spectral function of the Holstein polaron at finite temperature, *Phys. Rev. B* **100**, 094307 (2019).
- [41] J. Bonča and S. A. Trugman, Dynamic properties of a polaron coupled to dispersive optical phonons, *Phys. Rev. B* **103**, 054304 (2021).
- [42] D. Jansen, J. Bonča, and F. Heidrich-Meisner, Finite-temperature density-matrix renormalization group method for electron-phonon systems: Thermodynamics and Holstein-polaron spectral functions, *Phys. Rev. B* **102**, 165155 (2020).
- [43] M. Grover and R. Silbey, Exciton migration in molecular crystals, *J. Chem. Phys.* **54**, 4843 (1971).
- [44] D. R. Yarkony and R. Silbey, Variational approach to exciton transport in molecular crystals, *J. Chem. Phys.* **67**, 5818 (1977).
- [45] R. Silbey and R. W. Munn, General theory of electronic transport in molecular crystals. I. Local linear electron-phonon coupling, *J. Chem. Phys.* **72**, 2763 (1980).
- [46] K. Hannewald and P. A. Bobbert, Anisotropy effects in phonon-assisted charge-carrier transport in organic molecular crystals, *Phys. Rev. B* **69**, 075212 (2004).
- [47] Y.-C. Cheng and R. J. Silbey, A unified theory for charge-carrier transport in organic crystals, *J. Chem. Phys.* **128**, 114713 (2008).
- [48] F. Ortmann, F. Bechstedt, and K. Hannewald, Theory of charge transport in organic crystals: Beyond Holstein's small-polaron model, *Phys. Rev. B* **79**, 235206 (2009).
- [49] N. Prodanović and N. Vukmirović, Charge carrier mobility in systems with local electron-phonon interaction, *Phys. Rev. B* **99**, 104304 (2019).
- [50] J. H. Fetherolf, D. Golež, and T. C. Berkelbach, A Unification of the Holstein Polaron and Dynamic Disorder Pictures of Charge Transport in Organic Crystals, *Phys. Rev. X* **10**, 021062 (2020).
- [51] S. Fratini and S. Ciuchi, Dynamical Mean-Field Theory of Transport of Small Polarons, *Phys. Rev. Lett.* **91**, 256403 (2003).

- [52] S. Fratini and S. Ciuchi, Optical properties of small polarons from dynamical mean-field theory, *Phys. Rev. B* **74**, 075101 (2006).
- [53] G. L. Goodvin, A. S. Mishchenko, and M. Berciu, Optical Conductivity of the Holstein Polaron, *Phys. Rev. Lett.* **107**, 076403 (2011).
- [54] A. S. Mishchenko, N. Nagaosa, G. De Filippis, A. de Candia, and V. Cataudella, Mobility of Holstein Polaron at Finite Temperature: An Unbiased Approach, *Phys. Rev. Lett.* **114**, 146401 (2015).
- [55] W. Li, J. Ren, and Z. Shuai, Finite-temperature TD-DMRG for the carrier mobility of organic semiconductors, *J. Phys. Chem. Lett.* **11**, 4930 (2020).
- [56] Y. Tanimura, Stochastic Liouville, Langevin, Fokker–Planck, and master equation approaches to quantum dissipative systems, *J. Phys. Soc. Jpn.* **75**, 082001 (2006).
- [57] R.-X. Xu and Y. J. Yan, Dynamics of quantum dissipation systems interacting with bosonic canonical bath: Hierarchical equations of motion approach, *Phys. Rev. E* **75**, 031107 (2007).
- [58] A. Ishizaki and G. R. Fleming, Unified treatment of quantum coherent and incoherent hopping dynamics in electronic energy transfer: Reduced hierarchy equation approach, *J. Chem. Phys.* **130**, 234111 (2009).
- [59] Y. Tanimura, Numerically “exact” approach to open quantum dynamics: The hierarchical equations of motion (HEOM), *J. Chem. Phys.* **153**, 020901 (2020).
- [60] R.P. Feynman and F.L. Vernon, The theory of a general quantum system interacting with a linear dissipative system, *Ann. Phys. (NY)* **24**, 118 (1963).
- [61] Q. Shi, L. Chen, G. Nan, R.-X. Xu, and Y. Yan, Efficient hierarchical Liouville space propagator to quantum dissipative dynamics, *J. Chem. Phys.* **130**, 084105 (2009).
- [62] H.-D. Zhang, R.-X. Xu, X. Zheng, and Y. Yan, Statistical quasi-particle theory for open quantum systems, *Mol. Phys.* **116**, 780 (2018).
- [63] A. Ishizaki and G. R. Fleming, Theoretical examination of quantum coherence in a photosynthetic system at physiological temperature, *Proc. Natl. Acad. Sci. USA* **106**, 17255 (2009).
- [64] J. Strümpfer and K. Schulten, Open quantum dynamics calculations with the hierarchy equations of motion on parallel computers, *J. Chem. Theory Comput.* **8**, 2808 (2012).
- [65] D. M. Wilkins and N. S. Dattani, Why quantum coherence is not important in the Fenna–Matthews–Olsen complex, *J. Chem. Theory Comput.* **11**, 3411 (2015).
- [66] T. Kramer, M. Noack, A. Reinefeld, M. Rodríguez, and Y. Zelinsky, Efficient calculation of open quantum system dynamics and time-resolved spectroscopy with distributed memory HEOM (DM-HEOM), *J. Comput. Chem.* **39**, 1779 (2018).
- [67] V. Janković and T. Mančal, Exact description of excitonic dynamics in molecular aggregates weakly driven by light, *J. Chem. Phys.* **153**, 244122 (2020).
- [68] V. Janković and T. Mančal, Nonequilibrium steady-state picture of incoherent light-induced excitation harvesting, *J. Chem. Phys.* **153**, 244110 (2020).
- [69] D. Wang, L. Chen, R. Zheng, L. Wang, and Q. Shi, Communications: A nonperturbative quantum master equation approach to charge carrier transport in organic molecular crystals, *J. Chem. Phys.* **132**, 081101 (2010).
- [70] L. Song and Q. Shi, A new approach to calculate charge carrier transport mobility in organic molecular crystals from imaginary time path integral simulations, *J. Chem. Phys.* **142**, 174103 (2015).
- [71] L. Chen, Y. Zhao, and Y. Tanimura, Dynamics of a one-dimensional Holstein polaron with the hierarchical equations of motion approach, *J. Phys. Chem. Lett.* **6**, 3110 (2015).
- [72] L. Song and Q. Shi, Calculation of correlated initial state in the hierarchical equations of motion method using an imaginary time path integral approach, *J. Chem. Phys.* **143**, 194106 (2015).
- [73] T. Kuhn, Density matrix theory of coherent ultrafast dynamics, in *Theory of Transport Properties of Semiconductor Nanostructures*, edited by E. Schöl (Springer Science+Business Media, Dordrecht, 1998).
- [74] M. Kira and S.W. Koch, *Semiconductor Quantum Optics* (Cambridge University Press, New York, 2012).
- [75] I. S. Dunn, R. Tempelaar, and D. R. Reichman, Removing instabilities in the hierarchical equations of motion: Exact and approximate projection approaches, *J. Chem. Phys.* **150**, 184109 (2019).
- [76] H. Liu, L. Zhu, S. Bai, and Q. Shi, Reduced quantum dynamics with arbitrary bath spectral densities: Hierarchical equations of motion based on several different bath decomposition schemes, *J. Chem. Phys.* **140**, 134106 (2014).
- [77] J. Seibt and T. Mančal, Treatment of Herzberg–Teller and non-Condon effects in optical spectra with hierarchical equations of motion, *Chem. Phys.* **515**, 129 (2018).
- [78] Y. Yan, T. Xing, and Q. Shi, A new method to improve the numerical stability of the hierarchical equations of motion for discrete harmonic oscillator modes, *J. Chem. Phys.* **153**, 204109 (2020).
- [79] G. Mahan, *Many-Particle Physics* (Kluwer Academic, New York, 2000).
- [80] See Supplemental Material at <http://link.aps.org/supplemental/10.1103/PhysRevB.105.054311> for more detailed discussions on (i) the definition of and interrelations between the greater and lesser Green’s functions and the spectral function; (ii) the QMC method for thermodynamic expectation values; (iii) the weak-coupling limit of the HEOM method; (iv) the strong-coupling limit of the HEOM method; (v) the interpretation of the artificial broadening of spectral lines within the HEOM method; (vi) time- and frequency-domain HEOM-method results for different maximum hierarchy depths; (vii) HEOM and QMC data for the electronic momentum distribution; (viii) HEOM-method results in the adiabatic regime; (ix) the reduction of the statistical noise in the QMC data with increasing the sample size; and (x) the HEOM and QMC imaginary-time correlation functions in the antiadiabatic and adiabatic regime.
- [81] Y. Tanimura, Reduced hierarchical equations of motion in real and imaginary time: Correlated initial states and thermodynamic quantities, *J. Chem. Phys.* **141**, 044114 (2014).
- [82] J. M. Moix, Y. Zhao, and J. Cao, Equilibrium-reduced density matrix formulation: Influence of noise, disorder, and temperature on localization in excitonic systems, *Phys. Rev. B* **85**, 115412 (2012).

- [83] H.-D. Zhang, Q. Qiao, R.-X. Xu, X. Zheng, and Y. Yan, Efficient steady-state solver for hierarchical quantum master equations, *J. Chem. Phys.* **147**, 044105 (2017).
- [84] L. Zhu, H. Liu, W. Xie, and Q. Shi, Explicit system-bath correlation calculated using the hierarchical equations of motion method, *J. Chem. Phys.* **137**, 194106 (2012).
- [85] R.-X. Xu, P. Cui, X.-Q. Li, Y. Mo, and Y. J. Yan, Exact quantum master equation via the calculus on path integrals, *J. Chem. Phys.* **122**, 041103 (2005).
- [86] I.G. Lang and Yu. A. Firsov, Kinetic theory of semiconductors with low mobility, *J. Exptl. Theoret. Phys. (U.S.S.R.)* **43**, 1843 (1962) [*Sov. Phys. JETP* **16**, 1301 (1962)].
- [87] V. May and O. Kühn, *Charge and Energy Transfer Dynamics in Molecular Systems*, 3rd ed. (WILEY-VCH, Weinheim, 2011).
- [88] S. Mukamel, *Principles of Nonlinear Optical Spectroscopy* (Oxford University Press, New York, 1995).
- [89] C. Lin, F. H. Zong, and D. M. Ceperley, Twist-averaged boundary conditions in continuum quantum Monte Carlo algorithms, *Phys. Rev. E* **64**, 016702 (2001).
- [90] J. P. F. LeBlanc, A. E. Antipov, F. Becca, I. W. Bulik, G. K.-L. Chan, C.-M. Chung, Y. Deng, M. Ferrero, T. M. Henderson, C. A. Jiménez-Hoyos, E. Kozik, X.-W. Liu, A. J. Millis, N. V. Prokof'ev, M. Qin, G. E. Scuseria, H. Shi, B. V. Svistunov, L. F. Tocchio, I. S. Tupitsyn *et al.*, (Simons Collaboration on the Many-Electron Problem), Solutions of the Two-Dimensional Hubbard Model: Benchmarks and Results from a Wide Range of Numerical Algorithms, *Phys. Rev. X* **5**, 041041 (2015).
- [91] S. Karakuzu, L. F. Tocchio, S. Sorella, and F. Becca, Superconductivity, charge-density waves, antiferromagnetism, and phase separation in the Hubbard-Holstein model, *Phys. Rev. B* **96**, 205145 (2017).
- [92] M. Hohenadler, M. Aichhorn, and W. von der Linden, Spectral function of electron-phonon models by cluster perturbation theory, *Phys. Rev. B* **68**, 184304 (2003).
- [93] P. Mitić, V. Janković, N. Vukmirović, and D. Tanasković, Spectral functions of the Holstein polaron: Exact and approximate solutions, [arXiv:2112.15542](https://arxiv.org/abs/2112.15542).
- [94] R. Kevin Kessing, P.-Y. Yang, S. R. Manmana, and J. Cao, Long-range non-equilibrium coherent tunneling induced by fractional vibronic resonances, [arXiv:2111.06137](https://arxiv.org/abs/2111.06137).
- [95] J. Vučićević, J. Kokalj, R. Žitko, N. Wentzell, D. Tanasković, and J. Mravlje, Conductivity in the Square Lattice Hubbard Model at High Temperatures: Importance of Vertex Corrections, *Phys. Rev. Lett.* **123**, 036601 (2019).
- [96] S. Poncé, W. Li, S. Reichardt, and F. Giustino, First-principles calculations of charge carrier mobility and conductivity in bulk semiconductors and two-dimensional materials, *Rep. Prog. Phys.* **83**, 036501 (2020).
- [97] C.-Y. Hsieh and J. Cao, A unified stochastic formulation of dissipative quantum dynamics. I. Generalized hierarchical equations, *J. Chem. Phys.* **148**, 014103 (2018).
- [98] C.-Y. Hsieh and J. Cao, A unified stochastic formulation of dissipative quantum dynamics. II. Beyond linear response of spin baths, *J. Chem. Phys.* **148**, 014104 (2018).
- [99] J. Loos, M. Hohenadler, A. Alvermann, and H. Fehske, Phonon spectral function of the Holstein polaron, *J. Phys.: Condens. Matter* **18**, 7299 (2006).
- [100] L. Vidmar, J. Bonča, and S. A. Trugman, Emergence of states in the phonon spectral function of the Holstein polaron below and above the one-phonon continuum, *Phys. Rev. B* **82**, 104304 (2010).
- [101] V. Chorošajev, O. Rancova, and D. Abramavicius, Polaronic effects at finite temperatures in the B850 ring of the LH2 complex, *Phys. Chem. Chem. Phys.* **18**, 7966 (2016).
- [102] V. M. Axt and S. Mukamel, Nonlinear optics of semiconductor and molecular nanostructures; a common perspective, *Rev. Mod. Phys.* **70**, 145 (1998).
- [103] M. Berciu, Exact Green's functions for the two-site Hubbard-Holstein Hamiltonian, *Phys. Rev. B* **75**, 081101(R) (2007).
- [104] K. Nakamura and Y. Tanimura, Optical response of laser-driven charge-transfer complex described by Holstein-Hubbard model coupled to heat baths: Hierarchical equations of motion approach, *J. Chem. Phys.* **155**, 064106 (2021).
- [105] A. Gelzinis, D. Abramavicius, and L. Valkunas, Non-Markovian effects in time-resolved fluorescence spectrum of molecular aggregates: Tracing polaron formation, *Phys. Rev. B* **84**, 245430 (2011).
- [106] W. H. Zurek, Decoherence, einselection, and the quantum origins of the classical, *Rev. Mod. Phys.* **75**, 715 (2003).
- [107] M. Schlosshauer, *Decoherence and the Quantum-To-Classical Transition* (Springer-Verlag, Berlin, 2007).
- [108] Y. Yan, M. Xu, T. Li, and Q. Shi, Efficient propagation of the hierarchical equations of motion using the Tucker and hierarchical Tucker tensors, *J. Chem. Phys.* **154**, 194104 (2021).
- [109] A. Krotz and R. Tempelaar, A reciprocal-space formulation of surface hopping, *J. Chem. Phys.* **156**, 024105 (2022).
- [110] E. Collini and G. D. Scholes, Coherent intrachain energy migration in a conjugated polymer at room temperature, *Science* **323**, 369 (2009).

Exact description of excitonic dynamics in molecular aggregates weakly driven by light

Cite as: J. Chem. Phys. 153, 244122 (2020); doi: 10.1063/5.0029914

Submitted: 17 September 2020 • Accepted: 7 December 2020 •

Published Online: 29 December 2020



View Online



Export Citation



CrossMark

Veljko Janković^{1,2,a)}  and Tomáš Mančal^{1,b)} 

AFFILIATIONS

¹Faculty of Mathematics and Physics, Charles University, Ke Karlovu 5, 121 16 Prague 2, Czech Republic

²Scientific Computing Laboratory, Center for the Study of Complex Systems, Institute of Physics Belgrade, University of Belgrade, Pregrevica 118, 11080 Belgrade, Serbia

^{a)} Author to whom correspondence should be addressed: veljko.jankovic@ipb.ac.rs

^{b)} Electronic mail: mancal@karlov.mff.cuni.cz

ABSTRACT

We present a rigorous theoretical description of excitonic dynamics in molecular light-harvesting aggregates photoexcited by weak-intensity radiation of arbitrary properties. While the interaction with light is included up to the second order, the treatment of the excitation–environment coupling is exact and results in an exact expression for the reduced excitonic density matrix that is manifestly related to the spectroscopic picture of the photoexcitation process. This expression takes fully into account the environmental reorganization processes triggered by the two interactions with light. This is particularly important for slow environments and/or strong excitation–environment coupling. Within the exponential decomposition scheme, we demonstrate how our result can be recast as the hierarchy of equations of motion (HEOM) that explicitly and consistently includes the photoexcitation step. We analytically describe the environmental reorganization dynamics triggered by a delta-like excitation of a single chromophore and demonstrate how our HEOM, in appropriate limits, reduces to the Redfield equations comprising a pulsed photoexcitation and the nonequilibrium Förster theory. We also discuss the relation of our formalism to the combined Born–Markov–HEOM approaches in the case of excitation by thermal light.

Published under license by AIP Publishing. <https://doi.org/10.1063/5.0029914>

I. INTRODUCTION

Recent years have seen vigorous interest in unveiling the basic physical mechanisms governing the electronic solar energy conversion in photosynthetic systems.^{1–4} The developments in this field are expected to provide new ways of improving the light-to-charge conversion in artificial systems, e.g., organic photovoltaics (OPVs).⁵ A thorough understanding of the solar energy conversion in molecular light-harvesting systems calls for a detailed description of light absorption, excitation energy transfer (EET), charge separation, and charge transport.^{6,7} Our current understanding of these steps has been shaped by ultrafast spectroscopy experiments, which can provide insights into the dynamics of electronic excitations on time scales as short as a couple of femtoseconds.^{8–11} Such experiments, therefore, can also temporally resolve nuclear motions induced by photoexcitation, i.e., nuclear reorganization processes, which take place on ~10 fs–100 fs time scales. Moreover, photosynthetic EET falls into the so-called intermediate coupling regime,^{2,3,12} in which

the energy scales representative of electronic couplings, excitation–environment couplings, and static disorder in local transition energies are comparable to one another. Correspondingly, a proper interpretation of ultrafast experimental signatures necessitates development of explicitly time-dependent theoretical approaches that can accurately capture the non-Markovian dynamical interplay between temporal evolution of electronic excitations and their environment.^{3,12} Examples of such methods include hierarchical equations of motion (HEOM)¹³ and some wavefunction-based methods.¹⁴

Apart from the nonperturbative treatment of the interaction with the environment, a comprehensive theoretical analysis of the dynamics of electronic excitations created during ultrafast spectroscopy experiments should explicitly consider the exciting radiation field. However, the explicit inclusion of the photoexcitation process has received only a limited attention so far. The photoexcitation is commonly assumed to be infinitely short, i.e., delta-like, so that it instantaneously produces excited-state populations,

whose further evolution on ultrashort time scales is followed.^{15,16} On the other hand, theoretical methods of nonlinear spectroscopy,¹⁷ which explicitly keep track of the interaction with exciting pulses, have been employed in conjunction with HEOM to examine certain features of spectroscopic signals.¹⁸ However, there has not been much discussion on how to explicitly include the photoexcitation and respect the nonperturbative treatment of the excitation–environment coupling.¹⁹ The importance of the photoexcitation step is typically discussed within the debate on the relevance of the results of ultrafast experiments for the photosynthetic operation *in vivo*.^{20–24} It is argued that due to different properties of natural sunlight compared to laser pulses employed in experiments, photoexcitation of photosynthetic complexes under natural conditions triggers different dynamics from the one observed in ultrafast experiments. Nevertheless, under the common assumption that the electronic system is initially unexcited, any nontrivial dynamics under both excitation conditions is ultimately induced by the interaction with the radiation. In a nonlinear spectroscopy experiment, the signal depends on the appropriate power of the exciting field, i.e., the perturbation expansion in the interaction with radiation is appropriate.^{17,25} Similarly, the weakness of the excitation of photosynthetic complexes under natural conditions makes the second-order treatment of the interaction with light plausible.^{20–22,24}

Indeed, it has been shown²⁰ that the excited-state dynamics of a molecular system weakly driven by light of arbitrary properties is completely determined by the first-order radiation correlation function and the reduced evolution superoperator. It can be said that the information required for constructing the dynamics under arbitrary (weak) driving can only be obtained by ultrafast spectroscopy,²¹ which provides access to the reduced evolution superoperator. However, the analysis conducted in Ref. 20 is quite general and does not provide any details on the form and properties of this superoperator. Certainly, it should contain information about the nonequilibrium evolution of the environment taking place between consecutive interactions with light.²⁶ Along these lines, attempts have been made to examine the importance of these dynamical environmental effects for the second-order light-induced dynamics by augmenting the usual quantum master equation by terms that depend on the delay between the two interactions.²⁷ The analysis of the second-order photoinduced dynamics in Ref. 28 suggested that the nonequilibrium bath evolution between the two interactions with light is reflected in the so-called photoinduced correlation term. Let us note that the analyses conducted in Refs. 26–28 are essentially perturbative in the excitation–environment coupling.

On the other hand, in the field of ultrafast semiconductor optics,^{29–31} the photoexcitation step and the nonequilibrium dynamics of thus induced electronic excitations are typically studied within the density matrix (DM) theory complemented with the so-called dynamics controlled truncation (DCT) scheme.^{29,32} The DCT scheme classifies DMs according to the lowest power with which they scale in the exciting field and, therefore, provides a recipe to analyze the dynamics up to any given order in the exciting field in terms of a finite number of electronic DMs. A DCT-based approach has been recently applied by one of us to study exciton generation and subsequent charge separation in photoexcited OPVs.^{33,34} However, the truncation of the environment-assisted branch of the hierarchy within the DCT scheme still has to be performed separately,³¹ and it is commonly done in a low order in the

excitation–environment coupling.^{29,33,35} In a similar vein, the explicit consideration of the excitation by incoherent light is also combined with a Redfield-like treatment of the excitation–environment coupling.^{36–38} The individual excitation and de-excitation events may be treated within the Born–Markov quantum optical approximation^{39,40} or by constructing the Bloch–Redfield quantum master equation.^{37,41} Adopting the standpoint of the theory of open quantum systems, the effects of incoherent radiation may be taken into account by introducing an appropriate spectral density of the light–matter coupling.^{36,38,42}

While the explicit inclusion of the light–matter coupling is typically accompanied by a perturbative treatment of the excitation–environment coupling, there are also studies concentrating on a (numerically) exact treatment of the latter, at the expense of a less transparent inclusion of the former.^{43–45} When the semiclassical description of light–matter interaction is appropriate, the time-dependent electric field can be straightforwardly incorporated in the HEOM formalism,^{45,46} whose relation to the spectroscopic picture of sequential interactions with light is not manifest. When the quantum description of light–matter interaction is in place,^{43,44} the interaction with the radiation is treated from the standpoint of quantum optics using the so-called hybrid master-equation–HEOM approach.⁴⁷ In essence, the interaction with radiation appears in the form of Markovian corrections to HEOM. In the end, there are also studies that propose a numerically exact treatment of both the couplings to environment and radiation,⁴⁸ which, however, comes with a complex formalism and huge computational costs.

In this work, we build on the results of Ref. 20. Our approach is based on the two cornerstones of the theory of photosynthetic excitons.⁴⁹ Section II introduces the Frenkel exciton model of a molecular light-harvesting aggregate. In Sec. III, we shed new light on the existing approaches^{45,46} to include the interaction with pulsed laser fields into the HEOM formalism. We realize that there is a close connection between the space on which the EET dynamics has to be formulated and the maximum order up to which the interaction with the exciting field has to be included. This is very similar to the situation in the nonlinear response-function theory.¹⁷ We obtain a new form of HEOM that explicitly includes the interaction with pulsed laser fields up to the second order in the field, which is fully consistent with the single-exciton Frenkel Hamiltonian commonly employed in the study of light-induced coherent EET. The analysis of Sec. III is actually not limited to the second-order response, and we provide a prescription for treating laser-induced nonlinearities of arbitrary order in conjunction with a numerically exact treatment of the interaction of photoinduced electronic excitations with the environment. Section IV presents the central result of our analysis, which is valid for weak light of arbitrary properties. There, we perform a second-order treatment of the light–matter coupling and a nonperturbative treatment of the excitation–environment coupling to obtain an expression for weak light-induced excitonic dynamics that is manifestly related to the spectroscopic picture and fully includes the dynamical interplay between nonequilibrium electronic dynamics and environmental reorganization processes. The exact result that we obtain does not allow easy analytical manipulations, and we demonstrate how it can be recast as HEOM, both in the case of semiclassical (Sec. V, which actually rederives the second-order results of Sec. III) and quantum (Sec. VI) treatments of the interaction with light. In addition, we analytically solve for the

environmental reorganization dynamics triggered by a delta-like excitation of a single molecule (Sec. V A) and relate our results to existing approaches, such as the Redfield theory with photoexcitation (Sec. V B), the nonequilibrium Förster theory (Sec. V C), and hybrid Born–Markov–HEOM approaches (Sec. VI). These discussions further emphasize the advantages of our method, which are once again summarized in Sec. VII.

II. MODEL HAMILTONIAN

The system of interest consists of a molecular aggregate M that is in contact with the thermal bath B representing its environment and with the radiation R . The total Hamiltonian reads as

$$H = H_M + H_B + H_R + H_{M-B} + H_{M-R}. \quad (1)$$

The electronic excitations of the aggregate are described within the Frenkel exciton model^{49–52}

$$H_M = \sum_j \varepsilon_j B_j^\dagger B_j + \sum_{jk} J_{jk} B_j^\dagger B_k. \quad (2)$$

In Eq. (2), ε_j are the so-called site energies, while J_{jk} are resonance couplings (we take $J_{kk} = 0$). The operators B_j and B_j^\dagger describe the destruction and creation of an excitation on site j , respectively, and they obey Paulion commutation relations.^{29,50,52}

The environment is assumed to be composed of sets of independent harmonic oscillators associated with each site

$$H_B = \sum_{j\xi} \hbar\omega_\xi b_{j\xi}^\dagger b_{j\xi}. \quad (3)$$

The oscillators are labeled by site index j and mode index ξ , and phonon creation and annihilation operators $b_{j\xi}^\dagger$ and $b_{j\xi}$ satisfy Bose commutation relations. The interaction of aggregate excitations and the environment is taken to be linear in mode displacements and local to each chromophore (Holstein-like coupling⁵³),

$$H_{M-B} = \sum_{j\xi} B_j^\dagger B_j g_{j\xi} (b_{j\xi}^\dagger + b_{j\xi}) \equiv \sum_j B_j^\dagger B_j u_j, \quad (4)$$

where u_j is the collective environment coordinate associated with chromophore j . The coupling constants $g_{j\xi}$ may be related to the displacement of the equilibrium configuration of mode ξ between the ground and excited electronic states of chromophore j .^{50,51}

The coupling between aggregate excitations and the radiation is taken in the dipole and rotating-wave approximations

$$H_{M-R} = -\boldsymbol{\mu}_{eg} \cdot \mathbf{E}^{(+)} - \boldsymbol{\mu}_{ge} \cdot \mathbf{E}^{(-)}. \quad (5)$$

The dipole-moment operator $\boldsymbol{\mu}$ is assumed to be a purely electronic operator $\boldsymbol{\mu} = \sum_j \mathbf{d}_j (B_j^\dagger + B_j) = \boldsymbol{\mu}_{eg} + \boldsymbol{\mu}_{ge}$, where transition dipole moment \mathbf{d}_j of chromophore j does not depend on environmental coordinates (Condon approximation), part $\boldsymbol{\mu}_{eg}$ contains only operators B_j^\dagger , while $\boldsymbol{\mu}_{ge}$ contains only operators B_j . $\mathbf{E}^{(\pm)}$ denotes the positive- and negative-frequency parts of the (time-independent) operator of the (transversal) electric field so that we treat both electronic excitations and the radiation generating them on the quantum level.

We assume that at the initial instant t_0 of our dynamics, the total statistical operator $W(t_0)$ representing the state of the combined system of aggregate excitations, environment, and radiation can be factorized as follows:

$$W(t_0) = |g\rangle\langle g| \otimes \rho_B^g \otimes \rho_R. \quad (6)$$

In Eq. (6), the aggregate is taken to be initially unexcited, the state of the environment ρ_B^g is adapted to the collective electronic ground state $|g\rangle$ of the aggregate [$T = (k_B\beta)^{-1}$ is the temperature],

$$\rho_B^g = \frac{\exp(-\beta H_B)}{\text{Tr}_B \exp(-\beta H_B)}, \quad (7)$$

while ρ_R describes the state of the radiation.

III. EQUATIONS OF MOTION: SEMICLASSICAL TREATMENT OF LIGHT-MATTER INTERACTION

The excitation by an arbitrary time-dependent (classical) electric field $\mathcal{E}(t)$ can be incorporated into the HEOM formalism by taking that the total purely electronic Hamiltonian is $H_M + H_{M-R}(t)$.^{45,46} Here, $H_{M-R}(t)$ is obtained from H_{M-R} in Eq. (5) by replacing electric-field operators $\mathbf{E}^{(\pm)}$ by the corresponding time-dependent quantities $\mathcal{E}^{(\pm)}(t)$. Indeed, all the steps in the derivation conducted in Ref. 54 can be repeated to obtain equations of motion for the reduced DM (RDM) $\rho(t) \equiv \sigma_0(t)$ and auxiliary DMs (ADMs) $\sigma_n(t)$. ADMs are fully specified by vector \mathbf{n} of non-negative integers $n_{j,m}$,

$$\mathbf{n} = \left\{ \underbrace{(n_{0,0}, n_{0,1}, \dots)}_{\mathbf{n}_0}, \dots, \underbrace{(n_{N-1,0}, n_{N-1,1}, \dots)}_{\mathbf{n}_{N-1}} \right\}. \quad (8)$$

The index $j = 0, \dots, N-1$ enumerates chromophores, while index m , in principle, does not have an upper limit and is related to the following expansion of the bath correlation function in terms of exponentially decaying factors ($t > 0$):

$$C_j(t) = \text{Tr}_B \left\{ u_j^{(I)}(t) u_j(0) \rho_B^g \right\} = \sum_m c_{j,m} e^{-\mu_{j,m} t}. \quad (9)$$

The time dependence of the collective coordinate $u_j^{(I)}(t)$ in Eq. (9) is with respect to the free-phonon Hamiltonian [Eq. (3)]. While expansion coefficients $c_{j,m}$ may be complex, the decay rates $\mu_{j,m}$ are assumed to be real and positive. We note that apart from the exponential decomposition scheme [Eq. (9)] adopted in this work, there are other decompositions of $C_j(t)$ from which a HEOM approach may be derived.⁵⁵ The bath correlation function is commonly expressed in terms of the so-called spectral density $J_j(\omega)$,

$$C_j(t) = \frac{\hbar}{\pi} \int_{-\infty}^{+\infty} d\omega J_j(\omega) \frac{e^{i\omega t}}{e^{\beta\hbar\omega} - 1}, \quad (10)$$

which conveniently combines information on the density of environmental-mode states and the respective coupling strengths to electronic excitations.^{50,51}

The equation of motion for ADM $\sigma_{\mathbf{n}}(t)$ reads as⁵⁴

$$\begin{aligned} \partial_t \sigma_{\mathbf{n}}(t) = & -\frac{i}{\hbar} [H_M, \sigma_{\mathbf{n}}(t)] + \frac{i}{\hbar} [\boldsymbol{\mu}_{eg} \mathcal{E}^{(+)}(t) + \boldsymbol{\mu}_{ge} \mathcal{E}^{(-)}(t), \sigma_{\mathbf{n}}(t)] \\ & - \left(\sum_j \sum_m n_{j,m} \mu_{j,m} \right) \sigma_{\mathbf{n}}(t) + i \sum_j \sum_m [V_j, \sigma_{\mathbf{n}_{j,m}^+}(t)] \\ & + i \sum_j \sum_m n_{j,m} \left(\frac{c_{j,m}}{\hbar^2} V_j \sigma_{\mathbf{n}_{j,m}^-}(t) - \frac{c_{j,m}^*}{\hbar^2} \sigma_{\mathbf{n}_{j,m}^-}(t) V_j \right), \end{aligned} \quad (11)$$

where $V_j = B_j^\dagger B_j$. Since the coupling to the radiation is explicitly included in the electronic Hamiltonian, the HEOM in Eq. (11) treats nonperturbatively not only the interaction with the bath, as usually, but also that with light. Keeping in mind that our formulation of the model Hamiltonian supports states with an arbitrary number of excitations, the result embodied in Eq. (11) is quite general. In principle, it can describe in great detail various nonlinear effects (nonlinear with respect to the exciting electric field). However, once we fix the highest order in the electric field we are interested in, there will be many elements of the DMs that do not contribute to the optical response up to that order. In other words, solving coupled equation (11) as it stands, we obtain much more information than necessary to reconstruct the optical response up to a given order. Moreover, we lack the intuitive physical picture characteristic of nonlinear spectroscopy, which is in terms of Liouville pathways, block structure of the statistical operator and evolution superoperator, etc.^{17,25} In order to circumvent these deficiencies, it is enough to make a projection of the dynamics on relevant excitonic subspaces. The second-order response is fully characterized by the reduction to the subspace that can accommodate at most one excitation. This is discussed in greater detail further in this section and in Sec. SI of the [supplementary material](#). Practically, the appropriate reduction to obtain the second-order response consists in the following replacements in the model Hamiltonian:

$$B_j \rightarrow |g\rangle\langle j|, \quad B_j^\dagger \rightarrow |j\rangle\langle g|, \quad B_j^\dagger B_k \rightarrow |j\rangle\langle k|. \quad (12)$$

In Eq. (12), $|j\rangle$ is the collective singly excited state featuring a selective excitation of site j .

Therefore, to obtain the second-order response, we should calculate the expectation values $n_{g,\mathbf{n}}(t) \equiv \langle g | \sigma_{\mathbf{n}}(t) | g \rangle$, $y_{e,\mathbf{n}}(t) \equiv \langle e | \sigma_{\mathbf{n}}(t) | g \rangle$, and $n_{ee,\mathbf{n}}(t) \equiv \langle e | \sigma_{\mathbf{n}}(t) | \bar{e} \rangle$, where $\{|e\rangle\}$ is an arbitrary basis of singly excited states (the notation is similar to that in Ref. 29). If $\mathbf{n} = \mathbf{0}$, these three expectation values, respectively, represent the ground-state population, optical coherences, and singly excited-state populations and intraband coherences. Since the electronic subsystem starts from $|g\rangle\langle g|$ and since the light-matter coupling H_{M-R} is the only part of the Hamiltonian that can cause transitions from the ground state to singly excited states, the following scaling relations hold:⁵⁶

$$n_{g,\mathbf{n}}(t) = \delta_{\mathbf{n},\mathbf{0}} + \sum_{k=1}^{+\infty} n_{g,\mathbf{n}}^{(2k)}(t), \quad n_{g,\mathbf{n}}^{(2k)}(t) \propto \mathcal{E}^{2k}, \quad (13a)$$

$$y_{e,\mathbf{n}}(t) = \sum_{k=0}^{+\infty} y_{e,\mathbf{n}}^{(2k+1)}(t), \quad y_{e,\mathbf{n}}^{(2k+1)}(t) \propto \mathcal{E}^{2k+1}, \quad (13b)$$

$$n_{ee,\mathbf{n}}(t) = \sum_{k=1}^{+\infty} n_{ee,\mathbf{n}}^{(2k)}(t), \quad n_{ee,\mathbf{n}}^{(2k)}(t) \propto \mathcal{E}^{2k}. \quad (13c)$$

In other words, optical coherences are dominantly linear in the applied field, while excited-state populations are at least quadratic in the applied field. The environmental assistance, which actually enters through vector \mathbf{n} ,⁵⁷ does not affect the scaling laws (13).³²

Formulating equations of motion for $y_{e,\mathbf{n}}(t)$ and $n_{ee,\mathbf{n}}(t)$ actually enables us to formulate operator equations for sectors eg and ee of $\sigma_{\mathbf{n}}(t)$. Namely, using Eqs. (13) and keeping only terms that are at most of the second order in the applied field, we form the following equations for the eg sector $\sigma_{eg,\mathbf{n}}(t)$ and for the ee sector $\sigma_{ee,\mathbf{n}}(t)$:

$$\begin{aligned} \partial_t \sigma_{eg,\mathbf{n}}(t) = & -\frac{i}{\hbar} [H_M, \sigma_{eg,\mathbf{n}}(t)] - \left(\sum_j \sum_m n_{j,m} \mu_{j,m} \right) \sigma_{eg,\mathbf{n}}(t) \\ & + \delta_{\mathbf{n},\mathbf{0}} \frac{i}{\hbar} \mathcal{E}^{(+)}(t) \boldsymbol{\mu}_{eg} + i \sum_j \sum_m V_j \sigma_{eg,\mathbf{n}_{j,m}^+}(t) \\ & + i \sum_j \sum_m n_{j,m} \frac{c_{j,m}}{\hbar^2} V_j \sigma_{eg,\mathbf{n}_{j,m}^-}(t), \end{aligned} \quad (14)$$

$$\begin{aligned} \partial_t \sigma_{ee,\mathbf{n}}(t) = & -\frac{i}{\hbar} [H_M, \sigma_{ee,\mathbf{n}}(t)] - \left(\sum_j \sum_m n_{j,m} \mu_{j,m} \right) \sigma_{ee,\mathbf{n}}(t) \\ & + \frac{i}{\hbar} \mathcal{E}^{(+)}(t) \boldsymbol{\mu}_{eg} \sigma_{eg,\mathbf{n}}^\dagger(t) - \frac{i}{\hbar} \sigma_{eg,\mathbf{n}}(t) \boldsymbol{\mu}_{ge} \mathcal{E}^{(-)}(t) \\ & + i \sum_j \sum_m [V_j, \sigma_{ee,\mathbf{n}_{j,m}^+}(t)] \\ & + i \sum_j \sum_m n_{j,m} \frac{c_{j,m}}{\hbar^2} V_j \sigma_{ee,\mathbf{n}_{j,m}^-}(t) \\ & - i \sum_j \sum_m n_{j,m} \frac{c_{j,m}^*}{\hbar^2} \sigma_{ee,\mathbf{n}_{j,m}^-}(t) V_j, \end{aligned} \quad (15)$$

where now $V_j \rightarrow |j\rangle\langle j|$. By reducing our dynamics to the subspace containing at most one excitation, we transform Eq. (11) into coupled equations describing the evolution of optical coherences [Eq. (14)] and excited-state populations and intraband coherences [Eq. (15)]. The crucial step in the transformation is the application of scaling laws in Eqs. (13), which ensure that our dynamics is consistently up to the second order in the exciting field.

Instead of the path we have taken, one could have started from the model Hamiltonian in which the low-density replacements of Eq. (12) are performed and solved Eq. (11) without ever considering the scaling laws in Eqs. (13). In that case, one would in principle obtain the solution that is exact to all orders in the exciting field. However, this exactness is only apparent because the proper treatment of higher orders in the exciting field requires enlarging the space on which the Hamiltonian is formulated, as we discuss in more detail in Sec. SI of the [supplementary material](#). Temporal evolutions of higher-order sectors of the DM (which are not taken into account) would then influence evolutions of optical coherences, excited-state populations, and intraband coherences. For example, as demonstrated in Ref. 29, already in the third order in the electric field, equations of motion for optical coherences are coupled to equations of motion for biexcitonic amplitudes (coherences between the ground state and doubly excited states), meaning that a separate equation governing the evolution of $|jk\rangle\langle g|$ block of $\sigma_{\mathbf{n}}(t)$ has

to be formulated. This discussion emphasizes that once we treat the photogeneration step explicitly, we should be aware of the close connection between the largest order in the exciting field we include and the space on which the dynamics has to be formulated. Should we limit ourselves to the Frenkel Hamiltonian for the singly excited states and, at the same time, explicitly describe the excitation generation by light, we should do that only up to the second order in the applied field.

The presented framework can be considered as a DM equivalent of the response-function approach adopted in the theory of nonlinear spectroscopy.¹⁷ Our focus is on obtaining temporal evolution of various DM elements for a given waveform of the exciting electric field. This is different from the computation of nonlinear response functions, which represent the response of the system to a series of delta-like excitations. Nevertheless, there are two common assumptions underlying both our DM and response-function computations: (1) the electronic system is initially unexcited and (2) the number of interactions with the exciting field completely determines the excitonic subspace on which the computations have to be performed. Previous computations of coherent EET dynamics under the influence of laser fields⁵⁸ were practically limited to pulses of certain shapes due to the complications brought about by the time-dependent driving. On the other hand, our approach is valid for arbitrarily shaped laser pulses, and its treatment of the time-dependent driving is intuitive and consistently keeps track of interactions up to the second order.

The presented framework can be generalized to include processes that are of higher orders in the laser field. To that end, we recall that the central theorem of the DCT scheme mentioned in the Introduction (for more details, see Ref. 29 and references therein) guarantees that the expectation value of the normal-ordered product of n_B excitonic operators B^\dagger, B with respect to any $\sigma_n(t)$ entering Eq. (11) is at least of the order n_B in the applied laser field, i.e.,

$$\text{Tr}_M \left\{ \underbrace{B_{j_1}^\dagger \dots B_{j_{n_B}}}_{n_B} \sigma_n(t) \right\} = \mathcal{O}(\mathcal{E}^{n_B}).$$

The scaling relations [Eq. (13)],

which are valid for the second-order dynamics, thus represent a particular instance of the more general DCT scaling relations. This formulation of the central theorem of the DCT scheme is somewhat different from the original one in that an arbitrary-order environmental assistance of the original formulation is replaced by the expectation value with respect to an arbitrary ADM $\sigma_n(t)$. The formulation presented in this paragraph relies on the results of Ref. 57, which provide a formal correspondence between the environmental assistance of order $2n_E$ and the HEOM's ADMs on level n_E . Therefore, while the DCT scheme has been typically used to study optical field-induced processes in conjunction with a perturbative treatment of the interaction with the environment,^{29–35} the results presented in this section open up the possibility to simultaneously study arbitrary nonlinear effects induced by arbitrarily time-varying optical fields and yet treat the interaction with the environment in a numerically exact manner. The practical procedure may be summarized as follows. For a given order n_B in the exciting field, one formulates equations of motion for all possible expectation values of n_B normally ordered excitonic operators starting from Eq. (11). It may happen that some of these expectation values actually do not contribute to the optical response up to order n_B . For example, the central the-

orem of the DCT scheme predicts that the biexcitonic amplitudes $\text{Tr}_M \{B_{j_1} B_{j_2} \sigma_n(t)\}$ should contribute to the second-order response. However, on closer inspection, these quantities are completely decoupled from equations of motion for the expectation values of B_j (optical coherences) and $B_{j_1}^\dagger B_{j_2}$ (excited-state populations and intraband coherences) and it turns out that they contribute to the third-order optical response. The details of the model Hamiltonian combined with the specific Paulion statistics of excitonic creation and annihilation operators may thus lower the number of expectation values that contribute to the optical response up to any given order. Using the ideas presented in Sec. SI of the [supplementary material](#), one can then determine the subspace on which the laser-induced excited-state dynamics has to be formulated. Further analysis is beyond the scope of this work, in which we concentrate on the weak-light second-order treatment. For the generalization of our approach to the third-order dynamics, we refer the reader to Sec. VII of Ref. 29.

Let us conclude this section by noting that the results we have presented so far rely heavily on the form of the light-matter interaction Hamiltonian in the semiclassical approximation. If we want to treat light quantum mechanically, too, the results of Ref. 20 suggest that, up to the second order in the exciting field, the only information we need about light is its first-order (two-point) correlation function (indices i, j label Cartesian components of a vector),

$$G_{ij}^{(1)}(\tau_2, \tau_1) = \text{Tr}_R \left\{ \left\{ \mathbf{E}^{(-)}(\tau_2) \right\}_i \left\{ \mathbf{E}^{(+)}(\tau_1) \right\}_j \rho_R \right\}. \quad (16)$$

In the developments presented up to now, such a quantity does not directly enter Eqs. (11), (14), and (15). However, for (classical, transform-limited) pulses, this correlation function factorizes into products of expectation values of single electric-field operators, which define classical values of the electric field,^{59–61}

$$G_{ij}^{(1)}(\tau_2, \tau_1) = \mathcal{E}_i^{(-)}(\tau_2) \mathcal{E}_j^{(+)}(\tau_1), \quad (17a)$$

$$\mathcal{E}_i^{(\pm)}(\tau) = \text{Tr}_R \left\{ \left\{ \mathbf{E}^{(\pm)}(\tau) \right\}_i \rho_R \right\}. \quad (17b)$$

As will be demonstrated in more detail in Sec. V, it is precisely this factorization that enables us to formulate Eqs. (14) and (15) as they stand.

IV. GENERAL THEORY OF WEAK LIGHT-INDUCED DYNAMICS

This section presents the central result of our exact description of the dynamics triggered by weak light of arbitrary properties. While the derivation is elementary in all its steps, it is cumbersome and thus presented in Sec. SII of the [supplementary material](#). Here, we only analyze the final result for the reduced excited-state density matrix

$$\begin{aligned} \rho_{ee}^{(I)}(t) = & \int_{t_0}^t d\tau_2 \int_{t_0}^{\tau_2} d\tau_1 \vec{U}_{\text{red}}^{(I)}(t, \tau_2, \tau_1) A^{(I)}(\tau_2, \tau_1) \\ & + \int_{t_0}^t d\tau_2 \int_{t_0}^{\tau_2} d\tau_1 A^{(I)\dagger}(\tau_2, \tau_1) \overleftarrow{U}_{\text{red}}^{(I)}(t, \tau_2, \tau_1). \end{aligned} \quad (18)$$

In Eq. (18), superscript (I) denotes the interaction picture with respect to H_M ; τ_1 and τ_2 are the instants at which the interaction with

the radiation occurs, and the purely electronic operator $A^{(I)}(\tau_2, \tau_1)$ reads as

$$A^{(I)}(\tau_2, \tau_1) = \frac{1}{\hbar^2} \sum_{ij} G_{ij}^{(1)}(\tau_2, \tau_1) \left\{ \boldsymbol{\mu}_{eg}^{(I)}(\tau_1) \right\}_j |g\rangle \langle g| \left\{ \boldsymbol{\mu}_{ge}^{(I)}(\tau_2) \right\}_i. \quad (19)$$

The arrow above the reduced propagator sign indicates the direction of its action on the corresponding operator. The reduced propagator acting on the right reads as (T is the chronological time-ordering sign)

$$\vec{U}_{\text{red}}^{(I)}(t, \tau_2, \tau_1) = T \exp \left[\vec{\mathcal{W}}_c(\tau_2, \tau_1) + \vec{\mathcal{W}}_p(t, \tau_2) + \vec{\mathcal{W}}_{c-p}(t, \tau_2, \tau_1) \right], \quad (20a)$$

$$\begin{aligned} \vec{\mathcal{W}}_c(\tau_2, \tau_1) = & -\frac{1}{\hbar^2} \sum_j \int_{\tau_1}^{\tau_2} ds_2 \int_{\tau_1}^{s_2} ds_1 V_j^{(I)}(s_2)^C \\ & \times C_j(s_2 - s_1) V_j^{(I)}(s_1)^C, \end{aligned} \quad (20b)$$

$$\begin{aligned} \vec{\mathcal{W}}_p(t, \tau_2) = & -\frac{1}{\hbar^2} \sum_j \int_{\tau_2}^t ds_2 \int_{\tau_2}^{s_2} ds_1 V_j^{(I)}(s_2)^\times \\ & \times \left(C_j^r(s_2 - s_1) V_j^{(I)}(s_1)^\times + i C_j^i(s_2 - s_1) V_j^{(I)}(s_1)^\circ \right), \end{aligned} \quad (20c)$$

$$\begin{aligned} \vec{\mathcal{W}}_{c-p}(t, \tau_2, \tau_1) = & -\frac{1}{\hbar^2} \sum_j \int_{\tau_2}^t ds_2 \int_{\tau_1}^{\tau_2} ds_1 V_j^{(I)}(s_2)^\times \\ & \times C_j(s_2 - s_1) V_j^{(I)}(s_1)^C. \end{aligned} \quad (20d)$$

In Eq. (20c), $C_j^{r/i}$ denote the real and imaginary parts of the bath correlation function C_j [Eq. (9)], whereas the action of hyperoperators $V_j^{\times, \circ, C}$ on an operator O is defined as $V_j^\times O = [V_j, O]$, $V_j^\circ O = \{V_j, O\}$, $V_j^C O = V_j O$. A similar expression holds for the propagator acting on the left, as detailed in Sec. III of the [supplementary material](#).

Equations (18)–(20) present an exact solution (with respect to the aggregate–environment coupling) of the dynamics of an excitonic system weakly driven by light of arbitrary properties. The principal novelty compared to a similar analysis conducted in Refs. 20 and 21 is that, here, we provide an exact expression for the reduced evolution superoperator that is compatible with the interaction with light, i.e., it explicitly depends on the interaction instants τ_1 and τ_2 with the radiation and the observation instant t . The two summands on the right-hand side of Eq. (18) are Hermitian adjoints of one another, and they represent the two Liouville pathways from $|g\rangle\langle g|$ to $|e\rangle\langle e|$ that differ by the time order of the radiation interactions with the bra and ket.¹⁷

The RDM evolution can be conveniently represented in terms of diagrams showing how the state of electronic excitations changes due to interactions with radiation and due to absorptions and emissions of elementary environmental excitations.^{62,63} In this discussion, we assume that the instants τ_1 and τ_2 are fixed. We further focus on the first-order term of the reduced evolution superoperator [Eq. (20a)] and we also fix instants s_1 and s_2 [Eqs. (20b)–(20d)] that describe a single environmentally assisted process. In Figs. 1(a)–1(c), we present the three primitive diagrams corresponding to the hyperoperators in Eqs. (20b)–(20d), respectively. The diagram in Fig. 1(a)

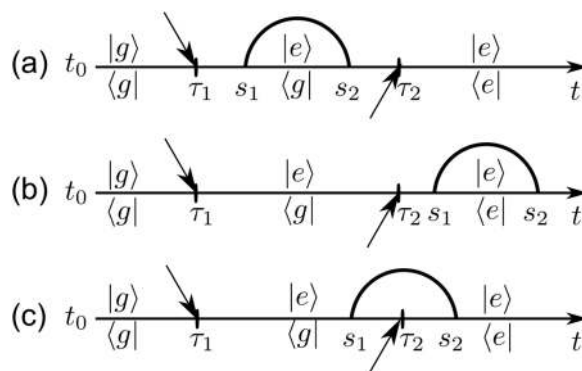


FIG. 1. Primitive diagrams describing the changes that the state of the electronic system undergoes due to the interaction with the radiation and environment-assisted processes. Only the diagrams characteristic for the first-order approximation to the reduced propagator [Eq. (20a)] in the first term of Eq. (18) are presented. The instants τ_1 and τ_2 at which the electronic system interacts with light, as well as the instants s_1 and s_2 determining the environmental assistance, are fixed. The arrows at τ_1 and τ_2 depict interactions with light, which are reflected in changes in the ket and bra of RDM. Circumferences represent the bath correlation function $C_j(s_2 - s_1)$. The observation time t satisfies $t \geq \tau_2 \geq \tau_1 \geq t_0$. Diagram (a) corresponds to Eq. (20b), diagram (b) corresponds to Eq. (20c), and diagram (c) corresponds to Eq. (20d).

describes a single-phonon-assisted process during which the electronic subsystem is in a state of optical coherence. The diagram in Fig. 1(b) describes a single-phonon-assisted process during which the electronic subsystem is entirely in the excited-state manifold. The single-phonon-assisted process represented by the primitive diagram in Fig. 1(c) starts when the electronic subsystem is in a state of optical coherence and ends when it is entirely in the excited-state manifold. There, the phonon propagator straddles two temporal sectors defined by the interactions with the radiation. These so-called straddling evolutions^{62,63} fully capture the nonequilibrium dynamics of the bath during different periods of photoinduced evolution.²⁶ They are intimately connected to the quantum coherence between electronic excitations and environment, and their presence is crucial to accurately describe photoinduced electronic dynamics.

Let us point out another viewpoint on the result embodied in Eq. (18). Due to the assumption of the initially unexcited system, any nontrivial dynamics is ultimately induced by the interaction with the radiation because the environment alone cannot cause transitions from the ground- to the excited-state manifold. This is reflected by the fact that the hyperoperator V^C in Eqs. (20b) and (20d) acts after the first and before the second interaction with the radiation, while hyperoperators $V_j^{\times/\circ}$ in Eqs. (20c) and (20d) act only after both interactions with radiation; see also Figs. 1(a)–1(c). Therefore, Eq. (18) can be reformulated by introducing a global time-ordering sign as follows:

$$\begin{aligned} \rho_{ee}^{(I)}(t) = & \int_{t_0}^t d\tau_2 \int_{t_0}^{\tau_2} d\tau_1 \frac{1}{\hbar^2} \sum_{ij} G_{ij}^{(1)}(\tau_2, \tau_1) \\ & \times T \left\{ \exp \left[\vec{\mathcal{W}}_c(\tau_2, \tau_1) + \vec{\mathcal{W}}_p(t, \tau_2) + \vec{\mathcal{W}}_{c-p}(t, \tau_2, \tau_1) \right] \right. \\ & \left. \times {}^C \left\{ \boldsymbol{\mu}_{ge}^{(I)}(\tau_2) \right\}_i \left\{ \boldsymbol{\mu}_{eg}^{(I)}(\tau_1) \right\}_j^C \right\} |g\rangle\langle g| + \text{H.c.} \end{aligned} \quad (21)$$

In Eq. (21), we introduced hyperoperator ${}^C V$ as ${}^C VO = OV$ for any operators V and O . This viewpoint will be useful in our discussion in Sec. V C, where we emphasize the similarities between the descriptions of the second-order photoexcitation process starting from the ground state and the Förster energy transfer from an excited donor to an unexcited acceptor.

Even though the result embodied in Eqs. (18)–(20) is remarkable, it is not very useful for actual computations, principally due to the time-ordering sign that renders analytical manipulations difficult. Nevertheless, whenever the bath correlation function $C_j(t)$ can be represented in the form given in Eq. (9), Eq. (18) can be recast as an infinite hierarchy of equations of motion for the RDM and ADMs.⁵⁴ However, the details of this procedure now depend on the form of operator $A^{(l)}(\tau_2, \tau_1)$ [Eq. (19)], i.e., on the temporal and statistical properties of the radiation.

V. EXCITATION BY WEAK (COHERENT) LASER PULSES

As has been recently discussed in Refs. 60 and 61, a pulse of light may be understood as a classical-like state of the electromagnetic field, whose energy density is localized and which can be specified by the spatial position around which it is localized, propagation direction, polarization, and spectral distribution. In essence, the quantum state representing the classical pulse whose bandwidth is determined by its spectral distribution is a coherent state that, as first realized by Glauber,⁵⁹ factorizes the $2n$ -point radiation correlation function into the product of $2n$ expectation values of the electric-field operator. In particular, $G_{ij}^{(1)}(\tau_2, \tau_1)$ is then factorized as predicted by Eq. (17) so that $A^{(l)}(\tau_2, \tau_1)$ [Eq. (19)] assumes the form

$$A^{(l)}(\tau_2, \tau_1) = \frac{1}{\hbar^2} \left[\boldsymbol{\mu}_{eg}^{(l)}(\tau_1) \cdot \mathcal{E}^{(+)}(\tau_1) \right] |g\rangle \langle g| \left[\boldsymbol{\mu}_{ge}^{(l)}(\tau_2) \cdot \mathcal{E}^{(-)}(\tau_2) \right]. \quad (22)$$

In other words, the result is the same as if we used the semiclassical form of the light–matter coupling from the very beginning, without any reference to electric-field operators. Therefore, further developments toward the HEOM have to result in Eqs. (14) and (15) that govern time evolution of optical coherences and excited-state populations and intraband coherences, respectively.

While the hierarchy counterpart of Eq. (18) for the RDM in the excited-state sector is Eq. (15), our previous discussion has not dealt with the RDM counterpart of the hierarchy for optical coherences [Eq. (14)]. In Sec. SII of the [supplementary material](#), we demonstrate that the exact solution (with respect to the excitation–environment coupling) in the eg sector reads as

$$\rho_{eg}^{(l)}(t) = \int_{t_0}^t d\tau U_{\text{red}}^{(l)}(t, \tau) \frac{1}{\hbar} \boldsymbol{\mu}_{eg}^{(l)}(\tau) \mathcal{E}^{(+)}(\tau) |g\rangle \langle g|, \quad (23)$$

where the reduced propagator for optical coherences reads as [see Eqs. (20a) and (20b)]

$$U_{\text{red}}^{(l)}(t, \tau) = \vec{U}_{\text{red}}^{(l)}(t, t, \tau) = T \exp \left[\vec{W}_c(t, \tau) \right]. \quad (24)$$

The manipulations that are necessary to recast Eqs. (23) and (18) as the HEOM presented in Eqs. (14) and (15), respectively,

proceed as usually.⁵⁴ For the sake of completeness, here, we only present the definitions of ADMs (in the interaction picture) for optical coherences,

$$\begin{aligned} \sigma_{eg, \mathbf{n}}^{(l)}(t) &= \int_{t_0}^t d\tau T \left\{ \prod_j \prod_m \left[\int_{\tau}^t ds e^{-\mu_{j,m}(t-s)} i \right. \right. \\ &\quad \times \left. \left. \frac{c_{j,m}}{\hbar^2} V_j^{(l)}(s) \right]^C \right] U_{\text{red}}^{(l)}(t, \tau) \left. \right\} \\ &\quad \times \frac{1}{\hbar} \boldsymbol{\mu}_{eg}^{(l)}(\tau) \mathcal{E}^{(+)}(\tau) |g\rangle \langle g|, \end{aligned} \quad (25)$$

and for excited-state populations and intraband coherences ($c_{j,m}^{r/i}$ denote the real/imaginary part of complex coefficients $c_{j,m}$),

$$\begin{aligned} \sigma_{ee, \mathbf{n}}^{(l)}(t) &= \int_{t_0}^t d\tau_2 \int_{t_0}^{\tau_2} d\tau_1 T \left\{ \prod_j \prod_m \left[\int_{\tau_2}^t ds e^{-\mu_{j,m}(t-s)} \right. \right. \\ &\quad \times \left(i \frac{c_{j,m}^r}{\hbar^2} V_j^{(l)}(s) \times - \frac{c_{j,m}^i}{\hbar^2} V_j^{(l)}(s) \circ \right) \\ &\quad \left. \left. + \int_{\tau_1}^{\tau_2} ds e^{-\mu_{j,m}(t-s)} i \frac{c_{j,m}}{\hbar^2} V_j^{(l)}(s) \right]^C \right] \\ &\quad \times \vec{U}_{\text{red}}^{(l)}(t, \tau_2, \tau_1) \left. \right\} A^{(l)}(\tau_2, \tau_1) + \text{H.c.} \end{aligned} \quad (26)$$

Before discussing the relation of the HEOM embodied in Eqs. (14) and (15) to existing theories of the dynamics of electronic excitations induced by weak laser pulses, let us briefly comment on the way in which the photoexcitation enters the HEOM. The electric field explicitly enters the hierarchy for optical coherences only on the level of RDM; see Eq. (14). Environmentally assisted optical coherences then act as source terms for environmentally assisted excited-state populations and intraband coherences; see Eq. (15). Moreover, the source term for the ee sector of ADM characterized by vector \mathbf{n} comprises only the eg sector of ADM characterized by the same vector \mathbf{n} . The hierarchy is schematically presented in Fig. 2 for $N = 2$ chromophores and $K = 1$ terms in the decomposition of the bath correlation function $C_j(t)$ in Eq. (9).

A. Impulsive photoexcitation of pure-dephasing spin-boson model: Analytical results

Let us now concentrate on the case of only one chromophore. The Hamiltonian [Eq. (1)] then reads as

$$\begin{aligned} H &= \varepsilon_e |e\rangle \langle e| + \sum_{\xi} \hbar \omega_{\xi} b_{\xi}^{\dagger} b_{\xi} + \sum_{\xi} g_{\xi} |e\rangle \langle e| (b_{\xi}^{\dagger} + b_{\xi}) \\ &\quad - \mathbf{d}_{eg} \cdot \left(\mathcal{E}^{(+)}(t) |e\rangle \langle g| + \mathcal{E}^{(-)}(t) |g\rangle \langle e| \right). \end{aligned} \quad (27)$$

Equation (27) is actually the pure-dephasing spin-boson Hamiltonian (or the independent-boson Hamiltonian, see Ref. 64), in which ε_e is the energy splitting between the two local energy levels (the ground state $|g\rangle$ and the singly excited state $|e\rangle$), and there is no tunneling between the two levels. The hyperoperators appearing in the reduced evolution superoperator [Eqs. (20)] are time-independent,

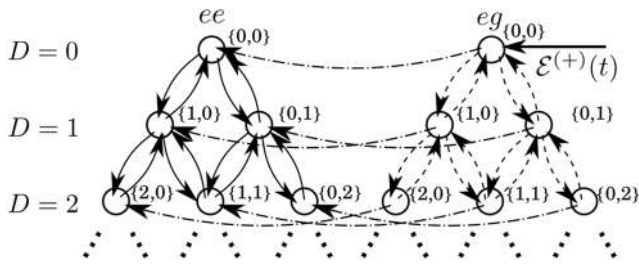


FIG. 2. Schematic representation of the HEOM for optical coherences and excited-state populations and intraband coherences in the case of excitation by a weak laser pulse. For the sake of simplicity, the aggregate comprises $N = 2$ chromophores and only $K = 1$ term in the exponential decomposition of the bath correlation function $C_j(t)$ is taken into account. Individual DMs are represented by circles, while the driving by the electric field $\mathcal{E}^{(+)}(t)$, which directly affects only the optical-coherence RDM, is presented by the straight horizontal arrow. D denotes the level of the hierarchy, and each DM is accompanied by the corresponding vector \mathbf{n} ; see Eq. (8). Curved dashed arrows represent hierarchical links between optical-coherence DMs, while curved solid arrows represent hierarchical links between excited-state DMs. The fact that DM $\sigma_{eg,\mathbf{n}}(t)$ acts as the source term in the EOM for $\sigma_{ee,\mathbf{n}}(t)$ is reflected in the diagram by the presence of curved dashed-dotted arrows pointing from $\sigma_{eg,\mathbf{n}}(t)$ toward $\sigma_{ee,\mathbf{n}}(t)$.

meaning that the time-ordering signs are not effective. This circumstance enables us to obtain analytical insights into the photoexcitation dynamics of the pure-dephasing spin-boson model in the impulsive limit.

The waveform of the positive-frequency part of the electric field is taken to be

$$\mathcal{E}^{(+)}(t) = \mathbf{e} \mathcal{E}_0 \delta(t) e^{-i\Omega_p t}, \quad (28)$$

where vector \mathbf{e} defines the polarization of the pulse, Ω_p is its central frequency, and \mathcal{E}_0 is its amplitude. If the initial instant is $t_0 < 0$, the excited-state RDM for $t > 0$ reads as⁵⁰

$$\rho_{ee}(t) = \frac{1}{\hbar^2} |(\mathbf{d}_{eg} \cdot \mathbf{e}) \mathcal{E}_0|^2 |e\rangle\langle e| \equiv P_e |e\rangle\langle e|. \quad (29)$$

At the same time, the optical-coherence RDM

$$\rho_{eg}(t) = \frac{i}{\hbar} (\mathbf{d}_{eg} \cdot \mathbf{e}) \mathcal{E}_0 e^{-ie_s t/\hbar} e^{-g(t)} |e\rangle\langle g| \quad (30)$$

exponentially decays to zero²⁵ on a time scale determined by the temporal behavior of the lineshape function

$$g(t) = \frac{1}{\hbar^2} \int_0^t ds_2 \int_0^{s_2} ds_1 C(s_1). \quad (31)$$

In a certain sense, Eqs. (29) and (30) formally demonstrate that the propagation scheme adopted in, e.g., Ref. 54, is physically sensible. Namely, optical coherences generated upon impulsive photoexcitation quickly decay to zero, and more importantly, they do not act as sources for excited-state populations and intraband coherences for $t > 0$; see Eqs. (14), (15), and (28). Therefore, upon a delta-like photoexcitation, it is justified to propagate only the excited-state dynamics. The reduced propagator for the excited-state sector [Eq. (20a)] then becomes the reduced propagator used in Ref. 54.

Although the excited-state RDM does not evolve in time, the impulsive photoexcitation triggers environmental reorganization

processes, whose dynamics is encoded in ADMs. Using the definition of the first-tier excited-state ADM in Eq. (26) and specializing to the single-chromophore case and impulsive excitation, we obtain

$$\sigma_{ee,0_m^+}(t) = -2 \frac{c_m^i}{\hbar^2} \frac{1 - e^{-\mu_m t}}{\mu_m} P_e |e\rangle\langle e|. \quad (32)$$

In essence, the only nontrivial contribution comes from the anti-commutator with $|e\rangle\langle e|$, which produces a factor of 2. A similar analysis can be conducted for d th-tier ($d \geq 1$) excited-state ADM with the final result

$$\sigma_{ee,0_{m_1 \dots m_d}^+}(t) = (-2)^d \prod_{p=1}^d \left(\frac{c_{m_p}^i}{\hbar^2} \frac{1 - e^{-\mu_{m_p} t}}{\mu_{m_p}} \right) P_e |e\rangle\langle e|. \quad (33)$$

Therefore, within the pure-dephasing spin-boson model, we can analytically compute the nonequilibrium environmental dynamics initiated by a delta-like photoexcitation. The result embodied in Eq. (33) becomes particularly interesting in the archetypal case of overdamped Brownian oscillator spectral density

$$J(\omega) = 2\lambda \frac{\omega\gamma}{\omega^2 + \gamma^2}, \quad (34)$$

when only the coefficient c_0 connected to the Drude pole $\mu_0 = \gamma$ has an imaginary part [see also Eq. (10)]

$$c_0 = \lambda \cdot \hbar\gamma \left[\cot\left(\frac{\beta\hbar\gamma}{2}\right) - i \right]. \quad (35)$$

In (this case, the only excited-state ADMs that exhibit a nontrivial temporal evolution are the ones featuring an exclusive excitation of the Drude pole. After performing suitable rescalings, which ensure that ADMs are dimensionless and indeed decay to zero in high enough hierarchical orders,⁶⁵ we finally obtain for $d \geq 0$

$$\langle e | \sigma_{ee,0_{m_1 \dots m_d}^{\text{resc}}}(t) | e \rangle / P_e = \delta_{m_1,0} \dots \delta_{m_d,0} \frac{2^d}{\sqrt{d!}} \left(\frac{\lambda}{\hbar\gamma} \right)^{d/2} \times \left[1 + \cot^2\left(\frac{\beta\hbar\gamma}{2}\right) \right]^{-d/4} (1 - e^{-\gamma t})^d. \quad (36)$$

In Fig. 3, we present the time evolution of the RDM and first four nontrivial ADMs that is predicted by Eq. (36). The numerical computations of the dynamics of impulsively photoexcited spin-boson model performed in Ref. 54 (see Fig. 1 and the corresponding discussion) employed the high-temperature approximation, in which the expansion of the bath correlation function [Eq. (9)] contains only the Drude contribution (term with $m = 0$). Interestingly, our analytical result [Eq. (36)] demonstrates that, in that case, the high-temperature approximation actually gives an exact solution.

Let us also note that the procedure outlined can be repeated to obtain optical-coherence ADMs. However, judging by Eq. (25), there will be no restrictions on m s that can be excited. This is not at variance with constraints present in Eq. (36) because, in the impulsive limit, optical coherences are not sources for purely excited-state dynamics.

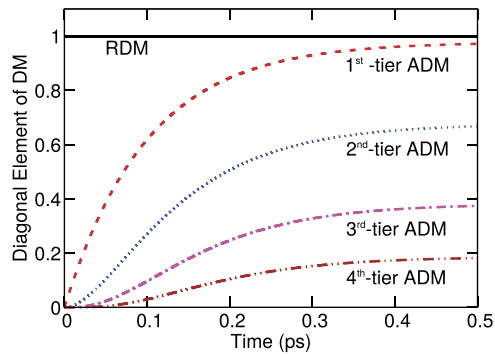


FIG. 3. Time evolution of the RDM and first four nontrivial ADMs following the impulsive excitation of the pure-dephasing spin–boson model. The spectral density of the excitation–environment interaction is assumed to be of the Drude–Lorentz type; see Eq. (34). The results are obtained using Eq. (36) with the following values of model parameters: reorganization energy $\lambda = 100 \text{ cm}^{-1}$, bath relaxation time $\gamma^{-1} = 100 \text{ fs}$, and temperature $T = 300 \text{ K}$.

B. Redfield theory with photoexcitation

Here, we discuss how, in the limit of weak excitation–environment interaction, our results for $\rho_{ee}^{(l)}(t)$ and $\rho_{eg}^{(l)}(t)$ reduce to the results of Refs. 29 and 35, where the photoexcitation is treated up to the second order in the optical field, while the environment-induced relaxation processes are described within the Redfield theory. Our strategy is similar to the one used in Ref. 54 to accomplish a similar goal.

If we assume that the characteristic decay time of the bath correlation function $C_j(t)$ is short compared to the time scales of the dynamics we are interested in, we can employ the Markov approximation to reduce Eqs. (18) and (23) to a system of coupled second-order equations for the excited-state and optical-coherence sectors of the RDM.^{50,51} The final result is commonly written in the exciton basis $\{|x\rangle\}$, defined by $H_M|x\rangle = \hbar\omega_x|x\rangle$, and assumes the form of Redfield equations with photoexcitation. The optical coherence $y_x(t) = \langle x|\rho_{eg}(t)|g\rangle$ evolves according to

$$\partial_t y_x(t) = -i\omega_x y_x(t) + \frac{i}{\hbar} \boldsymbol{\mu}_x \cdot \boldsymbol{\mathcal{E}}^{(+)}(t) - \sum_{x'} \left(\sum_{\bar{x}} \Gamma_{x\bar{x}x'} \right) y_{x'}(t), \quad (37)$$

while exciton populations and interexciton coherences $n_{xx}(t) = \langle x|\rho_{ee}(t)|\bar{x}\rangle$ obey

$$\begin{aligned} \partial_t n_{xx}(t) = & -i(\omega_x - \omega_{\bar{x}})n_{xx}(t) - \frac{i}{\hbar} \boldsymbol{\mu}_{\bar{x}}^* \cdot \boldsymbol{\mathcal{E}}^{(-)}(t) y_x(t) \\ & + \frac{i}{\hbar} y_{\bar{x}}^*(t) \boldsymbol{\mu}_x \cdot \boldsymbol{\mathcal{E}}^{(+)}(t) - \sum_{\bar{x}'x'} \mathcal{R}_{\bar{x}x\bar{x}'x'} n_{\bar{x}'x'}(t). \end{aligned} \quad (38)$$

In Eq. (37), the damping matrix $\Gamma_{x\bar{x}'x'}$ is defined as

$$\Gamma_{x\bar{x}'x'} = \sum_j \langle x|j\rangle \langle j|x'\rangle \langle \bar{x}|j\rangle \langle j|\bar{x}'\rangle \int_0^{+\infty} ds \frac{C_j(s)}{\hbar^2} e^{i(\omega_{x'} - \omega_x)s}, \quad (39)$$

while the Redfield tensor $\mathcal{R}_{\bar{x}x\bar{x}'x'}$ appearing in Eq. (38) assumes the standard form

$$\mathcal{R}_{\bar{x}x\bar{x}'x'} = -\Gamma_{\bar{x}'\bar{x}x} - \Gamma_{x'\bar{x}\bar{x}}^* + \delta_{\bar{x}'\bar{x}} \sum_{\bar{x}} \Gamma_{x\bar{x}\bar{x}x'} + \delta_{x'x} \sum_{\bar{x}} \Gamma_{\bar{x}\bar{x}\bar{x}x'}^*. \quad (40)$$

We have also introduced elements of the dipole-moment operator in the excitonic basis $\boldsymbol{\mu}_x = \langle x|\boldsymbol{\mu}_{eg}|g\rangle$. Although quite standard, the derivation of Eqs. (37) and (38) from Eqs. (18) and (23) deserves attention, and we present it in Sec. SIII of the [supplementary material](#).

In applications, it is common to neglect the imaginary parts of the Redfield tensor,^{29,50} which give rise to renormalizations of transition frequencies. However, as discussed in Ref. 66, this is not correct, especially when we discuss the Redfield equation without the secular approximation. Moreover, as the following discussion demonstrates, the application of Eqs. (37) and (38) to describe laser-induced dynamics of electronic excitations that are strongly coupled to relatively slow nuclear motions runs into more serious difficulties than those caused by neglecting renormalizations of transition frequencies or applying the secular approximation.

In Figs. 5(a1)–5(d2), we compare the photoinduced electronic dynamics of a dimer (see Fig. 4) treated by our HEOM formalism incorporating the photoexcitation [Eqs. (14) and (15)] and the Redfield formalism incorporating the photoexcitation [Eqs. (37) and (38)]. Relevant parameters of the model dimer are summarized in the caption of Fig. 4.

For the weakest excitation–environment coupling [see Figs. 5(a1) and 5(a2)], the results predicted by the two approaches are quite similar, as expected. However, as the excitation–environment coupling is increased, the dynamics predicted by the

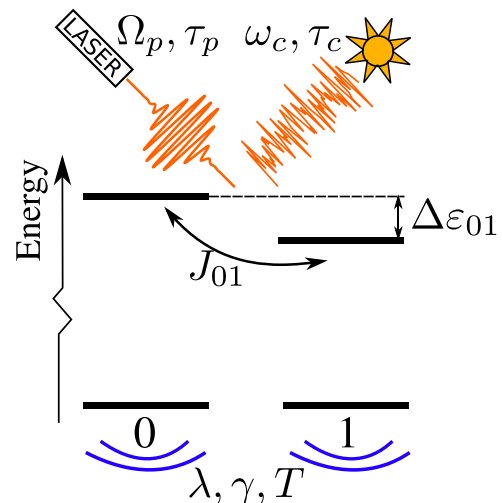


FIG. 4. Scheme of the model dimer. The difference between local energy levels is $\Delta\epsilon_{01} = \epsilon_0 - \epsilon_1 = 100 \text{ cm}^{-1}$, and the electronic coupling is $J_{01} = 100 \text{ cm}^{-1}$. The transition dipole moment of site 1 is assumed to be perpendicular to the polarization vector of the exciting field, whereas the magnitude of the projection of the transition dipole moment of site 0 onto the polarization vector is d_{eg} . Each chromophore is in contact with its thermal bath (schematically represented by the motion lines below chromophore numbers), and the spectral density of the excitation–environment interaction is assumed to be the Drude–Lorentz spectral density [see Eq. (34)] whose parameters γ and λ are identical on both sites. The bath relaxation time is $\gamma^{-1} = 100 \text{ fs}$, while the temperature is $T = 300 \text{ K}$. The initially unexcited dimer is excited by a weak laser pulse (characterized by the pulse central frequency Ω_p and duration τ_p , see Fig. 5) or by weak incoherent light (characterized by the central frequency ω_c and correlation time τ_c , see Figs. 6 and 7).

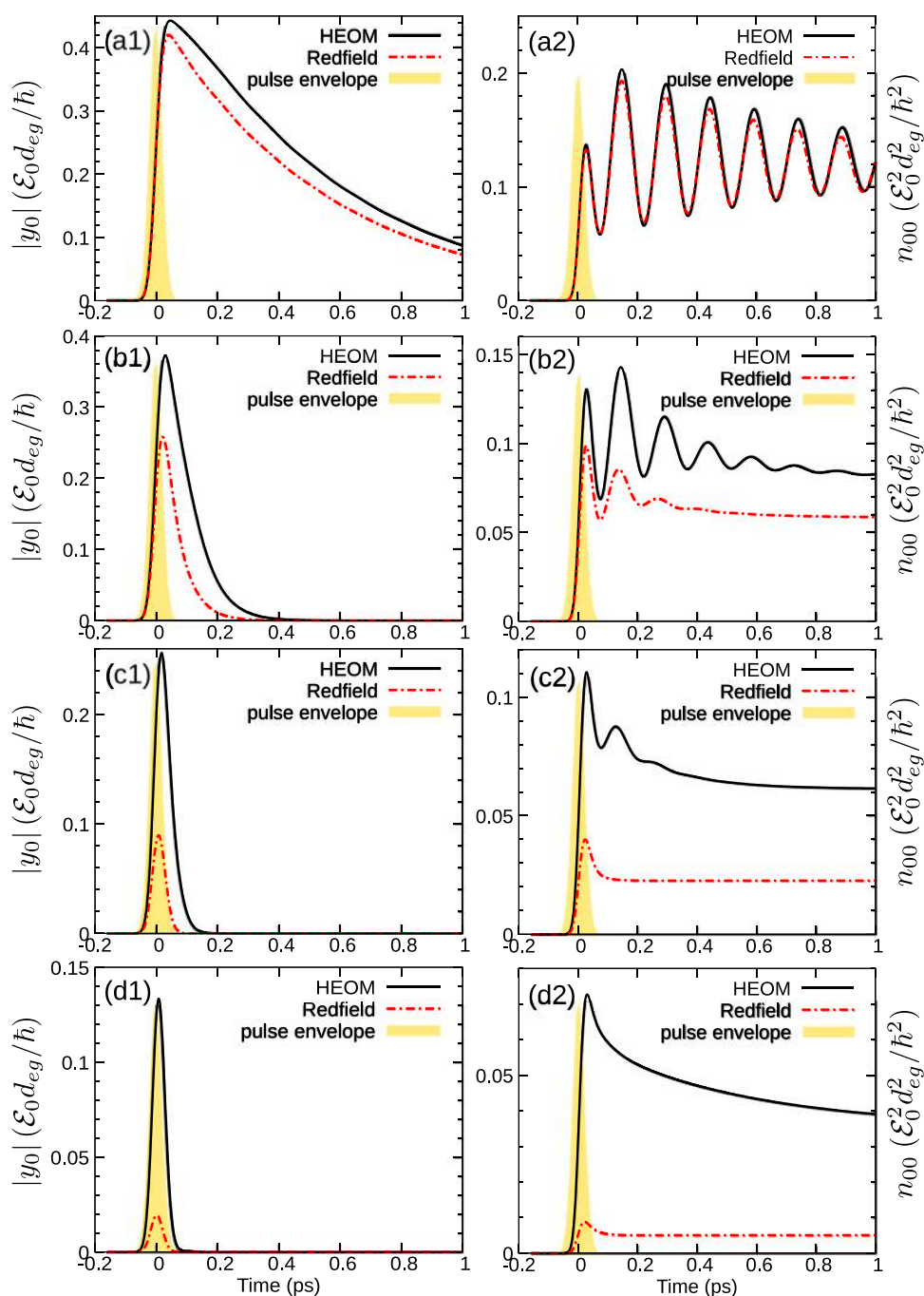


FIG. 5. Time evolution of the optical coherence modulus [(a1)–(d1)] and population [(b2)–(d2)] of site 0 following a pulsed photoexcitation of the model dimer (see Fig. 4). The computation is performed using the HEOM formalism incorporating the photoexcitation [Eqs. (14) and (15), solid curves] and the Redfield theory incorporating the photoexcitation [Eqs. (37) and (38), dashed-dotted curves], while the envelope of the photoexcitation is represented by shaded areas. The waveform of the excitation is $\mathcal{E}^{(+)}(t) = \mathcal{E}_0 \exp(-i\Omega_p t - t^2/(2\tau_p^2))/(\tau_p\sqrt{2\pi})$, where the duration of the pulse is $\tau_p = 20$ fs, while the central frequency Ω_p is tuned to the vertical transition frequency of site 0. The reorganization energy assumes the following values: $\lambda = 2$ cm^{-1} in (a1) and (a2), $\lambda = 20$ cm^{-1} in (b1) and (b2), $\lambda = 100$ cm^{-1} in (c1) and (c2), and $\lambda = 500$ cm^{-1} in (d1) and (d2).

Redfield theory deviates both qualitatively (e.g., absence of oscillatory features) and quantitatively from the numerically exact results [see Figs. 5(b1)–5(d2)]. The reasons for such deviations are summarized in the following.

First, the relaxation tensor employed in Eqs. (37) and (38) is time-independent, i.e., it cannot accurately capture the very first steps of the nuclear reorganization dynamics initiated by

photoexcitation. In the derivation of Eqs. (37) and (38), we obtained time-local equations because we ceased to keep track of the exact instants of the interaction with light by formally setting the difference between the observation instant t and the last instant of the interaction with light τ to infinity. Such an approximation is reasonable whenever the bath correlation time and/or the excitation–environment coupling are small enough. These conditions are

typically satisfied in ultrafast semiconductor optics,^{30,31} which explains the success of methods relying on equations such as Eqs. (37) and (38) to describe ultrafast semiconductor dynamics. On the other hand, in view of the intermediate regime to which photosynthetic EET belongs,^{2,3,12} transient features of light-triggered nuclear reorganization dynamics become crucial to properly characterize electronic dynamics in photosynthetic aggregates. In other words, one has to keep track of the exact instants τ_1 and τ_2 of the interaction with light, which our formalism manifestly does. One may hope to partially cure the deficiencies of the dynamics predicted by Eqs. (37) and (38) by replacing the time-independent Redfield tensor by its time-dependent counterpart; see, e.g., Ref. 27. However, as argued in the [supplementary material](#) of Ref. 28, such a replacement in a time-local equation for RDM would have to rely on the rather arbitrary instant t_0 in which we prescribe the initial condition [Eq. (6)], which would give a reasonable description only in the limit of impulsive excitation at t_0 . For pulses of finite duration, the correct description of ultrafast dynamics has to be on the time-nonlocal level.

Second, the derivation presented in the [supplementary material](#) suggests that Eqs. (37) and (38) neglect the nonequilibrium dynamics of the bath in the period between the two interactions with light. Again, our formalism manifestly includes such dynamics through the HEOM for optical coherences. On the other hand, the change in the bath state in the period between the two interactions with the light can be partially taken into account, even on the time-local level, through the so-called photoinduced correlation term that was identified in Ref. 28 (and also, in a more specialized setting, in Ref. 27). In the language of the standard density matrix theory, the photoinduced correlation term arises from the combined action of the environmental assistance and the interaction with the exciting field. While the neglect of such a term can be justified in semiconductor optics,^{30,31} its effect on the dynamics may be nontrivial in the case of slow bath and/or strong excitation–environment coupling.

C. Nonequilibrium generalization of Förster theory

As pointed out in Ref. 54, the Förster limit⁶⁷ cannot be directly obtained from the analytical results presented there, simply because the initial environmental density matrix ρ_B^g is assumed to describe the equilibrium of environmental modes when there are no electronic excitations in the system. However, in the following, we demonstrate how, under appropriate approximations, the results of Ref. 54, i.e., our results in the limit of ultrashort excitation, lead to the nonequilibrium generalization of the Förster theory proposed in Refs. 68 and 69.

Let us limit our discussion to an aggregate containing two chromophores [see Fig. 4], one acting as the excitation donor (D , chromophore 0 in Fig. 4) and the other acting as the excitation acceptor (A , chromophore 1 in Fig. 4). Let an impulsive excitation selectively excite D at $t = 0$. Disregarding the dynamics of thus induced optical coherences, the reduced excited-state dynamics for $t > 0$ is described by

$$\rho_{ee}^{(I)}(t) = T \exp\left[\vec{\mathcal{W}}_p(t, 0)\right] |D\rangle\langle D|, \quad (41)$$

where we have dropped out the normalization constant similar to P_e in Eq. (29). We are interested in the rate at which the population of A ,

$$P_A(t) = \langle A | \tilde{U}_{DA}(t, 0) \rho_{ee}^{(I)}(t) \tilde{U}_{DA}^\dagger(t, 0) | A \rangle, \quad (42)$$

changes. In the last equation, a tilde over the operator denotes the interaction picture with respect to the electronic Hamiltonian of the noninteracting chromophores ($\varepsilon_D |D\rangle\langle D| + \varepsilon_A |A\rangle\langle A|$) and

$$\tilde{U}_{DA}(t, 0) = T \exp\left[-\frac{i}{\hbar} \int_0^t ds \tilde{H}_{DA}(s)\right] \quad (43)$$

with $H_{DA} = J_{DA}(|A\rangle\langle D| + |D\rangle\langle A|)$ being the DA electronic coupling.

Within the Förster theory, the population transfer from D to A is induced by two actions of H_{DA} on opposite sides of $|D\rangle\langle D|$, while environmental degrees of freedom are mere spectators in that process. Nevertheless, they do adapt to the change in the electronic state induced by the transfer, but they alone cannot induce it if we assume (as is usual) that no environmental mode couples to both D and A .⁶⁸ The situation is somehow similar to the photoexcitation process (see Sec. IV), where the excited-state sector ee is reached from the ground-state sector gg by applying two H_{M-R} from the opposite sides of $|g\rangle\langle g|$. The phonons just adapt to the new electronic configuration, but they alone cannot bring about to the ground-to-excited state transition. Having all these things considered, it seems reasonable to attempt to replace all time-dependent operators $V_j^{(I)}(t)$ in Eq. (41) by time-independent operators V_j and to transform Eq. (42) by expanding $\tilde{U}_{DA}(t, 0)$ and keeping only contributions in which two $\tilde{H}_{DA}(\tau)$ act from the opposite sides of $\rho_{ee}^{(I)}(t)$. The above-described analogy with the photoexcitation process is most conveniently exploited from the standpoint of Eq. (21). The analogy then suggests that the Förster limit be obtained by enforcing the global chronological order in the hyperoperator product acting on $|D\rangle\langle D|$, which results in the following expression for the rate of population transfer from D to A :

$$k_{AD}^F(t) = \frac{2}{\hbar^2} \int_0^t d\tau \operatorname{Re} \left\{ \langle A | T \left[\tilde{H}_{DA}(t) \right]^C \exp\left[\vec{\mathcal{W}}_p(t, 0)\right] \times {}^C \tilde{H}_{DA}(\tau) |D\rangle\langle D| |A \rangle \right\}. \quad (44)$$

We then partition the integration domain in $\vec{\mathcal{W}}_p(t, 0)$ as follows [$\vec{\mathcal{F}}_p(s_2, s_1)$ denotes the hyperoperator under integral signs in Eq. (20c)]:

$$\vec{\mathcal{W}}_p(t, 0) = \int_0^\tau ds_2 \int_0^{s_2} ds_1 \vec{\mathcal{F}}_p(s_2, s_1) + \int_\tau^t ds_2 \int_\tau^{s_2} ds_1 \times \vec{\mathcal{F}}_p(s_2, s_1) + \int_\tau^t ds_2 \int_0^\tau ds_1 \vec{\mathcal{F}}_p(s_2, s_1). \quad (45)$$

Let us now analyze Eq. (44) order by order in $\vec{\mathcal{W}}_p(t, 0)$. This analysis bears certain resemblance to that conducted in Refs. 70 and 71. The approximation $V_j^{(I)}(s) \approx V_j$ is performed only after the global time-ordering prescription has been applied. Let us focus on the first-order term. The first summand on the right-hand side of Eq. (45) describes the single-phonon assistance before the first interaction H_{DA} takes place at instant τ . Upon making the approximation $V_j^{(I)}(s) \approx V_j$, we conclude that the corresponding contribution is equal to zero (cf. Sec. V A). The second summand in Eq. (45) is effective after the first interaction H_{DA} , when the electronic state is

that of D/A coherence, $|D\rangle\langle A|$. It is then easily checked that [see also Eq. (31)]

$$T\left[\tilde{H}_{DA}(t)^C \int_{\tau}^t ds_2 \int_{\tau}^{s_2} ds_1 \vec{\mathcal{F}}_p(s_2, s_1)^C \tilde{H}_{DA}(\tau)\right] |D\rangle\langle D| \approx -J_{DA}^2 e^{-i(\epsilon_D - \epsilon_A)(t-\tau)} [g_D(t-\tau) + g_A^*(t-\tau)] |A\rangle\langle A|. \quad (46)$$

We may anticipate that after the resummation, this term produces the well-known factors characteristic of donor emission [$e^{-g_D^*(t-\tau)}$] and acceptor absorption [$e^{-g_A(t-\tau)}$]. In the third summand in Eq. (45), one superoperator acts before, and the other after, the first interaction H_{DA} . This summand is expected to take into account corrections to the aforementioned donor emission factor due to the fact that the donor environment has not yet adapted to the electronic excited state. In greater detail,

$$T\left[\tilde{H}_{DA}(t)^C \int_{\tau}^t ds_2 \int_0^{\tau} ds_1 \vec{\mathcal{F}}_p(s_2, s_1)^C \tilde{H}_{DA}(\tau)\right] |D\rangle\langle D| \approx -J_{DA}^2 e^{-i(\epsilon_D - \epsilon_A)(t-\tau)} \frac{2i}{\hbar^2} \int_{\tau}^t ds_2 \int_0^{\tau} ds_1 C_D^i(s_2 - s_1) |A\rangle\langle A|. \quad (47)$$

One can convince themselves that the final result for the excitation transfer rate $k_{AD}^F(t)$ in this limit reads as

$$k_{AD}^F(t) = \frac{2J_{DA}^2}{\hbar^2} \int_0^t d\tau \operatorname{Re} \left\{ \exp\left(i(\epsilon_D - \epsilon_A)(t-\tau) - g_D^*(t-\tau) - g_A(t-\tau) + \frac{2i}{\hbar^2} \int_{\tau}^t ds_2 \int_0^{\tau} ds_1 C_D^i(s_2 - s_1)\right) \right\}. \quad (48)$$

To enable a direct comparison with Eq. (20) or Eq. (24) of Ref. 68, one should perform change of variables $t - \tau = \tau'$ and calculate all bath correlation functions by definition, starting from the general expression for u_j [Eq. (3)].

VI. EXCITATION BY WEAK INCOHERENT LIGHT

Here, we study in more detail the excitation by (weak) incoherent light, for which the factorized part [Eq. (17)] of the first-order light correlation function [Eq. (16)] identically vanishes. The HEOM, as formulated here, leans on the exponential decomposition of the environmental correlation function $C_j(t)$ [see Eq. (9)]. Therefore, it may be expected that if we can expand $G_{ij}^{(1)}(\tau_2 - \tau_1)$ as a weighted sum of exponential factors, we can proceed to formulate HEOM in the usual manner. We concentrate on thermal (chaotic) light whose propagation direction and polarization are well defined. It is known that quantum and classical theory predict the same form of the first-order light correlation function for such light,⁷²

$$G^{(1)}(\tau) = I_0 \exp(i\omega_c \tau - \tau/\tau_c). \quad (49)$$

In Eq. (49), I_0 is the intensity, ω_c is the central frequency, while τ_c is the coherence time of the radiation. In view of the well-defined polarization, we omit subscripts i, j labeling Cartesian coordinates of the electric field. This form of the first-order radiation correlation function has been used to gain insight into the dynamics of open²⁰

and closed⁷³ quantum systems weakly driven by light. Here, motivated by the aforementioned exponential decomposition, we show how the following light correlation function

$$G^{(1)}(\tau) = \sum_l I_{0,l} \exp(i\omega_{c,l} \tau - \tau/\tau_{c,l}) \quad (50)$$

can be used to recast Eq. (18) as the HEOM.

For incoherent light, the optical coherences defined in Eq. (23) are exactly equal to zero. Nevertheless, the general scheme of the hierarchy is still analogous to that we outlined in the case of classical excitation (see Fig. 2). One can introduce the following objects that act in the eg sector and are thus analogous to optical coherences, cf. Eq. (23),

$$\rho_{eg,l}^{(l)}(t) = \int_{t_0}^t d\tau U_{\text{red}}^{(l)}(t, \tau) \frac{i}{\hbar} \mu_{eg}^{(l)}(\tau) |g\rangle\langle g| \times I_{0,l} \exp[i\omega_{c,l}(t-\tau) - (t-\tau)/\tau_{c,l}], \quad (51)$$

where the dipole-moment operator μ_{eg} is the projection of μ_{eg} on the polarization direction. These optical coherence-like objects are counted by index l appearing in Eq. (50). In other words, each term in the exponential decomposition of the first-order radiation correlation function adds a new layer to the HEOM for “optical coherences,” which reads as

$$\begin{aligned} \partial_t \sigma_{eg,l,n}(t) = & -\frac{i}{\hbar} [H_M, \sigma_{eg,l,n}(t)] + (i\omega_{c,l} - \tau_{c,l}^{-1}) \sigma_{eg,l,n}(t) \\ & - \left(\sum_j \sum_m n_{j,m} \mu_{j,m} \right) \sigma_{eg,l,n}(t) + \delta_{n,0} \frac{i}{\hbar} I_{0,l} \mu_{eg} \\ & + i \sum_j \sum_m V_j \sigma_{eg,l,n_{j,m}^+}(t) \\ & + i \sum_j \sum_m n_{j,m} \frac{C_{j,m}}{\hbar^2} V_j \sigma_{eg,l,n_{j,m}^-}(t). \end{aligned} \quad (52)$$

Nevertheless, the HEOM for singly excited-state populations and intraband coherences does not feature any additional layers stemming from the decomposition in Eq. (50) and it reads as

$$\begin{aligned} \partial_t \sigma_{ee,n}(t) = & -\frac{i}{\hbar} [H_M, \sigma_{ee,n}(t)] - \left(\sum_j \sum_m n_{j,m} \mu_{j,m} \right) \sigma_{ee,n}(t) \\ & + \frac{i}{\hbar} \mu_{eg} \left(\sum_l \sigma_{eg,l,n}^\dagger(t) \right) - \frac{i}{\hbar} \left(\sum_l \sigma_{eg,l,n}(t) \right) \mu_{ge} \\ & + i \sum_j \sum_m [V_j, \sigma_{ee,n_{j,m}^+}(t)] + i \sum_j \sum_m n_{j,m} \frac{C_{j,m}}{\hbar^2} V_j \\ & \times \sigma_{ee,n_{j,m}^-}(t) - i \sum_j \sum_m n_{j,m} \frac{C_{j,m}^*}{\hbar^2} \sigma_{ee,n_{j,m}^-}(t) V_j. \end{aligned} \quad (53)$$

Our results embodied in Eqs. (52) and (53) are significant because they provide a viable route toward a description of excitonic dynamics triggered by thermal light. This description consistently combines both specific temporal and statistical properties of the radiation and a nonperturbative treatment of the excitation–environment coupling. It is well known that, in principle, the only sensible representation of thermal light is statistical, in terms of a set of all possible realizations. The recently suggested representation of natural incoherent light as an ensemble of transform-limited

pulses⁷⁴ would suggest that the dynamics it induces be computed by propagating the HEOM embodied in Eqs. (14) and (15) for individual ensemble realizations and then averaging over them. This would present a formidable task since propagating Eqs. (14) and (15) for one ensemble member is already numerically expensive. Equations (52) and (53) demonstrate how such complications can be circumvented within the second-order treatment of the interaction with light. The fact that the exponential decomposition of the first-order radiation correlation function does not affect the complexity of the HEOM in the excited-state sector is numerically advantageous. Namely, propagating the HEOM for “optical coherences” [Eq. (52)] is significantly less numerically demanding than propagating the HEOM in the excited-state sector [Eq. (53)]. Since the dynamics of “optical coherences” in our second-order treatment is not affected by the dynamics in the excited-state sector, we conclude that the overall numerical complexity of the problem as we formulate it is not significantly greater than in the case of pulsed photoexcitation [Eqs. (14) and (15)].

The proposed theory is valid in the limit of weak light–matter interaction. To provide a more quantitative criterion of this weakness, we recall that the maximum normal surface solar irradiance at sea level on a clear day is $\mathcal{I}_{\max} \approx 1 \text{ kW/m}^2$.⁷⁵ The electric field amplitude corresponding to this irradiance can be estimated by $E_0 = \sqrt{\frac{2\mathcal{I}_{\max}}{c\epsilon_0}}$ (c is the speed of light, while ϵ_0 is the vacuum permittivity), and we obtain $E_0 \approx 870 \text{ V/m}$. Keeping in mind that the magnitude of the transition dipole moment of the bacteriochlorophyll molecule is $d_{eg} \approx 6 \text{ D}$,⁴⁹ we can estimate the magnitude of the interaction energy of electronic excitations and radiation by $E_0 d_{eg} \sim 10^{-3} \text{ cm}^{-1}$. We see that this interaction energy is orders of magnitude smaller than the energies characteristic for excitonic couplings, exciton–environment interactions, and static disorder in transition energies ($\sim 10 \text{ cm}^{-1}$ – 100 cm^{-1}).² Keeping in mind that the lunar irradiance or the solar irradiance in habitats of some photosynthetic bacteria are even smaller than the maximum solar irradiance upon which the above estimates were based, we conclude that the weak-light assumption is well satisfied in various photosynthetically relevant situations. The same conclusion may be reached by estimating the rate of solar photons incident on a photosynthetic complex. To that end, we start from the fact that the normal surface solar irradiance of the photosynthetically available radiation (400 nm–700 nm) of the solar spectrum is $\mathcal{I}_{\text{PAR}} \approx 540 \text{ W/m}^2$.⁷⁵ In typical photosynthetic complexes, bacteriochlorophyll molecules most strongly absorb at wavelengths around $\lambda \approx 700 \text{ nm}$ – 800 nm .⁴⁹ Taking that the typical linear dimension of a photosynthetic complex is $a \sim 10 \text{ \AA}$,² we may estimate that the number of solar photons incident on a complex per unit time is $\frac{dN}{dt} = \mathcal{I}_{\text{PAR}} \frac{\lambda a^2}{2\pi\hbar c} \approx 2000 \text{ s}^{-1}$, which agrees well with the estimate provided in Ref. 36. The actual photon absorption rate, which also depends on the effective absorption cross section and the degree of radiation attenuation due to the specific habitat conditions, may be even smaller. The corresponding temporal scale is thus orders of magnitude longer than time scales typical for EET, excitation recombination, or extraction, which corroborates the plausibility of our weak-light assumption.

In the following, we compare our Eqs. (52) and (53) with the existing descriptions of photoexcitation by incoherent light.^{43,44,47} We concentrate on the light correlation function in Eq. (49). The aforementioned approaches exploit the fact that the

coherence time of natural sunlight $\tau_c \sim 1 \text{ fs}$ ^{76,77} is at least an order of magnitude shorter than the time scales typical for electronic couplings and nuclear reorganization processes (which assume values of $\sim 10 \text{ cm}^{-1}$ – 100 cm^{-1}).² We may then argue that we can disregard the nonequilibrium environmental dynamics taking place between the two interactions with the radiation, which was crucial to correctly describe excitonic dynamics induced by a pulsed photoexcitation; see the discussion accompanying Figs. 1(c) and 5(a1)–5(d2). In other words, we may assume that both interactions with the radiation occur essentially at the same instant, which means that Eq. (49) should be replaced by

$$G^{(1)}(\tau) = 2I_0\tau_c \delta(\tau). \quad (54)$$

This is the so-called white-noise model (WNM) of the radiation.⁴⁸ In this case, one has to propagate only the HEOM for excited-state populations and interband coherences and Eq. (53) should be replaced by

$$\begin{aligned} \partial_t \sigma_{ee,n}(t) = & -\frac{i}{\hbar} [H_M, \sigma_{ee,n}(t)] - \left(\sum_j \sum_m n_{j,m} \mu_{j,m} \right) \sigma_{ee,n}(t) \\ & + \delta_{n,0} \frac{2I_0\tau_c}{\hbar^2} \mu_{eg}|g\rangle\langle g| \mu_{ge} + i \sum_j \sum_m [V_j, \sigma_{ee,n_{j,m}^+}(t)] \\ & + i \sum_j \sum_m n_{j,m} \frac{c_{j,m}}{\hbar^2} V_j \sigma_{ee,n_{j,m}^-}(t) \\ & - i \sum_j \sum_m n_{j,m} \frac{c_{j,m}^*}{\hbar^2} \sigma_{ee,n_{j,m}^-}(t) V_j. \end{aligned} \quad (55)$$

In Figs. 6(a) and 6(b), we confront the dynamics of the dimer described in Fig. 4 that is triggered by suddenly turned on incoherent light and governed by Eqs. (52) and (53) (label “full”) and Eq. (55) (label “WNM”) for different values of light coherence times τ_c . Figure 6(a) presents the dimensionless source term for the total excited-state population for $G^{(1)}(\tau)$ given in Eq. (49) (curves labeled as “full”),

$$S_{\text{full}}(t) = \frac{i}{\hbar} \text{Tr}_M \{ \mu_{eg} \sigma_{eg,0}^\dagger(t) - \sigma_{eg,0}(t) \mu_{ge} \}, \quad (56)$$

and for $G^{(1)}(\tau)$ given in Eq. (54) (the curve labeled as “WNM”),

$$S_{\text{WNM}} = \frac{2I_0\tau_c}{\hbar^2} \text{Tr}_M \{ \mu_{eg}|g\rangle\langle g| \mu_{ge} \}. \quad (57)$$

Instead of presenting the data in absolute units, the dimensionless source term in Fig. 6(a) and the total population in Fig. 6(b) are given in units of $\gamma\tau_c I_0 d_{eg}^2 / (\hbar\gamma)^2$. The reason for choosing this unit is our second-order treatment of exciton–light interaction, which ensures that the excited-state populations and intraband coherences scale linearly in the light intensity I_0 [Eqs. (49), (50), and (54)] and quadratically in the transition dipole moment d_{eg} (see Fig. 4). On the formal side, one can convince themselves that $\gamma\tau_c I_0 d_{eg}^2 / (\hbar\gamma)^2$ is the appropriate unit for our purposes by analyzing Eqs. (52), (53), and (55). The presence of the factor $\gamma\tau_c$ in the unit enables us to compare on the same plot the data for different light coherence times. The value of this unit is estimated by recalling that the energy scale of the exciton–light interaction is $E_0 d_{eg} \sim 10^{-3} \text{ cm}^{-1}$ and that we use $\gamma^{-1} = 100 \text{ fs}$ (see the caption of Fig. 4). Therefore, for $\tau_c = 1.3$

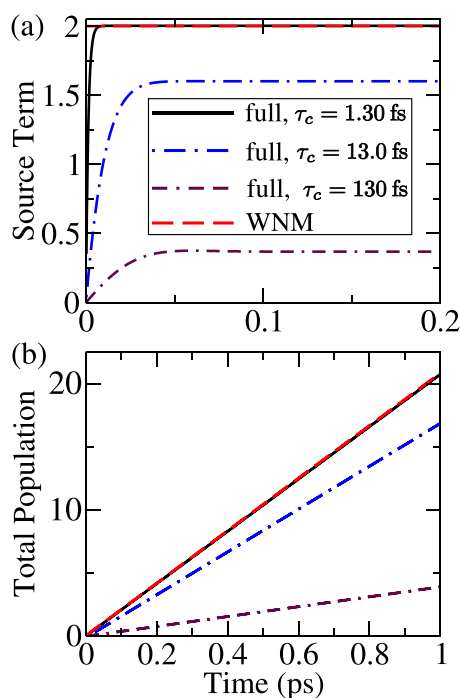


FIG. 6. (a) Source term [in units of $\gamma\tau_c I_0 d_{eg}^2 / (\hbar\gamma)^2$] in the equation for the total excited-state population of the model dimer (see Fig. 4) when the dynamics is governed by Eq. (55) (WNM, dashed line) and when the dynamics is governed by Eqs. (52) and (53) for $\tau_c = 1.30$ fs (solid line), $\tau_c = 13.0$ fs (dashed-dotted line), and $\tau_c = 130$ fs (double dashed-dotted line). (b) Total excited-state population [in units of $\gamma\tau_c I_0 d_{eg}^2 / (\hbar\gamma)^2$] after a sudden turn-on of incoherent light with $\tau_c = 1.30$ fs (solid line), $\tau_c = 13.0$ fs (dashed-dotted line), $\tau_c = 130$ fs (double dashed-dotted line), and $\tau_c \rightarrow 0$ (WNM, dashed line).

fs, $\gamma\tau_c I_0 d_{eg}^2 / (\hbar\gamma)^2 \simeq 4 \times 10^{-12}$ and for $\tau_c = 13$ fs, $\gamma\tau_c I_0 d_{eg}^2 / (\hbar\gamma)^2 \simeq 4 \times 10^{-11}$, while for $\tau_c = 130$ fs, $\gamma\tau_c I_0 d_{eg}^2 / (\hbar\gamma)^2 \simeq 4 \times 10^{-10}$. The value of τ_c determines the time scale on which the source term for the total excited-state population $S_{\text{full}}(t)$ reaches a constant value upon a sudden turn-on of incoherent radiation [see Fig. 6(a)]. For the shortest τ_c examined, the source term $S_{\text{full}}(t)$ saturates within the initial ~ 10 fs of the dynamics and the value it reaches excellently agrees with the source term S_{WNM} predicted by the WNM of the radiation. This is also reflected in Fig. 6(b), in which the total exciton populations predicted by the two models display a perfect agreement for the shortest τ_c . As τ_c is increased so that it becomes comparable to time scales of nuclear reorganization processes, the agreement between the results predicted by Eqs. (52), (53), and (55) deteriorates [see Figs. 6(a) and 6(b)] because the WNM cannot capture the nonequilibrium bath dynamics between the two interactions with the radiation. The larger is the coherence time τ_c , the more pronounced are the deviations of the exact dynamics from the WNM results.

We now turn our attention to the dynamics of interexciton coherences, which is displayed in Figs. 7(a)–7(d) for different values of the reorganization energy λ .

The initial (sub-picosecond) oscillatory dynamics of the interexciton coherence that is clearly observed for lower values

of λ [see Figs. 7(a) and 7(b)] is directly related to the oscillations displayed by the populations in the site basis upon an ultrafast excitation [see Figs. 5(a2) and 5(b2)].⁶⁶ As the reorganization energy is increased, the oscillatory features gradually disappear, cf. Figs. 5(b1)–5(d2), and certain steady behavior of the interexciton coherence, similar to a steady increase in the total exciton population observed in Fig. 6, sets in. In Figs. 7(b)–7(d), we see that the imaginary part of the interexciton coherence saturates in ~ 1 ps after the excitation starts. On the other hand, the real part of the interexciton coherence in Fig. 7(b) exhibits a steady increase for $t \gtrsim 1.25$ ps, while the corresponding start of the steady increase is shifted to ~ 0.75 ps and ~ 1.5 ps in Figs. 7(c) and 7(d), respectively. The time scale on which the steady increase in the interexciton coherence sets in is intimately related to the time scale on which the populations in the site basis [see Figs. 5(b2)–5(d2)] reach their limiting values following a very short photoexcitation. By virtue of basis transformation,⁶⁶ the latter is closely connected to the time scale of the dephasing of the interexciton coherence generated by a very short photoexcitation. Therefore, the oscillatory features under incoherent illumination originate from the sudden turn-on of the excitation at $t = 0$ ^{24,78} and they disappear on the time scale on which the interexciton coherence dephases after a short photoexcitation.⁴⁸ We note, in passing, that the magnitude of the interexciton coherence becomes much larger than populations, which is also in line with previous studies.^{24,48,74,78} The light-induced coherences observed in Figs. 7(a) and 7(b) are not expected to be directly relevant to excitation harvesting under natural conditions, which proceeds via nonequilibrium steady states.²⁴ Such states arise from a combination of the steady increase in populations and coherences [see Figs. 6(b) and 7(a)–7(d)] due to continuous generation and the steady excitation decay by trapping at the reaction center and recombination. What may be relevant for the efficiency of light harvesting driven by incoherent light are the relations among the RDM elements that establish themselves on time scales typical for excitation trapping and recombination, which are generally much longer than the time scales covered in this study. Further development of this idea is the topic of the accompanying paper.⁷⁹

This section explicitly deals with incoherent light whose first-order correlation function is of the form given in Eqs. (49) and (50). In the literature,^{43,44,47} it is common to formulate equations similar to Eq. (55), which tacitly lean on the WNM in which the source term describing the generation of state $|e\rangle$ (from the ground state) by incoherent sunlight is given in terms of the number of photons of energy ε_e at the temperature of the Sun's photosphere (~ 6000 K). In Sec. SIV of the supplementary material, we demonstrate how our description reduces to the above-described quantum-optical limit by virtue of the Weisskopf–Wigner approximation,⁸⁰ which has to be performed in the exciton basis.³⁹ In essence, exploiting the weakness of the excitation–light coupling, the quantum-optical approaches tacitly assume that the effects of this coupling can be simply added to the dynamics in the absence of radiation in the form of Markovian corrections that do not feature any modifications due to the presence of the environment.^{43,44,47} While such approaches do include a radiative recombination term, our approach does not contain such a term. As demonstrated in greater detail in Sec. SIV of the supplementary material, the reason for the absence of the radiative recombination term in Eqs. (52) and (53) or in Eq. (55) is the fact that our dynamics starts from the initially unexcited system and that it

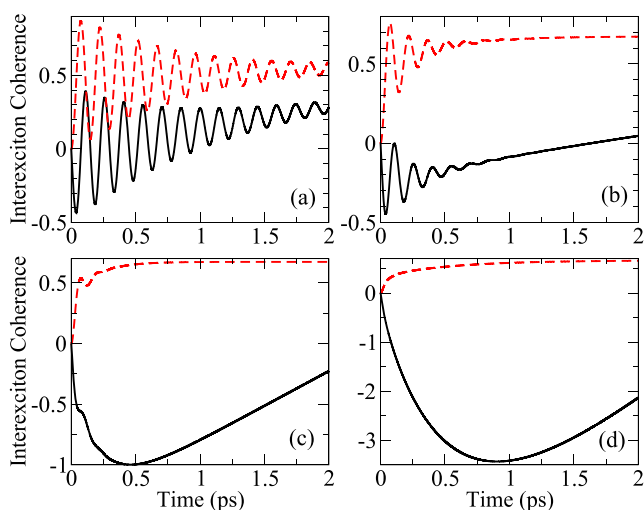


FIG. 7. Dynamics of the real (solid lines) and imaginary (dashed lines) parts of the interexciton coherence [in units of $\gamma\tau_c I_0 d_{eg}^2 / (\hbar\gamma)^2$] in the model dimer (see Fig. 4) for different values of the reorganization energy: (a) $\lambda = 2 \text{ cm}^{-1}$, (b) $\lambda = 20 \text{ cm}^{-1}$, (c) $\lambda = 100 \text{ cm}^{-1}$, and (d) $\lambda = 500 \text{ cm}^{-1}$. Light coherence time is $\tau_c = 1.3 \text{ fs}$.

consistently keeps track of interactions with light up to the second order. To describe nonequilibrium stationary states under incoherent light, our theoretical framework has to be augmented by additional drain terms that should take into account excitation recombination and possibly some other mechanisms by which the excitations may be lost (e.g., trapping at the reaction center). In our opinion, this feature of our formalism does not render it less suitable for steady-state calculations under incoherent light; see the accompanying paper.⁷⁹ However, a fully self-consistent approach to obtain the steady-state under incoherent light is still out of our reach because it asks for a solution to the fundamental problem of the nonadditivity of the excitation–light and excitation–environment coupling.¹⁹

VII. CONCLUSION

We have conducted a detailed theoretical investigation of the dynamics of electronic excitations in molecular aggregates induced by weak radiation of arbitrary properties. Starting from initially unexcited aggregate, our approach combines a perturbative treatment of the coupling to radiation with an exact treatment of the excitation–environment coupling in a manner that is manifestly compatible with the spectroscopic view of the photoexcitation. We express the reduced excited-state dynamics entirely in terms of the first-order radiation correlation function and the reduced evolution superoperator, for which we provide an exact expression within the Frenkel exciton model. The changes that the state of electronic excitations undergoes due to the photoexcitation and the interaction with the environment can be conveniently represented diagrammatically, in terms of elementary processes assisted by single quanta of environmental excitations. The fact that our general expression for the excited-state dynamics explicitly keeps track of the instants at

which the two interactions with light occur means that the corresponding differential equation is time-nonlocal. Within the exponential decomposition scheme, we outline how this temporal nonlocality can be circumvented by setting up a suitable HEOM scheme that explicitly takes into account the photoexcitation step. Such developments, however, turn out to heavily depend on radiation properties.

In the case of excitation by transform-limited pulses, when the radiation correlation function factorizes into the product of (classical) electric fields at two interaction instants, we relate the HEOM arising from our results to the HEOM obtained by considering the (semiclassical) light–matter coupling as a part of the aggregate Hamiltonian. The insights from nonlinear spectroscopy and semiconductor optics analyzed using the DCT scheme turn out to be crucial in establishing that relationship. Namely, the order in which the light–matter coupling is taken into account determines the subspace of the excitation Fock space on which the photoinduced dynamics should be formulated and vice versa. We demonstrate that the second-order response to light should be formulated on the subspace containing at most one excitation. The second-order results [Eqs. (14) and (15)] presented in Sec. III may be extended to treat laser-induced nonlinear effects of an arbitrary order and yet retain the numerically exact treatment of the interaction of photoinduced excitations with the environment. We believe that this result may be of relevance for future treatments of laser-induced coherent EET.

We analyze in detail the dynamics triggered by an impulsive excitation of a single chromophore, where we provide analytical results for environmental reorganization dynamics, which is encoded in ADMs. We further identify the approximations under which our general result reduces to the widely employed Redfield theory with photoexcitation and nonequilibrium Förster theory. Our comparison between the dynamics predicted by the HEOM and Redfield theory with photoexcitation further corroborates the advantages of our approach, which exactly describes light-induced environmental reorganization processes and fully takes into account the nonequilibrium evolution of the bath between the two interactions with light.

In the case of excitation by thermal light, we compare our approach to the widely used hybrid Born–Markov–HEOM approach, which treats the light–matter coupling within quantum-optical approximations. Since we employ the exponential decomposition scheme, the formulation of the HEOM relies on an exponential decomposition of the radiation correlation function. We find that the HEOM thus obtained is not significantly more numerically expensive than the HEOM as it is usually formulated. This is because additional layers stemming from the decomposition of radiation correlation function exist only in its optical-coherence-like part, which may be solved completely independently from its excited-state part. This paves the way toward viable simulations of the dynamics triggered by natural incoherent light that respect both the specific properties of the radiation and the need for a nonperturbative treatment of excitation–environment coupling.

We believe that despite its unfavorable numerical cost, the approach outlined here can be useful in further investigations of light-induced dynamics in both photosynthetic light-harvesting aggregates and OPVs. In particular, in both types of systems, the

relation of the insights gained in ultrafast spectroscopies to the actual operation under natural sunlight illumination has provoked long-standing debates. Our method promises to bridge these two standpoints and establish a new more suitable common viewpoint on energy conversion in these systems. Further work on bridging the two standpoints is under way in our respective research groups.

SUPPLEMENTARY MATERIAL

See the [supplementary material](#) for (a) a more detailed discussion of the second-order response to excitation by coherent light, (b) a detailed derivation of the exact evolution superoperator, (c) derivation of the Redfield equation comprising photoexcitation, and (d) a discussion of the quantum-optical limit in the case of excitation by incoherent light.

AUTHORS' CONTRIBUTIONS

V.J. and T.M. designed the research. V.J. performed all the analytical and numerical work under the supervision of T.M. V.J. prepared the initial version of this manuscript. Both authors contributed to the submitted version of this manuscript.

ACKNOWLEDGMENTS

We gratefully acknowledge the support from Charles University Research Centre Program No. UNCE/SCI/010. T.M. acknowledges the funding from the Czech Science Foundation (GAČR), Grant No. 18-18022S. The final stages of this work were supported by the Institute of Physics Belgrade, through the grant by the Ministry of Education, Science, and Technological Development of the Republic of Serbia.

DATA AVAILABILITY

The data that support the findings of this study are available from the corresponding author upon reasonable request.

REFERENCES

- 1 M. Mohseni, Y. Omar, G. Engel, and M. B. Plenio (Cambridge University Press, 2014).
- 2 S. J. Jang and B. Mennucci, "Delocalized excitons in natural light-harvesting complexes," *Rev. Mod. Phys.* **90**, 035003 (2018).
- 3 A. Chenu and G. D. Scholes, "Coherence in energy transfer and photosynthesis," *Annu. Rev. Phys. Chem.* **66**, 69–96 (2015).
- 4 F. Fassioli, R. Dinshaw, P. C. Arpin, and G. D. Scholes, "Photosynthetic light harvesting: Excitons and coherence," *J. R. Soc., Interface* **11**, 20130901 (2014).
- 5 J.-L. Brédas, E. H. Sargent, and G. D. Scholes, "Photovoltaic concepts inspired by coherence effects in photosynthetic systems," *Nat. Mater.* **16**, 35 (2016).
- 6 R. E. Blankenship, *Molecular Mechanisms of Photosynthesis* (Wiley Blackwell, 2014).
- 7 J.-L. Brédas, J. E. Norton, J. Cornil, and V. Coropceanu, "Molecular understanding of organic solar cells: The challenges," *Acc. Chem. Res.* **42**, 1691–1699 (2009).
- 8 G. S. Engel, T. R. Calhoun, E. L. Read, T.-K. Ahn, T. Mančal, Y.-C. Cheng, R. E. Blankenship, and G. R. Fleming, "Evidence for wavelike energy transfer through quantum coherence in photosynthetic systems," *Nature* **446**, 782–786 (2007).

- 9 F. D. Fuller, J. Pan, A. Gelzinis, V. Butkus, S. S. Senlik, D. E. Wilcox, C. F. Yocum, L. Valkunas, D. Abramavicius, and J. P. Ogilvie, "Vibronic coherence in oxygenic photosynthesis," *Nat. Chem.* **6**, 706–711 (2014).
- 10 E. Collini and G. D. Scholes, "Coherent intrachain energy migration in a conjugated polymer at room temperature," *Science* **323**, 369–373 (2009).
- 11 S. M. Falke, C. A. Rozzi, D. Brida, M. Maiuri, M. Amato, E. Sommer, A. De Sio, A. Rubio, G. Cerullo, E. Molinari, and C. Lienau, "Coherent ultrafast charge transfer in an organic photovoltaic blend," *Science* **344**, 1001–1005 (2014).
- 12 A. Ishizaki and G. R. Fleming, "Quantum coherence in photosynthetic light harvesting," *Annu. Rev. Condens. Matter Phys.* **3**, 333–361 (2012).
- 13 Y. Tanimura, "Stochastic Liouville, Langevin, Fokker–Planck, and master equation approaches to quantum dissipative systems," *J. Phys. Soc. Jpn.* **75**, 082001 (2006).
- 14 M. Beck, A. Jäckle, G. Worth, and H.-D. Meyer, "The multiconfiguration time-dependent Hartree (MCTDH) method: A highly efficient algorithm for propagating wavepackets," *Phys. Rep.* **324**, 1–105 (2000).
- 15 A. Ishizaki and G. R. Fleming, "Theoretical examination of quantum coherence in a photosynthetic system at physiological temperature," *Proc. Natl. Acad. Sci. U. S. A.* **106**, 17255–17260 (2009).
- 16 A. Kato and A. Ishizaki, "Non-Markovian quantum-classical ratchet for ultrafast long-range electron-hole separation in condensed phases," *Phys. Rev. Lett.* **121**, 026001 (2018).
- 17 S. Mukamel, *Principles of Nonlinear Optical Spectroscopy* (Oxford University Press, New York, 1995).
- 18 L. Chen, R. Zheng, Y. Jing, and Q. Shi, "Simulation of the two-dimensional electronic spectra of the Fenna-Matthews-Olson complex using the hierarchical equations of motion method," *J. Chem. Phys.* **134**, 194508 (2011).
- 19 H. Maguire, J. Iles-Smith, and A. Nazir, "Environmental nonadditivity and Franck–Condon physics in nonequilibrium quantum systems," *Phys. Rev. Lett.* **123**, 093601 (2019).
- 20 T. Mančal and L. Valkunas, "Exciton dynamics in photosynthetic complexes: Excitation by coherent and incoherent light," *New J. Phys.* **12**, 065044 (2010).
- 21 A. Chenu, P. Malý, and T. Mančal, "Dynamic coherence in excitonic molecular complexes under various excitation conditions," *Chem. Phys.* **439**, 100–110 (2014).
- 22 P. Brumer and M. Shapiro, "Molecular response in one-photon absorption via natural thermal light vs. pulsed laser excitation," *Proc. Natl. Acad. Sci. U. S. A.* **109**, 19575–19578 (2012).
- 23 I. Kassal, J. Yuen-Zhou, and S. Rahimi-Keshari, "Does coherence enhance transport in photosynthesis?," *J. Phys. Chem. Lett.* **4**, 362–367 (2013).
- 24 P. Brumer, "Shedding (incoherent) light on quantum effects in light-induced biological processes," *J. Phys. Chem. Lett.* **9**, 2946–2955 (2018).
- 25 T. Mančal, "Principles of multidimensional electronic spectroscopy," in *Quantum Effects in Biology*, edited by M. Mohseni, Y. Omar, G. Engel, and M. B. Plenio (Cambridge University Press, 2014), pp. 82–120.
- 26 T. Mančal and F. Šanda, "Quantum master equations for non-linear optical response of molecular systems," *Chem. Phys. Lett.* **530**, 140–144 (2012).
- 27 J. Olšina and T. Mančal, "Parametric projection operator technique for second order non-linear response," *Chem. Phys.* **404**, 103–115 (2012).
- 28 P. Malý, J. M. Gruber, R. van Grondelle, and T. Mančal, "Single molecule spectroscopy of monomeric LHCII: Experiment and theory," *Sci. Rep.* **6**, 26230 (2016).
- 29 V. M. Axt and S. Mukamel, "Nonlinear optics of semiconductor and molecular nanostructures; a common perspective," *Rev. Mod. Phys.* **70**, 145–174 (1998).
- 30 F. Rossi and T. Kuhn, "Theory of ultrafast phenomena in photoexcited semiconductors," *Rev. Mod. Phys.* **74**, 895–950 (2002).
- 31 V. M. Axt and T. Kuhn, "Femtosecond spectroscopy in semiconductors: A key to coherences, correlations and quantum kinetics," *Rep. Prog. Phys.* **67**, 433 (2004).
- 32 V. M. Axt, K. Victor, and A. Stahl, "Influence of a phonon bath on the hierarchy of electronic densities in an optically excited semiconductor," *Phys. Rev. B* **53**, 7244–7258 (1996).
- 33 V. Janković and N. Vukmirović, "Origin of space-separated charges in photoexcited organic heterojunctions on ultrafast time scales," *Phys. Rev. B* **95**, 075308 (2017).

- ³⁴V. Janković and N. Vukmirović, "Identification of ultrafast photophysical pathways in photoexcited organic heterojunctions," *J. Phys. Chem. C* **121**, 19602–19618 (2017).
- ³⁵K. Siantidis, V. M. Axt, and T. Kuhn, "Dynamics of exciton formation for near band-gap excitations," *Phys. Rev. B* **65**, 035303 (2001).
- ³⁶C. Chuang and P. Brumer, "LH1–RC light-harvesting photocycle under realistic light–matter conditions," *J. Chem. Phys.* **152**, 154101 (2020).
- ³⁷T. V. Tscherbul and P. Brumer, "Non-equilibrium stationary coherences in photosynthetic energy transfer under weak-field incoherent illumination," *J. Chem. Phys.* **148**, 124114 (2018).
- ³⁸L. A. Pachón, J. D. Botero, and P. Brumer, "Open system perspective on incoherent excitation of light-harvesting systems," *J. Phys. B: At., Mol. Opt. Phys.* **50**, 184003 (2017).
- ³⁹H.-P. Breuer and F. Petruccione, *The Theory of Open Quantum Systems* (Oxford University Press, 2002).
- ⁴⁰T. V. Tscherbul and P. Brumer, "Long-lived quasistationary coherences in a V-type system driven by incoherent light," *Phys. Rev. Lett.* **113**, 113601 (2014).
- ⁴¹T. V. Tscherbul and P. Brumer, "Partial secular Bloch-Redfield master equation for incoherent excitation of multilevel quantum systems," *J. Chem. Phys.* **142**, 104107 (2015).
- ⁴²L. A. Pachón and P. Brumer, "Incoherent excitation of thermally equilibrated open quantum systems," *Phys. Rev. A* **87**, 022106 (2013).
- ⁴³E. Fassio, A. Olaya-Castro, and G. D. Scholes, "Coherent energy transfer under incoherent light conditions," *J. Phys. Chem. Lett.* **3**, 3136–3142 (2012).
- ⁴⁴H. C. H. Chan, O. E. Gamel, G. R. Fleming, and K. B. Whaley, "Single-photon absorption by single photosynthetic light-harvesting complexes," *J. Phys. B: At., Mol. Opt. Phys.* **51**, 054002 (2018).
- ⁴⁵A. G. Dijkstra and A. Beige, "Efficient long-distance energy transport in molecular systems through adiabatic passage," *J. Chem. Phys.* **151**, 034114 (2019).
- ⁴⁶A. Kato and Y. Tanimura, "Hierarchical equations of motion approach to quantum thermodynamics," in *Thermodynamics in the Quantum Regime: Fundamental Aspects and New Directions*, edited by F. Binder, L. A. Correa, C. Gogolin, J. Anders, and G. Adesso (Springer International Publishing, Cham, 2018), pp. 579–595.
- ⁴⁷C. Kreisbeck, T. Kramer, M. Rodríguez, and B. Hein, "High-performance solution of hierarchical equations of motion for studying energy transfer in light-harvesting complexes," *J. Chem. Theory Comput.* **7**, 2166–2174 (2011).
- ⁴⁸J. Olsina, A. G. Dijkstra, C. Wang, and J. Cao, "Can natural sunlight induce coherent exciton dynamics?," [arXiv:1408.5385](https://arxiv.org/abs/1408.5385) [physics.chem-ph] (2014).
- ⁴⁹V. van Amerongen, L. Valkunas, and R. van Grondelle, *Photosynthetic Excitons* (World Scientific Publishing Co. Pte. Ltd., 2000).
- ⁵⁰V. May and O. Kühn, *Charge and Energy Transfer Dynamics in Molecular Systems*, 3rd ed. (Wiley-VCH Verlag GmbH & Co. KGaA, Weinheim, 2011).
- ⁵¹L. Valkunas, D. Abramavicius, and T. Mančal, *Molecular Excitation Dynamics and Relaxation* (Wiley-VCH Verlag GmbH & Co. KGaA, 2013).
- ⁵²V. M. Agranovich, *Excitations in Organic Solids* (Oxford University Press, New York, 2008).
- ⁵³T. Holstein, "Studies of polaron motion: Part I. The molecular-crystal model," *Ann. Phys.* **8**, 325–342 (1959).
- ⁵⁴A. Ishizaki and G. R. Fleming, "Unified treatment of quantum coherent and incoherent hopping dynamics in electronic energy transfer: Reduced hierarchy equation approach," *J. Chem. Phys.* **130**, 234111 (2009).
- ⁵⁵H. Rahman and U. Kleinekathöfer, "Chebyshev hierarchical equations of motion for systems with arbitrary spectral densities and temperatures," *J. Chem. Phys.* **150**, 244104 (2019).
- ⁵⁶V. M. Axt and S. Mukamel, "Influence of a phonon bath on electronic correlations and optical response in molecular aggregates," in *Nonlinear Optical Materials*, IMA Volume in Mathematics and Applications, edited by J. V. Moloney (Springer Science + Business Media, New York, 1998), pp. 1–32.
- ⁵⁷L. Zhu, H. Liu, W. Xie, and Q. Shi, "Explicit system-bath correlation calculated using the hierarchical equations of motion method," *J. Chem. Phys.* **137**, 194106 (2012).
- ⁵⁸Q. Ai, Y.-J. Fan, B.-Y. Jin, and Y.-C. Cheng, "An efficient quantum jump method for coherent energy transfer dynamics in photosynthetic systems under the influence of laser fields," *New J. Phys.* **16**, 053033 (2014).
- ⁵⁹R. J. Glauber, "Coherent and incoherent states of the radiation field," *Phys. Rev.* **131**, 2766–2788 (1963).
- ⁶⁰A. Chenu, A. M. Brańczyk, G. D. Scholes, and J. E. Sipe, "Thermal light cannot be represented as a statistical mixture of single pulses," *Phys. Rev. Lett.* **114**, 213601 (2015).
- ⁶¹A. Chenu, A. M. Brańczyk, and J. E. Sipe, "First-order decomposition of thermal light in terms of a statistical mixture of single pulses," *Phys. Rev. A* **91**, 063813 (2015).
- ⁶²A. Ishizaki and Y. Tanimura, "Nonperturbative non-Markovian quantum master equation: Validity and limitation to calculate nonlinear response functions," *Chem. Phys.* **347**, 185–193 (2008).
- ⁶³Y. Tanimura and S. Mukamel, "Description of nonlinear optical response using phase space wave packets," *J. Phys. Chem.* **97**, 12596–12601 (1993).
- ⁶⁴G. Mahan, *Many-Particle Physics* (Kluwer Academic, New York, 2000).
- ⁶⁵Q. Shi, L. Chen, G. Nan, R.-X. Xu, and Y. Yan, "Efficient hierarchical Liouville space propagator to quantum dissipative dynamics," *J. Chem. Phys.* **130**, 084105 (2009).
- ⁶⁶A. Ishizaki and G. R. Fleming, "On the adequacy of the Redfield equation and related approaches to the study of quantum dynamics in electronic energy transfer," *J. Chem. Phys.* **130**, 234110 (2009).
- ⁶⁷T. Förster, "Delocalized excitation and excitation transfer bulletin No. 18," Technical Report No. FSU-2690-18, Department of Chemistry, Florida State University, Tallahassee, 1964.
- ⁶⁸S. Jang, Y. Jung, and R. J. Silbey, "Nonequilibrium generalization of Förster-Dexter theory for excitation energy transfer," *Chem. Phys.* **275**, 319–332 (2002).
- ⁶⁹J. Seibt and T. Mančal, "Ultrafast energy transfer with competing channels: Non-equilibrium Förster and modified Redfield theories," *J. Chem. Phys.* **146**, 174109 (2017).
- ⁷⁰J. Wu and J. Cao, "Higher-order kinetic expansion of quantum dissipative dynamics: Mapping quantum networks to kinetic networks," *J. Chem. Phys.* **139**, 044102 (2013).
- ⁷¹J. Cao, "Effects of bath relaxation on dissipative two-state dynamics," *J. Chem. Phys.* **112**, 6719–6724 (2000).
- ⁷²R. Loudon, *The Quantum Theory of Light* (Oxford University Press, Oxford, 2000).
- ⁷³Z. S. Sadeq and P. Brumer, "Transient quantum coherent response to a partially coherent radiation field," *J. Chem. Phys.* **140**, 074104 (2014).
- ⁷⁴A. Chenu and P. Brumer, "Transform-limited-pulse representation of excitation with natural incoherent light," *J. Chem. Phys.* **144**, 044103 (2016).
- ⁷⁵L. Wald, "Basics in solar radiation at earth surface" (published online 2018), available at <https://hal-mines-paristech.archives-ouvertes.fr/hal-01676634>.
- ⁷⁶Y. Kano and E. Wolf, "Temporal coherence of black body radiation," *Proc. Phys. Soc.* **80**, 1273–1276 (1962).
- ⁷⁷C. L. Mehta, "Coherence-time and effective bandwidth of blackbody radiation," *Nuovo Cimento* **28**, 401–408 (1963).
- ⁷⁸A. Dodin, T. V. Tscherbul, and P. Brumer, "Coherent dynamics of V-type systems driven by time-dependent incoherent radiation," *J. Chem. Phys.* **145**, 244313 (2016).
- ⁷⁹V. Janković and T. Mančal, "Nonequilibrium steady-state picture of photosynthetic light harvesting," *J. Chem. Phys.* **153**(24), 244110 (2020).
- ⁸⁰M. O. Scully and M. S. Zubairy, *Quantum Optics* (Cambridge University Press, Cambridge, 1997).

Nonequilibrium steady-state picture of incoherent light-induced excitation harvesting

Cite as: J. Chem. Phys. 153, 244110 (2020); doi: 10.1063/5.0029918

Submitted: 17 September 2020 • Accepted: 7 December 2020 •

Published Online: 24 December 2020



View Online



Export Citation



CrossMark

Veljko Janković^{1,a)}  and Tomáš Mančal^{2,b)} 

AFFILIATIONS

¹Scientific Computing Laboratory, Center for the Study of Complex Systems, Institute of Physics Belgrade, University of Belgrade, Pregrevica 118, 11080 Belgrade, Serbia

²Faculty of Mathematics and Physics, Charles University, Ke Karlovu 5, 121 16 Prague 2, Czech Republic

^{a)} Author to whom correspondence should be addressed: veljko.jankovic@ipb.ac.rs

^{b)} Electronic mail: mancal@karlov.mff.cuni.cz

ABSTRACT

We formulate a comprehensive theoretical description of excitation harvesting in molecular aggregates photoexcited by weak incoherent radiation. An efficient numerical scheme that respects the continuity equation for excitation fluxes is developed to compute the nonequilibrium steady state (NESS) arising from the interplay between excitation generation, excitation relaxation, dephasing, trapping at the load, and recombination. The NESS is most conveniently described in the so-called preferred basis in which the steady-state excitonic density matrix is diagonal. The NESS properties are examined by relating the preferred-basis description to the descriptions in the site or excitonic bases. Focusing on a model photosynthetic dimer, we find that the NESS in the limit of long trapping time is quite similar to the excited-state equilibrium in which the stationary coherences originate from the excitation–environment entanglement. For shorter trapping times, we demonstrate how the properties of the NESS can be extracted from the time-dependent description of an incoherently driven but unloaded dimer. This relation between stationary and time-dependent pictures is valid, provided that the trapping time is longer than the decay time of dynamic coherences accessible in femtosecond spectroscopy experiments.

Published under license by AIP Publishing. <https://doi.org/10.1063/5.0029918>

I. INTRODUCTION

The observation of unexpectedly long-lived oscillatory features of ultrafast spectroscopic signals measured on photosynthetic pigment–protein complexes^{1,2} has generated much excitement during the past decade. The idea that (dynamic) coherences modulating these signals may be directly relevant to natural light harvesting,^{3,4} which is triggered by stationary incoherent sunlight,^{5,6} has been driving intense research activities in the field.^{7,8} Insights from ultrafast spectroscopies are indispensable in determining the underlying Hamiltonian of the system under investigation, from which the dynamics of excitation energy transfer (EET) under any excitation condition may be inferred (as long as the excitation is sufficiently weak).^{6,7,9–11} A number of experimental^{1,2} and theoretical^{12,13} studies speculating about a positive impact of coherences and entanglement on the biological EET have been

performed on the so-called unloaded systems. Such systems feature no transmission of photoinduced excitations to the reaction center (RC or load) from which the excitation energy is eventually harvested. Furthermore, the time scales addressed in these studies are generally much shorter than those representative of exciton recombination, either radiative or nonradiative.¹⁴ Direct experimental insights into the dynamics of molecular aggregates initiated by incoherent light are limited.¹⁵ Therefore, at present, the possible relevance of some sort of quantum coherence for EET under natural conditions is best examined within appropriate theoretical models.

Such models should contain a realistic description of photoexcitation by natural incoherent light, whose intensity is essentially constant from the molecular viewpoint. Thus, the physically plausible description of natural light harvesting should feature continuous generation of electronic excitations by light, their

continuous delivery to the RC, and their continuous loss by recombination.^{6,16–20} The EET is then studied from the standpoint of nonequilibrium steady states (NESSs), which arise as a result of excitation photogeneration, phonon-induced relaxation, dephasing, trapping at the RC, and recombination. Furthermore, the coupling between the radiation and absorbing pigments is, in general, weak so that its second-order treatment is reasonable. Then, the only information we need about the radiation is its first-order correlation function,⁹ which can be either modeled by appropriate expressions^{9,21} or obtained by a suitable ensemble average.^{21,22} Excitation and de-excitation events can be treated within the Born–Markov approximation²³ by Lindblad dissipators^{24,25} or by establishing the Bloch–Redfield quantum master equation.^{17,26} Approaching the problem from the perspective of open quantum systems, one can introduce an appropriate spectral density of light–matter coupling^{20,27–29} and possibly treat it even beyond the second order.²⁹

Reasonable models of photosynthetic EET should not overlook the non-Markovian interplay between photoinduced electronic excitations and nuclear reorganization processes,^{30,31} whose relevance is emphasized by ultrafast spectroscopic studies. To that end, a number of studies attempt to combine an explicit treatment of the photoexcitation step with a nonperturbative approach to the excitation–environment coupling.^{24,25,29,32–34} The method of choice for an exhaustive treatment of excitation–environment coupling are hierarchical equations of motion (HEOM).^{35,36} In the accompanying paper,³⁴ we combine HEOM with a second-order treatment of light–matter coupling for light of arbitrary properties. Our method correctly captures light-induced reorganization processes and nonequilibrium evolution of the bath between the two interactions with light.

Recently, a number of groups have suggested that stationary coherences in the energy basis (interexciton coherences) or local basis (intersite coherences) under incoherent illumination may improve the light-harvesting efficiency in photosynthetic systems.^{17,37–39} However, the majority of the existing theoretical approaches to NESSs in photosynthetic light harvesting typically feature a simplified treatment of the photoexcitation^{18,19,40} or a simplified treatment of excitation relaxation and dephasing.^{17,18,38–40} Also, efficient algorithms that avoid the explicit temporal propagation in the computation of NESSs induced by natural incoherent light have just begun to be developed.⁴¹ Therefore, there is still an urge to construct theoretical methods that circumvent the disparity between the time scales of EET dynamics and incoherent excitation sources and yet meet the two requirements outlined in the above text.

Another pertaining issue is the origin of stationary coherences, i.e., whether they are primarily induced by incoherent radiation or by the coupling to the protein environment. The authors of Ref. 29 argued that the NESS coherences ultimately stem from the entanglement of electronic excitations with the environment. This entanglement has been systematically studied both analytically^{42,43} and numerically^{42,44} within the undriven and unloaded spin–boson model. The two-level system displays noncanonical equilibrium statistics,^{45,46} whose deviation from the canonical equilibrium statistics can be conveniently measured by a single parameter.⁴² This parameter can be interpreted as the angle by which the basis in which the system’s Hamiltonian (or the system–bath

interaction Hamiltonian) is diagonal should be rotated to obtain the diagonal reduced density matrix (RDM). The basis in which the RDM is diagonal is thus singled out by the environment, and the corresponding basis states are known as the preferred (or pointer) states within the framework of the decoherence theory.^{47,48} The concept of preferred basis is useful whenever representation-dependent issues, such as the ones we are after in this study, arise.

In this paper, we extend the ideas developed in Ref. 42 to examine the properties of the NESS that arise in an incoherently driven and loaded excitonic aggregate. Adapting the algorithm presented in Ref. 49, we devise a procedure to find the NESS of our recently proposed HEOM that incorporates incoherent photoexcitation³⁴ and to properly define light-harvesting efficiency under incoherent illumination. Our theoretical approach fully respects the continuity equation for excitation fluxes. The NESS is most conveniently described in the so-called preferred basis in which the steady-state RDM is diagonal. Such a description of a driven and loaded aggregate may be regarded as analogous to the normal-mode description of a system of coupled harmonic oscillators. While our theoretical method is quite general and applicable to arbitrary excitonic networks, we investigate the properties of the NESS using the appropriately parameterized model dimer. For realistic values of the load extraction time, we conclude that light-induced coherences are completely irrelevant in the NESS, which is then close to the non-canonical equilibrium of the undriven and unloaded dimer. We find that the NESS of the driven and loaded dimer is intimately related to the dynamics of the driven but unloaded dimer, which takes place on the time scale of the excitation trapping at the load. This close connection between the dynamic and stationary picture is correct, provided that the load extraction time is longer than the time scale of coherence dephasing, which is, in principle, accessible in ultrafast spectroscopies.

This paper is structured as follows: The model and method are presented in Secs. II and III, respectively. In Sec. IV, we discuss the relation of the preferred-basis description of the NESS to more standard descriptions conducted in the site or excitonic basis. Section V presents numerical results with an emphasis on the relation between the time-dependent and stationary picture. In Sec. VI, we outline how the methodology presented in this work could be applied to multichromophoric systems. Section VII concludes this paper by summarizing its principal findings.

II. MINIMAL MODEL

We consider the simplest EET system, a molecular aggregate composed of two mutually coupled chromophores (a dimer and a spin–boson-like model⁵⁰). Although a similar model has been repeatedly used by many authors to gain insight into fundamentals of light harvesting under incoherent illumination,^{17,19,29,38,39,51,52} our analysis uses a rigorous theoretical approach to investigate in greater detail certain properties of the NESS that have not received enough attention so far. The dimer system can be considered as the minimal model of a photosynthetic antenna with delocalization in which one can study the effects of energy relaxation, dephasing, and (static) disorder in local transition energies (the so-called asymmetric dimer, see Sec. V A). To be specific, we speak about the model dimer, while we note that the model and the method to

be presented are quite general and applicable to multichromophoric situations.

Electronic excitations of the model dimer are modeled within the Frenkel exciton model,^{53,54} and the corresponding Hamiltonian reads as

$$H_M = \sum_j \varepsilon_j |l_j\rangle \langle l_j| + \sum_{jk} J_{jk} |l_j\rangle \langle l_k|. \quad (1)$$

In Eq. (1), $|l_j\rangle$ is the singly excited state localized on chromophore j and ε_j is its vertical excitation energy, while J_{jk} are resonance couplings (we take $J_{kk} \equiv 0$). We limit our discussion to the manifold of singly excited states, which is justified under the assumption that the driving by the radiation is sufficiently weak. The aggregate is in contact with the thermal bath, which represents its protein environment and is modeled as a collection of independent oscillators labeled by site index j and mode index ξ ,

$$H_B = \sum_{j\xi} \hbar \omega_\xi b_{j\xi}^\dagger b_{j\xi}. \quad (2)$$

The phonon creation and annihilation operators $b_{j\xi}^\dagger$ and $b_{j\xi}$ entering Eq. (2) satisfy Bose commutation relations. The aggregate is driven by weak radiation, and the generation of excitations is described in the dipole and rotating-wave approximations,

$$H_{M-R} = -\boldsymbol{\mu}_{eg} \cdot \mathbf{E}^{(+)} - \boldsymbol{\mu}_{ge} \cdot \mathbf{E}^{(-)}. \quad (3)$$

In Eq. (3), operators $\mathbf{E}^{(\pm)}$ are the positive- and negative-frequency part of the (time-independent) operator of the (transversal) electric field, while the eg part of the dipole-moment operator reads as

$$\boldsymbol{\mu}_{eg} = \boldsymbol{\mu}_{ge}^\dagger = \sum_j \mathbf{d}_j |l_j\rangle \langle g_j|. \quad (4)$$

We assume that transition dipole moment \mathbf{d}_j of chromophore j does not depend on nuclear coordinates (Condon approximation). The interaction of photoinduced excitations with the environment is taken to be in Holstein form, i.e., it is local and linear in oscillator displacements,

$$H_{M-B} = \sum_j |l_j\rangle \langle l_j| \sum_\xi g_{j\xi} (b_{j\xi}^\dagger + b_{j\xi}) \equiv \sum_j V_j u_j. \quad (5)$$

We assume that there are two possible channels through which photogenerated excitons may decay. The first one is their transfer to the charge-separated state in the RC, the case in which they are usefully harvested. On the other hand, exciton recombination, either radiative or nonradiative, is detrimental to the efficiency of EET. While our description of exciton photogeneration and the subsequent phonon-induced relaxation is exact (see Sec. III and Ref. 34), the description of exciton trapping by the RC and exciton recombination is only effective and relies on the results of more elaborate treatments performed in Refs. 55 and 56. There, it is realized that EET from one chromophore to another, as well as the radiative decay to the ground state, is actually mediated by the bath of environmental photons. Performing a second-order treatment of the appropriate interaction Hamiltonians, one ends up with

effective Liouville superoperators \mathcal{L}_{RC} and \mathcal{L}_{rec} that describe the excitation trapping and recombination on the level of reduced excitonic dynamics, respectively. In Secs. III and IV, we provide more details in the form of these effective Liouvillians and the manner in which they enter our description.

III. METHODS

We use our exact description of weak-light-induced exciton dynamics in molecular aggregates, which is developed in the accompanying paper.³⁴ The radiation correlation function, which is the only property of the radiation entering our reduced description, is modeled by the following expression:⁵⁷

$$G^{(1)}(\tau) = \left\langle E^{(-)}(\tau) E^{(+)}(0) \right\rangle_R = I_0 \exp(i\omega_c \tau - \tau/\tau_c), \quad (6)$$

where I_0 , ω_c , and τ_c are the intensity, central frequency, and coherence time of the radiation, respectively. The radiation is assumed to have well defined directions of propagation and polarization. The weak-light assumption underlying our theoretical approach is well satisfied in a wide variety of photosynthetically relevant situations. For example, for a bacteriochlorophyll molecule irradiated by ambient sunlight, the excitation–light interaction may be estimated to be of the order of 10^{-3} cm^{-1} (see the accompanying paper³⁴ and Ref. 25). This energy scale is much smaller than the typical energy scales ($\sim 10 \text{ cm}^{-1}$ – 100 cm^{-1}) of resonance couplings or the excitation–environment coupling. Also, the number of photons per unit time incident on a single photosynthetic complex under sunlight at the surface of the Earth can be estimated to be of the order of 1000 s^{-1} (see the accompanying paper³⁴ and Ref. 20). In other words, the corresponding time scale is orders of magnitude longer than time scales typical for excitation transport, trapping at the load, and recombination.

For the sake of simplicity, we assume that the baths on both sites are identical, but uncorrelated. The bath correlation function, which is the only property of the bath entering the reduced description, can be decomposed into the optimized exponential series⁵⁸ ($t \geq 0$),

$$C(t) = \langle u_j(t) u_j(0) \rangle_B = \sum_{m=0}^{K-1} c_m e^{-\mu_m t} + 2\Delta \delta(t). \quad (7)$$

In Eq. (7), the collective bath coordinate u_j is defined in Eq. (5) and the expansion coefficients c_m may be complex, while the corresponding decay rates μ_m , as well as the white-noise-residue strength Δ , are assumed to be real and positive. The bath correlation function is usually expressed in terms of the environmental spectral density $J(\omega)$ [$\beta = (k_B T)^{-1}$, where T is the temperature],

$$C(t) = \frac{\hbar}{\pi} \int_0^{+\infty} d\omega J(\omega) \frac{e^{i\omega t}}{e^{\beta\hbar\omega} - 1}, \quad (8)$$

which conveniently combines information on the density of environmental-mode states and the respective coupling strengths to electronic excitations.^{53,54} We explicitly treat only $K = N_{BE} + N_J$ terms in Eq. (7), where N_{BE} and N_J are the numbers of explicitly treated poles of the Bose–Einstein function and the bath spectral

density, respectively. We assume the environmental spectral density of the overdamped Brownian oscillator,

$$J(\omega) = 2\lambda \frac{\omega\gamma}{\omega^2 + \gamma^2}, \quad (9)$$

where λ is the reorganization energy, while γ^{-1} is the characteristic time scale for the decay of the bath correlation function $C(t)$.

The exponential decompositions embodied in Eqs. (6) and (7) enable us to formulate the problem as HEOM incorporating photoexcitation. As demonstrated in Ref. 34, the hierarchy consists of two parts: one in the eg sector and another in the ee sector. Each density matrix $\sigma_{\mathbf{n}}(t)$ is uniquely characterized by vector \mathbf{n} of non-negative integers $n_{j,m}$, where index j enumerates chromophores, while index m counts terms in the decomposition of $C(t)$ [Eq. (7)]. In order to describe excitation harvesting by the RC and recombination, we augment our formalism by effective Liouvillians describing these two processes. As demonstrated in Ref. 55, these Liouvillians appear on each level of HEOM. Performing the appropriate rescalings, which ensure that auxiliary density operators (ADOs) are all dimensionless and consistently smaller in deeper levels of the hierarchy,⁵⁹ we obtain the following equations describing the NESS we are interested in ($\gamma_{\mathbf{n}} = \sum_{j,m} n_{j,m} \mu_{j,m}$):

$$\begin{aligned} 0 = & -\frac{i}{\hbar\gamma} [H_M, \sigma_{eg,\mathbf{n}}^{ss}] - \frac{\gamma_{\mathbf{n}}}{\gamma} \sigma_{eg,\mathbf{n}}^{ss} + \left(i \frac{\omega_c}{\gamma} - (\tau_c\gamma)^{-1} \right) \sigma_{eg,\mathbf{n}}^{ss} \\ & - \frac{\Delta}{\hbar^2\gamma} \sum_j V_j \sigma_{eg,\mathbf{n}}^{ss} + \delta_{\mathbf{n},\mathbf{0}} \frac{i}{\hbar\gamma} I_0 \mu_{eg} \\ & + i \sum_j \sum_{m=0}^{K-1} \sqrt{1+n_{j,m}} \sqrt{\frac{|c_m|}{(\hbar\gamma)^2}} V_j \sigma_{eg,\mathbf{n}^+_{j,m}}^{ss} \\ & + i \sum_j \sum_{m=0}^{K-1} \sqrt{n_{j,m}} \frac{c_m/(\hbar\gamma)^2}{\sqrt{|c_m|/(\hbar\gamma)^2}} V_j \sigma_{eg,\mathbf{n}^-_{j,m}}^{ss}, \end{aligned} \quad (10)$$

$$\begin{aligned} 0 = & -\frac{i}{\hbar\gamma} [H_M, \sigma_{ee,\mathbf{n}}^{ss}] - \frac{\gamma_{\mathbf{n}}}{\gamma} \sigma_{ee,\mathbf{n}}^{ss} - \frac{\Delta}{\hbar^2\gamma} \sum_j V_j^\times V_j^\times \sigma_{ee,\mathbf{n}}^{ss} \\ & + \frac{i}{\hbar\gamma} \mu_{eg} \sigma_{eg,\mathbf{n}}^{ss\dagger} - \frac{i}{\hbar\gamma} \sigma_{eg,\mathbf{n}}^{ss} \mu_{eg}^\dagger + \gamma^{-1} \mathcal{L}_{\text{rec}}[\sigma_{ee,\mathbf{n}}^{ss}] \\ & + \gamma^{-1} \mathcal{L}_{\text{RC}}[\sigma_{ee,\mathbf{n}}^{ss}] + i \sum_j \sum_{m=0}^{K-1} \sqrt{1+n_{j,m}} \sqrt{\frac{|c_m|}{(\hbar\gamma)^2}} V_j^\times \sigma_{ee,\mathbf{n}^+_{j,m}}^{ss} \\ & + i \sum_j \sum_{m=0}^{K-1} \sqrt{n_{j,m}} \frac{c_m/(\hbar\gamma)^2}{\sqrt{|c_m|/(\hbar\gamma)^2}} V_j \sigma_{ee,\mathbf{n}^-_{j,m}}^{ss} \\ & - i \sum_j \sum_{m=0}^{K-1} \sqrt{n_{j,m}} \frac{c_m^*/(\hbar\gamma)^2}{\sqrt{|c_m|/(\hbar\gamma)^2}} \sigma_{ee,\mathbf{n}^-_{j,m}}^{ss} V_j. \end{aligned} \quad (11)$$

In the NESS, the continuity equation for exciton currents should be valid, i.e., the number of generated excitons per unit time must balance the sum of the recombination and trapping exciton fluxes. This is physically clear, and it is seen from a more formal perspective by taking the trace (with respect to the electronic system of interest) of Eq. (11) in which $\mathbf{n} = \mathbf{0}$. This results in

$$J_{\text{gen}} - J_{\text{RC}} - J_{\text{rec}} = 0. \quad (12)$$

In the continuity equation [Eq. (12)], we define all currents to be positive, while the sign is determined by the “direction” of the current (\pm if it leads to an increase/a decrease in the exciton number). In more detail, the definitions of currents, which are dimensionless in our description, are

$$J_{\text{gen}} = \frac{2}{\hbar\gamma} \text{Im Tr}_M \left\{ \sigma_{eg,\mathbf{0}}^{ss} \mu_{eg}^\dagger \right\}, \quad (13)$$

$$J_{\text{RC}} = -\gamma^{-1} \text{Tr}_M \left\{ \mathcal{L}_{\text{RC}}[\sigma_{ee,\mathbf{0}}^{ss}] \right\}, \quad (14)$$

$$J_{\text{rec}} = -\gamma^{-1} \text{Tr}_M \left\{ \mathcal{L}_{\text{rec}}[\sigma_{ee,\mathbf{0}}^{ss}] \right\}. \quad (15)$$

Let us immediately note that currents J_{gen} , J_{RC} , and J_{rec} are written in a basis-invariant manner. This feature is quite appealing, since one can express currents in terms of populations and coherences in any particular basis. The light-harvesting efficiency is defined as

$$\eta = \frac{J_{\text{RC}}}{J_{\text{gen}}}. \quad (16)$$

As discussed in the accompanying paper³⁴ and in Sec. VI, for realistic values of the light coherence time $\tau_c \sim 1$ fs, the expression for the generation current may be further simplified to

$$J_{\text{gen}} = 2 \frac{I_0 \gamma \tau_c}{(\hbar\gamma)^2} \text{Tr}_M \left\{ \mu_{eg} |g\rangle \langle g| \mu_{ge} \right\}. \quad (17)$$

In other words, possible enhancements in η due to coherences in any basis ultimately originate from the expression for the trapping Liouvillian \mathcal{L}_{RC} , as detailed in Sec. IV.

IV. DIFFERENT BASES

In the literature on the physics of photosynthetic light harvesting, two bases play special roles. The first one is basis $\{|l_j\rangle|j\rangle$ of singly excited states localized on single chromophores (local or site basis). While Hamiltonian parameters are usually known in the local basis, the description of absorption properties of a photosynthetic aggregate is usually performed in the excitonic basis $\{|x_j\rangle|j\rangle$, i.e., in the basis of stationary states of the isolated-aggregate Hamiltonian H_M . Claims about possible impact of coherences on the efficiency of photosynthetic light harvesting are usually made with the coherences in the excitonic or local basis in mind.

Tomasi and Kassal have recently classified different types of possible coherent enhancements of light harvesting efficiency according to the basis in which the excitation decay mechanisms are defined.³⁷ Let us now focus on the trapping at the RC. Two forms for the Liouvillian $\mathcal{L}_{\text{RC}}[\rho]$ are widely used in the literature.^{17,19,38–40} If site j_0 is closest to the RC so that it is essentially the sole site coupled to it, one uses the so-called localized-trapping Liouvillian,^{17,19,40}

$$\mathcal{L}_{\text{RC}}^{\text{loc}}[\rho] = \tau_{\text{RC}}^{-1} \left(|\text{RC}\rangle \langle l_{j_0} | \rho | l_{j_0} \rangle \langle \text{RC}| - \frac{1}{2} \{ |l_{j_0}\rangle \langle l_{j_0}|, \rho \} \right), \quad (18)$$

where τ_{RC} is the characteristic time scale on which the populations are delivered from site j_0 to the RC. However, even in such a situation, the excitation transfer to the RC should be regarded as the multichromophoric Förster transfer^{60,61} so that it is more appropriate to employ the so-called delocalized-trapping Liouvillian,^{17,40}

$$\mathcal{L}_{RC}^{\text{deloc}}[\rho] = \tau_{RC}^{-1} \sum_j |\langle x_j | l_{j_0} \rangle|^2 \left(|\text{RC}\rangle \langle x_j | \rho | x_j \rangle \langle \text{RC}| - \frac{1}{2} \{ |x_j\rangle \langle x_j|, \rho \} \right). \quad (19)$$

The recombination occurs due to both radiative and nonradiative processes. In other words, the lifetime of chromophores' excited states is determined not only by the fluorescent decay but also to a great extent by the conversion of the singlet states to triplets. While the radiative recombination is most naturally described in the excitonic basis, the nonradiative processes likely occur in a different basis of states, depending on how the triplet states are coupled among themselves. Overall, it is not possible to say that recombination occurs straightforwardly in neither the delocalized nor local basis. For definiteness, we assume that the (nonradiative) recombination may occur from each site with the same rate constant τ_{rec} , and the appropriate Liouvillian reads as

$$\mathcal{L}_{\text{rec}}^{\text{loc}}[\rho] = \tau_{\text{rec}}^{-1} \sum_j \left(|g\rangle \langle l_j | \rho | l_j \rangle \langle g| - \frac{1}{2} \{ |l_j\rangle \langle l_j|, \rho \} \right). \quad (20)$$

The fact that we have chosen the local version of the recombination should not, however, influence our results because the recombination process is generally much slower than every other process and it occurs on the time scale of nanoseconds, i.e., several orders of magnitude slower than trapping and other processes (see Sec. V). In situations in which the radiative decay is the major loss channel, it may be more appropriate to consider the recombination Liouvillian in the excitonic basis,

$$\mathcal{L}_{\text{rec}}^{\text{deloc}}[\rho] = \sum_j \tau_j^{-1} \left(|g\rangle \langle x_j | \rho | x_j \rangle \langle g| - \frac{1}{2} \{ |x_j\rangle \langle x_j|, \rho \} \right), \quad (21)$$

where τ_j^{-1} is the Weisskopf-Wigner spontaneous emission rate²⁵ from excitonic state $|x_j\rangle$.

If we assume the trapping at the RC to be governed by Eq. (18), the trapping current J_{RC} in Eq. (14) depends only on site populations and on both exciton populations and interexciton coherences. If, on the other hand, we assume that the trapping is governed by Eq. (19), J_{RC} is expressed in terms of exciton populations only, while its expression in the local basis contains both site populations and intersite coherences. This has been recognized in recent studies, which ascertain that possible coherent enhancements of the efficiency can be achieved only when the coherence occurs in a basis different from that in which the trapping or recombination is modeled.^{17,37}

However, we feel that the notion of coherent efficiency enhancements is not defined well enough. The word "enhancement" would suggest that there is a reference value of the efficiency (which should be smaller than unity) with respect to which we can expect to achieve an enhancement. Moreover, since the enhancement is supposed to be coherent, one could imagine that the aforementioned reference value should depend on populations only so that

the subsequent inclusion of coherences should enhance the efficiency above that reference value. Whatever the form of the effective trapping and recombination Liouvillians is, there will always be a basis in which J_{RC} is entirely expressed in terms of basis-state populations only. Such a basis will be denoted as $\{|p_j\rangle|j\rangle\}$ and termed the preferred basis of the NESS under investigation. The trapping current is then expressed only in terms of the RDM diagonal elements so that the efficiency value calculated in the preferred basis could be regarded as the reference value above which coherent enhancements due to non-zero values of coherences in some other basis (e.g., in the local or excitonic basis) may be possible. However, our definition of the efficiency [Eq. (16)] is basis-independent, and the fact that the coherences in the excitonic or local basis are non-zero should not be expected to bring about any efficiency enhancements.

While the above discussion about coherent efficiency enhancements is quite general, it will not be the main topic of our numerical investigations, which focus on a model photosynthetic dimer and in which the efficiency is close to unity (see Sec. V A). Our central question is how the stationary state of the incoherently driven and loaded molecular system looks like and how it relates to the two standard pictures: the picture of local states and the delocalized-states picture. Nevertheless, to the best of our knowledge, our work is among the first works that properly describe the principal physical features of excitation harvesting under incoherent light and properly define the light-harvesting efficiency.^{20,38,39} The arguments of the previous paragraph suggest that, once a proper description of the state in which the photosynthetic systems under incoherent illumination and load find themselves, the involvement of the coherences in the description of photosynthetic light harvesting should be critically reassessed. We thus believe that future applications of our NESS methodology to larger systems (see Sec. VI) could significantly contribute to the debate on possible coherent efficiency enhancements.

The excited-state sector of the steady-state RDM ρ_{ee}^{ss} in the preferred basis reads as

$$\rho_{ee}^{\text{ss}} \equiv \sigma_{ee,0}^{\text{ss}} = \sum_j p_j |p_j\rangle \langle p_j|. \quad (22)$$

The preferred basis is determined by the competition between excitation generation, pure dephasing, energy relaxation, excitation trapping at the RC, and recombination.

The excitonic (or site) basis and the preferred basis of the NESS are connected through a unitary transformation. For our model dimer, the most general transformation of that kind can be parameterized by four real parameters so that the basis vectors in the preferred basis are expressed in terms of the basis vectors in the excitonic basis as follows:⁶²

$$\begin{pmatrix} |p_0\rangle \\ |p_1\rangle \end{pmatrix} = e^{i\varphi_{px}/2} \begin{pmatrix} e^{i\psi_{px}} & 0 \\ 0 & e^{-i\psi_{px}} \end{pmatrix} \begin{pmatrix} \cos \theta_{px} & \sin \theta_{px} \\ -\sin \theta_{px} & \cos \theta_{px} \end{pmatrix} \begin{pmatrix} e^{i\Delta_{px}} & 0 \\ 0 & e^{-i\Delta_{px}} \end{pmatrix} \begin{pmatrix} |x_0\rangle \\ |x_1\rangle \end{pmatrix}. \quad (23)$$

Due to the phase freedom, we can immediately remove parameters φ_{px} and ψ_{px} from further discussion so that we are left with only two parameters, θ_{px} and Δ_{px} . From our subsequent discussion, it will emerge that the rotation angle θ_{px} is closely related to the analogous rotation angle, which measures the deviation from the

non-canonical statistics in the undriven and unloaded system (no generation, trapping, and recombination).⁴² The phase Δ_{px} is intimately connected to the rates of excitation trapping and recombination, which remove excitations from the system.

The parameters θ_{px} and Δ_{px} can be related to the Bloch angles θ_B^x and ϕ_B^x that are commonly used to characterize the basis in which the RDM is diagonal.^{42,44} Specifically, one can always normalize ρ_{ee}^{ss} to obtain $\tilde{\rho}_{ee}^{ss}$ whose trace is unity and whose eigenvalues will be denoted as \tilde{p}_j . For the model dimer, the operator $\tilde{\rho}_{ee}^{ss}$ can always be expressed as

$$\tilde{\rho}_{ee}^{ss} = \frac{1}{2}(\mathbb{I} + \mathbf{a} \cdot \boldsymbol{\sigma}), \quad (24)$$

where \mathbb{I} is the 2×2 unity matrix, while $\boldsymbol{\sigma} = \{\sigma_1, \sigma_2, \sigma_3\}$ are three Pauli matrices. Let σ_3 be diagonal in the excitonic basis (i.e., $\sigma_3 = |x_0\rangle\langle x_0| - |x_1\rangle\langle x_1|$) and let \mathbf{a}^x be the corresponding vector in Eq. (24). Then, it can be shown that the spherical angles θ_B^x and ϕ_B^x on the Bloch sphere are related to parameters θ_{px} and Δ_{px} as follows:

$$\cos \theta_B^x = \frac{a_3^x}{|\mathbf{a}^x|} = \text{sgn}(2\tilde{p}_0 - 1) \cdot \cos(2\theta_{px}), \quad (25)$$

$$\tan \phi_B^x = \frac{a_2^x}{a_1^x} = -\tan(2\Delta_{px}). \quad (26)$$

Equations (25) and (26) relate θ_{px} and Δ_{px} to the Bloch angles θ_B^x and ϕ_B^x , respectively, that are straightforwardly obtained from vector \mathbf{a}^x . In a similar manner, one obtains parameters θ_{pl} and Δ_{pl} of the unitary transformation that connects the preferred and the local basis. The rotation angle θ_{px} can always be chosen in the range $(0, \pi/4)$, while $\Delta_{px} \in (-\pi/4, \pi/4)$. This is discussed in greater detail in Sec. SI of the [supplementary material](#).

V. NUMERICAL RESULTS

A. Model parameterization and numerical implementation

Numerical computations are performed on an asymmetric dimer, which is schematically presented in Fig. 1. The parameters of our model are summarized in Table I.

In brief, we selectively and resonantly ($\hbar\omega_c = \varepsilon_0$) excited site 0 by weak-intensity radiation whose coherence time τ_c assumes the value representative of the natural sunlight.^{63,64} Such a selective excitation of one site was also a feature of previous studies on model dimers.^{17,19} As mentioned in Sec. III, the propagation direction and the polarization vector of the radiation are assumed to be well defined. While the transition dipole moment of site 1 is assumed to be orthogonal to the polarization vector, the magnitude of the projection of the transition dipole moment of site 0 onto the polarization vector will be further denoted as d_{eg} . While we assume the selective excitation of site 0, the excitation trapping at the load is modeled by Eq. (18) or Eq. (19) in which we assume that the load is coupled only to site 1, i.e., $j_0 = 1$ in Eqs. (18) and (19). Such an assumption is motivated by our wish to include the spatial transfer of excitations within our dimer model. The difference $\Delta\varepsilon_{01} = \varepsilon_0 - \varepsilon_1$ between the local energy levels, resonance coupling J_{01} , and bath relaxation time γ^{-1} assumes values typical of the Fenna–Matthews–Olson (FMO) complex.^{65,66} The value of the recombination time

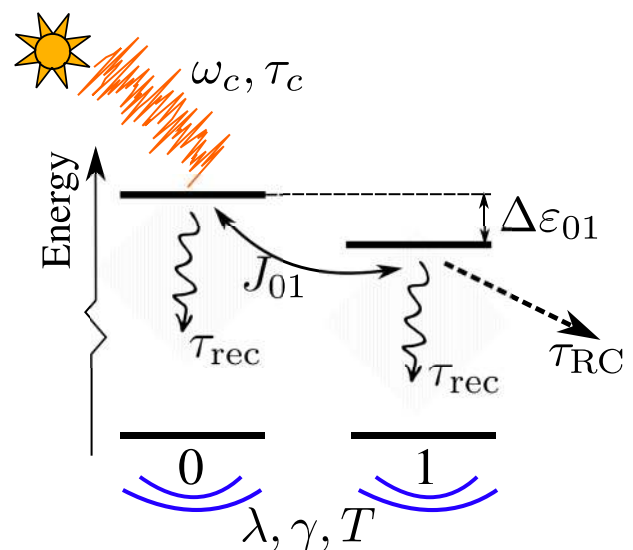


FIG. 1. Scheme of the model dimer. The electronic parameters of the dimer are the resonance coupling J_{01} and the difference between the local energy levels $\Delta\varepsilon_{01}$. The dimer is excited by thermal light (schematically represented by Sun and chaotic signal) characterized by the central frequency ω_c and coherence time τ_c [see Eq. (6)]. The transition dipole moment of site 1 is assumed to be perpendicular to the radiation polarization vector, whereas the magnitude of the projection of the transition dipole moment of site 0 onto the polarization vector is d_{eg} . Each chromophore is in contact with its thermal bath (schematically represented by the motion lines below chromophore numbers) characterized by the reorganization energy λ , correlation time γ^{-1} , and temperature T [see Eqs. (8) and (9)]. The time scale of the excitation harvesting, which is governed by Eq. (18) or Eq. (19), is τ_{RC} . The time scale of the excitation loss in recombination events, which is governed by Eq. (20), is τ_{rec} .

constant τ_{rec} is chosen on the basis of the measured exciton lifetime in the FMO complex^{67,68} and is similar to the value used in previous theoretical studies.^{17,19,40,69} Let us note that the recombination time scale is significantly longer than all other time scales in the problem. Also, in our model dimer, it is quite unlikely that an excitation would be prevented from reaching the RC during its lifetime. Therefore, the recombination is not probable, the precise value of τ_{rec} is not important, and the light-harvesting efficiency will always be close to 1 in the model dimer.^{19,38} The recombination is explicitly treated in order to formulate the continuity equation [Eq. (12)], and the efficiency η is not of primary interest in this work, which will be focused on other relevant properties of the NESS. Within our simplified model, there is a certain level of arbitrariness in the choice

TABLE I. Values of model parameters used in computations.

$\Delta\varepsilon_{01}$ (cm ⁻¹)	100
J_{01} (cm ⁻¹)	100
γ^{-1} (fs)	100
T (K)	300
$\hbar\omega_c$	ε_0
τ_c (fs)	1.3
τ_{rec} (ns)	1.0

of the appropriate value of τ_{RC} . Specifically, a more elaborate treatment of excitation harvesting should explicitly consider both the forward and backward excitation transfer from the absorbing aggregate to the state of the primary electron donor in the RC, as well as the primary charge separation, after which the excitation may be considered as usefully harvested.^{70–72} Previous theoretical works employing a simplified description of excitation harvesting, as we do here, typically assumed that τ_{RC} is of the order of picoseconds.^{66,69} On the other hand, experiments on various species of photosynthetic bacteria, as well as computational studies, suggest that the appropriate value of our parameter τ_{RC} may be as large as a couple of tens of picoseconds.^{71,73–75} The reported values of the reorganization energy in the FMO complex range from tens to hundreds of inverse centimeters.^{75–77} Having all these things considered, the values of τ_{RC} and λ will be varied in wide yet physically relevant ranges in order to examine how they impact the properties of the NESS.

The NESS is obtained by solving coupled Eqs. (10) and (11) by adapting the algorithm that was introduced in Ref. 49. The computational approach of Ref. 49 was developed to compute the equilibrium RDM of an undriven and unloaded system and it relies on the Jacobi iterative procedure to solve a diagonally dominant system of linear algebraic equations. The procedure is repeated until a convergence criterion, which, in Ref. 49, was related to the magnitude of the ADO elements, is satisfied. Here, we deal with a driven and loaded system, and our computations are terminated once the continuity equation [Eq. (12)] is satisfied with a desired numerical accuracy. More details on our numerical scheme to compute the NESS of a driven and loaded dimer can be found in Sec. SII of the [supplementary material](#).

B. Results: Long trapping times

Figures 2 and 3 summarize the dependence of the parameters of the unitary transformation between the preferred and excitonic (local) basis on the reorganization energy and the trapping time at the RC. The trapping is assumed to be governed by the localized Liouvillian [see Eq. (18)], while the recombination is described by the Liouvillian in Eq. (20). When the trapping at the RC is so slow that τ_{RC} is (much) longer than characteristic time scales for excitation dephasing and energy relaxation, phases Δ_{px} and Δ_{pl} tend to zero [see Figs. 2(a) and 3(a) for $\tau_{RC} \sim 20$ ps–100 ps]. These time scales are still much shorter than those relevant for recombination. Therefore, the obtained NESS is expected to be quite similar to the equilibrium state of an undriven and unloaded aggregate.²⁹ To confirm this expectation, in Figs. 4(a) and 4(b), we plot angles θ_{px} and θ_{pl} as functions of the reorganization energy for different values of τ_{RC} . We conclude that, as τ_{RC} is increased, angles θ_{px} and θ_{pl} tend to the values specific to the thermal equilibrium of undriven and unloaded dimers (in which we may formally identify $\tau_{RC}, \tau_{rec} \rightarrow +\infty$). For small reorganization energies, angle θ_{px} tends to zero [see Fig. 4(a)], and the preferred basis is close to the excitonic basis. At the same time, the limiting value reached by θ_{pl} as the reorganization energy is decreased [see Fig. 4(b)] corresponds to the angle of the rotation by which the excitonic basis is transformed into the local basis (the mixing angle θ_{xl} is given as $\tan(2\theta_{xl}) = 2J_{01}/\Delta\epsilon_{01}$). As the reorganization energy is increased, the preferred basis continuously changes from the excitonic basis [in which H_M is diagonal, see Eq. (1)] toward

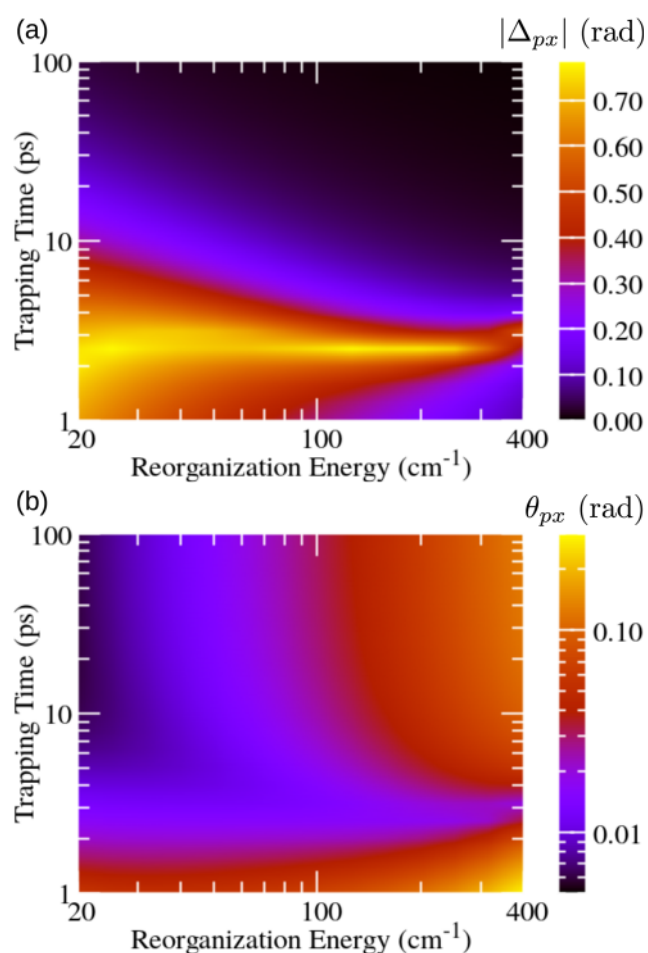


FIG. 2. Dependence of transformation parameter (a) Δ_{px} and (b) θ_{px} between the preferred and excitonic basis on the reorganization energy λ and the trapping time τ_{RC} at the RC. Trapping at the RC is governed by the localized-trapping Liouvillian [Eq. (18)], while the recombination is described by the Liouvillian in Eq. (20). Both axes feature logarithmic scale and the scale of the color bar in (a) is linear, while that of the color bar in (b) is logarithmic. The maximal value on the color bar in (a) is $\pi/4$.

the local basis [in which H_{M-B} is diagonal, see Eq. (5)].⁴² Therefore, the magnitude of θ_{px} increases [see Fig. 4(a)], while the magnitude of θ_{pl} decreases [see Fig. 4(b)] with the increase in reorganization energy.

C. Results: Short trapping times. Relation between stationary and time-dependent pictures

On the other hand, when the trapping at the RC is faster, phases Δ_{px} and Δ_{pl} increase in magnitude [see Figs. 2(a) and 3(a)], while the values of angles θ_{px} and θ_{pl} start to deviate from the respective values in the thermal equilibrium [see Figs. 2(b) and 3(b)]. These deviations are more pronounced as the trapping time is decreased and the reorganization energy is increased [see the lower right corners of Figs. 2(b) and 3(b)]. At the same time, the magnitude of phase Δ_{px}

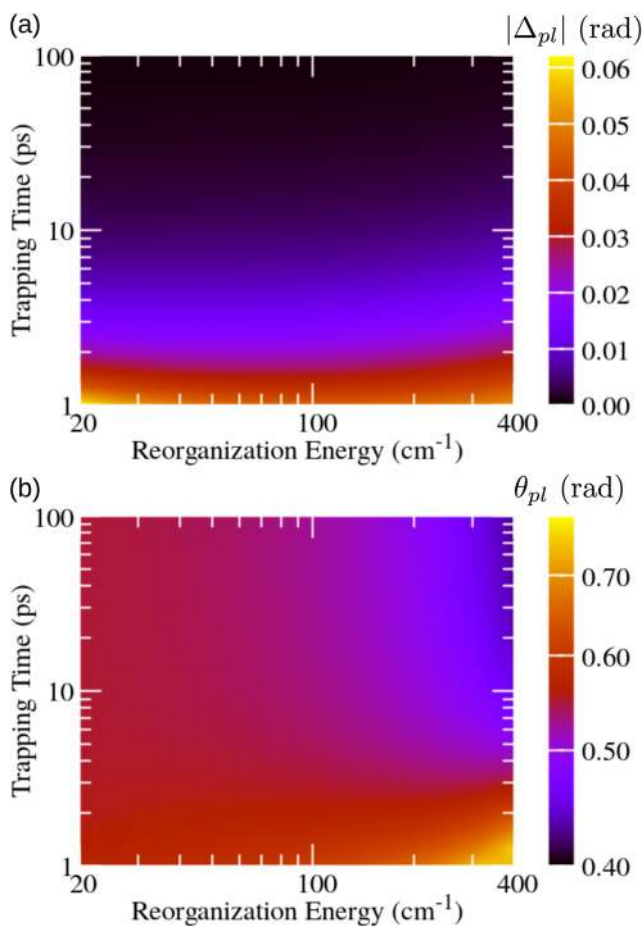


FIG. 3. Dependence of transformation parameter (a) Δ_{pl} and (b) θ_{pl} between the preferred and local basis on the reorganization energy λ and the trapping time τ_{RC} at the RC. Trapping at the RC is governed by the localized-trapping Liouvillian [Eq. (18)], while the recombination is described by the Liouvillian in Eq. (20). Both axes feature logarithmic scale and the scale of the color bar in (a) is linear, while that of the color bar in (b) is logarithmic. The maximal value on the color bar in (b) is $\pi/4$.

is large in the region of fast trapping and relatively small reorganization energy [see the lower left corner in Fig. 2(a)], while the increase that $|\Delta_{pl}|$ displays as the trapping time is reduced is virtually the same for all considered values of reorganization energy [see Fig. 3(a)]. It was suggested that the trapping time practically determines the temporal frame in which the intrinsic dimer's dynamics is interrogated.²⁹ It is therefore interesting to examine if the dependence of the transformation parameters between the excitonic (or site) and the preferred basis of the NESS on the trapping time (vertical cuts in Figs. 2 and 3) can somehow be recovered from the dynamics of the unloaded dimer initiated by suddenly turned-on incoherent light.

To gain some intuition on the relation between the stationary and time-dependent pictures, let us consider the differential equation

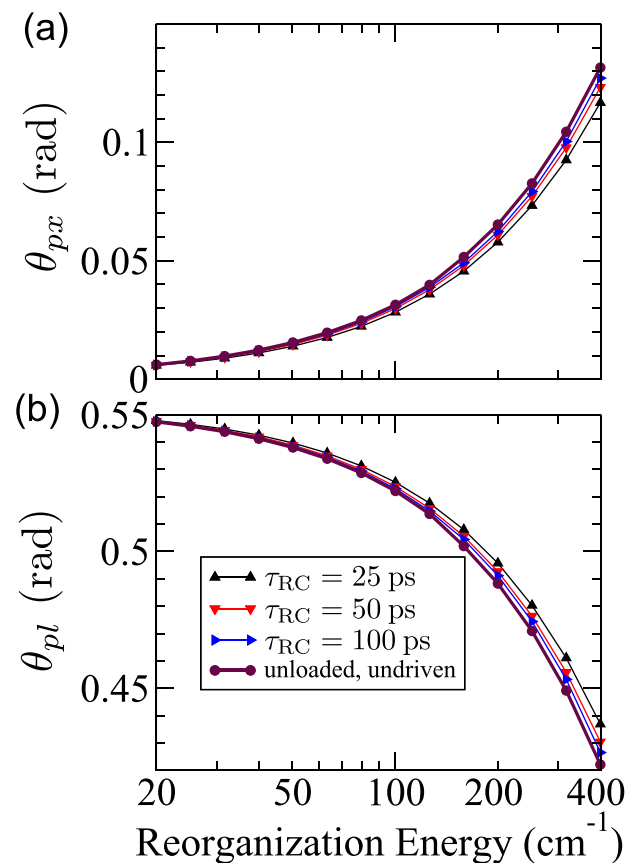


FIG. 4. Dependence of transformation parameter (a) θ_{px} (between the preferred and excitonic basis) and (b) θ_{pl} (between the preferred and site basis) on the reorganization energy λ for fixed values of the trapping time at the RC ($\tau_{RC} = 25$ ps, 50 ps, and 100 ps) and for the undriven and unloaded dimers (formally, $\tau_{RC} \rightarrow +\infty$). Trapping at the RC is governed by the localized-trapping Liouvillian [Eq. (18)], while the recombination is described by the Liouvillian in Eq. (20).

$$\frac{df(t)}{dt} = G - Df(t). \quad (27)$$

This equation models the system, characterized by quantity f , that is subjected to continuous pumping (source term G) and continuous decay (decay rate D). It resembles the equation for the total excited-state population that may be obtained by taking the trace of the temporal counterpart of Eq. (11) for $\mathbf{n} = \mathbf{0}$ (on the level of the RDM). The stationary point of Eq. (27) is $f^{ss} = G/D$. If one considers the driven system in the absence of decay channels, its dynamics is governed by $\frac{df^{ul}(t)}{dt} = G$ (the superscript “ul” specifies that the system is unloaded). To solve the last equation, we assume that the driving is suddenly turned on at instant $t = 0$ and that the initial condition is $f^{ul}(0) = 0$ (which would correspond to the initially unexcited system). One immediately realizes that $f^{ul}(D^{-1}) = f^{ss}$, i.e., the steady-state solution f^{ss} under constant driving and decay can be obtained from the temporal evolution $f^{ul}(t)$ of the driven system without decay channels at instant $t = D^{-1}$ corresponding to the characteristic decay time.

In the following, we develop the above-described simple argument in the situation of our interest. While the argument is quite formal, some of its parts will be specifically developed for the case of our model dimer, and in Sec. VI, we discuss its validity in multichromophoric situations.

Let us first note that there is a hierarchy of temporal scales characteristic for the dimer's dynamics under weak incoherent light. The shortest time scales (roughly speaking, tens to hundreds of femtoseconds) stem from the intrinsic dimer's dynamics. The time scale of the trapping at the load is of the order of 1 ps–10 ps in the photosynthetically relevant range of parameters. The longest time scale characterizes the excitation loss by recombination, and it is of the order of nanoseconds. The assumption of weak light actually means that the radiation is so weak that the number of incident photons per unit time is very small and the corresponding time scale is the longest time scale in the problem (we may loosely say that the light intensity is so low that the absorption of incident radiation is the rate-limiting process).

We now concentrate on the NESS Eqs. (10) and (11). Within our second-order treatment of the light–matter interaction, one can first solve Eq. (10) and obtain the steady-state in the *eg* sector, $\{\sigma_{eg,n}^{ss}|\mathbf{n}\}$, and then use this solution to compute the source term in the *ee* sector [the third term on the RHS of Eq. (11)]. Given the known source term in the *ee* sector, which will be denoted as \mathbf{G} , Eq. (11) can be recast as

$$0 = \mathbf{G} - (\hat{A} + \hat{D})\rho^{ss}, \quad (28)$$

where ρ^{ss} is the HEOM-space representation of the RDM and ADMs and \hat{A} is the HEOM-space representation of the hierarchical links between DMs [it comprises terms 1, 2, and 5–7 on the RHS of Eq. (11)], while \hat{D} is the HEOM-space representation of the recombination and trapping at the load [term 4 on the RHS of Eq. (11)]. Equation (28) is solved by

$$\rho^{ss} = (\hat{A} + \hat{D})^{-1}\mathbf{G}. \quad (29)$$

While the matrix \hat{A} is off-diagonal in the HEOM space and non-symmetric, the matrix \hat{D} is diagonal in the HEOM space. Whatever the form of the trapping and recombination Liouvillians is, all the matrix elements of \hat{D} are of the same magnitude, $\sim \tau_{RC}^{-1}$ (due to the above-mentioned hierarchy of dimer's temporal scales, the recombination rate, τ_{rec}^{-1} , is completely irrelevant). Moreover, the eigenvalues of matrix \hat{A} , which represent the rates of the internal dimer's dynamics, are much larger than τ_{RC}^{-1} . Therefore, computing the inverse $(\hat{A} + \hat{D})^{-1}$, we can regard \hat{D} as a small isotropic correction to \hat{A} . In the lowest-order approximation, the spectral decomposition of $(\hat{A} + \hat{D})^{-1}$ can be formulated as

$$(\hat{A} + \hat{D})^{-1} \approx \sum_k (a_k + d_k)^{-1} |a_k^R\rangle \langle a_k^L|, \quad (30)$$

where a_k , $|a_k^R\rangle$, and $\langle a_k^L|$ are the eigenvalues and right and left eigenvectors of matrix \hat{A} , respectively, while d_k are the elements of \hat{D} (they are all approximately the same).

Let us now focus on the temporal counterparts of Eqs. (10) and (11) in which the trapping and recombination Liouvillians

are omitted. Within our second-order treatment of the light–matter interaction, one can first solve the dynamics in the *eg* sector [Eq. (10)] and then use this solution as a known time-dependent source term in Eq. (11), which describes the *ee* sector we are primarily interested in. However, as advocated in the accompanying paper,³⁴ for realistic values of the light coherence time (of the order of 1 fs for natural sunlight), this source term is approximately time-independent (see also the expression for the generation current in the limit of short coherence time of light) and thus equal to \mathbf{G} introduced in the above discussion. The temporal counterpart of Eq. (11) without trapping and recombination then reads as

$$\partial_t \rho^{ul}(t) = \mathbf{G} - \hat{A} \rho^{ul}(t). \quad (31)$$

Assuming that the light is abruptly turned on at $t = 0$ and that $\rho^{ul}(0) = \mathbf{0}$, the solution is

$$\rho^{ul}(t) = \int_0^t ds e^{-\hat{A}(t-s)} \mathbf{G}. \quad (32)$$

In the spectral representation of \hat{A} , the solution reads as

$$\rho^{ul}(t) = \sum_k \left(\int_0^t ds e^{-a_k(t-s)} \right) |a_k^R\rangle \langle a_k^L| \mathbf{G}. \quad (33)$$

It is known from the literature⁷⁸ that, for the spin–boson model whose coupling to the environment has the overdamped Brownian oscillator spectral density [Eq. (9)], at least one of the eigenvalues of matrix \hat{A} is equal to zero, while non-zero eigenvalues appear in complex conjugate pairs and have positive real parts. Assuming that $a_0 = 0$, the time-dependent solution for a driven but unloaded system [Eq. (32)] can be recast as

$$\rho^{ul}(t) = t |0^R\rangle \langle 0^L| \mathbf{G} + \sum_{k \neq 0} \frac{1 - e^{-a_k t}}{a_k} |a_k^R\rangle \langle a_k^L| \mathbf{G}. \quad (34)$$

The same observations enable us to recast the spectral form of the NESS solution under driving and load as

$$\rho^{ss} \approx \frac{1}{d_0} |a_0^R\rangle \langle a_0^L| \mathbf{G} + \sum_{k \neq 0} \frac{1}{a_k} \left(1 + \frac{d_k}{a_k} \right)^{-1} |a_k^R\rangle \langle a_k^L| \mathbf{G}. \quad (35)$$

Remembering that $d_0 \sim \tau_{RC}^{-1}$ and that $|d_k/a_k|$ is sufficiently smaller than 1 for all $k \neq 0$, we can approximate $e^{-a_k/\tau_{RC}} \approx 0$ in Eq. (34) and $(1 + d_k/a_k)^{-1} \approx 1$ in Eq. (35) to finally obtain that

$$\rho^{ul}(\tau_{RC}) \approx \rho^{ss} \approx \tau_{RC} |a_0^R\rangle \langle a_0^L| \mathbf{G} + \sum_{k \neq 0} \frac{1}{a_k} |a_k^R\rangle \langle a_k^L| \mathbf{G}. \quad (36)$$

We have just demonstrated that the dimer's NESS can be reconstructed from the time evolution of the initially unexcited, driven, but unloaded dimer at instant $t \sim \tau_{RC}$ after a sudden turn-on of the driving. This result establishes an interesting relationship between the stationary (with load) and time-dependent (without load) pictures under incoherent driving.

While the physical relevance of the sudden turn-on of incoherent light may be questionable (see Ref. 6 and references therein),

this formal argument demonstrates that there is a formal connection between this seemingly unphysical setting and the NESS picture. However unphysical the sudden turn-on may be, the final-value theorem from the theory of Laplace transforms ensures that Eq. (32) in which the load is added, i.e., $\hat{A} \rightarrow \hat{A} + \hat{D}$, can be used to obtain the NESS in Eq. (29) by temporal propagation up to sufficiently long time $t \rightarrow +\infty$.

In the following, we concentrate on a numerical demonstration of this relationship. First, we propagate the temporal counterparts of Eqs. (10) and (11) in which the trapping and recombination Liouvillians are omitted [see Figs. 5(a1)–5(d2)]. The RDM elements [in Figs. 5(a1)–5(d2), in the excitonic basis] are measured in units of $I_0 d_{eg}^2 / (\hbar\gamma)^2$ and not in absolute units, as is customarily done. Our reason for choosing this unit lies in our perturbative treatment of

the interaction with light, which ensures that singly excited-state populations and intraband coherences are proportional to the light intensity I_0 [see Eq. (6)] and to the excited-state oscillator strength d_{eg}^2 (see the caption of Fig. 1). Analyzing Eqs. (10) and (11), one can readily conclude that $I_0 d_{eg}^2 / (\hbar\gamma)^2$ is the natural unit to measure populations and coherences. The absolute value of this unit may be estimated by using the estimate for the magnitude of the excitation–light interaction given in Sec. III, $\sqrt{I_0 d_{eg}^2} \sim 10^{-3} \text{ cm}^{-1}$, so that for the value of γ given in Table I, we obtain $I_0 d_{eg}^2 / (\hbar\gamma)^2 \simeq 4 \times 10^{-10}$. Second, we use the RDM $\sigma_{ee,0}(\tau_{RC})$ at $t = \tau_{RC}$ to determine the transformation parameters Δ and θ by virtue of Eqs. (24)–(26). The results emerging from these real-time computations are confronted with the results emerging from NESS computations in Figs. 5(a3)–5(d4)

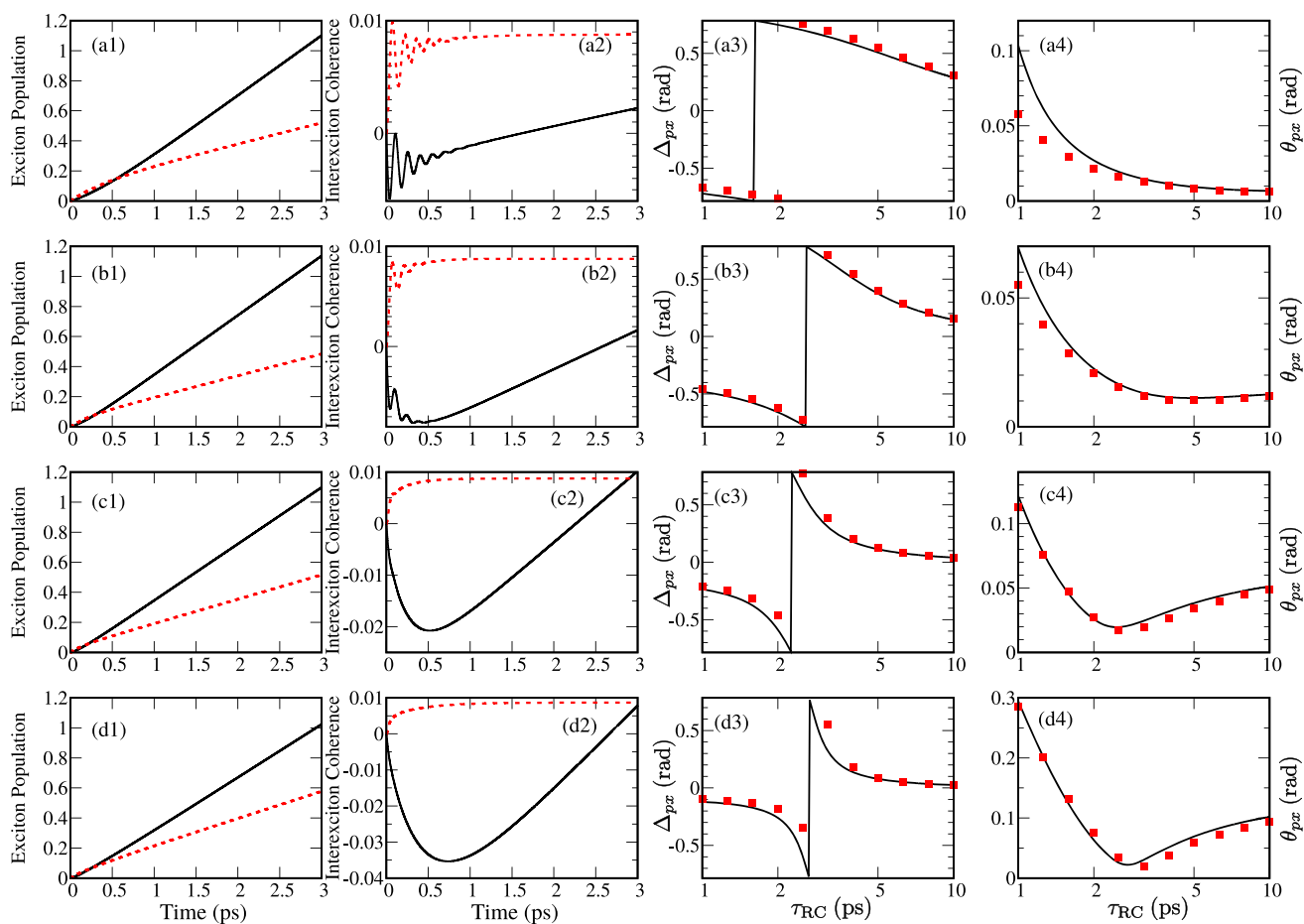


FIG. 5. (a1)–(d1) Time dependence of populations of exciton states $|x_0\rangle$ (solid line) and $|x_1\rangle$ (dashed line) of the incoherently driven and unloaded model dimer for different values of the reorganization energy. [(a2)–(d2)] Time dependence of the real (solid line) and imaginary (dashed line) parts of the interexciton coherence of the incoherently driven and unloaded model dimer for different values of the reorganization energy. Both exciton populations and interexciton coherences are measured in units of $I_0 d_{eg}^2 / (\hbar\gamma)^2$. The excitation is suddenly turned on at $t = 0$. Dependence of the transformation parameters Δ_{px} [(a3)–(d3)] and θ_{px} [(a4)–(d4)] between the excitonic basis and the preferred basis of the NESS on the trapping time constant $\tau_{RC} \in (1, 10)$ ps for different values of the reorganization energy. Solid lines are computed using time traces of a driven and unloaded model dimer at $t = \tau_{RC}$, while squares emerge from the computation of the NESS using Eqs. (10) and (11). The scale on the abscissa (τ_{RC}) in (a3)–(d4) is logarithmic. Trapping at the RC is governed by the localized-trapping Liouvillian [Eq. (18)], while the recombination is described by the Liouvillian in Eq. (20). The values of the reorganization energy are 20 cm^{-1} [(a1)–(a4)], 50 cm^{-1} [(b1)–(b4)], 200 cm^{-1} [(c1)–(c4)], and 400 cm^{-1} [(d1)–(d4)].

for a couple of values of the reorganization energy. It is observed that the two methods predict quite similar values of transformation parameters Δ_{px} and θ_{px} for all the examined values of the reorganization energy and trapping time. This result, together with the RDM dynamics initiated by a sudden turn-on of incoherent radiation, can help us better understand the dependence of Δ_{px} and Δ_{pl} on τ_{RC} for $\tau_{RC} \sim 1$ ps–10 ps. The discontinuous change from $-\pi/4$ to $\pi/4$ that phase Δ_{px} undergoes at around 2 ps–3 ps [see the bright area in Fig. 2(a)] should be attributed to the fact that the real part of interexciton coherence in an incoherently driven but unloaded dimer becomes equal to zero at around 2 ps–3 ps [see solid curves in Figs. 5(a2)–5(d2)]. The imaginary part of the interexciton coherence saturates somewhat earlier [see dashed curves in Figs. 5(a2)–5(d2)]. As τ_{RC} is further increased, Δ_{px} decreases because the real part of the interexciton coherence is increasing [see also Eq. (26)].

The relation between the NESS and RDM dynamics in real time leans on the above-mentioned hierarchy of time scales of the dimer's dynamics, i.e., on the fact that the trapping time scale is long enough. Specifically, in time traces of a driven and unloaded dimer for $t \gtrsim 1$ ps, one observes that the behavior of both exciton populations [Figs. 5(a1)–5(d1)] and interexciton coherences [Figs. 5(a2)–5(d2)] displays certain steadiness. In other words, populations, as well as the real part of the interexciton coherence, linearly increase in time, while the imaginary part of the interexciton coherence reaches a constant value (see also the accompanying paper).³⁴ When the trapping time constant is $\tau_{RC} \gtrsim 1$ ps so that at $t = \tau_{RC}$, the steadiness has already been established, the dynamical quantities of a driven but unloaded dimer may be used to quite accurately reconstruct the NESS. On the other hand, when $\tau_{RC} \lesssim 1$ ps so that the steadiness has not been established yet, the reconstruction of the NESS from the quantities of a driven and unloaded dimer computed at τ_{RC} would be less accurate. This is particularly clear for low values of the reorganization energy [see Figs. 5(a3) and 5(a4)], when oscillations in the interexciton coherence are damped on a time scale of ~ 200 fs–300 fs [see Fig. 5(a2)]. A similar situation can be expected for slow bath when the bath correlation time γ^{-1} is long enough.³⁵ In such cases, the reconstruction of NESS from the dynamics of the incoherently driven and unloaded dimer is not accurate because τ_{RC} is comparable to the time scales of the intrinsic dimer's dynamics. At this point, it is useful to remember that the information extracted from ultrafast spectroscopic signals can be used to determine the Hamiltonian parameters of the system under consideration, i.e., to determine the rate constants $\text{Re}\{a_k\}$ and the frequencies $\text{Im}\{a_k\}$ of the oscillatory features of the intrinsic dimer's dynamics that enter Eqs. (30) and (32)–(36).^{6,7,9–11} The dynamics of a driven but unloaded system in which the driving is abruptly turned on at $t = 0$ [see Eq. (32) and Figs. 5(a1)–5(d2)] can be formally regarded as the interference of all possible outcomes $e^{-\hat{A}(t-s)}\mathbf{G}$ of ultrafast experiments in which the delta-like excitation is centered at instant $s \in (0, t)$ and which freely evolve for the time interval of length $t-s$. The initial condition is set by the ratios (the initial condition has to be dimensionless!) of the components of the generation vector \mathbf{G} , which can be shown to be basically proportional to the square of the transition dipole moments and dependent on their mutual alignments (see Sec. VI). The oscillatory features stemming from the abruptly turned-on incoherent light in Figs. 5(a2) and 5(b2) are thus tightly connected to the oscillatory features characteristic of the excitation by very short pulses. The

time scales on which the oscillatory features can be observed thus set the lower limit on τ_{RC} for which the above-described relationship between the stationary and dynamic pictures is valid. Therefore, the decay time of dynamical coherences observed in spectroscopies may still be relevant in the natural setting, although the dynamical coherences themselves are absent in the NESS.⁷⁹ In Sec. SIII of the [supplementary material](#), we estimate the time scales characteristic of exciton decoherence by suitable fitting procedures. For the values of model parameters adopted in this work, we find that the characteristic decay times of exciton coherence are shorter than reasonable values of τ_{RC} .

The previous discussion was conducted for interexciton coherences. Similar conclusions can be also reached in the site basis (see Fig. 3). While we have already discussed the limit of long trapping time in Fig. 4(b), the case of relatively short $\tau_{RC} \sim 1$ ps–10 ps is analyzed in greater detail in Fig. S2 of the [supplementary material](#). The analysis is completely analogous to that accompanying Figs. 5(a1)–5(d4).

The choice of instant $t = \tau_{RC}$ at which time-dependent quantities are extracted to obtain the properties of the NESS is somewhat arbitrary because τ_{RC} is not really the time, but the characteristic time scale of the trapping. This is also apparent from our formal demonstration of the relation between the stationary and time-dependent pictures in which we only used the fact that all d_k are of the order of τ_{RC}^{-1} , while their precise values were not important. Moreover, in the results presented so far, we used the trapping [Eq. (18)] and recombination [Eq. (20)] Liouvillians that are diagonal in the local basis. It is, therefore, not obvious if and how the above-discussed relation between the dynamic and stationary pictures under incoherent driving changes when the trapping or recombination Liouvillian that is diagonal in the excitonic basis [Eqs. (19) and (21)] is employed. In Figs. 6(a) and 6(b), which are analogous to Figs. 2(a) and 2(b), respectively, we examine the dependence of the transformation parameters Δ_{px} and θ_{px} on λ and τ_{RC} under the assumption of delocalized trapping, while we retain the recombination Liouvillian in Eq. (20). The main features of Figs. 2(a) and 2(b) are clearly recognizable in Figs. 6(a) and 6(b). This is particularly true at long trapping times. However, at short trapping times, the maximum that $|\Delta_{px}|$ reaches in Fig. 2(a) at $\tau_{RC} \sim 2$ ps–3 ps is shifted toward $\tau_{RC} \sim 1$ ps–2 ps in Fig. 6(a). A similar discussion applies to Fig. 6(b), where the decrease that θ_{px} exhibits as τ_{RC} is increased from 1 ps is shifted to shorter trapping times with respect to Fig. 2(b). We believe that the maximum in $|\Delta_{px}|$, which occurs at $\tau_{RC} \sim 1$ ps–2 ps for delocalized trapping, should still be interpreted to originate from the fact that the real part of the interexciton coherence in the driven and unloaded dimer changes its sign on a picosecond time scale. If the real part of the interexciton coherence is equal to zero at instant t_0 , it is not guaranteed that the magnitude of Δ_{px} (computed from the NESS) reaches its maximal value of $\pi/4$ exactly at $\tau_{RC} = t_0$ [this is also observed in Figs. 5(a3)–5(d3)]. Our point here is that the magnitude of Δ_{px} reaches $\pi/4$ at $\tau_{RC} \sim t_0$ irrespective of the precise form of the trapping Liouvillian.

D. Further results

In the following, we discuss how the variations in the electronic parameters of the model, particularly in the difference $\Delta\varepsilon_{01}$ between local energy levels, affect the properties of the NESS. We fix the

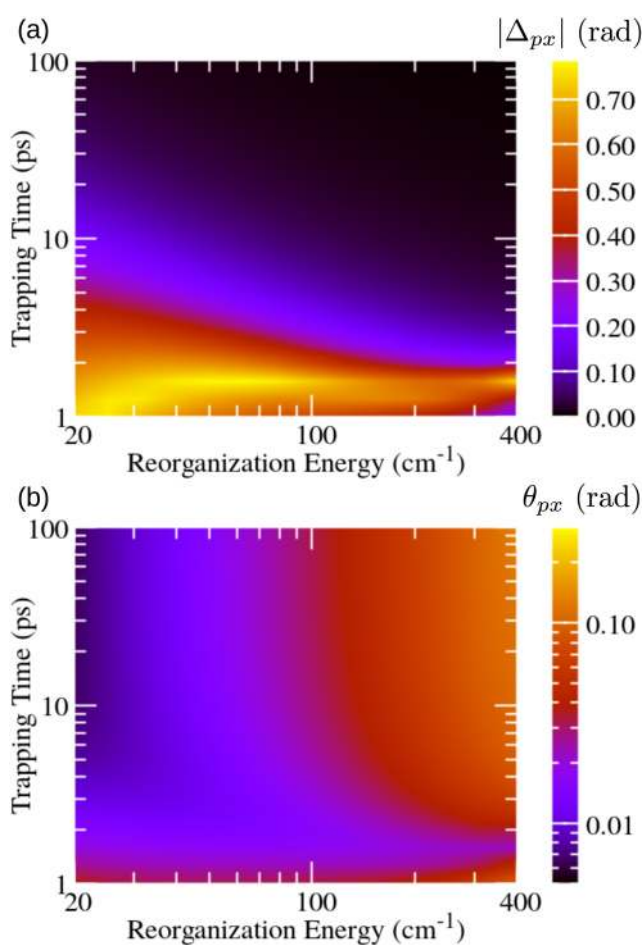


FIG. 6. Dependence of transformation parameter (a) Δ_{px} and (b) θ_{px} between the preferred and excitonic basis on the reorganization energy λ and the trapping time τ_{RC} at the RC. Trapping at the RC is governed by the delocalized-trapping Liouvillian [Eq. (19)], while the recombination is described by the Liouvillian in Eq. (20). Both axes feature logarithmic scale and the scale of the color bar in (a) is linear, while that of the color bar in (b) is logarithmic. The maximal value on the color bar in (a) is $\pi/4$. To facilitate the comparison with Fig. 2, the ranges of color bars in (a) and (b) are identical to the ranges of color bars in Figs. 2(a) and 2(b), respectively.

reorganization energy to 150 cm^{-1} . Figures 7(a) and 7(b) present the dependence of transformation parameters Δ_{px} and θ_{px} on τ_{RC} and $\Delta\epsilon_{01}$. We varied $\Delta\epsilon_{01}$ from 30 cm^{-1} to 300 cm^{-1} on the basis of the literature values of site-energy differences in the FMO complex.^{65,75} Let us first focus on the long trapping times when the magnitude of the phase Δ_{px} is small [see the upper half of Fig. 7(a)], and the NESS obtained is quite similar to the excited-state equilibrium. For small values of $\Delta\epsilon_{01}$ for which $J_{01}/\Delta\epsilon_{01} \gtrsim 2$, exciton delocalization prevails over the localizing effect of the environment, which is reflected in relatively small values of the rotation angle θ_{px} [see the upper left part of Fig. 7(b)]. As the local energy levels become more off-resonant, the environment-induced localization becomes more pronounced than exciton delocalization so that the rotation angle from the excitonic basis to the preferred basis of the NESS increases.

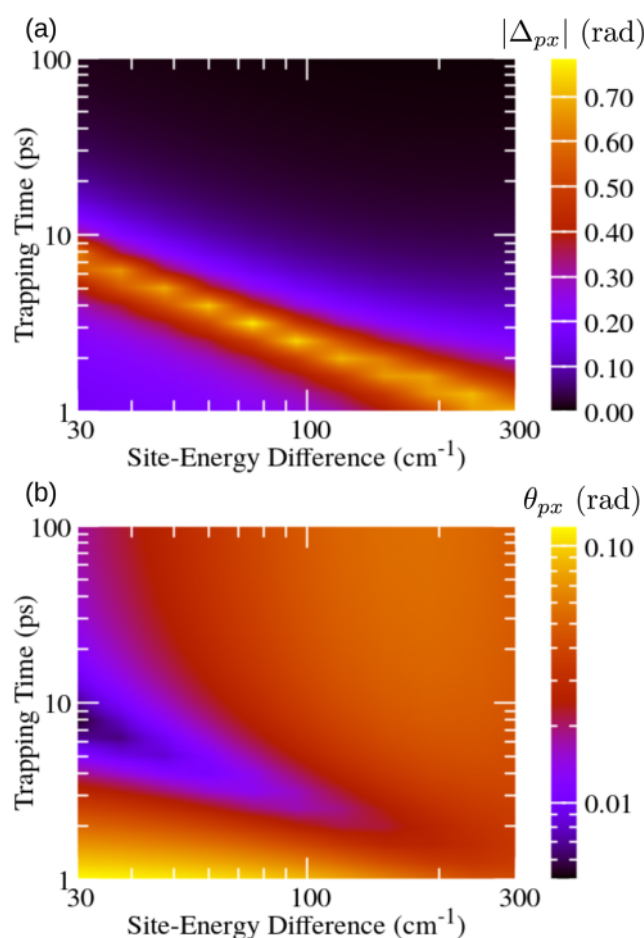


FIG. 7. Dependence of transformation parameter (a) Δ_{px} and (b) θ_{px} between the preferred and excitonic basis on the site-energy difference $\Delta\epsilon_{01}$ and the trapping time τ_{RC} at the RC. Trapping at the RC is governed by the localized-trapping Liouvillian [Eq. (18)], while the recombination is described by the Liouvillian in Eq. (20). Both axes feature a logarithmic scale and the scale of the color bar in (a) is linear, while that of the color bar in (b) is logarithmic. The maximal value of the color bar in (a) is $\pi/4$. The reorganization energy assumes the value of 150 cm^{-1} .

However, when $\Delta\epsilon_{01}$ is large enough so that $\Delta\epsilon_{01}/J_{01} \gtrsim 2$, the excitonic basis is already localized enough and, for the chosen value of λ , the localizing effect of the environment is effectively suppressed. This leads to a decrease in the rotation angle θ_{px} . As the trapping time is shortened, the deviations from the above-established picture become more pronounced. The magnitude of Δ_{px} reaches its maximum at $\tau_{RC} = 1 \text{ ps} - 10 \text{ ps}$ depending on the particular value of $\Delta\epsilon_{01}$ [see Fig. 7(a)], while angle θ_{px} exhibits a minimum in the very same region of the $\Delta\epsilon_{01} - \tau_{RC}$ space [see Fig. 7(b)].

VI. POSSIBLE APPLICATIONS TO MULTICHROMOPHORIC AGGREGATES

So far, we have employed our novel theoretical approach to study in great detail the NESS of an incoherently driven and loaded

dimer. The dimer represents the only model in which one can represent the character of the NESS by only two parameters—the angle of the basis rotation θ with respect to a chosen basis and the phase Δ that is closely connected with the excitation decay rates—and the difference between different NESSs is easy to understand. In other words, the dimer is the only model, where relatively simple “understanding” of the role of different parameters in establishing the preferred basis can be derived. Whether our results can be translated to larger systems is, of course, an important question. This section aims at presenting the basic steps that have to be taken in order to apply our NESS formalism to multichromophoric situations.

We start from the fact that the realistic coherence time of light $\tau_c \sim 1$ fs is much shorter than any other time scale in the problem. All our results for the dimer are obtained by solving Eqs. (10) and (11) and do not lean on any assumption about the coherence time τ_c entering Eq. (6). In the accompanying paper,³⁴ we have argued that, in the limit of small τ_c , the first-order light correlation function defined in Eq. (6) may be replaced by

$$G^{(1)}(\tau) = 2I_0\tau_c\delta(\tau), \quad (37)$$

which represents the so-called white-noise model of the radiation.²⁹ Equation (10) is then omitted from further discussion, while the source term (the third term) of Eq. (11) reads as³⁴

$$S_{\mathbf{n}}^{\text{WNM}} = \delta_{\mathbf{n},\mathbf{0}} \frac{2I_0\gamma\tau_c}{(\hbar\gamma)^2} \mu_{eg} |g\rangle \langle g| \mu_{eg}^\dagger. \quad (38)$$

We recall that the operator $\mu_{eg} = \mathbf{e} \cdot \boldsymbol{\mu}_{eg}$ is the projection of the dipole-moment operator $\boldsymbol{\mu}_{eg}$ onto the radiation polarization vector \mathbf{e} . Using the definition of μ_{eg} in Eq. (4), the matrix elements of the source term in the basis $\{|b_j\rangle|j\rangle\}$ of the single-excitation manifold can be expressed as

$$\langle b_k | S_{\mathbf{n}}^{\text{WNM}} | b_j \rangle = \delta_{\mathbf{n},\mathbf{0}} \frac{2I_0\gamma\tau_c}{(\hbar\gamma)^2} \sum_{k'j'} (\mathbf{d}_{k'} \cdot \mathbf{e})(\mathbf{d}_{j'} \cdot \mathbf{e}) \langle b_k | l_{k'} \rangle \langle l_{j'} | b_j \rangle. \quad (39)$$

The basis $\{|b_j\rangle|j\rangle\}$ is, in principle, arbitrary; it can be the local basis ($b = l$), the excitonic basis ($b = x$), the preferred basis ($b = p$), or any other basis in the single-excitation manifold. Equation (39) is in the form in which the rotational average can be straightforwardly performed with the final result,⁸⁰

$$\begin{aligned} \langle b_k | S_{\mathbf{n}}^{\text{WNM}} | b_j \rangle^{(\text{avg})} &= \delta_{\mathbf{n},\mathbf{0}} \frac{2I_0\gamma\tau_c}{(\hbar\gamma)^2} \frac{1}{3} \sum_{k'j'} (\mathbf{d}_{k'} \cdot \mathbf{d}_{j'}) \langle b_k | l_{k'} \rangle \langle l_{j'} | b_j \rangle \\ &= \delta_{\mathbf{n},\mathbf{0}} \frac{2I_0\gamma\tau_c}{(\hbar\gamma)^2} \frac{1}{3} \mathbf{d}_{b_k} \cdot \mathbf{d}_{b_j}^*, \end{aligned} \quad (40)$$

where $\mathbf{d}_{b_k} = \sum_{k'} \mathbf{d}_{k'} \langle b_k | l_{k'} \rangle$ is the transition dipole moment of state $|b_k\rangle$. In a typical situation, the system of interest consists of many photosynthetic complexes in solution, and the rotational average is performed over random orientation of individual chromophores' dipole moments with respect to the polarization direction. The source term in Eq. (40) depends only on relative orientations of transition dipole moments, which are known for the

widely investigated Q_y-band excitations of the FMO complex.⁸¹ Representing Eq. (11) in basis $\{|b_j\rangle|j\rangle\}$ and using the rotationally averaged source term given in Eq. (40), we obtain a description of incoherent-light driven EET that exploits both the light incoherence (short τ_c) and experimentally available data on relative orientations of transition dipole moments. Such a description features a much more realistic excitation condition than the one we have employed in the study of model dimer (the selective excitation of a local site).

Our NESS approach can also be used to follow the pathways of light-induced excitations from the point of their generation, through the chromophore network, to the point of their extraction at the load. To elaborate this, we compute the $|b_k\rangle\langle b_k|$ matrix element of Eq. (11) for the RDM ($\mathbf{n} = \mathbf{0}$) and obtain

$$J_{\text{gen}}^{b_k} - J_{\text{RC}}^{b_k} - J_{\text{rec}}^{b_k} + \sum_{k'(\neq k)} J^{b_k b_{k'}} + J_{\text{res}}^{b_k} = 0. \quad (41)$$

In Eq. (41), $J_{\text{gen}}^{b_k}$ is the excitation generation flux into the singly excited state $|b_k\rangle$,

$$J_{\text{gen}}^{b_k} = \frac{2}{\hbar\gamma} \text{Im} \langle b_k | \sigma_{eg,\mathbf{0}}^{ss} \mu_{eg}^\dagger | b_k \rangle, \quad (42)$$

$J_{\text{RC}}^{b_k}$ is the excitation trapping flux from $|b_k\rangle$,

$$J_{\text{RC}}^{b_k} = -\gamma^{-1} \langle b_k | \mathcal{L}_{\text{RC}} [\sigma_{ee,\mathbf{0}}^{ss}] | b_k \rangle, \quad (43)$$

and $J_{\text{rec}}^{b_k}$ is the excitation recombination flux from $|b_k\rangle$,

$$J_{\text{rec}}^{b_k} = -\gamma^{-1} \langle b_k | \mathcal{L}_{\text{rec}} [\sigma_{ee,\mathbf{0}}^{ss}] | b_k \rangle, \quad (44)$$

while $J^{b_k b_{k'}}$ (for $k' \neq k$) is the net flux of excitations that are exchanged between states $|b_k\rangle$ and $|b_{k'}\rangle$,

$$\begin{aligned} J^{b_k b_{k'}} &= \frac{2}{\hbar\gamma} \text{Im} \{ \langle b_k | H_M | b_{k'} \rangle \langle b_{k'} | \sigma_{ee,\mathbf{0}}^{ss} | b_k \rangle \} + 2 \sum_j \sum_{m=0}^{K-1} \sqrt{\frac{|c_m|}{(\hbar\gamma)^2}} \\ &\times \text{Im} \{ \langle b_{k'} | l_j \rangle \langle l_j | b_k \rangle \langle b_k | \sigma_{ee,\mathbf{0}}^{ss} | b_{k'} \rangle \}. \end{aligned} \quad (45)$$

The last term in Eq. (41), $J_{\text{res}}^{b_k}$, stems from the residual term $2\Delta\delta(t)$ in the decomposition of the bath correlation function into the optimized exponential series [see Eq. (7)]. This term can therefore be made arbitrarily small by explicitly treating a sufficient number K of exponentially decaying terms in Eq. (7) and will not be considered in the further discussion. For the sake of completeness, let us also note that, if the light incoherence is exploited on the level of Eqs. (37)–(40), Eq. (42) for the generation flux should be replaced by

$$J_{\text{gen}}^{b_k} = \frac{2I_0\gamma\tau_c}{(\hbar\gamma)^2} |\mathbf{d}_{b_k}|^2. \quad (46)$$

Similar to Eq. (12), all the fluxes entering Eq. (41) are dimensionless and the sign in front of them is determined by the

“direction” of the flux (\pm if it leads to an increase/a decrease in the population of state $|b_k\rangle$). One can prove that the (global) continuity equation [Eq. (12)] is obtained by adding Eq. (41) for different states $|b_k\rangle$. Therefore, Eq. (41) can be regarded as the local continuity equation in the basis $\{|b_k\rangle\}$. Here, the term “local” is in no manner connected to the local basis because Eq. (41) is formulated in an arbitrary basis $\{|b_j\rangle\}$. The local continuity equation establishes the balance (on the level of a single-excitation state) between the excitation generation, trapping, and recombination on the one hand and the excitation flow from the considered state toward other states on the other hand.

We believe that the local continuity equation is a potentially interesting feature of our NESS picture because it enables us to track the steady-state excitation pathways. The excitation flux $J^{b_k b_{k'}}$ satisfies $J^{b_k b_{k'}} = -J^{b_{k'} b_k}$, and it is positive when the net excitation flow is directed from $b_{k'}$ to b_k , while it is negative when the net excitation flow is directed from b_k to $b_{k'}$. One may, therefore, identify the states in which the generation, trapping, and recombination predominantly occur and then individuate the pathways along which the excitations travel. Such a discussion can be performed in an arbitrary basis of singly excited states, enabling one to follow the excitation pathways in the local, excitonic, or preferred basis.

We conclude this section by discussing the generality of the relationship between the stationary and time-dependent pictures that we established for the model dimer in Sec. V C. This relationship relies on the hierarchy of time scales of the dimer’s dynamics under incoherent light that is also introduced in Sec. V C. On the other hand, in a multichromophoric aggregate, the rates of excitation transfer between various states can be of the different orders of magnitude, and the excitation may be trapped in certain states so that the recombination time scale may also become important. As an example, let us take a single unit of the FMO complex that, despite the fact that its contribution to direct light harvesting is minor, has become a paradigmatic system to discuss quantum effects in biological systems.⁸² It is known that the intraunit energy transfer predominantly proceeds on subpicosecond time scales.⁸³ The excitation transfer from the considered unit of the FMO complex to the RC typically occurs on a ~ 20 ps time scale, while the decay time of the lowest FMO level is around 250 ps.⁸⁴ We may thus speculate that the hierarchy of time scales introduced in Sec. V C is valid in this example and that the reconstruction of the NESS from the dynamics of the driven but unloaded system is possible. However, in this multichromophoric example, the value of the efficiency genuinely depends on a complex interplay between the excitation generation, relaxation, dephasing, trapping at the RC, and recombination and, as such, it cannot be predicted in advance (as is the case for the dimer model). This is even more pronounced in photosynthetically more relevant situations in which the excitations initially created in antenna complexes reach the RC after many steps of the relatively slow interpigment transfer.²⁰ The application of our NESS formalism to such situations is out of the scope of this paper.

VII. DISCUSSION AND CONCLUSION

We have provided a detailed and rigorous theoretical description of light harvesting by a molecular aggregate under conditions

that are representative of photosynthetic light harvesting as it occurs in nature. The picture established in this work takes into account the excitation generation by means of weak incoherent light and their subsequent relaxation and dephasing, as well as excitation trapping by a load (the RC) and recombination. While the generation, relaxation, and dephasing are described in a (numerically) exact manner, which we have reported in the accompanying paper, the excitation trapping and recombination are included on the level of effective Liouvillians.

This piece of research addresses a recurrent question of the possible relevance of quantum coherent effects (understood in a very broad sense) for the natural light harvesting. Our NESS approach provides a physically transparent definition of the light-harvesting efficiency [Eq. (16)] that is basis-invariant so that we are in a position to embark upon the study of possible coherent enhancements of the efficiency. Recent reports have suggested that these coherent enhancements strongly depend on the basis in which the effective trapping and/or recombination Liouvillians are diagonal. Here, we use the fact that the state of an incoherently driven and loaded aggregate is most naturally represented and studied in the so-called preferred basis of the NESS in which the steady-state RDM is diagonal. This definition of the preferred basis implies that this basis sublimates the joint effect of excitation generation, relaxation, dephasing, trapping, and recombination. The preferred-basis description of the NESS under driving and load can be seen as an analog of the description of a system of coupled harmonic oscillators in terms of normal modes. While finding that the preferred basis is highly nontrivial, as demonstrated throughout this paper, this concept may shed new light on the debate on the role of coherences in the energy transfer under incoherent light.

We have examined the properties of the preferred basis of the NESS of an incoherently driven and loaded dimer by studying the manners in which it is connected to two widely used representations: namely, those employing the excitonic and the local bases. The recombination time scale is, in general, significantly longer than any other time scale in the problem so that, in the limit of long trapping time, the NESS is very similar to the previously studied excited-state equilibrium of an undriven and unloaded system. We also find that the NESS under driving and load carries information that is encoded in the temporal evolution of the unloaded system driven by the suddenly turned-on incoherent light. If the radiation is abruptly turned on at $t = 0$, the properties of the NESS that arises due to the excitation trapping with time constant τ_{RC} can be quite reliably extracted from the RDM at $t \sim \tau_{RC}$. We conclude that the trapping time scales for which such a relation between the NESS and the dynamics of the driven but unloaded system is sensible are basically determined by the time scales of decoherence and relaxation, which are accessible in ultrafast spectroscopy experiments. Since realistic trapping times are, in general, much longer than decoherence and relaxation time scales, the relation we found between the steady-state and time-dependent pictures is quite general.

We again note that our theoretical and computation approach to obtain the NESS under incoherent driving is general and not limited to the model dimer studied here. We opted for the dimer because the relationships between basis vectors of the preferred basis and the excitonic or local basis can be parameterized by only

two real parameters, which have certain physical significance and whose dependence on model parameters can be studied in a systematic manner. In the case of a more complex excitonic aggregate, one should resort to more involved parameterizations of unitary matrices.

SUPPLEMENTARY MATERIAL

See the [supplementary material](#) for (a) the derivation of equations for the transformation parameters θ and Δ , (b) detailed numerical procedure to compute the nonequilibrium steady state, (c) analysis of the dynamics initiated by a delta-like photoexcitation, and (d) the comparison of transformation parameters θ_{pl} and Δ_{pl} obtained from stationary and time-dependent pictures in the case of fast trapping.

AUTHORS' CONTRIBUTIONS

T.M. gave the initial impetus for this work, which started during the stay of V.J. in Prague. V.J. developed the methodology, conducted all numerical computations, analyzed their results, and prepared the initial version of the manuscript. Both authors contributed to the submitted version of the manuscript.

ACKNOWLEDGMENTS

The initial stages of this work were supported by Charles University Research Center Program No. UNCE/SCI/010 and the Czech Science Foundation (GAČR; Grant No. 18-18022S). The final stages of this work were supported by the Institute of Physics Belgrade, through the grant by the Ministry of Education, Science, and Technological Development of the Republic of Serbia. Computational resources were supplied by the project “e-Infrastruktura CZ” (Grant No. e-INFRA LM2018140) provided within the program Projects of Large Research, Development and Innovations Infrastructures. Numerical computations were also performed in the PARADOX supercomputing facility at the Scientific Computing Laboratory of the Institute of Physics, Belgrade.

DATA AVAILABILITY

The data that support the findings of this study are available from the corresponding author upon reasonable request.

REFERENCES

- ¹G. S. Engel, T. R. Calhoun, E. L. Read, T.-K. Ahn, T. Mančal, Y.-C. Cheng, R. E. Blankenship, and G. R. Fleming, “Evidence for wavelike energy transfer through quantum coherence in photosynthetic systems,” *Nature* **446**, 782–786 (2007).
- ²G. Panitchayangkoon, D. Hayes, K. A. Fransted, J. R. Caram, E. Harel, J. Wen, R. E. Blankenship, and G. S. Engel, “Long-lived quantum coherence in photosynthetic complexes at physiological temperature,” *Proc. Natl. Acad. Sci. U. S. A.* **107**, 12766–12770 (2010).
- ³Y.-C. Cheng and G. R. Fleming, “Dynamics of light harvesting in photosynthesis,” *Annu. Rev. Phys. Chem.* **60**, 241–262 (2009).
- ⁴A. Ishizaki and G. R. Fleming, “On the interpretation of quantum coherent beats observed in two-dimensional electronic spectra of photosynthetic light harvesting complexes,” *J. Phys. Chem. B* **115**, 6227–6233 (2011).
- ⁵P. Brumer and M. Shapiro, “Molecular response in one-photon absorption via natural thermal light vs pulsed laser excitation,” *Proc. Natl. Acad. Sci. U. S. A.* **109**, 19575–19578 (2012).
- ⁶P. Brumer, “Shedding (incoherent) light on quantum effects in light-induced biological processes,” *J. Phys. Chem. Lett.* **9**, 2946–2955 (2018).
- ⁷T. Mančal, “A decade with quantum coherence: How our past became classical and the future turned quantum,” *Chem. Phys.* **532**, 110663 (2020).
- ⁸J. Cao, R. J. Cogdell, D. F. Coker, H.-G. Duan, J. Hauer, U. Kleinekathöfer, T. L. C. Jansen, T. Mančal, R. J. D. Miller, J. P. Ogilvie, V. I. Prokhorenko, T. Renger, H.-S. Tan, R. Tempelaar, M. Thorwart, E. Thyryhaug, S. Westenhoff, and D. Zigmantas, “Quantum biology revisited,” *Sci. Adv.* **6**, eaaz4888 (2020).
- ⁹T. Mančal and L. Valkunas, “Exciton dynamics in photosynthetic complexes: Excitation by coherent and incoherent light,” *New J. Phys.* **12**, 065044 (2010).
- ¹⁰A. Chenu, P. Malý, and T. Mančal, “Dynamic coherence in excitonic molecular complexes under various excitation conditions,” *Chem. Phys.* **439**, 100–110 (2014).
- ¹¹G. D. Scholes, “Coherence from light harvesting to chemistry,” *J. Phys. Chem. Lett.* **9**, 1568–1572 (2018).
- ¹²A. Ishizaki and G. R. Fleming, “Theoretical examination of quantum coherence in a photosynthetic system at physiological temperature,” *Proc. Natl. Acad. Sci. U. S. A.* **106**, 17255–17260 (2009).
- ¹³M. Sarovar, A. Ishizaki, G. R. Fleming, and K. B. Whaley, “Quantum entanglement in photosynthetic light-harvesting complexes,” *Nat. Phys.* **6**, 462–467 (2010).
- ¹⁴V. van Amerongen, L. Valkunas, and R. van Grondelle, *Photosynthetic Excitons* (World Scientific Publishing Co. Pte. Ltd., 2000).
- ¹⁵D. B. Turner, D. J. Howey, E. J. Sutor, R. A. Hendrickson, M. W. Gealy, and D. J. Ulness, “Two-dimensional electronic spectroscopy using incoherent light: Theoretical analysis,” *J. Phys. Chem. A* **117**, 5926–5954 (2013).
- ¹⁶I. Kassal, J. Yuen-Zhou, and S. Rahimi-Keshari, “Does coherence enhance transport in photosynthesis?,” *J. Phys. Chem. Lett.* **4**, 362–367 (2013).
- ¹⁷T. V. Tscherbul and P. Brumer, “Non-equilibrium stationary coherences in photosynthetic energy transfer under weak-field incoherent illumination,” *J. Chem. Phys.* **148**, 124114 (2018).
- ¹⁸D. Manzano, “Quantum transport in networks and photosynthetic complexes at the steady state,” *PLoS One* **8**, e57041 (2013).
- ¹⁹S. Jesenko and M. Žnidarič, “Excitation energy transfer efficiency: Equivalence of transient and stationary setting and the absence of non-Markovian effects,” *J. Chem. Phys.* **138**, 174103 (2013).
- ²⁰C. Chuang and P. Brumer, “LH1–RC light-harvesting photocycle under realistic light–matter conditions,” *J. Chem. Phys.* **152**, 154101 (2020).
- ²¹Z. S. Sadeq and P. Brumer, “Transient quantum coherent response to a partially coherent radiation field,” *J. Chem. Phys.* **140**, 074104 (2014).
- ²²A. Chenu and P. Brumer, “Transform-limited-pulse representation of excitation with natural incoherent light,” *J. Chem. Phys.* **144**, 044103 (2016).
- ²³H.-P. Breuer and F. Petruccione, *The Theory of Open Quantum Systems* (Oxford University Press, 2002).
- ²⁴F. Fassio, A. Olaya-Castro, and G. D. Scholes, “Coherent energy transfer under incoherent light conditions,” *J. Phys. Chem. Lett.* **3**, 3136–3142 (2012).
- ²⁵H. C. H. Chan, O. E. Gamel, G. R. Fleming, and K. B. Whaley, “Single-photon absorption by single photosynthetic light-harvesting complexes,” *J. Phys. B: At., Mol. Opt. Phys.* **51**, 054002 (2018).
- ²⁶T. V. Tscherbul and P. Brumer, “Partial secular Bloch-Redfield master equation for incoherent excitation of multilevel quantum systems,” *J. Chem. Phys.* **142**, 104107 (2015).
- ²⁷L. A. Pachón and P. Brumer, “Incoherent excitation of thermally equilibrated open quantum systems,” *Phys. Rev. A* **87**, 022106 (2013).
- ²⁸L. A. Pachón, J. D. Botero, and P. Brumer, “Open system perspective on incoherent excitation of light-harvesting systems,” *J. Phys. B: At., Mol. Opt. Phys.* **50**, 184003 (2017).
- ²⁹J. Olšina, A. G. Dijkstra, C. Wang, and J. Cao, “Can natural sunlight induce coherent exciton dynamics?,” [arXiv:1408.5385](https://arxiv.org/abs/1408.5385) [physics.chem-ph] (2014).

- ³⁰A. Ishizaki and G. R. Fleming, "Quantum coherence in photosynthetic light harvesting," *Annu. Rev. Condens. Matter Phys.* **3**, 333–361 (2012).
- ³¹A. Chenu and G. D. Scholes, "Coherence in energy transfer and photosynthesis," *Annu. Rev. Phys. Chem.* **66**, 69–96 (2015).
- ³²H. Maguire, J. Iles-Smith, and A. Nazir, "Environmental nonadditivity and Franck-Condon physics in nonequilibrium quantum systems," *Phys. Rev. Lett.* **123**, 093601 (2019).
- ³³A. G. Dijkstra and A. Beige, "Efficient long-distance energy transport in molecular systems through adiabatic passage," *J. Chem. Phys.* **151**, 034114 (2019).
- ³⁴V. Janković and T. Mančal, "Exact description of excitonic dynamics in molecular aggregates weakly driven by light," *J. Chem. Phys.* (in press); [arXiv:2001.07180](https://arxiv.org/abs/2001.07180) [physics.chem-ph] (2020).
- ³⁵A. Ishizaki and G. R. Fleming, "Unified treatment of quantum coherent and incoherent hopping dynamics in electronic energy transfer: Reduced hierarchy equation approach," *J. Chem. Phys.* **130**, 234111 (2009).
- ³⁶Y. Tanimura, "Numerically 'exact' approach to open quantum dynamics: The hierarchical equations of motion (HEOM)," *J. Chem. Phys.* **153**, 020901 (2020).
- ³⁷S. Tomasi and I. Kassal, "Classification of coherent enhancements of light-harvesting processes," *J. Phys. Chem. Lett.* **11**, 2348–2355 (2020).
- ³⁸P.-Y. Yang and J. Cao, "Steady-state analysis of light-harvesting energy transfer driven by incoherent light: From dimers to networks," *J. Phys. Chem. Lett.* **11**, 7204–7211 (2020).
- ³⁹K. A. Jung and P. Brumer, "Energy transfer under natural incoherent light: Effects of asymmetry on efficiency," *J. Chem. Phys.* **153**, 114102 (2020).
- ⁴⁰R. d. J. León-Montiel, I. Kassal, and J. P. Torres, "Importance of excitation and trapping conditions in photosynthetic environment-assisted energy transport," *J. Phys. Chem. B* **118**, 10588–10594 (2014).
- ⁴¹S. Axelrod and P. Brumer, "An efficient approach to the quantum dynamics and rates of processes induced by natural incoherent light," *J. Chem. Phys.* **149**, 114104 (2018).
- ⁴²C. K. Lee, J. Cao, and J. Gong, "Noncanonical statistics of a spin-boson model: Theory and exact Monte Carlo simulations," *Phys. Rev. E* **86**, 021109 (2012).
- ⁴³C. K. Lee, J. Moix, and J. Cao, "Accuracy of second order perturbation theory in the polaron and variational polaron frames," *J. Chem. Phys.* **136**, 204120 (2012).
- ⁴⁴J. Cerrillo and J. Cao, "Non-Markovian dynamical maps: Numerical processing of open quantum trajectories," *Phys. Rev. Lett.* **112**, 110401 (2014).
- ⁴⁵J. Strümpfer and K. Schulten, "Light harvesting complex II B850 excitation dynamics," *J. Chem. Phys.* **131**, 225101 (2009).
- ⁴⁶J. M. Moix, Y. Zhao, and J. Cao, "Equilibrium-reduced density matrix formulation: Influence of noise, disorder, and temperature on localization in excitonic systems," *Phys. Rev. B* **85**, 115412 (2012).
- ⁴⁷W. H. Zurek, "Decoherence, einselection, and the quantum origins of the classical," *Rev. Mod. Phys.* **75**, 715–775 (2003).
- ⁴⁸M. Schlosshauer, *Decoherence and the Quantum-To-Classical Transition* (Springer-Verlag Berlin Heidelberg, 2007).
- ⁴⁹H.-D. Zhang, Q. Qiao, R.-X. Xu, X. Zheng, and Y. Yan, "Efficient steady-state solver for hierarchical quantum master equations," *J. Chem. Phys.* **147**, 044105 (2017).
- ⁵⁰E. N. Zimanyi and R. J. Silbey, "Theoretical description of quantum effects in multi-chromophoric aggregates," *Philos. Trans. R. Soc., A* **370**, 3620–3637 (2012).
- ⁵¹T. V. Tscherbul and P. Brumer, "Long-lived quasistationary coherences in a *v*-type system driven by incoherent light," *Phys. Rev. Lett.* **113**, 113601 (2014).
- ⁵²S. Tomasi, S. Baghbanzadeh, S. Rahimi-Keshari, and I. Kassal, "Coherent and controllable enhancement of light-harvesting efficiency," *Phys. Rev. A* **100**, 043411 (2019).
- ⁵³L. Valkunas, D. Abramavicius, and T. Mančal, *Molecular Excitation Dynamics and Relaxation* (Wiley-VCH Verlag GmbH & Co. KGaA, 2013).
- ⁵⁴V. May and O. Kühn, *Charge and Energy Transfer Dynamics in Molecular Systems*, 3rd ed. (Wiley-VCH Verlag GmbH & Co. KGaA, Weinheim, 2011).
- ⁵⁵C. Kreisbeck, T. Kramer, M. Rodríguez, and B. Hein, "High-performance solution of hierarchical equations of motion for studying energy transfer in light-harvesting complexes," *J. Chem. Theory Comput.* **7**, 2166–2174 (2011).
- ⁵⁶V. N. Shatokhin, M. Walschaers, F. Schlawin, and A. Buchleitner, "Coherence turned on by incoherent light," *New J. Phys.* **20**, 113040 (2018).
- ⁵⁷R. Loudon, *The Quantum Theory of Light* (Oxford University Press, Oxford, 2000).
- ⁵⁸H.-D. Zhang, R.-X. Xu, X. Zheng, and Y. Yan, "Statistical quasi-particle theory for open quantum systems," *Mol. Phys.* **116**, 780–812 (2018).
- ⁵⁹Q. Shi, L. Chen, G. Nan, R.-X. Xu, and Y. Yan, "Efficient hierarchical Liouville space propagator to quantum dissipative dynamics," *J. Chem. Phys.* **130**, 084105 (2009).
- ⁶⁰S. Jang, M. D. Newton, and R. J. Silbey, "Multichromophoric Förster resonance energy transfer," *Phys. Rev. Lett.* **92**, 218301 (2004).
- ⁶¹J. Ma and J. Cao, "Förster resonance energy transfer, absorption and emission spectra in multichromophoric systems. I. Full cumulant expansions and system-bath entanglement," *J. Chem. Phys.* **142**, 094106 (2015).
- ⁶²F. Murnaghan, *The Unitary and Rotation Groups* (Spartan Books, Washington DC, 1962).
- ⁶³Y. Kano and E. Wolf, "Temporal coherence of black body radiation," *Proc. Phys. Soc.* **80**, 1273–1276 (1962).
- ⁶⁴C. L. Mehta, "Coherence-time and effective bandwidth of blackbody radiation," *Il Nuovo Cimento* **28**, 401–408 (1963).
- ⁶⁵S. J. Jang and B. Mennucci, "Delocalized excitons in natural light-harvesting complexes," *Rev. Mod. Phys.* **90**, 035003 (2018).
- ⁶⁶J. Moix, J. Wu, P. Huo, D. Coker, and J. Cao, "Efficient energy transfer in light-harvesting systems, III: The influence of the eighth bacteriochlorophyll on the dynamics and efficiency in FMO," *J. Phys. Chem. Lett.* **2**, 3045–3052 (2011).
- ⁶⁷W. Zhou, R. LoBrutto, S. Lin, and R. E. Blankenship, "Redox effects on the bacteriochlorophyll α -containing Fenna-Matthews-Olson protein from *Chlorobium tepidum*," *Photosynth. Res.* **41**, 89–96 (1994).
- ⁶⁸N. C. M. Magdaong, R. G. Saer, D. M. Niedzwiedzki, and R. E. Blankenship, "Ultrafast spectroscopic investigation of energy transfer in site-directed mutants of the Fenna-Matthews-Olson (FMO) antenna complex from *Chlorobaculum tepidum*," *J. Phys. Chem. B* **121**, 4700–4712 (2017).
- ⁶⁹M. B. Plenio and S. F. Huelga, "Dephasing-assisted transport: Quantum networks and biomolecules," *New J. Phys.* **10**, 113019 (2008).
- ⁷⁰R. E. Blankenship, *Molecular Mechanisms of Photosynthesis* (John Wiley & Sons, 2014).
- ⁷¹A. Damjanović, T. Ritz, and K. Schulten, "Excitation energy trapping by the reaction center of *Rhodobacter Sphaeroides*," *Int. J. Quantum Chem.* **77**, 139–151 (2000).
- ⁷²F. Caycedo-Soler, C. A. Schroeder, C. Autenrieth, A. Pick, R. Ghosh, S. F. Huelga, and M. B. Plenio, "Quantum redirection of antenna absorption to photosynthetic reaction centers," *J. Phys. Chem. Lett.* **8**, 6015–6021 (2017).
- ⁷³K. Timpmann, A. Freiberg, and V. Sundström, "Energy trapping and detraping in the photosynthetic bacterium *Rhodospseudomonas viridis*: Transfer-to-trap-limited dynamics," *Chem. Phys.* **194**, 275–283 (1995).
- ⁷⁴J. Strümpfer and K. Schulten, "Excited state dynamics in photosynthetic reaction center and light harvesting complex 1," *J. Chem. Phys.* **137**, 065101 (2012).
- ⁷⁵J. Adolphs and T. Renger, "How proteins trigger excitation energy transfer in the FMO complex of green sulfur bacteria," *Biophys. J.* **91**, 2778–2797 (2006).
- ⁷⁶X. Wang, G. Ritschel, S. Wüster, and A. Eisfeld, "Open quantum system parameters for light harvesting complexes from molecular dynamics," *Phys. Chem. Chem. Phys.* **17**, 25629–25641 (2015).
- ⁷⁷C. W. Kim, B. Choi, and Y. M. Rhee, "Excited state energy fluctuations in the Fenna-Matthews-Olson complex from molecular dynamics simulations with interpolated chromophore potentials," *Phys. Chem. Chem. Phys.* **20**, 3310–3319 (2018).
- ⁷⁸I. S. Dunn, R. Tempelaar, and D. R. Reichman, "Removing instabilities in the hierarchical equations of motion: Exact and approximate projection approaches," *J. Chem. Phys.* **150**, 184109 (2019).

- ⁷⁹K. M. Pelzer, T. Can, S. K. Gray, D. K. Morr, and G. S. Engel, “Coherent transport and energy flow patterns in photosynthesis under incoherent excitation,” *J. Phys. Chem. B* **118**, 2693–2702 (2014).
- ⁸⁰B. Hein, C. Kreisbeck, T. Kramer, and M. Rodríguez, “Modelling of oscillations in two-dimensional echo-spectra of the Fenna–Matthews–Olson complex,” *New J. Phys.* **14**, 023018 (2012).
- ⁸¹E. L. Read, G. S. Schlau-Cohen, G. S. Engel, J. Wen, R. E. Blankenship, and G. R. Fleming, “Visualization of excitonic structure in the Fenna–Matthews–Olson photosynthetic complex by polarization-dependent two-dimensional electronic spectroscopy,” *Biophys. J.* **95**, 847–856 (2008).
- ⁸²J. Pšenčík and T. Mančal, “Light harvesting in green bacteria,” in *Light Harvesting in Photosynthesis*, edited by R. Croce, R. van Grondelle, H. van Amerongen, and I. van Stokkum (Taylor & Francis/CRC Press, 2017), Chap. 7, pp. 121–154.
- ⁸³E. Thyryhaug, K. Židek, J. Dostál, D. Bína, and D. Zigmantas, “Exciton structure and energy transfer in the Fenna–Matthews–Olson complex,” *J. Phys. Chem. Lett.* **7**, 1653–1660 (2016).
- ⁸⁴J. Dostál, J. Pšenčík, and D. Zigmantas, “*In situ* mapping of the energy flow through the entire photosynthetic apparatus,” *Nat. Chem.* **8**, 705–710 (2016).

Energy-Temporal Pathways of Free-Charge Formation at Organic Bilayers: Competition of Delocalization, Disorder, and Polaronic Effects

Veljko Janković and Nenad Vukmirović*

Cite This: *J. Phys. Chem. C* 2020, 124, 4378–4392

Read Online

ACCESS |



Metrics & More

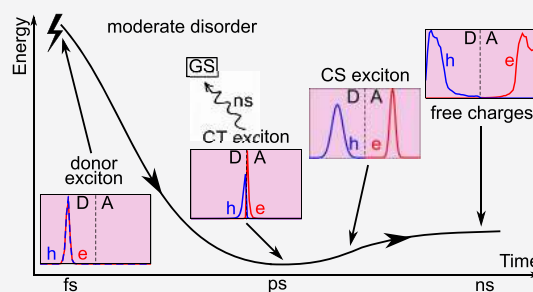


Article Recommendations



Supporting Information

ABSTRACT: We investigated the charge separation process in organic semiconductor bilayers from the moment of creation of a donor exciton to the time when all charge pairs have either recombined or reached external contacts. The system was modeled using a one-dimensional microscopic Hamiltonian that includes the effects of carrier delocalization, electron–hole interaction, static disorder, and carrier–phonon interaction. Transition rates between excitonic states were modeled using modified Redfield approach which takes into account polaronic effects by exact treatment of diagonal exciton–phonon interaction. An efficient numerical scheme was developed that enabled us to obtain the time dependence of energy-resolved populations of relevant exciton states on a time scale as long as 1 μ s. Our results indicated that charge separation proceeds via the so-called *cold pathway* in which donor excitons convert to relaxed charge-transfer excitons which further transform to the states of separated charges. We found that for lower disorder strengths the time scale for conversion of donor excitons to charge transfer excitons is $\sim(1–10)$ ps, while further separation to free charges takes place on the time scale reaching ~ 1 ns. These time scales are extended for larger disorder strengths because diffusion of donor excitons to the interface and transport of separated charges toward external contacts are slowed down. We also found that charge separation yield has a rather weak dependence on electron–phonon interaction strength.



INTRODUCTION

Operation of organic photovoltaic (OPV) devices is based on separation of electron–hole pairs (excitons) generated by incident sunlight into free charges. Although significant research efforts have been put in the last two decades to understand and improve the performance of OPVs, the details of charge separation mechanism are still not fully understood. The active region in OPVs typically consists of two organic semiconductor materials. The conventional picture of the charge separation process at the interface of these materials is as follows.^{1–3} Incident sunlight initially generates bound excitons in the donor material (donor excitons, XD) which then migrate to the interface of two materials into so-called charge transfer (CT) excitons, which consist of an electron in the acceptor material and a hole in the donor material that are both localized close to the interface. The next step in the separation process is transformation of CT excitons into charge separated (CS) states in which electron in the acceptor and hole in the donor are spatially separated. Electrons and holes in CS states are free to migrate toward external contacts and form current in external circuit.

The challenge to this conventional picture comes from the fact that in most efficient OPV devices almost each absorbed photon produces one electron–hole pair in external circuit, that is, internal quantum efficiency is close to one.⁴ Since

binding energy of electrons and holes in CT states is much larger than thermal energy at room temperature,¹ it remained unclear how is separation of electrons and holes from CT states possible. Along this line, there were suggestions that in the course of separation process excitons do not reach strongly bound CT states but remain in energetically higher and weakly bound CT states (so-called hot CT states) and further transform into CS states from these states.^{5,6} In such a picture, this transfer has to occur before relaxation to cold states⁷ and it was therefore believed that it takes place on very short sub-picosecond time scale. On the other hand, the conventional picture which involves separation from low energy strongly bound CT states (so-called cold CT states) was not abandoned. In particular, experimental results which show that internal quantum efficiency is nearly independent of the energy of the initial state point in favor of this picture.^{8–10}

In our previous theoretical work,^{11,12} we first investigated exciton dynamics on a sub-picosecond time scale using a fully quantum mechanical model of the heterojunction based on

Received: November 20, 2019

Revised: January 28, 2020

Published: February 3, 2020



density matrix theory. Our results indicated that donor excitons generated by a pulsed photoexcitation predominantly remain in these states and that there is no significant charge transfer on this time scale.¹² To assess the possibility of charge separation on longer time scale, we used a master equation approach to find steady-state populations of relevant states and calculate the charge separation yield.¹³ Our analysis indicated that efficient separation of charges from an initial strongly bound CT state is possible. Strong binding of the electron and hole in a CT state is overcome due to a sequence of transitions to higher energy and more loosely bound CT states from which further transitions to CS states take place. We found that the separation process is most efficient at moderate values of disorder and that it is enhanced by charge carrier delocalization.¹³

However, our previous efforts did not take into account polaronic effects, which are sometimes regarded as highly important for a realistic description of exciton and charge dynamics in organic semiconductors.¹⁴ Namely, when the strength of (static) disorder is comparable to the magnitude of electronic couplings, and both of these are comparable to the coupling of electronic excitations to vibrations, there is no obvious small parameter in which a perturbation expansion can be performed. Techniques that can circumvent this problem exist, for example wave function-based methods¹⁵ or hierarchical equations of motion.¹⁶ However, their direct application to the problem of long-time charge separation, in which we necessitate an accurate description of processes occurring on time scales spanning the range from femtoseconds (nuclear dynamics) to at least nanoseconds (recombination), is computationally prohibitive. The application of these numerically exact techniques is thus typically limited to ultrafast dynamics.^{17,18} A similar situation is encountered in photosynthetic excitonic complexes, where, however, one can find various approximate approaches taking into account the competition between delocalization, disorder, and polaronic effects at least partially.^{19–21} One of these approaches, which is suited for disordered excitonic systems, is the so-called modified Redfield theory.^{22,23} In such systems, due to disorder, the overlap between different excitonic wave functions is expected to be small, so that the off-diagonal exciton–phonon couplings should be much smaller than the diagonal ones. The modified Redfield theory takes advantage of this circumstance by treating the diagonal part of the exciton–phonon interaction exactly, while its off-diagonal part is treated perturbatively.

In this work, we analyze in detail exciton dynamics on long time scales reaching $\sim 1 \mu\text{s}$, when all charge pairs have either recombined or reached external contacts. We have extended our previous model where transition rates between different exciton states were calculated assuming relatively weak electron–phonon coupling to include polaronic effects in the framework of modified Redfield approach. We obtain spectrally resolved time dependence of populations of exciton states from which we construct a full picture of charge separation process starting from generation of donor or CT exciton and ending with fully separated charges in external contacts. From the results obtained, we identify the time scales for different parts of the charge separation process and establish the effect of most relevant system parameters on these time scales. Our results point in favor of conventional cold separation mechanism.

MODEL AND METHOD

Model. The model that we use to study charge separation on an organic bilayer is essentially the same as the one we have used in our recent studies of the same phenomenon.¹³ Therefore, the model itself is presented in greater detail in section S1.1 of the Supporting Information (SI), while here we only describe its features that are relevant to the formulation of the theoretical approach. Figure 1a provides a schematic diagram of our model.

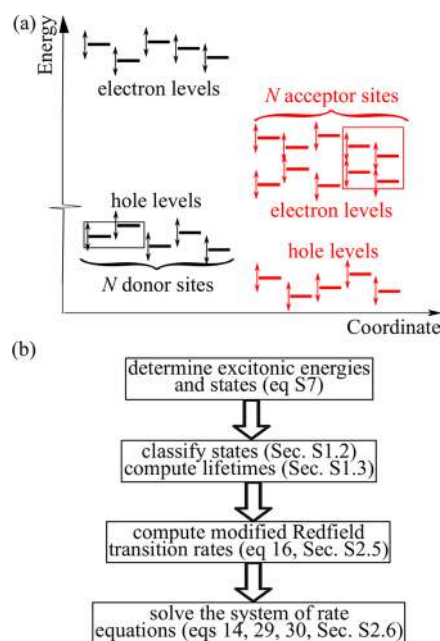


Figure 1. (a) Scheme of the one-dimensional electron–hole lattice model used to describe charge separation at the donor/acceptor interface. It consists of N donor and N acceptor sites, each of which can accommodate a number of single-electron and single-hole levels presented by horizontal lines. To mimic the existence of higher-than-LUMO orbitals that are energetically close to the LUMO level of the widely used electronic acceptor PCBM, we take two single-electron levels per acceptor site.¹³ Energies of single-carrier levels differ from site to site due to the diagonal static disorder, while two-sided vertical arrows standing on the left of each level represent its dynamical modulation by Holstein-like interaction with nuclear degrees of freedom. In a free-charge state, the electron (the hole) is mainly located in the spatial region within the rectangle in the acceptor part (the donor part) of the interface. More details can be found in ref 13 and section S1.4 of the SI. (b) Diagram outlining the main steps that have to be taken in order to compute the dynamics in a single disorder realization. Relevant equations and sections of the main text and SI are given in parentheses.

The interface between two organic semiconductors of different electronic properties is described using a one-dimensional electron–hole lattice model, in which each of the materials is modeled within the standard semiconductor model. As we have already discussed,¹³ our model takes into account on a fully quantum level all the physical effects that are regarded as relevant for the problem of charge separation in OPVs. Namely, the model includes electron and hole delocalization, attractive electron–hole interaction that binds them into excitons, static disorder, which is omnipresent in organic semiconductors, as well as the interaction of electrons and holes with nuclear degrees of freedom.

While the model itself is formulated in the electron–hole picture, theoretical developments are conducted in the excitonic basis, that is, in the basis of stationary states of an electron–hole pair that are compatible with our model interface. We limit our discussion to the subspace of singly excited states $\{|x\rangle\}$, in which the model Hamiltonian assumes the following form:

$$H = \sum_x \hbar\omega_x |x\rangle\langle x| + \sum_\mu \hbar\omega_\mu b_\mu^\dagger b_\mu + \sum_{\bar{x}\mu} \Gamma_{\bar{x}x}^\mu |x\rangle\langle x| (b_\mu^\dagger + b_\mu) \quad (1)$$

In eq 1, $\hbar\omega_x$ is the vertical excitation energy of exciton state $|x\rangle$, and index μ labels phonon modes whose energies are $\hbar\omega_\mu$, while b_μ^\dagger (b_μ) are the corresponding Bose creation (annihilation) operators. The third term in eq 1 is the exciton–phonon interaction, whose coupling constants $\Gamma_{\bar{x}x}^\mu$ satisfy $\Gamma_{\bar{x}x}^\mu = \Gamma_{x\bar{x}}^{\mu*}$.

The exciton–phonon interaction Hamiltonian stems from the electron–phonon and hole–phonon interaction Hamiltonians, which are taken to be of the Holstein type. Each site is assumed to be equipped with a set of phonon modes, and the relevant parameter sets on all sites (phonon frequencies and local electron–phonon and hole–phonon interaction constants) are taken to be identical. The limit of macroscopic phonon bath is taken by introducing the appropriate spectral density.

Based on their spatial properties, exciton states can be classified as donor, acceptor, CT, CS, and free-charge states. In the last three groups of states, the electron is predominantly located in the acceptor, and the hole is mainly in the donor. The discrimination between CT, CS, and free-charge states is established essentially on the basis of the mean electron–hole separation. The electron and hole in a CT state are quite close to one another and pinned to the interface. In a CS state, their mutual separation is somewhat larger. In free-charge states, charges are mainly located on the opposite edges of the interface, so that these states mimic the ones from which carrier extraction to electrodes is possible. In that spirit, we take that, once an exciton reaches a free-charge state, it permanently remains in that state. As discussed in ref 13, the disorder in on-site transition energies is crucial to identify free-charge states. Here, we introduce disorder by drawing electron and hole on-site energies from the Gaussian distribution with standard deviation σ and center at an appropriate energy. For more details, see refs 12, 13 and Section S1.2 of SI.

The model Hamiltonian is parametrized so that the values of band gaps, bandwidths, band offsets, and binding energies of the donor, acceptor, and CT exciton within our model agree with the literature values for typical OPV materials. In particular, we choose the values of model parameters to be representative of the prototypical P3HT/PCBM interface, as detailed in Section S1.4 of SI and ref 13.

METHOD

The exciton dynamics governed by Hamiltonian H is studied using the modified Redfield theory. As has been mentioned in Introduction, the essential criterion for the applicability of the modified Redfield theory is the smallness of the off-diagonal exciton–phonon couplings, which are treated perturbatively, with respect to the diagonal ones, which are treated exactly. In Results, we present numerical evidence that our model system

satisfies this criterion. Here, let us only mention that the magnitude of exciton–phonon couplings is governed by the spatial-proximity factor, which is determined by the electron and hole overlap in the two exciton states.¹³ In order to achieve high coupling between two (different) exciton states, both the electron and the hole in these states have to overlap, a condition that is difficult to meet in the presence of static disorder whose strength is comparable to electronic couplings.

The modified Redfield theory has become a standard tool in the chemical physics community,^{19,20,24} where it is commonly applied to study exciton dynamics within models containing a relatively small number of chromophores (~ 10), that is, a relatively small number of excitonic states.^{25,26} To the best of our knowledge, our work is among the first works employing the modified Redfield theory to describe excitonic dynamics in a condensed-phase system, in which the number of relevant excitonic levels is of the order of 1000. Therefore, the main steps toward the derivation of the relevant equations of motion are presented in the main body of the paper, whereas further technical details can be found in section S2 of the SI. Our presentation relies on the results of ref 27, which, in fact, in the limit of the macroscopic bath, present a lucid rederivation of the modified Redfield theory.

As the first step, the total Hamiltonian is rewritten as

$$H = H_0 + V \quad (2)$$

where the unperturbed Hamiltonian H_0 contains the diagonal part of the exciton–phonon interaction

$$H_0 = \sum_x |x\rangle \left(\hbar\omega_x + \sum_\mu \Gamma_{xx}^\mu (b_\mu^\dagger + b_\mu) \right) \langle x| + \sum_\mu \hbar\omega_\mu b_\mu^\dagger b_\mu \quad (3)$$

while the perturbation V contains its off-diagonal part

$$V = \sum'_{\bar{x}\mu} \Gamma_{\bar{x}x}^\mu |x\rangle \langle x| (b_\mu^\dagger + b_\mu) \quad (4)$$

In eq 4, the prime on the sum indicates that only terms in which $\bar{x} \neq x$ are considered.

Hamiltonian H_0 can be diagonalized by performing the polaron transformation

$$U = e^{-S} \quad (5)$$

where

$$S = \sum_{\bar{x}\mu} \frac{\Gamma_{\bar{x}x}^\mu}{\hbar\omega_\mu} |x\rangle \langle x| (b_\mu^\dagger - b_\mu) \quad (6)$$

In the polaron frame, Hamiltonian H_0 becomes (an operator in the polaron frame is denoted by a tilde above its symbol)

$$\tilde{H}_0 = U^\dagger H_0 U = \sum_x \hbar\tilde{\omega}_x |x\rangle \langle x| + \sum_\mu \hbar\omega_\mu b_\mu^\dagger b_\mu \quad (7)$$

where energies of excitonic states are renormalized due to the adaptation of the nuclei to the excited-state configuration

$$\hbar\tilde{\omega}_x = \hbar\omega_x - \sum_\mu \frac{[\Gamma_{xx}^\mu]^2}{\hbar\omega_\mu} \equiv \hbar\omega_x - \lambda_x \quad (8)$$

Hamiltonian V in the polaron frame reads as

$$\tilde{V} = U^\dagger V U = \sum'_{\bar{x}\mu} |\bar{x}\rangle \langle x| M_{\bar{x}\mu} \quad (9)$$

where the transition from exciton state $|x\rangle$ to exciton state $|\bar{x}\rangle$ is mediated by the dressed phonon operator

$$\sum_{\mu} M_{\bar{x}x\mu} = \sum_{\mu} \Gamma_{\bar{x}x}^{\mu} \exp \left[\sum_{\nu} \frac{\Gamma_{\bar{x}x}^{\nu} - \Gamma_{xx}^{\nu}}{\hbar\omega_{\nu}} (b_{\nu}^{\dagger} - b_{\nu}) \right] \left(b_{\mu}^{\dagger} + b_{\mu} - 2 \frac{\Gamma_{xx}^{\mu}}{\hbar\omega_{\mu}} \right) \quad (10)$$

This should be contrasted with the undressed phonon operator that mediates the same transition within the Redfield theory

$$\sum_{\mu} M_{\bar{x}x\mu}^{\text{Red}} = \sum_{\mu} \Gamma_{\bar{x}x}^{\mu} (b_{\mu}^{\dagger} + b_{\mu}) \quad (11)$$

We see that, while the Redfield theory does not take into account neither the displacements (with respect to the ground state) of equilibrium nuclear configurations in excited states nor multiphonon processes, the modified Redfield theory takes into account both these effects.²⁸ The presence of the displaced phonon operator $b_{\mu}^{\dagger} + b_{\mu} - 2\Gamma_{xx}^{\mu}/(\hbar\omega_{\mu})$ in eq 10, which is characteristic for the equilibrium configuration of the nuclei when the electronic subsystem is in state $|x\rangle$, means that the first effect is taken into account. Processes in which an arbitrary number of vibrational quanta is exchanged with the bath to accomplish the transition $|x\rangle \rightarrow |\bar{x}\rangle$ are taken into account in eq 10 by the presence of the exponential of phonon operators.

We assume that the initial density matrix is factorized as

$$\rho(0) = |x_0\rangle\langle x_0| \otimes \frac{\exp \left[-\beta \sum_{\mu} (\hbar\omega_{\mu} b_{\mu}^{\dagger} b_{\mu} + \Gamma_{x_0x_0}^{\mu} (b_{\mu}^{\dagger} + b_{\mu})) \right]}{\text{Tr}_B \exp \left[-\beta \sum_{\mu} (\hbar\omega_{\mu} b_{\mu}^{\dagger} b_{\mu} + \Gamma_{x_0x_0}^{\mu} (b_{\mu}^{\dagger} + b_{\mu})) \right]} \quad (12)$$

so that the excitonic subsystem is taken to be in excitonic state $|x_0\rangle$, while the nuclear degrees of freedom have already adapted themselves to the displaced equilibrium configuration corresponding to the excited state $|x_0\rangle$. In eq 12, $\beta = (k_B T)^{-1}$, T is the temperature, and Tr_B denotes (partial) trace over phonon bath. Such an initial condition tacitly assumes that the adaptation of nuclear degrees of freedom to the displaced equilibrium characteristic for excited states is much faster than the population transfer between excited states. Its relevance to the problem of charge separation in OPVs can be understood from our recent investigations of the phenomenon in question.¹² Namely, we have concluded that, on a sub-picosecond time scale after photoexcitation, the majority of excitons are found in strongly bound donor or CT states, which act as traps for ultrafast charge separation. The escape from these states, therefore, occurs on time scales much longer than typical time scales for nuclear relaxation, which are of the order of 100 fs. Moreover, the fact that our origin of the time axis loosely corresponds to $t \sim 100$ fs to 1 ps after the photoexcitation is not of particular importance for our analysis, which targets processes that happen on much longer time scales. Bearing in mind that we estimate time scales (i.e., orders of magnitude), we can safely think about $t = 0$ as the moment of exciton generation. The initial condition (eq 12) in the polaron frame reads as

$$\tilde{\rho}(0) = |x_0\rangle\langle x_0| \otimes \frac{\exp \left[-\beta \sum_{\mu} \hbar\omega_{\mu} b_{\mu}^{\dagger} b_{\mu} \right]}{\text{Tr}_B \exp \left[-\beta \sum_{\mu} \hbar\omega_{\mu} b_{\mu}^{\dagger} b_{\mu} \right]} \quad (13)$$

Working in the polaron frame in this case is thus technically advantageous, since all partial traces over phonon bath are computed in its canonical equilibrium.

By employing the usual second-order perturbation theory with respect to \tilde{V} , together with Markovian approximation, we obtain that population $f_x(t)$ of exciton state $|x\rangle$ evolves according to

$$\partial f_x(t) = - \sum_{x'(\neq x)} w_{x'x} f_x(t) + \sum_{x'(\neq x)} w_{xx'} f_{x'}(t) \quad (14)$$

where transition rates $w_{xx'}$ from state $|x'\rangle$ to state $|x\rangle$ are expressed in terms of the Fourier component of the correlation function of dressed phonon operators

$$w_{xx'} = \frac{1}{\hbar^2} \int_{-\infty}^{+\infty} d\tau e^{i(\tilde{\omega}_{x'} - \tilde{\omega}_x)\tau} \sum_{\mu\nu} \langle M_{x'\mu}^{(0)}(\tau) M_{xx'\nu} \rangle_{\text{eq}} \quad (15)$$

In the last equation, time dependence of phonon operators is with respect to the free-phonon Hamiltonian appearing in \tilde{H}_0 (see eq 7), whereas the averaging $\langle \dots \rangle_{\text{eq}}$ is with respect to the canonical equilibrium of the phonon bath (see eq 13). More details are provided in section S2.1 of the SI. The calculation of the phonon correlation function appearing in eq 15 is a straightforward, but rather tedious task, whose technical details are presented in section S2.2 of the SI. Here, we only quote the final result in the form that is commonly encountered in the literature

$$w_{xx'} = \frac{1}{\hbar^2} \int_{-\infty}^{+\infty} d\tau e^{i(\tilde{\omega}_{x'} - \tilde{\omega}_x)\tau} \exp \left[-\frac{1}{\hbar^2} (g_{x'x',x'x'}(\tau) - 2g_{x'x',xx}(\tau) + g_{xx,xx}(\tau)) \right] \exp \left[-\frac{i}{\hbar} (\lambda_{x'x',x'x'} - 2\lambda_{x'x',xx} + \lambda_{xx,xx})\tau \right] \left[\ddot{g}_{x'x',xx}(\tau) - \left(\frac{1}{\hbar} \dot{g}_{x'x',xx}(\tau) - \frac{1}{\hbar} \dot{g}_{x'x',x'x'}(\tau) - 2i\lambda_{x'x',x'x'} \right) \left(\frac{1}{\hbar} \dot{g}_{xx,xx}(\tau) - \frac{1}{\hbar} \dot{g}_{xx,x'x'}(\tau) - 2i\lambda_{xx,x'x'} \right) \right] \quad (16)$$

Transition rates within the modified Redfield theory are entirely expressed in terms of quantity

$$\ddot{g}_{\bar{x}_2x_2, \bar{x}_1x_1}(\tau) = \sum_{\mu_2\mu_1} \langle M_{\bar{x}_2x_2\mu_2}^{\text{Red}}(\tau) M_{\bar{x}_1x_1\mu_1}^{\text{Red}} \rangle_{\text{eq}} \quad (17)$$

and its integrals. The quantity $\ddot{g}_{\bar{x}_2x_2, \bar{x}_1x_1}(\tau)$ represents the (equilibrium) correlation function of undressed phonon operators mediating the transition between states $|\bar{x}_2\rangle$ and $|x_2\rangle$ and the transition between states $|\bar{x}_1\rangle$ and $|x_1\rangle$, see eq 11. The function $\dot{g}_{\bar{x}_2x_2, \bar{x}_1x_1}(\tau)$ and the so-called line shape function $g_{\bar{x}_2x_2, \bar{x}_1x_1}(\tau)$ are defined as

$$\dot{g}_{\bar{x}_2x_2, \bar{x}_1x_1}(\tau) = \int_0^{\tau} ds \ddot{g}_{\bar{x}_2x_2, \bar{x}_1x_1}(s) \quad (18)$$

$$g_{\bar{x}_2x_2, \bar{x}_1x_1}(\tau) = \int_0^\tau ds_2 \int_0^{s_2} ds_1 \ddot{g}_{\bar{x}_2x_2, \bar{x}_1x_1}(s_1) \quad (19)$$

while quantity $\lambda_{\bar{x}_2x_2, \bar{x}_1x_1}$ represents a generalization of the expression for λ_x (see eq 8) and reads as

$$\lambda_{\bar{x}_2x_2, \bar{x}_1x_1} = \sum_{\mu} \frac{\Gamma_{\bar{x}_2x_2}^{\mu} \Gamma_{\bar{x}_1x_1}^{\mu}}{\hbar\omega_{\mu}} \quad (20)$$

We note here that the derivation in section S2.1 of the SI actually results in rate eqs (eq 14) with time-dependent modified Redfield rates, $w_{xx'}(t)$, which are given by eq 16 in which the integration limits $-\infty$ and $+\infty$ are replaced by $-t$ and t , respectively. Therefore, strictly speaking, the dynamics predicted by eq 14 is not correct for times t shorter than the decay time of the phonon correlation function entering eq 15. On these time scales, non-Markovian effects become important. This circumstance, however, is not expected to affect our principal conclusions. Physically relevant treatment of short-time dynamics should proceed from an initial condition that should be appropriate for a sudden exciton photogeneration and that is different from that in eq 12. In the Discussion, we discuss why we believe the details of short-time dynamics are not particularly relevant for the long-time separation dynamics, which is of primary interest in this work.

Equation 15 nicely illustrates why this approach bears the name modified Redfield theory. Namely, population transition rates within the Redfield theory are also expressed in terms of the Fourier component of the correlation function, this time of undressed phonon operators (eq 11)¹⁹

$$w_{xx'}^{\text{Red}} = \frac{1}{\hbar^2} \int_{-\infty}^{+\infty} d\tau e^{i(\omega_x - \omega_{x'})\tau} \sum_{\mu\nu} \langle M_{x'x\mu}^{(0)\text{Red}}(\tau) M_{xx'\nu}^{(0)\text{Red}} \rangle_{\text{eq}} \quad (21)$$

Note also that, in eq 21, there is no renormalization of excitonic energies, that is, $\tilde{\omega}_x = \omega_x$. Evaluating eq 21, we obtain the familiar expression for rates in the case when only one phonon can be exchanged with the bath to perform transition $|x'\rangle \rightarrow |x\rangle$

$$w_{xx'}^{\text{Red}} = \frac{2\pi}{\hbar} \sum_{\mu} |\Gamma_{xx'}^{\mu}|^2 \delta(\hbar\omega_{x'} - \hbar\omega_x + \hbar\omega_{\mu}) n_{\text{BE}}(\hbar\omega_{\mu}) + \frac{2\pi}{\hbar} \sum_{\mu} |\Gamma_{xx'}^{\mu}|^2 \delta(\hbar\omega_{x'} - \hbar\omega_x - \hbar\omega_{\mu}) (1 + n_{\text{BE}}(\hbar\omega_{\mu})) \quad (22)$$

with $n_{\text{BE}}(E) = (e^{\beta E} - 1)^{-1}$.

As mentioned in the model description, index μ enumerating phonon modes can be understood as composite index $(i\xi)$, where i labels individual sites, while ξ counts individual phonon modes on each site. Bearing in mind our assumption that sets of phonon modes and local electron–phonon and hole–phonon interaction constants are identical on each site, the passage to the limit of macroscopic phonon bath is most conveniently done by introducing the spectral function (for $E > 0$)

$$J(E) = \sum_{\xi} g_{\xi}^2 \delta(E - \hbar\omega_{\xi}) \quad (23)$$

In eq 23, g_{ξ} are local carrier–phonon interaction constants. Under the aforementioned assumptions, correlation function $\ddot{g}_{\bar{x}_2x_2, \bar{x}_1x_1}(\tau)$ factorizes as follows

$$\ddot{g}_{\bar{x}_2x_2, \bar{x}_1x_1}(\tau) = P_{\bar{x}_2x_2, \bar{x}_1x_1} \ddot{g}(\tau) \quad (24)$$

where quantity $P_{\bar{x}_2x_2, \bar{x}_1x_1}$ depends only on spatial properties of exciton states involved, while

$$\ddot{g}(\tau) = \int_0^{+\infty} dE J(E) \left[\coth\left(\frac{\beta E}{2}\right) \cos\left(\frac{E\tau}{\hbar}\right) - i \sin\left(\frac{E\tau}{\hbar}\right) \right] \quad (25)$$

depends only on spectral density $J(E)$. Analogous factorizations also hold for $\dot{g}_{\bar{x}_2x_2, \bar{x}_1x_1}(\tau)$, $g_{\bar{x}_2x_2, \bar{x}_1x_1}(\tau)$, and $\lambda_{\bar{x}_2x_2, \bar{x}_1x_1}$ as detailed in section S2.3 of the SI. Here, let us only mention that quantity $P_{\bar{x}_2x_2, \bar{x}_1x_1}$ is a generalization of the spatial proximity factor $P_{x'x, xx'}$, which is the only quantity entering the Redfield population transition rates

$$w_{xx'}^{\text{Red}} = \frac{2\pi}{\hbar} P_{x'x, xx'} J(\hbar\omega_x - \hbar\omega_{x'}) n(\hbar\omega_x - \hbar\omega_{x'}) \quad (26)$$

Equation 26 can be obtained from eq 22 by passing to the limit of macroscopic bath, while

$$n(E) = \begin{cases} n_{\text{BE}}(E), & E > 0 \\ 1 + n_{\text{BE}}(-E), & E < 0 \end{cases} \quad (27)$$

In this work, we assume that the spectral density is of the Drude–Lorentz form

$$J(E) = \frac{2}{\pi} \lambda \frac{E \cdot \hbar\gamma}{E^2 + (\hbar\gamma)^2} \quad (28)$$

The parameter λ , which can be interpreted as the polaron binding energy, measures the overall strength of carrier–phonon coupling. The inverse of parameter γ , γ^{-1} , is the characteristic time scale of the decay of bath correlation function $\ddot{g}(\tau)$ in eq 25. The Drude–Lorentz spectral density is widely employed in computational studies of excitonic dynamics in models of photosynthetic excitonic aggregates^{29,30} and OPVs,^{18,31,32} mainly due to the existence of relatively simple analytical expressions for $\ddot{g}(\tau)$.

The exciton recombination is taken into account on the same level as in our recent work.¹³ Equation 14 is then augmented by the following term

$$(\partial f_x(t))_{\text{rec}} = -\tau_x^{-1} f_x(t) \quad (29)$$

where lifetime τ_x of state $|x\rangle$ basically depends on the overlap of moduli of electron and hole distributions in that state. The recombination events are assumed to be unidirectional and they are tracked by following the time evolution of the ground-state (GS) population

$$\partial f_{\text{GS}}(t) = \sum_x \tau_x^{-1} f_x(t) \quad (30)$$

Further details are given in section S1.3 of the SI and in ref 13.

Our aim is to examine pathways of charge separation on time scales spanning a very broad range, from shortest time scales stemming from nuclear dynamics (~ 10 – 100 fs) all the way to time scales characteristic for recombination events (~ 100 ps to 10 ns). Computational approaches that rely on

the direct propagation of eq 14 complemented with eq 29 are thus quite expensive, especially keeping in mind that we want to follow populations of ~ 1000 excitonic levels. Rewriting eqs 14 and 29 in matrix form, we formulate an efficient algorithm to calculate exponent of a nonsymmetric matrix, which completely obviates the need for direct temporal propagation. The details of our numerical scheme are presented in sections S2.5 and S2.6 of the SI. The flow diagram summarizing the main steps in the computation of the dynamics in a single disorder realization is given in Figure 1b.

RESULTS

Calculations of the time dependence of populations of various types of exciton states were performed using the approach presented in previous section. The default parameters in the calculations were: polaron binding energy $\lambda = 80$ meV, disorder strength $\sigma = 100$ meV, temperature $T = 300$ K, $\gamma = 10$ ps $^{-1}$. Some of these parameters were varied to understand the effect of relevant factors on time scales of charge separation process. The values of the parameters that were varied will be explicitly specified in the presentation of results in this section, while for all other parameters the default values will be assumed. The transition rates were evaluated within modified Redfield theory using eq 16. Two different types of initial conditions (see eq 12) were considered. The first type assumed that initial state (state $|x_0\rangle$ in eq 12) is an XD state with energy in the range $(E - \Delta E, E + \Delta E)$ (with $\Delta E = 50$ meV) which has highest matrix element for its optical generation. The second type assumed that initial state is the lowest-energy CT state among those whose recombination lifetime is shorter than 10 ns. The first type of initial conditions is chosen to mimic the effect of external excitation by a short pulse of central frequency E/\hbar . We will examine the dynamics starting from initial donor states of different energies E in order to understand how excess electronic energy supplied by the excitation of high-energy donor states affects charge separation pathways and time scales. As quantitatively demonstrated in Figure S2 of the SI, higher lying donor states also display a higher degree of carrier delocalization. Whether or not the excess electronic energy or better carrier delocalization can enhance separation of initial donor excitons has been the subject of experimental studies performed both on sub-picosecond⁵ and much longer³³ time scales. The second type of initial conditions was chosen to understand the separation process once the exciton reached the lowest energy CT state. Such an initial condition is also experimentally relevant. In refs 34 and 35, it was concluded that charge separation predominantly occurs upon the fast relaxation to the bottom of the CT manifold, on time scales ranging from tens to hundreds of picoseconds.³⁵ Moreover, the authors of ref 9 succeeded in selectively exciting (from the ground state) the low energy interface-pinned CT state. The condition on the exciton recombination lifetime was introduced to avoid the possibility of selecting some state whose energy was significantly lowered due to effects of disorder, while its overlap of electron and hole wave functions is so small that it essentially does not represent the conventional CT state with both electron and hole being close to the interface. In Figure S3 of the SI, we present numerical evidence that our criterion for the choice of the initial CT state indeed gives a CT state with small electron–hole separation and quite localized carriers. In the calculation, we include all exciton states with energies lower than $E_{\text{init}} + 20k_{\text{B}}T$, where E_{init} is the energy of

initial state. All of the results presented were averaged over 256 realizations of disorder, which is sufficient to get converged results for quantities presented.¹³ In Figure 2a–d we present

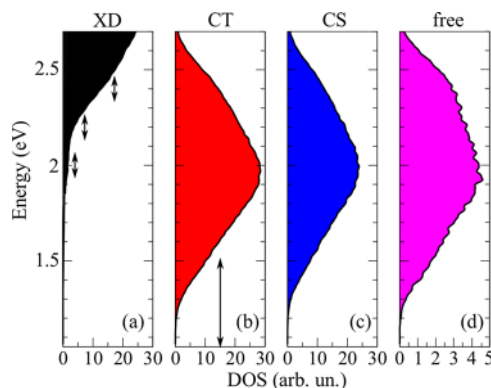


Figure 2. Disorder-averaged densities of (a) XD, (b) CT, (c) CS, and (d) free-charge states (in arbitrary units). The vertical arrows indicate energy ranges in which the initial (a) XD and (b) CT state is located. The excitonic DOS in a single disorder realization is computed by broadening each exciton level by a Gaussian with standard deviation of 5 meV.

disorder-averaged densities of XD, CT, CS, and free-charge states, respectively. The vertical arrows indicate the energy range in which the initial XD (Figure 2a) and CT (Figure 2b) state is located.

Our approach is based on the assumption that off-diagonal exciton–phonon coupling parameters (which can be quantified by the terms $P_{x_i x_j, x_f x_i}$ when $x_i \neq x_j$) are much smaller than the diagonal exciton–phonon coupling parameters (which can be quantified by the terms $P_{x_i x_i, x_i x_i}$). To check if this assumption is satisfied we present in Figure 3 the average over different disorder realizations of the quantity

$$h(E_i, E_f) = \frac{\sum_{x_j, x_g} P_{x_j x_g, x_f x_j} \exp\left(-\frac{(E_{x_j} - E_i)^2 + (E_{x_g} - E_f)^2}{2\sigma_E^2}\right)}{\sum_{x_j, x_g} \exp\left(-\frac{(E_{x_j} - E_i)^2 + (E_{x_g} - E_f)^2}{2\sigma_E^2}\right)} \quad (31)$$

which is basically the dependence of $P_{x_j x_g, x_f x_j}$ on the energies of states E_{x_i} and E_{x_f} . The results are presented for two disorder strengths, $\sigma = 50$ meV and $\sigma = 100$ meV. In each disorder realization, as well as on both axes in Figure 3, the energies $E_{i,f}$ have been rescaled to the $[0,1]$ range using the formula $e = \frac{E - E_{\text{min}}}{E_{\text{max}} - E_{\text{min}}}$, where E is the unrescaled energy, e is the rescaled energy which is shown on the axes, E_{min} and E_{max} are the minimal and maximal energy of exciton states considered for a given realization of disorder. Neither of the aforementioned energies is renormalized in the sense of eq 8. The reasons for such a rescaling will be given together with the presentation of energy–temporal pathways of charge separation, see Figure 6a–d. The results in Figure 3 point out that $h(E_i, E_f)$ is much smaller for states of different energies than for states of close energies, as can be evidenced by the fact that the off-diagonal contributions are at least an order of magnitude smaller than the diagonal contributions. Such results confirm our assumption that off-diagonal exciton–phonon coupling parameters are much smaller than the

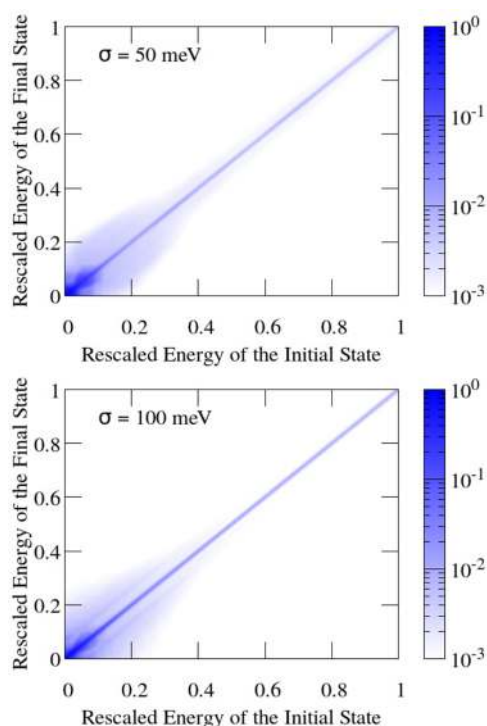


Figure 3. Dependence of spatial proximity factor $h(E_i, E_f)$ (eq 31) averaged over different disorder realizations on rescaled energy of the initial and final state for two different values of disorder strength σ . Standard deviation of the Gaussian function used to broaden the spatial proximity factor is $\sigma_E = 5$ meV. The data are shown for exciton states considered when the initial state is XD state with energy around 2200 meV.

diagonal exciton–phonon coupling parameters. We also checked the sensitivity of our results to the parameter of the spectral function γ . The results shown in Figures S7 and S8 of the SI indicate that the change of γ within reasonable limits $\gamma \in (10 - 20)$ ps $^{-1}$ has almost no effect on time dependence of populations.

To understand the time evolution of populations of various types of exciton states, we present in Figure 4 these dependences at four different values of disorder strength σ for initial XD state with energy of around 2200 meV, see the middle vertical arrow in Figure 2a. First step in the separation process is the transformation from the initial XD state to a CT state. In the initial XD state, electron and hole wave functions have strong overlap which means that the electron and the hole are localized around the same position in space. To transform into a CT state both electron and hole need to reach the interface and the effects of disorder slow down this process. This effect can be clearly seen from Figure 4. While for lowest disorder strength CT excitons outnumber XD excitons already at around 1 ps, for largest disorder strength this happens more than 100 ps after initial excitation. These time scales are comparable to the XD exciton recombination time and there is therefore a possibility that the XD exciton will recombine before transforming into a CT exciton. In Figure 5 (left panels) we present the time dependence of the number of excitons that have recombined from various groups of exciton states. For strong disorder the exciton remains in the donor for long time and therefore a significant portion of these excitons gets recombined (around 50% for $\sigma = 100$ meV, see bottom left panel in Figure 5). For low disorder strength a large portion of XD excitons transform into CT excitons before recombining

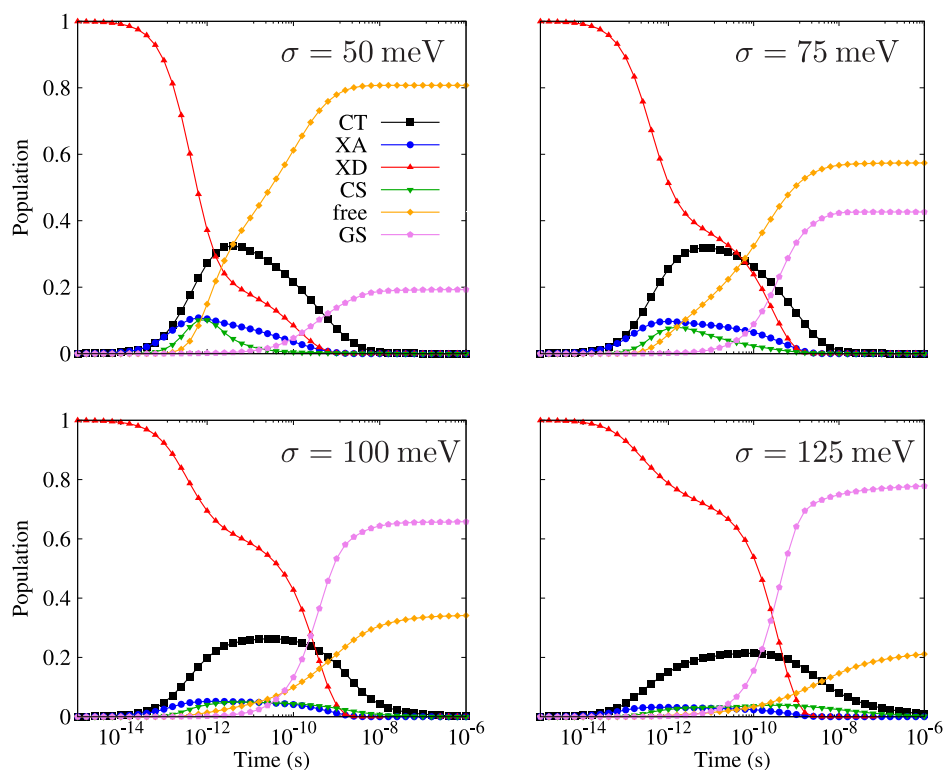


Figure 4. Time dependence of the number of CT excitons, acceptor (XA) excitons, XD excitons, CS excitons, free charges (free), and recombined pairs (GS) when initial state is XD state with energy around 2200 meV. The results are shown at four different values of disorder strength σ .

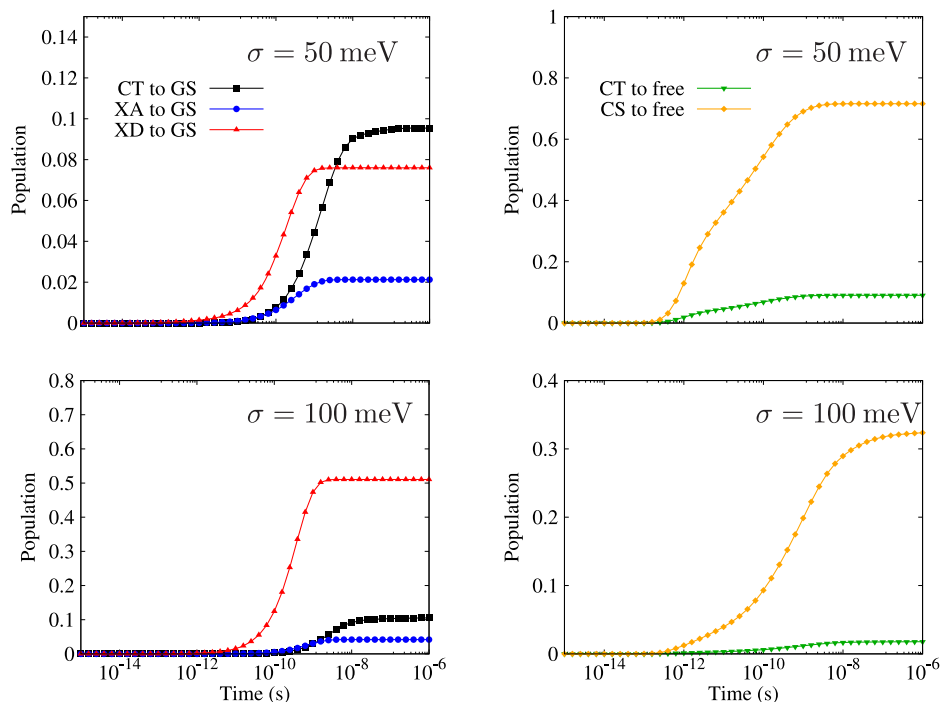


Figure 5. Left panels: Time dependence of the number of recombined pairs from CT states (CT to GS), from XA states (XA to GS) and from XD states (XD to GS). Right panels: Time dependence of the number of free charges created from CT states (CT to free) and from CS states (CS to free). The results are presented at two different values of disorder strength σ . Initial state is XD state with energy around 2200 meV.

and recombination from XD states is no longer the dominant source of recombination (see top left panel in Figure 5).

From Figure 4 we see that time scale for further separation from CT state toward free charges also strongly depends on disorder strength σ and increases as σ increases. This can be evidenced from the increase of time when free charge population reaches saturation. In our previous work,¹³ we investigated the separation from lowest CT state in detail and found that for low and moderate disorder strength it can be understood in terms of a four-state kinetic model involving the ground state, the lowest CT state, intermediate CT states and CS states. In this model an exciton that escapes from intermediate CT states to CS states reaches external contacts without any additional obstacles. For larger disorder strengths additional obstacle is caused by slow transport from CS state toward external contacts. For all disorder strengths the states from which conversion to free charges takes places are predominantly CS states. This can be seen from right panels in Figure 5. Despite the fact that almost all excitons that separate into free charges pass through CS states, their populations remain relatively small at all times. This is a consequence of the fact that no exciton remains for a long period of time in a CS state—it either makes a transition to other CS or CT states or converts into free charges. To additionally verify the statements of this paragraph regarding further evolution of an exciton that has reached a CT state, we have performed the computation where initial state is a low energy CT state chosen according to the criterion discussed in the first paragraph of this section. The results obtained are given in Figure S9 of SI and also demonstrate an increase of time scale for conversion into free charges from $\sim(1 - 10)$ ns at low and moderate disorder strength $\sigma = (50 - 75)$ meV toward $\sim 1 \mu\text{s}$ time scale at $\sigma = 125$ meV. In this case, all recombination events take place from CT states, as shown in

the left part of Figure S10 of the SI, and free states are again predominantly reached by transitions from CS states, as presented in the right part of that figure.

Next, we would like to gain insight in time evolution of exciton energies which will unravel whether hot or cold charge separation mechanism is in place. For this reason, we calculate the time evolution of spectral distribution of excitons defined as

$$A_G(E, t) = \frac{1}{N_X(t)} \sum_{x \in G} g(E - \hbar\omega_x, \sigma_E) f_x(t) \quad (32)$$

where $N_X(t)$ is the total excitonic population at time t and $g(x, \sigma_E) = \frac{1}{\sigma_E \sqrt{2\pi}} \exp\left(-\frac{x^2}{2\sigma_E^2}\right)$ is the Gaussian function with standard deviation σ_E . The summation in eq 32 is performed over all exciton states from group G . This distribution for various exciton groups is shown in Figure 6 along with corresponding densities of states. More precisely, the quantity $a_G(e, t)$ shown in Figure 6 is $a_G(e, t) = A_G(E, t)$, where the relation between the rescaled energy e and the unrescaled energy E is presented in the discussion of Figure 3. Spectral distribution and density of states obtained in this way were then averaged over different realizations of disorder. We believe that this way of energy rescaling is excellent to gain insight into energy-temporal pathways of various groups of excitons. On the other hand, if the rescaling were not performed, lowest energy CT states would have quite different energies for various realizations of disorder, see Figure 2b. In the course of averaging over different realizations of disorder, lowest energy CT states for some configurations would be at the same energy as some high-energy states of other configurations and it would be hard to gain insight into exciton pathways in the course of charge separation. From Figure 6a we see that donor excitons that do not recombine or

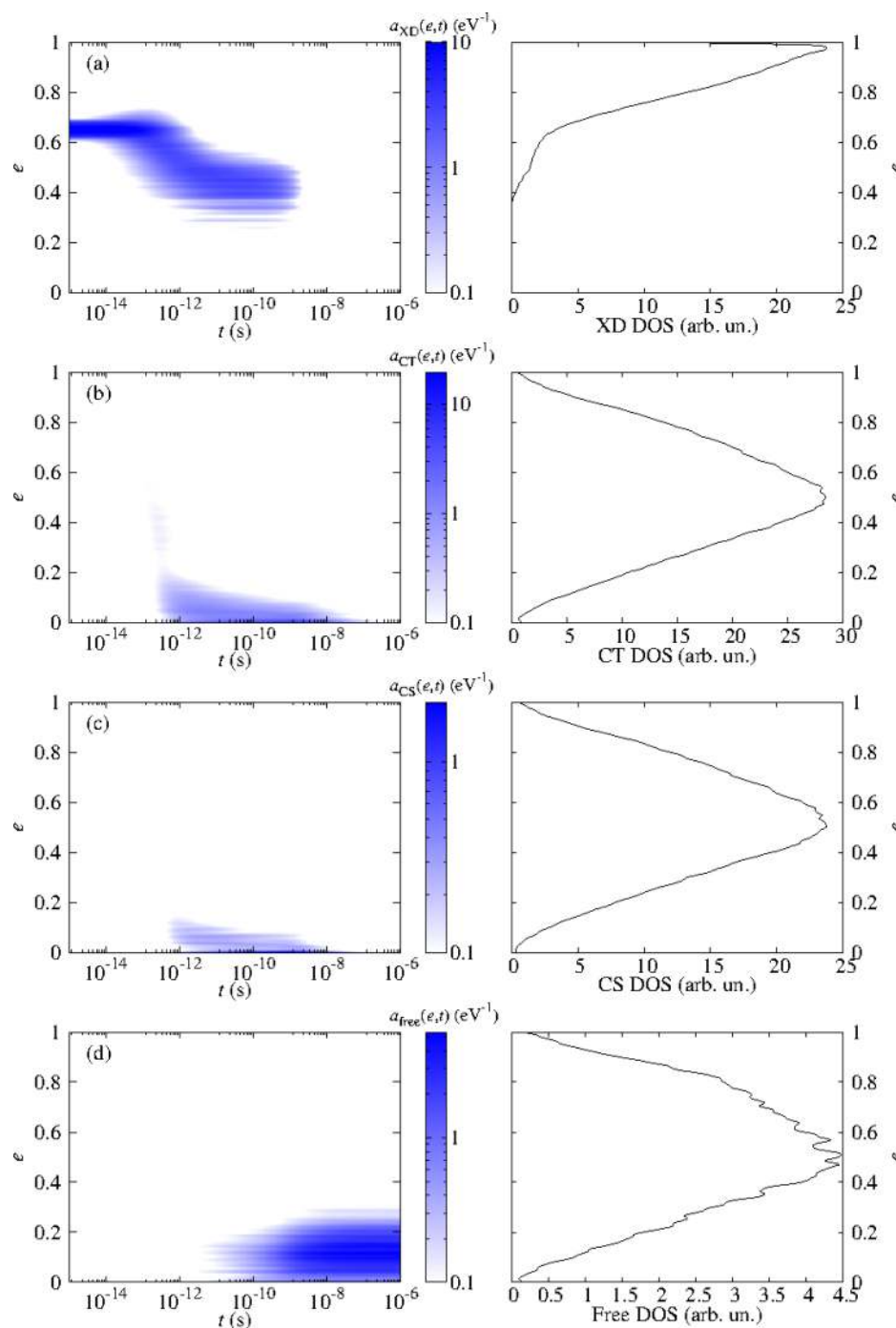


Figure 6. Energy- and time-resolved population of XD states [$a_{\text{XD}}(e, t)$], CT states [$a_{\text{CT}}(e, t)$], CS states [$a_{\text{CS}}(e, t)$], and free charges [$a_{\text{free}}(e, t)$]. Gaussian broadening of $\sigma_E = 5$ meV was used to calculate these quantities. The energy of free charges is taken at the moment of time when they are created. Initial state is XD state with energy around 2200 meV. Corresponding DOS (in arbitrary units) for each group of states is given as a reference in panels on the right. Energy axis has been rescaled in such a way that 0 corresponds to lowest energy in a certain configuration, while 1 corresponds to highest energy of that configuration.

convert to CT states relax to lower energies. Since the beginning of creation of CT states (at about 0.1–1 ps, see Figure 6b), the low energy part of CT manifold is populated, and the energy distribution is further shifted toward lower energies as the time progresses. CS states become populated at about similar times as CT states and only cold CS states are populated, as seen in Figure 6c. Figure 6d shows the distribution of energies of free charges that were created and also indicates that only low energy free charges are created.

Note that our model does not consider further evolution of free charges after their creation. Consequently, the energies of free charges in Figure 6d correspond to the moment of time when they were created. The results in Figure 6 clearly point in favor of cold separation mechanism since only low energy CT and CS excitons are present in the system and only low energy free charges are generated. We obtain the same conclusion from analogous figures obtained for different initial XD

energies (depicted by vertical arrows in Figure 2a) and for different disorder strengths, see Figures S11–S13 of the SI.

To further support the charge separation mechanism proposed, we present in Figure 7 the quantity defined as

$$N_T(t)_{G_2 G_1} = \sum_{x_1 \in G_1, x_2 \in G_2} [f_{x_1}(t)w_{x_2 x_1} - f_{x_2}(t)w_{x_1 x_2}] \quad (33)$$

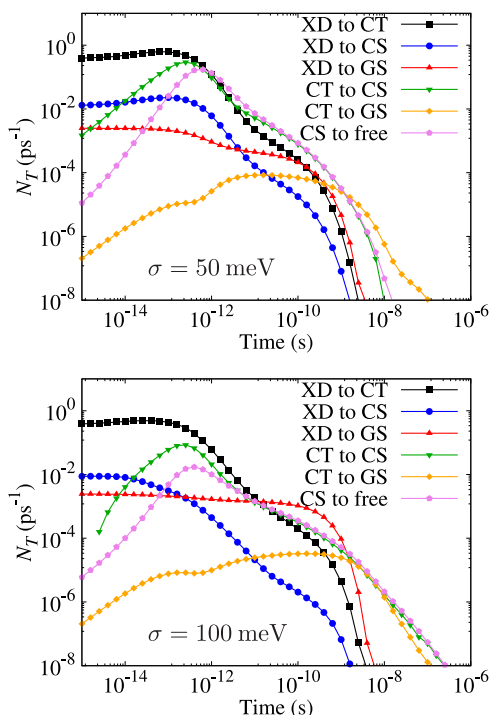


Figure 7. Time dependence of the number of transitions per unit time between most relevant groups of exciton states for disorder strengths of $\sigma = 50$ and 100 meV. Initial state is XD state with energy around 2200 meV.

This quantity represents the net number of exciton transitions per unit time from the states of group G_1 to the states of group G_2 . Figure 7 shows that dominant transitions in the system up to ~ 1 ps are the transitions from XD to CT states. After this time, for lower disorder strength of $\sigma = 50$ meV, the dominant transitions in the system are those from CT to CS states and from CS to the states of free charges. Interestingly, the value of N_T for these two groups of transitions is almost the same at those times (as can be seen in Figure 7), suggesting that almost each conversion between CT and CS states is followed by conversion from CS to free charge states. For larger times (after ~ 1 ns) recombination of a small number of remaining CT excitons dominates. For larger disorder strength of $\sigma = 100$ meV, we see that from $\sim (10 - 1000)$ ps XD recombination dominates. Nevertheless, there is again the balance between CT to CS and CS to free charge conversion, which become dominant events at times after ~ 10 ns. All these results unambiguously imply that the dominant pathway of excitons that avoid recombination is from XD, via cold CT to cold CS states, and eventually to free-charge states.

We further study the impact of polaron binding energy on exciton dynamics in general and charge separation yield in particular. Similarly as in ref 13, the separation yield is defined as the long-time limit of the total free-charge population. In

Figure 8 we present the dependence of separation yield from initial XD state on polaron binding energy at two different

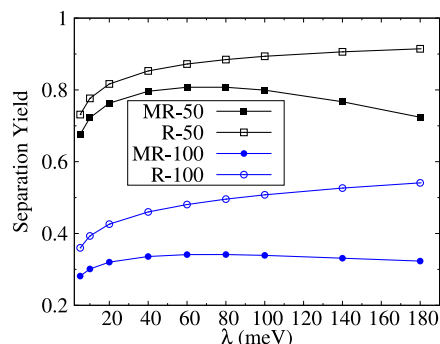


Figure 8. Dependence of separation yield on polaron binding energy λ when transition rates are modeled within modified Redfield theory for disorder strength of $\sigma = 50$ meV (label MR-50) and $\sigma = 100$ meV (label MR-100) and when transition rates are modeled within Redfield theory for disorder strength of $\sigma = 50$ meV (label R-50) and $\sigma = 100$ meV (label R-100). Initial state is XD state with energy around 2200 meV.

values of disorder strength in cases where transition rates were modeled using modified Redfield (eq 16) and Redfield (eq 26) approaches. The effect of electron–phonon interaction, whose strength is in our model quantified by polaron binding energy, on exciton transport is twofold. On the one hand, the increase in electron–phonon interaction increases the phonon-assisted scattering between exciton states and hence the transition rates between the states. This effect is included both in Redfield and modified Redfield rates. On the other hand, the increase in electron–phonon interaction tends to “dress” the carriers by the respective phonon cloud, which leads to a decrease in the transition rates between the states. This effect is captured only within the modified Redfield approach. As a consequence of previous facts, the transition rates always increase with increase in electron–phonon interaction strength within Redfield approach. For this reason, the separation yield is a monotonously increasing function of λ within Redfield approach. On the other hand, within modified Redfield approach, the transition rates and the separation yield are not monotonous functions of λ , which can be seen in Figure 8. The maximum in the dependence of the yield on λ is more pronounced for smaller disorder strength. In this case, relative role of localization induced due to polaron effects in comparison to localization induced by disorder is larger, leading to a more pronounced dependence of yield on λ . Nevertheless, we see from Figure 8 that in practice the separation yield depends only weakly on λ . This is true in particular in the range from 10 to 100 meV, which is the range of realistic values of λ .^{14,36} Some quantitative differences between separation yield from Redfield and modified Redfield approach exist, as can be seen in Figure 8. The separation yield is consistently smaller in the modified Redfield than in the Redfield approach, and the difference between the two yields increases as the magnitude of the carrier–phonon interaction is increased. Nevertheless, the overall conclusions regarding the time scales for conversion between different exciton types and separation mechanism are not expected to be affected by the choice between the two models for transition rates. This is confirmed by the results presented in Figure S5 of the SI, which compares the dynamics of excitonic populations and

recombination events produced by modified Redfield and Redfield transition rates. Since the excitonic dynamics in the two cases is similar, see Figure S5a,c,e, the correlation between the values of the respective transition rates is expected, as evidenced by Figure S6 of the SI, which shows pairs (w_R , w_{MR}) of transition rates predicted by Redfield (w_R) and modified Redfield (w_{MR}) approaches. For most transitions, the two models predict transition rates that are of the same order of magnitude. However, the difference in the separation yields presented in Figure 8 means that the most important transitions for the full charge separation (from XD to CT and from CT to CS states), which involve a significant spatial transfer of charge, are somewhat slower in the modified Redfield than in the Redfield approach. The effect is more pronounced for stronger couplings to vibrations and is also reflected in recombination data in Figure S5b,d,f. Higher recombination probabilities from both XD and CT states within the modified Redfield approach (with respect to the Redfield approach) reflect smaller escape rates from XD toward CT and from CT toward CS states. The preceding discussion clearly demonstrates that the approach adopted in this work takes into account (at least partially) the “dressing” of electronic excitations by phonons. For completeness, we present in Figure S14 of the SI the dependence of separation yield from initial CT state on λ . This dependence exhibits the same features as in the case of initial XD state, with a slight difference that it is somewhat more pronounced.

In our previous work,¹³ we used the transition rates which are equivalent to Redfield rates, with somewhat different spectral function (Ohmic with exponential cutoff instead of Drude–Lorentz). Since we have established that exciton dynamics and separation mechanism are expected to be similar both within Redfield and modified Redfield approach and we have previously shown¹³ that the choice between Drude–Lorentz and Ohmic (with exponential cutoff) spectral function does not strongly affect the separation yield from initial XD state, it is expected that all the trends obtained when a particular parameter of the Hamiltonian is changed (such as transfer integrals, band offsets, on-site Coulomb interaction, temperature, energy of initial donor state, electric field strength) will remain qualitatively similar as in our previous study. For example, we found in our previous work¹³ (in agreement with other studies^{17,32}) that the dependence of charge separation yield on electric field is a monotonously increasing function that is nearly constant at fields below $\sim 10^6$ – 10^7 V/m, which then increases and eventually reaches one at fields on the order $\sim 10^7$ – 10^8 V/m and we expect overall similar behavior here. Because of these expectations and the fact that the evaluation of modified Redfield rates is significantly more computationally prohibitive than the evaluation of Redfield rates, we do not repeat the analysis of these dependences from our previous work here.

DISCUSSION

Connection to Experimental Results. We now discuss the connection of our results to available experimental results from the literature. The most common experimental technique for investigating the time dependence of populations is pump–probe transient absorption spectroscopy. Within this technique, one initially excites the system by the pump pulse that creates excitons and then probes the system by another optical pulse. Optical response to the second pulse gives information about populations of certain groups of exciton states. Two time

scales were typically identified in the signals obtained from the application of this technique to polymer/fullerene blends: a very short ~ 100 fs time scale and a longer ~ 10 ps time scale.^{34,37–40} The longer ~ 10 ps time scale originates from conversion of XD to CT excitons. On the other hand, the short time scale may originate from ultrafast transfer of excitons generated very close to the interface which do not need to diffuse to the interface to convert into CT excitons. We will discuss in particular the results on P3HT/PCBM blend since the parameters of our model were chosen to mimic this system. In ref 41, the authors analyzed exciton and charge dynamics in P3HT/PCBM blends of varying degree of disorder: (i) regiorandom P3HT; (ii) regioregular P3HT; (iii) annealed regioregular P3HT. They found that in cases (i) and (ii) recombination from CT states occurs with a time constant of 2 ns with more recombination events in case (i). Such results are in overall agreement with our results regarding the time scale for recombination (see Figure 5) and its independence on disorder strength. The time scale for conversion of XD to CT states is less than 100 fs in cases (i) and (ii) in ref 41; however, one should note that these samples consist of a blend where there is a PCBM molecule close to each P3HT chain and therefore XD excitons do not need to diffuse to the interface to transform to CT states. On the other hand, our model mimics the P3HT/PCBM bilayer and predicted XD to CT conversion time scales should be compared to annealed samples [case (iii) in ref 41] where regions of pure P3HT are formed. The time scale for XD to CT conversion in case (iii) in ref 41 was reported to be approximately 9 ps and is comparable to our results, see Figure 6a,b, or Figure 4.

Since excitons in different states may respond to the same probe, it is difficult to reliably distinguish between different groups of states in a typical transient absorption experiment. It turns out in practice that XD excitons can be reliably identified but that it is quite difficult to distinguish between CT and CS states.¹¹ These difficulties can be circumvented in a time-delayed collection-field experiment, which exclusively measures free (extractable) charges.⁴² Charge generation by an energy-selective photoexcitation is followed by application of a high reverse bias voltage to extract free charges. In a recent study employing this experimental technique,³³ it is shown that the relaxation to the bottom of the CT manifold cannot be avoided, no matter how large the excess energy stemming from the excitation of high-energy donor states is. Moreover, the authors demonstrate that the majority of recombination, as well as the separation events occur starting from CT manifold, and that most photogenerated species either recombine or transform into free carriers within a couple of nanoseconds following the photoexcitation. The results we present in this work, in particular the energy- and time-resolved pathways summarized in Figures 6 and S7–S9, and the resolution of separation and recombination events performed in Figure 5 are thus in agreement with the central conclusions of ref 33.

Dynamics of excitons in polymer/fullerene blends was also studied using several other time-resolved techniques. In ref 40, interpretation of polarization-sensitive transient absorption measurement of P3HT/PCBM blends implied the time-scale of $\sim (0.1 - 20)$ ps for the formation of CT states and up to ~ 100 ps time scale for further conversion into free charges. In ref 43 time-resolved electric field-induced second harmonic method was used to monitor the charge separation process. It was shown that the charges separate by several nanometers during the first several picoseconds, while further separation

and formation of free carriers takes place on a subnanosecond time scale. In ref 7 the authors used time-resolved two-photon photoemission technique to visualize the time dependence of spectral distribution of excitons in a phthalocyanine/fullerene blend. They found that formation of CT states and their further relaxation occurs on a picosecond time scale. Time scales in these experiments are comparable with what we obtain for lower values of disorder strength.

Discussion on Theoretical Approach and Model.

Theoretical and simulation studies that investigated time dependence of exciton populations in organic heterojunctions were certainly performed in the past. Nevertheless, the studies based on model Hamiltonians were restricted to short (sub-picosecond) time scales.^{17,18,32,44–49} Consequently, these studies could capture at most the process of XD to CT conversion and could not capture further charge separation. Some of these studies also included polaronic effects to a certain extent.^{17,18,32,44,45,49} The studies on longer time scales were exclusively based on the assumption that electrons and holes are hopping between a predefined set of sites and relevant properties are typically extracted from a kinetic Monte Carlo simulation.^{50–56} Such studies typically do not include polaronic and delocalization effects, while in some cases delocalization is added through its effect on site energies⁵⁶ and polaronic effects are sometimes added if hopping rates are calculated using the Marcus expression.⁵² On the other hand, our study starts from a model Hamiltonian whose parameters were chosen to mimic a particular bilayer and includes both the effects of delocalization and polaronic effects in the same approach.

The modified Redfield theory interpolates between widely used theories of exciton/charge transport to which it reduces in appropriate limits.²⁵ Standard Redfield rates (eq 26) are obtained from eq 16 by neglecting all terms $\dot{g}_{\bar{x}_2 x_2, \bar{x}_1 x_1}'$, $g_{\bar{x}_2 x_2, \bar{x}_1 x_1}'$, $\lambda_{\bar{x}_2 x_2, \bar{x}_1 x_1}$ in which $\bar{x}_2 = x_2$ or $\bar{x}_1 = x_1$. In this limit, electronic couplings are treated in all orders, while the interaction with phonons is considered in the second order. The path toward the Förster and Marcus transition rates is presented in section S2.4 of the SI. In these limits, the interaction with phonons is treated in all orders, while electronic couplings are considered in the second order. The modified Redfield theory can thus be regarded as a viable route to go beyond all conventional limits and include both delocalization and the most important part of the couplings to vibrations in a nonperturbative manner. It is applicable to transitions in which the spatial overlap between the carriers in the excitonic states involved is relatively small. In our model, the disorder strength is comparable to electronic couplings, so that the carriers in excitonic states are only partially delocalized. This is shown in Figure S4, which presents data on the participation ratio of the electron and hole in various excitonic states. We see in Figure S4 that in the XD, CT, and CS states that are mainly involved in the separation process (see blue traces in Figure 6), the carriers are localized on only a couple of neighboring units. Full charge separation is achieved by transitions (from XD to CT, from CT to CS, and to CS to free-charge states) in which the spatial positions of the electron and hole are significantly changed. Therefore, the spatial overlap of the initial and final states in transitions that are crucial to reach free-charge states is expected to be small, and the rates predicted by the modified Redfield theory are expected to be reliable.

As already mentioned, the initial condition embodied in eq 12 is appropriate to describe the dynamics starting on time scales ~ 100 fs to 1 ps after a sudden photoexcitation event. Our approach is not intended to capture ultrafast dynamics right after exciton photogeneration. Should one want to examine such dynamics, and still treat polaronic effects on the level presented in our study, one should resort to the so-called nonequilibrium modified Redfield theory.^{28,57} The appropriate initial condition to describe sudden photogeneration in excitonic state $|x_0\rangle$ is of the form given on the right-hand side of eq 13, where nuclear degrees of freedom have not had time to accommodate themselves to the displaced equilibrium characteristic for $|x_0\rangle$, but are in their canonical equilibrium (which is associated with the ground state). A derivation that is similar to (but somewhat more involved than) that presented in section S2.1 of the SI produces rate equations (eq 14) with time-dependent nonequilibrium modified Redfield rates, which capture non-Markovian effects and dynamical interplay between nuclear relaxation toward equilibrium in electronically excited state and population transfer. It is shown that, already after a couple of γ^{-1} (in our case, a couple of hundreds of femtoseconds) after exciton photogeneration, time-dependent nonequilibrium modified Redfield rates reach their asymptotic values, which coincide with the modified Redfield rates given in eq 16.⁵⁷ In other words, nuclear relaxation toward nuclear equilibrium in excited states (see phonon factor of the initial condition in eq 12) is completed a couple of hundreds of femtoseconds after a sudden photogeneration. Our recent analysis¹² of ultrafast exciton dynamics triggered by a short photoexcitation suggests that, on sub-picosecond time scales following exciton photogeneration, population transfer mainly occurs within the manifold of donor states, while transitions toward states of spatially separated charges predominantly take place on much longer time scales. These conclusions are not expected to change when polaronic effects are taken into account. We thus believe that, in order to gain insight into time scales and pathways of long-time charge separation, it is reasonable to use time-independent modified Redfield rates (eq 16) along with the initial condition in eq 12.

Next, we comment on the possible influence of the dimensionality of the model on the results. Our main conclusion is that the main path of charge separation includes the transition from XD states to low energy CT states (step 1), followed by conversion of CT states to CS states (step 2) and eventual transport from CS states to free charge states (step 3). We will discuss next how the effect of dimensionality could affect the transport over these routes. Step 2 involves the transition from low energy CT state to intermediate CT state with somewhat larger energy and larger electron–hole separation and the transition from that state to some CS state. Since only a few transitions constitute this step, the effect of dimensionality is not expected to play any role on this step. On the other hand, the effect of dimensionality might be important when charge (or exciton) transport over larger distance takes place. In this case, additional dimensions might help the charge to find additional routes if direct one-dimensional route is not accessible. As a consequence, one might expect that higher dimensionality might accelerate steps 1 and 3. The results of our previous work¹⁵ suggest that step 2 is actually the rate limiting step for low and moderate disorder strengths (say up to $\sigma \sim 80$ meV). Therefore, for these disorder strengths, steps 1 and 3 are already fast enough and their further acceleration will not enhance the separation yield.

On the other hand, steps 1 and 3 do become rate limiting for larger disorder strengths and it is possible that higher dimensionality will accelerate these steps and increase the separation yield.

Next, we comment on the extent by which dimensionality affects the efficiency of steps 1 and 3 and consequently the separation yield. An important point to note in this regard is that the exciton states in our model exhibit a certain degree of delocalization. As a consequence, a donor exciton in step 1 can reach a CT state after making only a few transitions—it does not need to travel slowly site by site. In a similar manner, an electron and a hole in step 3 can also reach the free charge state in a few steps only and not by passing each site. It is therefore important to note that our model is different than frequently used hopping models in which an exciton (or a charge) is localized at a site and can usually hop only to nearest neighbor sites. In such models, the transport can be very slow in one dimension in the presence of disorder and adding new dimensions strongly accelerates the transport. For example, in ref 56 the authors showed that separation yield at low electric fields in one dimension is rather low (between 10^{-4} and 10^{-2} depending on the parameters) and that the separation yield in 2D model can be 2 orders of magnitude larger than in 1D model. In our model, the transport is already relatively efficient in 1D as can be evidenced by reasonably large separation yields of at least 20% even at highest disorder strength (see Figure 4d). Therefore, we expect that additional dimension will only slightly increase the separation yield at large disorder strength, while it will hardly affect it at low and moderate disorder strengths.

This expectation can rigorously be confirmed only by extending the model to higher dimensions which is at present a significant challenge both from computational and conceptual side. On the computational side, higher dimension introduces a significantly larger number of relevant exciton states, which then introduces the need for a much larger number of transition rates that need to be calculated and a larger eigenvalue problem and the system of linear equations that need to be solved to obtain time dependence of populations. On the conceptual side, real morphology of the materials near the interface is not well-known. Ideally, one would like to start in the simulation from the atomic structure of the materials near the interface, then parametrize an effective model similar to ours and use that model further. However, in the case of P3HT/PCBM several questions arise regarding for example the orientation of P3HT chains with respect to the interface, the sharpness of the interface, the amount of order/disorder in each of the materials near the interface, etc.

CONCLUSIONS

In conclusion, we presented the method for simulation of charge separation process in organic semiconductor bilayers from the creation of exciton in the donor to the final time (which can be as long as 1 μ s later), when there are no more charge pairs present in the system. In the course of separation process, donor excitons first relax to lower energies and eventually transform into a CT state. Charge transfer excitons then convert into CS and free-charge states via intermediate CT states which have higher energies and larger electron–hole separation. In more disordered systems the processes of conversion between XD and CT states and the conversion from CT toward free carrier states are slowed down and charge separation yield is lowered since some XD or CT excitons

recombine before they convert to other exciton types. Polaronic effects were included in the computations and it turned out that in relevant range of electron–phonon interaction parameters charge separation yield rather weakly depends on electron–phonon interaction strength. Computation results indicate that it is the conventional cold charge separation mechanism that takes place in organic heterojunctions.

ASSOCIATED CONTENT

Supporting Information

The Supporting Information is available free of charge at <https://pubs.acs.org/doi/10.1021/acs.jpcc.9b10862>.

Detailed description of the model, theoretical approach, and numerical scheme, together with additional figures complementing the discussion in the main text (PDF)

AUTHOR INFORMATION

Corresponding Author

Nenad Vukmirović – Scientific Computing Laboratory, Center for the Study of Complex Systems, Institute of Physics Belgrade, University of Belgrade, 11080 Belgrade, Serbia; orcid.org/0000-0002-4101-1713; Phone: +381 11 3713152; Email: nenad.vukmirovic@ipb.ac.rs

Author

Veljko Janković – Scientific Computing Laboratory, Center for the Study of Complex Systems, Institute of Physics Belgrade, University of Belgrade, 11080 Belgrade, Serbia; Institute of Physics, Faculty of Mathematics and Physics, Charles University, CZ–121 16 Prague 2, Czech Republic; orcid.org/0000-0002-0297-2167

Complete contact information is available at: <https://pubs.acs.org/doi/10.1021/acs.jpcc.9b10862>

Notes

The authors declare no competing financial interest.

ACKNOWLEDGMENTS

We gratefully acknowledge the support by the Ministry of Education, Science and Technological Development of the Republic of Serbia (Project No. ON171017). Numerical computations were performed on the PARADOX supercomputing facility at the Scientific Computing Laboratory of the Institute of Physics Belgrade. V.J. acknowledges stimulating discussions with Dr Tomáš Maňal. V.J.'s work in Prague is supported by Charles University Research Centre Program No. UNCE/SCI/010 and the Czech Science Foundation (GACR) through Grant No. 17-22160S.

REFERENCES

- (1) Brédas, J. L.; Norton, J. E.; Cornil, J.; Coropceanu, V. Molecular Understanding of Organic Solar Cells: The Challenges. *Acc. Chem. Res.* **2009**, *42*, 1691–1699.
- (2) Clarke, T. M.; Durrant, J. R. Charge Photogeneration in Organic Solar Cells. *Chem. Rev.* **2010**, *110*, 6736–6767.
- (3) Few, S.; Frost, J. M.; Nelson, J. Models of Charge Pair Generation in Organic Solar Cells. *Phys. Chem. Chem. Phys.* **2015**, *17*, 2311–2325.
- (4) Park, S. H.; Roy, A.; Beaupré, S.; Cho, S.; Coates, N.; Moon, J. S.; Moses, D.; Leclerc, M.; Lee, K.; Heeger, A. J. Bulk Heterojunction Solar Cells with Internal Quantum Efficiency Approaching 100%. *Nat. Photonics* **2009**, *3*, 297–302.

- (5) Grancini, G.; Maiuri, M.; Fazzi, D.; Petrozza, A.; Egelhaaf, H.-J.; Brida, D.; Cerullo, G.; Lanzani, G. Hot Exciton Dissociation in Polymer Solar Cells. *Nat. Mater.* **2013**, *12*, 29–33.
- (6) Bakulin, A. A.; Rao, A.; Pavelyev, V. G.; van Loosdrecht, P. H. M.; Pshenichnikov, M. S.; Niedzialek, D.; Cornil, J.; Beljonne, D.; Friend, R. H. The Role of Driving Energy and Delocalized States for Charge Separation in Organic Semiconductors. *Science* **2012**, *335*, 1340–1344.
- (7) Jailaubekov, A. E.; Willard, A. P.; Tritsch, J. R.; Chan, W.-L.; Sai, N.; Gearba, R.; Kaake, L. G.; Williams, K. J.; Leung, K.; Rossky, P. J.; et al. Hot Charge-Transfer Excitons Set the Time Limit for Charge Separation at Donor/Acceptor Interfaces in Organic Photovoltaics. *Nat. Mater.* **2013**, *12*, 66–73.
- (8) Lee, J.; Vandewal, K.; Yost, S. R.; Bahlke, M. E.; Goris, L.; Baldo, M. A.; Manca, J. V.; Van Voorhis, T. Charge Transfer State Versus Hot Exciton Dissociation in Polymer–Fullerene Blended Solar Cells. *J. Am. Chem. Soc.* **2010**, *132*, 11878–11880.
- (9) Vandewal, K.; Albrecht, S.; Hoke, E. T.; Graham, K. R.; Widmer, J.; Douglas, J. D.; Schubert, M.; Mateker, W. R.; Bloking, J. T.; Burkhard, G. F.; et al. Efficient Charge Generation by Relaxed Charge-Transfer States at Organic Interfaces. *Nat. Mater.* **2014**, *13*, 63–68.
- (10) van der Hofstad, T. G. J.; Di Nuzzo, D.; van den Berg, M.; Janssen, R. A. J.; Meskers, S. C. J. Influence of Photon Excess Energy on Charge Carrier Dynamics in a Polymer–Fullerene Solar Cell. *Adv. Energy Mater.* **2012**, *2*, 1095–1099.
- (11) Janković, V.; Vukmirović, N. Origin of Space-Separated Charges in Photoexcited Organic Heterojunctions on Ultrafast Time Scales. *Phys. Rev. B: Condens. Matter Mater. Phys.* **2017**, *95*, 075308.
- (12) Janković, V.; Vukmirović, N. Identification of Ultrafast Photophysical Pathways in Photoexcited Organic Heterojunctions. *J. Phys. Chem. C* **2017**, *121*, 19602–19618.
- (13) Janković, V.; Vukmirović, N. Combination of Charge Delocalization and Disorder Enables Efficient Charge Separation at Photoexcited Organic Bilayers. *J. Phys. Chem. C* **2018**, *122*, 10343–10359.
- (14) Coropceanu, V.; Cornil, J.; da Silva Filho, D. A.; Olivier, Y.; Silbey, R.; Brédas, J.-L. Charge Transport in Organic Semiconductors. *Chem. Rev.* **2007**, *107*, 926–952.
- (15) Beck, M.; Jäckle, A.; Worth, G.; Meyer, H.-D. The Multiconfiguration Time-Dependent Hartree (MCTDH) Method: A Highly Efficient Algorithm for Propagating Wavepackets. *Phys. Rep.* **2000**, *324*, 1–105.
- (16) Tanimura, Y. Stochastic Liouville, Langevin, Fokker–Planck, and Master Equation Approaches to Quantum Dissipative Systems. *J. Phys. Soc. Jpn.* **2006**, *75*, 082001.
- (17) Tamura, H.; Burghardt, I. Ultrafast Charge Separation in Organic Photovoltaics Enhanced by Charge Delocalization and Vibronically Hot Exciton Dissociation. *J. Am. Chem. Soc.* **2013**, *135*, 16364–16367.
- (18) Kato, A.; Ishizaki, A. Non-Markovian Quantum-Classical Ratchet for Ultrafast Long-Range Electron-Hole Separation in Condensed Phases. *Phys. Rev. Lett.* **2018**, *121*, 026001.
- (19) May, V.; Kühn, O. *Charge and Energy Transfer Dynamics in Molecular Systems*, 3rd ed.; Wiley-VCH: Weinheim, 2011.
- (20) Valkunas, L.; Abramavicius, D.; Mančal, T. *Molecular Excitation Dynamics and Relaxation*; Wiley-VCH, 2013.
- (21) Xu, D.; Cao, J. Non-Canonical Distribution and Non-Equilibrium Transport beyond Weak System-Bath Coupling Regime: A Polaron Transformation Approach. *Front. Phys.* **2016**, *11*, 110308.
- (22) Zhang, W. M.; Meier, T.; Chernyak, V.; Mukamel, S. Exciton-Migration and Three-Pulse Femtosecond Optical Spectroscopies of Photosynthetic Antenna Complexes. *J. Chem. Phys.* **1998**, *108*, 7763–7774.
- (23) Yang, M.; Fleming, G. R. Influence of Phonons on Exciton Transfer Dynamics: Comparison of the Redfield, Förster, and Modified Redfield Equations. *Chem. Phys.* **2002**, *275*, 355–372.
- (24) Renger, T. In *Primary Processes of Photosynthesis—Part 1: Principles and Apparatus*; Renger, G., Ed.; RSC Publishing: Cambridge, 2008; pp 39–97.
- (25) Abramavicius, D.; Mukamel, S. Energy-Transfer and Charge-Separation Pathways in the Reaction Center of Photosystem II Revealed by Coherent Two-Dimensional Optical Spectroscopy. *J. Chem. Phys.* **2010**, *133*, 184501.
- (26) Novoderezhkin, V. I.; Palacios, M. A.; van Amerongen, H.; van Grondelle, R. Energy-Transfer Dynamics in the LHCII Complex of Higher Plants: Modified Redfield Approach. *J. Phys. Chem. B* **2004**, *108*, 10363–10375.
- (27) Pereverzev, A.; Bittner, E. R. Time-Convolutionless Master Equation for Mesoscopic Electron-Phonon Systems. *J. Chem. Phys.* **2006**, *125*, 104906.
- (28) Dinh, T.-C.; Renger, T. Lineshape Theory of Pigment-Protein Complexes: How the Finite Relaxation Time of Nuclei Influences the Exciton Relaxation-Induced Lifetime Broadening. *J. Chem. Phys.* **2016**, *145*, 034105.
- (29) Kell, A.; Feng, X.; Reppert, M.; Jankowiak, R. On the Shape of the Phonon Spectral Density in Photosynthetic Complexes. *J. Phys. Chem. B* **2013**, *117*, 7317–7323.
- (30) Ishizaki, A.; Fleming, G. R. Theoretical Examination of Quantum Coherence in a Photosynthetic System at Physiological Temperature. *Proc. Natl. Acad. Sci. U. S. A.* **2009**, *106*, 17255–17260.
- (31) Lee, M. H.; Aragón, J.; Troisi, A. Charge Dynamics in Organic Photovoltaic Materials: Interplay between Quantum Diffusion and Quantum Relaxation. *J. Phys. Chem. C* **2015**, *119*, 14989–14998.
- (32) Yan, Y.; Song, L.; Shi, Q. Understanding the Free Energy Barrier and Multiple Timescale Dynamics of Charge Separation in Organic Photovoltaic Cells. *J. Chem. Phys.* **2018**, *148*, 084109.
- (33) Kurpiers, J.; Ferron, T.; Roland, S.; Jakoby, M.; Thiede, T.; Jaiser, F.; Albrecht, S.; Janietz, S.; Collins, B. A.; Howard, I. A.; et al. Probing the Pathways of Free Charge Generation in Organic Bulk Heterojunction Solar Cells. *Nat. Commun.* **2018**, *9*, 2038.
- (34) Grupp, A.; Ehrenreich, P.; Kalb, J.; Budweg, A.; Schmidt-Mende, L.; Brida, D. Incoherent Pathways of Charge Separation in Organic and Hybrid Solar Cells. *J. Phys. Chem. Lett.* **2017**, *8*, 4858–4864.
- (35) Devišis, A.; De Jonghe-Risse, J.; Hany, R.; Nüesch, F.; Jenatsch, S.; Gulbinas, V.; Moser, J.-E. Dissociation of Charge Transfer States and Carrier Separation in Bilayer Organic Solar Cells: A Time-Resolved Electroabsorption Spectroscopy Study. *J. Am. Chem. Soc.* **2015**, *137*, 8192–8198.
- (36) Poelking, C.; Daoulas, K.; Troisi, A.; Andrienko, D. In *P3HT Revisited – From Molecular Scale to Solar Cell Devices*; Ludwigs, S., Ed.; Springer: Berlin, 2014; pp 139–180.
- (37) Hwang, I.-W.; Moses, D.; Heeger, A. J. Photoinduced Carrier Generation in P3HT/PCBM Bulk Heterojunction Materials. *J. Phys. Chem. C* **2008**, *112*, 4350–4354.
- (38) Scheblykin, I. G.; Yartsev, A.; Pullerits, T.; Gulbinas, V.; Sundström, V. Excited State and Charge Photogeneration Dynamics in Conjugated Polymers. *J. Phys. Chem. B* **2007**, *111*, 6303–6321.
- (39) Piris, J.; Dykstra, T. E.; Bakulin, A. A.; Loosdrecht, P. H. v.; Knulst, W.; Trinh, M. T.; Schins, J. M.; Siebbeles, L. D. Photogeneration and Ultrafast Dynamics of Excitons and Charges in P3HT/PCBM Blends. *J. Phys. Chem. C* **2009**, *113*, 14500–14506.
- (40) Matheson, A. B.; Pearson, S. J.; Ruseckas, A.; Samuel, I. D. W. Charge Pair Dissociation and Recombination Dynamics in a P3HT-PC₆₀BM Bulk Heterojunction. *J. Phys. Chem. Lett.* **2013**, *4*, 4166–4171.
- (41) Howard, I. A.; Mauer, R.; Meister, M.; Laquai, F. Effect of Morphology on Ultrafast Free Carrier Generation in Polythiophene-Fullerene Organic Solar Cells. *J. Am. Chem. Soc.* **2010**, *132*, 14866–14876.
- (42) Kniepert, J.; Schubert, M.; Blakesley, J. C.; Neher, D. Photogeneration and Recombination in P3HT/PCBM Solar Cells Probed by Time-Delayed Collection Field Experiments. *J. Phys. Chem. Lett.* **2011**, *2*, 700–705.

(43) Vithanage, D. A.; Devizis, A.; Abramavicius, V.; Infahsaeng, Y.; Abramavicius, D.; MacKenzie, R. C. I.; Keivanidis, P. E.; Yartsev, A.; Hertel, D.; Nelson, J.; et al. Visualizing Charge Separation in Bulk Heterojunction Organic Solar Cells. *Nat. Commun.* **2013**, *4*, 2334.

(44) Tamura, H.; Bittner, E. R.; Burghardt, I. Exciton Dissociation at Donor-Acceptor Polymer Heterojunctions: Quantum Nonadiabatic Dynamics and Effective-Mode Analysis. *J. Chem. Phys.* **2007**, *126*, 021103.

(45) Bera, S.; Gheeraert, N.; Fratini, S.; Ciuchi, S.; Florens, S. Impact of Quantized Vibrations on the Efficiency of Interfacial Charge Separation in Photovoltaic Devices. *Phys. Rev. B: Condens. Matter Mater. Phys.* **2015**, *91*, 041107.

(46) Sun, Z.; Stafström, S. Dynamics of Exciton Dissociation in Donor-Acceptor Polymer Heterojunctions. *J. Chem. Phys.* **2013**, *138*, 164905.

(47) Sun, Z.; Stafström, S. Dynamics of Charge Separation at an Organic Donor-Acceptor Interface. *Phys. Rev. B: Condens. Matter Mater. Phys.* **2014**, *90*, 115420.

(48) Smith, S. L.; Chin, A. W. Phonon-Assisted Ultrafast Charge Separation in the PCBM Band Structure. *Phys. Rev. B: Condens. Matter Mater. Phys.* **2015**, *91*, 201302.

(49) Richler, K.-D.; Mayou, D. Influence of Static Disorder and Polaronic Band Formation on the Interfacial Electron Transfer in Organic Photovoltaic Devices. *Phys. Rev. B: Condens. Matter Mater. Phys.* **2019**, *99*, 195151.

(50) Watkins, P. K.; Walker, A. B.; Verschoor, G. L. B. Dynamical Monte Carlo Modelling of Organic Solar Cells: The Dependence of Internal Quantum Efficiency on Morphology. *Nano Lett.* **2005**, *5*, 1814–1818.

(51) Casalegno, M.; Raos, G.; Po, R. Methodological Assessment of Kinetic Monte Carlo Simulations of Organic Photovoltaic Devices: The Treatment of Electrostatic Interactions. *J. Chem. Phys.* **2010**, *132*, 094705.

(52) Jones, M. L.; Dyer, R.; Clarke, N.; Groves, C. Are Hot Charge Transfer States the Primary Cause of Efficient Free-Charge Generation in Polymer:Fullerene Organic Photovoltaic Devices? A Kinetic Monte Carlo Study. *Phys. Chem. Chem. Phys.* **2014**, *16*, 20310–20320.

(53) Shi, L.; Lee, C. K.; Willard, A. P. The Enhancement of Interfacial Exciton Dissociation by Energetic Disorder Is a Non-equilibrium Effect. *ACS Cent. Sci.* **2017**, *3*, 1262–1270.

(54) van Eersel, H.; Janssen, R. A. J.; Kemerink, M. Mechanism for Efficient Photoinduced Charge Separation at Disordered Organic Heterointerfaces. *Adv. Funct. Mater.* **2012**, *22*, 2700–2708.

(55) Albes, T.; Gagliardi, A. Influence of Permittivity and Energetic Disorder on the Spatial Charge Carrier Distribution and Recombination in Organic Bulk-Heterojunctions. *Phys. Chem. Chem. Phys.* **2017**, *19*, 20974–20983.

(56) Athanasopoulos, S.; Tscheuschner, S.; Bäessler, H.; Köhler, A. Efficient Charge Separation of Cold Charge-Transfer States in Organic Solar Cells Through Incoherent Hopping. *J. Phys. Chem. Lett.* **2017**, *8*, 2093–2098.

(57) Seibt, J.; Mančal, T. Ultrafast Energy Transfer with Competing Channels: Non-Equilibrium Förster and Modified Redfield Theories. *J. Chem. Phys.* **2017**, *146*, 174109.

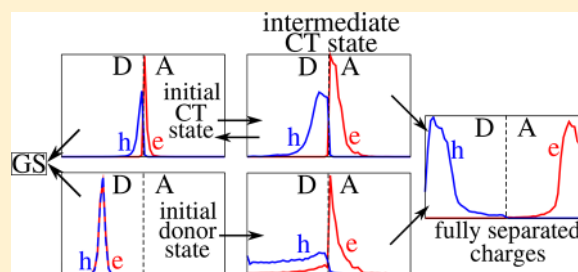
Combination of Charge Delocalization and Disorder Enables Efficient Charge Separation at Photoexcited Organic Bilayers

Veljko Janković¹ and Nenad Vukmirović*¹

Scientific Computing Laboratory, Center for the Study of Complex Systems, Institute of Physics Belgrade, University of Belgrade, Pregrevica 118, Belgrade 11080, Serbia

Supporting Information

ABSTRACT: We study incoherent charge separation in a lattice model of an all-organic bilayer. Charge delocalization is taken into account by working in the basis of electron–hole pair eigenstates, and the separation is described as a series of incoherent hops between these states. We find that relatively weak energetic disorder, in combination with good charge delocalization, can account for efficient and weakly field- and temperature-dependent separation of the strongly bound charge transfer (CT) state. The separation efficiency is determined by the competition between the recombination from the initial CT state and the escape toward intermediate CT states, from which free-charge states can be reached with certainty. The separation of donor excitons also exhibits quite high yields, less bound excitons separating more efficiently. Overall, our results support the notion that efficient charge separation can be achieved even out of strongly bound pair states without invoking coherent effects.



INTRODUCTION

The outstanding problem of charge carrier photogeneration at an interface between an electron-donating (donor) and an electron-accepting (acceptor) organic material has inspired coordinated and interdisciplinary research efforts in the field of organic photovoltaics (OPVs).^{1–4} A photoexcitation of such an interface creates strongly bound donor (or acceptor) excitons that, after the diffusion to the donor/acceptor (D/A) interface, dissociate forming the charge transfer (CT) state. Although the magnitude of the Coulomb interaction between the electron and hole in the CT state is much larger than the thermal energy at room temperature, the subsequent charge separation and eventual formation of free charges that can be extracted at the electrodes is very efficient.^{5,6}

Numerous mechanisms have been invoked to understand the origins of such an efficient conversion of strongly bound excitons to free charges. One group of mechanisms (coherent mechanisms) suggests that free-charge generation occurs on an ultrafast (100 fs) time scale by virtue of the high-energy (“hot”) CT states in which electrons and holes are highly delocalized and spatially separated.^{7–10} The charge separation competes with the subpicosecond exciton relaxation toward strongly bound and localized CT states, which are regarded as traps for further separation.⁷ Another group of mechanisms (incoherent mechanisms) conceives charge separation as a much slower process that starts from the strongly bound (“cold”) CT states and converts them into free carriers by means of the hopping between localized states that is possibly assisted by the interfacial electric field.^{6,11–14} The characteristic time scale for the incoherent charge separation is of the order of tens to hundreds of picoseconds.^{11,12} However, what actually drives the

separation from “cold” CT states despite their strong binding and pronounced localization remains elusive.²

The coherent and incoherent separation mechanisms do not contradict each other, and both may be at play in an efficient OPV cell.¹⁵ Indeed, from our recent theoretical studies,^{16,17} which focus upon the ultrafast dynamics following photoexcitation of a model heterointerface, emerges that on picosecond time scales after photoexcitation the majority of charges are still bound in states of donor or CT excitons. In other words, there is some (coherent) charge separation on subpicosecond time scales, but the vast majority of charges remains in strongly bound states on picosecond time scales, which is in agreement with recent experimental results.¹³ Therefore, examining charge separation on longer time scales is crucial to fully understand charge photogeneration in OPVs.

Recent theoretical studies have challenged the common view that the separation from the CT state requires surmounting an immense energy barrier.^{18–21} These studies emphasize the influence of the entropy on charge separation. In this context, the entropy is related to the number of configurations in which an electron–hole pair may be arranged. It is suggested that the combined effect of entropy and disorder²⁰ or entropy and carrier delocalization²¹ can substantially reduce (or even eliminate) the Coulomb barrier, so that the electron and hole in the CT state are not thermodynamically bound and thus might separate if there are no kinetic obstacles.

Received: April 2, 2018

Revised: April 19, 2018

Published: April 19, 2018

The charge separation from the strongly bound CT state has been extensively studied within the framework of the Onsager–Braun model^{22,23} and its modifications.²⁴ Basically, the separation probability is determined by the competition between the electric field- and temperature-dependent dissociation of a localized electron–hole pair and its recombination to the ground state. While such a treatment has been revealed successful in reproducing experimental photodissociation yields in bulk molecular D/A crystals,²⁵ it has been recognized as unsuitable for conjugated polymer/fullerene blends.²⁶ The reasons for this inadequacy may be summarized as follows. First, the Onsager–Braun model employs the approximation of localized point charge carriers, which does not hold in a polymer/fullerene blend. In this regard, it has been proposed that the hole delocalization along conjugated segments of polymer chains can enhance charge separation^{27–29} because the kinetic energy of hole oscillations along chains lowers the Coulomb barrier between the electron and hole. The combination of the effects due to the hole delocalization and the presence of dark interfacial dipoles^{30,31} has been demonstrated to reproduce the essential features of experimental photocurrent data.³² Furthermore, the combination of the on-chain hole delocalization and the dimensional (entropic) effects has been suggested as the main reason for weakly field-dependent and very efficient charge separation in polymer/fullerene bilayers.³³ Second, for the Onsager–Braun model to reproduce experimental data, the mobility-lifetime product should assume unrealistically high values, meaning that either carrier mobility or pair lifetime should be unrealistically large. Kinetic Monte Carlo (kMC) studies have demonstrated that efficient and weakly field- and temperature-dependent charge separation can be achieved when relevant parameters are carefully chosen on the basis of experimental data.^{34,35} Third, the Onsager–Braun model does not capture the effects of the (energetic and/or spatial) disorder on charge separation. In ref 36, an analytical treatment of charge separation in a one-dimensional disordered chain is presented, and it was suggested that, at least at low interfacial electric fields, the disorder may enhance the separation of geminate electron–hole pairs. Recent kMC results also point toward the beneficial role of not too strong energetic disorder on charge separation.³⁷

Here, we investigate the separation of geminate electron–hole pairs in a one-dimensional lattice model of a bilayer. The model takes into account energetic disorder, carrier delocalization, carrier–carrier interaction, carrier recombination, and the interaction of carriers with the phonon bath and the interfacial electric field. The carrier delocalization is properly taken into account by transferring the description of charge separation from the usually used position space to the space spanned by the exciton basis states, that is, by stationary states of an electron–hole pair on the model interface. The charge separation is then conceived as a sequence of transitions between exciton basis states that are mediated by the interaction with the phonon bath. The separation yield is computed from the stationary solution to the rate equations for basis states populations in two cases, for the separation starting from CT states and donor exciton states. We find that moderate energetic disorder and carrier delocalization promote efficient and relatively weakly field-dependent separation of the strongly bound CT exciton. In this process, the vital role is played by long-lived intermediate CT states, from which further charge separation proceeds practically without obstacles. The separation of the strongly bound donor exciton is also efficient,

but requires quite strong electric fields to occur with certainty. On the other hand, more separated and weakly bound donor excitons separate with efficiency close to 1.

MODEL AND METHODS

Model Hamiltonian, Exciton States, and Their Classification. To describe the bilayer of two organic semiconductors, we employ the standard semiconductor model on a lattice with multiple single-electron and single-hole states per site. The model to be presented is quite general and may also be used (upon appropriate adjustments) to study the electric field-assisted charge generation in other D/A structures. The numerical computations are performed on a one-dimensional system consisting of $2N$ sites located on a lattice of constant a . The sites $0, \dots, N - 1$ represent the donor part, while sites $N, \dots, 2N - 1$ represent the acceptor part of the bilayer. The single-electron levels on lattice site i are counted by index β_i , so that Fermi operators $c_{i\beta_i}^\dagger$ ($c_{i\beta_i}$) create (destroy) an electron on site i and in single-electron state β_i . The single-hole levels on site i are counted by index α_i and Fermi operators $d_{i\alpha_i}^\dagger$ ($d_{i\alpha_i}$) create (annihilate) a hole in single-hole state α_i on site i . The phonon bath is assumed to consist of a multitude of localized phonon modes on each lattice site, and the sets of phonon modes on all sites are identical. The Bose operators $b_{i\lambda}^\dagger$ ($b_{i\lambda}$) create (annihilate) a phonon on site i and in phonon mode λ . The model Hamiltonian assumes the form:

$$H = H_c + H_p + H_{c-p} + H_{c-f} \quad (1)$$

where H_c describes interacting carriers:

$$H_c = \sum_{\substack{i\beta_i \\ j\beta_j}} \epsilon_{(i\beta_i)(j\beta_j)}^c c_{i\beta_i}^\dagger c_{j\beta_j} - \sum_{\substack{i\alpha_i \\ j\alpha_j}} \epsilon_{(i\alpha_i)(j\alpha_j)}^v d_{i\alpha_i}^\dagger d_{j\alpha_j} + \frac{1}{2} \sum_{\substack{i\beta_i \\ j\beta_j}} V_{ij} c_{i\beta_i}^\dagger c_{j\beta_j}^\dagger c_{j\beta_j} c_{i\beta_i} + \frac{1}{2} \sum_{\substack{i\alpha_i \\ j\alpha_j}} V_{ij} d_{i\alpha_i}^\dagger d_{j\alpha_j}^\dagger d_{j\alpha_j} d_{i\alpha_i} - \sum_{\substack{i\beta_i \\ j\alpha_j}} V_{ij} c_{i\beta_i}^\dagger d_{j\alpha_j}^\dagger d_{j\alpha_j} c_{i\beta_i} \quad (2)$$

$$H_p = \sum_{i\lambda} \hbar \omega_\lambda b_{i\lambda}^\dagger b_{i\lambda} \quad (3)$$

describes the phonon bath, H_{c-p} accounts for the interaction of carriers with the phonon bath:

$$H_{c-p} = \sum_{i\beta_i} \sum_{\lambda} g_{i\beta_i\lambda}^c c_{i\beta_i}^\dagger c_{i\beta_i} (b_{i\lambda}^\dagger + b_{i\lambda}) - \sum_{i\alpha_i} \sum_{\lambda} g_{i\alpha_i\lambda}^v d_{i\alpha_i}^\dagger d_{i\alpha_i} (b_{i\lambda}^\dagger + b_{i\lambda}) \quad (4)$$

whereas H_{c-f} represents the interaction of carriers with the interfacial electric field \mathbf{F} , which is assumed to be uniform throughout the system:

$$H_{c-f} = \sum_{i\beta_i} q\mathbf{F} \cdot \mathbf{r}_i c_{i\beta_i}^\dagger c_{i\beta_i} - \sum_{i\alpha_i} q\mathbf{F} \cdot \mathbf{r}_i d_{i\alpha_i}^\dagger d_{i\alpha_i} \quad (5)$$

In eq 2, we take that quantities $\epsilon_{(i\beta_i)(j\beta_j)}^c$ ($\epsilon_{(i\alpha_i)(j\alpha_j)}^v$), which represent electron (hole) on-site energies and transfer integrals, assume nonzero values only for particular combinations of their

indices. In more detail, we assume that $\varepsilon_{(i\beta)(j\beta')}^c \neq 0$ when it represents

- (1) on-site energy $\varepsilon_{i\beta_i}^c$ of single-electron level β_i on site i , for $i = j$ and $\beta_i = \beta'_i$;
- (2) negative electron transfer integral between single-electron levels on nearest-neighboring sites belonging to the same band β_i , $-J_{i\beta_i}^{c,int}$, for i and j both belonging to the same part of the bilayer, $|i - j| = 1$, and $\beta_i = \beta'_j$;
- (3) negative electron transfer integral between single-electron levels on nearest-neighboring sites belonging to different bands, $-J_{i\beta_i}^{c,ext}$, for i and j both belonging to the same part of the bilayer, $|i - j| = 1$, and $\beta_i \neq \beta'_j$; or
- (4) negative electron transfer integral between different parts of the bilayer, $-J_{D,A}^c$, for $i = N - 1$ and $j = N$ or vice versa.

The Coulomb interaction (eq 2) is taken into account in the lowest monopole–monopole approximation, and the interaction potential V_{ij} is assumed to be the Ohno potential:

$$V_{ij} = \frac{U}{\sqrt{1 + \left(\frac{r_{ij}}{r_0}\right)^2}} \quad (6)$$

where U is the on-site Coulomb interaction, r_{ij} is the distance between sites i and j , $r_0 = q^2/(4\pi\varepsilon_0\varepsilon_r U)$ is the characteristic length, and ε_r is the relative dielectric constant. Charge carriers are assumed to be locally and linearly coupled to the phonon bath (Holstein-type interaction), as given in eq 4. In eq 5, $q > 0$ is the elementary charge, \mathbf{r}_i is the position vector of site i , and vector \mathbf{F} is assumed to be perpendicular to the interface and directed opposite the internal electric field of a space-separated electron–hole pair (vide infra). The interfacial electric field may originate from the different Fermi levels of the electrodes,³⁸ or from some other source.³⁹

Similar to other numerical studies, which obtain charge separation efficiency by tracking the faith of a single electron–hole pair, we confine ourselves to the subspace of a single electron–hole pair. We describe charge separation in the exciton basis, whose basis vectors are stationary states of an electron–hole pair supported by the model interface. The most general state of an electron–hole pair can be written as $|x\rangle = \sum_{i\alpha_i} \sum_{j\beta_j} \psi_{(i\alpha_i)(j\beta_j)}^x c_{j\beta_j}^\dagger d_{i\alpha_i}^\dagger |0\rangle$, where $|0\rangle$ is the vacuum of electron–hole pairs. The exciton basis states are obtained by solving the eigenvalue problem $(H_c + H_{c-f})|x\rangle = \hbar\omega_x|x\rangle$, which in the basis of single-particle states localized at lattice sites reads as

$$\sum_{\substack{i'\alpha'_i \\ j\beta'_j}} \left(\delta_{ii'} \delta_{\alpha_i\alpha'_i} \varepsilon_{(j\beta_j)(j'\beta'_j)}^c - \delta_{jj'} \delta_{\beta_j\beta'_j} \varepsilon_{(i\alpha_i)(i'\alpha'_i)}^v - \delta_{ii'} \delta_{\alpha_i\alpha'_i} \delta_{jj'} \delta_{\beta_j\beta'_j} \right) \psi_{(i'\alpha'_i)(j'\beta'_j)}^x \times (V_{ij} - q\mathbf{F} \cdot (\mathbf{r}_j - \mathbf{r}_i)) \psi_{(i\alpha_i)(j\beta_j)}^x = \hbar\omega_x \psi_{(i\alpha_i)(j\beta_j)}^x \quad (7)$$

We take into account the diagonal static disorder; that is, on-site energies $\varepsilon_{i\beta_i}^c$ and $\varepsilon_{i\alpha_i}^v$ depend on site index i . The disorder is the essential element of our model, because disorder-induced localization effects enable us to isolate exciton states that are similar to states of free charges, as will be detailed in the next paragraph.

It is convenient to classify the exciton basis states in a manner similar to that we employed in our previous studies,^{16,17} where we differentiated between

- (1) donor exciton (XD) states, in which both carriers are mainly in the donor part of the bilayer,
- (2) acceptor exciton (XA) states, in which both carriers are mainly in the acceptor part of the bilayer, and
- (3) space-separated exciton states, in which the electron is mainly in the acceptor, while the hole is mainly in the donor part of the bilayer.

Here, we are interested in full charge separation, which results in almost free carriers capable of producing electric current. Therefore, we have to individuate exciton states of our model that resemble these free-carrier states. To this end, we introduce the notion of the contact region of the bilayer, which consists of sites $0, \dots, l_c - 1$ in the donor part and sites $2N - l_c, \dots, 2N - 1$ in the acceptor part of the bilayer. If both electron and hole are primarily located in the contact region (the electron in its acceptor part and the hole in its donor part), we consider them as fully separated carriers. More quantitatively, we say that space-separated exciton state x is a contact state (state of fully separated carriers) if

$$\sum_{i=0}^{l_c-1} \sum_j \sum_{\alpha\beta} |\psi_{(i\alpha)(j\beta)}^x|^2 \geq 0.7 \quad (8)$$

and

$$\sum_i \sum_{j=2N-l_c}^{2N-1} |\psi_{(i\alpha)(j\beta)}^x|^2 \geq 0.7 \quad (9)$$

The space-separated states that are not contact states will be further referred to as CT states. We point out that the localization induced by disorder is crucial to identify contact states. In the perfectly ordered system, there are no space-separated states that meet the criteria of spatial localization given in eqs 8 and 9.

Theoretical Approach to Incoherent Charge Separation. Our aim is to analyze the incoherent charge separation, that is, charge separation that occurs on long time scales so that coherent features are not pronounced and consequently carrier dynamics can be well described in terms of populations only. Here, we work in the basis of electron–hole pair states x and study charge separation by finding a stationary solution to an appropriate equation for populations f_x of exciton states. Similar to ref 36, we assume that contact states act as absorbing states in the course of charge separation; that is, once an exciton reaches a contact state, it is removed from the system. This removal may be interpreted as the extraction of the fully separated electron and hole at the electrodes. Therefore, we find the stationary solution to equations for populations f_x of exciton states x that do not belong to the group of contact states (further denoted as C). These equations are Pauli master equations in which the interaction with the phonon bath leads to transitions between exciton states. The time evolution of the population of exciton state $x \notin C$ is described by

$$\frac{df_x}{dt} = g_x - \tau_x^{-1} f_x - \sum_{x'} w_{x'x} f_{x'} + \sum_{x' \notin C} w_{xx'} f_{x'} \quad (10)$$

where g_x is the generation rate of state x (the number of excitons generated per unit time in state x), τ_x is the lifetime of

exciton state x , $w_{x'x}$ is the rate of phonon bath-induced transition from state x to state x' , while the condition $x' \notin C$ on the summation in the fourth term is due to the assumption of absorbing contact states.

We are searching for the stationary solution f_x^0 to eq 10, which satisfies

$$0 = g_x - \tau_x^{-1} f_x^0 - \sum_{x'} w_{x'} f_{x'}^0 + \sum_{x' \notin C} w_{xx'} f_{x'}^0 \quad (11)$$

With the stationary populations of exciton states at hand, we can compute the separation probability:

$$\varphi = \frac{\sum_{x' \in C} \sum_{x \notin C} w_{x'} f_{x'}^0}{\sum_{x \notin C} g_x} \quad (12)$$

and the recombination probability:

$$\rho = \frac{\sum_{x \notin C} \tau_x^{-1} f_x^0}{\sum_{x \notin C} g_x} \quad (13)$$

Using eq 10, it can be shown that $\varphi + \rho = 1$. Different choices of g_x allow us to investigate incoherent charge separation starting from different initial states.

The phonon bath-assisted transition rates from exciton state x to exciton state x' , $w_{x'x}$ can be obtained using the Fermi golden rule. First, it is convenient to rewrite the carrier–phonon bath interaction H_{c-p} (eq 4) in the relevant subspace of single electron–hole excitations as¹⁶

$$H_{c-p} = \sum_{x'x} \Gamma_{x'x}^{i\lambda} |x'\rangle \langle x| (b_{i\lambda}^\dagger + b_{i\lambda}) \quad (14)$$

where the interaction constants in the exciton basis read as

$$\Gamma_{x'x}^{i\lambda} = \sum_{\beta_i} \sum_{j\alpha_j} g_{i\beta_j\lambda}^c \Psi_{(j\alpha_j)(i\beta_j)}^{x'*} \Psi_{(j\alpha_j)}^x - \sum_{\alpha_i} \sum_{j\beta_j} g_{i\alpha_j\lambda}^v \Psi_{(i\alpha_i)(j\beta_j)}^{x'*} \Psi_{(i\alpha_i)(j\beta_j)}^x \quad (15)$$

Therefore, the phonon bath-assisted transition rate from state x to state x' is

$$w_{x'x} = \frac{2\pi}{\hbar} \sum_{i\lambda} |\Gamma_{x'x}^{i\lambda}|^2 \delta(\hbar\omega_{x'} - \hbar\omega_x - \hbar\omega_\lambda) n_{\text{BE}}(\hbar\omega_\lambda) + \frac{2\pi}{\hbar} \sum_{i\lambda} |\Gamma_{x'x}^{i\lambda}|^2 \delta(\hbar\omega_{x'} - \hbar\omega_x + \hbar\omega_\lambda) (1 + n_{\text{BE}}(\hbar\omega_\lambda)) \quad (16)$$

where $n_{\text{BE}}(E) = (e^{\beta E} - 1)^{-1}$ is the Bose–Einstein occupation number at temperature $T = (k_B\beta)^{-1}$. The right-hand side of eq 16 can be simplified by assuming that all of the interaction constants $g_{i\beta_j\lambda}^c$ and $g_{i\alpha_j\lambda}^v$ are independent of site and band indices and equal to g_λ . Introducing the spectral density $J(E)$ by

$$J(E) = \sum_{\lambda} |g_\lambda|^2 \delta(E - \hbar\omega_\lambda) \quad (17)$$

we obtain

$$w_{x'x} = \frac{2\pi}{\hbar} P_{x'x} J(|\hbar\omega_{x'} - \hbar\omega_x|) n(\hbar\omega_{x'} - \hbar\omega_x) \quad (18)$$

where

$$P_{x'x} = \sum_i \left| \sum_{\beta_i} \sum_{j\alpha_j} \Psi_{(j\alpha_j)(i\beta_j)}^{x'*} \Psi_{(j\alpha_j)(i\beta_j)}^x - \sum_{\alpha_i} \sum_{j\beta_j} \Psi_{(i\alpha_i)(j\beta_j)}^{x'*} \Psi_{(i\alpha_i)(j\beta_j)}^x \right|^2 \quad (19)$$

whereas

$$n(E) = \begin{cases} n_{\text{BE}}(E), & E > 0 \\ 1 + n_{\text{BE}}(-E), & E < 0 \end{cases} \quad (20)$$

The transition rates $w_{x'x}$ do not depend solely on the energy difference $\hbar\omega_{x'} - \hbar\omega_x$ between exciton states x' and x , but also on spatial properties (e.g., spatial localization and mutual overlap) of these states, which is described by quantity $P_{x'x}$ (the so-called spatial proximity factor). The spatial proximity factor between exciton states of the same character is in general much larger than that between states of different characters. In other words, for the same energy difference $\hbar\omega_{x'} - \hbar\omega_x$ the transition probability $w_{x'x}$ (eq 18) is much larger when states x' and x are of the same character than when their characters are different. The last point will be repeatedly used in further discussion.

Parametrization of the Model Hamiltonian. The values of model parameters used in our computations are summarized in Table 1. They are selected so that the values of band gaps,

Table 1. Values of Model Parameters Used in Computations

parameter	value
N	30
l_c	11
a (nm)	1.0
U (eV)	0.65
ϵ_r	3.0
$\epsilon_{D,0}^c$ (eV)	2.63
$J_{D,0}^{\text{int}}$ (eV)	0.1
$\epsilon_{D,0}^v$ (eV)	−0.3
$J_{D,0}^{\text{int}}$ (eV)	−0.15
$\epsilon_{A,0}^c$ (eV)	1.565
$\epsilon_{A,1}^c$ (eV)	1.865
$J_{A,0}^{\text{int}}$ (eV)	0.05
$J_{A,1}^{\text{int}}$ (eV)	0.025
$J_{A,0}^{\text{ext}}$ (eV)	0.02
$\epsilon_{A,0}^v$ (eV)	−1.03
$J_{A,0}^{\text{int}}$ (eV)	−0.15
J_{DA} (eV)	0.1
J_{DA} (eV)	−0.1
σ (meV)	50
η	1.5
E_c (meV)	10
τ_0 (ps)	250
$A_{A/D}$	0.5
T (K)	300

bandwidths, band offsets, and binding energies of the donor, acceptor, and CT exciton that emerge from our model are in agreement with the literature values for typical OPV materials. While the present values are largely chosen to be representative of the P3HT/PCBM interface, we emphasize that our aim is to unveil fundamental physical effects responsible for very efficient charge separation at an all-organic bilayer. Therefore, many of the parameters listed in Table 1 will be varied (within reasonable limits), and the effects of these variations on charge

separation yield will be rationalized. This is also of practical relevance, because the trends observed in such variations may suggest which material properties should be tuned to maximize the separation efficiency.

Actual computations are performed on the model system having one single-electron level per site in the donor and one single-hole level per site in both the donor and the acceptor. To mimic the presence of higher-than-LUMO orbitals energetically close to the LUMO level, which is a situation typical of fullerenes,^{40,41} we take two single-electron levels per acceptor site. The HOMO level of the ordered donor material is taken as the zero of the energy scale. The model is schematically depicted in Figure 1. The choice of the values of model

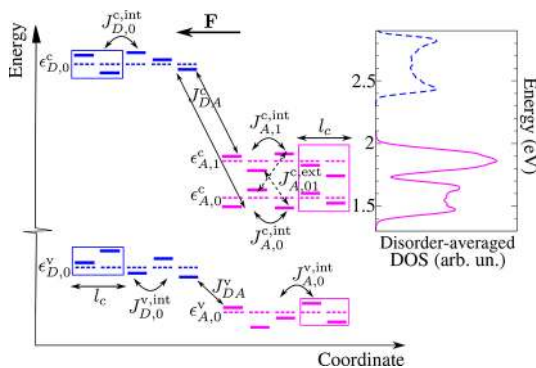


Figure 1. Schematic view of the model system indicating different transfer integrals and average on-site energies listed in Table 1. The dashed lines represent average on-site energies, while the solid lines represent actual on-site energies, which vary from site to site due to the diagonal static disorder. The contact region of the bilayer is denoted by rectangles. \mathbf{F} is the vector of the interfacial electric field. The plot on the right presents the single-particle DOS for electrons in the isolated acceptor (full line) and donor (dashed line) regions of the bilayer averaged over different disorder realizations. For each disorder realization, the electronic states of the isolated regions are obtained by diagonalizing the free-electron Hamiltonian (the first term on the right-hand side of eq 2) in which the D/A coupling J_{DA}^c is set to 0. The DOS for that disorder realization is computed by broadening each of the single-electron states obtained by a Gaussian whose standard deviation is equal to 10 meV.

parameters is almost the same as in our recent investigation of ultrafast dynamics at a D/A heterointerface.¹⁶ Therefore, here, we only briefly summarize the essential features of this parameter set, while the details can be found in our recent article.

Within each region of the bilayer, the on-site energies of electrons and holes are drawn from a Gaussian distribution function. For example, the probability density that the energy of the electron on donor site i ($0 \leq i \leq N - 1$) is in the vicinity of $\epsilon_{i,0}^c$ can be expressed as

$$f(\epsilon_{i,0}^c) = \frac{1}{\sigma\sqrt{2\pi}} \exp\left(-\frac{(\epsilon_{i,0}^c - \epsilon_{D,0}^c)^2}{2\sigma^2}\right) \quad (21)$$

where $\epsilon_{D,0}^c$ is the average electron on-site energy in the donor, and σ is the standard deviation of the Gaussian distribution. We assume that the deviations of on-site energies from their average values are uncorrelated; this assumption regards both on-site energies of electrons (holes) on different sites and on-site energies of electrons and holes on the same site. The disorder strength is determined by parameter σ , which typically

assumes values of the order of 100 meV.⁴² To obtain analytical insights into charge separation efficiency, we opt for a lower value of $\sigma = 50$ meV, which does lead to localization effects, but does not completely destroy charge delocalization. Moreover, the disorder-averaged values of relevant quantities, such as exciton binding energies, LUMO–LUMO, and HOMO–HOMO offsets, assume values that are quite close (within few tens of meV) to the respective values in the ordered system, which will thus often be used in the discussion.

The lattice constant a is comparable to typical distances between neighboring constitutive elements of ordered polymers⁴³ (fullerene aggregates⁴⁴). The number N of lattice sites in the donor and acceptor is then chosen so that the length of the model bilayer is similar to the linear dimensions of the polymer/fullerene bilayers used in experiments.^{26,29,32} Our choice of the value of the hole transfer integral $J_{D,0}^{v,int}$ is motivated by the literature values of the HOMO bandwidth along the π -stacking direction of the regioregular P3HT^{45,46} and the values of the hole transfer integral along the π -stacking direction of the same material.^{47,48} Such a choice tacitly assumes that the hole transport in the donor part of the bilayer takes place among different polymer chains. However, our Hamiltonian is quite general, so that a different selection of the values of its parameters can describe a different physical situation, for example, the hole transport along a polymer chain. The single-particle and optical gap of the ordered donor part of the bilayer are tuned to be around 2.43 and 2.0 eV, respectively,^{49,50} so that the exciton binding energy of the ordered donor material is around 0.43 eV. The electronic parameters of the acceptor (transfer integrals $J_{A,0}^{c,int}$, $J_{A,1}^{c,int}$, and $J_{A,0,1}^{c,ext}$ and the energy difference $\epsilon_{A,1}^c - \epsilon_{A,0}^c$ between average values of electronic on-site energies) are selected so that the single-electron density of states (DOS) of the ordered acceptor part reproduces the most important features of the DOS of fullerene aggregates.^{40,51} The single-particle gap and the binding energy of the ordered acceptor part are tuned to the values of around 2.2 and 0.45 eV.⁴⁹ The values of the LUMO–LUMO (ca. 0.97 eV) and HOMO–HOMO (ca. 0.73 eV) offsets between the donor and acceptor part of the ordered bilayer are chosen by adjusting the energy differences Δ_{XD-CT} and Δ_{XA-CT} between the lowest excited state of the heterojunction (the lowest CT state) and the lowest exciton states in the donor and acceptor to the typical literature values.^{49,52,53} The magnitudes of the transfer integrals J_{DA}^c and J_{DA}^v between the two materials are taken to be similar to the values obtained in ref 54.

For the spectral density of the phonon bath, we take the Ohmic spectral density:⁵⁵

$$J(E) = \eta E e^{-E/E_c} \quad (22)$$

which is characterized by two parameters: the dimensionless parameter η describes the strength of the system–bath coupling, while E_c is the energy cutoff determining the energy range of phonon modes that are strongly coupled to the system. For the Holstein-like system–bath coupling and in the limiting case of a charge carrier localized on a single lattice site, the polaron binding energy is given by $E_{pol} = \sum_{\lambda} |g_{\lambda}|^2 / (\hbar\omega_{\lambda})$.⁵⁶ In terms of spectral density $J(E)$, and specifically for the Ohmic spectral density, the polaron binding energy can be expressed as

$$E_{pol} = \int_0^{+\infty} dE \frac{J(E)}{E} = \eta E_c \quad (23)$$

It is equal to the geometry relaxation energy Λ_{rel} upon charging a molecule and to one-half of the reorganization energy Λ_{reorg} .⁵⁶ In ref 40, the relaxation energy of the PC₆₀BM anion was estimated to be $\Lambda_{\text{rel}} = 15$ meV. The authors of ref 57 found that the polaron binding energy in a long straight polythiophene chain is of the order of 10 meV. We use these estimates and take the polaron binding energy $E_{\text{pol}} = 15$ meV (the reorganization energy is then $\Lambda_{\text{reorg}} = 30$ meV). We assume that the system–bath coupling is strongest for the low-frequency phonon modes and therefore take that $E_c = 10$ meV and $\eta = 1.5$. All of these assumptions will be reassessed in the Discussion.

There are different kinds of recombination processes that limit the efficiency of organic solar cells.⁵⁸ The recombination of an electron–hole pair that originates from the absorption of a single photon is geminate recombination. On the other hand, an electron and a hole undergoing a nongeminate recombination event do not originate from the same photon. Here, we consider only geminate recombination, which at a D/A interface may occur as (a) the recombination of excitons photogenerated in a neat donor or acceptor material, or (b) the recombination of excitons in CT states. The recombination can be further classified as radiative or nonradiative. In neat polymers, recombination predominantly occurs via nonradiative processes.⁵⁹ In D/A blends, the major part of charges recombine nonradiatively either at the interface or in the donor material.⁶⁰ However, there is no simple model that describes the rate of nonradiative recombination in terms of microscopic material properties. It is intuitively clear that the smaller is the overlap between the electron and hole probability densities, the smaller is the rate of their recombination and the larger is the lifetime of the pair. In previous model studies of charge separation at D/A interfaces, the last point has been recognized as the steep dependence of the exciton lifetime on the electron–hole separation,⁶¹ so that the recombination is assumed to occur exclusively from the strongly bound CT state,^{32,36,61} or a formula describing the aforementioned distance dependence is proposed.³³ Here, to each exciton state x , be it a state in the neat material or a CT state, we assign the lifetime τ_x that is inversely proportional to the weighted overlap of the electron and hole wave function moduli:

$$\tau_x = \tau_0 \left(\sum_{i=0}^{N-1} |\phi_i^{x,e}| |\phi_i^{x,h}| + A_{A/D} \sum_{i=N}^{2N-1} |\phi_i^{x,e}| |\phi_i^{x,h}| \right)^{-1} \quad (24)$$

In the last expression, the moduli of the wave function of the electron and hole in exciton state x are defined as

$$|\phi_i^{x,e}| = \sqrt{\sum_{\beta_i} \sum_{j\alpha_j} |\psi_{(j\alpha_j)(i\beta_i)}^x|^2} \quad (25)$$

$$|\phi_i^{x,h}| = \sqrt{\sum_{\alpha_i} \sum_{j\beta_j} |\psi_{(i\alpha_i)(j\beta_j)}^x|^2} \quad (26)$$

while τ_0 and $A_{A/D}$ are constants that are determined so that the lifetimes of the lowest CT, XD, and XA states in the ordered system agree with the values reported in the literature. The expression for the lifetime given in eq 24 captures the previously described trend. Singlet exciton lifetimes in a variety of conjugated polymers used in organic solar cells are of the order of hundreds of picoseconds.⁵⁹ Time-resolved photoluminescence measurements yield the singlet exciton lifetime in neat P3HT around 470 ps and in neat PCBM around 740 ps.⁶²

From the transient absorption measurements performed in blends of P3HT and different fullerenes, the lifetime of the CT state was determined to be around 3 ns.⁶³ For the values of model parameters listed in Table 1, the lifetime of the lowest CT state in the ordered system is $\tau_{\text{CT}}^{\text{ord}} \approx 2.5$ ns, the lifetime of the lowest XD state in the ordered system is $\tau_{\text{XD}}^{\text{ord}} \approx 400$ ps, and the lifetime of the lowest XA state in the ordered system is $\tau_{\text{XA}}^{\text{ord}} \approx 800$ ps.

NUMERICAL RESULTS

In this section, we present the results concerning the yield of charge separation starting from CT and donor states. In all of the computations, we average over different disorder realizations, and all of the results to be presented are averaged over 256 disorder realizations. To facilitate the discussion, in Figure 2a–e we present disorder-averaged DOS for different

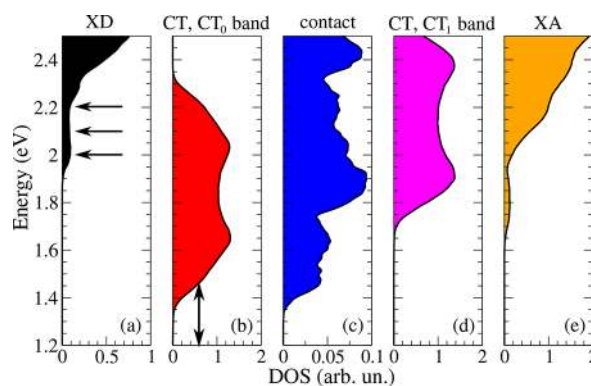


Figure 2. Disorder-averaged exciton DOS (in arbitrary units and at $F = 0$) for (a) donor exciton states, (b) CT states belonging to CT₀ band, (c) contact states, (d) CT states belonging to CT₁ band, and (e) acceptor exciton states. The horizontal arrows in (a) indicate approximate energies of XD states serving as initial states of charge separation. The vertical double-sided arrow in (b) indicates the energy range of the CT states acting as initial states of charge separation. The DOS in a single disorder realization is obtained by broadening each exciton level by a Gaussian whose standard deviation is equal to 10 meV.

groups of exciton states. Similar to our recent study, we discriminate between CT states belonging to CT₀ and CT₁ bands.¹⁶ We say that a CT state belongs to the CT₀ (CT₁) band if its electron primarily belongs to the electronic band in the acceptor part of the bilayer arising from the single-electron level of average energy $\epsilon_{A,0}^c$ ($\epsilon_{A,1}^c$).

Charge Separation from the Strongly Bound CT State.

As starting states for the charge separation process, here we consider CT states belonging to the CT₀ band. One particular CT state out of all of the states in the CT₀ band is chosen by requiring that the mean electron–hole separation, which for exciton state x reads as

$$\langle r_{e-h} \rangle_x = \sum_{i\alpha_i} \sum_{j\beta_j} |i - j| |\psi_{(i\alpha_i)(j\beta_j)}^x|^2 \quad (27)$$

be minimal. We will further refer to such a state as the strongly bound CT state. The strongly bound CT state is located on the lower edge of the disorder-averaged DOS of CT excitons belonging to the CT₀ band; see the vertical double-sided arrow in Figure 2b. We set the generation rate g_x appearing in eq 10 to be different from zero only for the strongly bound CT state.

The field-dependent separation yield from this state is presented by circles in Figure 3a. The separation yield is above

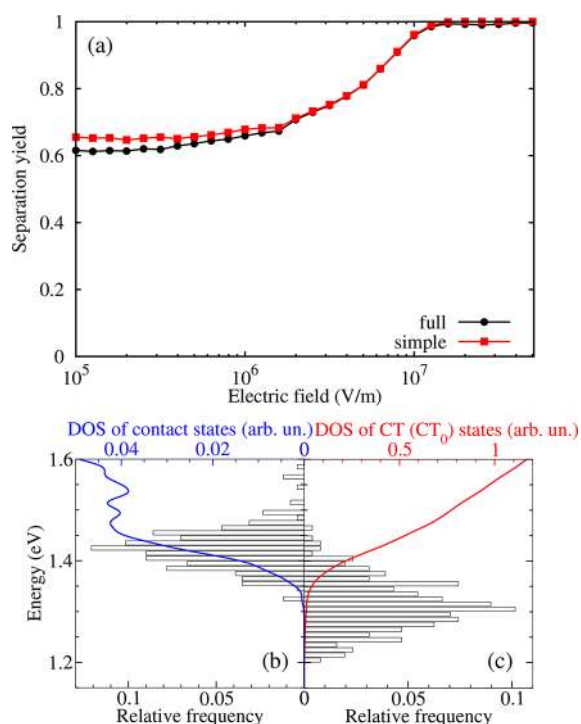


Figure 3. (a) Field-dependent yield of charge separation from the strongly bound CT state. The data labeled by “full” are obtained by numerically solving eq 10, while the data labeled by “simple” are computed using eq 34. The low-energy edges of the disorder-averaged DOS (full lines) for (b) contact states and (c) CT states belonging to the CT_0 band. The bars depict histograms of the distribution of the energy of (b) the lowest-energy contact state and (c) the initial strongly bound CT state. The width of the bins on the energy axis is 10 meV, while $F = 0$.

0.6 for all of the examined values of the electric field down to $F = 0$. Figure 3b presents the low-energy tail of the DOS of contact states (see Figure 2c) along with the distribution of energies of the lowest-energy contact state. Figure 3c shows the low-energy tail of the DOS of CT states (see Figure 2b) together with the distribution of energies of the initial strongly bound CT state. The disorder-averaged energy difference between the lowest-energy contact state and the initial CT state may serve as an estimate of the average energy barrier that an electron–hole pair in the initial CT state has to surmount to reach the nearest free-charge state. We obtain the average barrier of approximately 0.13 eV ($\sim 5 k_B T$ at room temperature), which is lower (at least by a factor of 2) than usually assumed when considering separation of the strongly bound CT exciton.⁶⁴ Further discussion reveals that the actual barrier to be overcome is smaller than the energy difference between the lowest-energy contact state and the initial CT state. The intermediate CT states, lying between the initial CT state and the lowest-energy contact state and exhibiting larger electron–hole distances as compared to the initial CT state, are crucial to the successful separation of the initial strongly bound pairs. Stronger electric field is beneficial to exciton separation, which, combined with the fact that the separation yield is above 0.5 even at $F = 0$, implies that it exhibits relatively weak dependence on the magnitude of the electric field.

It is instructive to analyze the results presented in Figure 3a from the viewpoint of single disorder realizations. In Figure 4a–d we present distributions of the separation yield in single

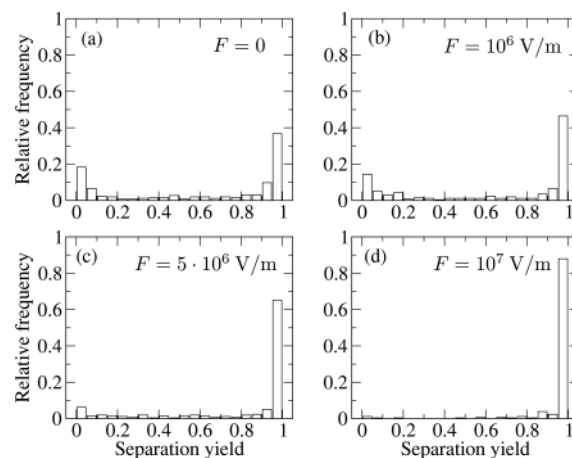


Figure 4. Histograms showing the distribution of the yield of charge separation from the strongly bound CT state for different strengths of the electric field: (a) $F = 0$, (b) $F = 10^6$ V/m, (c) $F = 5 \times 10^6$ V/m, and (d) $F = 10^7$ V/m. The width of the bins for the separation yield is 0.05.

disorder realizations at different strengths of the electric field. A distinctive feature of all of the histograms is a quite small number of disorder realizations for which the separation yield assumes values in an intermediate range (say between 0.2 and 0.8). Even at zero electric field, the number of disorder realizations in which the separation yield is high (above 0.8) is greater than the number of those in which the separation yield is low (below 0.2), which can account for the mean separation yield above 0.5 even at zero field. As the electric field is increased, the number of disorder realizations in which the separation yield is low or intermediate decreases, while the number of disorder realizations in which the separation yield is high increases; see Figure 4b–d. At $F = 10^7$ V/m, the separation yield is between 0.95 and 1 for somewhat less than 90% of disorder realizations, see Figure 4d, meaning that the mean yield is close to 1. Relevant to this discussion are also the relative positions of the lower-energy tails of the DOS of CT states belonging to the CT_0 band and the DOS of contact states, which are presented in Figure S1a–d. We observe that the effect of increasing F on the DOS tails consists of decreasing the energy difference between the edges of CT and contact DOS. For sufficiently strong field, the lowest contact state is situated energetically below the strongly bound CT state.

We now establish which factors primarily determine the separation yield and propose an analytical formula that is capable of reproducing the separation yield in single disorder realizations (and consequently the mean separation yield) quite well. Let us begin by noticing that the initial CT state is usually strongly coupled (by means of phonon bath-assisted transitions) to only a couple of exciton states, which are of CT character and whose electron–hole separation (and consequently the lifetime) is larger than in the initial CT state. We further refer to these states as intermediate states. Moreover, intermediate states are in general very well coupled to other space-separated states, meaning that, in principle, there is no kinetic obstacle for an exciton in the intermediate state to

undergo a series of phonon bath-assisted transitions in which the electron–hole separation gradually increases, and finally reach a contact state. However, because the coupling among the initial state and intermediate states is appreciable, the “implosion” of the pair, that is, the back-transfer from intermediate states to the initial CT state followed by the recombination event, should not be omitted from the analysis. The recombination from intermediate states, as well as from all of the subsequent states paving the way toward contact states, is not probable, because the lifetimes of all of these states are quite long as compared to the inverse transition rates among them. In other words, the recombination occurs almost exclusively from the initial CT state. We may therefore assume that the only rate-limiting step during charge separation is the escape from the initial strongly bound CT state x_{init} . The separation yield is then determined by the competition between the recombination rate in the initial CT state, the escape rate from the initial CT state toward intermediate states, and the back-transfer rate from intermediate states to the initial CT state. This competition may be described using a simple kinetic model whose variables are populations of the initial CT state and intermediate states (which are considered as a single state). Recombination is possible only from the initial CT state, while contact states may be reached from intermediate states. The stationarity of the initial CT state population f_{init}^0 demands that

$$g_{\text{init}} = (\tau_{\text{init}}^{-1} + w_{\text{inter,init}})f_{\text{init}}^0 - w_{\text{init,inter}}f_{\text{inter}}^0 \quad (28)$$

while a similar condition for the stationary population f_{inter}^0 of intermediate states reads as

$$(w_{\text{init,inter}} + w_{\text{contact,inter}})f_{\text{inter}}^0 = w_{\text{inter,init}}f_{\text{init}}^0 \quad (29)$$

In eqs 28 and 29, g_{init} is the generation rate of the initial CT state, τ_{init} is its lifetime, $w_{\text{inter,init}}$ is the total escape rate from the initial CT state x_{init} toward intermediate states x_{inter} :

$$w_{\text{inter,init}} = \sum_{x_{\text{inter}}} w_{x_{\text{inter}},x_{\text{init}}} \quad (30)$$

and $w_{\text{init,inter}}$ is the total back-transfer rate to the initial CT state from intermediate states:

$$w_{\text{init,inter}} = \sum_{x_{\text{inter}}} w_{x_{\text{init}},x_{\text{inter}}} \quad (31)$$

The total escape rate from all of the intermediate states toward contact states is

$$w_{\text{contact,inter}} = \sum_{x_{\text{inter}}} \sum_{x_{\text{f}}} w_{x_{\text{f}},x_{\text{inter}}} \quad (32)$$

where, for each intermediate state x_{inter} , the summation over final states x_{f} is carried out only over the states from which further transitions toward contact states are possible (it should not include the transitions back to the initial CT state). An adaptation of eq 12 to the problem at hand gives the following expression for the separation yield:

$$\varphi = \frac{w_{\text{contact,inter}}f_{\text{inter}}^0}{g_{\text{init}}} \quad (33)$$

Combining eqs 28, 29, and 33, we obtain the following expression for the separation yield:

$$\varphi = \frac{1}{1 + (\tau_{\text{init}}w_{\text{inter,init}})^{-1} \left(1 + \frac{w_{\text{init,inter}}}{w_{\text{contact,inter}}}\right)} \quad (34)$$

We point out that all four quantities (τ_{init} , $w_{\text{inter,init}}$, $w_{\text{init,inter}}$, and $w_{\text{contact,inter}}$) entering eq 34 are characteristic of each disorder realization; that is, eq 34 contains no free parameters. It is then remarkable that it reproduces quite well the field-dependent separation yield for each disorder realization, and consequently the disorder-averaged separation yield, which is presented by squares in Figure 3a.

The preceding discussion suggests that the barrier the initial CT exciton has to surmount to reach a contact state is determined by the energy difference $\hbar\omega_{\text{inter}} - \hbar\omega_{\text{init}}$ between the initial CT state and the intermediate CT state exhibiting strongest coupling to the initial state. In Figure 5a,b we present

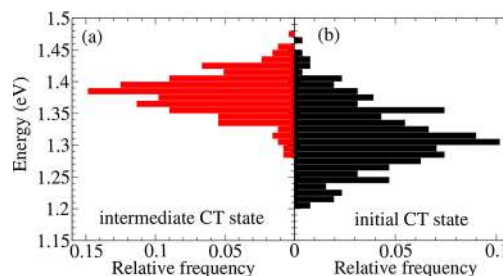


Figure 5. Histograms showing distributions of energies of (a) the intermediate CT state (which is most strongly coupled to the initial CT state) and (b) the initial CT state. The histograms are computed for $F = 0$.

distributions of energies of the intermediate (Figure 5a) and the initial (Figure 5b) CT state at $F = 0$. We estimate that the average energy difference $\langle \hbar\omega_{\text{inter}} - \hbar\omega_{\text{init}} \rangle$ is around 0.07 eV, which is smaller than the average energy difference between the lowest contact state and the initial CT state. Therefore, already at $F = 0$, the average energy barrier opposing the separation from the initial CT state is $\sim 3 k_{\text{B}}T$ at room temperature. For stronger F , the height of the barrier decreases, and the barrier is almost eliminated at $F \gtrsim 10^7$ V/m, as is presented in more detail in Figure S2a–d.

Equation 34 gives the separation yield that is always an upper bound to the true separation yield obtained by numerically solving rate equations embodied in eq 10. Deriving eq 34, we assume that there is only one rate-limiting step in the process of charge separation from the initial CT state (the escape from the initial CT state to intermediate states), while further transitions from intermediate states toward contact states occur with certainty. However, in reality, some of these further transitions may present another obstacle to full charge separation, and, to fully reproduce the numerical data, eq 34 should be corrected so as to take other rate-limiting steps into account (it turns out that such corrections are really important only for strong enough disorder, vide infra). We can elaborate more on the last point by noticing that eq 34 is actually a version of the Rubel’s formula³⁶ that describes the separation of an exciton initially in state 1 through a series of incoherent hops $1 \rightleftharpoons 2 \rightleftharpoons \dots \rightleftharpoons n \rightarrow n + 1$ among localized states, which terminates when free-charge state $n + 1$ is reached:

$$\varphi_{\text{Rubel}} = \frac{1}{1 + (\tau_1 w_{21})^{-1} \left(1 + \sum_{i=2}^n \prod_{j=2}^i \frac{w_{j-1,j}}{w_{j+1,j}} \right)} \quad (35)$$

One of the main assumptions behind the Rubel's formula is that the recombination event is possible only from the initial CT state 1, its rate being τ_1^{-1} . This assumption is satisfied in our computations, as we obtain that the major part of recombination events occurs from the initial CT state, so that we may identify τ_{init} in eq 34 with τ_1 in eq 35. The first rate-limiting step is the escape from the initial CT state to more separated (and thus longer-lived) intermediate states, which justifies the identification of $w_{i,\text{inter,init}}$ in eq 34 with w_{21} in eq 35. Further rate-limiting steps are taken into account in eq 35 by the term $\sum_{i=2}^n \prod_{j=2}^i \frac{w_{j-1,j}}{w_{j+1,j}}$, which takes care of the fact that, at each step j that has to be completed to reach state i , there is a competition between the escape rate $w_{j+1,j}$ toward the free-charge state $n+1$ and the back-transfer rate $w_{j-1,j}$ toward the initial state 1. Rubel et al. have assumed that the pathway from the initial to the final state is such that hops are possible only between neighboring states in the sequence $1 \rightleftharpoons 2 \rightleftharpoons \dots \rightleftharpoons n \rightarrow n+1$, while in our model hops are in principle possible among any two exciton states. Thus, in our model it is difficult to isolate particular separation paths and ensure that they do not interfere among themselves. Nevertheless, as evidenced by quite good agreement between the results presented in Figure 3a, taking into account only the first rate-limiting step is a reasonable approximation to the full numerical data. This approximation is, however, plausible only for not too strong disorder. For stronger disorder, disorder-induced localization effects become more pronounced, and, on its way toward contact states, an exciton may reach a state exhibiting strong localization. Because of its strong localization, this state is poorly coupled to other states, meaning that it may act as another recombination center, or it may "reflect" excitons toward the initial state; that is, it acts as a trap state for charge separation. Neither of these two possibilities is captured by eq 34; therefore, it cannot accurately reproduce the separation yield for stronger disorder, as we discuss in the next paragraph.

We continue our discussion on the effects of disorder by investigating the separation yield for different disorder strengths σ at zero electric field. Along with the data emerging from numerically solving eq 10, in Figure 6 we present the data obtained by means of eq 34. We observe that the dependence of φ on σ is not monotonic. For very low values of σ (typically $\sigma < 20$ meV in our one-dimensional model), contact states are generally absent from the spectrum (the disorder is so weak that disorder-induced localization effects are not pronounced), and consequently the separation yield within our model is exactly equal to zero in the majority of disorder realizations. This is different from predictions of other models describing incoherent charge separation,^{36,37} according to which the separation yield is different from zero for all of the values of disorder strength down to $\sigma = 0$. Therefore, the predictions of our model are not reliable for too low disorder. Bearing in mind that typical disorder strength in organic semiconductors is considered to be of the order of 100 meV,⁴² the aforementioned feature of our model does not compromise its relevance. For stronger disorder (typically $\sigma > 20$ meV), contact states start to appear in the spectrum, and their number grows with increasing σ . At the same time, the average energy difference $\langle \hbar\omega_{\text{inter}} - \hbar\omega_{\text{init}} \rangle$ between the intermediate state and

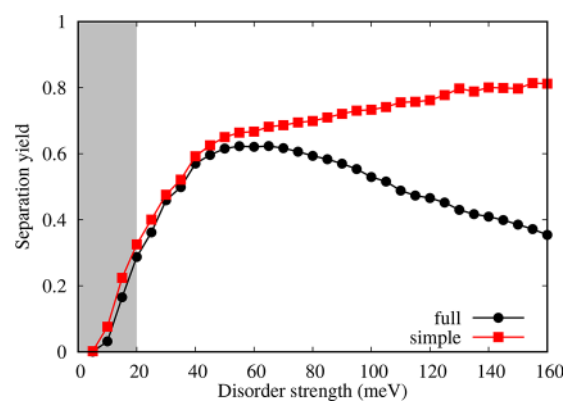


Figure 6. Yield of charge separation from the strongly bound CT state at $F = 0$ for different strengths σ of the diagonal static disorder. The gray area indicates the range of disorder strength in which the predictions of our model are not reliable. The data labeled by "full" are obtained by numerically solving rate equations (eq 10), while the data labeled by "simple" are computed using eq 34.

the initial CT state decreases (see Figure S3), and the escape rate $w_{i,\text{inter,init}}$ from the initial CT state to intermediate states increases (see eq 18). Because the disorder is still not too strong, further separation from intermediate states is much more probable than the "implosion" of the pair, meaning that typically $w_{\text{init,inter}}/w_{\text{contact,inter}} \ll 1$. The last statement, combined with the fact that τ_{init} essentially does not depend on σ , gives that the separation yield determined by eq 34 increases with increasing σ . However, there exists an optimal disorder strength σ_{opt} for which the separation yield attains a maximum value, so that for $\sigma > \sigma_{\text{opt}}$ an increase in the disorder strength leads to a decreased separation yield. In our numerical computations, σ_{opt} is around 60 meV, in good agreement with the results of ref 37, which also point toward the existence of the optimal disorder strength. Although for strong disorder the number of contact states is large, the pronounced disorder-induced localization starts to impede phonon-assisted transitions among exciton states. The number of trap states for charge separation (cf., previous paragraph) increases, meaning that there is more than just a single rate-limiting step during the separation of the initial electron-hole pair. This leads to an increased probability of the "implosion" of the pair into the initial CT state or the pair recombination directly from trap states. Therefore, the separation yield is decreased. As can be inferred from Figure 6, the yield computed using eq 34 (circles) is again an upper bound to the separation yield obtained by numerically solving rate equations (eq 10, squares) and approximates it quite well only for $\sigma \lesssim \sigma_{\text{opt}}$ while for $\sigma > \sigma_{\text{opt}}$ the two separation yields exhibit opposite trends with increasing disorder strength. While the true separation yield decreases for $\sigma > \sigma_{\text{opt}}$, the yield given by eq 34 monotonically increases in the entire examined range of disorder strength, consistent with the fact that $\langle \hbar\omega_{\text{inter}} - \hbar\omega_{\text{init}} \rangle$ monotonically decreases with increasing σ . Equation 34 does not capture further rate-limiting steps in the course of charge separation, and the highly successful escape from the initial CT state to intermediate states does not guarantee full charge separation.

The apparent simplicity of our model enables us to systematically study the effects of variations of different model parameters on the efficiency of charge separation starting from the strongly bound CT state. Let us first examine how the variations in the electron delocalization in the acceptor

(mimicked by variations in the transfer integral $J_{A,0}^{\text{int}}$) and in the hole delocalization in the donor (mimicked by variations in the transfer integral $J_{D,0}^{\text{int}}$) affect the separation yield. We obtain that better delocalization of carriers promotes higher separation yields; see Figure 7a,b. This can be rationalized using eq 34,

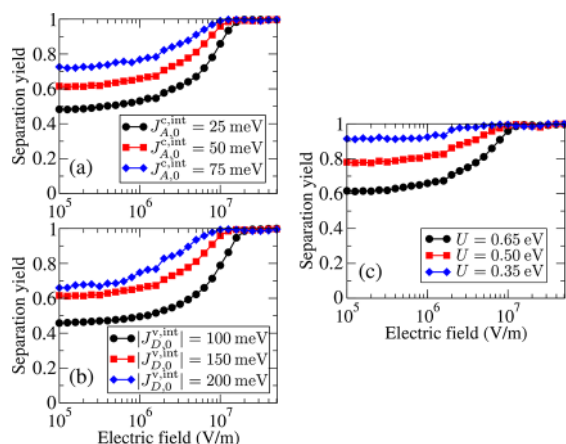


Figure 7. Field-dependent separation yield from the strongly bound CT state for different values of (a) the electron transfer integral $J_{A,0}^{\text{int}}$ in the acceptor, (b) the hole transfer integral $J_{D,0}^{\text{int}}$ in the donor, and (c) the on-site Coulomb interaction U .

which determines the separation yield as a function of only a couple of parameters, and following the variation of these parameters with varying carrier delocalization. When the separation yield is high (greater than 0.8 already at zero field and for the lowest investigated values of $J_{A,0}^{\text{int}}$ and $J_{D,0}^{\text{int}}$, cf., the discussion of Figure 4a–d), reasonable variations in $J_{A,0}^{\text{int}}$ and $J_{D,0}^{\text{int}}$ do not dramatically influence the separation yield, which remains high. When the separation yield is low or intermediate (less than 0.8 at zero field and for the lowest investigated values of $J_{A,0}^{\text{int}}$ and $J_{D,0}^{\text{int}}$), it exhibits a pronounced increase with increasing transfer integrals $J_{A,0}^{\text{int}}$ and $J_{D,0}^{\text{int}}$. Better carrier delocalization leads to an increase in the escape rate $w_{\text{inter,init}}$ from the initial CT state, which, along with the fact that τ_{init} remains largely unaffected by variations in $J_{A,0}^{\text{int}}$ and $J_{D,0}^{\text{int}}$, means that the separation yield determined by eq 34 is higher.

Next, we comment on the variations that the separation yield undergoes when the magnitude of the on-site Coulomb interaction U is changed. In Figure 7c we observe that weaker electron–hole interaction leads to more efficient charge separation from the strongly bound CT state. Again, this beneficial effect of weaker Coulomb interaction may be attributed to the product $\tau_{\text{init}}w_{\text{inter,init}}$ being (on average) larger for weaker Coulomb interaction. On a more intuitive level, the trends in the separation yield presented in Figure 7a–c may be rationalized by following the changes in the disorder-averaged energy difference $\langle \hbar\omega_{\text{inter}} - \hbar\omega_{\text{init}} \rangle$ with changing the degree of carrier delocalization and the strength of the electron–hole interaction. In Figure S4a1–c3, we compare values of $\langle \hbar\omega_{\text{inter}} - \hbar\omega_{\text{init}} \rangle$, as well as the energy distributions of the initial and intermediate CT state, for different $J_{A,0}^{\text{int}}$, $J_{D,0}^{\text{int}}$, and U . We conclude that better carrier delocalization and weaker electron–hole interaction favor lower values of $\langle \hbar\omega_{\text{inter}} - \hbar\omega_{\text{init}} \rangle$, or, in other words, lower the separation barrier from the CT state. Let us also note that each of the effects studied can on its own improve the separation from the strongly bound CT state, because its binding energy strongly depends both on the

degree of carrier delocalization and on the Coulomb interaction; compare to the discussion of the results (Figure 11a–c) concerning charge separation from the closely separated donor exciton state.

We have also studied the temperature dependence of the process of charge separation from the strongly bound CT state. We observe an approximately 6-fold decrease in the separation yield when the temperature is decreased from 300 to 100 K; see Figure 8a. On temperature reduction from 300 to below 50 K,

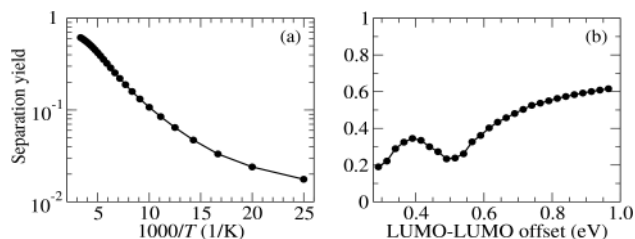


Figure 8. Yield of charge separation from the strongly bound CT state at zero electric field as a function of (a) the temperature (in Arrhenius representation) and (b) the LUMO–LUMO offset. The reported values of the LUMO–LUMO offset refer to the ordered system.

the separation yield reduces for more than an order of magnitude. These observations are in agreement with other numerical studies of charge separation from the strongly bound CT state,³⁴ and with experimentally obtained temperature dependence of the photocurrent under an excitation at the low-energy edge of the CT manifold.⁶⁵

The effect of the variations in the LUMO–LUMO offset on the separation yield was studied by changing average on-site energies $\varepsilon_{A,0}^c$, $\varepsilon_{A,1}^c$, and $\varepsilon_{A,0}^v$ in the acceptor part of the bilayer (see Figure 1) by the same amount, keeping all of the other model parameters listed in Table 1 unchanged. In first approximation, these variations manifest themselves in Figure 2a–e as rigid translations of the DOS of space-separated exciton states (Figure 2b–d) with respect to the DOS of donor and acceptor exciton states (Figure 2a,e). Figure 8b presents the dependence of the separation yield at zero electric field on the LUMO–LUMO offset. For the LUMO–LUMO offset greater than approximately 0.5 eV, we observe that the separation yield monotonically decreases with decreasing the LUMO–LUMO offset; see Figure 8b. A decrease in the LUMO–LUMO offset leads to a decreased energy difference between the lowest acceptor (and also donor) state and the initial CT state; see also Figure 2a–e. We may thus expect that a sufficient decrease in the LUMO–LUMO offset results in the involvement of acceptor and donor states in the separation from the strongly bound CT state. The transitions from the space-separated manifold toward the acceptor (donor) manifold are in general much less probable than those inside the space-separated manifold. However, once an exciton enters the acceptor (donor) manifold, it can easily recombine, because the typical lifetime of acceptor (donor) states is shorter than the lifetime of the initial CT state. In other words, the fact that acceptor (donor) states participate in the separation of the strongly bound CT exciton is seen as a decrease in the separation yield, which is due to the enhanced recombination from acceptor (donor) states. This is shown in more detail in Figure S5a,b, which provide data on recombination from different groups of exciton states. While the recombination from acceptor states can partially account for the decrease in

the separation yield observed for LUMO–LUMO offsets below 0.65 eV, the recombination from donor states is reflected in the decrease seen for LUMO–LUMO offsets below 0.4 eV. We can estimate these numbers using Figure 2a–e and having in mind that the LUMO–LUMO offset for that arrangement of exciton energies is ca. 0.97 eV. A rigid translation of Figure 2b–d by approximately 0.3 eV (upward in energy) makes the initial CT state energetically close to the acceptor states in the low-energy tail of the acceptor DOS, meaning that they can participate in the separation of the initial CT state. Similarly, a rigid translation of Figure 2b–d by approximately 0.55 eV makes the initial CT state energetically close to the donor states in the low-energy tail of the donor DOS. However, to understand the behavior of the separation yield in the whole range of LUMO–LUMO offsets displayed in Figure 8b, we have to remember that lower LUMO–LUMO offset promotes better coupling between the two parts of the bilayer, which is mediated by the D/A couplings J_{DA}^E and J_{DA}^D . As a consequence, reducing the LUMO–LUMO offset enhances the electron–hole overlap in CT states, thus decreasing their lifetime and increasing the recombination from CT states, which is shown in Figures S6 and S5b. Therefore, enhanced recombination from CT states can explain the decrease in the separation yield observed for LUMO–LUMO offsets above approximately 0.65 eV.

Charge Separation from a Donor Exciton State. Here, we aim at understanding which factors control charge separation starting from a donor exciton state. In numerical computations, the generation rate g_x appearing in eq 10 is set to a nonzero value only for donor states. We have noted in our previous publications that the low-energy (closely separated and strongly bound) donor states are essentially isolated from the manifold of space-separated states and thus act as trap states for the separation of the initial donor excitons on subpicosecond time scales.^{16,17} On the contrary, higher-energy (more separated and loosely bound) donor states exhibit appreciable coupling to the space-separated manifold, and we may thus expect that charge separation starting from these states should be more probable than that starting from closely separated donor states.

We perform computations of the yield of the separation of donor excitons of different energies. We focus on the energy windows centered around $E_{\text{init}} = 2.0$ eV (the optical gap of the ordered donor material), $E_{\text{init}} = 2.1$ eV, and $E_{\text{init}} = 2.2$ eV (significantly above the optical gap of the ordered donor material), which is indicated by horizontal arrows in Figure 2a. Because the precise energies of donor states are determined by the disorder, we choose the initial donor state among the states that lie in the 50 meV-wide energy windows centered around the aforementioned energies. One particular donor state out of the chosen states is selected by the requirement that the squared modulus of the dipole moment for the direct generation of donor exciton state x , which is proportional to $\left| \sum_{i \in D; \alpha, \beta} \psi_{(i\alpha)(i\beta)}^x \right|^2$,¹⁶ be maximum. In other words, among donor states in a given energy window, we select the state whose direct generation from the ground state is most probable. Such a choice of the initial donor state is motivated by our recent computations in which we have observed that quite a high fraction of photogenerated excitons remain in the initially photoexcited donor state on a picosecond time scale following the excitation.¹⁶

In Figure 9, we compare the yields of charge separation starting from donor states of different energies. As we have

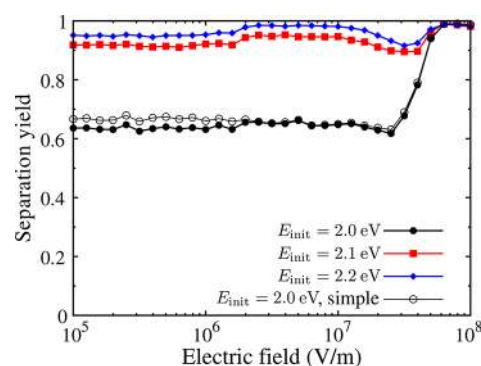


Figure 9. Field-dependent yield of charge separation starting from donor exciton states of different energies. The data represented by filled symbols are obtained by solving the full set of rate equations (eq 10). The data represented by empty circles are obtained by solving the reduced set of rate equations (eq 36) in case $E_{\text{init}} = 2.0$ eV.

expected, charge separation starting from a higher-energy donor state is more efficient than that starting from a closely separated donor state. The yield of the separation from a donor state situated around $E_{\text{init}} = 2.2$ eV is practically field-independent and greater than 0.9 for all of the examined values of the electric field down to $F = 0$. The yield is somewhat higher for $E_{\text{init}} = 2.2$ eV than for $E_{\text{init}} = 2.1$ eV. On the other hand, the yield of the separation from a closely separated donor state ($E_{\text{init}} = 2.0$ eV) is lower: it is almost constant for electric fields $F \lesssim 5 \times 10^7$ V/m, its value being around 0.6, after which it rises and reaches values close to 1 at $F \sim 10^8$ V/m. The value of the electric field at which the separation from a closely separated donor state occurs with certainty is almost an order of magnitude larger than in the case of charge separation from the strongly bound CT state, see Figure 3a, which is consistent with the fact that the binding energy of the donor exciton is larger than the binding energy of the CT exciton.

Let us now analyze in more detail the separation of the closely separated donor exciton ($E_{\text{init}} = 2.0$ eV). Our data suggest that the major part of recombination events occur from donor exciton states. This is consistent with the fact that phonon bath-assisted transitions starting from the closely separated donor exciton state couple it most strongly to other donor states, while coupling to the space-separated manifold is in principle much weaker (we note that its coupling to an acceptor state is practically negligible). The states of the space-separated manifold to which the closely separated donor state can couple are typically well spatially separated, long-lived, and exhibit good coupling to other space-separated states. In other words, despite the weak coupling, once an exciton in the closely separated donor state performs a transition to the space-separated manifold, it is highly probable that it will eventually reach a fully separated state. Instead of finding the stationary solution to the full set of rate equations (eq 10) for all exciton states (excluding contact states), we may compute the separation yield by solving the rate equations in which we explicitly consider only donor states $x \in XD$ and treat exciton states x' that are not of donor character as absorbing states:

$$0 = g_x - \tau_x^{-1} f_x^0 - \sum_{x'} w_{x',x} f_x^0 + \sum_{x' \in XD} w_{xx'} f_{x'}^0 \quad (36)$$

The separation yield, computed by inserting the solution to eq 36 into an expression analogous to eq 12, which reads as

$$\varphi = \frac{\sum_{x' \notin \text{XD}} \sum_{x \in \text{XD}} w_{x'} f_x^0}{\sum_{x \in \text{XD}} g_x} \quad (37)$$

is presented in case $E_{\text{init}} = 2.0$ eV by empty circles in Figure 9. We note that the agreement between the two results (full and empty circles in Figure 9) is quite good, thus validating our simple picture of charge separation from a low-energy donor state. The same procedure can be repeated when considering the separation starting from higher-energy donor states, but the agreement between the results obtained by solving eq 36 and the full system of rate equations (eq 10) is worse. An analysis of recombination events suggests that, in these cases, the acceptor exciton states are an equally important recombination channel as the donor exciton states. When the initial donor state is loosely bound, its direct coupling to acceptor states cannot be neglected. Further discussion on the limits of validity of the simple picture of charge separation from donor states embodied in eq 36 is presented in the next paragraph.

We now turn to the influence of the diagonal static disorder on the yield of charge separation starting from donor exciton states of different energies at zero electric field. We focus our attention on the initial donor states whose energies are around $E_{\text{init}} = 2.0$ eV and $E_{\text{init}} = 2.2$ eV. Together with the separation yield emerging from numerically solving the full set of rate equations given in eq 10 (the true separation yield), in Figure 10a,b we also present the data obtained by solving the reduced

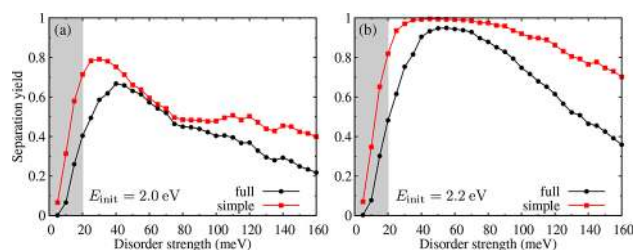


Figure 10. Separation yield at zero electric field for different strengths σ of the diagonal static disorder. The initial state of charge separation is a donor exciton state of energy around (a) $E_{\text{init}} = 2.0$ eV and (b) $E_{\text{init}} = 2.2$ eV. The data labeled by “full” are obtained by numerically solving the full set of rate equations (eq 10), whereas the data labeled by “simple” emerge from the numerical solution to the reduced set of rate equations (eq 36). Similar to Figure 6, the gray area indicates the range of disorder strength in which the predictions of our model are not reliable.

set of rate equations (eq 36). We observe that the separation yield exhibits similar trends with varying disorder strength as when the separation starts from the strongly bound CT state (cf., Figure 6). In particular, for not too strong disorder, the yield increases with increasing disorder strength, it attains the maximum value when the disorder assumes its optimal value, after which it decreases. For all of the examined values of disorder strength, the yield of the separation starting from the donor state of energy $E_{\text{init}} = 2.2$ eV is higher than in the case $E_{\text{init}} = 2.0$ eV; compare data represented by circles in Figure 10a,b, which again suggests that excitons initially in higher-energy donor states separate more efficiently than those initially in lower-energy donor states. While the maximum yield of separation starting from the donor state of energy $E_{\text{init}} = 2.0$ eV is around 0.7, the maximum yield in the case $E_{\text{init}} = 2.2$ eV is above 0.9. For both initial states of charge separation, the yield computed by numerically solving the reduced set of rate

equations (squares in Figure 10a,b) is an upper bound to the true separation yield (circles in Figure 10a,b) for all of the examined values of σ . For $E_{\text{init}} = 2.0$ eV, the separation yield computed by solving the reduced set of rate equations reproduces the true separation yield very well when the disorder strength is from around 40 meV to around 90 meV, while for stronger disorder the agreement between the yields computed in two manners deteriorates. This suggests that, for moderate disorder strength, our simple picture of charge separation from the closely separated donor state, embodied in eq 36, is plausible. At stronger disorder, the localization effects become more important, and recombination may occur from states that do not belong to the donor manifold as well. On the other hand, the agreement between the two separation yields in case $E_{\text{init}} = 2.2$ eV, see Figure 10b, is less satisfactory than that in case $E_{\text{init}} = 2.0$ eV.

We have also examined the dependence of the separation yield starting from the closely separated donor state on the magnitude of electron ($J_{D,0}^{c,\text{int}}$) and hole ($J_{D,0}^{v,\text{int}}$) transfer integrals in the donor part of the bilayer. We find that reasonable variations in these quantities do not induce major changes in the separation yield; see Figure 11a,b. The reason for this

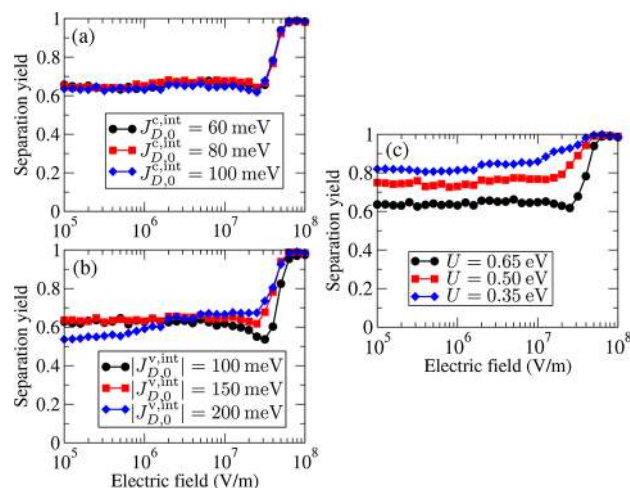


Figure 11. Field-dependent yield of charge separation starting from the closely separated donor exciton state ($E_{\text{init}} = 2.0$ eV) for different values of (a) the electron transfer integral $J_{D,0}^{c,\text{int}}$ in the donor, (b) the hole transfer integral $J_{D,0}^{v,\text{int}}$ in the donor, and (c) the on-site Coulomb interaction U .

behavior is the fact that the donor exciton binding energy, which is a rough measure of the energy barrier that has to be overcome for free charges to form, is not strongly dependent on the carrier delocalization in the donor. The factor that primarily determines the binding energy of the donor exciton is the strength of the Coulomb interaction. In Figure 11c we present the field-dependent separation yield for different values of the on-site Coulomb interaction U . As anticipated, we find that lowering U leads to a higher separation yield.

The temperature-dependent separation yield at zero electric field is shown in Figure 12a. We see that lower temperature leads to lower separation yield because the phonon bath-assisted processes transferring an exciton in a donor state to the space-separated manifold (and, eventually, to a state of fully separated charges) are weaker. The separation yield exhibits a 6-fold decrease when the temperature is lowered from the room temperature to around 50 K. The intensity of the temperature

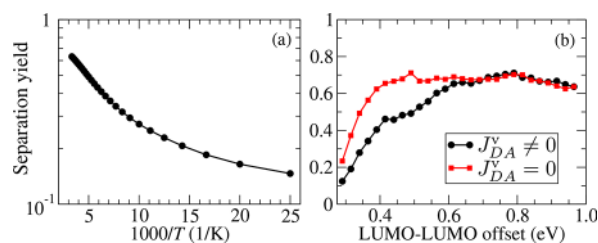


Figure 12. Yield of charge separation starting from the closely separated donor state ($E_{\text{init}} = 2.0$ eV) at zero electric field as a function of (a) the temperature (in Arrhenius representation) and (b) the LUMO–LUMO offset. The reported values of the LUMO–LUMO offset refer to the ordered system. In (b), we present results in which acceptor states are included ($J_{DA}^v \neq 0$) and excluded ($J_{DA}^v = 0$) from the computation.

variation-induced effect on the separation yield is somewhat smaller than in case of the separation starting from the strongly bound CT state; compare to Figure 8a.

In the end, we examine how the value of the LUMO–LUMO offset affects charge separation from the closely separated donor state. Figure 12b presents the separation yield as a function of the LUMO–LUMO offset for the values of model parameters listed in Table 1 ($J_{DA}^v \neq 0$, circles), as well as for $J_{DA}^v = 0$ (squares), that is, when states of acceptor excitons are excluded from the computation. For the LUMO–LUMO offset above approximately 0.6 eV, we observe that the separation yield in both cases is essentially the same and weakly dependent on the particular value of the LUMO–LUMO offset. This indicates that, in this range of LUMO–LUMO offsets, charge separation starting from the closely separated donor state does not involve acceptor exciton states, which once again validates our simple picture of charge separation from that state (formally embodied in eq 36). However, when the LUMO–LUMO offset is below 0.6 eV, the separation yield in case $J_{DA}^v \neq 0$ starts to decrease with decreasing the LUMO–LUMO offset. On the other hand, in case $J_{DA}^v = 0$, a similar decrease in the separation yield is observed only when the LUMO–LUMO offset is lower than approximately 0.4 eV. The different behavior of the separation yield in the two cases signals that, when the LUMO–LUMO offset assumes values lower than ca. 0.6 eV, states of acceptor excitons are involved in charge separation, and the observed decrease is due to the recombination from acceptor states. As we have already noted in the analysis of Figure 8b, when the LUMO–LUMO offset is around 0.6 eV, the low-energy tails of the CT and acceptor exciton DOS become energetically close. Further analysis of recombination events from different groups of exciton states, which is presented in Figure S7, shows that the contribution of the recombination from acceptor states to the total recombination probability becomes appreciable when the LUMO–LUMO offset is around 0.6 eV. When acceptor states are excluded from the computation, the independence of the separation yield on the LUMO–LUMO offset is disturbed when the energy of the strongly bound CT state is approximately equal to the energy of the initial donor state, which occurs for the LUMO–LUMO offset below around 0.4 eV. For even smaller values of the LUMO–LUMO offset, all of the space-separated states are energetically above the initial donor state, meaning that full charge separation can be achieved only by means of energetically upward processes. The decrease in the separation yield with decreasing LUMO–LUMO offset

can then be attributed to an increased probability of recombination from donor states.

DISCUSSION

This section is devoted to a more detailed discussion of some aspects of our model.

Let us start by commenting on our results in view of the reduced dimensionality of our model. Although formally one-dimensional, the proposed model of a bilayer can be regarded as a two (or three)-dimensional model consisting of periodically repeated chains similar to that shown in Figure 1 that are isolated from each other; that is, the transfer integrals between (neighboring) chains are equal to zero. We have established that, within our one-dimensional model, the degree of charge delocalization, quantified by the values of the electron and hole transfer integrals, is one of the factors influencing the (CT exciton) separation efficiency; see Figure 7a,b. On simple grounds, better delocalization is beneficial to charge separation because it increases the mean distance (in the direction of a single chain, which is perpendicular to the D/A interface) between the electron and hole located in the acceptor and donor, respectively. If we assigned nonzero values to transfer integrals coupling different chains, the charges could also delocalize along the direction perpendicular to the chains (parallel to the D/A interface) and further increase their separation. Therefore, it may be expected that the separation yield would be enhanced in such a genuinely two (or three)-dimensional model. This line of reasoning is supported by studies highlighting the beneficial role of hole delocalization along polymer chains in charge separation,^{28,33} particularly if we keep in mind that the values of the intrachain transfer integrals are typically larger than those employed in this study. We may also say that the separation yields we obtain using an effectively one-dimensional model are the lower limit to those that would be obtained in a higher-dimensional system. Another possible interpretation of our results is that they suggest that, to describe fundamental reasons for efficient charge separation at all-organic bilayers, it is more important to properly account for charge delocalization than for dimensionality effects.

Next, we discuss our assumptions concerning the strength of the carrier–bath interaction. We take that the polaron binding energy is $E_{\text{pol}} = 15$ meV, which is significantly lower than values commonly reported in electronic-structure studies of single PCBM molecules.^{44,66} The selection of the values of model parameters implicitly suggests that each lattice site may be imagined to substitute a polymer chain or a group of fullerene molecules. In this regard, carrier transfer from one site to another should not be interpreted as transfer between single molecules supporting localized carrier states, but rather as transfer between two aggregates of molecules supporting delocalized carrier states. It has been demonstrated recently that, in such a case, the definition of E_{pol} (given in the text between eqs 22 and 23) should be corrected so as to take into account delocalization effects, which can substantially reduce E_{pol} .⁶⁷ Having all of these things considered, we believe that our choice of the magnitude of E_{pol} is reasonable. Larger E_{pol} (while keeping all other model parameters fixed) would result in a higher separation yield, because the phonon bath-induced transition rates (eq 18) would be larger. In this sense, our results may also be regarded as the lower limit to the separation yield computed for larger E_{pol} .

Another common choice for the spectral density $J(E)$ (eq 17) when studying charge separation in photosynthetic⁵⁵ and

OPV systems^{51,68} is the so-called Drude–Lorentz spectral density. Because of its algebraic decay at high energies, the Drude–Lorentz spectral density generally favors coupling to a wider range of phonon modes than does the Ohmic spectral density employed here. In Figure S8a–d, we find that the Drude–Lorentz spectral density promotes higher separation yield than the ohmic spectral density.

The next comment concerns the number of disorder realizations over which the averaging is performed and our definition of the contact region and contact states (eqs 8 and 9). In Figure S9a,b, we present the dependence of the (average) separation yield at zero electric field on the number of disorder realizations over which we average. We see that averaging over more than 200–300 disorder realizations does not lead to substantial changes in the separation yield. Figure S10a,b confirms that our results remain qualitatively (and to a good extent quantitatively) the same when the linear dimension l_c of the contact region and the threshold probability on the right-hand sides of eqs 8 and 9 are varied within reasonable limits.

In the end, we note that an approach to the separation of strongly bound CT state similar to ours (eq 34) has been recently implemented in ref 37. We point out that eq 34 can, for moderate disorder, reproduce the separation yield in single disorder realizations without any tunable parameters. On the other hand, the authors of ref 37 reproduce the nonmonotonic dependence of the separation yield on the disorder strength using a formula similar to eq 34, which contains disorder-averaged transition rates and a tunable parameter. Let us also mention that eq 34 bears certain similarity to the exciton dissociation probability in unintentionally doped polymer materials proposed by Arkhipov et al.⁶⁹ These authors also assumed that the formation of free carriers is a two-step process: the initial exciton dissociates by the electron transfer to the dopant, while the subsequent charge separation is due to combined effects of the internal electric field, hole delocalization, and carrier recombination. However, the phenomenon of our interest, that is, the formation of free charges at D/A interfaces, is significantly different from free-charge formation in lightly doped conjugated polymers. The model introduced in ref 69 was devised to rationalize the weak field and temperature dependence exhibited by the free-charge yield in doped polymers, which is much smaller than unity. To understand very efficient charge separation at organic D/A interfaces, this model was further amended in refs 28 and 30–32.

CONCLUSION

Using a one-dimensional model of an all-organic bilayer, we have modeled and investigated the process of incoherent charge separation. Our model is microscopic, its parameters have clear physical significance, and their values are selected on the basis of literature data on OPV materials. The main advantage of our model is that it properly takes into account carrier delocalization, whose importance for efficient charge separation in OPV systems has been repeatedly recognized.^{26–28,30,32,33} However, many studies on charge separation at organic heterointerfaces either employ the approximation of point-like charges,^{34,35,61,70} or account for delocalization effects in an effective way (e.g., by introducing the carrier effective mass^{26,28,30,32,33} or evenly smearing charge throughout the delocalization region²⁷). On the other hand, here, carrier delocalization is fully and naturally taken into account by working in the exciton basis. The charge separation is then conceived as a sequence of environment-assisted transitions

among exciton basis states that terminates once a free-charge state is reached. Another important ingredient of our model is the diagonal static disorder, which is crucial to identify the counterparts of free-charge states within our description. We emphasize that the model and method employed in this study are very general. They may be potentially used, upon appropriate Hamiltonian modifications and suitable choice of the values of model parameters, to describe field-dependent charge generation in many different physical systems, for example, in a neat polymer material,^{14,71} or at an interface between two polymer materials.

We obtain that the synergy between moderate energetic disorder and carrier delocalization can explain quite high and relatively weakly field-dependent separation efficiencies observed in solar cells photoexcited at the low-energy edge of the CT manifold;⁶ see Figure 3a. At electric fields typically encountered in a working organic solar cell ($F \sim 5\text{--}10\text{ V}/\mu\text{m}$), the efficiency of the separation of the strongly bound CT exciton is above 0.8. Our analytical treatment, which is sensible for not too strong disorder, reveals that the separation of the strongly bound CT exciton is actually governed by only a couple of parameters, see eq 34, among which the most important are the recombination rate from the initial CT state and the escape rate toward more separated and long-lived intermediate states. Because further separation from intermediate states can proceed without kinetic obstacles, the competition between the two aforementioned rates describes the separation quite well. However, strong disorder destroys this simple picture, because full charge separation then involves more than just a single rate-limiting step; compare the two curves in Figure 6. The remedy may then be enhancing carrier delocalization; see Figure 7a,b. This result is also in agreement with conclusions of ref 6, which emphasize that, in most efficient solar cells, the “cold” CT state is only weakly bound and quite delocalized. Moreover, we observe a much milder temperature dependence of the separation yield than the (predominantly) exponential one predicted by the Onsager–Braun model, see Figure 8a, in agreement with experimental⁶⁵ and theoretical studies.³⁴ The fact that larger LUMO–LUMO offsets favor more efficient free-charge generation out of the strongly bound CT state is attributed to an increased recombination probability from acceptor and donor states observed for smaller LUMO–LUMO offsets; see Figure 8b.

The separation of donor excitons is also quite efficient, and its yield depends on the exciton energy; see Figure 9. The electric field required to separate the closely separated donor exciton with certainty is almost an order of magnitude higher than that needed to separate the strongly bound CT exciton. Our results suggest that the separation of the closely separated donor exciton exhibits only one rate-limiting step, that is, the escape to the space-separated manifold. Carrier delocalization does not strongly influence this escape; see Figure 11a,b. The donor exciton separation shows weak temperature dependence, see Figure 12a, while its decrease with decreasing the LUMO–LUMO offset is attributed to the recombination from acceptor states, as in Figure 12b. Relatively weak disorder is beneficial to donor exciton separation, while strong disorder suppresses it; see Figure 10a,b.

In summary, our results provide unambiguous evidence that efficient charge separation can be achieved even out of strongly bound pair states and are supported by experiments^{6,13} suggesting that free-charge generation predominantly occurs on long time scales, from localized initial conditions.

■ ASSOCIATED CONTENT**Supporting Information**

The Supporting Information is available free of charge on the ACS Publications website at DOI: 10.1021/acs.jpcc.8b03114.

Numerical data complementing the discussion on the influence of various model parameters on the separation yield (PDF)

■ AUTHOR INFORMATION**Corresponding Author**

*Phone: +381 (0)11 3713152. E-mail: nenad.vukmirovic@ipb.ac.rs.

ORCID

Veljko Janković: 0000-0002-0297-2167

Nenad Vukmirović: 0000-0002-4101-1713

Notes

The authors declare no competing financial interest.

■ ACKNOWLEDGMENTS

We gratefully acknowledge the support by the Ministry of Education, Science and Technological Development of the Republic of Serbia (project no. ON171017) and the European Commission under H2020 project VI-SEEM, grant no. 675121, as well as the contribution of the COST Action MP1406. Numerical computations were performed on the PARADOX supercomputing facility at the Scientific Computing Laboratory of the Institute of Physics Belgrade.

■ REFERENCES

- (1) Gao, F.; Inganäs, O. Charge Generation in Polymer-Fullerene Bulk-Heterojunction Solar Cells. *Phys. Chem. Chem. Phys.* **2014**, *16*, 20291–20304.
- (2) Bäessler, H.; Köhler, A. "Hot or Cold": How do Charge Transfer States at the Donor-Acceptor Interface of an Organic Solar Cell Dissociate? *Phys. Chem. Chem. Phys.* **2015**, *17*, 28451–28462.
- (3) Ostroverkhova, O. Organic Optoelectronic Materials: Mechanisms and Applications. *Chem. Rev.* **2016**, *116*, 13279–13412.
- (4) Ponceca, C. S.; Chábera, P.; Uhlig, J.; Persson, P.; Sundström, V. Ultrafast Electron Dynamics in Solar Energy Conversion. *Chem. Rev.* **2017**, *117*, 10940–11024.
- (5) Park, S. H.; Roy, A.; Beaupré, S.; Cho, S.; Coates, N.; Moon, J. S.; Moses, D.; Leclerc, M.; Lee, K.; Heeger, A. J. Bulk Heterojunction Solar Cells with Internal Quantum Efficiency Approaching 100%. *Nat. Photonics* **2009**, *3*, 297–303.
- (6) Vandewal, K.; Albrecht, S.; Hoke, E. T.; Graham, K. R.; Widmer, J.; Douglas, J. D.; Schubert, M.; Mateker, W. R.; Bloking, J. T.; Burkhard, G. F.; et al. Efficient Charge Generation by Relaxed Charge-Transfer States at Organic Interfaces. *Nat. Mater.* **2014**, *13*, 63–68.
- (7) Jailaubekov, A. E.; Willard, A. P.; Tritsch, J. R.; Chan, W.-L.; Sai, N.; Gearba, R.; Kaake, L. G.; Williams, K. J.; Leung, K.; Rossky, P. J.; et al. Hot Charge-Transfer Excitons Set the Time Limit for Charge Separation at Donor/Acceptor Interfaces in Organic Photovoltaics. *Nat. Mater.* **2013**, *12*, 66–73.
- (8) Grancini, G.; Maiuri, M.; Fazzi, D.; Petrozza, A.; Egelhaaf, H.-J.; Brida, D.; Cerullo, G.; Lanzani, G. Hot Exciton Dissociation in Polymer Solar Cells. *Nat. Mater.* **2013**, *12*, 29–33.
- (9) Bakulin, A. A.; Rao, A.; Pavelyev, V. G.; van Loosdrecht, P. H. M.; Pshenichnikov, M. S.; Niedzialek, D.; Cornil, J.; Beljonne, D.; Friend, R. H. The Role of Driving Energy and Delocalized States for Charge Separation in Organic Semiconductors. *Science* **2012**, *335*, 1340–1344.
- (10) Falke, S. M.; Rozzi, C. A.; Brida, D.; Maiuri, M.; Amato, M.; Sommer, E.; de Sio, A.; Rubio, A.; Cerullo, G.; Molinari, E.; et al. Coherent Ultrafast Charge Transfer in an Organic Photovoltaic Blend. *Science* **2014**, *344*, 1001–1005.
- (11) Vithanage, D. A.; Devižis, A.; Abramavičius, V.; Infahsaeng, Y.; Abramavičius, D.; MacKenzie, R. C. I.; Keivanidis, P. E.; Yartsev, A.; Hertel, D.; Nelson, J.; et al. Visualizing Charge Separation in Bulk Heterojunction Organic Solar Cells. *Nat. Commun.* **2013**, *4*, 2334.
- (12) Devižis, A.; De Jonghe-Risse, J.; Hany, R.; Nüesch, F.; Jenatsch, S.; Gulbinas, V.; Moser, J.-E. Dissociation of Charge Transfer States and Carrier Separation in Bilayer Organic Solar Cells: A Time-Resolved Electroabsorption Spectroscopy Study. *J. Am. Chem. Soc.* **2015**, *137*, 8192–8198.
- (13) Grupp, A.; Ehrenreich, P.; Kalb, J.; Budweg, A.; Schmidt-Mende, L.; Brida, D. Incoherent Pathways of Charge Separation in Organic and Hybrid Solar Cells. *J. Phys. Chem. Lett.* **2017**, *8*, 4858–4864.
- (14) Gerhard, M.; Arndt, A. P.; Bilal, M.; Lemmer, U.; Koch, M.; Howard, I. A. Field-Induced Exciton Dissociation in PTB7-Based Organic Solar Cells. *Phys. Rev. B: Condens. Matter Mater. Phys.* **2017**, *95*, 195301.
- (15) Gerhard, M.; Arndt, A. P.; Howard, I. A.; Rahimi-Iman, A.; Lemmer, U.; Koch, M. Temperature- and Energy-Dependent Separation of Charge-Transfer States in PTB7-Based Organic Solar Cells. *J. Phys. Chem. C* **2015**, *119*, 28309–28318.
- (16) Janković, V.; Vukmirović, N. Identification of Ultrafast Photophysical Pathways in Photoexcited Organic Heterojunctions. *J. Phys. Chem. C* **2017**, *121*, 19602–19618.
- (17) Janković, V.; Vukmirović, N. Origin of Space-Separated Charges in Photoexcited Organic Heterojunctions on Ultrafast Time Scales. *Phys. Rev. B: Condens. Matter Mater. Phys.* **2017**, *95*, 075308.
- (18) Clarke, T. M.; Durrant, J. R. Charge Photogeneration in Organic Solar Cells. *Chem. Rev.* **2010**, *110*, 6736–6767.
- (19) Gregg, B. A. Entropy of Charge Separation in Organic Photovoltaic Cells: The Benefit of Higher Dimensionality. *J. Phys. Chem. Lett.* **2011**, *2*, 3013–3015.
- (20) Hood, S. N.; Kassal, I. Entropy and Disorder Enable Charge Separation in Organic Solar Cells. *J. Phys. Chem. Lett.* **2016**, *7*, 4495–4500.
- (21) Ono, S.; Ohno, K. Combined Impact of Entropy and Carrier Delocalization on Charge Transfer Exciton Dissociation at the Donor-Acceptor Interface. *Phys. Rev. B: Condens. Matter Mater. Phys.* **2016**, *94*, 075305.
- (22) Onsager, L. Initial Recombination of Ions. *Phys. Rev.* **1938**, *54*, 554–557.
- (23) Braun, C. L. Electric Field Assisted Dissociation of Charge Transfer States as a Mechanism of Photocarrier Production. *J. Chem. Phys.* **1984**, *80*, 4157–4161.
- (24) Wojcik, M.; Tachiya, M. Accuracies of the Empirical Theories of the Escape Probability Based on Eigen Model and Braun Model Compared with the Exact Extension of Onsager Theory. *J. Chem. Phys.* **2009**, *130*, 104107.
- (25) Goliber, T. E.; Perlstein, J. H. Analysis of Photogeneration in a Doped Polymer System in Terms of a Kinetic Model for Electric-Field-Assisted Dissociation of Charge-Transfer States. *J. Chem. Phys.* **1984**, *80*, 4162–4167.
- (26) Schwarz, C.; Tscheuschner, S.; Frisch, J.; Winkler, S.; Koch, N.; Bäessler, H.; Köhler, A. Role of the Effective Mass and Interfacial Dipoles on Exciton Dissociation in Organic Donor-Acceptor Solar Cells. *Phys. Rev. B: Condens. Matter Mater. Phys.* **2013**, *87*, 155205.
- (27) Deibel, C.; Strobel, T.; Dyakonov, V. Origin of the Efficient Polaron-Pair Dissociation in Polymer-Fullerene Blends. *Phys. Rev. Lett.* **2009**, *103*, 036402.
- (28) Nenashev, A. V.; Baranovskii, S. D.; Wiemer, M.; Jansson, F.; Österbacka, R.; Dvurechenskii, A. V.; Gebhard, F. Theory of Exciton Dissociation at the Interface Between a Conjugated Polymer and an Electron Acceptor. *Phys. Rev. B: Condens. Matter Mater. Phys.* **2011**, *84*, 035210.
- (29) Schwarz, C.; Bäessler, H.; Bauer, I.; Koenen, J.-M.; Preis, E.; Scherf, U.; Köhler, A. Does Conjugation Help Exciton Dissociation? A Study on Poly(p-phenylene)s in Planar Heterojunctions with C₆₀ or TNF. *Adv. Mater.* **2012**, *24*, 922–925.
- (30) Arkhipov, V. I.; Heremans, P.; Bäessler, H. Why is Exciton Dissociation So Efficient at the Interface Between a Conjugated

(71) Menšík, M.; Pflieger, J.; Rybak, A.; Jung, J.; Ulański, J.; Halašová, K.; Vohlídal, J. Photogeneration of Free Charge Carriers in Tenuously Packed π Conjugated Polymer Chains. *Polym. Adv. Technol.* **2011**, *22*, 2075–2083.

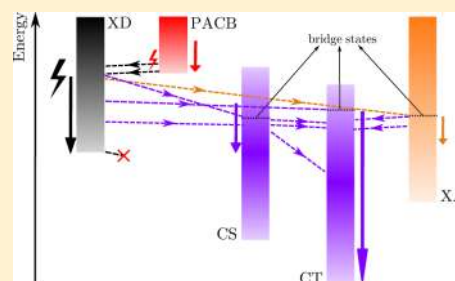
Identification of Ultrafast Photophysical Pathways in Photoexcited Organic Heterojunctions

Veljko Janković¹ and Nenad Vukmirović*

Scientific Computing Laboratory, Center for the Study of Complex Systems, Institute of Physics Belgrade, University of Belgrade, Pregrevica 118, 11080 Belgrade, Serbia

Supporting Information

ABSTRACT: The exciton dissociation and charge separation occurring on subpicosecond time scales following the photoexcitation are studied in a model donor/acceptor heterojunction using a fully quantum approach. Higher-than-LUMO acceptor orbitals which are energetically aligned with the donor LUMO orbital participate in the ultrafast interfacial dynamics by creating photon-absorbing charge-bridging states in which charges are spatially separated and which can be directly photoexcited. Along with the states brought about by single-particle resonances, the two-particle (exciton) mixing gives rise to bridge states in which charges are delocalized. Bridge states open up a number of photophysical pathways that indirectly connect the initial donor states with states of spatially separated charges and compete with the efficient progressive deexcitation within the manifold of donor states. The diversity and efficiency of these photophysical pathways depend on a number of factors, such as the precise energy alignment of exciton states, the central frequency of the excitation, and the strength of carrier–phonon interaction.



INTRODUCTION

Tremendous research efforts have been devoted to understanding the microscopic mechanisms governing efficient and ultrafast (happening on a $\lesssim 100$ fs time scale) free-charge generation observed in time-resolved experiments on donor/acceptor (D/A) heterojunction organic photovoltaic (OPV) devices.^{1–4} The photogenerated exciton in the donor material is commonly believed to transform into the charge transfer (CT) exciton.^{5,6} In the CT exciton, the electron and hole are tightly bound and localized at the D/A interface. The Coulomb barrier preventing the electron and hole in the CT state from further charge separation and formation of a charge separated (CS) state is much higher than the thermal energy at room temperature, so that the actual mechanism of the emergence of spatially separated charges on such short time scales remains an open question.^{7–10}

Electronically hot CT states, which are essentially resonant with the initial states of donor excitons and exhibit significant charge delocalization,^{11,12} are believed to be precursors to separated charges present on ultrafast time scales following the excitation.^{1,2,13–16} The delocalization of carriers can also reduce the Coulomb barrier and allow the transition from CT to CS exciton.^{3,17–19} The ultrafast exciton dissociation and charge separation are not purely electronic processes, but are instead mediated by the carrier–phonon coupling.^{17,20–26} The phonon-mediated ultrafast exciton dissociation and charge separation can proceed via the so-called intermediate bridge states,^{20,25} the vibronically hot CT states,¹⁷ or can occur without any intermediate CT state.²⁴ The exciton states of mixed donor and CS character are found to open up different photophysical pathways for ultrafast dissociation of initial

donor excitons, which are concurrent with vibronically assisted transitions within the donor exciton manifold.²³

We have recently investigated the exciton dynamics occurring on a subpicosecond time scale following the excitation of the model D/A heterojunction.²⁷ Our model explicitly takes into account the physical mechanisms regarded as highly relevant for the ultrafast heterojunction dynamics, such as the carrier delocalization and the carrier–phonon interaction. Moreover, the exciton generation, exciton dissociation, and further charge separation are treated on equal footing and on a fully quantum level, which is essential to correctly describe processes taking place on ultrafast time scales. For the model parameters representative of a low-bandgap polymer/fullerene blend, we found that the major part of space-separated charges present on 100 fs time scales after the excitation originates from the direct optical generation from the ground state rather than from the ultrafast population transfer from initially generated donor excitons. The resonant mixing between single-electron states in the two materials leads to the redistribution of oscillator strengths between states of donor excitons and space-separated charges, the latter becoming accessible by direct photoexcitation.

In this study, we aim at giving a more detailed description of the ultrafast heterojunction dynamics in terms of particular photophysical pathways along which it proceeds. In order to keep the numerical effort within reasonable limits, we still use one-dimensional model of a heterojunction, but we extend it by

Received: June 7, 2017

Revised: August 3, 2017

Published: August 17, 2017



taking into account more than only one single-electron (single-hole) state per site. The model parameters are chosen to be representative of the prototypical blend of poly-3-hexylthiophene (P3HT) and [6,6]-phenyl-C₆₁ butyric acid methyl ester (PCBM). The aforementioned extension of the model is important in many aspects. First, the degeneracy of the LUMO, LUMO+1, and LUMO+2 orbitals of the C₆₀ molecule is broken in its functionalized derivative PCBM,^{28–30} giving rise to three energetically close bands of electronic states of PCBM aggregates. This fact was shown to be important for efficient and ultrafast charge separation observed in D/A blends containing PCBM as the acceptor.^{14,25,31} Upon the functionalization of C₆₀, together with the degeneracy of its LUMO, LUMO+1, and LUMO+2 orbitals, the degeneracy of its LUMO+3, LUMO+4, and LUMO+5 orbitals, which are situated at around 1 eV above the LUMO, LUMO+1, and LUMO+2 orbitals, is also broken. Second, according to the results of Ma and Troisi,³² the precise energy alignment of higher-than-LUMO orbitals of the acceptor can modulate the exciton dissociation rate by orders of magnitude by opening up new exciton dissociation channels. The LUMO–LUMO offset in the P3HT/PCBM blend can be quite large (around 1 eV)^{33–35} and thus comparable to the energy separation between LUMO and LUMO+3 orbitals of the PCBM molecule. It can therefore be expected that the electronic states of a PCBM aggregate, which arise from LUMO+3, LUMO+4, and LUMO+5 orbitals of the PCBM molecule may play nontrivial role in the ultrafast interfacial dynamics. Surprisingly, it seems that the effect of these orbitals has not received enough attention in previous model studies of the P3HT/PCBM heterojunction. The ultrafast electron transfer observed in ref 36 has been ascribed to the energy overlap between the state of the photoexcited electron and the electronic states of the fullerene aggregate. The result presented in Figure 3e of ref 36 suggests that this overlap involves the electronic states of the fullerene aggregate stemming from the LUMO+3, LUMO+4, and LUMO+5 orbitals of the PCBM molecule.

Our results indicate that the exciton states in which the charges are delocalized throughout the heterojunction play a crucial role in the ultrafast heterojunction dynamics. In the low-energy part of the exciton spectrum, such states emerge due to the resonant mixing between different exciton (i.e., two-particle) states, and we denote them as bridge states. However, in the high-energy region of the exciton spectrum, such states form as a consequence of the resonant mixing between single-electron states in the donor and acceptor (states originating from LUMO+3, LUMO+4, and LUMO+5 orbitals of the PCBM molecule). The relevant exciton states of this kind are those in which the charges are spatially separated (the electron is mainly in the acceptor, while the hole is mainly in the donor) and we denote them as photon-absorbing charge-bridging (PACB) states,^{28,37,38} since they can be directly reached by a photoexcitation. Exciting well above the lowest donor state, we find that excitons are generated in both donor and PACB states, while the major part of space-separated charges present on a 100 fs time scale following the excitation resides in PACB states. The deexcitation of initial PACB excitons proceeds via the donor exciton manifold, while single-phonon-assisted processes involving a PACB state and CT and CS states belonging to the low-energy part of the spectrum are virtually absent. The donor excitons mainly deexcite within the donor exciton manifold and, before reaching the lowest donor exciton state, may perform transitions to bridge states, which are

gateways into the space-separated manifold. The lowest donor state, being essentially decoupled from the space-separated manifold, is a trap state for exciton dissociation. The bridge states can be either intermediate or final states in the course of the charge separation. Once a space-separated state is reached, the gradual energy loss within the space-separated manifold leads to the population of low-energy CT states on a picosecond time scale. The participation of PACB excitons in the total exciton population strongly depends on the central frequency of the excitation. The probability of a bridge state being accessed during the exciton deexcitation sensitively depends on the distribution of initially generated excitons, the energy level alignment, and the carrier–phonon interaction strength.

MODEL AND METHODS

Model Hamiltonian. We use the standard semiconductor Hamiltonian with multiple single-electron/single-hole states per site. The model heterojunction consists of $2N$ sites located on a one-dimensional lattice of constant a : sites $0, \dots, N-1$ belong to the donor part, while sites $N, \dots, 2N-1$ belong to the acceptor part of the heterojunction. The single-electron levels on site i are counted by index β_i , so that Fermi operators $c_{i\beta_i}^\dagger$ ($c_{i\beta_i}$) create (destroy) electrons on site i and in single-electron state β_i . Analogously, single-hole levels on site i are counted by index α_i , so that Fermi operators $d_{i\alpha_i}^\dagger$ ($d_{i\alpha_i}$) create (destroy) holes on site i and in single-hole state α_i . Each site contributes a number of localized phonon modes and the corresponding Bose operators $b_{i\lambda_i}^\dagger$ ($b_{i\lambda_i}$) create (annihilate) phonons belonging to mode λ_i on site i . The Hamiltonian has the form

$$H = H_c + H_p + H_{c-p} + H_{c-f} \quad (1)$$

where H_c describes interacting carriers

$$H_c = \sum_{\substack{i\beta_i \\ j\beta_j}} \epsilon_{(i\beta_i)(j\beta_j)}^c c_{i\beta_i}^\dagger c_{j\beta_j} - \sum_{\substack{i\alpha_i \\ j\alpha_j}} \epsilon_{(i\alpha_i)(j\alpha_j)}^v d_{i\alpha_i}^\dagger d_{j\alpha_j} \\ + \frac{1}{2} \sum_{\substack{i\beta_i \\ j\beta_j}} V_{ij} c_{i\beta_i}^\dagger c_{j\beta_j}^\dagger c_{j\beta_j} c_{i\beta_i} + \frac{1}{2} \sum_{\substack{i\alpha_i \\ j\alpha_j}} V_{ij} d_{i\alpha_i}^\dagger d_{j\alpha_j}^\dagger d_{j\alpha_j} d_{i\alpha_i} \\ - \sum_{\substack{i\beta_i \\ j\alpha_j}} V_{ij} c_{i\beta_i}^\dagger d_{j\alpha_j}^\dagger d_{j\alpha_j} c_{i\beta_i} \quad (2)$$

$$H_p = \sum_{i\lambda_i} \hbar\omega_{i\lambda_i} b_{i\lambda_i}^\dagger b_{i\lambda_i} \quad (3)$$

is the phonon part of the Hamiltonian, H_{c-p} accounts for the carrier–phonon interaction

$$H_{c-p} = \sum_{i\beta_i} \sum_{\lambda_i} g_{i\beta_i\lambda_i}^c c_{i\beta_i}^\dagger c_{i\beta_i} (b_{i\lambda_i}^\dagger + b_{i\lambda_i}) \\ - \sum_{i\alpha_i} \sum_{\lambda_i} g_{i\alpha_i\lambda_i}^v d_{i\alpha_i}^\dagger d_{i\alpha_i} (b_{i\lambda_i}^\dagger + b_{i\lambda_i}) \quad (4)$$

whereas H_{c-f} represents the interaction of carriers with the external electric field $E(t)$

$$H_{c-f} = -E(t) \sum_{i\alpha_i\beta_i} d_{i\alpha_i}^{c\nu} (c_{i\beta_i}^\dagger d_{i\alpha_i}^\dagger + d_{i\alpha_i} c_{i\beta_i}) \quad (5)$$

In our model, quantities $\epsilon_{(i\beta_i)(j\beta_j)}^c$ ($\epsilon_{(i\alpha_i)(j\alpha_j)}^v$), which represent electron (hole) on-site energies and transfer integrals, are

nonzero only for certain combinations of their indices. Namely, $\epsilon_{(i\beta')(j\beta'')}^c$ is nonzero when it represents

- (1) on-site energy $\epsilon_{i\beta_i}^c$ of electron level β_i on site i for $i = j$ and $\beta_i = \beta'_i$;
- (2) negative electron transfer integral between nearest neighbors of band $\beta_i - J_{i\beta_i}^{\text{int}}$, for i and j both belonging to the same part of the heterojunction, $|i - j| = 1$, and $\beta_i = \beta'_i$;
- (3) negative electron transfer integral between nearest neighbors of different bands, $-J_{i\beta_i\beta'_i}^{\text{ext}}$, for i and j both belonging to the same part of the heterojunction, $|i - j| = 1$, and $\beta_i \neq \beta'_i$;
- (4) negative electron transfer integral between different parts of the heterojunctions, $-J_{DA}^c$ for $i = N - 1$ and $j = N$ or vice versa.

The Coulomb interaction described by eq 2 is taken into account in the lowest monopole–monopole approximation and the interaction potential V_{ij} is assumed to be the Ohno potential

$$V_{ij} = \frac{U}{\sqrt{1 + \left(\frac{r_{ij}}{r_0}\right)^2}} \quad (6)$$

where U is the on-site Coulomb interaction, r_{ij} is the distance between sites i and j , $r_0 = e^2/(4\pi\epsilon_0\epsilon_r U)$ is the characteristic length, and ϵ_r is the relative dielectric constant. Charge carriers are assumed to be locally and linearly coupled to the set of phonon modes (Holstein-type interaction), as given in eq 4. We assume that the frequency of the external electric field is such that it creates electron–hole excitations, the interband matrix elements of the dipole moment being $d_{i\alpha\beta}^{\text{cv}}$, and neglect all intraband dipole matrix elements.

Theoretical Framework. Ultrafast exciton dynamics governed by the model Hamiltonian defined in eqs 1–5 is treated using the density matrix formalism complemented with the dynamics controlled truncation (DCT) scheme.^{27,39–42} Exciton generation (from initially unexcited heterojunction) by means of a pulsed excitation and subsequent evolution of thus created nonequilibrium state of the system are treated on equal footing. We consider the case of weak excitation and low carrier densities. The carrier branch of the hierarchy of equations produced by the density matrix formalism can then be truncated retaining only contributions up to the second order in the exciting field. The truncation of the phonon branch of the hierarchy is performed to ensure the conservation of the particle-number and energy after the pulsed excitation.⁴²

It is advantageous to formulate theory in the subspace of single electron–hole excitations, which is spanned by the so-called exciton basis. The most general electron–hole pair state is of the form $|x\rangle = \sum_{i\alpha_j} \psi_{(i\alpha)(j\beta)}^x c_{j\beta}^\dagger d_{i\alpha}^\dagger |0\rangle$, where $|0\rangle$ is the vacuum of electron–hole pairs. The exciton basis states are obtained by solving the eigenvalue problem $H_c|x\rangle = \hbar\omega_x|x\rangle$,

which in the basis of single-particle states localized at lattice sites reads as

$$\sum_{\substack{i'\alpha'_i \\ i'\beta'_j}} (\delta_{ii'}\delta_{\alpha\alpha'}\epsilon_{(j\beta')(j'\beta'')}^c - \delta_{jj'}\delta_{\beta\beta'}\epsilon_{(i\alpha)(i'\alpha')}^v) \psi_{(i'\alpha')(j'\beta'')}^x - \delta_{ii'}\delta_{\alpha\alpha'}\delta_{jj'}\delta_{\beta\beta'}V_{ij})\psi_{(i'\alpha')(j'\beta'')}^x = \hbar\omega_x\psi_{(i\alpha)(j\beta)}^x \quad (7)$$

The operator which creates an exciton in state x is defined through

$$X_x^\dagger = \sum_{\substack{i\alpha \\ j\beta}} \psi_{(i\alpha)(j\beta)}^x c_{j\beta}^\dagger d_{i\alpha}^\dagger \quad (8)$$

The total Hamiltonian (eq 1), in which we keep only operators whose expectation values are at most of the second order in the exciting field, can be expressed in terms of exciton creation and annihilation operators as

$$H = \sum_x \hbar\omega_x X_x^\dagger X_x + \sum_{i\lambda_i} \hbar\omega_{i\lambda_i} b_{i\lambda_i}^\dagger b_{i\lambda_i} + \sum_{\substack{\bar{x}x \\ i\lambda_i}} (\Gamma_{\bar{x}x}^{i\lambda_i} X_{\bar{x}}^\dagger X_x b_{i\lambda_i}^\dagger + \Gamma_{\bar{x}x}^{i\lambda_i*} X_x^\dagger X_{\bar{x}} b_{i\lambda_i}) - E(t) \sum_x (M_x^* X_x + M_x X_x^\dagger). \quad (9)$$

Dipole-moment matrix elements for the direct generation (from the ground state) of excitons in state x are given as

$$M_x = \sum_i \sum_{\alpha\beta} \psi_{(i\alpha)(i\beta)}^{x*} d_{i\alpha\beta}^{\text{cv}} \quad (10)$$

while exciton–phonon matrix elements describing transitions from exciton state x to exciton state \bar{x} assisted by phonon ($i\lambda_i$) are

$$\Gamma_{\bar{x}x}^{i\lambda_i} = \sum_{\beta_i} \sum_{j\alpha_j} g_{i\beta_j\lambda_i}^c \psi_{(j\alpha)(i\beta)}^{\bar{x}*} \psi_{(j\alpha)(i\beta)}^x - \sum_{\alpha_i} \sum_{j\beta_j} g_{i\alpha_j\lambda_i}^v \psi_{(i\alpha)(j\beta)}^{\bar{x}*} \psi_{(i\alpha)(j\beta)}^x \quad (11)$$

Active variables in our formalism are electronic density matrices $y_x = \langle X_x \rangle$ and $n_{\bar{x}x} = \langle X_{\bar{x}}^\dagger X_x \rangle$, along with their single-phonon-assisted counterparts $y_{x(i\lambda_i)^-} = \langle X_x b_{i\lambda_i} \rangle$, $y_{x(i\lambda_i)^+} = \langle X_x b_{i\lambda_i}^\dagger \rangle$, and $n_{\bar{x}x(i\lambda_i)^+} = \langle X_{\bar{x}}^\dagger X_x b_{i\lambda_i}^\dagger \rangle$. The equations of motion for these variables are given in the Supporting Information. Since the phonon branch of the hierarchy is truncated at the level of second-order phonon assistance, our treatment of the electron–phonon interaction does not capture properly the processes with higher-order phonon assistance, which are important for stronger electron–phonon interaction. In this case, the feedback effects of electronic excitations on phonons would have to be taken into account as well. To this end, in our recent publication²⁷ we performed a computation of subpicosecond dynamics using surface hopping approach (which, however, treats lattice dynamics classically) and found that the feedback effects were not very pronounced. In order to treat the electron–phonon interaction more accurately, other approaches based on state-of-the-art multiconfigurational techniques,²³ infinite resummation within Green's function formalism^{43,44} or variational ansätze for the wave function of electron–phonon system⁴⁵ can be used.

The early stages of our numerical experiment (during and immediately after the pulsed excitation) are dominated by exciton coherences with the ground state y_x and their phonon-assisted counterparts. The corresponding coherent exciton populations $|y_x|^2$ are not a measure of the number of truly bound electron–hole pairs and generally decay quickly after the pulsed excitation, converting into incoherent exciton populations. This conversion from coherent to incoherent exciton populations is in our model mediated by the carrier–phonon interaction. The incoherent exciton populations are defined as

$$\bar{n}_{xx} = n_{xx} - |y_x|^2 \quad (12)$$

They represent numbers of Coulomb-correlated electron–hole pairs and typically exist for a long time after the decay of coherent populations. The incoherent populations of various groups X of exciton states are defined as

$$N_X^{\text{incoh}} = \sum_{x \in X} \bar{n}_{xx} \quad (13)$$

and are frequently and conveniently normalized to the total exciton population

$$N_{\text{tot}} = \sum_x n_{xx} \quad (14)$$

which is conserved after the excitation. Once created from coherent populations, incoherent populations redistribute among various exciton states, the redistribution being mediated by the carrier–phonon interaction. In order to gain insight into the pathways along which these redistribution processes proceed, we define energy- and time-resolved exciton populations $\varphi_X(E, t)$ of states belonging to group X as

$$\varphi_X(E, t) = \frac{1}{N_{\text{tot}}} \sum_{x \in X} n_{xx}(t) \delta(E - \hbar\omega_x) \quad (15)$$

so that $\varphi_X(E, t) \Delta E$ is the number (normalized to N_{tot}) of excitons from group X residing in the states whose energies are between E and $E + \Delta E$. Bearing in mind eq 12, relating the coherent, incoherent, and total exciton population of state x , quantity $\varphi_X(E, t)$ can be decomposed into its coherent

$$\varphi_X^{\text{coh}}(E, t) = \frac{1}{N_{\text{tot}}} \sum_{x \in X} |y_x(t)|^2 \delta(E - \hbar\omega_x) \quad (16)$$

and incoherent part

$$\varphi_X^{\text{incoh}}(E, t) = \frac{1}{N_{\text{tot}}} \sum_{x \in X} \bar{n}_{xx}(t) \delta(E - \hbar\omega_x) \quad (17)$$

The plots of φ_X^{coh} as a function of E and t provide information about states in which excitons are initially generated (the initial exciton distribution) and the time scale on which the conversion from coherent to incoherent exciton populations takes place. The plots of φ_X^{incoh} as a function of E and t reveal actual pathways along which (incoherent) excitons are redistributed, starting from the initial exciton distribution.

Parameterization of the Model Hamiltonian. Our model is parametrized with the aim of describing ultrafast exciton dissociation and charge separation in the direction perpendicular to the D/A interface. This is motivated by recent studies of ultrafast exciton dissociation⁴⁶ and charge separation¹⁹ in two-dimensional models of a D/A polymeric heterojunction which have suggested that these processes crucially depend on the electronic properties and geometry in the direction

perpendicular to the interface. In actual computations, we take one single-electron level per site in the donor and one single-hole level per site in both the donor and acceptor. In order to mimic the presence of higher-than-LUMO orbitals energetically close to the LUMO level (which is a situation typical of fullerenes), as well as to investigate the effects of single-electron levels situated at around 1.0 eV above the LUMO level on the exciton dissociation, we take four single-electron levels per site in the acceptor. Different types of electronic couplings are schematically indicated in Figure 1, while the values of model parameters

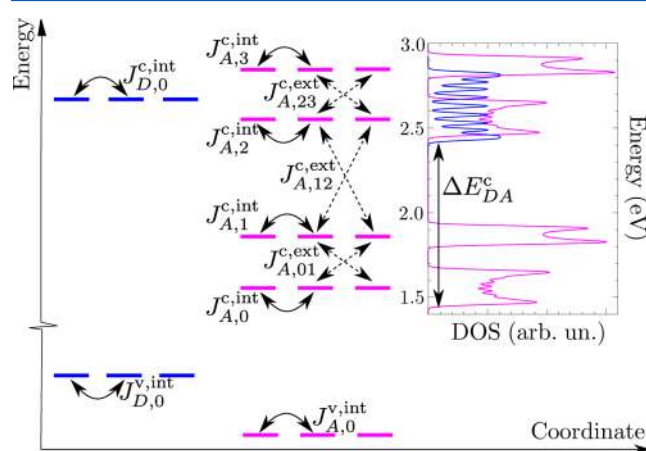


Figure 1. Illustration of the model system indicating different transfer integrals present in Table 1. The plot on the right shows the single-particle DOS for electrons in the neat donor (blue curve) and acceptor (magenta curve) materials obtained using the values of relevant parameters listed in Table 1. The electronic states of the isolated materials are computed by diagonalizing the free-electron Hamiltonian (the first term on the right-hand side of eq 2) in which the D/A coupling is set to 0. The DOS was then calculated by broadening each of the states obtained by a Gaussian with the standard deviation of 10 meV.

used in computations are summarized in Table 1. These values are selected so that the main characteristics of the single-particle and exciton spectrum (band widths, band alignments, exciton and charge transfer state binding energies) within the model correspond to the ones observed in P3HT/PCBM material system. We take the HOMO level of the donor material to be the zero of the energy scale.

The value of the lattice spacing a agrees with the typical distance between constitutive elements of organic semiconductors. The number of sites in a single material $N = 11$ is reasonable since typical linear dimensions of phase segregated domains in bulk heterojunction morphology are 10–20 nm.⁴⁷ The value of the transfer integral $J_{D,0}^{v,int}$ was chosen so as to agree with the HOMO bandwidth along the π -stacking direction of the regioregular P3HT^{48,49} and the values of the hole transfer integral along the π -stacking direction of the same material.^{50,51} The electron transfer integral $J_{D,0}^{c,int}$ should be of similar magnitude as the hole transfer integral along the π -stacking direction.⁵⁰ Energies of the single-electron and single-hole levels in the donor, as well as the on-site Coulomb interaction U , were chosen so that the lowest donor exciton state is located at around 2.0 eV, while the HOMO–LUMO gap (single-particle gap) is around 2.4 eV, i.e., the binding energy of the donor exciton is around 0.4 eV.^{52,53}

Electron transfer integrals in the acceptor $J_{A,0}^{c,int}$, $J_{A,1}^{c,int}$ and $J_{A,0,1}^{c,ext}$, together with the energy difference $\epsilon_{A,1}^c - \epsilon_{A,0}^c$ between

Table 1. Values of Model Parameters Used in Computations

parameter	value
N	11
a (nm)	1.0
U (eV)	0.65
ϵ_r	3.0
$\epsilon_{D,0}^c$ (eV)	2.63
$J_{D,0}^{\text{int}}$ (eV)	0.1
$\epsilon_{D,0}^v$ (eV)	-0.3
$J_{D,0}^{\text{int}}$ (eV)	-0.15
$\epsilon_{A,0}^c$ (eV)	1.565
$\epsilon_{A,1}^c$ (eV)	1.865
$\epsilon_{A,2}^c$ (eV)	2.565
$\epsilon_{A,3}^c$ (eV)	2.865
$J_{A,0}^{\text{int}}$ (eV)	0.05
$J_{A,1}^{\text{int}}$ (eV)	0.025
$J_{A,2}^{\text{int}}$ (eV)	0.05
$J_{A,3}^{\text{int}}$ (eV)	0.025
$J_{A,01}^{\text{ext}}$ (eV)	0.02
$J_{A,12}^{\text{ext}}$ (eV)	0.02
$J_{A,23}^{\text{ext}}$ (eV)	0.02
$\epsilon_{A,0}^v$ (eV)	-1.03
$J_{A,0}^{\text{int}}$ (eV)	-0.15
J_{DA}^c (eV)	0.1
J_{DA}^v (eV)	-0.1
$\hbar\omega_{p,1}$ (meV)	10.0
g_1 (meV)	42.0
$\hbar\omega_{p,2}$ (meV)	185.0
g_2 (meV)	94.0
T (K)	300.0

single-electron states, are chosen to reproduce the most important features of the low-energy part of the electronic density of states (DOS) of fullerene aggregates,^{14,25} such as the combined (total) bandwidth of 0.4–0.5 eV and the presence of two separated groups of allowed states. Let us note that, because of the reduced dimensionality of our model, we cannot expect to reproduce details of the actual DOS, but only its gross features. We therefore believe that taking two instead of three orbitals energetically close to the LUMO orbital is reasonable within our model. The electronic DOS in the acceptor produced by our model is shown in the inset of Figure 1. Magnitudes of transfer integrals in the acceptor are also in agreement with the values reported in the literature.^{54,55} We have also included the single-electron fullerene states which are located at around 1 eV above the lowest single-electron state. It is well-known that these states in C₆₀ are also triply degenerate and that this degeneracy is lifted in PC₆₀BM. Since we use a model system, we take, for simplicity, that the degeneracy is lifted in the same manner as in the case of lowest single-electron levels, i.e., we take $J_{A,0}^{\text{int}} = J_{A,2}^{\text{int}} = J_{A,1}^{\text{int}} = J_{A,3}^{\text{int}}$, $J_{A,01}^{\text{int}} = J_{A,23}^{\text{int}}$, and $\epsilon_{A,3}^c - \epsilon_{A,2}^c = \epsilon_{A,1}^c - \epsilon_{A,0}^c$, while $\epsilon_{A,2}^c - \epsilon_{A,0}^c = 1.0$ eV. For the magnitudes of the energy difference $\epsilon_{A,0}^c - \epsilon_{A,0}^v$ and the transfer integral $J_{A,0}^{\text{int}}$ listed in Table 1, the single-particle gap in the acceptor part of the heterojunction assumes the value of 2.2 eV, which is similar to the literature values for PCBM.⁵²

The energy differences Δ_{XD-CT} and Δ_{XA-CT} between the lowest excited state of the heterojunction (the lowest CT state) and the lowest exciton states in the donor and acceptor respectively, are directly related to LUMO–LUMO and HOMO–HOMO energy offsets between the materials. Literature values of Δ_{XD-CT} representative of P3HT/PCBM

blends are usually calculated for the system consisting of one PCBM molecule and one oligomer and range from 0.7 eV³³ to 1.3 eV.³⁴ Liu and Troisi³⁵ obtained $\Delta_{XD-CT} = 0.97$ eV and pointed out that taking into account partial electron delocalization over fullerene molecules can significantly lower the XD-CT energy difference. For parameters listed in Table 1, $\Delta_{XD-CT} = 0.68$ eV, which is a reasonable value, since we do account for carrier delocalization effects. The LUMO–LUMO offset ΔE_{DA}^c (see Figure 1) produced by the model parameters is around 0.96 eV and the lowest CT state is located at 1.32 eV. The energy difference $\Delta_{XA-CT} = 0.42$ eV, so that the HOMO–HOMO offset is around 0.73 eV and the lowest XA state is approximately at 1.74 eV, both of which compare well with the available data.⁵² The magnitudes of the transfer integrals J_{DA}^c and J_{DA}^v between the two materials are taken to be similar to the values obtained in ref 28.

Interband matrix elements of the dipole moment $d_{i\alpha\beta}^{cv}$ are assumed not to depend on band indices α, β, i and to be equal on all sites belonging to the single material, $d_{i\alpha\beta}^{cv} = d_D^{cv}$ for $i = 0, \dots, N - 1$ and $d_{i\alpha\beta}^{cv} = d_A^{cv}$ for $i = N, \dots, 2N - 1$. Since the focus of our study is on the dissociation of donor excitons, in all the computations we set $d_A^{cv} = 0$.

We assume that each site contributes one low-frequency and one high-frequency phonon mode. The energies of the phonon modes, as well as the carrier–phonon interaction constants, are taken to be equal in both parts of the heterojunction. The phonon mode of energy 185 meV, present in both materials, was shown to be important for ultrafast charge transfer in the P3HT/PCBM blend,²⁶ while low-energy ($\lesssim 10$ meV) phonon modes of P3HT exhibit strong coupling to carriers.⁵⁶ The strength of the carrier–phonon interaction can be quantified by the polaron binding energy, which can be estimated using the result of the second-order weak-coupling perturbation theory at $T = 0$ in the vicinity of the point $k = 0$:⁵⁷

$$\epsilon_b^{\text{pol}} = \sum_{i=1}^2 \epsilon_{b,i}^{\text{pol}} = \sum_{i=1}^2 \frac{g_i^2}{2|J|} \frac{1}{\sqrt{\left(1 + \frac{\hbar\omega_{p,i}}{2|J|}\right)^2 - 1}} \quad (18)$$

where $\epsilon_{b,i}^{\text{pol}}$ are the contributions of high- and low-frequency phonon modes to the polaron binding energy. The values of g_1 and g_2 in Table 1 are obtained assuming that $\epsilon_b^{\text{pol}} = 50$ meV and $\epsilon_{b,1}^{\text{pol}} = \epsilon_{b,2}^{\text{pol}}$ and setting $|J| = 125$ meV.

Classification of Exciton States. The classification of exciton states is unambiguous only for $J_{DA}^c = J_{DA}^v = 0$ (noninteracting heterojunction), when each exciton state $\psi_{(i\alpha)(j\beta)}^{x(0)}$ can be classified as a donor exciton state (XD), a space-separated state, an acceptor exciton state (XA) or a state in which the electron is in the donor, while the hole is in the acceptor (eDhA). Because eDhA states are very well separated (in energy) from other groups of exciton states, we will not further consider them. In the group of space-separated states, CT and CS states can further be distinguished by the mean electron–hole distance

$$\langle r_{e-h} \rangle_{x(0)} = \sum_{\substack{i\alpha_i \\ j\beta_j}} |\psi_{(i\alpha)(j\beta)}^{x(0)}|^2 |i - j| \quad (19)$$

If the electron–hole interaction is set to zero, the mean electron–hole distance for all the space-separated states is equal to N . For the nonzero Coulomb interaction, we consider a

space-separated state as a CS state if its mean electron–hole distance is larger than (or equal to) N , otherwise we consider it as a CT state.

In general case, when at least one of J_{DA}^c, J_{DA}^v is different from zero (interacting heterojunction), it is useful to explicitly separate the D/A interaction from the interacting-carrier part of the Hamiltonian (eq 2),

$$H_c = H_c^{(0)} + H_{DA} \quad (20)$$

where

$$H_{DA} = -J_{DA}^c \sum_{\substack{\beta_{N-1} \\ \beta_N}} \left(c_{(N-1)\beta_{N-1}}^\dagger c_{N\beta_N} + \text{H. c.} \right) + J_{DA}^v \sum_{\substack{\alpha_{N-1} \\ \alpha_N}} \left(d_{(N-1)\alpha_{N-1}}^\dagger d_{N\alpha_N} + \text{H. c.} \right) \quad (21)$$

is the D/A interaction, and $H_c^{(0)}$ describes interacting carriers at the noninteracting heterojunction. Exciton states of the noninteracting heterojunction $\psi_{(i\alpha_i)(j\beta_j)}^{x(0)}$ and corresponding exciton energies $\hbar\omega_x^{(0)}$ are obtained solving the electron–hole pair eigenproblem of $H_c^{(0)}$. Exciton states of the interacting heterojunction $\psi_{(i\alpha_i)(j\beta_j)}^x$ are linear combinations of exciton states of the noninteracting heterojunction

$$\psi_{(i\alpha_i)(j\beta_j)}^x = \sum_{x^{(0)}} C_{xx^{(0)}} \psi_{(i\alpha_i)(j\beta_j)}^{x^{(0)}} \quad (22)$$

and their character is obtained using this expansion. Namely, for each group $X^{(0)}$ of the exciton states of the noninteracting heterojunction, we compute the overlap of state x (of the interacting heterojunction) with states belonging to this group

$$C_{X^{(0)}}^x = \sum_{x^{(0)} \in X^{(0)}} |C_{xx^{(0)}}|^2 \quad (23)$$

The character of state x is then the character of the group $X^{(0)}$ for which the overlap $C_{X^{(0)}}^x$ is maximum.

The electron in a space-separated state is predominantly located in the acceptor part of the heterojunction, while the hole is located in the donor part. Since there is a number of single-electron levels per acceptor site, the electron in a space-separated state can be in different electronic bands originating from these single-electron levels. A useful quantity for further classification of space-separated states is

$$p_x(\beta) = \sum_{j=N}^{2N-1} \sum_{i\alpha_i} |\psi_{(i\alpha_i)(j\beta)}^x|^2 \quad (24)$$

which represents the conditional probability that, given that the electron in state x is in the acceptor, it belongs to the electronic band stemming from the single-electron level β . The index of the electronic band β_x to which the electron in space-separated state x predominantly belongs is then the value of β for which the conditional probability p_x is maximal. In other words, space-separated state x belongs to the CT_{β_x} band.

Let us note here that, because of the large energy separation between the lower two (0 and 1) and the higher two (2 and 3) single-electron levels in the acceptor, the electronic coupling $J_{A,12}^{\text{ext}}$, which couples space-separated states belonging to CT_0 and CT_1 bands to the ones belonging to CT_2 and CT_3 bands, is not effective. Therefore, the space-separated states from CT_0 and CT_1 bands are very weakly mixed with (and essentially

isolated from) space-separated states of CT_2 and CT_3 bands, which permits us to separately analyze these two subgroups of space-separated states.

Role of the Donor–Acceptor Coupling and the Resonant Mixing Mechanism. In this section, we show that the D/A coupling is at the root of the resonant mixing mechanism, which explains the presence of space-separated (and XA) states that have a certain amount of donor character, can be reached by means of a photoexcitation, and act as gateways to the space-separated manifold for the initial donor excitons. However, the precise role of the D/A coupling is different in different energy regions of the exciton spectrum. In the low-energy region of the exciton spectrum, which is dominated by the space-separated states belonging to CT_0 and CT_1 bands, this coupling leads to the resonant mixing of two-particle (exciton) states. On the other hand, in the high-energy region of the exciton spectrum, in which space-separated states belong to CT_2 and CT_3 bands, it gives rise to the resonant mixing of single-electron states in the donor and acceptor.

To better appreciate the role of couplings J_{DA}^c, J_{DA}^v , it is convenient to schematically represent exciton wave functions $\psi_{(i\alpha_i)(j\beta_j)}^{x(0)}$ and $\psi_{(i\alpha_i)(j\beta_j)}^x$ in the coordinate space. For the clarity of the discussion, we assume that we have only one single-electron and single-hole state per site throughout the system. This assumption does not compromise the validity of the conclusions to be presented in the case of more single-particle states per site. On the abscissa of our coordinate space is the hole coordinate, while the electron coordinate is on the ordinate.

The wave functions of exciton states $x^{(0)}$ of the noninteracting heterojunction are confined to a single quadrant of our coordinate space, see Figure 2a. For example, the wave

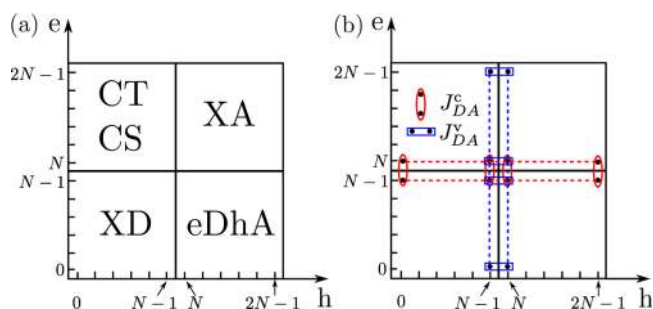


Figure 2. (a) At the noninteracting heterojunction, the wave function of each exciton state is confined to a single quadrant in the position space of the electron and hole. (b) The points at which the sums in eq 26 are evaluated: the points relevant to the computation of the first and the second sum are grouped by red ellipses, the points relevant to the computation of the third and the fourth sum are grouped by blue rectangles.

function of a donor exciton state is nonzero only when both electron and hole coordinates are between 0 and $N - 1$, and similarly for other groups of exciton states. Because of the D/A interaction H_{DA} (eq 21), exciton states x of the interacting heterojunction are mixtures of different exciton states $x^{(0)}$ of the noninteracting heterojunction, see eq 22. Therefore, the wave function of a general exciton state at the interacting heterojunction is not confined to the quadrant which is in Figure 2a labeled by its prevalent character, but is nonzero also in other quadrants. The D/A interaction H_{DA} is written in the noninteracting-heterojunction exciton basis as

$$H_{\text{DA}} = \sum_{\bar{x}^{(0)}, x^{(0)}} h_{\bar{x}^{(0)}, x^{(0)}} |\bar{x}^{(0)}\rangle \langle x^{(0)}| \quad (25)$$

with

$$\begin{aligned} h_{\bar{x}^{(0)}, x^{(0)}} = & -J_{\text{DA}}^{\text{c}} \sum_{k\alpha_k} \psi_{(k\alpha_k)(N-1, \beta_{N-1})}^{\bar{x}^{(0)*}} \psi_{(k\alpha_k)(N\beta_N)}^{x^{(0)}} \\ & - J_{\text{DA}}^{\text{c}} \sum_{k\alpha_k} \psi_{(k\alpha_k)(N\beta_N)}^{\bar{x}^{(0)*}} \psi_{(k\alpha_k)(N-1, \beta_{N-1})}^{x^{(0)}} \\ & + J_{\text{DA}}^{\text{v}} \sum_{k\beta_k} \psi_{(N-1, \alpha_{N-1})(k\beta_k)}^{\bar{x}^{(0)*}} \psi_{(N\alpha_N)(k\beta_k)}^{x^{(0)}} \\ & + J_{\text{DA}}^{\text{v}} \sum_{k\beta_k} \psi_{(N\alpha_N)(k\beta_k)}^{\bar{x}^{(0)*}} \psi_{(N-1, \alpha_{N-1})(k\beta_k)}^{x^{(0)}} \end{aligned} \quad (26)$$

The points at which the sums in the last equation (disregarding band indices) are to be evaluated are presented in Figure 2b. The first two sums in eq 26 are nonzero only when one state is of XD, and the other is of space-separated character. Similarly, the other two sums in eq 26 are nonzero only when one state is of XA, and the other is of space-separated character. Therefore, if $J_{\text{DA}}^{\text{c}} \neq 0$ and $J_{\text{DA}}^{\text{v}} = 0$, XA states of the interacting heterojunction are identical to XA states of the noninteracting heterojunction, while XD (space-separated) states of the interacting heterojunction are generally combinations of XD and space-separated states of the noninteracting heterojunction. Similarly, if $J_{\text{DA}}^{\text{c}} = 0$ and $J_{\text{DA}}^{\text{v}} \neq 0$, XD states of the interacting heterojunction are identical to XD states of the noninteracting heterojunction, while XA (space-separated) states of the interacting heterojunction are generally combinations of XA and space-separated states of the noninteracting heterojunction.

The exact mechanism of this mixing is different in different parts of the exciton spectrum. Let us start with the lower-energy part of the spectrum, which contains space-separated states belonging to CT_0 and CT_1 bands. Single-electron states in the acceptor which originate from levels 0 and 1 do not exhibit strong resonant mixing with single-electron states in the donor, thanks to the large energy separation between these two groups of states. Therefore, the relevant partitioning of the interacting-carrier Hamiltonian H_{c} is the one embodied in eq 20. Coefficients $C_{xx}^{(0)}$ in the expansion of exciton state x (of the interacting heterojunction) in terms of exciton states $x^{(0)}$ (of the noninteracting heterojunction) are obtained as solutions to the eigenvalue problem

$$\sum_{x^{(0)}} (\delta_{x^{(0)}, \bar{x}^{(0)}} \hbar\omega_{x^{(0)}} + h_{\bar{x}^{(0)}, x^{(0)}}) C_{xx}^{(0)} = \hbar\omega_x C_{x\bar{x}}^{(0)} \quad (27)$$

Since $h_{\bar{x}^{(0)}, x^{(0)}}$ contains products of two exciton wave functions, $|h_{\bar{x}^{(0)}, x^{(0)}}|$ is generally much smaller than $|J_{\text{DA}}^{\text{c}}|$. Therefore, most of the states in the lower-energy part of the interacting heterojunction are almost identical to the respective states of the noninteracting heterojunction. However, whenever $|h_{\bar{x}^{(0)}, x^{(0)}}| \sim |\hbar\omega_{\bar{x}^{(0)}} - \hbar\omega_{x^{(0)}}|$, there exists at least one state of the interacting heterojunction which is a mixture of states $\bar{x}^{(0)}$ and $x^{(0)}$ (which have different characters!) of the noninteracting heterojunction. In other words, states $\bar{x}^{(0)}$ and $x^{(0)}$, which are virtually resonant in energy, exhibit resonant mixing to form the so-called bridge states of the interacting heterojunction. Apart from their dominant character, which is obtained as previously explained, bridge states also have nontrivial overlaps

with noninteracting-heterojunction states of other characters. For example, if $J_{\text{DA}}^{\text{c}} = 0$, all the bridge states of the interacting heterojunction are of mixed XD and space-separated character; if $J_{\text{DA}}^{\text{v}} = 0$, all the bridge states of the interacting heterojunction are of mixed XA and space-separated character; if both couplings are nonzero, bridge states of the interacting heterojunction are of mixed XD, XA, and space-separated character. The emergence of bridge states in the low-energy part of the exciton spectrum requires subtle energy alignment of exciton, i.e., two-particle, states. Bridge states formed by resonances between two-particle states are thus rather scarce. Having a certain amount of the donor character, bridge states acquire oscillator strengths from donor states and can thus be directly generated from the ground state. In the rest of our paper, it is convenient to consider as a bridge state any state (in the lower-energy part of the exciton spectrum) of dominant CS, CT, or XA character whose amount of donor character is at least 0.01.

On the other hand, in the high-energy region of the exciton spectrum, which contains space-separated states belonging to CT_2 and CT_3 bands, there is significant mixing between single-electron states in the acceptor stemming from levels 2 and 3 and single-electron states in the donor. In this case, instead of the decomposition of the interacting-carrier part of the Hamiltonian given in eq 20, it is more convenient to separate the carrier-carrier interaction (last three terms in eq 2) from the part describing noninteracting carriers (first two terms in eq 2). The latter part of the interacting-carrier Hamiltonian then gives rise to single-electron states of the whole heterojunction which are delocalized on both the donor and acceptor as a consequence of the resonant mixing between single-electron states in the two materials. Since one single-electron state of the entire system generally participates in many two-particle states, exciton states having at least one carrier delocalized throughout the heterojunction are ubiquitous in the high-energy region of the spectrum. They also generally have greater amount of donor character than the bridge states in the low-energy part of the spectrum, *vide infra*, making them easily accessible from the ground state by a (suitable) photoexcitation. The dominant character of these states can be different and to our further discussion are relevant space-separated (CT and CS) states of CT_2 and CT_3 bands with partial donor character, which will be further termed photon-absorbing charge-bridging (PACB) states. This term has been repeatedly used in the literature to denote space-separated states in which charges are delocalized throughout the system.^{28,37,38} We note that the PACB states within our model do not have any other immediate relationship with PACB states reported in ab initio studies of D/A interfaces apart from the charge-bridging property and relatively large oscillator strengths permitting their direct optical generation.

The bridge states owe their name to the fact that they indirectly connect, via phonon-assisted processes, a state of pure XD character to a state of pure space-separated character. In our model, these two states cannot be involved in a single-phonon-assisted process because of the form of exciton-phonon matrix elements $\Gamma_{xx}^{i,j}$ (eq 11), which contain products of exciton wave functions taken at the same point. Therefore, single-phonon-assisted transitions among exciton states of the same character are most intensive and probable. A state of pure XD character can, however, also be coupled (via processes mediated by a donor phonon) to a bridge state, which can then be coupled to a state of pure space-separated character (via single-phonon processes mediated by acceptor phonons).

In the remaining part of our study, we will for ease of presentation adopt the following classification of the exciton states. Since space-separated states belonging to CT₂ and CT₃ bands which are relevant to our study are PACB states, we will not discriminate between CT and CS states in CT₂ and CT₃ bands, but rather refer to all of them as PACB states. We will, however, distinguish between CS and CT states in CT₀ and CT₁ bands and, for brevity of discussion, we will denote them simply as CS and CT states. This classification facilitates the understanding of the role that PACB states play in ultrafast interfacial dynamics by enabling direct comparison between results obtained with all four and only two lower orbitals per acceptor site, *vide infra*. The comparison is plausible since there is a well-defined correspondence between XA, CT, and CS states in the lower-energy part of the exciton spectrum (four orbitals per acceptor site) and the corresponding states when only two orbitals per acceptor site are taken into account. The part of the exciton spectrum which is relevant for our study is shown in Figure 3.

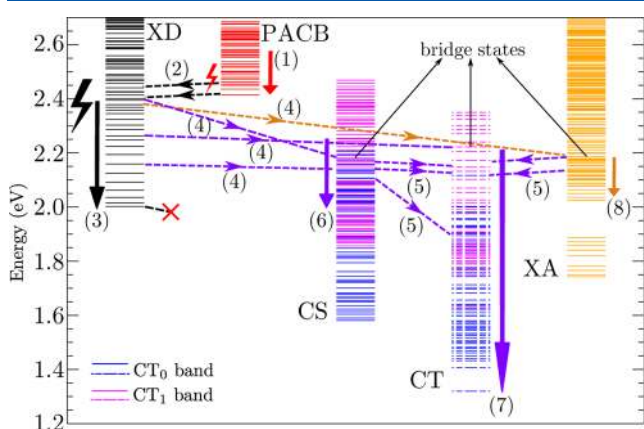


Figure 3. Exciton states relevant for our study divided in different groups. In the third (the fourth) column (from the left), blue and magenta lines denote CS (CT) states belonging to CT₀ and CT₁ band, respectively. Ultrafast exciton dynamics proceeds along the photophysical pathways denoted by (1)–(8), which are further specified in the Numerical Results section. The solid arrows [pathways (1), (3), (6), (7), and (8)] indicate the deexcitation processes occurring within one group of exciton states, whereas the dashed arrows [pathways (2), (4), and (5)] denote transitions among different groups of exciton states. The black (red) bolt denotes the direct photoexcitation of excitons in donor (PACB) states.

NUMERICAL RESULTS

In this section, we present results for the exciton dynamics at the model heterojunction during and after its pulsed excitation. The form of the excitation is

$$E(t) = E_0 \cos(\omega_c t) \exp\left(-\frac{t^2}{\tau_G^2}\right) \theta(t + t_0) \theta(t_0 - t) \quad (28)$$

where ω_c is its central frequency, $2t_0$ is its duration, τ_G is the characteristic time of the Gaussian envelope, and $\theta(t)$ is the Heaviside step function. In all the computations, we set $t_0 = 50$ fs and $\tau_G = 20$ fs. Computing the energy- and time-resolved exciton populations $\varphi_X(E, t)$ (eqs 16 and 17) or the exciton DOS, we represent δ functions by a Gaussian with the standard deviation of 10 meV.

We start with the analysis of the ultrafast exciton dynamics when model parameters assume the values listed in Table 1 and

the system is excited at the bright donor state located around $\hbar\omega_c = 2.35$ eV, which is significantly above the lowest donor state. We also present the results obtained taking into account only two lower single-electron levels (of energies $\epsilon_{A,0}^c$ and $\epsilon_{A,1}^c$) in the acceptor per site, while the values of all other model parameters are as listed in Table 1. The comparison of these results helps us understand the effects that the presence of two higher single-electron levels in the acceptor has on ultrafast exciton dynamics in our model.

In Figure 4a we show the time dependence of the total coherent exciton population $N_{\text{tot}}^{\text{coh}} = \sum_x |y_x|^2$, total incoherent exciton population $N_{\text{tot}}^{\text{incoh}} = \sum_x \bar{n}_{x,v}$ and total exciton population N_{tot} (eq 14). Exciting well above the lowest donor state, the conversion from coherent to incoherent exciton populations is rapid and is completed in a couple of tens of femtoseconds after the end of the pulsed excitation. Figure 5a–e presents density plots of energy- and time-resolved distributions $\varphi_X^{\text{coh}}(E, t)$ of coherent exciton populations for different groups of exciton states X . Comparing the ranges of color bars in Figure 5a–e, we conclude that the excitation predominantly generates donor excitons. We observe in Figure 5a that the initially populated donor states are the states located around 2.35 and 2.42 eV, together with the lowest donor state at around 2 eV. Even though we pump well above the lowest donor state, this state is prone to the direct optical generation because of its very large dipole moment M_x (eq 10) for direct generation from the ground state and the spectral width of the pulse. Apart from donor states, PACB states are also initially populated (see Figure 5b). In Figure 5c–e we see that energy positions of the bright spots in the density plots on the left correspond very well to the energy positions of red bars, which indicate bridge states of dominant CS, CT, and XA character, on the right. In other words, these states can be directly optically generated from the ground state, as already discussed.

The time dependence of normalized incoherent populations of different groups of exciton states is presented in Figure 4b. Figure 4c shows normalized incoherent populations in the model with only two accessible electronic states (of energies $\epsilon_{A,0}^c$ and $\epsilon_{A,1}^c$) at each acceptor site. Comparing panels b and c of Figure 4, we conclude that the presence of PACB states significantly affects exciton dynamics on ultrafast time scales. In the presence of only two lower electronic levels in the acceptor, the number of donor excitons decreases, while the numbers of CS, CT, and XA excitons increase after the excitation (see Figure 4c). On the other hand, taking into account the presence of higher-lying electronic orbitals in the acceptor and pumping well above the lowest donor exciton, the populations of XD, XA, CT, and CS states increase, while the population of PACB states decreases after the excitation. The fact that donor states acquire population after the end of the pulse may at first seem counterintuitive, since initially generated donor excitons are expected to dissociate, performing transitions to the space-separated manifold. Having significant amount of donor character, PACB states are well coupled (via single-phonon-assisted processes) to the manifold of donor excitons, while their coupling to space-separated states belonging to CT₀ and CT₁ bands is essentially negligible (see also the paragraph following eq 24). Therefore, instead of performing single-phonon-assisted transitions to lower-energy space-separated states, initially generated PACB excitons perform transitions toward donor states, i.e., the number of donor excitons increases at the expense of excitons initially generated in PACB states. While, at the end of the pulse, excitons in PACB states comprise

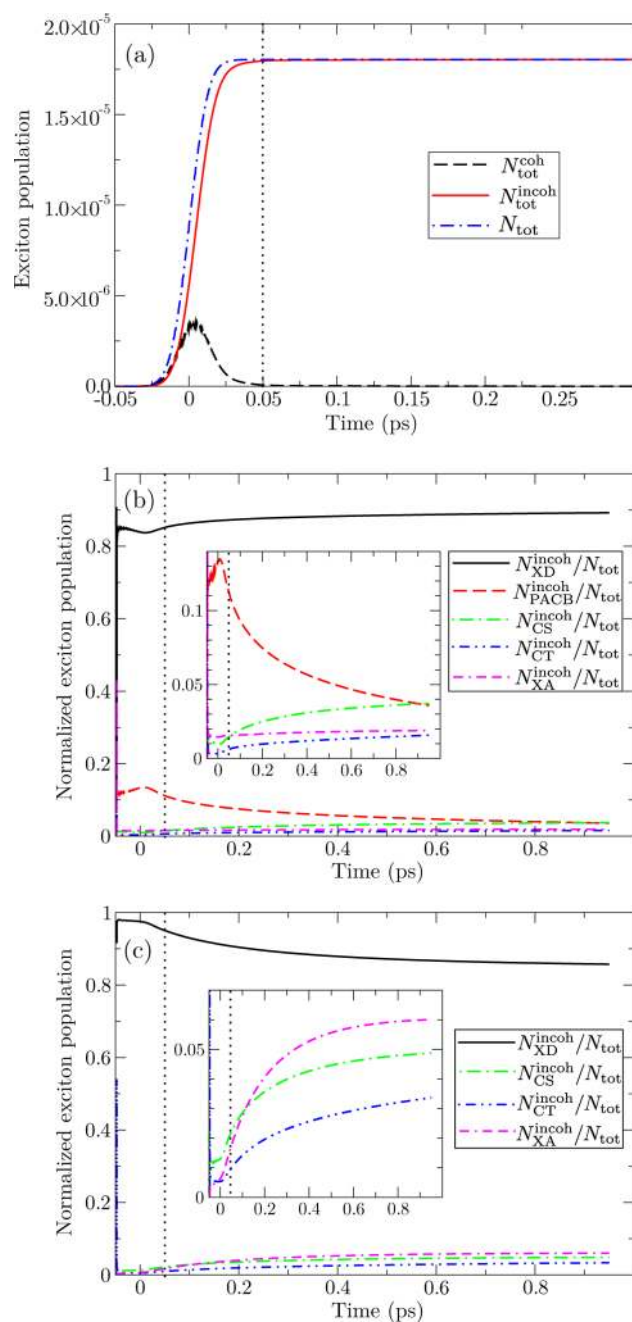


Figure 4. Time dependence of (a) the total exciton population and its coherent and incoherent parts, (b,c) normalized incoherent populations of different groups of exciton states. In panels a and b, we take four single-electron levels per acceptor site, while in panel c we take only two lower single-electron levels ($\epsilon_{A,0}^x$ and $\epsilon_{A,1}^x$) per acceptor site. The dotted vertical lines denote the end of the excitation.

around 11% of the total exciton population, 900 fs after the pulse their participation in the total population reduces to 4%. At the same time, the normalized number of donor excitons increases from around 85% to around 89% of the total exciton population, meaning that some of the donor excitons are converted into XA, CT, and CS states, which is seen in Figure 4b as the increase in the populations of these states.

In the model with four accessible electronic orbitals per acceptor site, the major part of space-separated states that are populated on 100 fs time scales following the excitation are directly generated PACB states. This conclusion is in line with

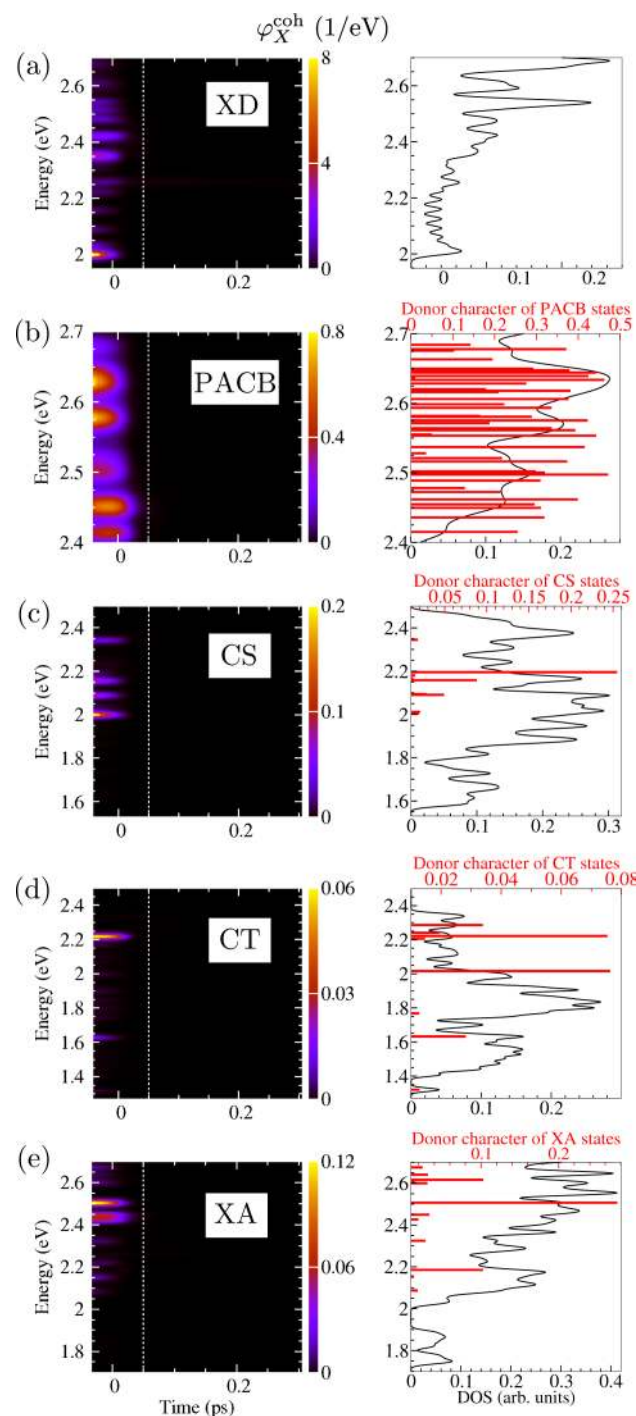


Figure 5. Density plots of $\varphi_X^{\text{coh}}(E,t)$ for (a) XD, (b) PACB, (c) CS, (d) CT, and (e) XA states. Each density plot is complemented with the plot of the corresponding exciton DOS. In panels b–e, exciton DOS plots contain amounts of the donor character of exciton states (see eq 23) [in panels c–e, as long as it is greater than 0.01].

our recent results regarding ultrafast photophysics in a model where the LUMO–LUMO offset is comparable to the effective bandwidth of the LUMO band of the acceptor.²⁷ Namely, we have recognized that the resonant mixing between single-electron states in the LUMO bands of the two materials is at the root of the ultrafast direct optical generation of space-separated charges. Here, the same mechanism is responsible for the observed direct generation of excitons in PACB states, which now acquire nonzero oscillator strengths due to the

energy alignment between single-electron states stemming from the donor LUMO orbital and higher-than-LUMO acceptor orbitals. On the contrary, if only electronic orbitals close to the LUMO orbital are taken into account, populations of space-separated states present on 100 fs time scales after the excitation mainly reside in bridge states, which are formed by two-particle resonant mixing. The populations of bridge states are dominantly built by phonon-assisted transitions from initially generated donor excitons (since the direct generation of excitons in bridge states is not very pronounced for the excitation studied). Therefore, in our model, the PACB states can enhance the generation of space-separated charges on ultrafast time scales by allowing for their direct optical generation and not by acting as intermediate states of charge separation starting from initial donor excitons.

In order to understand the photophysical pathways of ultrafast exciton dynamics, in Figure 6a–e we depict the density plots of $\varphi_X^{\text{incoh}}(E,t)$ for various groups X of exciton states. For the completeness of the discussion, in the Supporting Information we provide the density plots of $\varphi_X^{\text{incoh}}(E,t)$ in the model with only two lower electronic orbitals per acceptor site and compare them to the plots presented here. As already explained, the excitons initially generated in PACB states (red bolt in Figure 3) undergo deexcitation within the PACB manifold (pathway (1) in Figure 3) followed by phonon-mediated transitions toward the manifold of donor states (pathway (2) in Figure 3; see Figure 6b). Donor excitons (either the ones initially generated in higher-lying bright states (black bolt in Figure 3) or the ones originating from PACB excitons) are involved in a series of ultrafast phonon-assisted transitions toward lower-energy states. Most of these transitions happen within the XD manifold (pathway (3) in Figure 3; see the series of more or less bright bands in the density plot of Figure 6a), which is consistent with the fact that donor excitons comprise the largest part of the total exciton population at every instant. The deexcitation within the XD manifold proceeds until the lowest XD state is reached. In fact, we see that already for $t \gtrsim 250$ fs, XD population resides mainly in the lowest donor state at around 2 eV and the donor state at around 2.13 eV. The lowest donor state is almost uncoupled from the space-separated manifold, acting as a trap state for exciton dissociation, which is in line with other studies.²³ The other donor state (at around 2.13 eV) acting as a trap state for exciton dissociation is specific to our computation.

In the course of the deexcitation from the higher-lying donor states and before reaching a trap state for exciton dissociation, a donor exciton can perform a transition to a bridge state (pathway (4) in Figure 3). As seen in Figure 6c–e, the energy positions of the bright bands in the density plots on the left match exactly the energy positions of red bars displaying the amount of donor character of dominantly space-separated or XA states on the right. Figure 7b–d depicts probability distributions of the electron and hole in representative bridge states of different dominant characters, while Figure 7a shows the same quantities for particular PACB states. All the bridge states exhibit carrier delocalization throughout the system; this property makes them accessible from the initial states of donor excitons. The same holds for PACB states: since the carriers in these states are delocalized throughout the heterojunction, these states inherit oscillator strengths from donor excitons and may thus be directly accessed by an optical excitation. Moreover, this property enables efficient phonon-assisted coupling between PACB states and donor states. The bridge

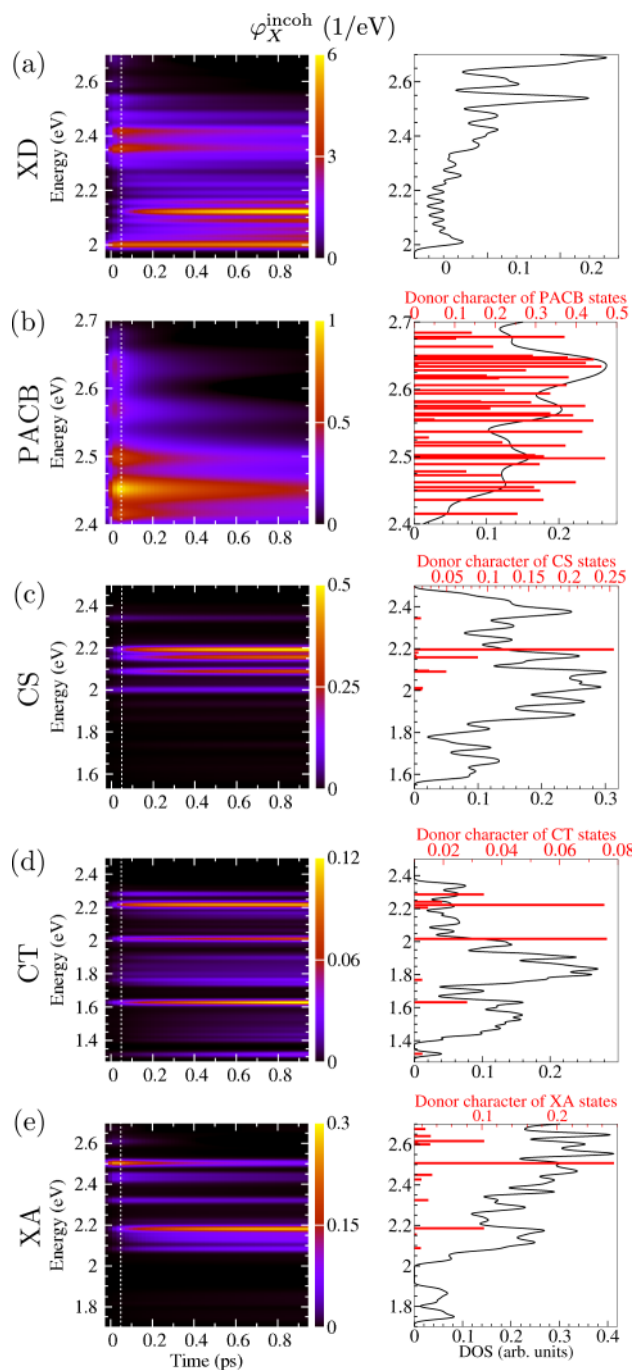


Figure 6. Density plots of $\varphi_X^{\text{incoh}}(E,t)$ for (a) XD, (b) PACB, (c) CS, (d) CT, and (e) XA states. Each density plot is accompanied by the plot of the corresponding exciton DOS. In panels b–e, the exciton DOS plots contain the amount of the donor character of exciton states (see eq 23) [in panels c–e, as long as it is greater than 0.01].

states gain significant populations during the first 100 fs following the excitation (pathway (4) in Figure 3) and concomitantly the excitons initially generated in PACB states perform phonon-mediated transitions toward donor states (pathway (2) in Figure 3).

Once the exciton has reached a bridge state, it can deexcite within the manifold of its dominant character (pathways (6)–(8) in Figure 3) or it can perform a transition to the CT manifold (pathway (5) in Figure 3) followed by a number of downward transitions within this manifold (pathway (7) in Figure 3; see the

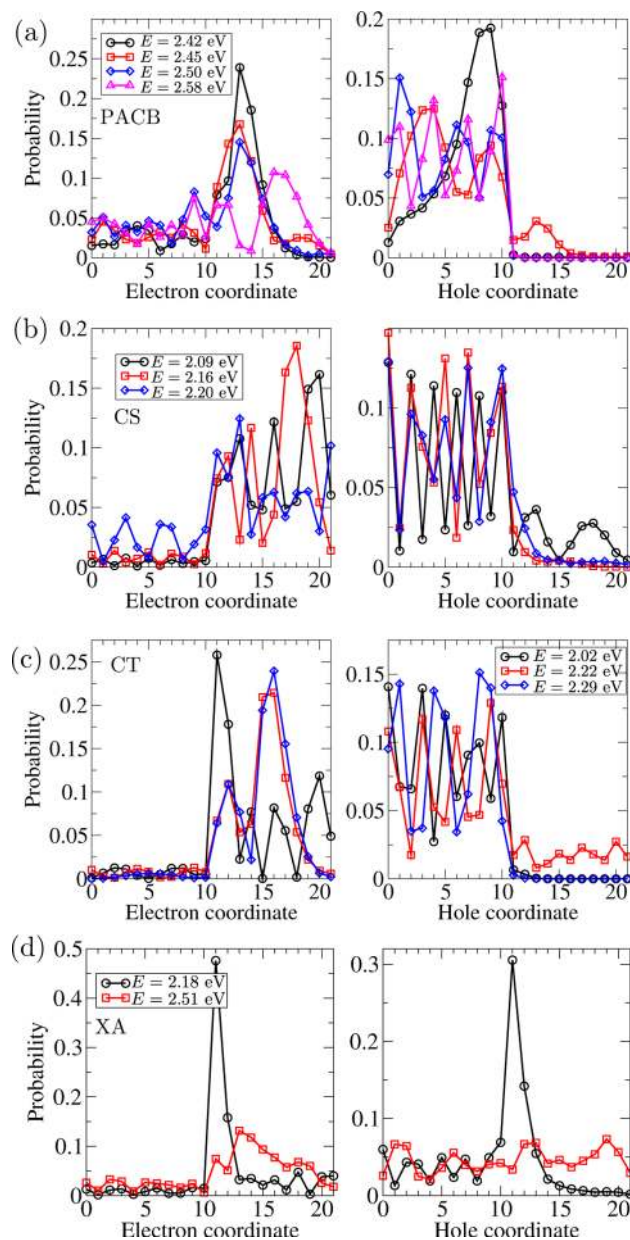


Figure 7. Probability distributions of the electron (left) and hole (right) in representative (a) PACB states and bridge states of dominant (b) CS, (c) CT, and (d) XA character.

series of more or less bright bands between 1.3 and 2.2 eV in the density plot of Figure 6d). The gradual deexcitation within the CT manifold leads to the delayed buildup of populations of low-energy CT states (pathway (7) in Figure 3; see bright bands at around 1.62 and 1.32 eV in the density plot in Figure 6d), which happens on a picosecond time scale. Apart from mediating the charge separation, bridge states can also act as competing final states. In our computation, at every instant, virtually all CS excitons reside in bridge states of dominant CS character, and the progressive deexcitation within the CS manifold (pathway (6) in Figure 3) is not pronounced (see Figure 6c). Analogous situation is observed analyzing the energy- and time-resolved populations of XA states (pathway (8) in Figure 3) in Figure 6e. This 2-fold role of bridge states observed in our computations is in agreement with conclusions of previous studies.²⁰

Ultrafast Exciton Dynamics for Various Central Frequencies. The exact photophysical pathways along which

the exciton dynamics proceeds on ultrafast time scales strongly depend on the frequency of the excitation, the exciton dissociation being more pronounced for larger excess energy.^{1,58} Here, we examine ultrafast exciton dynamics for three different excitations of central frequencies $\hbar\omega_c = 2.35, 2.25,$ and 2 eV (excitation at the lowest donor state). As the central frequency of the excitation is decreased, i.e., as the initially generated donor excitons are closer in energy to the lowest donor state, the conversion from coherent to incoherent exciton population is slower and the time scale on which exciton coherences with the ground state dominate the interfacial dynamics is longer (see Figure 8b). At the same time, the participation of excitons

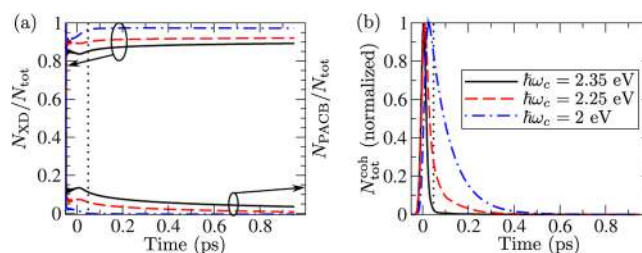


Figure 8. Time dependence of (a) the normalized number of excitons in donor and PACB states, and (b) the total coherent exciton population, for different central frequencies of the excitation. For convenience, the total coherent population shown in panel b is normalized so that its maximal value is equal to 1.

in PACB states in the total exciton population is decreased, whereas donor excitons comprise larger part of the total population (see Figure 8a). Namely, as the central frequency is lowered toward the lowest donor state, the initial optical generation of excitons in PACB states is less pronounced and the pathways (1) and (2) in Figure 3 become less important, while the possible photophysical pathways of the initially generated donor excitons become less diverse. Therefore, the phonon-assisted processes responsible for the conversion from coherent to incoherent exciton populations and for the ultrafast phonon-mediated transitions from donor states toward space-separated states are less effective. As a consequence, the conversion from coherent to incoherent exciton populations is slower, and initially generated donor excitons tend to remain within the manifold of donor states (pathway (3) in Figure 3, down to the lowest donor state, is preferred to pathways (4)–(7), which may lead to space-separated states). The latter fact is especially pronounced exciting at the lowest donor state, which is very weakly coupled to the space-separated manifold, when around 80% of the total exciton population lies in the lowest donor state, meaning that the ultrafast charge transfer upon excitation at this state is not significant. In the Supporting Information, we present the density plots of $\phi_X^{\text{incoh}}(E,t)$ for different groups of exciton states X and excitations of different central frequencies.

Influence of Small Variations of the LUMO–LUMO Offset on Ultrafast Exciton Dynamics. In this work, we deal with rather large LUMO–LUMO offsets, when the bridge states emerge as a consequence of the energy resonance between two-particle (exciton) states. The energies of these states, as well as their number and amount of the donor character, are therefore very sensitive to the particular exciton energy level alignment at the heterojunction. On the other hand, the properties of PACB states are not expected to be particularly sensitive to the details of the energy level alignment,

since they originate from resonances between single-electron states in the donor and acceptor. In order to demonstrate this difference between bridge states and PACB states, we performed computations with different, but very close, values of the LUMO–LUMO offset. The LUMO–LUMO offset is varied by changing all the parameters $\epsilon_{A,0}^c, \epsilon_{A,1}^c, \epsilon_{A,2}^c, \epsilon_{A,3}^c, \epsilon_{A,0}^v$ in Table 1 by the same amount, keeping all the other model parameters fixed. The effects of small variations of LUMO–LUMO offset are studied for $J_{DA}^v = 0$, when all the bridge states are of mixed XD and space-separated character and, since $d_A^{cv} = 0$, XA states do not participate in the ultrafast exciton dynamics. The exclusion of XA states from the dynamics significantly decreases the numerical effort and at the same time allows us to concentrate on the dynamics of ultrafast electron transfer, instead of considering both electron transfer and exciton transfer. The main qualitative features of the ultrafast exciton dynamics described earlier remain the same, as detailed in the Supporting Information.

The system is excited at $\hbar\omega_c = 2.35$ eV. Figure 9a presents the time dependence of the normalized number excitons in

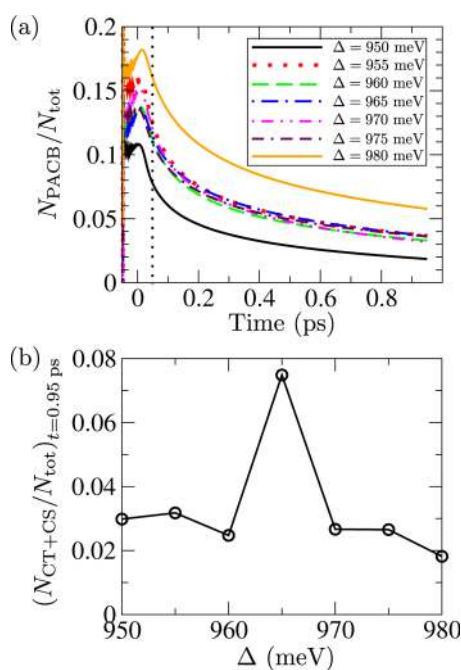


Figure 9. (a) Time dependence of the normalized number of PACB excitons for different LUMO–LUMO offsets Δ . (b) The relative number of excitons in space-separated (CT and CS) states 900 fs after the excitation for different LUMO–LUMO offsets Δ .

PACB states, while Figure 9b shows the normalized number of excitons in space-separated states 900 fs after the excitation for different LUMO–LUMO offsets ranging from 950 to 980 meV in steps of 5 meV. Small variations of the LUMO–LUMO offset between 955 and 975 meV weakly affect the portion of PACB excitons in the total exciton population. However, for the LUMO–LUMO offset of 980 meV, the normalized number of excitons in PACB states is somewhat higher than for the other considered values, while this number is somewhat smaller for the LUMO–LUMO offset of 950 meV. Namely, for larger LUMO–LUMO offsets, the lowest state of CT_2 band is closer to the central frequency of the excitation, and the direct optical generation of excitons in PACB states is more pronounced. For smaller LUMO–LUMO offsets, the initial generation of

excitons in PACB states is to a certain extent suppressed because the energy difference between the lowest state of CT_2 band and the central frequency of the excitation is larger. On the other hand, the relative number of space-separated excitons can change up to three times as a result of small changes in the LUMO–LUMO offset. The different behavior displayed by the relative numbers of PACB excitons and space-separated excitons is a consequence of different mechanisms by which PACB states and bridge states emerge. The peak in the normalized number of space-separated excitons observed for the LUMO–LUMO offset of 965 meV signals that the exciton-level alignment at this point favors either (i) formation of more bridge states of dominant space-separated character than at other points or (ii) formation of bridge states that couple more strongly to initial donor states than bridge states at other points.

Influence of Carrier–Phonon Interaction Strength and Temperature on Ultrafast Exciton Dynamics.

We have analyzed the ultrafast exciton dynamics for different strengths of the carrier–phonon coupling, exciting the system at $\hbar\omega_c = 2.35$ eV. The polaron binding energy ϵ_{pol}^b (eq 18), which is a measure of the carrier–phonon interaction strength, assumes values of 20, 50, and 70 meV.

Since the carrier–phonon interaction mediates the conversion from coherent to incoherent exciton populations, weaker carrier–phonon coupling makes this conversion somewhat slower (see Figure 10a). We note that, for all the interaction strengths considered, the total coherent population decays 100 times (compared to its maximal value) in $\lesssim 100$ fs following the excitation, meaning that the conversion is in all three cases relatively fast.

The normalized number of excitons in PACB states is smaller for stronger carrier–phonon interaction (see Figure 10b). The characteristic time scale for the decay of the population of PACB states is shorter for stronger carrier–phonon interaction, which is a consequence of stronger phonon-mediated coupling among PACB states and donor states (pathway (2) in Figure 3). For larger interaction strength, the populations of CS and CT states comprise larger part of the total exciton population (see Figure 10d,e). Namely, the stronger the carrier–phonon interaction, the more probable the transitions from donor excitons to bridge states (pathway (4) in Figure 3) and the larger the populations of CS and CT states (pathways (5)–(7) in Figure 3). The relative number of acceptor excitons does not change very much with the carrier–phonon interaction strength (see Figure 10b). The variation in the relative number of donor excitons brought about by the changes in the interaction strength is governed by a number of competing factors. First, stronger carrier–phonon interaction favors larger number of donor excitons, since phonon-assisted transitions from PACB to XD states (pathway (2) in Figure 3) are more pronounced. Second, for stronger interaction, the transitions from XD to bridge states are more probable (pathway (4) in Figure 3). Third, since phonon-mediated transitions are most pronounced between exciton states of the same character, stronger interaction may also favor deexcitation of donor populations within the XD manifold (down to the lowest XD state, pathway (3) in Figure 3) to possible transitions (via bridge states) to the space-separated manifold (pathways (4)–(7) in Figure 3). From Figure 10c we see that, as a result of all these factors, the relative number of donor excitons does not change monotonously with the interaction strength.

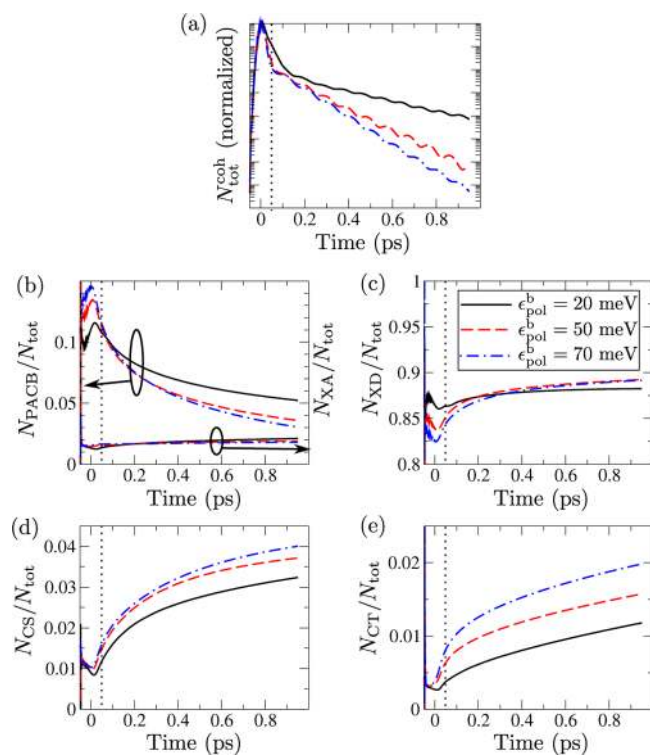


Figure 10. (a) Time dependence of the total coherent exciton population $N_{\text{tot}}^{\text{coh}}$ for different carrier–phonon interaction strengths. For convenience, $N_{\text{tot}}^{\text{coh}}$ is normalized so that its maximum assumes the same value for all studied interaction strengths. Dynamics of normalized incoherent excitation populations of (b) PACB and XA, (c) XD, (d) CS, and (e) CT states, for different interaction strengths.

In order to understand how the changes in carrier–phonon interaction strength affect the photophysical pathways along which the ultrafast exciton dynamics proceeds, in Figure 11a–l we present energy- and time-resolved incoherent populations of various groups of exciton states (in different rows) and for different interaction strengths (in different columns).

While for the strongest studied interaction initially generated higher-lying donor excitons and excitons in PACB states leave the initial states rapidly (see Figure 11i,j), for the weakest studied interaction strength, significant exciton population remains in these states during the first picosecond of the exciton dynamics (see Figure 11a,b). The deexcitation of donor excitons takes place predominantly within the XD manifold (pathway (3) in Figure 3) for all three interaction strengths (compare the ranges of color bars in Figure 11a,e,i). For the weakest studied interaction, the lowest donor state, which is a trap for the exciton dissociation, is largely bypassed in the course of the deexcitation, whereas for stronger carrier–phonon interactions, this state acquires significant population already from the beginning of the excitation. Energy- and time-resolved populations of CS states are very nearly the same for all three interaction strengths studied (see Figure 11c,g,k). The major part of the CS population resides in bridge states, and the deexcitation within the subset of CS states (pathway (6) in Figure 3) is not very pronounced. On the other hand, the deexcitation within the subset of CT states (pathway (7) in Figure 3), down to the lowest CT state, is observed for all the interaction strengths considered (see the series of more or less bright bands in Figure 11d,h,l). While for the weakest interaction the largest portion of the CT population resides in

the bridge state of CT character located at around 2.2 eV, for the strongest interaction, the major part of the CT population is located in the lowest state of CT_1 band at around 1.63 eV.

The carrier–phonon coupling thus acts in two different ways. On the one hand, stronger carrier–phonon interaction enhances exciton dissociation and subsequent charge separation by (i) enabling phonon-assisted transitions from a donor state to space-separated states via bridge states (pathways (4) and (5) in Figure 3) and (ii) enabling phonon-assisted transitions within the space-separated manifold once a space-separated state is reached (pathways (6) and (7) in Figure 3). On the other hand, stronger carrier–phonon coupling is detrimental to exciton dissociation and further charge separation because (i) it makes donor states more easily accessible from initially generated PACB excitons (pathway (2) in Figure 3), and, similarly, it may favor backward transitions from a bridge state to a donor state with respect to transitions to the space-separated manifold and (ii) downward phonon-assisted transitions make low-energy CT states, which are usually considered as traps for charge separation, populated on a picosecond time scale following the excitation (pathway (7) in Figure 3).

In the Supporting Information we examine the temperature dependence of the ultrafast heterojunction dynamics. We find that the effect of temperature variations on exciton dynamics occurring on subpicosecond time scales is not particularly pronounced, as has been repeatedly recognized in the literature.^{59–61}

DISCUSSION AND CONCLUSION

Using a relatively simple, but physically grounded model of an all-organic heterointerface, we have investigated subpicosecond dynamics of exciton dissociation and charge separation in the framework of the density matrix theory complemented with the DCT scheme. Our model is constructed as an effective model intended to describe the dynamics of excitation transport in the direction perpendicular to the interface, and it is parametrized using the literature data for the P3HT/PCBM blend.

Apart from the electronic states of the fullerene aggregate that originate from molecular orbitals close to the LUMO orbital of PCBM, we also account for the electronic states stemming from orbitals situated at around 1 eV above the LUMO orbital. Our analysis reveals the importance of the space-separated states that inherit nonzero oscillator strengths from donor states (bridge states and PACB states) and exhibit charge delocalization in ultrafast exciton dynamics. Depending on the energy region of the exciton spectrum, the origin of these states is different. In the low-energy region of the spectrum, bridge states are formed as a consequence of the resonant mixing among exciton (i.e., two-particle) states, while in the opposite part of the spectrum the resonant mixing between single-electron states in the two materials brings about the formation of PACB states.

The resonant mixing has been suggested to be the key physical mechanism responsible for the presence of separated charges on ultrafast time scales following the excitation of a D/A heterojunction.^{1,11,12,62–65} Employing the model of reduced dimensionality and studying its subpicosecond dynamics on a fully quantum level, we reach similar conclusions, and thus believe that our one-dimensional model is capable of describing the essential physics behind ultrafast interfacial processes. Our one-dimensional model does not provide a detailed description of, e.g., the role of fullerene cluster size and packing in the ultrafast dynamics. However, it takes into account the most important consequences of the aforementioned effects, i.e., the

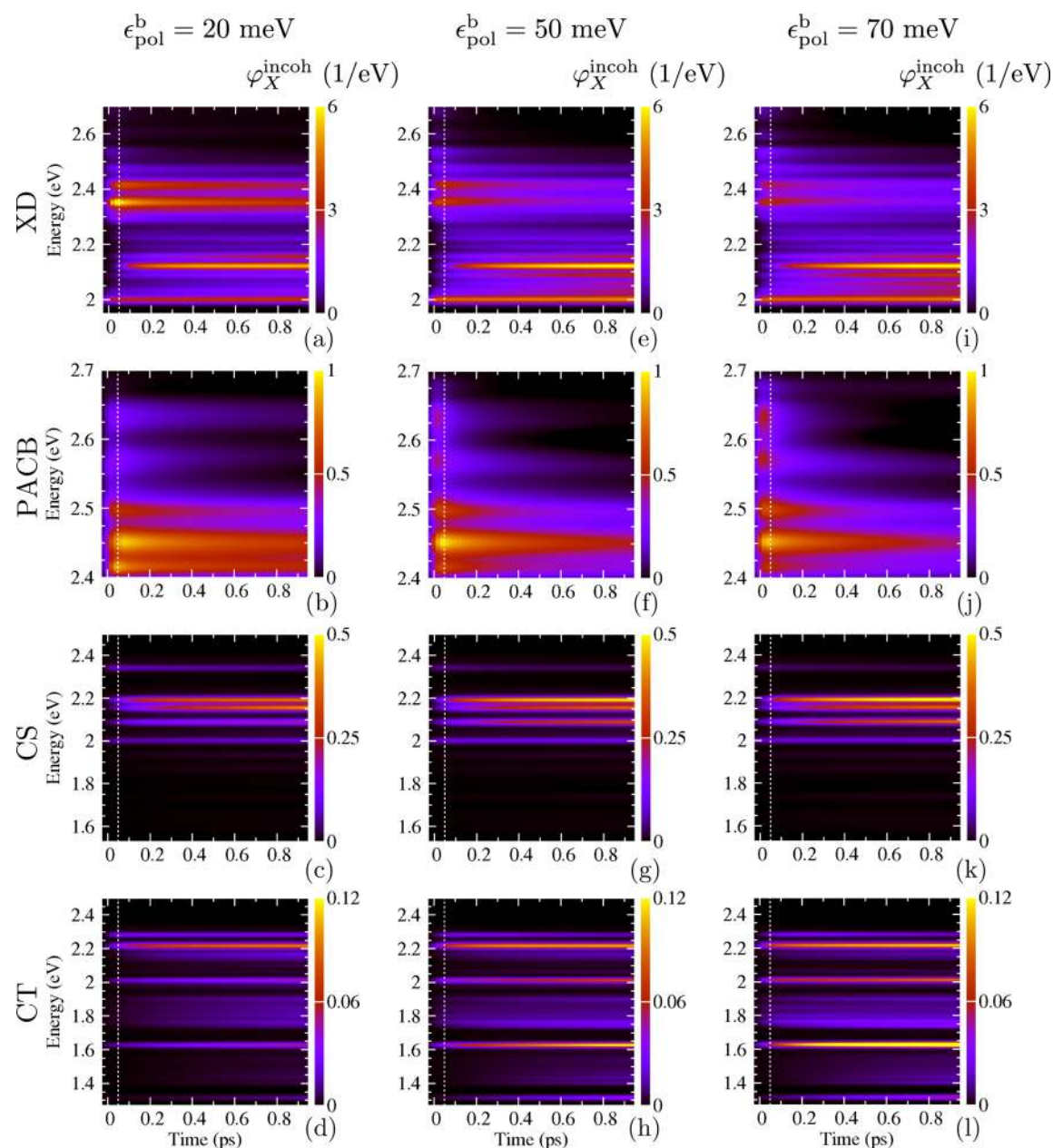


Figure 11. Energy- and time-resolved incoherent exciton populations $\phi_X^{\text{incoh}}(E, t)$ for different carrier–phonon interaction strengths: (a–d) $g_1 = 26.7$ meV, $g_2 = 59.7$ meV; (e–h) $g_1 = 42.2$ meV, $g_2 = 94.3$ meV; (i–l) $g_1 = 54.0$ meV, $g_2 = 111.6$ meV. Groups of exciton states: (a,e,i) XD states; (b,f,j) PACB states; (c,g,k) CS states; (d,h,l) CT states.

delocalization of electronic states and the accessibility of delocalized states of space-separated charges from the states of donor excitons.⁶⁴ The effects of the dimensionality of the model become crucial on somewhat longer time and length scales. Namely, on $\gtrsim 10$ ps time scales, the diffusion-controlled charge separation by incoherent hops throughout the respective materials takes place,⁶⁶ and one has to take into consideration all possible separation paths the electron and hole can follow, which can be done correctly only within a three-dimensional model of the heterojunction. The effects of electric polarization and screening at realistic interfaces are rather complex and strongly dependent on the details of the interface.⁶⁷ Here, however, we take a minimal model of the electron–hole interaction that reproduces the most important features of the energetics of exciton states obtained from experimental data or from more sophisticated models of polarization and screening

at interfaces. In that sense, our model can be considered as an effective model whose parameters were adjusted to yield realistic energetics of relevant exciton states.

While the PACB states in our model enhance ultrafast charge separation by acting as additional interfacial photon-absorbing states, the most important characteristic of the bridge states is not their direct accessibility from the ground state, but their good coupling with the manifold of donor states. Therefore, for donor excitons, the bridge states act as gateways to the space-separated manifold, so that the populations of low-lying space-separated states are built by progressive deexcitation within the space-separated manifold on a picosecond time scale following the excitation.

The ultrafast exciton dynamics strongly depends on the central frequency of the excitation. While exciting well above the lowest donor state, there are a number of photophysical

pathways enabling subpicosecond exciton dissociation, exciting at the lowest donor state, the major part of generated excitons reside in this state, and ultrafast exciton dissociation is not pronounced. Stronger carrier–phonon interaction enhances phonon-mediated transitions from donor states to bridge states and is thus beneficial to exciton dissociation on ultrafast time scales.

Our results indicate that the number of space-separated charges that are present 1 ps after photoexcitation is rather small, being typically less than 10% of the number of excited electron–hole pairs (see, e.g., Figures 4 and 10). On the other hand, in most efficient solar cell devices internal quantum efficiencies (IQE) close to 100% have been reported. In light of an ongoing debate on the origin of high IQE and the time scale necessary for the charge separation process to occur, our results indicate that longer time scales are needed to separate the charges. Many of the photophysical pathways that we identify eventually lead to occupation of low-lying CT states (e.g., in Figure 3, the pathway starting from initial donor excitons (black bolt) [\rightarrow (3)] \rightarrow (4) \rightarrow (5) \rightarrow (7) or the pathway starting from initial PACB excitons (red bolt) [\rightarrow (1)] \rightarrow (2) [\rightarrow (3)] \rightarrow (4) \rightarrow (5) \rightarrow (7)). We also find that on subpicosecond time scales a large portion of excitons remains in donor states. Therefore, a mechanism that leads to escape of charges from low-lying CT states and donor states on longer time scales and consequently to high IQE needs to exist. Several recent experimental^{68,69} and theoretical^{70–72} studies have provided evidence that the separation of charges residing in these states is indeed possible. Along these lines, our model could potentially be part of a multiscale model of the OPV devices, as it yields the populations of different states at \sim 1 ps after photoexcitation. The output of our model could then be used as input for a semiclassical model that would consider the charge separation and transport on a longer time scale.

■ ASSOCIATED CONTENT

Supporting Information

The Supporting Information is available free of charge on the ACS Publications website at DOI: 10.1021/acs.jpcc.7b05582.

Equations of motion for active density matrices and further details on ultrafast exciton dynamics complementing the main discussion (PDF)

■ AUTHOR INFORMATION

Corresponding Author

*E-mail: nenad.vukmirovic@ipb.ac.rs; Phone: +381 (0)11 3713152.

ORCID

Veljko Janković: 0000-0002-0297-2167

Notes

The authors declare no competing financial interest.

■ ACKNOWLEDGMENTS

We gratefully acknowledge the support by the Ministry of Education, Science and Technological Development of the Republic of Serbia (Project No. ON171017) and the European Commission under H2020 project VI-SEEM, Grant No. 675121, as well as the contribution of the COST Action MP1406. Numerical computations were performed on the PARADOX supercomputing facility at the Scientific Computing Laboratory of the Institute of Physics Belgrade.

■ REFERENCES

- (1) Grancini, G.; Maiuri, M.; Fazzi, D.; Petrozza, A.; Egelhaaf, H.-J.; Brida, D.; Cerullo, G.; Lanzani, G. Hot Exciton Dissociation in Polymer Solar Cells. *Nat. Mater.* **2013**, *12*, 29–33.
- (2) Jaiilaubekov, A. E.; Willard, A. P.; Tritsch, J. R.; Chan, W.-L.; Sai, N.; Gearba, R.; Kaake, L. G.; Williams, K. J.; Leung, K.; Rossky, P. J.; et al. Hot Charge-Transfer Excitons Set the Time Limit for Charge Separation at Donor/Acceptor Interfaces in Organic Photovoltaics. *Nat. Mater.* **2013**, *12*, 66–73.
- (3) Gélinas, S.; Rao, A.; Kumar, A.; Smith, S. L.; Chin, A. W.; Clark, J.; van der Poll, T. S.; Bazan, G. C.; Friend, R. H. Ultrafast Long-Range Charge Separation in Organic Semiconductor Photovoltaic Diodes. *Science* **2014**, *343*, 512–516.
- (4) Paracattil, A. A.; Banerji, N. Charge Separation Pathways in a Highly Efficient Polymer: Fullerene Solar Cell Material. *J. Am. Chem. Soc.* **2014**, *136*, 1472–1482.
- (5) Clarke, T. M.; Durrant, J. R. Charge Photogeneration in Organic Solar Cells. *Chem. Rev.* **2010**, *110*, 6736–6767.
- (6) Deibel, C.; Strobel, T.; Dyakonov, V. Role of the Charge Transfer State in Organic Donor-Acceptor Solar Cells. *Adv. Mater.* **2010**, *22*, 4097–4111.
- (7) Gao, F.; Inganäs, O. Charge Generation in Polymer-Fullerene Bulk-Heterojunction Solar Cells. *Phys. Chem. Chem. Phys.* **2014**, *16*, 20291–20304.
- (8) Few, S.; Frost, J. M.; Nelson, J. Models of Charge Pair Generation in Organic Solar Cells. *Phys. Chem. Chem. Phys.* **2015**, *17*, 2311–2325.
- (9) Bässlér, H.; Köhler, A. "Hot or Cold": How do Charge Transfer States at the Donor-Acceptor Interface of an Organic Solar Cell Dissociate? *Phys. Chem. Chem. Phys.* **2015**, *17*, 28451–28462.
- (10) Ostroverkhova, O. Organic Optoelectronic Materials: Mechanisms and Applications. *Chem. Rev.* **2016**, *116*, 13279–13412.
- (11) Troisi, A. How Quasi-Free Holes and Electrons are Generated in Organic Photovoltaic Interfaces. *Faraday Discuss.* **2013**, *163*, 377–392.
- (12) Vázquez, H.; Troisi, A. Calculation of Rates of Exciton Dissociation into Hot Charge-Transfer States in Model Organic Photovoltaic Interfaces. *Phys. Rev. B: Condens. Matter Mater. Phys.* **2013**, *88*, 205304.
- (13) Bakulin, A. A.; Rao, A.; Pavelyev, V. G.; van Loosdrecht, P. H. M.; Pshenichnikov, M. S.; Niedzialek, D.; Cornil, J.; Beljonne, D.; Friend, R. H. The Role of Driving Energy and Delocalized States for Charge Separation in Organic Semiconductors. *Science* **2012**, *335*, 1340–1344.
- (14) Savoie, B. M.; Rao, A.; Bakulin, A. A.; Gelinias, S.; Movaghar, B.; Friend, R. H.; Marks, T. J.; Ratner, M. A. Unequal Partnership: Asymmetric Roles of Polymeric Donor and Fullerene Acceptor in Generating Free Charge. *J. Am. Chem. Soc.* **2014**, *136*, 2876–2884.
- (15) Nan, G.; Zhang, X.; Lu, G. Do "Hot" Charge-Transfer Excitons Promote Free Carrier Generation in Organic Photovoltaics? *J. Phys. Chem. C* **2015**, *119*, 15028–15035.
- (16) Chen, K.; Barker, A. J.; Reish, M. E.; Gordon, K. C.; Hodgkiss, J. M. Broadband Ultrafast Photoluminescence Spectroscopy Resolves Charge Photogeneration via Delocalized Hot Excitons in Polymer-Fullerene Photovoltaic Blends. *J. Am. Chem. Soc.* **2013**, *135*, 18502–18512.
- (17) Tamura, H.; Burghardt, I. Ultrafast Charge Separation in Organic Photovoltaics Enhanced by Charge Delocalization and Vibronically Hot Exciton Dissociation. *J. Am. Chem. Soc.* **2013**, *135*, 16364–16367.
- (18) Smith, S. L.; Chin, A. W. Ultrafast Charge Separation and Nongeminate Electron-Hole Recombination in Organic Photovoltaics. *Phys. Chem. Chem. Phys.* **2014**, *16*, 20305–20309.
- (19) Sun, Z.; Stafström, S. Dynamics of Charge Separation at an Organic Donor-Acceptor Interface. *Phys. Rev. B: Condens. Matter Mater. Phys.* **2014**, *90*, 115420.
- (20) Tamura, H.; Ramon, J. G. S.; Bittner, E. R.; Burghardt, I. Phonon-Driven Ultrafast Exciton Dissociation at Donor-Acceptor Polymer Heterojunctions. *Phys. Rev. Lett.* **2008**, *100*, 107402.

- (21) Tamura, H.; Burghardt, I.; Tsukada, M. Exciton Dissociation at Thiophene/Fullerene Interfaces: The Electronic Structures and Quantum Dynamics. *J. Phys. Chem. C* **2011**, *115*, 10205–10210.
- (22) Tamura, H.; Martinazzo, R.; Ruckebauer, M.; Burghardt, I. Quantum Dynamics of Ultrafast Charge Transfer at an Oligothiophene-Fullerene Heterojunction. *J. Chem. Phys.* **2012**, *137*, 22A540.
- (23) Huix-Rotllant, M.; Tamura, H.; Burghardt, I. Concurrent Effects of Delocalization and Internal Conversion Tune Charge Separation at Regioregular Polythiophene-Fullerene Heterojunctions. *J. Phys. Chem. Lett.* **2015**, *6*, 1702–1708.
- (24) Bittner, E. R.; Silva, C. Noise-Induced Quantum Coherence Drives Photo-Carrier Generation Dynamics at Polymeric Semiconductor Heterojunctions. *Nat. Commun.* **2014**, *5*, 3119.
- (25) Smith, S. L.; Chin, A. W. Phonon-Assisted Ultrafast Charge Separation in the PCBM Band Structure. *Phys. Rev. B: Condens. Matter Mater. Phys.* **2015**, *91*, 201302.
- (26) Falke, S. M.; Rozzi, C. A.; Brida, D.; Maiuri, M.; Amato, M.; Sommer, E.; De Sio, A.; Rubio, A.; Cerullo, G.; Molinari, E.; et al. Coherent Ultrafast Charge Transfer in an Organic Photovoltaic Blend. *Science* **2014**, *344*, 1001–1005.
- (27) Janković, V.; Vukmirović, N. Origin of Space-Separated Charges in Photoexcited Organic Heterojunctions on Ultrafast Time Scales. *Phys. Rev. B: Condens. Matter Mater. Phys.* **2017**, *95*, 075308.
- (28) Kanai, Y.; Grossman, J. C. Insights on Interfacial Charge Transfer Across P3HT/Fullerene Photovoltaic Heterojunction from Ab Initio Calculations. *Nano Lett.* **2007**, *7*, 1967–1972.
- (29) Sheng, C.-Q.; Wang, P.; Shen, Y.; Li, Y.-J.; Zhang, W.-H.; Xu, F.-Q.; Zhu, J.-F.; Lai, G.-Q.; Li, H.-N. Electronic Structure of PCBM. *Chin. Phys. B* **2012**, *21*, 017102.
- (30) Idé, J.; Fazzi, D.; Casalegno, M.; Meille, S. V.; Raos, G. Electron Transport in Crystalline PCBM-Like Fullerene Derivatives: A Comparative Computational Study. *J. Mater. Chem. C* **2014**, *2*, 7313–7325.
- (31) Liu, T.; Troisi, A. What Makes Fullerene Acceptors Special as Electron Acceptors in Organic Solar Cells and How to Replace Them. *Adv. Mater.* **2013**, *25*, 1038–1041.
- (32) Ma, H.; Troisi, A. Modulating the Exciton Dissociation Rate by up to More than Two Orders of Magnitude by Controlling the Alignment of LUMO + 1 in Organic Photovoltaics. *J. Phys. Chem. C* **2014**, *118*, 27272–27280.
- (33) Grancini, G.; Polli, D.; Fazzi, D.; Cabanillas-Gonzalez, J.; Cerullo, G.; Lanzani, G. Transient Absorption Imaging of P3HT:PCBM Photovoltaic Blend: Evidence For Interfacial Charge Transfer State. *J. Phys. Chem. Lett.* **2011**, *2*, 1099–1105.
- (34) Yi, Y.; Coropceanu, V.; Bredas, J.-L. A Comparative Theoretical Study of Exciton-Dissociation and Charge-Recombination Processes in Oligothiophene/Fullerene and Oligothiophene/Perylene diimide Complexes for Organic Solar Cells. *J. Mater. Chem.* **2011**, *21*, 1479–1486.
- (35) Liu, T.; Troisi, A. Absolute Rate of Charge Separation and Recombination in a Molecular Model of the P3HT/PCBM Interface. *J. Phys. Chem. C* **2011**, *115*, 2406–2415.
- (36) Li, Z.; Zhang, X.; Lu, G. Electron Structure and Dynamics at Poly(3-hexylthiophene)/Fullerene Photovoltaic Heterojunctions. *Appl. Phys. Lett.* **2011**, *98*, 083303.
- (37) Liu, T.; Cheung, D. L.; Troisi, A. Structural Variability and Dynamics of the P3HT/PCBM Interface and its Effects on the Electronic Structure and the Charge-Transfer Rates in Solar Cells. *Phys. Chem. Chem. Phys.* **2011**, *13*, 21461–21470.
- (38) Fujii, M.; Shin, W.; Yasuda, T.; Yamashita, K. Photon-Absorbing Charge-Bridging States in Organic Bulk Heterojunctions Consisting of Diketopyrrolopyrrole Derivatives and PCBM. *Phys. Chem. Chem. Phys.* **2016**, *18*, 9514–9523.
- (39) Axt, V.; Stahl, A. A Dynamics-Controlled Truncation Scheme for the Hierarchy of Density Matrices in Semiconductor Optics. *Z. Phys. B: Condens. Matter* **1994**, *93*, 195–204.
- (40) Axt, V. M.; Victor, K.; Stahl, A. Influence of a Phonon Bath on the Hierarchy of Electronic Densities in an Optically Excited Semiconductor. *Phys. Rev. B: Condens. Matter Mater. Phys.* **1996**, *53*, 7244–7258.
- (41) Axt, V. M.; Mukamel, S. Nonlinear Optics of Semiconductor and Molecular Nanostructures; A Common Perspective. *Rev. Mod. Phys.* **1998**, *70*, 145–174.
- (42) Janković, V.; Vukmirović, N. Dynamics of Exciton Formation and Relaxation in Photoexcited Semiconductors. *Phys. Rev. B: Condens. Matter Mater. Phys.* **2015**, *92*, 235208.
- (43) Král, K.; Khás, Z. Electron Self-Energy in Quantum Dots. *Phys. Rev. B: Condens. Matter Mater. Phys.* **1998**, *57*, R2061–R2064.
- (44) Menšík, M.; Pflieger, J.; Toman, P. Dynamics of Photogenerated Polarons and Polaron Pairs in P3HT Thin Films. *Chem. Phys. Lett.* **2017**, *677*, 87–91.
- (45) Bera, S.; Gheeraert, N.; Fratini, S.; Ciuchi, S.; Florens, S. Impact of Quantized Vibrations on the Efficiency of Interfacial Charge Separation in Photovoltaic Devices. *Phys. Rev. B: Condens. Matter Mater. Phys.* **2015**, *91*, 041107.
- (46) Sun, Z.; Stafström, S. Dynamics of Exciton Dissociation in Donor-Acceptor Polymer Heterojunctions. *J. Chem. Phys.* **2013**, *138*, 164905.
- (47) Cowan, S. R.; Banerji, N.; Leong, W. L.; Heeger, A. J. Charge Formation, Recombination, and Sweep-Out Dynamics in Organic Solar Cells. *Adv. Funct. Mater.* **2012**, *22*, 1116–1128.
- (48) Northrup, J. E. Atomic and Electronic Structure of Polymer Organic Semiconductors: P3HT, PQT, and PBTBT. *Phys. Rev. B: Condens. Matter Mater. Phys.* **2007**, *76*, 245202.
- (49) Maillard, A.; Rochefort, A. Structural and Electronic Properties of Poly(3-hexylthiophene) π -stacked Crystals. *Phys. Rev. B: Condens. Matter Mater. Phys.* **2009**, *79*, 115207.
- (50) Lan, Y.-K.; Huang, C.-I. A Theoretical Study of the Charge Transfer Behavior of the Highly Regioregular Poly-3-hexylthiophene in the Ordered State. *J. Phys. Chem. B* **2008**, *112*, 14857–14862.
- (51) Cheung, D. L.; McMahan, D. P.; Troisi, A. Computational Study of the Structure and Charge-Transfer Parameters in Low-Molecular-Mass P3HT. *J. Phys. Chem. B* **2009**, *113*, 9393–9401.
- (52) Street, R. A.; Hawks, S. A.; Khlyabich, P. P.; Li, G.; Schwartz, B. J.; Thompson, B. C.; Yang, Y. Electronic Structure and Transition Energies in Polymer-Fullerene Bulk Heterojunctions. *J. Phys. Chem. C* **2014**, *118*, 21873–21883.
- (53) Bhatta, R. S.; Tsige, M. Chain Length and Torsional Dependence of Exciton Binding Energies in P3HT and PTB7 Conjugated Polymers: A First-Principles Study. *Polymer* **2014**, *55*, 2667–2672.
- (54) Cheung, D. L.; Troisi, A. Theoretical Study of the Organic Photovoltaic Electron Acceptor PCBM: Morphology, Electronic Structure, and Charge Localization. *J. Phys. Chem. C* **2010**, *114*, 20479–20488.
- (55) Tamura, H.; Tsukada, M. Role of Intermolecular Charge Delocalization on Electron Transport in Fullerene Aggregates. *Phys. Rev. B: Condens. Matter Mater. Phys.* **2012**, *85*, 054301.
- (56) Lücke, A.; Ortmann, F.; Panhans, M.; Sanna, S.; Rauls, E.; Gerstmann, U.; Schmidt, W. G. Temperature-Dependent Hole Mobility and Its Limit in Crystal-Phase P3HT Calculated from First Principles. *J. Phys. Chem. B* **2016**, *120*, 5572–5580.
- (57) Cheng, Y.-C.; Silbey, R. J. A Unified Theory for Charge-Carrier Transport in Organic Crystals. *J. Chem. Phys.* **2008**, *128*, 114713.
- (58) Schulze, M.; Hänsel, M.; Tegeder, P. Hot Excitons Increase the Donor/Acceptor Charge Transfer Yield. *J. Phys. Chem. C* **2014**, *118*, 28527–28534.
- (59) Pensack, R. D.; Asbury, J. B. Beyond the Adiabatic Limit: Charge Photogeneration in Organic Photovoltaic Materials. *J. Phys. Chem. Lett.* **2010**, *1*, 2255–2263.
- (60) Chenel, A.; Mangaud, E.; Burghardt, I.; Meier, C.; Desouter-Lecomte, M. Exciton Dissociation at Donor-Acceptor Heterojunctions: Dynamics Using the Collective Effective Mode Representation of the Spin-Boson Model. *J. Chem. Phys.* **2014**, *140*, 044104.
- (61) Hughes, K. H.; Cahier, B.; Martinazzo, R.; Tamura, H.; Burghardt, I. Non-Markovian Reduced Dynamics of Ultrafast Charge

Transfer at an Oligothiophene-Fullerene Heterojunction. *Chem. Phys.* **2014**, *442*, 111–118.

(62) D'Avino, G.; Muccioli, L.; Olivier, Y.; Beljonne, D. Charge Separation and Recombination at Polymer-Fullerene Heterojunctions: delocalization and Hybridization Effects. *J. Phys. Chem. Lett.* **2016**, *7*, 536–540.

(63) Ma, H.; Troisi, A. Direct Optical Generation of Long-Range Charge-Transfer States in Organic Photovoltaics. *Adv. Mater.* **2014**, *26*, 6163–6167.

(64) Savoie, B. M.; Rao, A.; Bakulin, A. A.; Gelinas, S.; Movaghar, B.; Friend, R. H.; Marks, T. J.; Ratner, M. A. Unequal Partnership: Asymmetric Roles of Polymeric Donor and Fullerene Acceptor in Generating Free Charge. *J. Am. Chem. Soc.* **2014**, *136*, 2876–2884.

(65) Yao, Y.; Xie, X.; Ma, H. Ultrafast Long-Range Charge Separation in Organic Photovoltaics: Promotion by Off-Diagonal Vibronic Couplings and Entropy Increase. *J. Phys. Chem. Lett.* **2016**, *7*, 4830–4835.

(66) Vithanage, D. A.; Devižis, A.; Abramavičius, V.; Infahsaeng, Y.; Abramavičius, D.; MacKenzie, R. C. I.; Keivanidis, P. E.; Yartsev, A.; Hertel, D.; Nelson, J.; et al. Visualizing Charge Separation in Bulk Heterojunction Organic Solar Cells. *Nat. Commun.* **2013**, *4*, 2334.

(67) D'Avino, G.; Mothy, S.; Muccioli, L.; Zannoni, C.; Wang, L.; Cornil, J.; Beljonne, D.; Castet, F. Energetics of Electron-Hole Separation at P3HT/PCBM Heterojunctions. *J. Phys. Chem. C* **2013**, *117*, 12981–12990.

(68) Vandewal, K.; Albrecht, S.; Hoke, E. T.; Graham, K. R.; Widmer, J.; Douglas, J. D.; Schubert, M.; Mateker, W. R.; Bloking, J. T.; Burkhard, G. F.; et al. Efficient Charge Generation by Relaxed Charge-Transfer States at Organic Interfaces. *Nat. Mater.* **2014**, *13*, 63–68.

(69) Gerhard, M.; Arndt, A. P.; Bilal, M.; Lemmer, U.; Koch, M.; Howard, I. A. Field-Induced Exciton Dissociation in PTB7-Based Organic Solar Cells. *Phys. Rev. B: Condens. Matter Mater. Phys.* **2017**, *95*, 195301.

(70) Burke, T. M.; McGehee, M. D. How High Local Charge Carrier Mobility and an Energy Cascade in a Three-Phase Bulk Heterojunction Enable > 90% Quantum Efficiency. *Adv. Mater.* **2014**, *26*, 1923–1928.

(71) Hood, S. N.; Kassal, I. Entropy and Disorder Enable Charge Separation in Organic Solar Cells. *J. Phys. Chem. Lett.* **2016**, *7*, 4495–4500.

(72) Athanasopoulos, S.; Tscheuschner, S.; Bäessler, H.; Köhler, A. Efficient Charge Separation of Cold Charge-Transfer States in Organic Solar Cells Through Incoherent Hopping. *J. Phys. Chem. Lett.* **2017**, *8*, 2093–2098.

Origin of space-separated charges in photoexcited organic heterojunctions on ultrafast time scales

Veljko Janković* and Nenad Vukmirović†

Scientific Computing Laboratory, Center for the Study of Complex Systems, Institute of Physics Belgrade, University of Belgrade, Pregrevica 118, 11080 Belgrade, Serbia

(Received 29 December 2016; published 21 February 2017)

We present a detailed investigation of ultrafast (subpicosecond) exciton dynamics in the lattice model of a donor/acceptor heterojunction. Exciton generation by means of a photoexcitation, exciton dissociation, and further charge separation are treated on equal footing. The experimentally observed presence of space-separated charges at $\lesssim 100$ fs after the photoexcitation is usually attributed to ultrafast transitions from excitons in the donor to charge-transfer and charge-separated states. Here, we show, however, that the space-separated charges appearing on $\lesssim 100$ -fs time scales are predominantly directly optically generated. Our theoretical insights into the ultrafast pump-probe spectroscopy challenge usual interpretations of pump-probe spectra in terms of ultrafast population transfer from donor excitons to space-separated charges.

DOI: [10.1103/PhysRevB.95.075308](https://doi.org/10.1103/PhysRevB.95.075308)**I. INTRODUCTION**

The past two decades have seen rapidly growing research efforts in the field of organic photovoltaics (OPVs), driven mainly by the promise of economically viable and environmentally friendly power generation [1–5]. In spite of vigorous and interdisciplinary research activities, there is a number of fundamental questions that still have to be properly answered in order to rationally design more efficient OPV devices. It is commonly believed [1,6] that photocurrent generation in OPV devices is a series of the following sequential steps. Light absorption in the donor material creates an exciton, which subsequently diffuses towards the donor/acceptor (D/A) interface where it dissociates producing an interfacial charge transfer (CT) state. The electron and hole in this state are tightly bound and localized at the D/A interface. The CT state further separates into a free electron and a hole [the so-called charge-separated (CS) state], which are then transported to the respective electrodes. On the other hand, several recent spectroscopic studies [7–10] have indicated the presence of spatially separated electrons and holes on ultrafast ($\lesssim 100$ fs) time scales after the photoexcitation. These findings challenge the described picture of free-charge generation in OPV devices as the following issues arise. (i) It is not expected that an exciton created in the donor can diffuse in such a short time to the D/A interface since the distance it can cover in 100 fs is rather small compared to the typical size of phase segregated domains in bulk heterojunctions. [11] (ii) The mechanism by which a CT state would transform into a CS state is not clear. The binding energy of a CT exciton is rather large [6,12] and there is an energy barrier preventing it from the transition to a CS state, especially at such short time scales.

To resolve question (ii), many experimental [7,8,13,14] and theoretical [15–19] studies have challenged the implicit assumption that the lowest CT state is involved in the process. These studies emphasized the critical role of electronically hot (energetically higher) CT states as intermediate states before the transition to CS states. Having significantly larger

electron-hole separations, i.e., more delocalized carriers, compared to the interface-bound CT states, these hot CT states are also more likely to exhibit ultrafast charge separation and thus bypass the relaxation to the lowest CT state. The time scale of the described hot exciton dissociation mechanism is comparable to the time scale of hot CT exciton relaxation to the lowest CT state [8,18]. Other studies suggested that electron delocalization in the acceptor may reduce the Coulomb barrier [9,20,21] and allow the transition from CT to CS states. Experimental results of Vandewal *et al.* [22], who studied the consequences of the direct optical excitation of the lowest CT state, suggest that the charge separation can occur very efficiently from this state. To resolve issue (i), it has been proposed that a direct transition from donor excitons to CS states provides an efficient route for charge separation [23,24].

All the aforementioned studies implicitly assume that an optical excitation creates a donor exciton and address the mechanisms by which it can evolve into a CT or CS state on a ~ 100 -fs time scale. In this work, we demonstrate that the majority of space-separated charges that are present ~ 100 fs after photoexcitation are directly optically generated, in contrast to the usual belief that they originate from optical generation of donor excitons followed by some of the proposed mechanisms of transfer to CT or CS states. We note that in a recent theoretical work Ma and Troisi [25] concluded that space-separated electron-hole pairs significantly contribute to the absorption spectrum of the heterojunction, suggesting the possibility of their direct optical generation. A similar conclusion was also obtained in the most recent study of D'Avino *et al.* [26]. These works, however, do not provide information about the relative importance of direct optical generation of space-separated charges in comparison to other hypothesized mechanisms of their generation. On the other hand, in the framework of a simple, yet physically grounded model, we simulate the time evolution of populations of various exciton states during and after optical excitation. Working with a model Hamiltonian whose parameters have clear physical meanings, we are able to vary model parameters and demonstrate that these variations do not violate our principal conclusion that the space-separated charges present at ~ 100 fs following photoexcitation originate from direct optical generation. In addition, we numerically investigate the

*veljko.jankovic@ipb.ac.rs

†nenad.vukmirovic@ipb.ac.rs

ultrafast pump-probe spectroscopy and find that the signal on ultrafast time scales is dominated by coherences rather than by state populations. This makes the interpretation of the experimental spectra in terms of state populations rather difficult.

The paper is organized as follows. Section II introduces the model, its parametrization, and the theoretical treatment of ultrafast exciton dynamics. The central conclusion of our study is presented in Sec. III, where we also assess its robustness against variations of most of the model parameters. Section IV is devoted to the theoretical approach to ultrafast pump-probe experiments and numerical computations of the corresponding pump-probe signals. We discuss our results and draw conclusions in Sec. V.

II. THEORETICAL FRAMEWORK

In this section, we lay out the essential elements of the model (Sec. II A) and of the theoretical approach (Sec. II B) we use to study ultrafast exciton dynamics at a heterointerface. Section II C presents the parametrization of the model Hamiltonian and analyzes its spectrum.

A. One-dimensional lattice model of a heterojunction

In this study, a one-dimensional two-band lattice semiconductor model is employed to describe a heterojunction. It takes into account electronic couplings, carrier-carrier, and carrier-phonon interactions, as well as the interaction of carriers with the external electric field. There are $2N$ sites in total, see Fig. 2(a); first N sites (labeled by $0, \dots, N-1$) belong to the donor part of the heterojunction, while sites labeled by $N, \dots, 2N-1$ belong to the acceptor part. Each site i has one valence-band and one conduction-band orbital and also contributes localized phonon modes counted by index λ_i . The model Hamiltonian is pictorially presented in Fig. 1(a), the total Hamiltonian being

$$H = H_c + H_p + H_{c-p} + H_{c-f}. \quad (1)$$

Interacting carriers are described by

$$H_c = \sum_{i=0}^{2N-1} \left(H_c^i + H_h^i + \sum_{\substack{j=0 \\ j \neq i}}^{2N-1} (H_e^{ij} + H_h^{ij}) + \sum_{j=0}^{2N-1} H_{e-h}^{ij} \right), \quad (2)$$

the phonon Hamiltonian is

$$H_p = \sum_{i=0}^{2N-1} H_p^i, \quad (3)$$

the carrier-phonon interaction is

$$H_{c-p} = \sum_{i=0}^{2N-1} (H_{e-p}^i + H_{h-p}^i), \quad (4)$$

while the interaction of carriers with the external exciting field $E(t)$ is given as

$$H_{c-f} = \sum_{i=0}^{2N-1} H_{c-f}^i. \quad (5)$$

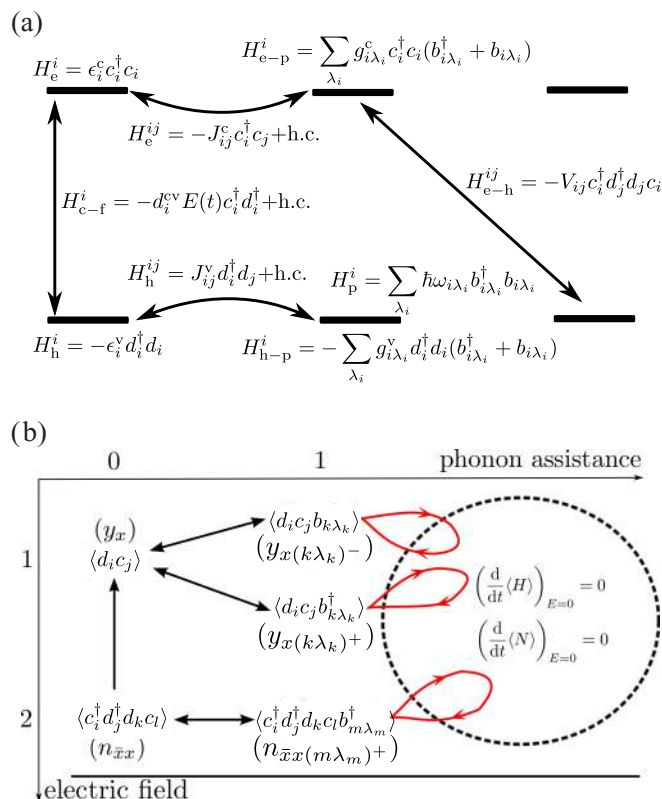


FIG. 1. (a) Illustration of the model Hamiltonian used in our study. (b) Active variables in the density matrix formalism and their interrelations in the resulting hierarchy of equations. The direction of a straight arrow indicates that in the equation for the variable at its start appears the variable at its end. Loops represent couplings to higher-order phonon-assisted density matrices which are truncated so that the particle number and energy of the free system are conserved.

In Fig. 1(a), Fermi operators c_i^\dagger and d_i^\dagger (c_i and d_i) create (destroy) electrons and holes on site i , whereas Bose operators $b_{i\lambda_i}^\dagger$ ($b_{i\lambda_i}$) create (destroy) phonons in mode λ_i on site i . ϵ_i^c and ϵ_i^v are electron and hole on-site energies, while J_{ij}^c and J_{ij}^v denote electron and hole transfer integrals, respectively. The carrier-phonon interaction is taken to be of the Holstein form, where a charge carrier is locally and linearly coupled to dispersionless optical modes, and $g_{i\lambda_i}^c$ and $g_{i\lambda_i}^v$ are the interaction strengths with electrons and holes, respectively. Electron-hole interaction is accounted for in the lowest monopole-monopole approximation and V_{ij} is the carrier-carrier interaction potential. Interband dipole matrix elements are denoted by d_i^{cv} .

B. Theoretical approach to exciton dynamics

We examine the ultrafast exciton dynamics during and after pulsed photoexcitation of a heterointerface in the previously developed framework of the density matrix theory complemented with the dynamics controlled truncation (DCT) scheme [27–29] (see Ref. [30] and references therein), starting from initially unexcited heterojunction. We confine ourselves to the case of weak optical field and low carrier densities, in which it is justified to work in the subspace of single-

exciton excitations (spanned by the so-called exciton basis) and truncate the carrier branch of the hierarchy of equations for density matrices retaining only contributions up to the second order in the optical field. The phonon branch of the hierarchy is truncated independently so as to ensure the particle-number and energy conservation after the pulsed excitation, as described in detail in Ref. [30].

In more detail, the exciton basis is obtained solving the eigenvalue problem

$$\sum_{i'j'} (\delta_{i'i} \epsilon_{jj'}^c - \delta_{j'j} \epsilon_{ii'}^v - \delta_{i'i} \delta_{j'j} V_{ij}) \psi_{i'j'}^x = \hbar \omega_x \psi_{ij}^x, \quad (6)$$

where indices i, i' (j, j') correspond to the position of the hole (electron) and quantities ϵ_{mn}^c (ϵ_{mn}^v) denote on-site electron (hole) energies (for $m = n$) or electron (hole) transfer integrals (for $m \neq n$) in the donor, in the acceptor, or between the donor and the acceptor. The creation operator for the exciton in the state x is then defined as

$$X_x^\dagger = \sum_{ij} \psi_{ij}^x c_j^\dagger d_i^\dagger. \quad (7)$$

As we pointed out [30], the total Hamiltonian, in which only contributions whose expectation values are at most of the second order in the optical field are kept, can be expressed in terms of exciton operators X_x^\dagger, X_x as

$$\begin{aligned} H = & \sum_x \hbar \omega_x X_x^\dagger X_x + \sum_{i\lambda_i} \hbar \omega_{i\lambda_i} b_{i\lambda_i}^\dagger b_{i\lambda_i} \\ & + \sum_{\substack{\bar{x}x \\ i\lambda_i}} (\Gamma_{\bar{x}x}^{i\lambda_i} X_{\bar{x}}^\dagger X_x b_{i\lambda_i}^\dagger + \Gamma_{\bar{x}x}^{i\lambda_i*} X_x^\dagger X_{\bar{x}} b_{i\lambda_i}) \\ & - E(t) \sum_x (M_x^* X_x + M_x X_x^\dagger), \end{aligned} \quad (8)$$

where the exciton-phonon coupling constants are given as

$$\Gamma_{\bar{x}x}^{i\lambda_i} = g_{i\lambda_i}^c \sum_j \psi_{ji}^{\bar{x}*} \psi_{ji}^x - g_{i\lambda_i}^v \sum_j \psi_{ij}^{\bar{x}*} \psi_{ij}^x, \quad (9)$$

while the dipole moment for the generation of the state x from the ground state is

$$M_x = \sum_i \psi_{ii}^{x*} d_i^{cv}. \quad (10)$$

Active variables in our formalism are the coherences between exciton state x and the ground state, $y_x = \langle X_x \rangle$, exciton populations (for $\bar{x} = x$), and exciton-exciton coherences (for $\bar{x} \neq x$) $n_{\bar{x}x} = \langle X_{\bar{x}}^\dagger X_x \rangle$, together with their single-phonon-assisted counterparts $y_{x(i\lambda_i)^-} = \langle X_x b_{i\lambda_i} \rangle$, $y_{x(i\lambda_i)^+} = \langle X_x b_{i\lambda_i}^\dagger \rangle$, and $n_{\bar{x}x(i\lambda_i)^+} = \langle X_{\bar{x}}^\dagger X_x b_{i\lambda_i}^\dagger \rangle$. Their mutual interrelations in the resulting hierarchy are schematically shown in Fig. 1(b), while the equations themselves are presented in Ref. [31]. In order to quantitatively monitor ultrafast processes at the model heterojunction during and after its pulsed photoexcitation, the incoherent population of exciton state x , which gives the number of truly bound (Coulomb-correlated) electron-hole pairs in the state x ,

$$\bar{n}_{xx} = n_{xx} - |y_x|^2, \quad (11)$$

will be used. Coherent populations of exciton states, $|y_x|^2$, dominate early stages of the optical experiment, typically decay quickly due to different scattering mechanisms (in our case, the carrier-phonon interaction), and do not represent bound electron-hole pairs. The populations of truly bound electron-hole pairs build up on the expense of coherent exciton populations. We frequently normalize \bar{n}_{xx} to the total exciton population in the system,

$$N_{\text{tot}} = \sum_x n_{xx}, \quad (12)$$

which, together with the expectation value of the Hamiltonian $\langle H \rangle$, is conserved in the absence of the external field. Probabilities $f_e(t, r)$ [$f_h(t, r)$] that an electron (a hole) is located at site r at instant t can be obtained using the so-called contraction identities (see, e.g., Ref. [29]) and are given as

$$f_e(t, r) = \frac{\sum_{\bar{x}x} (\sum_{r_h} \psi_{r_h r}^{\bar{x}*} \psi_{r_h r}^x) n_{\bar{x}x}(t)}{\sum_x n_{xx}(t)}, \quad (13)$$

$$f_h(t, r) = \frac{\sum_{\bar{x}x} (\sum_{r_e} \psi_{r r_e}^{\bar{x}*} \psi_{r r_e}^x) n_{\bar{x}x}(t)}{\sum_x n_{xx}(t)}. \quad (14)$$

Consequently, the probability that an electron is in the acceptor at time t is

$$P_A^e(t) = \sum_{r=N}^{2N-1} f_e(t, r). \quad (15)$$

C. Model parameters and Hamiltonian spectrum

The model Hamiltonian was parameterized to yield values of band gaps, bandwidths, band offsets, and exciton binding energies that are representative of typical OPV materials. The values of model parameters used in numerical computations are summarized in Table I. While these values largely correspond to the PCPDTBT/PCBM interface, we note that our goal is to reach general conclusions valid for a broad class of interfaces. Consequently, later in this study, we also vary most of the model parameters and study the effects of these variations. Figures 2(a) and 2(b) illustrate the meaning of some of the model parameters.

All electron and hole transfer integrals are restricted to nearest neighbors. The single-particle band gap of the donor $E_{g,D}$, as well as the offset ΔE_{DA}^c between the lowest single-electron levels in the donor and acceptor, assume values that are representative of the low-band-gap PCPDTBT polymer used in the most efficient solar cells [32,33]. The single-particle band gap of the acceptor $E_{g,A}$ and electron/hole transfer integrals $J_A^{c/v}$ are tuned to values typical of fullerene and its derivatives [34,35]. Electron/hole transfer integrals $J_D^{c/v}$ in the donor were extracted from the conduction and valence bandwidths of the PCPDTBT polymer. To obtain the bandwidths, an electronic structure calculation was performed on a straight infinite polymer. The calculation is based on the density functional theory (DFT) in the local density approximation (LDA), as implemented in the QUANTUM ESPRESSO [36] package. Transfer integrals were then obtained as 1/4 of the respective bandwidth. The values of the transfer integral between the two materials are chosen to be similar to the values obtained in the

TABLE I. Values of model parameters used in calculations.

Parameter ^a	Value
$E_{g,D}$ (meV)	1500
$E_{g,A}$ (meV)	1950
ΔE_{DA}^c (meV)	500
$ J_D^c $ (meV)	105
$ J_D^v $ (meV)	295
$ J_A^c $ (meV)	150
$ J_A^v $ (meV)	150
$ J_{DA}^c , J_{DA}^v $ (meV)	75
ϵ_r	3.0
N	11
a (nm)	1.0
U (meV)	480
$\hbar\omega_{p,1}$ (meV)	10
g_1 (meV)	28.5
$\hbar\omega_{p,2}$ (meV)	185
g_2 (meV)	57.0
T (K)	300
t_0 (fs)	50

^a $E_{g,D}$ ($E_{g,A}$) is the single-particle band gap in the donor (acceptor). ΔE_{DA}^c denotes LUMO-LUMO energy offset. $J_D^{c/v}$ ($J_A^{c/v}$) are electron/hole transfer integrals in the donor (acceptor). $J_{DA}^{c/v}$ are electron/hole transfer integrals between the donor and acceptor. ϵ_r is the relative dielectric constant. N is the number of lattice sites in the donor and acceptor ($2N$ sites in total). a is the lattice constant. U denotes the on-site Coulomb interaction. $\hbar\omega_{p,1/2}$ are energies of local phonon modes, while $g_{1/2}$ are carrier-phonon coupling constants. T denotes temperature. The duration of the pulse is $2t_0$.

ab initio study of P3HT/PCBM heterojunctions [37]. We set the number of sites in a single material to $N = 11$, which is reasonable having in mind that the typical dimensions of phase segregated domains in bulk heterojunction morphology are considered to be 10–20 nm [11]. The electron-hole interaction potential V_{ij} is modeled using the Ohno potential

$$V_{ij} = \frac{U}{\sqrt{1 + \left(\frac{r_{ij}}{a_0}\right)^2}}, \quad (16)$$

where r_{ij} is the distance between sites i and j , and $a_0 = e^2/(4\pi\epsilon_0\epsilon_r U)$ is the characteristic length. The relative dielectric constant ϵ_r assumes a value typical for organic materials, while the magnitude of the on-site Coulomb interaction U was chosen so that the exciton binding energy in both the donor and the acceptor is around 300 meV. Following common practice when studying all-organic heterojunctions [38,39], we take one low-energy and one high-energy phonon mode. For simplicity, we assume that energies of both phonon modes, as well as their couplings to carriers, have the same values in both materials. The high-frequency phonon mode of energy 185 meV ($\approx 1500 \text{ cm}^{-1}$), which is present in both materials, was suggested to be crucial for ultrafast electron transfer in the P3HT/PCBM blend [40]. Recent theoretical calculations of the phonon spectrum and electron-phonon coupling constants in P3HT indicate the presence of low-energy phonon modes ($\lesssim 10$ meV) that strongly couple to carriers [41]. The chosen

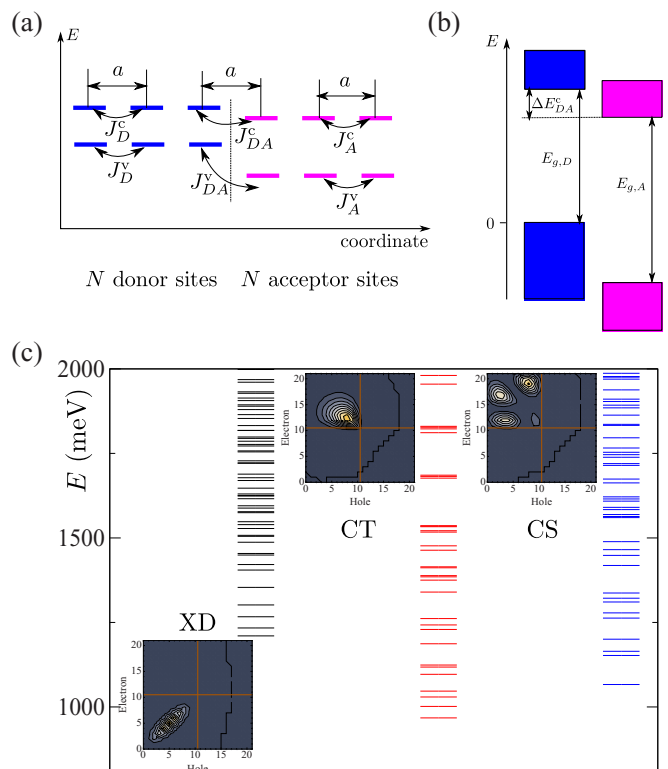


FIG. 2. (a) One-dimensional lattice model of a heterojunction. Various types of electronic couplings (in the donor, in the acceptor, and among them) are indicated. There is an energy offset between single-electron/hole levels in the donor and acceptor. (b) Band alignment produced by our model. (c) Energies of exciton states, in particular of donor excitons (black lines), CT (red lines), and CS (blue lines) states. Exciton wave function square moduli are shown for the lowest donor, CT, and CS state.

values of phonon-mode energies fall in the ranges in which the phonon density of states in conjugated polymers is large [42] and the local electron-vibration couplings in PCBM are pronounced [43]. We estimate the carrier-phonon coupling constants from the value of polaron binding energy, which can be estimated using the result of the second-order weak-coupling perturbation theory at $T = 0$ in the vicinity of the point $k = 0$ [44]:

$$\epsilon_b^{\text{pol}} = \sum_{i=1}^2 \frac{g_i^2}{2|J|} \frac{1}{\sqrt{\left(1 + \frac{\hbar\omega_{p,i}}{2|J|}\right)^2 - 1}}. \quad (17)$$

We took $g_2/g_1 = 2$ and estimated the numerical values assuming that $\epsilon_b^{\text{pol}} = 20$ meV and $|J| = 125$ meV. The electric field is centered around $t = 0$ and assumes the form

$$E(t) = E_0 \cos(\omega_c t) \theta(t + t_0) \theta(t_0 - t), \quad (18)$$

where ω_c is its central frequency, $\theta(t)$ is the step function, and the duration of the pulse is $2t_0$. The time t_0 should be chosen large enough so that the pulse is spectrally narrow enough (the energy of the initially generated excitons is around the central frequency of the pulse). On the other hand, since our focus is on processes happening on subpicosecond time scale, the pulse should be as short as possible in order

to disentangle the carrier generation during the pulse from free-system evolution after the pulse. Trying to reconcile the aforementioned requirements, we choose $t_0 = 50$ fs. We note that the results and conclusions to be presented do not crucially depend on the particular value of t_0 nor on the wave form of the excitation. This is shown in greater detail in Ref. [31], see Figs. 1 and 2, where we present the dynamics for shorter pulses of wave forms given in Eqs. (18) and (33). Interband dipole matrix elements d_i^{cv} are zero in the acceptor ($i = N, \dots, 2N - 1$), while in the donor they all assume the same value d^{cv} so that $d^{cv} E_0 = 0.2$ meV (weak excitation).

Figure 2(c) displays part of the exciton spectrum produced by our model. Exciton states can be classified according to the relative position of the electron and the hole. The classification is straightforward only for the noninteracting heterojunction ($J_{DA}^{c/v} = 0$), in which case any exciton state can be classified into four groups: (a) both the electron and the hole are in the donor [donor exciton (XD) state], (b) both the electron and the hole are in the acceptor (acceptor exciton state), (c) the electron is in the acceptor, while the hole is in the donor (space-separated exciton state), and (d) the electron is in the donor, while the hole is in the acceptor.

Space-separated excitons can be further discriminated according to their mean electron-hole distance defined as

$$\langle r_{e-h} \rangle_x = \sum_{ij} |i - j| |\psi_{ij}^x|^2. \quad (19)$$

When the electron-hole interaction is set to zero, the mean electron-hole distance for all the states from group (c) is equal to N . For the nonzero Coulomb interaction, we consider a space-separated exciton as a CS exciton if its mean electron-hole distance is larger than (or equal to) N , otherwise we consider it as a CT exciton. In the general case, the character of an exciton state is established by calculating its overlap with each of the aforementioned groups of the exciton states at the noninteracting heterojunction; this state then inherits the character of the group with which the overlap is maximal.

III. NUMERICAL RESULTS

Here, the results of our numerical calculations on the model system defined in Sec. II are presented. In Sec. III A, we observe that the populations of CT and CS states predominantly build up during the action of the excitation, and that the changes in these populations occurring on ~ 100 -fs time scales after the excitation are rather small. This conclusion, i.e., the direct optical generation as the principal source of space-separated charges on ultrafast time scales following the excitation, is shown in Sec. III B to be robust against variations of model parameters. Since the focus of our study is on the ultrafast exciton dynamics at photoexcited heterojunctions, all the computations are carried out for 1 ps in total (involving the duration of the pulse).

A. Interfacial dynamics on ultrafast time scales

Figure 3(a) shows the time dependence of the numbers of donor, CT, and CS excitons for the 100-fs-long excitation with central frequency $\hbar\omega_c = 1500$ meV, which excites the system well above the lowest donor or space-separated exciton

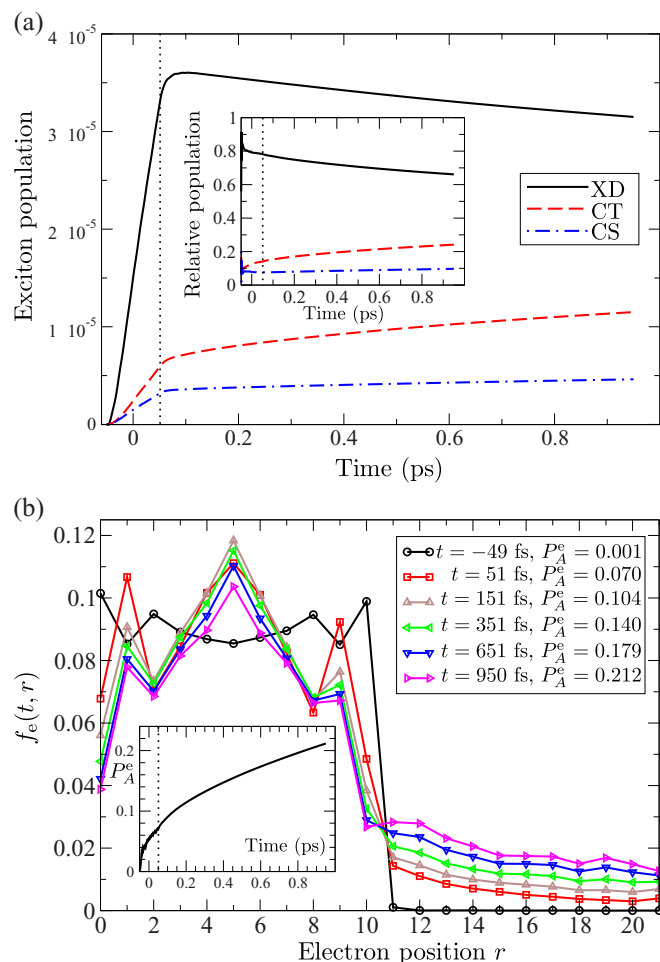


FIG. 3. (a) Time dependence of the numbers of donor (XD), CT, and CS excitons. The inset shows the time dependence of these quantities normalized to the total exciton population in the system. (b) Probability that at time t an electron is located at site r as a function of r for various values of t . In the legend, the probability that at instant t an electron is located in the acceptor is given, while the inset shows its full time dependence. Dotted vertical lines indicate the end of the excitation.

state, see Fig. 2(c). The number of all three types of excitons grows during the action of the electric field, whereas after the electric field has vanished, the number of donor excitons decreases and the numbers of CT and CS excitons increase. However, the changes in the exciton numbers brought about by the free-system evolution alone are much less pronounced than the corresponding changes during the action of the electric field, as is shown in Fig. 3(a). The population of CS excitons builds up during the action of the electric field, so that after the first 100 fs of the calculation, CS excitons comprise 7.6% of the total exciton population, see the inset of Fig. 3(a). In the remaining 900 fs, when the dynamics is governed by the free Hamiltonian, the population of CS excitons further increases to 9.6%. A similar, but less extreme, situation is also observed in the relative number of CT excitons, which at the end of the pulse form 14% of the total population and in the remaining 900 fs of the computation their number further grows to 24%. Therefore, if only the free-system

evolution were responsible for the conversion from donor to CT and CS excitons, the population of CT and CS states at the end of the pulsed excitation would assume much smaller values than we observe. We are led to conclude that the population of CT and CS excitons on ultrafast ($\lesssim 100$ -fs) time scales is mainly established by direct optical generation. Transitions from donor to CT and CS excitons are present, but on this time scale are not as important as is currently thought.

Exciton dissociation and charge separation can also be monitored using the probabilities $f_e(t,r)$ [$f_h(t,r)$] that an electron (a hole) is located on site r at instant t , as well as the probability $P_A^e(t)$ that an electron is in the acceptor at time t , see Eqs. (13)–(15). Figure 3(b) displays quantity f_e as a function of site index r at different times t . The probability of an electron being in the acceptor is a monotonically increasing function of time t , see the inset of Fig. 3(b). It increases, however, more rapidly during the action of the electric field than after the electric field has vanished: in the first 100 fs of the calculation, it increases from virtually 0 to 0.070, while in the next 100 fs it only rises from 0.070 to 0.104, and at the end of the computation it assumes the value 0.210. The observed time dependence of the probability that an electron is located in the acceptor further corroborates our hypothesis of direct optical generation as the main source of separated carriers on ultrafast time scales. If only transitions from donor to CT and CS excitons led to ultrafast charge separation starting from a donor exciton, the values of the considered probability would be smaller than we observe.

The rationale behind the direct optical generation of space-separated charges is the resonant coupling between donor excitons and (higher-lying) space-separated states, which stems from the resonant mixing between single-electron states in the donor and acceptor modulated by the electronic coupling between materials, see the level alignment in Fig. 2(b). This mixing leads to higher-lying CT and CS states having non-negligible amount of donor character and acquiring nonzero dipole moment from donor excitons; these states can thus be directly generated from the ground state. It should be stressed that the mixing, in turn, influences donor states, which have certain amount of space-separated character.

B. Impact of model parameters on ultrafast exciton dynamics

Our central conclusion was so far obtained using only one set of model parameters and it is therefore important to check its sensitivity on system parameters. To this end, we vary one model parameter at a time, while all the other parameters retain the values listed in Table I.

We start by investigating the effect of the transfer integral between the donor and acceptor $J_{DA}^{c/v}$. Higher values of $J_{DA}^{c/v}$ favor charge separation, since the relative numbers of CT and CS excitons, together with the probability that an electron is in the acceptor, increase, whereas the relative number of donor excitons decreases with increasing $J_{DA}^{c/v}$, see Figs. 4(a)–4(c). In light of the proposed mechanism of ultrafast direct optical generation of space-separated charges, the observed trends can be easily rationalized. Stronger electronic coupling between materials leads to stronger mixing between donor and space-separated states, i.e., a more pronounced donor character of

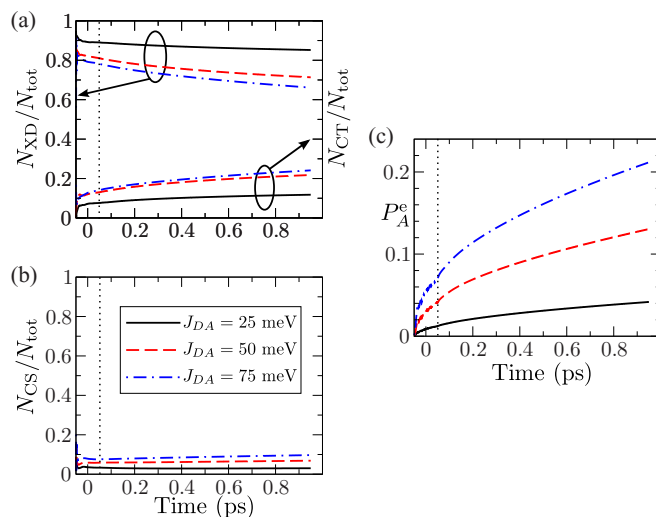


FIG. 4. Time dependence of the relative number of (a) donor and CT, (b) CS excitons, and (c) the probability P_A^e that an electron is in the acceptor, for different values of the transfer integrals $|J_{DA}^c| = |J_{DA}^v| = J_{DA}$ between the donor and the acceptor. Dotted vertical lines indicate the end of the excitation.

CT and CS states and consequently a larger dipole moment for direct creation of CT and CS states from the ground state.

The results concerning the effects of the energy offset ΔE_{DA}^c between LUMO levels in the donor and acceptor are summarized in Figs. 5(a)–5(c). The parameter ΔE_{DA}^c determines the energy width of the overlap region between single-electron states in the donor and acceptor, see Fig. 2(b). The smaller is ΔE_{DA}^c , the greater is the number of virtually resonant single-electron states in the donor and in the acceptor and therefore the greater is the number of (higher-lying) CT and CS states that inherit nonzero dipole moments from donor states and may thus be directly excited from the ground state.

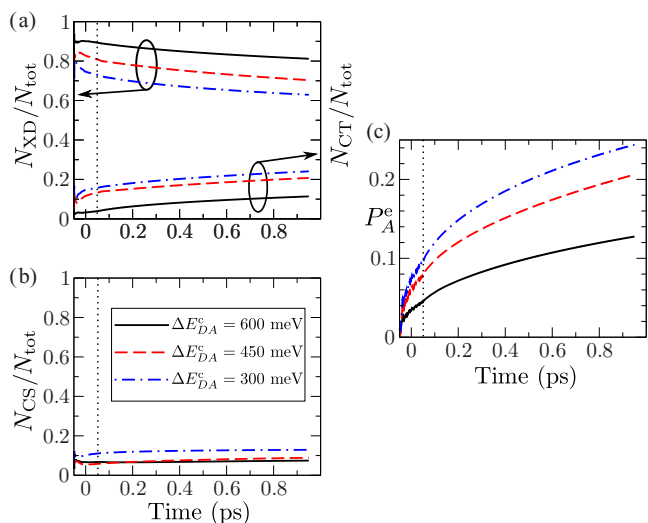


FIG. 5. Time dependence of the relative number of (a) donor and CT, (b) CS excitons, and (c) the probability P_A^e that an electron is in the acceptor, for different values of the LUMO-LUMO energy offset ΔE_{DA}^c . Dotted vertical lines indicate the end of the excitation.

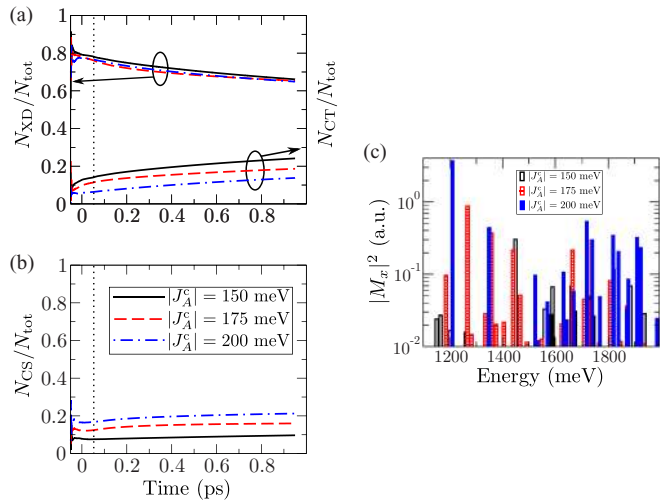


FIG. 6. Time dependence of the relative number of (a) donor and CT and (b) CS excitons, for different values of electronic coupling in the acceptor J_A^c . (c) Squared moduli of dipole matrix elements (in arbitrary units) for direct generation of CS excitons from the ground state for different values of electronic coupling in the acceptor J_A^c . Dotted vertical lines indicate the end of the excitation. Note that, globally, squared moduli of dipole matrix elements are largest for $|J_A^c| = 200$ meV (completely filled bars).

This manifests as a larger number of CT and CS excitons, as well as a larger probability that an electron is in the acceptor, with decreasing ΔE_{DA}^c .

Figures 6(a)–6(c) show the effects of electron delocalization in the acceptor on the ultrafast dynamics at the model heterojunction. Delocalization effects are mimicked by varying the electronic coupling in the acceptor. While increasing $|J_A^c|$ has virtually no effect on the relative number of donor excitons, it leads to an increased participation of CS and a decreased participation of CT excitons in the total exciton population. CT states, in which the electron-hole interaction is rather strong, are mainly formed from lower-energy single-electron states in the acceptor and higher-energy single-hole states in the donor. These single-particle states are not subject to strong resonant mixing with single-particle states of the other material. However, CS states are predominantly composed of lower-energy single-hole donor states and higher-energy single-electron acceptor states; the mixing of the latter group of states with single-electron donor states is stronger for larger $|J_A^c|$, just as in case of smaller ΔE_{DA}^c , see Fig. 2(b). Therefore the dipole moments for direct generation of CS excitons generally increase when increasing $|J_A^c|$, see Fig. 6(c), whereas the dipole moments for direct generation of CT excitons at the same time change only slightly, which can account for the trends of the participation of CS and CT excitons in Figs. 6(a) and 6(b).

We now turn our attention to the effects that the strength of the carrier-phonon interaction has on the ultrafast exciton dynamics at heterointerfaces. In Figs. 7(a)–7(d), we present the results with the fixed ratio $g_2/g_1 = 2.0$ and the polaron binding energies defined in Eq. (17) assuming the values of approximately 20, 40, 60, and 140 meV, in ascending order of g_1 . We note that it is not straightforward to predict the

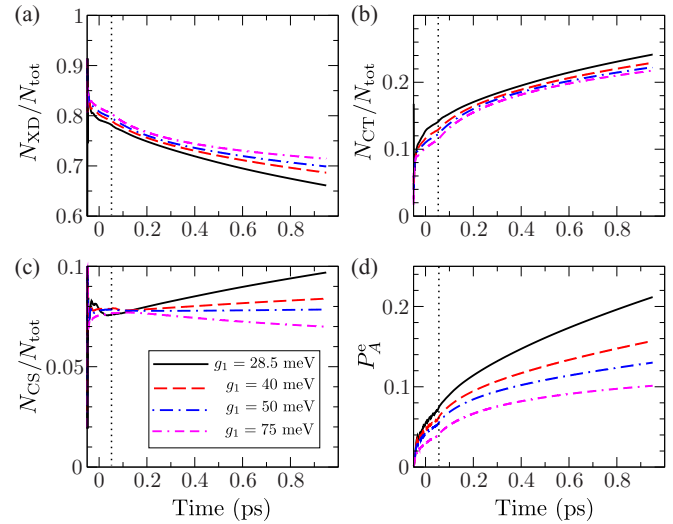


FIG. 7. Time dependence of the relative number of (a) donor, (b) CT, (c) CS excitons, and (d) the probability P_A^e that an electron is in the acceptor, for different strengths of the carrier-phonon interaction. Dotted vertical lines indicate the end of the excitation.

effect of the variations of carrier-phonon interaction strength on the population of space-separated states. Single-phonon-assisted processes preferentially couple exciton states of the same character, i.e., a donor exciton state is more strongly coupled to another donor state, than to a space-separated state. On the one hand, stronger carrier-phonon interaction implies more pronounced exciton dissociation and charge separation because of stronger coupling between donor and space-separated states. On the other hand, stronger carrier-phonon interaction leads to faster relaxation of initially generated donor excitons within the donor exciton manifold to low-lying donor states. Low-lying donor states are essentially uncoupled from space-separated states, i.e., they exhibit low probabilities of exciton dissociation and charge separation. Our results, shown in Figs. 7(a)–7(d), indicate that stronger carrier-phonon interaction leads to smaller number of CT and CS excitons, as well as the probability that an electron is in the acceptor, and to greater number of donor excitons. We also note that stronger carrier-phonon interaction changes the trend displayed by the population of CS states. While for the weakest interaction studied CS population grows after the excitation, for the strongest interaction studied CS population decays after the excitation. This is a consequence of more pronounced phonon-assisted processes leading to population of low-energy CT states once a donor exciton performs a transition to a space-separated state. This discussion can rationalize the changes in relevant quantities summarized in Figs. 7(a)–7(d); the magnitudes of the changes observed are, however, rather small. In previous studies [38,45], which did not deal with the initial exciton generation step, stronger carrier-phonon interaction is found to suppress quite strongly the charge separation process. The weak influence of the carrier-phonon interaction strength on ultrafast heterojunction dynamics that we observe supports the mechanism of ultrafast direct optical generation of space-separated charges. If the charge separation process at heterointerfaces were mainly

driven by the free-system evolution, greater changes in the quantities describing charge separation efficiency would be expected with varying carrier-phonon interaction strength.

Additionally, we have performed computations for a fixed value of ϵ_b^{pol} [Eq. (17)] and different values of the ratio g_2/g_1 among coupling constants of high- and low-frequency phonon modes. The result, which is presented in Ref. [31] (see Fig. 4), shows that the increase of the ratio g_2/g_1 increases the number of CT excitons and decreases the number of donor excitons, while the population of CS states exhibits only a weak increase. Stronger coupling to the high-frequency phonon mode (with respect to the low-frequency one) enhances charge separation by decreasing the number of donor excitons, but at the same time promotes phonon-assisted processes towards more strongly bound CT states, so that the population of CS states remains nearly constant.

Our formalism takes into account the influence of phonons on excitons. However, if this influence were too strong, the hierarchy of equations would have to be truncated at a higher level, which would make it computationally intractable. When the effects of lattice motion on excitons are strong, one has, in turn, to consider the feedback of excitons on phonons, which is not captured by the current approach. The feedback of excitons on the lattice motion can be easily included in a mixed quantum/classical approach, where excitons are treated quantum mechanically, while the lattice motion is treated classically. To estimate the importance of the feedback of excitons on the lattice motion, we have performed the computation using the surface hopping approach [46,47] (see Ref. [31] for more details). In Fig. 3 of Ref. [31], we show the time dependence of the probability that an electron is in the acceptor obtained from simulations with and without feedback effects. The result is nearly the same in both cases, suggesting that feedback effects are small. As a consequence, our approach is sufficient for properly taking into account the influence of phonons on excitons.

We have also studied the influence of the temperature on the ultrafast exciton dynamics at a heterojunction. It exhibits a weak temperature dependence, see Fig. 5 of Ref. [31], which is consistent with existing theoretical [48] and experimental [49] insights, and also with the mechanism of direct optical generation of space-separated carriers.

Finally, the consequences of introducing diagonal static disorder in our model will be studied. It is done by drawing the (uncorrelated) on-site energies of electrons and holes in the donor and the acceptor from Gaussian distributions centered at the values that can be obtained from Table I. We have for simplicity assumed that the standard deviations of all the Gaussian distributions are equal to σ . As we do not intend to obtain any of the system properties by a statistical analysis of various realizations of disorder, but merely to check whether or not the presence of disorder may significantly alter qualitative features of the proposed picture of ultrafast exciton dynamics at heterointerfaces, we present our results only for a couple of different disorder realizations and compare them to the results for ordered system. In Figs. 8(a)–8(d), we show the time dependence of the relative number of space-separated (CS and CT) excitons and of the probability P_A^e for three different realizations of disorder with standard deviations $\sigma = 50$ and 100 meV. For these disorder realizations, the quantities

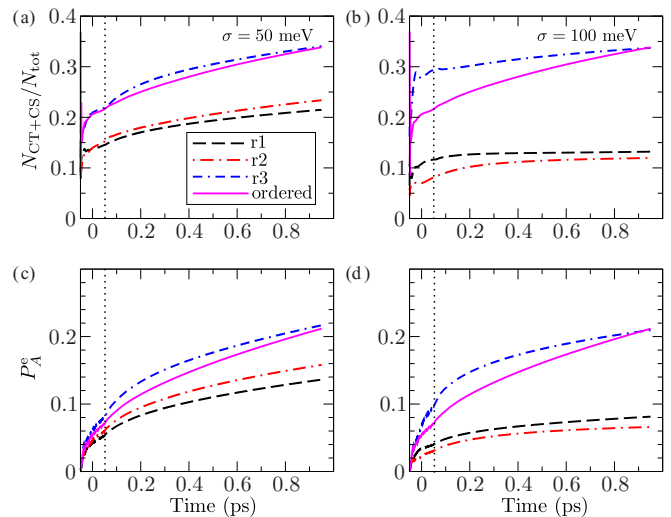


FIG. 8. (a) and (b) Time dependence of the relative number of space-separated (CT and CS) excitons for three different disorder realizations (r1, r2, and r3). (c) and (d) Time dependence of the probability that an electron is in the acceptor for three different disorder realizations. Time evolution of the respective quantities in ordered system is shown on each graph for comparison. Disorder is diagonal (affects only on-site energies), static, and Gaussian, standard deviations being $\sigma = 50$ [(a) and (c)] and 100 meV [(b) and (d)].

we use to describe ultrafast heterojunction dynamics show qualitatively similar behavior to the case of the ordered system. Namely, changes in the relative number of space-separated excitons and the probability of an electron being in the acceptor are more pronounced during the action of the pulse than after its end. The characteristic time scales of these changes (for the disorder realizations studied) are not drastically different from the corresponding time scale in the ordered system. The presence of disorder in our model does not necessarily lead to less efficient charge separation as monitored by the two aforementioned quantities. Our results based on the considered disorder realizations are in agreement with the more detailed study of the effects of disorder on charge separation at model D/A interfaces [16], from which emerged that regardless of the degree of disorder, the essential physics of free hole and electron generation remains the same.

In summary, we find that regardless of the particular values of varied model parameters ($J_{DA}^{c/v}$, ΔE_{DA}^c , J_A^c , carrier-phonon coupling constants), the majority of CT and CS states that are present at ~ 100 fs after photoexcitation have been directly generated during the excitation. Trends in quantities describing ultrafast heterojunction dynamics that we observe varying model parameters can be explained by taking into consideration the proposed mechanism of ultrafast direct optical generation of space-separated charges.

IV. ULTRAFAST SPECTROSCOPY SIGNATURES

Exciton dynamics on ultrafast time scales is typically probed experimentally using the ultrafast pump-probe spectroscopy, see, e.g., Refs. [7,8]. In such experiments, the presence of space-separated charges on ultrafast time scales after photoexcitation has been established and the energy

resonance between donor exciton and space-separated states was identified as responsible for efficient charge generation [7], in agreement with our numerical results. However, while our results indicate that the majority of space-separated charges that are present at ~ 100 fs after photoexcitation have been directly optically generated, interpretation of experiments [7] suggests that these states become populated by the transition from donor exciton states. To understand the origin of this apparent difference, we numerically compute ultrafast pump-probe signals in the framework of our heterojunction model. In Sec. IV A, we present the theoretical treatment of ultrafast pump-probe experiments adapted for the system at hand. Assuming that the probe pulse is delta-like, we obtain an analytic expression relating the differential transmission ΔT to the nonequilibrium state of the system “seen” by the probe pulse. The expression provides a very clear and direct interpretation of the results of ultrafast pump-probe experiments and allows to distinguish between contributions stemming from exciton populations and coherences, challenging the existing interpretations. It is used in Sec. IV B to numerically compute differential transmission signals.

A. Theoretical treatment of the ultrafast pump-probe spectroscopy

In a pump-probe experiment, the sample is firstly irradiated by an energetic pump pulse and the resulting excited (nonequilibrium) state of the sample is consequently examined using a second, weaker, probe pulse, whose time delay with respect to the pump pulse can be tuned [50–52]. Our theoretical approach to a pump-probe experiment considers the interaction with the pump pulse as described in Sec. II B and Ref. [30], i.e., within the density matrix formalism employing the DCT scheme up to the second order in the pump field. The interaction with the probe pulse is assumed not to change significantly the nonequilibrium state created by the pump pulse and is treated in the linear response regime. The corresponding nonequilibrium dipole-dipole retarded correlation function is then used to calculate pump-probe signals [52,53].

To study pump-probe experiments, we extended our two-band lattice semiconductor model including more single-electron (single-hole) energy levels per site. Multiple single-electron (single-hole) levels on each site should be dipole-coupled among themselves in order to enable probe-induced dipole transitions between various exciton states. We denote by $c_{i\beta_i}^\dagger$ ($c_{i\beta_i}$) creation (annihilation) operators for electrons on site i in conduction-band orbital β_i ; similarly, $d_{i\alpha_i}^\dagger$ ($d_{i\alpha_i}$) create (annihilate) a hole on site i in valence-band orbital α_i . The dipole-moment operator in terms of electron and hole operators assumes the form

$$P = \sum_{\substack{i \\ \beta_i \alpha_i}} (d_i^{\text{cv}} c_{i\beta_i}^\dagger d_{i\alpha_i}^\dagger + \text{H.c.}) + \sum_{\substack{i \\ \beta_i \neq \beta'_i}} d_i^{\text{cc}} c_{i\beta_i}^\dagger c_{i\beta'_i} - \sum_{\substack{i \\ \alpha_i \neq \alpha'_i}} d_i^{\text{vv}} d_{i\alpha_i}^\dagger d_{i\alpha'_i}. \quad (20)$$

Intraband dipole matrix elements d_i^{cc} (d_i^{vv}) describe electron (hole) transitions between different single-electron (single-hole) states on site i , as opposed to the interband matrix

elements d_i^{cv} , which are responsible for the exciton generation. Performing transition to the exciton basis, which is defined analogously to Eq. (6), dipole matrix elements for transitions from the ground state to exciton state x are

$$M_x = \sum_{\substack{i \\ \beta_i \alpha_i}} d_i^{\text{cv}} \psi_{(i\alpha_i)(i\beta_i)}^{x*}, \quad (21)$$

while those for transitions from exciton state x to exciton state \bar{x} are

$$M_{\bar{x}}^x = \sum_{\substack{i \\ \alpha_i \neq \alpha'_i}} \sum_{\substack{j \\ \beta_j}} \psi_{(i\alpha_i)(j\beta_j)}^{\bar{x}*} d_i^{\text{vv}} \psi_{(i\alpha'_i)(j\beta_j)}^x - \sum_{\substack{i \\ \beta_i \neq \beta'_i}} \sum_{\substack{j \\ \alpha_j}} \psi_{(j\alpha_j)(i\beta'_i)}^{\bar{x}*} d_i^{\text{cc}} \psi_{(j\alpha_j)(i\beta_i)}^x. \quad (22)$$

Operator P [Eq. (20)] expressed in terms of operators X_x, X_x^\dagger assumes the form (keeping only contributions whose expectation values are at most of the second order in the pump field)

$$P = \sum_x (M_x X_x^\dagger + M_x^* X_x) - \sum_{\bar{x}} M_{\bar{x}}^x X_{\bar{x}}^\dagger X_x. \quad (23)$$

We concentrate on the so-called nonoverlapping regime [52], in which the probe pulse, described by its electric field $e(t)$, acts after the pump pulse. We take that our system meets the condition of optical thinness, i.e., the electromagnetic field originating from probe-induced dipole moment can be neglected compared to the electromagnetic field of the probe. In the following considerations, the origin of time axis $t = 0$ is taken to be the instant at which the probe pulse starts. The pump pulse finishes at $t = -\tau$, where τ is the time delay between (the end of) the pump and (the start of) the probe. The pump creates a nonequilibrium state of the system which is, at the moment when the probe pulse starts, given by the density matrix $\rho(0)$, which implicitly depends on the pump-probe delay τ .

In the linear-response regime, the probe-induced dipole moment $d_p(t)$ for $t > 0$ is expressed as [52]

$$d_p(t) = \int dt' \chi(t, t') e(t'), \quad (24)$$

where $\chi(t, t')$ is the nonequilibrium retarded dipole-dipole correlation function

$$\chi(t, t') = -\frac{i}{\hbar} \theta(t - t') \text{Tr}(\rho(0)[P(t), P(t')]). \quad (25)$$

Time dependence in Eq. (25) is governed by the Hamiltonian of the system in the absence of external fields [Eq. (8)]:

$$H_{E(t)=0} = H_0 + H_{\text{e-ph}}, \quad (26)$$

where H_0 is the noninteracting Hamiltonian of excitons in the phonon field [the first two terms in Eq. (8)], while $H_{\text{e-ph}}$ accounts for exciton-phonon interaction [the third term in Eq. (8)]. For an ultrashort probe pulse, $e(t) = e_0 \delta(t)$, the probe-induced dipole moment assumes the form

$$d_p(t) = e_0 \chi(t, 0) = e_0 \left(-\frac{i}{\hbar} \right) \text{Tr}(\rho(0)[P(t), P(0)]). \quad (27)$$

Probe pulse tests the possibility of transitions between various exciton states, i.e., it primarily affects carriers. Therefore,

as a reasonable approximation to the full time dependent operator $P(t)$ appearing in Eq. (27), operator $P^{(0)}(t)$, evolving according to the noninteracting Hamiltonian H_0 in Eq. (26), may be used. This leads us to the central result for the probe-induced dipole moment:

$$d_p(t) = e_0 \left(-\frac{i}{\hbar} \right) \text{Tr}(\rho(0)[P^{(0)}(t), P(0)]). \quad (28)$$

Deriving the commutator in Eq. (28), in the expression for $d_p(t)$ we obtain two types of contributions, see Eq. (A3) in Appendix. Contributions of the first type oscillate at frequencies ω_x corresponding to probe-induced transitions between the ground state and exciton state x , while those of the second type oscillate at frequencies $\omega_{\bar{x}} - \omega_x$ corresponding to probe-induced transitions between exciton states \bar{x} and x . Here, we focus our attention to the process of photoinduced absorption (PIA), in which an exciton in state x performs a transition to another state \bar{x} under the influence of the probe field. Therefore we will further consider only the second type of contributions.

The frequency-dependent transmission coefficient $T(\omega)$ is defined as (we use SI units)

$$T(\omega) = 1 + \frac{c\mu_0}{S\hbar} \text{Im} \left[\hbar\omega \frac{d_p(\omega)}{e(\omega)} \right], \quad (29)$$

where $d_p(\omega)$ and $e(\omega)$ are Fourier transformations of $d_p(t)$ and $e(t)$, respectively, while S is the irradiated area of the sample. The differential transmission is given as

$$\Delta T(\tau; \omega) = T^{\text{neq}}(\tau; \omega) - T^{\text{eq}}(\omega). \quad (30)$$

The transmission of a system, which is initially (before the action of the probe) unexcited, is denoted by $T^{\text{eq}}(\omega)$. The transmission of a pump-driven system $T^{\text{neq}}(\tau; \omega)$ depends on the time delay τ between the pump and the probe through the nonequilibrium density matrix $\rho(0)$. Since our aim is to study the process of PIA and since $T^{\text{eq}}(\omega)$ is expected to reflect only transitions involving the ground state, we will not further consider this term. After a derivation, the details of which are given in Appendix, we obtain the expression for the part of the differential transmission signal $\Delta T_{\text{PIA}}(\tau; \omega)$ accounting for the PIA:

$$\begin{aligned} \Delta T_{\text{PIA}}(\tau; \omega) \propto \text{Im} & \left[\sum_{xx'} \left((M_x M_{x'})^* \frac{\hbar\omega}{\hbar\omega - (\hbar\omega_{x'} - \hbar\omega_x) + i\eta} y_{x'}(0) - M_x M_{x'}^* \frac{\hbar\omega}{\hbar\omega + (\hbar\omega_{x'} - \hbar\omega_x) + i\eta} y_{x'}^*(0) \right) \right. \\ & + \sum_{\bar{x}xx'} \left(M_{x'}^x M_{\bar{x}}^{\bar{x}} \frac{\hbar\omega}{\hbar\omega + (\hbar\omega_{x'} - \hbar\omega_x) + i\eta} y_{x'}^*(0) y_{\bar{x}}(0) - M_x^x M_{\bar{x}}^{\bar{x}} \frac{\hbar\omega}{\hbar\omega - (\hbar\omega_{x'} - \hbar\omega_x) + i\eta} y_{\bar{x}}^*(0) y_{x'}(0) \right) \\ & \left. + \sum_{\bar{x}xx'} \left(M_{x'}^x M_{\bar{x}}^{\bar{x}} \frac{\hbar\omega}{\hbar\omega + (\hbar\omega_{x'} - \hbar\omega_x) + i\eta} \bar{n}_{x'\bar{x}}(0) - M_x^x M_{\bar{x}}^{\bar{x}} \frac{\hbar\omega}{\hbar\omega - (\hbar\omega_{x'} - \hbar\omega_x) + i\eta} \bar{n}_{\bar{x}x'}(0) \right) \right]. \quad (31) \end{aligned}$$

In the last equation, we have explicitly separated the coherent contributions by introducing the correlated parts of exciton populations and exciton-exciton coherences $\bar{n}_{\bar{x}x} = n_{\bar{x}x} - y_{\bar{x}}^* y_x$ [see also Eq. (11) defining incoherent exciton populations], while η is a positive parameter effectively accounting for the spectral line broadening [53]. $y_x(0)$ denotes the value of the electronic density matrix y_x at the moment when the probe pulse starts, and similarly for $\bar{n}_{\bar{x}x}(0)$. The coherences between exciton states and the ground state $y_x(0)$, as well as correlated parts of exciton-exciton coherences $\bar{n}_{\bar{x}x}(0)$ ($\bar{x} \neq x$), are expected to approach zero for sufficiently long time delays between the pump and the probe [54]. In this limit, Eq. (31) contains only the incoherent exciton populations \bar{n}_{xx} :

$$\Delta T_{\text{PIA}}(\tau; \omega) \propto \sum_{xx'} |M_{x'}^x|^2 \left[-\frac{\eta \cdot \hbar\omega}{(\hbar\omega + (\hbar\omega_{x'} - \hbar\omega_x))^2 + \eta^2} + \frac{\eta \cdot \hbar\omega}{(\hbar\omega - (\hbar\omega_{x'} - \hbar\omega_x))^2 + \eta^2} \right] \bar{n}_{x'x}(0). \quad (32)$$

This expression is manifestly negative when it describes probe-induced transitions from exciton state x' to some higher-energy exciton state x . The last conclusion is in agreement with the usual experimental interpretation of pump-probe spectra, where a negative differential transmission signal corresponds either to PIA or to stimulated emission [51]. Our expression [Eq. (31)] demonstrates, however, that this correspondence can not be uniquely established in the ultrafast regime, where it is expected that both coherences between exciton states and the ground state $y_x(0)$ and exciton-exciton coherences $\bar{n}_{\bar{x}x}(0)$ ($\bar{x} \neq x$), along with incoherent exciton populations $\bar{n}_{xx}(0)$, play significant role. This is indeed the case in our numerical computations of pump-probe spectra, which are presented in the following subsection. For each studied case, we separately show the total signal [full Eq. (31)], the y -part of the signal

[the first two terms in Eq. (31)], and the \bar{n} -part of the signal [the third term in Eq. (31)]. We note that it would be possible to further separate the \bar{n} -part of the signal into the contribution stemming from incoherent exciton populations \bar{n}_{xx} [Eq. (32)] and exciton-exciton coherences $\bar{n}_{\bar{x}x}$ ($\bar{x} \neq x$). As shown in more detail in Ref. [31] (see Fig. 7), the overall \bar{n} -part of the signal is qualitatively very similar to its contribution stemming from incoherent exciton populations. Therefore, for the simplicity of further discussion, we may consider the \bar{n} -part of the signal as completely originating from incoherent exciton populations.

B. Numerical results: ultrafast pump-probe signals

In order to compute pump-probe signals and at the same time keep the numerics manageable, we extended our model

by introducing only one additional single-electron level both in the donor and in the acceptor and one additional single-hole level in the donor. Additional energy levels in the donor and the corresponding bandwidths are extracted from the aforementioned electronic structure calculation on the infinitely long PCPDTBT polymer. The additional single-electron level is located at 1160 meV above the single-electron level used in all the calculations and the bandwidth of the corresponding zone is estimated to be 480 meV. The additional single-hole level is located at 1130 meV below the single-hole level used in all the calculations and the bandwidth of the corresponding zone is estimated to be 570 meV. The additional single-electron level in the acceptor is extracted from an electronic structure calculation on the C_{60} molecule. The calculation is based on DFT using either LDA or B3LYP exchange-correlation functional (both choices give similar results) and 6-31G basis set and was performed using the NWCHEM package [55]. We found that the additional single-electron level lies around 1000 meV above the single-electron level used in all the calculations. The bandwidth of the corresponding zone is set to 600 meV, see Table I.

In this section, we assume that the waveform of the pump pulse is

$$E(t) = E_0 \cos(\omega_c t) \exp\left(-\frac{t^2}{\tau_G^2}\right) \theta(t + t_0) \theta(t_0 - t), \quad (33)$$

where we take $\tau_G = 20$ fs and $t_0 = 50$ fs, while the probe is

$$e(t) = e_0 \delta(t - (t_0 + \tau)), \quad (34)$$

with variable pump-probe delay τ . The intraband dipole matrix elements d_i^{cc}, d_i^{vv} in Eq. (20) are assumed to be equal in the whole system:

$$d_i^{cc} = d_i^{vv} = d^{\text{intra}} = \frac{1}{2} d^{cv}. \quad (35)$$

The positive parameter η , which effectively accounts for the line broadening, is set to $\eta = 50$ meV. We have checked that variations in η do not change the qualitative features of the presented PIA spectra, see Fig. 6 in Ref. [31]. In actual computations of the signal given in Eq. (31), we should remember that the pump pulse finishes at instant t_0 , while in Eq. (31), all the quantities are taken at the moment when the probe starts, which is now $t_0 + \tau$; in other words, $y_x(0) \rightarrow y_x(t_0 + \tau)$, $\bar{n}_{\bar{x}x}(0) \rightarrow \bar{n}_{\bar{x}x}(t_0 + \tau)$ when we compute pump-probe signals using Eq. (31) and the pump and probe are given by Eqs. (33) and (34), respectively.

In Figs. 9(a) and 9(b), we show the PIA signal from space-separated states after the excitation by the pump at 1500 meV. The frequency ω in Eq. (31) is set to 1000 meV, which is (for the adopted values of model parameters) appropriate for observing PIA from space-separated states. At small pump-probe delays ($\tau \lesssim 300$ fs), we see that the oscillatory features stemming from coherences between exciton states and the ground state (y -part of the signal) dominate the dynamics. At larger delays, the part originating from established (incoherent) exciton populations (\bar{n} -part of the signal) prevails, see Fig. 9(b), and the shape of the signal resembles the shapes of signals from space-separated states in Fig. 4(c) of Ref. [7]. The signal decreases at larger delays, which correlates very well with the fact that the numbers of CT and CS excitons increase,

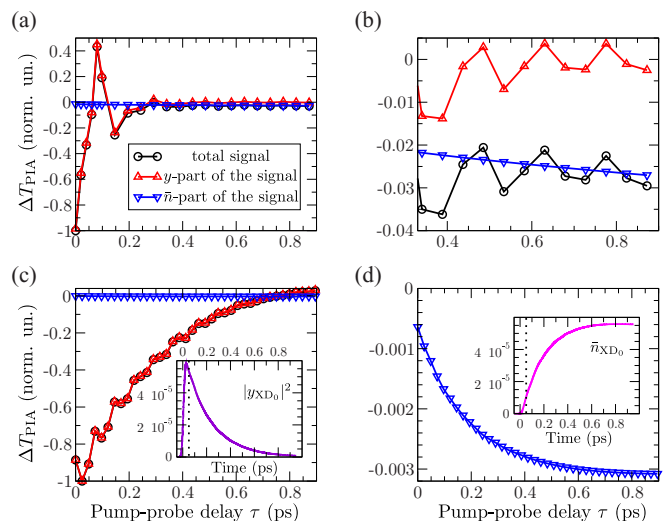


FIG. 9. Differential transmission signal ΔT_{PIA} [Eq. (31)] as a function of the pump-probe delay for (a) pump at 1500 meV (826 nm) and probe at 1000 meV (1240 nm) testing PIA dynamics from space-separated states, and (c) pump resonant with the lowest donor exciton (1210 meV, 1025 nm) and probe at 1130 meV (1096 nm) testing PIA dynamics from donor states. The inset of (c) shows the coherent exciton population $|y_{XD_0}|^2$ of the lowest donor state XD_0 . (b) The same signal as in (a) at longer pump-probe delays (>300 fs). (d) The same signal as in (c); the inset displays the incoherent exciton population \bar{n}_{XD_0} of the lowest donor state.

see Fig. 3(a). In other words, at larger pump-probe delays, at which the influence of coherences between exciton states and the ground state is small, the signal can be unambiguously interpreted in terms of charge transfer from the donor to the acceptor.

Figures 9(c) and 9(d) display PIA signal from donor excitons following the pump excitation at the lowest donor exciton (1210 meV). The frequency ω in Eq. (31) is set to 1130 meV. The overall signal shape is qualitatively similar to the shape of donor exciton PIA signal in Fig. 4(a) of Ref. [7], but its interpretation is rather different. While the authors of Ref. [7] suggest that the monotonically increasing PIA signal from donor excitons reflects their transfer to space-separated states, our signal predominantly originates from coherences between donor states and the ground state [y -part of the signal in Fig. 9(c)]. Furthermore, the shape of the total signal matches very well the decay of the coherent population of the lowest donor exciton, see the inset of Fig. 9(c), while the shape of the \bar{n} -part of the signal corresponds well to the changes in the incoherent population of the lowest donor state, see the inset of Fig. 9(d). This incoherent population does not decay during our computation: immediately after the pump pulse, it rises and at longer times it reaches a plateau, which signals that the donor exciton population is “blocked” in the lowest donor state. The lowest donor exciton is very strongly dipole-coupled to the ground state, its population comprising around 75% of the total generated population. Therefore, according to our numerical results, the observed PIA signal from donor excitons in this case mimics the conversion from coherent to incoherent exciton population

of the lowest donor state. This, however, does not necessarily mean that the concomitant charge transfer is completely absent in this case. Instead, the presence of coherences between exciton states and the ground state, which dominate the signal for all pump-probe delays we studied, prevents us from attributing the signal to the population transfer from donor excitons to space-separated states. The aforementioned conversion from coherent to incoherent exciton population of the lowest donor state is rather slow because of the relatively weak coupling between low-lying donor excitons on the one hand and space-separated states on the other hand (this weak coupling was also appreciated in Ref. [7]). On the other hand, pumping well above the lowest donor and space-separated states, the couplings between these species are stronger and more diverse than for the pump resonant with the lowest donor exciton; this situation resembles the one encountered for the excitation condition in Fig. 4(c) of Ref. [7].

In conclusion, our computations yield spectra which overall agree with experimental spectra [7], and we find that the shape of the spectrum in Figs. 9(c) and 9(d) originates from the decay of coherences between donor excitons and the ground state, rather than from transitions from donor excitons to space-separated states.

V. DISCUSSION AND CONCLUSION

We studied ultrafast exciton dynamics in a one-dimensional model of a heterointerface. Even though similar theoretical models have been lately proposed [38,56], we believe that our theoretical treatment goes beyond the existing approaches, since it treats both the exciton generation and their further separation on equal footing and it deals with all the relevant interactions on a fully quantum level. Namely, the vast majority of the existing theoretical studies on charge separation at heterointerfaces does not treat explicitly the interaction with the electric field which creates excitons from an initially unexcited system [17,19,38,45,56], but rather assumes that the exciton has already been generated and then follows its evolution at the interface between two materials. If we are to explore the possibility of direct optical generation of space-separated charges, we should certainly monitor the initial process of exciton generation, which we are able to achieve with the present formalism. We find that the resonant electronic coupling between donor and space-separated states not only enhances transfer from the former to the latter group of states [7,15], but also opens up a new pathway to obtain space-separated charges: their direct optical generation [25,26]. While this mechanism has been proposed on the basis of electronic structure and model Hamiltonian calculations (which did not include any dynamics), our study is, to the best of our knowledge, the first to investigate the possibility of direct optical generation of separated charges studying the ultrafast exciton dynamics at a heterointerface. We conclude that the largest part of space-separated charges which are present ~ 100 fs after the initial photoexcitation are directly optically generated, contrary to the general belief that they originate from ultrafast transitions from donor excitons. Although the D/A coupling in our model is restricted to only two nearest sites (labeled by $N - 1$ and N) in the donor and acceptor, there are space-separated states which

acquire nonzero dipole moment from donor excitons. The last point was previously highlighted in studies conducted on two- [25] and three-dimensional [26] heterojunction models, in which the dominant part of the D/A coupling involves more than a single pair of sites. We thus speculate that the main conclusions of our study would remain valid in a more realistic higher-dimensional model of a heterointerface. While there is absorption intensity transfer from donor to space-separated states brought about by their resonant mixing, the absorption still primarily occurs in the donor part of a heterojunction. Our results show that on ultrafast time scales the direct optical generation as a source of space-separated carriers is more important than transitions from donor to space-separated states. This, however, does not mean that initially generated donor excitons do not transform into space-separated states. They indeed do, see Figs. 3(a) and 3(b), but the characteristic time scale on which populations of space-separated states change due to the free-system evolution is longer than 100 fs.

The ultrafast generation of separated charges at heterointerfaces is more pronounced when the electronic coupling between materials is larger or when the energy overlap region between single-electron states in the donor and acceptor is wider, either by increasing the electronic coupling in the acceptor or decreasing the LUMO-LUMO offset between the two materials, see Fig. 2(b). Our results are therefore in agreement with studies emphasizing the beneficial effects of larger electronic couplings among materials [56], charge delocalization, [17,21,38,56], and smaller LUMO-LUMO offset [57] on charge separation. We find that strong carrier-phonon interaction suppresses charge separation, in agreement with previous theoretical studies [38,45] in which the effects of variations of carrier-phonon coupling constants have been systematically investigated. However, changes in the quantities we use to monitor charge separation with variations of carrier-phonon coupling strength are rather small, which we interpret to be consistent with the ultrafast direct optical generation of space-separated charges. Our theoretical treatment of ultrafast exciton dynamics is fully quantum, but it is expected to be valid for not too strong coupling of excitons to lattice vibrations, since the phonon branch of the hierarchy is truncated at a finite order, see Sec. I in Ref. [31]. Results of our mixed quantum/classical approach to exciton dynamics show that the feedback effect of excitons on the lattice motion, which is expected to be important for stronger exciton-phonon interaction, is rather small. We therefore expect that more accurate treatment of exciton-phonon interaction is not crucial to describe heterojunction dynamics on ultrafast time scales. If one wants to treat more accurately strong exciton-phonon interaction and yet remain in the quantum framework, other theoretical approaches, such as the one adopted in Ref. [45], have to be employed.

Despite a simplified model of organic semiconductors, our theoretical treatment takes into account all relevant effects. Consequently, our approach to ultrafast pump-probe experiments produces results that are in qualitative agreement with experiments and confirms the previously observed dependence of the exciton dynamics on the excess photon energy [7]. Our results indicate that the interpretation of ultrafast pump-probe signals is involved, as it is hindered by coherences (dominantly by those between exciton states and the ground state) which

cannot be neglected on the time scales studied. Time scales on which coherent features are prominent depend on the excess photon energy. We find that higher values of the excess photon energy enable faster disappearance of the coherent part of the signal since they offer diverse transitions between exciton states which make conversion from coherent to incoherent exciton populations faster. Pumping at the lowest donor exciton, our signal is (at subpicosecond pump-probe delays) dominated by its coherent part, conversion from coherent to incoherent exciton populations is slow, and therefore it cannot be interpreted in terms of exciton population transfer between various states.

ACKNOWLEDGMENTS

We gratefully acknowledge the support by the Ministry of Education, Science and Technological Development of the Republic of Serbia (Project No. ON171017) and European Community FP7 Marie Curie Career Integration Grant

(ELECTROMAT), as well as the contribution of the COST Action MP1406. Numerical computations were performed on the PARADOX supercomputing facility at the Scientific Computing Laboratory of the Institute of Physics Belgrade.

APPENDIX: DETAILS OF THE THEORETICAL TREATMENT OF PUMP-PROBE EXPERIMENTS

The commutator in Eq. (28) is to be evaluated in the nonequilibrium state $\rho(0)$ at the moment when the probe pulse starts. Therefore, deriving this commutator, only contributions whose expectation values are at most of the second order in the pump field should be retained. The commutation relations of exciton operators, which are correct up to the second order in the pump field, read as

$$[X_x, X_{\bar{x}}^\dagger] = \delta_{x\bar{x}} - \sum_{\bar{x}'x'} C_{\bar{x}x}^{\bar{x}'x'} X_{\bar{x}'}^\dagger X_{x'}, \quad (\text{A1})$$

where four-index coefficients $C_{\bar{x}x}^{\bar{x}'x'}$ are given as

$$C_{\bar{x}x}^{\bar{x}'x'} = \sum_{\substack{\bar{j}\bar{\beta}_j \\ j\beta_j}} \left(\sum_{i\alpha_i} \psi_{(i\alpha_i)(\bar{j}\bar{\beta}_j)}^{\bar{x}'*} \psi_{(i\alpha_i)(j\beta_j)}^{x'} \right) \left(\sum_{i\alpha_i} \psi_{(i\alpha_i)(\bar{j}\bar{\beta}_j)}^{\bar{x}} \psi_{(i\alpha_i)(j\beta_j)}^{x*} \right) + \sum_{\substack{\bar{i}\bar{\alpha}_i \\ i\alpha_i}} \left(\sum_{j\beta_j} \psi_{(\bar{i}\bar{\alpha}_i)(j\beta_j)}^{\bar{x}'*} \psi_{(i\alpha_i)(j\beta_j)}^{x'} \right) \left(\sum_{j\beta_j} \psi_{(\bar{i}\bar{\alpha}_i)(j\beta_j)}^{\bar{x}} \psi_{(i\alpha_i)(j\beta_j)}^{x*} \right). \quad (\text{A2})$$

The final result for the commutator $[P^{(0)}(t), P(0)]$ is

$$\begin{aligned} [P^{(0)}(t), P(0)] &= \sum_x |M_x|^2 (e^{-i\omega_x t} - e^{i\omega_x t}) - \sum_{\bar{x}_1 x_1} \sum_{x x'} (M_x^* M_{x'} C_{x'x}^{\bar{x}_1 x_1} e^{-i\omega_x t} - M_x M_{x'}^* C_{xx'}^{\bar{x}_1 x_1} e^{i\omega_x t}) X_{\bar{x}_1}^\dagger X_{x_1} \\ &\quad - \sum_{x x'} (M_x M_{x'}^*)^* e^{-i\omega_x t} X_{x'} + \sum_{x x'} M_x M_{x'}^* e^{i\omega_x t} X_{x'}^\dagger + \sum_{x x'} (M_x M_{x'}^x)^* e^{-i(\omega_{x'} - \omega_x)t} X_{x'} \\ &\quad - \sum_{x x'} M_x M_{x'}^x e^{i(\omega_{x'} - \omega_x)t} X_{x'}^\dagger + \sum_{\bar{x} x x'} M_{x'}^x M_x^{\bar{x}} e^{i(\omega_{x'} - \omega_x)t} X_{x'}^\dagger X_{\bar{x}} - \sum_{\bar{x} x x'} M_x^{x'} M_{\bar{x}}^x e^{-i(\omega_{x'} - \omega_x)t} X_{\bar{x}}^\dagger X_{x'}. \quad (\text{A3}) \end{aligned}$$

The expectation values [with respect to $\rho(0)$] of the operators appearing in the last equation are simply the active purely electronic density matrices of our formalism computed when the probe pulse starts, i.e., $\text{Tr}(\rho(0)X_x) = y_x(0)$ and $\text{Tr}(\rho(0)X_{\bar{x}}^\dagger X_x) = n_{\bar{x}x}(0)$.

As already mentioned, in order to study the process of PIA, in Eq. (A3) only terms which oscillate at differences of two exciton frequencies should be retained. Computing the Fourier transformation of $d_p(t)$ [Eq. (28)], we obtain integrals of the type

$$\int_0^{+\infty} dt e^{i(\omega - \Omega + i\eta)t} = \frac{i}{\omega - \Omega + i\eta}, \quad (\text{A4})$$

where we have introduced a positive infinitesimal parameter η to ensure the integral convergence. Physically, introducing η effectively accounts for the line broadening. For simplicity, we assume that only one value of η is used in all the integrals of the type (A4). Using the computed Fourier transformation $d_p(\omega)$ in Eqs. (29) and (30), we obtain the result for $\Delta T_{\text{PIA}}(\tau; \omega)$ given in Eq. (31).

-
- [1] T. M. Clarke and J. R. Durrant, Charge photogeneration in organic solar cells, *Chem. Rev.* **110**, 6736 (2010).
 [2] C. Deibel and V. Dyakonov, Polymer-fullerene bulk heterojunction solar cells, *Rep. Prog. Phys.* **73**, 096401 (2010).
 [3] F. Gao and O. Inganäs, Charge generation in polymer-fullerene bulk-heterojunction solar cells, *Phys. Chem. Chem. Phys.* **16**, 20291 (2014).

- [4] A. Zhugayevych and S. Tretiak, Theoretical description of structural and electronic properties of organic photovoltaic materials, *Annu. Rev. Phys. Chem.* **66**, 305 (2015).
 [5] H. Bässler and A. Köhler, "Hot or cold": how do charge transfer states at the donor-acceptor interface of an organic solar cell dissociate? *Phys. Chem. Chem. Phys.* **17**, 28451 (2015).

- [6] J. L. Brédas, J. E. Norton, J. Cornil, and V. Coropceanu, Molecular understanding of organic solar cells: the challenges, *Acc. Chem. Res.* **42**, 1691 (2009).
- [7] G. Grancini, M. Maiuri, D. Fazzi, A. Petrozza, H.-J. Egelhaaf, D. Brida, G. Cerullo, and G. Lanzani, Hot exciton dissociation in polymer solar cells, *Nat. Mater.* **12**, 29 (2013).
- [8] A. E. Jailaubekov, A. P. Willard, J. R. Tritsch, W.-L. Chan, N. Sai, R. Gearba, L. G. Kaake, K. J. Williams, K. Leung, P. J. Rossky, and X.-Y. Zhu, Hot charge-transfer excitons set the time limit for charge separation at donor/acceptor interfaces in organic photovoltaics, *Nat. Mater.* **12**, 66 (2013).
- [9] S. Gélinas, A. Rao, A. Kumar, S. L. Smith, A. W. Chin, J. Clark, T. S. van der Poll, G. C. Bazan, and R. H. Friend, Ultrafast long-range charge separation in organic semiconductor photovoltaic diodes, *Science* **343**, 512 (2014).
- [10] A. A. Paraecattil and N. Banerji, Charge separation pathways in a highly efficient polymer:fullerene solar cell material, *J. Am. Chem. Soc.* **136**, 1472 (2014).
- [11] S. R. Cowan, N. Banerji, W. L. Leong, and A. J. Heeger, Charge formation, recombination, and sweep-out dynamics in organic solar cells, *Adv. Funct. Mater.* **22**, 1116 (2012).
- [12] C. Deibel, T. Strobel, and V. Dyakonov, Role of the charge transfer state in organic donor-acceptor solar cells, *Adv. Mater.* **22**, 4097 (2010).
- [13] A. A. Bakulin, A. Rao, V. G. Pavelyev, P. H. M. van Loosdrecht, M. S. Pshenichnikov, D. Niedzialek, J. Cornil, D. Beljonne, and R. H. Friend, The role of driving energy and delocalized states for charge separation in organic semiconductors, *Science* **335**, 1340 (2012).
- [14] K. Chen, A. J. Barker, M. E. Reish, K. C. Gordon, and J. M. Hodgkiss, Broadband ultrafast photoluminescence spectroscopy resolves charge photogeneration via delocalized hot excitons in polymer:fullerene photovoltaic blends, *J. Am. Chem. Soc.* **135**, 18502 (2013).
- [15] A. Troisi, How quasi-free holes and electrons are generated in organic photovoltaic interfaces, *Faraday Discuss.* **163**, 377 (2013).
- [16] H. Vázquez and A. Troisi, Calculation of rates of exciton dissociation into hot charge-transfer states in model organic photovoltaic interfaces, *Phys. Rev. B* **88**, 205304 (2013).
- [17] Z. Sun and S. Stafström, Dynamics of charge separation at an organic donor-acceptor interface, *Phys. Rev. B* **90**, 115420 (2014).
- [18] G. Nan, X. Zhang, and G. Lu, Do “hot” charge-transfer excitons promote free carrier generation in organic photovoltaics? *J. Phys. Chem. C* **119**, 15028 (2015).
- [19] S. L. Smith and A. W. Chin, Phonon-assisted ultrafast charge separation in the PCBM band structure, *Phys. Rev. B* **91**, 201302 (2015).
- [20] H. Tamura and I. Burghardt, Ultrafast charge separation in organic photovoltaics enhanced by charge delocalization and vibronically hot exciton dissociation, *J. Am. Chem. Soc.* **135**, 16364 (2013).
- [21] S. L. Smith and A. W. Chin, Ultrafast charge separation and nongeminate electron-hole recombination in organic photovoltaics, *Phys. Chem. Chem. Phys.* **16**, 20305 (2014).
- [22] K. Vandewal, S. Albrecht, E. T. Hoke, K. R. Graham, J. Widmer, J. D. Douglas, M. Schubert, W. R. Mateker, J. T. Bloking, G. F. Burkhard, A. Sellinger, J. M. J. Fréchet, A. Amassian, M. K. Riede, M. D. McGehee, D. Neher, and A. Salleo, Efficient charge generation by relaxed charge-transfer states at organic interfaces, *Nat. Mater.* **13**, 63 (2014).
- [23] E. R. Bittner and C. Silva, Noise-induced quantum coherence drives photo-carrier generation dynamics at polymeric semiconductor heterojunctions, *Nat. Commun.* **5**, 3119 (2014).
- [24] B. M. Savoie, A. Rao, A. A. Bakulin, S. Gélinas, B. Movaghar, R. H. Friend, T. J. Marks, and M. A. Ratner, Unequal partnership: Asymmetric roles of polymeric donor and fullerene acceptor in generating free charge, *J. Am. Chem. Soc.* **136**, 2876 (2014).
- [25] H. Ma and A. Troisi, Direct optical generation of long-range charge-transfer states in organic photovoltaics, *Adv. Mater.* **26**, 6163 (2014).
- [26] G. D’Avino, L. Muccioli, Y. Olivier, and D. Beljonne, Charge separation and recombination at polymer-fullerene heterojunctions: delocalization and hybridization effects, *J. Phys. Chem. Lett.* **7**, 536 (2016).
- [27] V.M. Axt and A. Stahl, A dynamics-controlled truncation scheme for the hierarchy of density matrices in semiconductor optics, *Z. Phys. B* **93**, 195 (1994).
- [28] V. M. Axt, K. Victor, and A. Stahl, Influence of a phonon bath on the hierarchy of electronic densities in an optically excited semiconductor, *Phys. Rev. B* **53**, 7244 (1996).
- [29] V. M. Axt and S. Mukamel, Nonlinear optics of semiconductor and molecular nanostructures; a common perspective, *Rev. Mod. Phys.* **70**, 145 (1998).
- [30] V. Janković and N. Vukmirović, Dynamics of exciton formation and relaxation in photoexcited semiconductors, *Phys. Rev. B* **92**, 235208 (2015).
- [31] See Supplemental Material at <http://link.aps.org/supplemental/10.1103/PhysRevB.95.075308> for equations of motion of active density matrices, further results concerning the impact of model parameters on ultrafast exciton dynamics, the mixed quantum/classical approach to exciton dynamics, and additional details regarding numerical computations of ultrafast pump-probe spectra.
- [32] I.-W. Hwang, C. Soci, D. Moses, Z. Zhu, D. Waller, R. Gaudiana, C. J. Brabec, and A. J. Heeger, Ultrafast electron transfer and decay dynamics in a small band gap bulk heterojunction material, *Adv. Mater.* **19**, 2307 (2007).
- [33] D. Mühlbacher, M. Scharber, M. Morana, Z. Zhu, D. Waller, R. Gaudiana, and C. Brabec, High photovoltaic performance of a low-bandgap polymer, *Adv. Mater.* **18**, 2884 (2006).
- [34] R. A. Street, S. A. Hawks, P. P. Khlyabich, G. Li, B. J. Schwartz, B. C. Thompson, and Y. Yang, Electronic structure and transition energies in polymer-fullerene bulk heterojunctions, *J. Phys. Chem. C* **118**, 21873 (2014).
- [35] H. Tamura and M. Tsukada, Role of intermolecular charge delocalization on electron transport in fullerene aggregates, *Phys. Rev. B* **85**, 054301 (2012).
- [36] P. Giannozzi *et al.*, Quantum espresso: a modular and open-source software project for quantum simulations of materials, *J. Phys.: Condens. Matter* **21**, 395502 (2009).
- [37] Y. Kanai and J. C. Grossman, Insights on interfacial charge transfer across P3HT/fullerene photovoltaic heterojunction from ab initio calculations, *Nano Lett.* **7**, 1967 (2007).
- [38] M. H. Lee, J. Aragón, and A. Troisi, Charge dynamics in organic photovoltaic materials: Interplay between quantum diffusion and quantum relaxation, *J. Phys. Chem. C* **119**, 14989 (2015).

- [39] E. R. Bittner and J. G. S. Ramon, Exciton and charge-transfer dynamics in polymer semiconductors, in *Quantum Dynamics of Complex Molecular Systems*, edited by D. A. Micha and I. Burghardt (Springer-Verlag, Berlin Heidelberg, 2007).
- [40] S. M. Falke, C. A. Rozzi, D. Brida, M. Maiuri, M. Amato, E. Sommer, A. De Sio, A. Rubio, G. Cerullo, E. Molinari, and C. Lienau, Coherent ultrafast charge transfer in an organic photovoltaic blend, *Science* **344**, 1001 (2014).
- [41] A. Lücke, F. Ortmann, M. Panhans, S. Sanna, E. Rauls, U. Gerstmann, and W. G. Schmidt, Temperature-dependent hole mobility and its limit in crystal-phase P3HT calculated from first principles, *J. Phys. Chem. B* **120**, 5572 (2016).
- [42] N. Vukmirović and L.-W. Wang, Charge carrier motion in disordered conjugated polymers: A multiscale ab initio study, *Nano Lett.* **9**, 3996 (2009).
- [43] D. L. Cheung and A. Troisi, Theoretical study of the organic photovoltaic electron acceptor PCBM: Morphology, electronic structure, and charge localization, *J. Phys. Chem. C* **114**, 20479 (2010).
- [44] Y.-C. Cheng and R. J. Silbey, A unified theory for charge-carrier transport in organic crystals, *J. Chem. Phys.* **128**, 114713 (2008).
- [45] S. Bera, N. Gheeraert, S. Fratini, S. Ciuchi, and S. Florens, Impact of quantized vibrations on the efficiency of interfacial charge separation in photovoltaic devices, *Phys. Rev. B* **91**, 041107 (2015).
- [46] J. C. Tully, Molecular dynamics with electronic transitions, *J. Chem. Phys.* **93**, 1061 (1990).
- [47] L. Wang and O. V. Prezhdo, A simple solution to the trivial crossing problem in surface hopping, *J. Phys. Chem. Lett.* **5**, 713 (2014).
- [48] A. Chenel, E. Mangaud, I. Burghardt, C. Meier, and M. Desouter-Lecomte, Exciton dissociation at donor-acceptor heterojunctions: Dynamics using the collective effective mode representation of the spin-boson model, *J. Chem. Phys.* **140**, 044104 (2014).
- [49] R. D. Pensack and J. B. Asbury, Beyond the adiabatic limit: Charge photogeneration in organic photovoltaic materials, *J. Phys. Chem. Lett.* **1**, 2255 (2010).
- [50] S. Mukamel, *Principles of Nonlinear Optical Spectroscopy* (Oxford University Press, New York, 1995).
- [51] J. Cabanillas-Gonzalez, G. Grancini, and G. Lanzani, Pump-probe spectroscopy in organic semiconductors: Monitoring fundamental processes of relevance in optoelectronics, *Adv. Mater.* **23**, 5468 (2011).
- [52] E. Perfetto and G. Stefanucci, Some exact properties of the nonequilibrium response function for transient photoabsorption, *Phys. Rev. A* **91**, 033416 (2015).
- [53] J. Walkenhorst, U. De Giovannini, A. Castro, and A. Rubio, Tailored pump-probe transient spectroscopy with time-dependent density-functional theory: controlling absorption spectra, *Eur. Phys. J. B* **89**, 128 (2016).
- [54] Coherences between exciton states and the ground state y_x typically decay on $\lesssim 100$ -fs time scale after the pump field has vanished, while exciton-exciton coherences typically decay on picosecond time scales or longer. Therefore, in our computations, we expect to see the decay of coherences between exciton states and the ground state, but not of the exciton-exciton coherences, and time scales on which Eq. (32) is valid are in principle at least picosecond or longer.
- [55] M. Valiev, E. J. Bylaska, N. Govind, K. Kowalski, T. P. Straatsma, H. J. J. Van Dam, D. Wang, J. Nieplocha, E. Apra, T. L. Windus, and W. A. de Jong, NWChem: A comprehensive and scalable open-source solution for large scale molecular simulations, *Comput. Phys. Commun.* **181**, 1477 (2010).
- [56] A. A. Kocherzhenko, D. Lee, M. A. Forsuelo, and K. B. Whaley, Coherent and incoherent contributions to charge separation in multichromophore systems, *J. Phys. Chem. C* **119**, 7590 (2015).
- [57] L. J. A. Koster, V. D. Mihailetchi, and P. W. M. Blom, Ultimate efficiency of polymer/fullerene bulk heterojunction solar cells, *Appl. Phys. Lett.* **88**, 093511 (2006).

Dynamics of exciton formation and relaxation in photoexcited semiconductors

Veljko Janković* and Nenad Vukmirović†

Scientific Computing Laboratory, Institute of Physics Belgrade, University of Belgrade, Pregrevica 118, 11080 Belgrade, Serbia

(Received 21 October 2015; revised manuscript received 4 December 2015; published 22 December 2015)

We investigate the dynamics of the exciton formation and relaxation on a picosecond time scale following a pulsed photoexcitation of a semiconductor. The study is conducted in the framework of the density matrix theory complemented with the dynamics controlled truncation scheme. We truncate the phonon branch of the resulting hierarchy of equations and propose the form of coupling among single-phonon-assisted and higher-order phonon-assisted density matrices so as to ensure the energy and particle-number conservation in a closed system. Time scales relevant for the exciton formation and relaxation processes are determined from numerical investigations performed on a one-dimensional model for the values of model parameters representative of a typical organic and inorganic semiconductor. The exciton dynamics is examined for different values of central frequency of the exciting field, temperature, and microscopic model parameters, such as the strengths of carrier-carrier and carrier-phonon couplings. We find that for typical organic semiconductor parameters, formation of bound excitons occurs on a several-hundred-femtosecond time scale, while their subsequent relaxation and equilibration take at least several picoseconds. These time scales are consistent with recent experimental studies of the exciton formation and relaxation in conjugated polymer-based materials.

DOI: [10.1103/PhysRevB.92.235208](https://doi.org/10.1103/PhysRevB.92.235208)

PACS number(s): 71.35.-y, 71.10.-w

I. INTRODUCTION

The continual and ever-increasing demand for economic and efficient ways of utilizing solar energy drives a huge part of current research activities. In particular, organic solar cells have developed rapidly in the past decade and have become promising candidates for economically viable large-scale power generation due to their flexibility, cost effectiveness, relatively simple fabrication techniques, and mass production [1,2]. Processes upon which the operation of solar cells is based are the light absorption in a semiconducting material and the subsequent conversion of photons into mobile charge carriers that produce an electric current [3,4]. An optical excitation of a semiconductor creates an exciton, i.e., an electron-hole pair in which Coulomb attraction between oppositely charged electron and hole prevents their separation. In a conventional inorganic semiconductor, relatively weak Coulomb interaction (primarily due to large dielectric constant) results in the exciton binding energy of the order of 10 meV [5–7]. Thus, thermal excitations are likely to split the exciton in an electron and a hole. On the other hand, in a typical organic semiconductor, the attraction between an electron and a hole is much stronger (mainly due to low dielectric constant), the exciton binding energy being of the order of or larger than 500 meV [3,8]. Therefore, while optical absorption in an inorganic semiconductor results in almost immediate generation of free charges, in an organic semiconductor it leads to formation of tightly bound electron-hole pairs, which should be separated in order to generate current [1,3,4]. This last conclusion has an enormous impact on the design and geometry of organic photovoltaic devices.

Photoexcitation of a semiconductor creates electron-hole pairs in a highly nonequilibrium state. Apart from the Coulomb interaction, which primarily induces correlations, the carrier-phonon interaction is also vital for a thorough understanding

of nonequilibrium processes taking place in photoexcited semiconductors. Theoretical approaches for treating these processes are most often based on the density matrix theory [9,10] or the nonequilibrium Green's functions formalism [11]. Density matrix theory has become the preferred technique in the treatment of experiments with ultrashort pulses since it deals with quantities that depend on one time argument and are directly related to observables.

Previous theoretical studies of the exciton formation process after an ultrafast optical excitation of a semiconductor were typically focused on inorganic semiconductors. Early studies were conducted in the framework of the semiclassical Boltzmann approach [12,13]. The fully microscopic and quantum theory for the interacting system of electrons, holes, photons, and phonons, capable of treating a wide variety of optical and excitonic effects after an ultrafast optical excitation of a semiconductor, was elaborated in Refs. [14–18]. On the other hand, the exciton formation from an initial state of two opposite charges in organic semiconductors was typically modeled by simulating the time evolution of empirical Hamiltonians applied to small systems, where the effects of the lattice are not included or are treated classically [19,20].

The main aim of this work was to investigate the dynamics of exciton formation on short (up to several ps) time scale. This time scale is of particular relevance for the operation of organic solar cells since it has been well established that the exciton separation at the interface of donor and acceptor materials occurs on a subpicosecond time scale [21,22]. However, the details of the exciton formation and separation process and the factors that determine its efficiency are still not well understood. In recent years, significant insights have been obtained from subpicosecond time-resolved experiments performed both on neat materials [23,24] and blends [25–29]. The results of all these experiments highlight the importance of nonequilibrium nature of excitons formed after photoexcitation.

In our study, we employ the Hamiltonian which includes all relevant physical effects in the system: electronic coupling which leads to band formation, electron-hole interaction

*veljko.jankovic@ipb.ac.rs

†nenad.vukmirovic@ipb.ac.rs

which causes exciton formation, electron-phonon interaction that leads to relaxation, and the interaction with external electromagnetic field. We do not, however, include the effects of stimulated emission which lead to radiative recombination of excitons since we are interested in the exciton dynamics on a short time scale, where these effects are negligible. From the time evolution of relevant quantities, we identify the time scale of the processes of formation of free charges and bound excitons and their subsequent relaxation. Rather than focusing on the details of one particular material system, we have chosen a Hamiltonian whose parameters can be easily varied so that we can identify the influence of different physical effects on relevant time scales. The study is conducted in the framework of the density matrix formalism combined with the so-called dynamics controlled truncation (DCT) scheme, first developed in 1994 by Axt and Stahl [30,31]. This method is particularly suited for a system described by a pair-conserving Hamiltonian which is initially unexcited and was successfully applied to study the dynamics of exciton formation for near-band-gap excitations and low-excitation densities [32–34]. Here, we truncate the phonon branch of the hierarchy so as to ensure that the resulting equations are compatible with the energy and particle-number conservation in a closed system. Furthermore, we propose the form of coupling between single-phonon-assisted and higher-order phonon-assisted electronic density matrices which is compatible with the energy conservation in a closed system.

The paper is organized as follows. In Sec. II, the general form of the Hamiltonian, along with the equations which describe the exciton formation process, is presented. Section III is devoted to the results of our numerical investigations of the exciton formation process which are carried out on a one-dimensional model system. The discussion of our results in light of recent experimental investigations of ultrafast exciton dynamics is presented in Sec. IV, whereas concluding remarks are given in Sec. V.

II. THEORETICAL FRAMEWORK

We use the standard two-band semiconductor model which takes into account the interaction of carriers with the external electromagnetic field applied to the semiconductor, as well as carrier-carrier and carrier-phonon interactions. We will work in the electron-hole picture which is particularly suited for describing the effects which arise after the optical excitation of an initially unexcited semiconductor. Notation from Ref. [35] will be used. The Hamiltonian has the form

$$H = H_c + H_{\text{ph}} + H_{\text{c-ph}} + H_{\text{c-f}}, \quad (1)$$

where H_c describes interacting carriers

$$\begin{aligned} H_c = & \sum_{q \in \text{CB}} \epsilon_q^c c_q^\dagger c_q - \sum_{q \in \text{VB}} \epsilon_q^v d_q^\dagger d_q \\ & + \frac{1}{2} \sum_{pqkl \in \text{CB}} V_{pqkl}^{\text{cccc}} c_p^\dagger c_k^\dagger c_l c_q + \frac{1}{2} \sum_{pqkl \in \text{VB}} V_{pqkl}^{\text{vvvv}} d_q^\dagger d_l^\dagger d_k d_p \\ & + \sum_{\substack{pq \in \text{VB} \\ kl \in \text{CB}}} (V_{plkq}^{\text{vcv}} - V_{pqkl}^{\text{vcc}}) c_k^\dagger d_q^\dagger d_p c_l, \end{aligned} \quad (2)$$

$$H_{\text{ph}} = \sum_{\mu} \hbar \omega_{\mu} b_{\mu}^{\dagger} b_{\mu} \quad (3)$$

is the free-phonon Hamiltonian, $H_{\text{c-ph}}$ describes the carrier-phonon interaction

$$\begin{aligned} H_{\text{c-ph}} = & \sum_{\substack{pq \in \text{CB} \\ \mu}} (\gamma_{pq}^{\mu} c_p^{\dagger} c_q b_{\mu}^{\dagger} + \gamma_{pq}^{\mu*} c_q^{\dagger} c_p b_{\mu}) \\ & - \sum_{\substack{pq \in \text{VB} \\ \mu}} (\gamma_{pq}^{\mu} d_q^{\dagger} d_p b_{\mu}^{\dagger} + \gamma_{pq}^{\mu*} d_p^{\dagger} d_q b_{\mu}), \end{aligned} \quad (4)$$

whereas the coupling to the optical field is given by

$$H_{\text{c-f}} = -\mathbf{E}(t) \cdot \left(\sum_{\substack{p \in \text{VB} \\ q \in \text{CB}}} \mathbf{M}_{pq}^{\text{vc}} d_p c_q + \sum_{\substack{p \in \text{CB} \\ q \in \text{VB}}} \mathbf{M}_{pq}^{\text{cv}} c_p^{\dagger} d_q^{\dagger} \right). \quad (5)$$

Fermi operators c_q^{\dagger} (c_q) create (annihilate) an electron of energy ϵ_q^c in the single-particle state q in the conduction band, while Fermi operators d_q^{\dagger} (d_q) create (annihilate) a hole of energy $-\epsilon_q^v$ in the single-particle state q in the valence band. Matrix elements of the Coulomb interaction potential $V(\mathbf{x} - \mathbf{y})$ are defined as

$$V_{pqkl}^{\lambda_p \lambda_q \lambda_k \lambda_l} = \int d\mathbf{x} d\mathbf{y} \phi_p^{\lambda_p*}(\mathbf{x}) \phi_q^{\lambda_q}(\mathbf{x}) V(\mathbf{x} - \mathbf{y}) \phi_k^{\lambda_k*}(\mathbf{y}) \phi_l^{\lambda_l}(\mathbf{y}), \quad (6)$$

where $\phi_p^{\lambda_p}(\mathbf{x})$ are single-particle eigenfunctions for an electron in the state p and in the band λ_p . Bose operators b_{μ}^{\dagger} (b_{μ}) create (annihilate) a phonon in mode μ , while γ_{pq}^{μ} are carrier-phonon matrix elements. We neglect intraband contributions to the carrier-field interaction and retain only interband dipole matrix elements.

We note that the Hamiltonian of interacting carriers [Eq. (2)] includes the limiting cases of Wannier and Frenkel excitons. Namely, when single-particle eigenfunctions are of the Bloch form labeled by a wave vector \mathbf{k} , then under suitable approximations, described, e.g., in Ref. [36], we obtain the Hamiltonian describing the limiting case of Wannier excitons. On the other hand, if single-particle eigenfunctions are taken to be atomic states labeled by a position vector \mathbf{R} , then using approximations that exploit localization properties of this basis set the Hamiltonian appropriate for the limiting case of Frenkel excitons is obtained [37].

We study the dynamics of exciton formation in photoexcited semiconductors in the framework of the density matrix theory. Differential equations for dynamic variables are formed and, due to the many-body nature of the problem, an infinite hierarchy of differential equations is obtained. The main approximation is then the truncation of the hierarchy, which can be based upon different physical pictures. The Hamiltonian defined by Eqs. (1)–(5) has the property that only the interaction with the optical field can change the number of pair excitations. The DCT scheme relies upon the aforementioned property of the Hamiltonian and classifies higher-order density matrices according to their leading order in the optical field [30,35,38]. Namely, when the system is initially in the

ground state represented by the vacuum of electron-hole pairs, the expectation value of the normal-ordered product of n_e electron operators c^\dagger and c , n_h hole operators d^\dagger and d and an arbitrary number of phonon operators b^\dagger and b is at least of the order $m = \max\{n_e, n_h\}$ in the applied field. Therefore, higher-order density matrices are also of higher order in the optical field and only a finite number of electronic density matrices contributes to the optical response at any given order in the optical field. The DCT scheme truncates only the electronic branch of the hierarchy and can be used along with any strategy to deal with the phonon-assisted branch of the hierarchy [7]. We limit ourselves to the case of weak optical field and low carrier densities, in which it is justified to neglect biexcitonic effects and keep only contributions up to the second order in the optical field. In Refs. [32,35] a reduced treatment of the phonon branch of the hierarchy, which can be combined with the DCT scheme for the electronic branch of the hierarchy, was presented. This treatment includes correlation expansion for phonon-assisted variables combined with the Markov approximation. As a result, phonon-assisted variables are eliminated from the formalism and only two types of electronic density matrices remain. These are the interband transition amplitude (excitonic amplitude)

$$Y_{ab} = \langle d_a c_b \rangle \quad (7)$$

and the electron-hole pair density (excitonic population)

$$N_{abcd} = \langle c_a^\dagger d_b^\dagger d_c c_d \rangle. \quad (8)$$

In this study, we adopt a different strategy for dealing with the phonon-assisted density matrices. In order to facilitate the truncation of the phonon-assisted branch of the hierarchy, the following generating functions for the phonon-assisted electronic density matrices are defined [35]:

$$Y_{ab}^{\alpha\beta} = \langle d_a c_b \hat{F}^{\alpha\beta} \rangle, \quad (9)$$

$$N_{abcd}^{\alpha\beta} = \langle c_a^\dagger d_b^\dagger d_c c_d \hat{F}^{\alpha\beta} \rangle, \quad (10)$$

$$F^{\alpha\beta} = \langle \hat{F}^{\alpha\beta} \rangle = \left\langle \exp \left(\sum_{\rho} \alpha_{\rho} b_{\rho}^\dagger \right) \exp \left(\sum_{\rho} \beta_{\rho} b_{\rho} \right) \right\rangle, \quad (11)$$

where $\{\alpha_{\rho}\}$ and $\{\beta_{\rho}\}$ are arbitrary sets of real parameters. As a consequence of the generating-function property, all phonon-assisted electronic density matrices can be obtained as derivatives of these functions taken at $\alpha_{\mu} = \beta_{\mu} = 0$. The electron and hole populations and correlations $\langle c_a^\dagger c_b \rangle$ and $\langle d_a^\dagger d_b \rangle$, as well as their phonon-assisted counterparts, do not have to be considered as independent variables in the formalism since they can be eliminated in favor of N by identities (contraction identities) that are exact within the second-order treatment [35,38]. The differential equations for variables $Y_{ab}^{\alpha\beta}$ and $N_{abcd}^{\alpha\beta}$ are given in Appendix A.

The most general form of an electron-hole pair state is [36]

$$|p\rangle = \sum_{\substack{a \in \text{VB} \\ b \in \text{CB}}} \psi_{ab} c_b^\dagger d_a^\dagger |0\rangle, \quad (12)$$

where $|0\rangle$ represents the state in which the conduction band is completely empty and the valence band is completely filled.

The excitonic basis is defined by the eigenvalue problem $H_c |p\rangle = E |p\rangle$ which can be transformed into equations for amplitudes ψ_{ab} :

$$(\epsilon_b^c - \epsilon_a^v) \psi_{ab}^x + \sum_{\substack{p \in \text{VB} \\ q \in \text{CB}}} (V_{pqba}^{\text{vccv}} - V_{pabq}^{\text{vccc}}) \psi_{pq}^x = \hbar \omega_x \psi_{ab}^x. \quad (13)$$

The excitonic basis is orthonormal

$$\sum_{\substack{a \in \text{VB} \\ b \in \text{CB}}} \psi_{ab}^{\bar{x}*} \psi_{ab}^x = \delta_{x\bar{x}}. \quad (14)$$

We perform all calculations in the excitonic basis and expand all density matrices in the excitonic basis, for example,

$$Y_{ab} = \sum_x \psi_{ab}^x y_x, \quad (15)$$

$$N_{abcd} = \sum_{\bar{x}x} \psi_{ba}^{\bar{x}*} \psi_{cd}^x n_{\bar{x}x}, \quad (16)$$

and similarly for the corresponding phonon-assisted electronic density matrices; in the case of single-phonon assistance, the explicit definitions are

$$Y_{ab\mu^+} \equiv \langle d_a c_b b_{\mu}^\dagger \rangle = \sum_x \psi_{ab}^x y_{x\mu^+}, \quad (17a)$$

$$N_{abcd\mu^+} \equiv \langle c_a^\dagger d_b^\dagger d_c c_d b_{\mu}^\dagger \rangle = \sum_{\bar{x}x} \psi_{ba}^{\bar{x}*} \psi_{cd}^x n_{\bar{x}x\mu^+}. \quad (17b)$$

The creation operator for the exciton in the state x can be defined as

$$X_x^\dagger = \sum_{\substack{a \in \text{CB} \\ b \in \text{VB}}} \psi_{ba}^x c_a^\dagger d_b^\dagger. \quad (18)$$

The number of excitons in the state x , after performing the decoupling (which is exact up to the second order in the optical field) $\langle c_a^\dagger d_b^\dagger d_c c_d \rangle = \langle c_a^\dagger d_b^\dagger \rangle \langle d_c c_d \rangle + \delta \langle c_a^\dagger d_b^\dagger d_c c_d \rangle$, where $\delta \langle c_a^\dagger d_b^\dagger d_c c_d \rangle$ stands for the correlated part of the electron-hole pair density, can be expressed as the sum

$$\langle X_x^\dagger X_x \rangle = |y_x|^2 + \bar{n}_{xx}, \quad (19)$$

where $\bar{n}_{xx} = n_{xx} - y_x^* y_x$. The first term in Eq. (19) describes the so-called coherent excitons, whereas the second term describes the incoherent excitons. Namely, an optical excitation of a semiconductor first induces single-particle excitations in form of optical polarizations and carrier densities. Optical polarizations decay very fast due to various scattering mechanisms present [15]. Therefore, their squared moduli, which are usually referred to as coherent excitonic populations [32], do not provide information about the true excitonic populations, which are the consequence of Coulomb-induced correlations between electrons and holes and which typically exist in the system for a long time after the decay of optical polarizations [7]. In order to describe true excitons, which are atomlike complexes of electrons and holes bound by the Coulomb attraction, we have to consider two-particle correlations between them, and not single-particle quantities [15]. The last conclusion justifies identification of the term $\delta \langle c_a^\dagger d_b^\dagger d_c c_d \rangle$ with the incoherent excitonic populations.

The dynamic equations for the relevant variables should be compatible with the energy conservation in a system without external fields. Our system, however, interacts with external optical field, but, since we consider a pulsed excitation, the energy of the system should be conserved after the field has vanished. The total energy of the system, i.e., the expectation value of the Hamiltonian $\langle H \rangle$ defined in Eqs. (1)–(5), is expressed as

$$\mathcal{E} = \mathcal{E}_c + \mathcal{E}_{\text{ph}} + \mathcal{E}_{\text{c-ph}} + \mathcal{E}_{\text{c-f}}, \quad (20)$$

where the carrier energy is

$$\mathcal{E}_c = \sum_x \hbar \omega_x n_{xx}, \quad (21)$$

the phonon energy is

$$\mathcal{E}_{\text{ph}} = \sum_{\mu} \hbar \omega_{\mu} \langle b_{\mu}^{\dagger} b_{\mu} \rangle, \quad (22)$$

the carrier-phonon interaction energy is

$$\mathcal{E}_{\text{c-ph}} = 2 \sum_{\bar{x}\mu} \text{Re} \{ \Gamma_{\bar{x}\mu}^{\mu} n_{\bar{x}\mu} \}, \quad (23)$$

and the carrier-field interaction energy is

$$\mathcal{E}_{\text{c-f}} = -\mathbf{E}(t) \sum_x (\mathbf{M}_x^* y_x + y_x^* \mathbf{M}_x). \quad (24)$$

In Eqs. (20)–(24) we have kept only contributions up to the second order in the external field and transferred to the excitonic basis. We also introduce excitonic dipole matrix elements

$$\mathbf{M}_x = \sum_{\substack{a \in \text{VB} \\ b \in \text{CB}}} \psi_{ab}^{x*} \mathbf{M}_{ba}^{\text{cv}}, \quad (25)$$

as well as matrix elements of the carrier-phonon interaction in the excitonic basis which describe the coupling to the phonon mode μ :

$$\Gamma_{xx'}^{\mu} = \sum_{\substack{a \in \text{VB} \\ b \in \text{CB}}} \psi_{ab}^{x*} \left(\sum_{k \in \text{CB}} \gamma_{bk}^{\mu} \psi_{ak}^{x'} - \sum_{k \in \text{VB}} \gamma_{ka}^{\mu} \psi_{kb}^{x'} \right). \quad (26)$$

Within previous approaches to solving the hierarchy of equations obtained after performing the DCT scheme, single-phonon-assisted density matrices $n_{\bar{x}\mu}^{\mu}$, which appear in Eq. (23), were not explicitly taken into account, but the respective differential equations were solved in the Markov and adiabatic approximations. However, it can be shown that the total energy under these approximations is not exactly conserved after the external field has vanished. In order to satisfy the energy conservation, we retain density matrices $n_{\bar{x}\mu}^{\mu}$ as independent dynamic variables in the formalism.

The dynamics should also conserve the particle number after the external field has vanished since all the other terms in the Hamiltonian given by Eqs. (1)–(5) commute with the total particle-number operator. The number of electrons (and also the number of holes, since carriers are generated in pairs in this model), with accuracy up to the second order in the

external field, is given as

$$N_{\text{tot}} = N_e = N_h = \sum_x n_{xx}. \quad (27)$$

The equations for the purely electronic relevant variables and phonon distribution function are

$$\begin{aligned} \partial_t y_x &= -i \omega_x y_x - \frac{1}{i\hbar} \mathbf{E}(t) \mathbf{M}_x \\ &+ \frac{1}{i\hbar} \sum_{\mu x'} \Gamma_{xx'}^{\mu} y_{x'\mu^+} + \frac{1}{i\hbar} \sum_{\mu x'} \Gamma_{x'\mu^+}^{\mu*} y_{x'\mu^-}, \end{aligned} \quad (28)$$

$$\begin{aligned} \partial_t n_{\bar{x}\mu} &= -i(\omega_x - \omega_{\bar{x}}) n_{\bar{x}\mu} - \frac{1}{i\hbar} \mathbf{E}(t) (y_{\bar{x}}^* \mathbf{M}_x - \mathbf{M}_{\bar{x}}^* y_x) \\ &+ \frac{1}{i\hbar} \sum_{\mu x'} \Gamma_{xx'}^{\mu} n_{\bar{x}x'\mu^+} - \frac{1}{i\hbar} \sum_{\mu \bar{x}'} \Gamma_{\bar{x}'\bar{x}}^{\mu} n_{\bar{x}'\mu^+} \\ &+ \frac{1}{i\hbar} \sum_{\mu x'} \Gamma_{x'\mu^+}^{\mu*} n_{\bar{x}\bar{x}'\mu^+} - \frac{1}{i\hbar} \sum_{\mu \bar{x}'} \Gamma_{\bar{x}\bar{x}'}^{\mu*} n_{\bar{x}\bar{x}'\mu^+}, \end{aligned} \quad (29)$$

$$\partial_t \langle b_{\mu}^{\dagger} b_{\mu} \rangle = \frac{2}{\hbar} \sum_{\bar{x}\mu} \text{Im} \{ \Gamma_{\bar{x}\mu}^{\mu} n_{\bar{x}\mu} \}. \quad (30)$$

Even at this level, without specifying the form of equations for one-phonon-assisted electronic density matrices, using Eq. (29) with vanishing electric field it is easily shown that, in the absence of external fields, our dynamics conserves the total number of particles.

We will neglect hot-phonon effects and assume that in all the equations for y_x , $n_{\bar{x}\mu}$, and their phonon-assisted counterparts the phonon numbers assume their equilibrium values $n_{\mu}^{\text{ph}} = (e^{\beta \hbar \omega_{\mu}} - 1)^{-1}$. We will, however, retain Eq. (30) in the formalism because it is necessary to prove the energy conservation.

In equations for phonon-assisted electronic density matrices we neglect the coupling to the light field, i.e., we neglect contributions arising from the combined action of the phonon coupling and the interaction with the light field (so-called cross terms) [35,39]. The equations for the electronic density matrices with one-phonon assistance contain electronic density matrices with two-phonon assistance, from which we explicitly separate the factorized part and the correlated part, for example

$$\langle c_a^{\dagger} d_b^{\dagger} d_c d_a b_{\mu}^{\dagger} b_{\rho} \rangle = \langle c_a^{\dagger} d_b^{\dagger} d_c d_a \rangle \delta_{\mu\rho} n_{\mu}^{\text{ph}} + \delta \langle c_a^{\dagger} d_b^{\dagger} d_c d_a b_{\mu}^{\dagger} b_{\rho} \rangle, \quad (31)$$

$$\langle d_a c_b b_{\mu}^{\dagger} b_{\rho} \rangle = \langle d_a c_b \rangle \delta_{\mu\rho} n_{\mu}^{\text{ph}} + \delta \langle d_a c_b b_{\mu}^{\dagger} b_{\rho} \rangle. \quad (32)$$

We should bear in mind that the two-phonon-assisted electronic density matrices with two creation (annihilation) phonon operators, whose factorized part vanishes, should be considered on this level of truncation of the phonon branch [40]. Further comments on the factorization performed in Eq. (31) are given in Appendix B. The following equations for the electronic density matrices with single-phonon assistance are

obtained:

$$\begin{aligned} \partial_t n_{\bar{x}x\mu^+} = & -i(\omega_x - \omega_{\bar{x}} - \omega_\mu) n_{\bar{x}x\mu^+} + \frac{n_\mu^{\text{ph}}}{i\hbar} \sum_{x'} \Gamma_{x'\bar{x}}^{\mu*} n_{\bar{x}x'} \\ & - \frac{1+n_\mu^{\text{ph}}}{i\hbar} \sum_{\bar{x}'} \Gamma_{\bar{x}\bar{x}'}^{\mu*} n_{\bar{x}'x} \\ & - \frac{1}{i\hbar} \sum_{\rho\bar{x}'} (\Gamma_{\bar{x}\bar{x}'}^{\rho*} \delta n_{\bar{x}'x\mu^+\rho^-} + \Gamma_{\bar{x}'\bar{x}}^\rho \delta n_{\bar{x}x'\mu^+\rho^+}) \\ & + \frac{1}{i\hbar} \sum_{\rho x'} (\Gamma_{x'\bar{x}}^{\rho*} \delta n_{\bar{x}x'\mu^+\rho^-} + \Gamma_{xx'}^\rho \delta n_{\bar{x}x'\mu^+\rho^+}), \end{aligned} \quad (33)$$

$$\begin{aligned} \partial_t y_{x\mu^+} = & -i(\omega_x - \omega_\mu) y_{x\mu^+} + \frac{n_\mu^{\text{ph}}}{i\hbar} \sum_{x'} \Gamma_{x'\bar{x}}^{\mu*} y_{x'} \\ & + \frac{1}{i\hbar} \sum_{\rho x'} (\Gamma_{xx'}^\rho \delta y_{x'\mu^+\rho^+} + \Gamma_{x'\bar{x}}^{\rho*} \delta y_{x'\mu^+\rho^-}), \end{aligned} \quad (34)$$

$$\begin{aligned} \partial_t y_{x\mu^-} = & -i(\omega_x + \omega_\mu) y_{x\mu^-} + \frac{1+n_\mu^{\text{ph}}}{i\hbar} \sum_{x'} \Gamma_{xx'}^\mu y_{x'} \\ & + \frac{1}{i\hbar} \sum_{\rho x'} (\Gamma_{xx'}^\rho \delta y_{x'\rho^+\mu^-} + \Gamma_{x'\bar{x}}^{\rho*} \delta y_{x'\rho^-\mu^-}). \end{aligned} \quad (35)$$

The correlated parts of two-phonon-assisted density matrices appearing in Eqs. (33) ($\delta n_{\bar{x}x\mu^+\rho^-}, \delta n_{\bar{x}x\mu^+\rho^+}$), (34), and (35) can be obtained solving their respective differential equations, in which all three-phonon-assisted density matrices have been appropriately factorized and their correlated parts have been neglected, in the Markov and adiabatic approximations. This procedure closes the phonon branch of the hierarchy. However, the full solution to these equations, when combined with Eq. (33), is cumbersome to evaluate, so further approximations are usually employed. The most common one is the so-called random phase approximation, which neglects sums over correlated parts of one-phonon-assisted electronic density matrices (which are complex quantities) due to random phases at different arguments of these density matrices [9]. After performing all the discussed approximations, the last two summands in Eq. (33), which represent the rate at which $n_{\bar{x}x\mu^+}$ changes due to the coupling to electronic density matrices with higher phonon assistance, reduce to

$$(\partial_t n_{\bar{x}x\mu^+})_{\text{higher}} = -\gamma_{\bar{x}x\mu} n_{\bar{x}x\mu^+}, \quad (36)$$

where $\gamma_{\bar{x}x\mu}$ is given as

$$\begin{aligned} \gamma_{\bar{x}x\mu} = & \frac{1}{2}(\Gamma_x + \Gamma_{\bar{x}}), \quad (37) \\ \Gamma_x = & \frac{2\pi}{\hbar} \sum_{\bar{x}\rho} [|\Gamma_{x\bar{x}}^\rho|^2 \delta(\hbar\omega_x - \hbar\omega_{\bar{x}} + \hbar\omega_\rho) n_\rho^{\text{ph}} \\ & + |\Gamma_{\bar{x}x}^\rho|^2 \delta(\hbar\omega_x - \hbar\omega_{\bar{x}} - \hbar\omega_\rho)(1 + n_\rho^{\text{ph}})]. \end{aligned} \quad (38)$$

Details of the procedure employed to close the phonon branch of the hierarchy are given in Appendix B.

It was recognized that this form of the coupling to higher-order phonon-assisted electronic density matrices is at variance with the energy conservation [9,10,41]. In this work, we will

use the following form of the coupling to higher-order phonon-assisted density matrices:

$$(\partial_t n_{\bar{x}x\mu}^{(+)})_{\text{higher}} = -\gamma_{\bar{x}x\mu} n_{\bar{x}x\mu}^{(+)} + \gamma_{\bar{x}x\mu} n_{\bar{x}x\mu}^{(+)*}, \quad (39)$$

where $\gamma_{\bar{x}x\mu}$ is, as before, defined by Eqs. (37) and (38). This form of $(\partial_t n_{\bar{x}x\mu}^{(+)})_{\text{higher}}$ is compatible with the energy conservation, as long as excitonic matrix elements of the carrier-phonon interaction $\Gamma_{\bar{x}x}^\mu$ are purely real, which is the case relevant for our numerical investigation in Sec. III. Namely, as is shown in Appendix C, the rate at which the total energy changes after the pulse is equal to the rate at which the carrier-phonon interaction energy changes due to the coupling of the single-phonon-assisted electronic density matrices $n_{\bar{x}x\mu^+}$ to density matrices with higher-order phonon assistance,

$$\begin{aligned} \partial_t \mathcal{E} = & (\partial_t \mathcal{E}_{\text{c-ph}})_{\text{higher}} \\ = & 2 \sum_{\bar{x}x\mu} \text{Re} \{ \Gamma_{\bar{x}x}^\mu (\partial_t n_{\bar{x}x\mu^+})_{\text{higher}} \}. \end{aligned} \quad (40)$$

It is then clear that, if all $\Gamma_{\bar{x}x}^\mu$ are real, the form of $(\partial_t n_{\bar{x}x\mu^+})_{\text{higher}}$ given in Eq. (39) does not violate the energy conservation. Furthermore, as $n_{\bar{x}x\mu^+}$ describes the elementary process in which an exciton initially in the state x is scattered to the state \bar{x} emitting the phonon from the mode μ , the reverse microscopic process, described by $n_{x\bar{x}\mu^-} = n_{\bar{x}x\mu^+}^*$, is also possible, so in the differential equation for $n_{\bar{x}x\mu^+}$ the quantity $n_{x\bar{x}\mu^-}^*$ may appear. In Appendix C, we comment on the energy conservation in greater detail.

Similar strategy can be adopted to simplify the coupling to electronic density matrices with higher phonon assistance in (34) and (35), with the final result

$$(\partial_t y_{x\mu}^{(\pm)})_{\text{higher}} = -\gamma_{x\mu} y_{x\mu}^{(\pm)}, \quad (41)$$

where

$$\gamma_{x\mu} = \frac{1}{2}\Gamma_x, \quad (42)$$

and Γ_x is defined in Eq. (38).

An alternative route to derive equations for the relevant variables is to rewrite the Hamiltonian given in Eq. (1) in terms of operators X_x, X_x^\dagger [see Eq. (18)], keeping only contributions whose expectation values are at most of the second order in the optical field. The result is

$$\begin{aligned} H = & \sum_x \hbar\omega_x X_x^\dagger X_x + \sum_\mu \hbar\omega_\mu b_\mu^\dagger b_\mu \\ & + \sum_{\mu\bar{x}x} \left(\Gamma_{\bar{x}x}^\mu X_{\bar{x}}^\dagger X_x b_\mu^\dagger + \Gamma_{\bar{x}x}^{\mu*} X_x^\dagger X_{\bar{x}} b_\mu \right) \\ & - \mathbf{E}(t) \sum_x (\mathbf{M}_x^* X_x + \mathbf{M}_x X_x^\dagger). \end{aligned} \quad (43)$$

The excitonic operators (up to the second order in the optical field) satisfy Bose commutation relations $[X_x, X_{\bar{x}}^\dagger] = \delta_{x\bar{x}}$. In this representation [42], the excitons are treated as noninteracting bosons and the form of the exciton-phonon interaction is transparent, with exciton-phonon coupling constants $\Gamma_{\bar{x}x}^\mu$ defined in Eq. (26).

III. ONE-DIMENSIONAL SEMICONDUCTOR MODEL AND NUMERICAL RESULTS

Numerical computations will be carried out on a two-band one-dimensional semiconductor model. We use a tight-binding model on a one-dimensional lattice with N sites and lattice spacing a to describe the semiconductor. Periodic boundary conditions are used. The Hamiltonian describing interacting carriers is given as

$$H_c = \sum_{i=0}^{N-1} \epsilon_0^c c_i^\dagger c_i - \sum_{i=0}^{N-1} J^c (c_i^\dagger c_{i+1} + c_{i+1}^\dagger c_i) - \sum_{i=0}^{N-1} \epsilon_0^v d_i^\dagger d_i + \sum_{i=0}^{N-1} J^v (d_i^\dagger d_{i+1} + d_{i+1}^\dagger d_i) + \frac{1}{2} \sum_{i,j=0}^{N-1} (c_i^\dagger c_i - d_i^\dagger d_i) V_{ij} (c_j^\dagger c_j - d_j^\dagger d_j). \quad (44)$$

It is assumed that the carrier transfer integrals J^c, J^v are nonzero only among nearest-neighbor pairs of sites. The Coulomb interaction is taken in the lowest monopole-monopole approximation [43], and the interaction potential V_{ij} is taken to be the Ohno potential

$$V_{ij} = \frac{U}{\sqrt{1 + \left(\frac{|i-j|a}{a_0}\right)^2}}. \quad (45)$$

U is the onsite carrier-carrier interaction, while a_0 is the characteristic length given as $a_0 = e^2/(4\pi\epsilon_0\epsilon_r U)$, where ϵ_r is the static relative dielectric constant. This form of carrier-carrier interaction is an interpolation between the onsite Coulomb interaction U and the ordinary Coulomb potential (in which the static relative dielectric constant is taken) $e^2/(4\pi\epsilon_0\epsilon_r r)$ when $r \rightarrow \infty$ (see, e.g., the discussion on the effective electron-hole interaction in Ref. [5]). The interaction with phonons is taken to be of the Holstein form, where a charge carrier is locally and linearly coupled to a dispersionless optical mode

$$H_{c-ph} = \sum_{i=0}^{N-1} g^c c_i^\dagger c_i (b_i + b_i^\dagger) - \sum_{i=0}^{N-1} g^v d_i^\dagger d_i (b_i + b_i^\dagger), \quad (46)$$

where the free-phonon Hamiltonian is

$$H_{ph} = \sum_{i=0}^{N-1} \hbar\omega_{ph} b_i^\dagger b_i. \quad (47)$$

Despite the fact that the carrier-phonon interaction in real materials has a more complicated form, we choose for our numerical investigations its simplest possible form [Eq. (46)] capable of providing the energy relaxation of the electronic subsystem. The interaction with the electric field is

$$H_{c-f} = -d_{cv} E(t) \sum_{i=0}^{N-1} (d_i c_i + c_i^\dagger d_i^\dagger). \quad (48)$$

As the system described is translationally symmetric, we can transfer to the momentum space and obtain the same Hamiltonian as described in Eqs. (1)–(5) with the following

values of parameters:

$$\epsilon_k^{c/v} = \epsilon_0^{c/v} - 2J^{c/v} \cos(ka), \quad (49a)$$

$$\gamma_{k_1 k_2}^q = \delta_{k_2, k_1+q} \frac{g^c}{\sqrt{N}} \quad \text{for } k_1, k_2 \in \text{CB}, \quad (49b)$$

$$\gamma_{k_1 k_2}^q = \delta_{k_1, k_2+q} \frac{g^v}{\sqrt{N}} \quad \text{for } k_1, k_2 \in \text{VB}, \quad (49c)$$

$$V_{pqkl}^{vccc} = \delta_{k+q, p+l} V_{k-l}, \quad V_{plkq}^{vccv} = 0. \quad (49d)$$

The signs of the transfer integrals are $J^c > 0$, $J^v < 0$. The constant energy $\epsilon_0^c > 0$, while $\epsilon_0^v < 0$ is chosen so that the maximum of the valence band is the zero of the energy scale. V_{k-l} is the Fourier transformation of the Ohno potential and it is computed numerically as

$$V_k = \frac{1}{N^2} \sum_{i,j=0}^{N-1} V_{ij} e^{-ika(i-j)}. \quad (50)$$

The translational symmetry of our model enables us to solve efficiently the eigenvalue problem (13) which defines the excitonic basis. Instead of solving eigenvalue problem of a $N^2 \times N^2$ matrix, we can solve N -independent eigenvalue problems of matrices of dimension $N \times N$, thus obtaining N^2 excitonic eigenstates and their eigenenergies, which are counted by the center-of-mass wave vector Q and the band index ν . Thus, the general index of an excitonic state x should be, in all practical calculations, replaced by combination (Q, ν) . This has the following consequences on the matrix elements in the excitonic basis: dipole matrix elements reduce to

$$M_{(Q\nu)} = \delta_{Q,0} d_{cv} \sum_{k_e} \psi_{Q-k_e, k_e}^{(Q\nu)*}, \quad (51)$$

whereas carrier-phonon interaction matrix elements reduce to

$$\Gamma_{(Q\nu)(Q'\nu')}^q = \delta_{Q', Q+q} \frac{1}{\sqrt{N}} \sum_{k_e} \psi_{Q-k_e, k_e}^{(Q\nu)*} \times (g^c \psi_{Q-k_e, Q'-Q+k_e}^{(Q'\nu')} - g^v \psi_{Q'-k_e, k_e}^{(Q'\nu')}). \quad (52)$$

Due to the translational symmetry of our model, only the dynamic variables for which the total created wave vector is equal to the total annihilated wave vector will have nontrivial values in the course of the system's evolution. For example, from all density matrices $\gamma_{(Q\nu)}$ only those with $Q = 0$ can have nonzero values.

Our objective is to analyze, in the framework of this relatively simple model, the characteristic time scales of exciton formation and relaxation in a photoexcited semiconductor, along with the impact that various model parameters have on these processes. Basic parameters in our model are transfer integrals J^c, J^v (which determine bandwidths of the conduction and valence bands), electron-phonon coupling constants g^c, g^v , the phonon energy $\hbar\omega_{ph}$, the dielectric constant ϵ_r , and the onsite Coulomb interaction U . We will, throughout the computations, assume for simplicity that $J^c = J^v = J$ and $g^c = g^v = g$.

As is well known, the main differences between a typical organic and inorganic semiconductor can be expressed in terms of bandwidths, dielectric constant, and the carrier-phonon

interaction strength. Namely, inorganic semiconductors are characterized by wide bands and high value of dielectric constant, whereas organic semiconductors have narrow bands and small value of dielectric constant. The carrier-phonon interaction is stronger in organic than in inorganic semiconductors. Having all these facts in mind, we propose two sets of model parameters which assume values typical of an organic and inorganic semiconductor. Values of our model parameters are adjusted to material parameters of GaAs for the inorganic case and pentacene for the organic case. Values of carrier-phonon coupling constants are chosen to correspond to typical values for mobility and/or typical values for the polaron binding energy.

Typical bandwidths in organic semiconductors are $W \sim 500$ meV [8], which corresponds to the transfer integral $J \sim 125$ meV, whereas inorganic semiconductors usually exhibit bandwidths of several electronvolts [8] and we take in our calculations the value of the transfer integral $J = 500$ meV. In both cases, the lattice constant was fixed to $a = 1$ nm. The dielectric constant in a typical inorganic semiconductor is of the order of 10 and in the calculations we take the value of static dielectric constant of GaAs $\epsilon_r = 12.9$. For a representative value of the dielectric constant in organic semiconductors we take $\epsilon_r = 3.0$ [4,8]. The value of the onsite Coulomb interaction U is chosen to give the correct order of magnitude for the exciton binding energy, which is calculated numerically. For the organic parameter set, we set $U = 480$ meV, which gives the exciton binding energy around 320 meV, while for the inorganic parameter set $U = 15$ meV and the corresponding exciton binding energy is roughly 10 meV.

The carrier-phonon coupling constants for the inorganic case are estimated from the mobility values. The mobility of carriers is estimated using the relation $\mu = e\tau/m^*$, where τ is the scattering time and m^* is the effective mass of a carrier. For cosine bands considered in this work, $m^* = \hbar^2/(2|J|a^2)$ in the vicinity of the band extremum. The scattering time is estimated from the expression for the carrier-phonon inelastic scattering rate based on the Fermi's golden rule, which around the band extremum $k = 0$ assumes the following form:

$$\frac{1}{\tau(k)} = \frac{g^2}{\hbar|J|} \frac{n^{\text{ph}}}{\sqrt{1 - \left(\cos(ka) - \frac{\hbar\omega_{\text{ph}}}{2|J|}\right)^2}}, \quad (53)$$

where $n^{\text{ph}} = (e^{\beta\hbar\omega_{\text{ph}}} - 1)^{-1}$. Therefore, the carrier-phonon coupling constant in terms of the carrier mobility reads as

$$g = |J| \sqrt{\frac{2ea^2}{\hbar\mu n^{\text{ph}}}} \left[1 - \left(1 - \frac{\hbar\omega_{\text{ph}}}{2|J|} \right)^2 \right]^{1/4}. \quad (54)$$

Using the value for the electron mobility in GaAs at 300 K $\mu_e \approx 8500$ cm²/(Vs) [44], we obtain $g \approx 25$ meV.

We can also estimate the carrier-phonon coupling constants from the polaron binding energy. As an estimate of this quantity, we use the result of the second-order weak-coupling perturbation theory at $T = 0$ in the vicinity of the point $k = 0$ [45]:

$$\epsilon_{\text{b}}^{\text{pol}}(k) = \frac{g^2}{2|J|} \frac{1}{\sqrt{(\cos(ka) + \frac{\hbar\omega_{\text{ph}}}{2|J|})^2 - 1}}. \quad (55)$$

TABLE I. Model parameters which are representative of a typical organic and inorganic semiconductor. References from which material parameters are taken are indicated.

Parameter	Inorganic	Organic
E_g (meV)	1519 [32]	2000 [47]
J (meV)	500	125
ϵ_r	12.9 [32]	3.0 [8]
g (meV)	25	40
$\hbar\omega_{\text{ph}}$ (meV)	36.4 [32]	10.0 [48,49]
U (meV)	15	480

It is known that polaron binding energies in typical inorganic semiconductors are $\epsilon_{\text{b}}^{\text{pol}} \sim 1$ meV and we used this fact along with Eq. (55) to check our estimate for g from the value of mobility; for $g \approx 25$ meV, we obtain $\epsilon_{\text{b}}^{\text{pol}} \approx 2$ meV. The polaron binding energies in polyacenes lie in the range between 21 and 35 meV [46]. The value of g in the set of model parameters representative of organic semiconductors was estimated from the polaron binding energy in pentacene, which is around 20 meV. We obtain that $g \approx 40$ meV. The values used for the organic/inorganic set of parameters are listed in Table I.

The form of the electric field is assumed to be a rectangular cosine pulse

$$E(t) = E_0 \cos(\omega_c t) \theta(t + t_0) \theta(t_0 - t), \quad (56)$$

where ω_c is the central frequency of the field and $\theta(t)$ is the Heaviside step function. Time t_0 is chosen large enough so that the pulse is so spectrally narrow that the notion of the central frequency makes sense. On the other hand, the pulse should be as short as possible, so that after its end we observe the intrinsic dynamics of our system, the one which is not accompanied by the carrier generation process, but merely shows how initially generated populations are redistributed among various states. Trying to reconcile the aforementioned requirements, we choose $t_0 = 250$ fs. The amplitude of the electric field E_0 and the interband dipole matrix element d_{cv} are chosen so that we stay in the low-density regime; particularly, we choose them so that the corresponding Rabi frequency $\hbar\omega_R = d_{\text{cv}}E_0$ assumes the value of 0.2 meV, which is smaller than any energy scale in our problem and ensures that the excitation is weak.

In order to quantitatively study the process of exciton formation after a pulsed excitation of a semiconductor, we solved the system of quantum kinetic equations for electronic density matrices $y_x, n_{\bar{x}x}$ and their single-phonon-assisted counterparts [Eqs. (28), (29), (33), (34), and (35) supplemented with Eqs. (36) and (41)] using the fourth-order Runge-Kutta algorithm. The computations are performed for the temperature $T = 300$ K and the central frequency of the pulse equal to the single-particle gap ($\hbar\omega_c = E_g$). The exciton is considered bound (unbound) if its energy $\hbar\omega_{(Qv)}$ is smaller (larger) than the smallest single-particle energy difference $\epsilon_{k_c}^c - \epsilon_{Q-k_c}^v$ [47]. The equation of the boundary line which

separates bound from unbound pair states reads as

$$\epsilon_{\text{sep}}(Q) = \epsilon_0^c - \epsilon_0^v - 2\sqrt{(J^c)^2 + (J^v)^2 - 2J^c J^v \cos(Qa)}. \quad (57)$$

An unbound exciton may be considered as (quasi)free electron and hole, so this way it is possible to distinguish between bound excitons and free carriers.

The pulsed excitation of a semiconductor leads, in the first step, to the generation of coherent electron-hole pairs that are described in our formalism by the coherent pair amplitudes y_x . The decay of the coherent pair occupation

$$N_{\text{coh}} = \sum_x |y_x|^2 \quad (58)$$

is due to the scattering processes which initiate already during the generation of the pairs and gives a direct measure of the loss of coherence [32]. At the same time, incoherent pair occupations start to grow, driven by the loss rate of coherent pair occupations [32,35]. In order to quantify the process of exciton formation, we will follow the time dependence of the total number of incoherent bound excitons

$$N_{\text{incoh,b}} = \sum_{x \in \text{bound}} (n_{xx} - |y_x|^2). \quad (59)$$

This quantity represents the number of truly bound electron-hole pairs which exist even after the optical field has vanished and as such is the direct measure of the efficiency of the exciton formation process. We will, when useful, also consider the number of incoherent excitons in a particular band ν , $N_{\text{incoh},\nu}$. The quantities $N_{\text{incoh,b}}$ and $N_{\text{incoh},\nu}$ will be normalized to the total number of excitons N_{tot} defined in Eq. (27).

A. Numerical results: Organic set of parameters

We start this section by an overview of properties of the excitonic spectrum, shown in Fig. 1(a), which will be relevant for further discussions of the exciton formation process. The lowest excitonic band is energetically well separated from the rest of the spectrum, the energy separation between the minima of the bands $\nu = 0$ and 1 being around 200 meV, which is much larger than both the value of $k_B T$ at room temperature and the phonon energy in our model (see Table I). As a consequence, downward transitions that end at the lowest excitonic band start almost exclusively from the states on $\nu = 1$ band and an exciton, which is at some instant in a state on the $\nu = 0$ band, cannot be scattered to an unbound excitonic state.

We briefly comment on the size of the exciton for these values of model parameters. From the exciton wave function $\psi_{Q-k_e, k_e}^{(Q\nu)}$ in k space, we can obtain the exciton wave function in real space performing the Fourier transformation

$$\begin{aligned} \psi_{r_e, r_h}^{(Q\nu)} &= \sum_{k_e} e^{i(Q-k_e)r_h} e^{ik_e r_e} \psi_{Q-k_e, k_e}^{(Q\nu)} \\ &= e^{iQ(r_e+r_h)/2} \sum_{k_e} e^{-i(Q-2k_e)(r_e-r_h)/2} \psi_{Q-k_e, k_e}^{(Q\nu)}. \end{aligned} \quad (60)$$

The exciton wave function in real space is a product of the plane wave which describes the motion of the center of mass

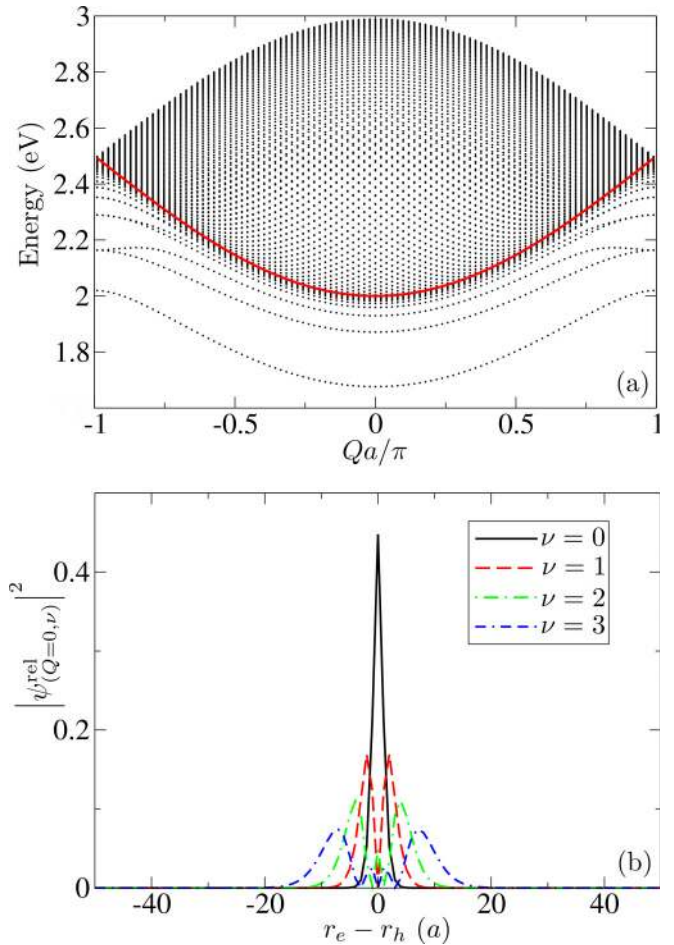


FIG. 1. (Color online) (a) Excitonic spectrum for the organic set of parameters. Dots represent individual excitonic states (Q, ν) , while thick red line is the boundary between bound and unbound excitonic states computed using Eq. (57). (b) Squared modulus of the wave function which describes the relative motion of an electron-hole pair [Eq. (61)] calculated for different states $(Q = 0, \nu)$. Mean electron-hole separations in these states are $0.7a$ ($\nu = 0$), $2.5a$ ($\nu = 1$), $4.6a$ ($\nu = 2$), and $7.8a$ ($\nu = 3$). Computations are performed for $N = 101$.

with the wave vector Q and the wave function of the relative motion of an electron and a hole:

$$\psi_{(Q,\nu)}^{\text{rel}} = \sum_{k_e} e^{-i(Q-2k_e)(r_e-r_h)/2} \psi_{Q-k_e, k_e}^{(Q\nu)}. \quad (61)$$

The latter part is directly related to the exciton size. We calculated squared modulus of the wave function of the relative motion of a pair for states $(Q = 0, \nu)$ in various bands. The result is shown in Fig. 1(b). It is clearly seen that an electron and a hole are tightly bound in these states and their relative separations are of the order of lattice constant, which is the typical value for the exciton radius in organic semiconductors. We point out that this does not mean that an exciton is localized; due to the translational symmetry of our system, it is delocalized over the whole lattice, as described by the plane-wave factor in the total wave function of a pair. Moreover, we note that the system size $N = 101$ is large enough for the results to be numerically accurate, as it is much larger than the typical size of the exciton in a bound state.

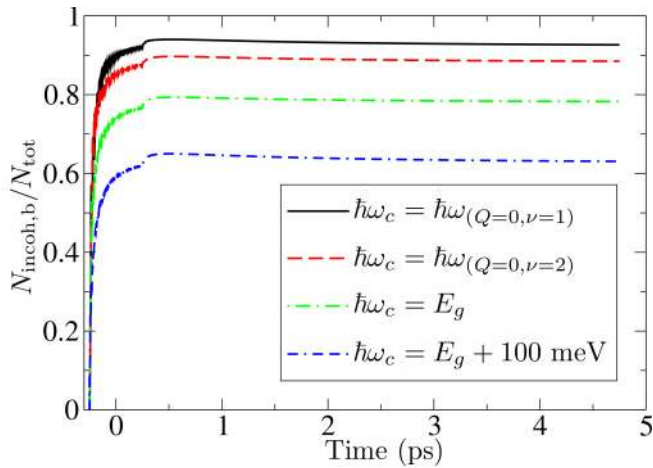


FIG. 2. (Color online) Time dependence of the relative number of incoherent bound excitons for different central frequencies of the pulse.

The impact that different parameters have on the exciton formation process is studied by changing one parameter, at the same time fixing the values of all the other parameters to the previously mentioned ones. We performed all the computations for a limited number of lowest excitonic bands, which crucially depends on the central frequency ω_c of the excitation. For the given excitation, we took into account all the bands whose minima lie below $\hbar\omega_c + \alpha k_B T$, where $\alpha \sim 5$ is a numerical constant.

We will first discuss the exciton formation process for different central frequencies of the exciting pulse. We have considered central frequencies in resonance with ($Q = 0$, $\nu = 1$) state, ($Q = 0$, $\nu = 2$) state, single-particle gap, and the central frequency which is 100 meV above the band gap. As can be noted from Fig. 2, raising the central frequency of the laser field leads to lower relative number of incoherent bound excitons. Namely, the higher is the central frequency, the higher (in energy) are the bands in which the initial coherent excitonic populations are created and the slower is the conversion of these coherent populations to incoherent populations in lower excitonic bands. However, in the long-time limit, the relative number of incoherent bound excitons should not depend on the central frequency of the laser, but tend to the value predicted by the Maxwell-Boltzmann distribution, which is above 99%. Such a high value is due to the large energy separation between the lowest excitonic band and the rest of the spectrum. We can thus infer, based on Fig. 2, that the semiconductor dynamics right after the pulsed excitation shows highly nonequilibrium features. Relaxation towards equilibrium occurs on a time scale longer than the picosecond one.

Next, we consider the dependence of the exciton formation process on temperature. The temperature enters our model only through phonon numbers n^{ph} . The overall behavior of the relative number of incoherent bound excitons for different temperatures is shown in Fig. 3. During the pulse, the relative number of incoherent bound excitons is highest for $T = 300$ K and lowest for $T = 100$ K, which is the consequence of the fact that scattering processes from higher excitonic bands (in which

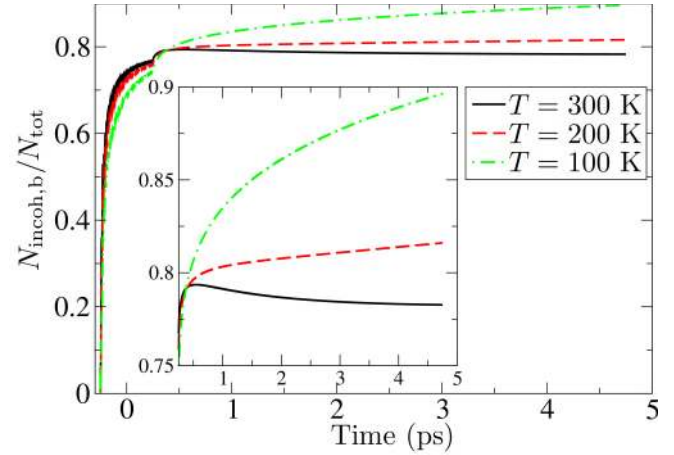


FIG. 3. (Color online) Time dependence of the relative number of incoherent bound excitons for different temperatures. The inset shows the portions of the same curves after the pulse.

initial coherent excitonic populations are created and which are situated both in the pair continuum and below it) towards lower excitonic bands are most efficient at $T = 300$ K. After the generation of carriers has been completed, phonon-mediated processes lead to the redistribution of created incoherent excitons among different excitonic states and the relative number of incoherent bound excitons increases with decreasing the temperature, which is the expected trend. In the inset of Fig. 3 we also note that the relative number of incoherent bound excitons after the pulse experiences an initial growth followed by a slow decay at $T = 300$ K, whereas at $T = 100$ K it monotonically rises. The initial growth at $T = 300$ K is attributed to downward scattering processes, but since at this temperature upward scattering events cannot be neglected, the following slow decay is due to the fact that some excitonic bands well below the pair continuum (bands $\nu = 1, 2, 3$) lose excitons both by downward scattering and upward scattering to excitonic states which are near to or belong to the pair continuum [see Figs. 4(a) and 4(b)]. At $T = 100$ K, these upward processes are much less probable than downward processes, thus the decay of the relative number of incoherent bound excitons is not observed; in Figs. 4(c) and 4(d) we see that lowest excitonic bands ($\nu = 0, 1, 2$) gain excitons, whereas bands which are near to or belong to the pair continuum ($\nu = 9, 11, 13, 15$) lose excitons. The population of the lowest excitonic band $\nu = 0$ continually grows at all the temperatures studied, due to the large energetic separation between this band and the rest of the spectrum.

We briefly comment on the behavior of the number of coherent excitons N_{coh} and its temperature dependence. Right after the start of the pulse, coherent excitons comprise virtually the total excitonic population (see Fig. 5). Due to the carrier-phonon interaction, the relative number of coherent excitons decays during the pulse, so that at its end coherent excitons comprise around 1% of the total excitonic population. The conversion from coherent to incoherent populations is thus almost completed by the end of the pulse. From the inset of Fig. 5, we note that $N_{\text{coh}}/N_{\text{tot}}$ exhibits a very fast decay after the pulse has vanished, with decay times of the order of 50 fs or less. Therefore, we infer that the transformation from coherent

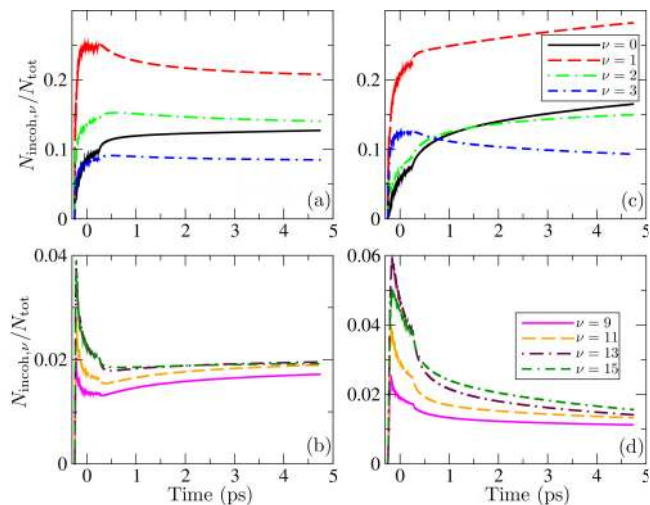


FIG. 4. (Color online) Time dependence of the relative population of various excitonic bands for different temperatures $T = 300$ K for panels (a) and (b) and $T = 100$ K for panels (c) and (d). Panels (a) and (c) concern bands which are well below the pair continuum ($\nu = 0, 1, 2, 3$), whereas panels (b) and (d) deal with the bands which are near the continuum ($\nu = 9$) or in the continuum ($\nu = 11, 13, 15$).

to incoherent excitonic populations takes place on a 50-fs time scale. Based on Fig. 5, we also note that the lower is the temperature, the slower is the transformation from coherent to incoherent excitonic populations, which is the expected trend.

We continue our investigation by examining the effects that changes in the carrier-phonon coupling constant g have on the exciton formation process. Since increasing (lowering) g increases (lowers) semiclassical transition rates, just as increasing (lowering) T does, the changes in g and T should have, in principle, similar effects on the exciton formation process. Considering first the relative number of incoherent bound excitons, whose time dependence for different values of g is shown in Fig. 6(a), we note that after the end of the

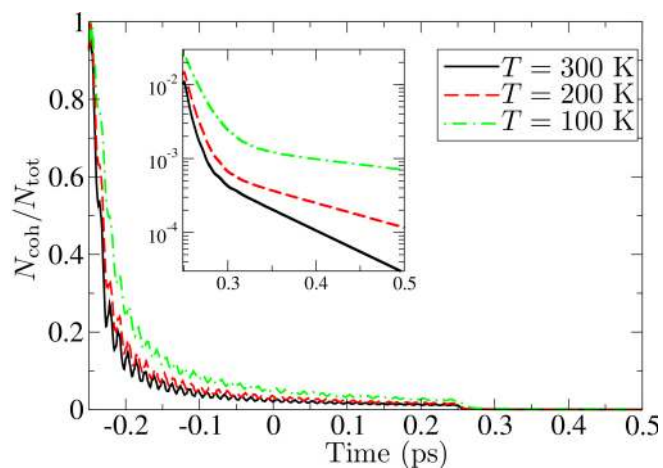


FIG. 5. (Color online) Time dependence of the relative number of coherent excitons for different temperatures. The inset shows the portions of the same curves (note the logarithmic scale on the vertical axis) after the pulse.

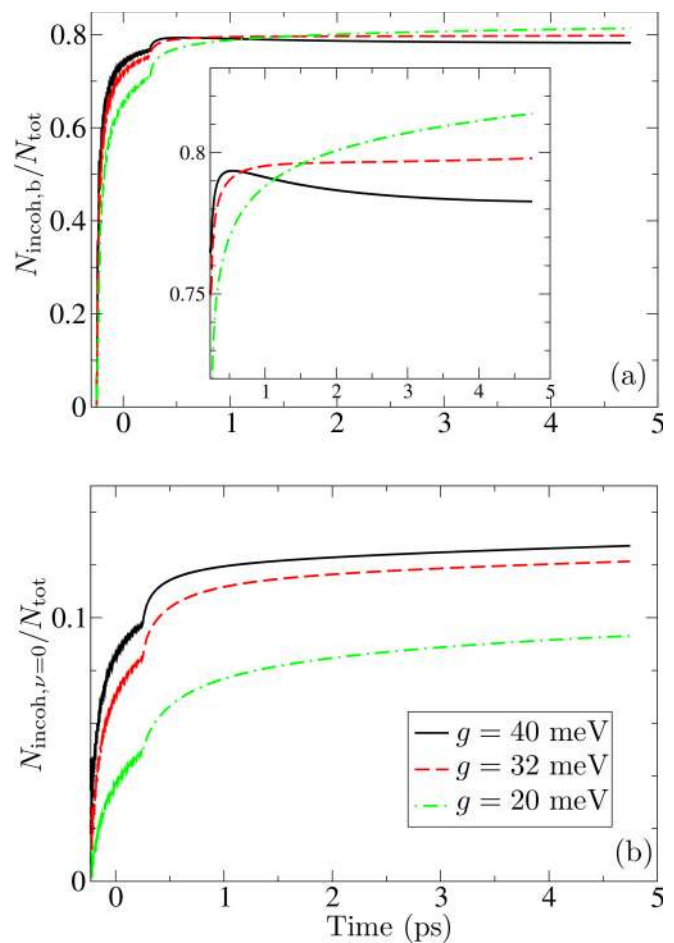


FIG. 6. (Color online) Time dependence of (a) the relative number of incoherent bound excitons, (b) the relative number of incoherent excitons in the $\nu = 0$ band, for various values of g . The inset in the panel (a) shows the portions of the same curves after the pulse.

pulse it increases with decreasing g . However, during the pulse, higher values of g lead to more incoherent bound excitons, as is expected since scattering processes which populate low-energy states are more intensive for larger g . We also show the time dependence of the relative number of excitons in $\nu = 0$ band in Fig. 6(b). It is observed that the lower is g , the lower is the number of excitons in the lowest excitonic band. This is due to the fact that populations on the lowest band are generated mainly via scattering processes from the $\nu = 1$ band and these processes are less efficient for smaller g .

We conclude this section by studying the effects that changes in the onsite Coulomb interaction U have on the process of exciton formation. Changing U has profound effects on the excitonic spectrum. Exciton binding energy lowers with lowering U along with the energy separation between the band $\nu = 0$ and the rest of the spectrum. We studied the impact of U on the exciton formation process for three values of U , $U = 480, 240,$ and 48 meV, for which the exciton binding energy is $\sim 320, \sim 175,$ and ~ 40 meV, respectively. Lowering U lowers the relative number of incoherent bound excitons, as is shown in Fig. 7. Smaller energy separation between the lowest excitonic band and the rest of the spectrum means that phonon-mediated transitions which start/end on the band $\nu =$

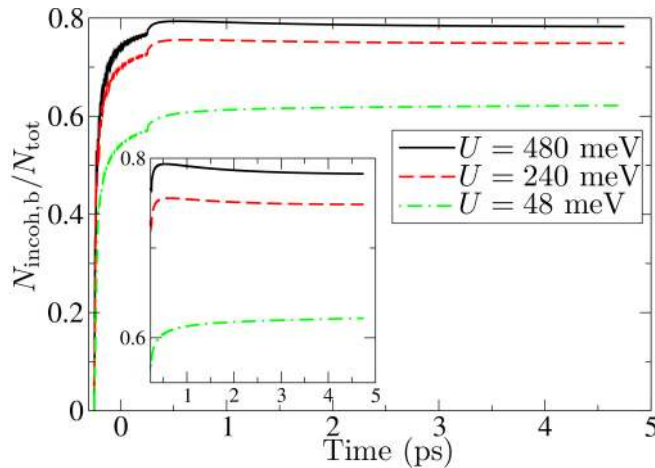


FIG. 7. (Color online) Time dependence of the relative number of incoherent bound excitons for various values of U . The inset shows the portions of the same curves after the pulse.

0 can end/start not predominantly on the band $\nu = 1$, but also on higher excitonic bands, which, for lower U , are more certain to belong to the electron-hole pair continuum than to the part of the spectrum which contains bound pair states. Thus, the lower is U , the more likely are the dissociation processes in which an exciton, initially in a bound state, after a phonon-mediated transition ends in an unbound pair state, which explains the observed trend in the relative number of incoherent bound excitons. This agrees with the usual picture according to which thermal fluctuations are likely to dissociate loosely bound electron-hole pairs. For $U = 48$ meV, in the long-time limit and according to the Maxwell-Boltzmann distribution, around 78% of the total number of excitons should be in bound states, whereas for the other two values of U this number is above 99%. Thus, the dynamics observed is highly nonequilibrium, but unlike the cases $U = 480$ and 240 meV, in which we cannot observe that the relative number of incoherent bound excitons starts to tend to its equilibrium value, for $U = 48$ meV we observe such a behavior (see the inset of Fig. 7).

In summary, we list the time scales of the exciton formation and relaxation that stem from our computations. The transformation from coherent to incoherent excitons takes place in less than 50 fs. A significant number of incoherent bound excitons are established on a time scale of several hundreds of femtoseconds, whereas the subsequent relaxation of excitonic populations occurs on a time scale longer than the picosecond one. Further discussion of these results is deferred for Sec. IV.

B. Numerical results: Inorganic set of parameters

In this section, we will investigate the exciton formation process in the case when material parameters assume values typical of inorganic semiconductors, i.e., relatively large bandwidths, large dielectric constant (weak Coulomb interaction), and weak carrier-phonon interaction. The excitonic spectrum is shown in Fig. 8(a). We see that almost all excitonic bands belong to the pair continuum, except for a couple of lowest bands, which is more clearly seen in the inset of Fig. 8(a). This is an entirely different situation from the one that we encounter

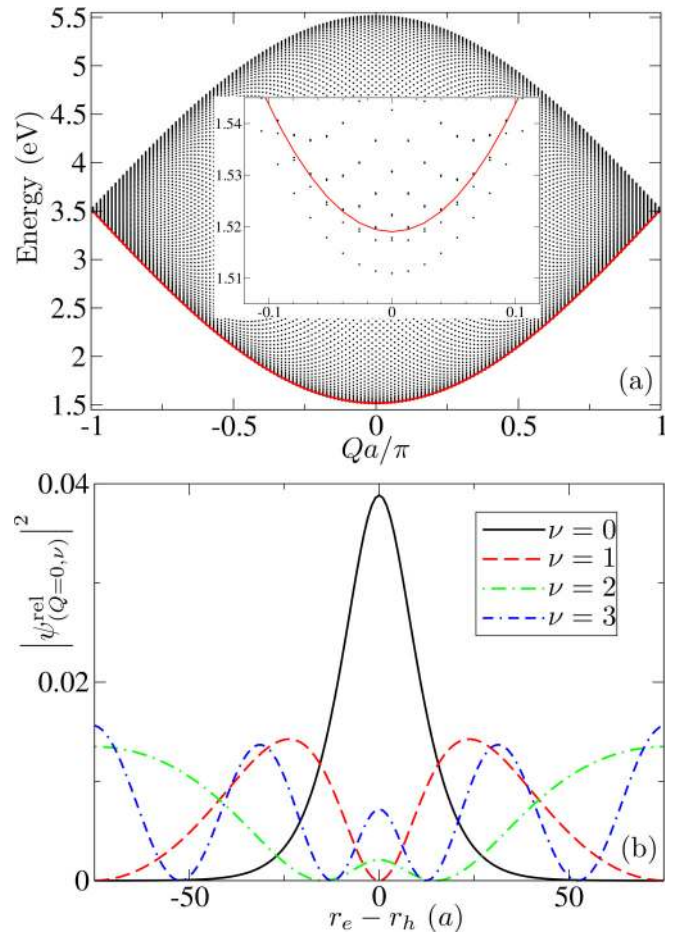


FIG. 8. (Color online) (a) Excitonic spectrum for the inorganic set of parameters. Dots represent individual excitonic states (Q, ν) , while thick red line is the boundary between bound and unbound excitonic states computed using Eq. (57). The inset shows the same spectrum in the range of energies around the single-particle gap. (b) Squared modulus of the wave function which describes the relative motion of an electron-hole pair [Eq. (61)] calculated for different states $(Q = 0, \nu)$. Mean electron-hole separations are $9.1a$ ($\nu = 0$) and $29.4a$ ($\nu = 1$), while states $(Q = 0, \nu = 2)$ and $(Q = 0, \nu = 3)$ are not bound. Computations are performed for $N = 151$.

for the organic set of parameters, where large energy separation of the lowest excitonic band from the rest of the spectrum was crucial to understand the exciton formation process. As a consequence, excitons in bound states are likely to scatter to a state in the pair continuum, in contrast to the situation for the model parameters representative of an organic semiconductor.

Having noted the important characteristics of the excitonic spectrum, we move on to comment briefly on the exciton size for the inorganic set of parameters. We plot in Fig. 8(b) the squared modulus of the wave function of the relative motion of the pair, which is defined in Eq. (61). We note that for the inorganic set of parameters, electron and hole are not as tightly bound as for the organic set of parameters, which is in accord with the fact that excitons in a typical inorganic semiconductor have large radii, typically of the order of 10 lattice constants [5,6]. From Fig. 8(b), it is also clear that, if we are to see the lowest excitonic state ($Q = 0, \nu = 0$) as a

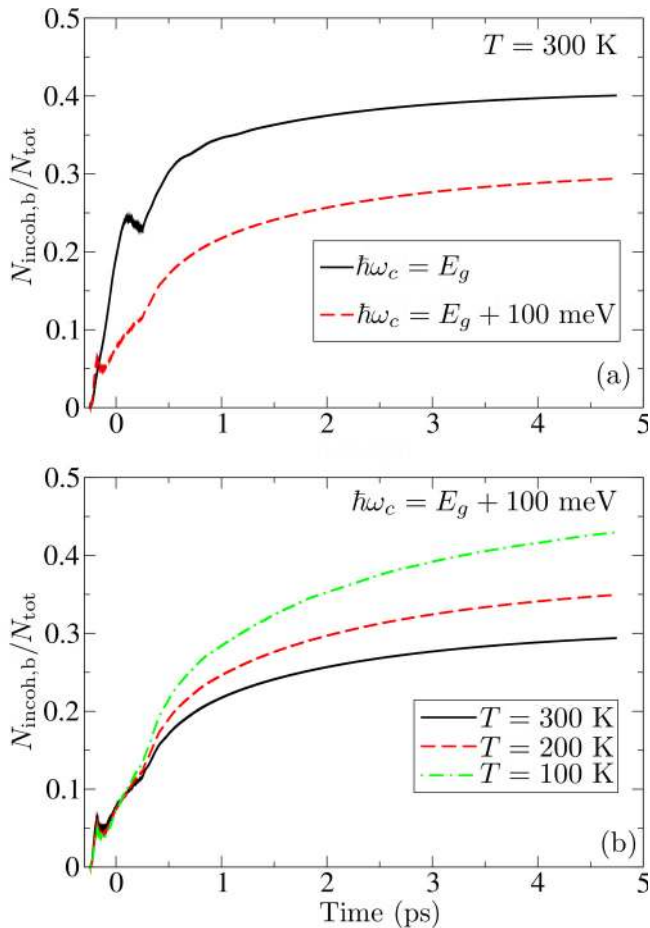


FIG. 9. (Color online) (a) Time dependence of the relative number of incoherent bound excitons for excitation resonant with the single-particle gap and the one which is 100 meV above it. The temperature in both cases is $T = 300$ K. (b) Time dependence of the relative number of incoherent bound excitons for various temperatures. The central frequency of the laser pulse is 100 meV above the single-particle gap.

bound pair, we should take the system size $N \gtrsim 120$. We opted for $N = 151$ because this value makes a good compromise between the minimal size of the system needed for the results to be numerically accurate and the computational time.

For the inorganic set of parameters, we note that incoherent unbound excitons comprise the major part of the total excitonic population [see Fig. 9(a)], which is different from the case when model parameters assume values representative of an organic semiconductor, when excitons in bound states prevail. Considering an unbound exciton as quasifree electron and hole, we interpret the last observation in the following manner: after an optical excitation of an organic semiconductor, (strongly) bound electron-hole pairs (excitons) are mainly generated, whereas in the case of an inorganic semiconductor an optical excitation predominantly generates (quasi)free charges. In Fig. 9, we also note that for higher central frequency of the laser field, the relative number of bound excitons is lower. However, in the long-time limit the number of incoherent bound excitons should assume the value predicted by the Maxwell-Boltzmann distribution, which is around 36.5%,

irrespective of the central frequency of the pulse. The values of the relative number of incoherent bound excitons at the end of our computations do not strongly deviate from the value predicted by the Maxwell-Boltzmann distribution, in contrast to the situation for the organic set of parameters, where this deviation was more pronounced (see Fig. 2). It can thus be inferred that nonequilibrium features of the semiconductor dynamics after a pulsed excitation are more pronounced for the organic than for the inorganic set of parameters.

Finally, we comment on the temperature dependence of the exciton formation process for the excitation whose central frequency is 100 meV above the single-particle gap. The lower is the temperature, the higher is the relative number of the incoherent bound excitons [see Fig. 9(b)]. During the pulse, higher temperature leads to higher relative number of incoherent bound excitons, which has already been explained in the section dealing with the organic set of parameters. The long-time limit values of the relative number of incoherent bound excitons are 44.7% for $T = 200$ K and 62.7% for $T = 100$ K. In all three cases, the dynamics is highly nonequilibrium, but it displays the trend of a slow, but monotonic, approach towards the equilibrium.

IV. DISCUSSION

In this section, we discuss the time scales of exciton formation and relaxation processes obtained from our calculations in light of recent subpicosecond time-resolved experiments. In Ref. [23], femtosecond-resolved fluorescence up-conversion spectroscopy was applied to investigate the exciton dynamics in pristine PCDTBT polymer. The results obtained were interpreted to originate from formation of free charges on less than 100 fs time scale, followed by formation of bound excitons in less than 1 ps and their further relaxation at a longer time scale. Similar results were obtained in Ref. [24] for P3HT polymer. Despite the fact that our Hamiltonian does not include the effects of disorder that are present in real materials and uses an oversimplified form of the carrier-phonon interaction, we obtain time scales consistent with these data in our computations. Namely, for the organic parameter set we find that significant population of bound excitons is formed on the time scale of several hundreds of femtoseconds and that their further relaxation occurs for at least several picoseconds. These conclusions are further corroborated by fitting the relative number of incoherent bound excitons $N_{\text{incoh,b}}/N_{\text{tot}}$ after the carrier generation has been completed to a sum of three exponentially decaying terms. For the organic parameter set, we obtain characteristic time scales of ~ 50 fs, ~ 500 fs and $\gtrsim 1$ ps. We attribute the fastest time scale to decoherence processes which are responsible for conversion from coherent ($|y_x|^2$) to incoherent (\bar{n}_{xx}) populations due to the interaction with phonons. The time scale of ~ 500 fs may be associated with the buildup of the Coulomb-induced correlations between electrons and holes by formation of bound incoherent electron-hole pairs via phonon-assisted scattering processes. After this time scale, however, intraband coherences $\bar{n}_{\bar{x}x}$ ($\bar{x} \neq x$), as well as single-phonon-assisted density matrices $n_{\bar{x}x\mu^+}$, still have significant values. In the long-time limit, these variables asymptotically vanish, and we remain only with incoherent populations whose dynamics will

eventually lead to thermalized distribution of excitons [35]. As our computations are certainly not long enough to observe these effects, we speculate that the slowest time scale we obtain may be related to the decay of the intraband coherences and/or phonon-assisted variables.

Next, we comment on the relation of our results with recent experimental insights which have challenged the commonly accepted physical picture of the generation of free charges in bulk heterojunction solar cells. Namely, it is widely believed that physical processes leading to current generation are formation of bound excitons due to light absorption in the donor material, their diffusion to the donor/acceptor interface, and their subsequent separation at the interface [4]. From the discrepancy between the distance that a donor exciton can diffuse in 100 fs and the distance it has to cover in order to reach the donor/acceptor interface in efficient bulk heterojunction solar cells, Cowan *et al.* [25] conclude that the subpicosecond charge transfer to the acceptor occurs before exciton formation in the donor. The results of our computations, which indicate that the formation of incoherent bound excitons occurs on a ~ 500 -fs time scale, are therefore consistent with their observations. The formation of hot charge transfer excitons which occurs in less than 100 fs and which is followed by their relaxation to lower energies and shorter electron-hole distances on a picosecond time scale was experimentally observed in a small molecule CuPc/fullerene blend using time-resolved second harmonic generation and time-resolved two-photon photoemission [28]. The presence of hot charge transfer excitons, which are delocalized, i.e., in which the electron-hole separation is rather large, and their essential role in subpicosecond charge separation in efficient OPV systems were also identified in Refs. [26,27,29]. Our simulation results that indicate exciton equilibration times longer than picoseconds are fully consistent with observations that during charge separation at the donor/acceptor interface the excitons remain out of equilibrium (hot excitons).

V. CONCLUSION

In conclusion, we have investigated the exciton dynamics in a photoexcited semiconductor on a picosecond time scale. The study was conducted on the two-band semiconductor Hamiltonian, which includes relevant physical effects in the system, using the density matrix theory combined with the DCT scheme. We truncate the phonon branch of the hierarchy and propose the form of coupling between electronic density matrices with single-phonon assistance and higher-order phonon assistance so as to achieve the compatibility of the resulting equations with the energy and particle-number conservation in a system without external fields. The numerical

study aiming at identifying time scales of exciton formation and relaxation processes was performed on a one-dimensional model system for the values of model parameters representative of a typical organic and inorganic semiconductor. We concluded that the dynamics on a picosecond time scale shows highly nonequilibrium features, relaxation processes towards equilibrium occurring on a longer time scale. While for the organic set of parameters the excitons generated are mainly tightly bound, for the inorganic set of parameters the major part of excitons is in unbound pair states and may thus be considered as (quasi)free electrons and holes. In other words, a photoexcitation of an initially unexcited organic semiconductor leads to creation of bound electron-hole pairs, whereas in an inorganic semiconductor it leads to generation of free charges. This difference can be mainly attributed to different properties of the excitonic spectrum, which for the organic set of parameters exhibits large energy separation between the lowest excitonic band and the rest of the spectrum. Furthermore, although the carrier-phonon interaction is stronger for the organic set of parameters, we have noted that the number of excitons in bound states more strongly deviates from its equilibrium value for the organic set of parameters than for the inorganic one. This observation emphasizes the importance of nonequilibrium effects for the proper understanding of the ultrafast dynamics of photoexcited organic semiconductors and unraveling the working principles of organic photovoltaic devices.

ACKNOWLEDGMENTS

We gratefully acknowledge the support by Serbian Ministry of Education, Science and Technological Development (Project No. ON171017) and European Community FP7 Marie Curie Career Integration Grant (ELECTROMAT) and the contribution of the COST Action MP1406. Numerical simulations were performed on the PARADOX supercomputing facility at the Scientific Computing Laboratory of the Institute of Physics Belgrade.

APPENDIX A: EQUATIONS OF MOTION

In this appendix, we present equations of motion for relevant dynamic variables. These are the same equations as in Ref. [35], with only slight modifications in notation, which are exact up to the second order in the external field. We point out that, according to the generating function property, differential equations for the corresponding phonon-assisted density matrices are obtained after performing appropriate differentiations and setting $\alpha_\mu = \beta_\mu = 0$:

$$\begin{aligned}
 i\hbar \partial_t Y_{ab}^{\alpha\beta} = & (\epsilon_b^c - \epsilon_a^v) Y_{ab}^{\alpha\beta} + \sum_{\substack{p \in \text{VB} \\ q \in \text{CB}}} (V_{pqba}^{\text{vccv}} - V_{pabq}^{\text{vccv}}) Y_{pq}^{\alpha\beta} + \sum_{\mu} \hbar\omega_{\mu} (\beta_{\mu} \partial_{\beta_{\mu}} - \alpha_{\mu} \partial_{\alpha_{\mu}}) Y_{ab}^{\alpha\beta} \\
 & + \sum_{\substack{k \in \text{CB} \\ \mu}} (\gamma_{bk}^{\mu} (\partial_{\alpha_{\mu}} + \beta_{\mu}) + \gamma_{kb}^{\mu*} \partial_{\beta_{\mu}}) Y_{ak}^{\alpha\beta} - \sum_{\substack{k \in \text{VB} \\ \mu}} (\gamma_{ka}^{\mu} (\partial_{\alpha_{\mu}} + \beta_{\mu}) + \gamma_{ak}^{\mu*} \partial_{\beta_{\mu}}) Y_{kb}^{\alpha\beta} - \mathbf{E}(t) \mathbf{M}_{ba}^{\text{cv}} F^{\alpha\beta}, \quad (\text{A1})
 \end{aligned}$$

$$\begin{aligned}
i\hbar \partial_t N_{abcd}^{\alpha\beta} &= (\epsilon_d^c - \epsilon_c^v + \epsilon_b^v - \epsilon_a^c) N_{abcd}^{\alpha\beta} + \sum_{\substack{p \in \text{VB} \\ q \in \text{CB}}} ((V_{pqdc}^{\text{vccv}} - V_{pcdq}^{\text{vccv}}) N_{abpq}^{\alpha\beta} - (V_{baqp}^{\text{vccv}} - V_{bpqa}^{\text{vccv}}) N_{qpdc}^{\alpha\beta}) \\
&+ \sum_{\mu} \hbar\omega_{\mu} (\beta_{\mu} \partial_{\beta_{\mu}} - \alpha_{\mu} \partial_{\alpha_{\mu}}) N_{abcd}^{\alpha\beta} + \sum_{\substack{k \in \text{CB} \\ \mu}} ((\gamma_{dk}^{\mu} (\partial_{\alpha_{\mu}} + \beta_{\mu}) + \gamma_{kd}^{\mu*} \partial_{\beta_{\mu}}) N_{abck}^{\alpha\beta} - (\gamma_{ka}^{\mu} \partial_{\alpha_{\mu}} + \gamma_{ak}^{\mu*} (\partial_{\beta_{\mu}} + \alpha_{\mu})) N_{kbcd}^{\alpha\beta}) \\
&- \sum_{\substack{k \in \text{VB} \\ \mu}} ((\gamma_{kc}^{\mu} (\partial_{\alpha_{\mu}} + \beta_{\mu}) + \gamma_{ck}^{\mu*} \partial_{\beta_{\mu}}) N_{abkd}^{\alpha\beta} - (\gamma_{bk}^{\mu} \partial_{\alpha_{\mu}} + \gamma_{kb}^{\mu*} (\partial_{\beta_{\mu}} + \alpha_{\mu})) N_{akcd}^{\alpha\beta}) - \mathbf{E}(t) (\mathbf{M}_{dc}^{\text{cv}} Y_{ba}^{\beta\alpha*} - \mathbf{M}_{ba}^{\text{vc}} Y_{cd}^{\alpha\beta}).
\end{aligned} \tag{A2}$$

APPENDIX B: CLOSING THE HIERARCHY OF EQUATIONS

In Eq. (33), correlated parts of two-phonon-assisted density matrices $\delta n_{\bar{x}\bar{x}\rho^+\sigma^-}$ and $\delta n_{\bar{x}\bar{x}\rho^+\sigma^+}$ appear. In their differential equations, three-phonon-assisted density matrices are present. In order to close the hierarchy of equations, we factorize them into all possible combinations of phonon distribution functions and phonon-assisted electronic density matrices and neglect their correlated parts. The strategy for the factorization is the one we employed in Eq. (31) where we considered an exciton as a basic entity and did not take into account contributions arising from the excitonic amplitude (with possible phonon assistance). Namely, the two-phonon-assisted electronic density matrix $\langle c_a^\dagger d_b^\dagger d_c c_d b_\mu^\dagger b_\rho \rangle$ can be written in terms of exciton creation and annihilation operators [see Eq. (18)] as $\sum_{\bar{x}\bar{x}} \psi_{ba}^{\bar{x}*} \psi_{cd}^{\bar{x}} \langle X_{\bar{x}}^\dagger X_{\bar{x}} b_\mu^\dagger b_\rho \rangle$. Since it appears in the equation of motion for one-phonon-assisted electronic density matrix $n_{\bar{x}\bar{x}\mu}^{(+)}$, which is coupled to Eq. (29) describing excitonic populations and intraband coherences, we treat an exciton as a basic entity and accordingly perform the factorization $\langle X_{\bar{x}}^\dagger X_{\bar{x}} b_\mu^\dagger b_\rho \rangle = \langle X_{\bar{x}}^\dagger X_{\bar{x}} \rangle \langle b_\mu^\dagger b_\rho \rangle + \delta \langle X_{\bar{x}}^\dagger X_{\bar{x}} b_\mu^\dagger b_\rho \rangle$. In the case of three-phonon-assisted electronic density matrices, the described factorization procedure, neglecting the correlated part, gives

$$\langle c_a^\dagger d_b^\dagger d_c c_d b_\mu^\dagger b_\rho \rangle = \delta_{\rho\sigma} \langle c_a^\dagger d_b^\dagger d_c c_d b_\mu^\dagger \rangle n_\rho^{\text{ph}} + \delta_{\mu\sigma} \langle c_a^\dagger d_b^\dagger d_c c_d b_\rho^\dagger \rangle n_\mu^{\text{ph}}. \tag{B1}$$

Performing transition to the excitonic basis, the following differential equation for the variable $\delta n_{\bar{x}\bar{x}\rho^+\sigma^-}$ is obtained:

$$\begin{aligned}
\partial_t \delta n_{\bar{x}\bar{x}\rho^+\sigma^-} &= -i(\omega_x - \omega_{\bar{x}} + \omega_\sigma - \omega_\rho) \delta n_{\bar{x}\bar{x}\rho^+\sigma^-} + \frac{1 + n_\sigma^{\text{ph}}}{i\hbar} \sum_{x'} \Gamma_{xx'}^\sigma n_{\bar{x}\bar{x}'\rho^+} - \frac{n_\sigma^{\text{ph}}}{i\hbar} \sum_{\bar{x}'} \Gamma_{\bar{x}'\bar{x}}^\sigma n_{\bar{x}'\bar{x}\rho^+} \\
&- \frac{1 + n_\rho^{\text{ph}}}{i\hbar} \sum_{\bar{x}'} \Gamma_{\bar{x}\bar{x}'}^{\rho*} n_{x\bar{x}'\sigma^+} + \frac{n_\rho^{\text{ph}}}{i\hbar} \sum_{x'} \Gamma_{x'\bar{x}}^{\rho*} n_{x'\bar{x}\sigma^+},
\end{aligned} \tag{B2}$$

and similarly for the variable $\delta n_{\bar{x}\bar{x}\rho^+\sigma^+}$. Solving Eq. (B2) in the Markov and adiabatic approximations [39,40], the following result is obtained:

$$\begin{aligned}
\delta n_{\bar{x}\bar{x}\rho^+\sigma^-} &= (1 + n_\sigma^{\text{ph}}) \sum_{x'} \Gamma_{xx'}^\sigma \mathcal{D}(\hbar\omega_{x'} - \hbar\omega_x - \hbar\omega_\sigma) n_{\bar{x}\bar{x}'\rho^+} - n_\sigma^{\text{ph}} \sum_{\bar{x}'} \Gamma_{\bar{x}'\bar{x}}^\sigma \mathcal{D}(\hbar\omega_{\bar{x}} - \hbar\omega_{\bar{x}'} - \hbar\omega_\sigma) n_{\bar{x}'\bar{x}\rho^+} \\
&+ (1 + n_\rho^{\text{ph}}) \sum_{\bar{x}'} \Gamma_{\bar{x}\bar{x}'}^{\rho*} \mathcal{D}^*(\hbar\omega_{\bar{x}'} - \hbar\omega_{\bar{x}} - \hbar\omega_\rho) n_{x\bar{x}'\sigma^+} - n_\rho^{\text{ph}} \sum_{x'} \Gamma_{x'\bar{x}}^{\rho*} \mathcal{D}^*(\hbar\omega_x - \hbar\omega_{x'} - \hbar\omega_\rho) n_{x'\bar{x}\sigma^+},
\end{aligned} \tag{B3}$$

where $\mathcal{D}(\epsilon) = -i\pi\delta(\epsilon) + \mathcal{P}(1/\epsilon)$. We thus expressed two-phonon-assisted electronic density matrices in terms of one-phonon-assisted electronic density matrices. When these results are inserted in Eq. (33), we neglect all terms involving principal values which, in principle, lead to polaron shifts in energies [9,40]. Furthermore, we note that the inserted terms involve multiple summations over excitonic indices x and we use the random phase approximation to simplify the expression obtained. This approximation is easier to understand and justify when we transfer to a particular representation for the excitonic index x , for example, the one that we used in our computational study, where we took advantage of the translational symmetry and had $x = (Q, \nu)$. Electronic density matrices with one-phonon assistance $n_{(\bar{Q}, \bar{\nu})(Q, \nu)q_\mu^\pm}$ are complex quantities, which acquire nontrivial values during the evolution provided that the condition $\bar{Q} + q_\mu = Q$ is satisfied. Having in mind the selection rule for carrier-phonon matrix elements in the excitonic basis [see Eq. (52)], we can express the first term which describes the coupling of the one-phonon-assisted electronic density matrix $n_{(Q-q_\mu, \bar{\nu})(Q, \nu)q_\mu^\pm}$ to density matrices with higher phonon assistance [see Eq. (33)] as

$$\begin{aligned}
& - \frac{1}{i\hbar} \sum_{\rho\bar{x}'} \Gamma_{\bar{x}\bar{x}'}^{\rho*} \delta n_{\bar{x}'\bar{x}\mu^+\rho^-} \\
& = \frac{\pi}{\hbar} \sum_{q_\rho, \nu', \bar{\nu}'} \Gamma_{(Q-q_\mu, \bar{\nu})(Q-q_\mu+q_\rho, \bar{\nu}')}^{q_\rho*} \Gamma_{(Q, \nu)(Q+q_\rho, \nu')}^{q_\rho} (1 + n_{q_\rho}^{\text{ph}}) \delta(\hbar\omega_{(Q+q_\rho, \nu')} - \hbar\omega_{(Q, \nu)} - \hbar\omega_{q_\rho}) n_{(Q-q_\mu+q_\rho, \bar{\nu}')(Q+q_\rho, \nu')q_\mu^\pm}
\end{aligned}$$

$$\begin{aligned}
& -\frac{\pi}{\hbar} \sum_{q_\rho, \bar{v}', \bar{v}''} \Gamma_{(Q-q_\mu, \bar{v})(Q-q_\mu+q_\rho, \bar{v}')}^{q_\rho*} \Gamma_{(Q-q_\mu, \bar{v}'')(Q-q_\mu+q_\rho, \bar{v}'')}^{q_\rho} n_{q_\rho}^{\text{ph}} \delta(\hbar\omega_{(Q-q_\mu+q_\rho, \bar{v}')} - \hbar\omega_{(Q-q_\mu, \bar{v}'')} - \hbar\omega_{q_\rho}) n_{(Q-q_\mu, \bar{v}'')(Q, v)q_\mu^+} \\
& -\frac{\pi}{\hbar} \sum_{q_\rho, \bar{v}', \bar{v}''} \Gamma_{(Q-q_\mu, \bar{v})(Q-q_\mu+q_\rho, \bar{v}')}^{q_\rho*} \Gamma_{(Q-q_\mu+q_\rho, \bar{v}')(Q+q_\rho, \bar{v}'')}^{q_\mu*} (1 + n_{q_\mu}^{\text{ph}}) \delta(\hbar\omega_{(Q+q_\rho, \bar{v}'')} - \hbar\omega_{(Q-q_\mu+q_\rho, \bar{v}')} - \hbar\omega_{q_\mu}) n_{(Q, v)(Q+q_\rho, \bar{v}'')q_\rho^+}^* \\
& +\frac{\pi}{\hbar} \sum_{q_\rho, \bar{v}', \bar{v}''} \Gamma_{(Q-q_\mu, \bar{v})(Q-q_\mu+q_\rho, \bar{v}')}^{q_\rho*} \Gamma_{(Q-q_\mu, \bar{v}')(Q, v)}^{q_\mu*} n_{q_\mu}^{\text{ph}} \delta(\hbar\omega_{(Q, v)} - \hbar\omega_{(Q-q_\mu, \bar{v}')} - \hbar\omega_{q_\mu}) n_{(Q-q_\mu, \bar{v}')(Q-q_\mu+q_\rho, \bar{v}'')q_\rho^+}^*. \tag{B4}
\end{aligned}$$

In the first, the third, and the fourth sums in the previous equation we perform summation of terms which involve complex-valued single-phonon-assisted electronic density matrices over the wave vector q_ρ , whereas in the second sum the summation is not carried out over any of the wave vectors describing the density matrix. In the lowest approximation, we can assume that all the sums apart from the second are negligible due to random phases at different wave vectors. For the sake of simplicity, in the second sum we keep only the contribution for $\bar{v}'' = \bar{v}$, thus expressing the coupling to higher-phonon-assisted density matrices only in terms of the single-phonon-assisted density matrix for which the equation is formed. Restoring the more general notation, we obtain the result

$$-\frac{1}{i\hbar} \sum_{\rho\bar{x}'} \Gamma_{\bar{x}\bar{x}'}^{\rho*} \delta n_{\bar{x}'x\mu^+\rho^-} = -\frac{\pi}{\hbar} \left(\sum_{\rho\bar{x}} |\Gamma_{\bar{x}\bar{x}}^\rho|^2 n_\rho^{\text{ph}} \delta(\hbar\omega_{\bar{x}} - \hbar\omega_{\bar{x}} + \hbar\omega_\rho) \right) n_{\bar{x}x\mu^+}. \tag{B5}$$

Repeating similar procedure with the remaining three terms which describe coupling to density matrices with higher-order phonon assistance in Eq. (33), we obtain the result embodied in Eqs. (36)–(38).

Analogously, the following results for two-phonon-assisted electronic density matrices $\delta y_{x\rho^+\sigma^-}, \delta y_{x\rho^+\sigma^+}$ are obtained, solving their respective differential equations in the Markov and adiabatic approximations

$$\delta y_{x\rho^+\sigma^-} = (1 + n_\sigma^{\text{ph}}) \sum_{x'} \Gamma_{xx'}^\sigma \mathcal{D}(\hbar\omega_{x'} - \hbar\omega_x - \hbar\omega_\sigma) y_{x'\rho}^{(+)} - n_\rho^{\text{ph}} \sum_{x'} \Gamma_{x'x}^{\rho*} \mathcal{D}^*(\hbar\omega_x - \hbar\omega_{x'} - \hbar\omega_\rho) y_{x'\sigma}^{(-)}, \tag{B6}$$

and similarly for the variable $\delta y_{x\rho^+\sigma^+}$. Inserting the results obtained in Eqs. (34) and (35) and performing the random phase approximation as described, the result given in Eqs. (41) and (42) is obtained.

APPENDIX C: COMMENTS ON THE ENERGY CONSERVATION IN THE MODEL

In this appendix, we will comment on the energy conservation in the model after the external field has vanished. Using Eqs. (21), (22), (29), and (30), we obtain the rate at which the energy of carriers and phonons changes after the pulse

$$\partial_t (\mathcal{E}_c + \mathcal{E}_{\text{ph}}) = -\frac{2}{\hbar} \sum_{\mu\bar{x}x} (\hbar\omega_x - \hbar\omega_{\bar{x}} - \hbar\omega_\mu) \text{Im} \{ \Gamma_{\bar{x}x}^\mu n_{\bar{x}x\mu^+} \}, \tag{C1}$$

which exactly cancels the part from $\partial_t \mathcal{E}_{c\text{-ph}}$ [see Eq. (23)] that originates from the free rotation term $-i(\omega_x - \omega_{\bar{x}} - \omega_\mu) n_{\bar{x}x\mu^+}$ in Eq. (33). The terms in $\partial_t \mathcal{E}_{c\text{-ph}}$ which arise from the second and third terms in Eq. (33) are identically equal to zero each since they are purely real, which is easily checked. Therefore, the rate at which the total energy changes after the pulse is equal to the rate at which the carrier-phonon interaction energy changes due to the coupling of single-phonon-assisted to higher-order phonon-assisted density matrices, $(\partial_t \mathcal{E}_{c\text{-ph}})_{\text{higher}}$, which is equal to [see Eq. (33)]

$$\begin{aligned}
(\partial_t \mathcal{E}_{c\text{-ph}})_{\text{higher}} = & -\frac{2}{\hbar} \text{Im} \left\{ \sum_{\substack{\mu\bar{x}x \\ \rho\bar{x}'}} \Gamma_{\bar{x}x}^\mu \Gamma_{\bar{x}\bar{x}'}^{\rho*} \delta n_{\bar{x}'x\mu^+\rho^-} \right\} - \frac{2}{\hbar} \text{Im} \left\{ \sum_{\substack{\mu\bar{x}x \\ \rho\bar{x}'}} \Gamma_{\bar{x}x}^\mu \Gamma_{\bar{x}'\bar{x}}^\rho \delta n_{\bar{x}'x\mu^+\rho^+} \right\} \\
& + \frac{2}{\hbar} \text{Im} \left\{ \sum_{\substack{\mu\bar{x}x \\ \rho x'}} \Gamma_{\bar{x}x}^\mu \Gamma_{x'x}^{\rho*} \delta n_{\bar{x}x\mu^+\rho^-} \right\} + \frac{2}{\hbar} \text{Im} \left\{ \sum_{\substack{\mu\bar{x}x \\ \rho x'}} \Gamma_{\bar{x}x}^\mu \Gamma_{xx'}^\rho \delta n_{\bar{x}x\mu^+\rho^+} \right\}. \tag{C2}
\end{aligned}$$

The first and the third terms on the right-hand side of Eq. (C2) are separately equal to zero (since the quantities under the sign of the imaginary part are purely real), whereas the second and the fourth terms exactly cancel each other, so the total energy is conserved. In particular, this is true for the form of the correlated parts of two-phonon-assisted density matrix $\delta n_{\bar{x}x\rho^+\sigma^-}$ given in Eq. (B3) and the similar form of the density matrix $\delta n_{\bar{x}x\rho^+\sigma^+}$. In Eq. (C2), all the sums are performed over all indices that are present in a particular expression, so the crux of the proof that the energy is conserved is the interchange of dummy indices combined with the properties $\delta n_{\bar{x}x\rho^+\sigma^-}^* = \delta n_{x\bar{x}\sigma^+\rho^-}$ and $\delta n_{\bar{x}x\rho^+\sigma^+} = \delta n_{x\bar{x}\sigma^+\rho^+}$. However, when we apply the random phase approximation, the aforementioned properties are lost and the energy is not conserved any more. For example,

the first term on the right-hand side in Eq. (C2) after performing the random phase approximation is not equal to zero, but to $-\frac{2\pi}{\hbar}(\sum_{\rho\bar{x}}|\Gamma_{\bar{x}\bar{x}}^{\rho}|^2n_{\rho}^{\text{ph}}\delta(\hbar\omega_{\bar{x}}-\hbar\omega_{\bar{x}}+\hbar\omega_{\rho}))\text{Re}\{\sum_{\mu\bar{x}x}\Gamma_{\bar{x}x}^{\mu}n_{\bar{x}x\mu^+}\}$ [see Eq. (B5)], which is just one term of the total rate $(\partial_t \mathcal{E}_{\text{c-ph}})_{\text{higher}}$ when we use the result from Eq. (36).

-
- [1] W. Tress, *Organic Solar Cells: Theory, Experiment, and Device Simulation*, Vol. 208 (Springer, Berlin, 2014).
- [2] C. Deibel and V. Dyakonov, *Rep. Prog. Phys.* **73**, 096401 (2010).
- [3] J.-L. Brédas, J. E. Norton, J. Cornil, and V. Coropceanu, *Acc. Chem. Res.* **42**, 1691 (2009).
- [4] T. M. Clarke and J. R. Durrant, *Chem. Rev.* **110**, 6736 (2010).
- [5] R. S. Knox, *Theory of Excitons* (Academic, New York, 1963).
- [6] J. Singh and H. E. Ruda, in *Optical Properties of Condensed Matter*, edited by J. Singh (Wiley, Hoboken, NJ, 2006).
- [7] V. M. Axt and T. Kuhn, *Rep. Prog. Phys.* **67**, 433 (2004).
- [8] H. Bässler and A. Köhler, in *Unimolecular and Supramolecular Electronics I*, edited by R. M. Metzger (Springer, Berlin, 2012).
- [9] T. Kuhn, in *Theory of Transport Properties of Semiconductor Nanostructures*, edited by E. Schöll (Chapman and Hall, London, 1998).
- [10] F. Rossi and T. Kuhn, *Rev. Mod. Phys.* **74**, 895 (2002).
- [11] H. Haug and A.-P. Jauho, *Quantum Kinetics in Transport and Optics of Semiconductors* (Springer, Berlin, 1996).
- [12] P. E. Selbmann, M. Gulia, F. Rossi, E. Molinari, and P. Lugli, *Phys. Rev. B* **54**, 4660 (1996).
- [13] M. Gulia, F. Rossi, E. Molinari, P. E. Selbmann, and P. Lugli, *Phys. Rev. B* **55**, R16049 (1997).
- [14] M. Kira and S. Koch, *Prog. Quantum Electron.* **30**, 155 (2006).
- [15] M. Kira and S. Koch, *Semiconductor Quantum Optics* (Cambridge University Press, New York, 2012).
- [16] M. Kira, W. Hoyer, T. Stroucken, and S. W. Koch, *Phys. Rev. Lett.* **87**, 176401 (2001).
- [17] W. Hoyer, M. Kira, and S. Koch, *Phys. Status Solidi B* **234**, 195 (2002).
- [18] W. Hoyer, M. Kira, and S. W. Koch, *Phys. Rev. B* **67**, 155113 (2003).
- [19] M. N. Kobrak and E. R. Bittner, *Phys. Rev. B* **62**, 11473 (2000).
- [20] K. Tandon, S. Ramasesha, and S. Mazumdar, *Phys. Rev. B* **67**, 045109 (2003).
- [21] N. S. Sariciftci, L. Smilowitz, A. J. Heeger, and F. Wudl, *Science* **258**, 1474 (1992).
- [22] I.-W. Hwang, D. Moses, and A. J. Heeger, *J. Phys. Chem. C* **112**, 4350 (2008).
- [23] N. Banerji, S. Cowan, M. Leclerc, E. Vauthey, and A. J. Heeger, *J. Am. Chem. Soc.* **132**, 17459 (2010).
- [24] N. Banerji, S. Cowan, E. Vauthey, and A. J. Heeger, *J. Phys. Chem. C* **115**, 9726 (2011).
- [25] S. R. Cowan, N. Banerji, W. L. Leong, and A. J. Heeger, *Adv. Funct. Mater.* **22**, 1116 (2012).
- [26] G. Grancini, M. Maiuri, D. Fazzi, A. Petrozza, H.-J. Egelhaaf, D. Brida, G. Cerullo, and G. Lanzani, *Nat. Mater.* **12**, 29 (2013).
- [27] A. A. Bakulin, A. Rao, V. G. Pavelyev, P. H. M. van Loosdrecht, M. S. Pshenichnikov, D. Niedzialek, J. Cornil, D. Beljonne, and R. H. Friend, *Science* **335**, 1340 (2012).
- [28] A. E. Jailaubekov, A. P. Willard, J. R. Tritsch, W.-L. Chan, N. Sai, R. Gearba, L. G. Kaake, K. J. Williams, K. Leung, P. J. Rossky, and X.-Y. Zhu, *Nat. Mater.* **12**, 66 (2013).
- [29] S. Gélinas, A. Rao, A. Kumar, S. L. Smith, A. W. Chin, J. Clark, T. S. van der Poll, G. C. Bazan, and R. H. Friend, *Science* **343**, 512 (2014).
- [30] V. Axt and A. Stahl, *Z. Phys. B* **93**, 195 (1994).
- [31] V. Axt and A. Stahl, *Z. Phys. B* **93**, 205 (1994).
- [32] K. Siantidis, V. M. Axt, and T. Kuhn, *Phys. Rev. B* **65**, 035303 (2001).
- [33] K. Siantidis, V. Axt, J. Wühr, and T. Kuhn, *Phys. Status Solidi A* **190**, 743 (2002).
- [34] K. Siantidis, T. Wolterink, V. Axt, and T. Kuhn, *Phys. B (Amsterdam)* **314**, 220 (2002).
- [35] V. M. Axt and S. Mukamel, *Rev. Mod. Phys.* **70**, 145 (1998).
- [36] E. Hanamura and H. Haug, *Phys. Rep.* **33**, 209 (1977).
- [37] M. Combescot and W. Pogosov, *Phys. Rev. B* **77**, 085206 (2008).
- [38] V. M. Axt, K. Victor, and A. Stahl, *Phys. Rev. B* **53**, 7244 (1996).
- [39] T. Kuhn and F. Rossi, *Phys. Rev. B* **46**, 7496 (1992).
- [40] J. Schilp, T. Kuhn, and G. Mahler, *Phys. Rev. B* **50**, 5435 (1994).
- [41] J. Schilp, T. Kuhn, and G. Mahler, *Phys. Status Solidi B* **188**, 417 (1995).
- [42] W. M. Zhang, T. Meier, V. Chernyak, and S. Mukamel, *Phys. Rev. B* **60**, 2599 (1999).
- [43] W. Huhn and A. Stahl, *Phys. Status Solidi B* **124**, 167 (1984).
- [44] *Handbook Series on Semiconductor Parameters*, Vol. 1, edited by M. Levinshtein, S. Rumyantsev, and M. Shur (World Scientific, Singapore, 1996).
- [45] Y.-C. Cheng and R. J. Silbey, *J. Chem. Phys.* **128**, 114713 (2008).
- [46] M. Pope and C. E. Swenberg, *Electronic Processes in Organic Crystals and Polymers* (Oxford University Press, Oxford, 1999).
- [47] P. Cudazzo, F. Sottile, A. Rubio, and M. Gatti, *J. Phys.: Condens. Matter* **27**, 113204 (2015).
- [48] A. Troisi and G. Orlandi, *Phys. Rev. Lett.* **96**, 086601 (2006).
- [49] K. Fujii, S. Kera, M. Oiwa, K. K. Okudaira, K. Sakamoto, and N. Ueno, *Surf. Sci.* **601**, 3765 (2007).

Nonequilibrium optical conductivity in materials with localized electronic states

Veljko Janković* and Nenad Vukmirović†

Scientific Computing Laboratory, Institute of Physics Belgrade, University of Belgrade, Pregrevica 118, 11080 Belgrade, Serbia

(Received 8 September 2014; revised manuscript received 20 November 2014; published 1 December 2014)

A wide range of disordered materials contain electronic states that are spatially well localized. In this work, we investigated the electrical response of such systems in nonequilibrium conditions to external electromagnetic field. We obtained the expression for optical conductivity valid for any nonequilibrium state of electronic subsystem. In the case of incoherent nonequilibrium state, this expression contains only the positions of localized electronic states, Fermi's golden rule transition probabilities between the states, and the populations of electronic states. The same form of expression is valid both in the case of weak electron-phonon interaction and weak electron-impurity interaction that act as perturbations of electronic Hamiltonian. The derivation was performed by expanding the general expression for ac conductivity in powers of small electron-phonon interaction or electron-impurity interaction parameter. Applications of the expression to two model systems, a simple one-dimensional Gaussian disorder model, and the model of a realistic three-dimensional organic polymer material, were presented as well.

DOI: [10.1103/PhysRevB.90.224201](https://doi.org/10.1103/PhysRevB.90.224201)

PACS number(s): 72.80.Ng, 72.80.Le

I. INTRODUCTION

Electronic transport in semiconductors has been attracting significant research attention for more than half a century. Particular classes of semiconductors where interesting physical effects arise in electronic transport are semiconductors where a certain type of disorder is present in the system which leads to localization of electronic states. These include amorphous inorganic semiconductors (such as amorphous Si or Ge) [1], inorganic crystals doped with randomly positioned impurities [2,3], and organic semiconductors based on conjugated polymers or small molecules [4–10]. The latter class of materials triggered a particular interest in the past two decades due to their low production cost, which led to the development of a variety of organic electronic devices [11–17].

There is currently a solid understanding of equilibrium electronic transport in disordered systems with localized electronic states. dc transport in such systems can be modeled using an equivalent network of resistors that connect each two sites where electronic states are localized [18,19]. Electronic conductivity or mobility in the material can then be calculated by finding the equivalent resistance of the network or estimated using percolation theory. However, dc mobility which quantifies electronic transport properties over long length scales is in many cases not the most relevant quantity when the description of electronic transport processes is concerned. In particular, in organic solar cells based on a bulk heterojunction of two organic semiconductors, charge carriers travel over very short length (on the order of nanometers) and time (on the order of picoseconds) scales before they reach the interface of two semiconductors [20–22]. The high frequency (terahertz) ac mobility is a much better measure of charge transport over such short time scales.

The approaches for simulation of ac conductivity are usually based on Kubo's formula which expresses the ac conductivity in terms of the mean square displacement of a diffusing carrier [23–27]. Such approaches therefore assume

that carriers are in equilibrium and that they are only slightly perturbed by external alternating electric field. However, in many realistic situations, the carriers are not in equilibrium; a typical example concerns the carriers created by external optical excitation across the band gap of a semiconductor. While general approaches for the treatment of nonequilibrium electronic transport, such as the density matrix formalism [28] or the nonequilibrium Green's function formalism [29–31], do exist, it is in practice quite difficult to apply them to disordered materials, where one needs to consider large portions of material to obtain reliable information about its properties.

The main goal of this work was to derive a simple expression that relates the optical conductivity of a material with localized electronic states to its microscopic parameters. To accomplish this goal, we first derive in Sec. II the relation between nonequilibrium optical conductivity and the corresponding current-current correlation function. Then, in Sec. III we derive an expression for the conductivity of the system of localized states with electron-phonon interaction that acts as perturbation valid for arbitrary nonequilibrium state of the electronic subsystem. In the case of incoherent nonequilibrium state, the obtained expression appears to have a rather simple form—the only quantities that appear in it are the positions of localized states, their populations, and the phonon-induced transition probabilities between the states. In Sec. IV we show that the same expression is obtained if additional static potential acts as a perturbation. In Sec. V, we present the results obtained from the application of the derived formula to a simple one-dimensional hopping model and to a realistic disordered conjugated polymer material. We discuss our results in light of the other results that exist in the literature in Sec. VI.

II. GENERAL EXPRESSION FOR NONEQUILIBRIUM OPTICAL CONDUCTIVITY

In this section, we consider an arbitrary quantum system described by the Hamiltonian \hat{H} whose state is given by the statistical operator $\hat{\rho}(t)$. We will derive the time evolution of $\hat{\rho}(t)$ due to a weak external perturbation $\hat{H}'(t)$ which is turned on at $t = 0$. Next, for the system that contains charged

*veljko.jankovic@ipb.ac.rs

†nenad.vukmirovic@ipb.ac.rs

particles, we will find the current density caused by external electric field that acts as a perturbation. While the results of this section are mostly available in the literature, we repeat them here for completeness of the paper, as well as to introduce the notation and terminology for the remainder of the paper.

A. Evolution of the density matrix

The equation for the density matrix $\hat{\rho}(t)$ describing the state of the system for $t > 0$ is

$$i\hbar \frac{d\hat{\rho}(t)}{dt} = [\hat{H} + \hat{H}'(t), \hat{\rho}(t)]. \quad (1)$$

We search for the solution of Eq. (1) in the form $\hat{\rho}(t) = \hat{\rho}_{\text{free}}(t) + \hat{f}(t)$, where

$$\hat{\rho}_{\text{free}}(t) = e^{-i\frac{\hat{H}}{\hbar}t} \hat{\rho}(0) e^{i\frac{\hat{H}}{\hbar}t} \quad (2)$$

is the statistical operator of the system in the absence of external perturbation, $\hat{\rho}(0)$ is the statistical operator describing the state of the system just before the external perturbation is turned on, while $\hat{f}(t)$ is the contribution to the statistical operator due to linear response of the system. It satisfies the differential equation

$$i\hbar \frac{d\hat{f}(t)}{dt} - [\hat{H}, \hat{f}(t)] = [\hat{H}'(t), \hat{\rho}_{\text{free}}(t)], \quad (3)$$

with the initial condition $\hat{f}(0) = \hat{0}$. After solving the last equation up to linear terms, we obtain [32]

$$\hat{\rho}(t) = e^{-i\frac{\hat{H}}{\hbar}t} \hat{\rho}(0) e^{i\frac{\hat{H}}{\hbar}t} + \frac{1}{i\hbar} e^{-i\frac{\hat{H}}{\hbar}t} \int_0^t dt' [\hat{H}'(t'), \hat{\rho}(0)] e^{i\frac{\hat{H}}{\hbar}t'}, \quad (4)$$

where $\hat{H}'(t) = e^{i\frac{\hat{H}}{\hbar}t} \hat{H}'(t) e^{-i\frac{\hat{H}}{\hbar}t}$. Equations given in this section are strictly valid only for an isolated quantum system and do not include the relaxation of the system from some nonequilibrium to the equilibrium state. In realistic systems, interaction of the system with the environment leads to relaxation of the system to the equilibrium state. Therefore, the equations that we will derive are valid only if the characteristic time of external perturbation is short compared to the relaxation time τ . Since we shall study the response to the electric field oscillating with a frequency ω , the aforementioned condition reads

$$\omega\tau \gg 1. \quad (5)$$

In that case, the relaxation of the system towards equilibrium during one period of the perturbation is negligible and can be ignored in the considerations.

B. Nonequilibrium optical conductivity

Next, we assume that the system contains mobile charged particles and that external electric field acts as a perturbation. The system responds to external electric field by nonzero value of current density. The current density operator is given by [33]

$$\hat{j}_a(\mathbf{r}) = \frac{1}{2m} \sum_n q(\hat{\mathbf{p}}_n \delta^{(3)}(\mathbf{r} - \hat{\mathbf{r}}_n) + \delta^{(3)}(\mathbf{r} - \hat{\mathbf{r}}_n) \hat{\mathbf{p}}_n)_a, \quad (6)$$

where q and m are the charge and the mass of a carrier, respectively, while $\hat{\mathbf{p}}_n$ and $\hat{\mathbf{r}}_n$ are the momentum and the

position operator for a single carrier, and a denotes the component of the current density operator (x , y , or z). Using Eq. (4), we find that the current density at time t is given as

$$\begin{aligned} \langle \hat{j}_a(\mathbf{r}) \rangle_t &= \text{Tr}(\hat{\rho}(t) \hat{j}_a(\mathbf{r})) \\ &= \text{Tr}(\hat{\rho}(0) \hat{j}_a(t, \mathbf{r})) \\ &\quad + \frac{1}{i\hbar} \int_0^t dt' \text{Tr}(\hat{\rho}(0) [\hat{j}_a(t, \mathbf{r}), \hat{H}'_I(t')]), \end{aligned} \quad (7)$$

where $\hat{j}_a(t, \mathbf{r}) = e^{i\frac{\hat{H}}{\hbar}t} \hat{j}_a(\mathbf{r}) e^{-i\frac{\hat{H}}{\hbar}t}$. The first term in Eq. (7) does not depend on the electric field, while we are interested in the response of the system to the applied electric field. Consequently, we shall further only consider the second term in Eq. (7) given as

$$\mathcal{J}_a(t, \mathbf{r}) = \frac{1}{i\hbar} \int_0^t dt' \text{Tr}(\hat{\rho}(0) [\hat{j}_a(t, \mathbf{r}), \hat{H}'_I(t')]). \quad (8)$$

We shall also assume that we are dealing with a spatially homogeneous system at the macroscopic scale. The current density averaged over the volume of the system

$$\mathcal{J}_a(t) = \frac{1}{V} \int d^3\mathbf{r} \mathcal{J}_a(t, \mathbf{r}) \quad (9)$$

will be considered as the response to the applied field. The Hamiltonian of interaction with electric field $\mathbf{E}(t)$ is given as [34]

$$\hat{H}'(t) = -\hat{\mathbf{\Pi}} \cdot \mathbf{E}(t), \quad (10)$$

where $\hat{\mathbf{\Pi}}$ is the electric dipole moment operator defined as

$$\hat{\mathbf{\Pi}} = q \sum_n \hat{\mathbf{r}}_n. \quad (11)$$

Using Eqs. (9), (8), and (10), the quantity $\mathcal{J}_a(t)$ can be expressed as

$$\mathcal{J}_a(t) = \int_0^t dt' \sigma_{ab}(t, t') E_b(t'), \quad (12)$$

where the tensor

$$\sigma_{ab}(t, t') = \frac{i}{\hbar V} \text{Tr}(\hat{\rho}(0) [\hat{J}_a(t), \hat{\Pi}_b(t')]) \quad (13)$$

describes the linear response to the applied electric field. In Eq. (13), the operator $\hat{J}_a(t)$ is defined as

$$\hat{J}_a(t) = \int d^3\mathbf{r} \hat{j}_a(t, \mathbf{r}) = \frac{q}{m} \sum_n (\hat{\mathbf{p}}_n)_a. \quad (14)$$

The operators $\hat{\Pi}_a(t)$ and $\hat{J}_b(t)$ satisfy the equal time commutation relation

$$[\hat{\Pi}_a(t), \hat{J}_b(t)] = i\hbar \frac{Nq^2}{m} \delta_{ab}, \quad (15)$$

where N is the number of carriers, and the continuity equation

$$\hat{j}_a(t) = \frac{d}{dt} \hat{\Pi}_a(t). \quad (16)$$

When the condition

$$[\hat{\rho}(0), \hat{H}] = \hat{0} \quad (17)$$

is satisfied, the tensor $\sigma_{ab}(t, t')$ defined in Eq. (13) does not depend separately on t and t' , but only on their difference

$u = t - t'$. The optical conductivity tensor can then be defined as $\sigma_{ab}(\omega) = \int_0^{+\infty} du \sigma_{ab}(u) e^{i\omega u}$ and reads

$$\sigma_{ab}(\omega) = \frac{i}{\hbar V} \int_0^{+\infty} dt e^{i\omega t} \text{Tr}(\hat{\rho}(0)[\hat{J}_a(t), \hat{\Pi}_b(0)]). \quad (18)$$

Using Eqs. (16) and (15), Eq. (18) can be cast into a more familiar form ($n = N/V$ is the concentration of carriers)

$$\sigma_{ab}(\omega) = i \frac{nq^2}{m\omega} \delta_{ab} + \frac{1}{\hbar\omega V} \int_0^{+\infty} dt e^{i\omega t} \times \text{Tr}(\hat{\rho}(0)[\hat{J}_a(t), \hat{J}_b(0)]). \quad (19)$$

The equation for the optical conductivity (19) can be considered as a generalization to the nonequilibrium stationary case of well-known results [35] which relate optical conductivity to the equilibrium current-current correlation function. Generalizations of this sort have already been proposed in the literature [in the context of the fluctuation-dissipation theorem, which relates the dissipative part of the optical conductivity to the (non)equilibrium current fluctuations] [36,37].

In the case, when $[\hat{\rho}(0), \hat{H}] \neq \hat{0}$, the tensor $\sigma_{ab}(t, t')$ defined in Eq. (13) depends separately on t and t'

$$\sigma_{ab}(t, t') = -\frac{1}{i\hbar V} \text{Tr}(e^{-\frac{i}{\hbar}\hat{H}t} \hat{\rho}(0) e^{\frac{i}{\hbar}\hat{H}t'} [\hat{J}_a(0), \hat{\Pi}_b(-(t-t'))]). \quad (20)$$

Using Eqs. (16) and (15), one obtains the following expression:

$$\sigma_{ab}(t, t') = \frac{nq^2}{m} \delta_{ab} - \frac{i}{\hbar V} \int_0^{t-t'} d\tau \times \text{Tr}(e^{-\frac{i}{\hbar}\hat{H}(t-\tau)} \hat{\rho}(0) e^{\frac{i}{\hbar}\hat{H}(t-\tau)} [\hat{J}_a(\tau), \hat{J}_b(0)]). \quad (21)$$

III. OPTICAL CONDUCTIVITY IN THE PRESENCE OF ELECTRON-PHONON INTERACTION

In this section, we derive the expression for optical conductivity of a system with localized electronic states in the presence of weak electron-phonon interaction. In Sec. III A we introduce the Hamiltonian of the system, derive the current operator, and obtain the frequency-time representation of the conductivity tensor. In Sec. III B, we derive the expression for conductivity valid for the arbitrary reduced density matrix of the electronic subsystem and in the limit of low carrier concentration. For incoherent density matrix of the electronic subsystem, this expression contains only the populations of single-particle electronic states, their spatial positions, and Fermi's golden rule transition probabilities between these states.

A. Model Hamiltonian and preliminaries

We consider the system of electrons and phonons described by the Hamiltonian

$$\hat{H} = \hat{H}_0 + \hat{H}_{\text{e-ph}} = \hat{H}_e + \hat{H}_{\text{ph}} + \hat{H}_{\text{e-ph}}, \quad (22)$$

where

$$\hat{H}_0 = \hat{H}_e + \hat{H}_{\text{ph}} = \sum_{\alpha} \epsilon_{\alpha} \hat{c}_{\alpha}^{\dagger} \hat{c}_{\alpha} + \sum_k \hbar\omega_k \hat{b}_k^{\dagger} \hat{b}_k \quad (23)$$

is the Hamiltonian of noninteracting electrons and phonons, while

$$\hat{H}_{\text{e-ph}} = \sum_k \sum_{\alpha\alpha'} (g_{\alpha\alpha',k}^{-} \hat{c}_{\alpha}^{\dagger} \hat{c}_{\alpha'} \hat{b}_k + g_{\alpha\alpha',k}^{+} \hat{c}_{\alpha}^{\dagger} \hat{c}_{\alpha'} \hat{b}_k^{\dagger}) \quad (24)$$

is the electron-phonon interaction Hamiltonian. In previous expressions, \hat{b}_k^{\dagger} (\hat{b}_k) are the creation (annihilation) operators for the phonon mode k that satisfy bosonic commutation relations, $\hat{c}_{\alpha}^{\dagger}$ (\hat{c}_{α}) are creation (annihilation) operators for electronic single-particle state α that satisfy fermion anticommutation relations, $\hbar\omega_k$ is the energy of a mode k phonon, while ϵ_{α} is the energy of electronic state α . Matrix elements of electron-phonon interaction satisfy the relation

$$g_{\alpha\alpha',k}^{\pm} = g_{\alpha'\alpha,k}^{\mp*} \quad (25)$$

and their particular form depends on details of the electron-phonon interaction mechanism.

We will assume that the phonon subsystem is in thermal equilibrium and therefore we will adopt the following factorization of the initial density matrix $\hat{\rho}(0)$:

$$\hat{\rho}(0) = \hat{\rho}_e \hat{\rho}_{\text{ph,eq}}. \quad (26)$$

The operator $\hat{\rho}_{\text{ph,eq}}$ describes the phonon subsystem in equilibrium at the temperature $T_{\text{ph}} = \frac{1}{k_B \beta_{\text{ph}}}$ and it is given as

$$\hat{\rho}_{\text{ph,eq}} = \frac{e^{-\beta_{\text{ph}} \hat{H}_{\text{ph}}}}{\text{Tr}_{\text{ph}} e^{-\beta_{\text{ph}} \hat{H}_{\text{ph}}}}, \quad (27)$$

whereas $\hat{\rho}_e$ is the reduced density matrix of the electronic subsystem. The state of the system described by Eq. (26) assumes that electrons are out of equilibrium, while the phonons are in equilibrium. Such states can arise naturally in several relevant physical scenarios. A typical example of such a scenario is a semiconductor structure excited with photons whose energy is larger than the band gap of the structure. Most of the energy of incident photons is then transferred to electronic degrees of freedom and therefore it is quite reasonable to assume that electrons are out of equilibrium, while the phonons are in equilibrium.

The electric dipole moment operator $\hat{\Pi}_a$ introduced in Eq. (11) can be expressed in the second quantization representation as

$$\hat{\Pi}_a = q \sum_{\alpha\beta} x_{\alpha;\alpha\beta} \hat{c}_{\alpha}^{\dagger} \hat{c}_{\beta}, \quad (28)$$

where $x_{\alpha;\alpha\beta} \equiv \langle \alpha | \hat{x}_a | \beta \rangle$ are the matrix elements of the single electron position operator. Using Eq. (16), we find that the operator \hat{J}_a reads $\hat{J}_a = \hat{J}_a^{(1)} + \hat{J}_a^{(2)}$, where

$$\hat{J}_a^{(1)} = \frac{iq}{\hbar} \sum_{\alpha\beta} (\epsilon_{\alpha} - \epsilon_{\beta}) x_{\alpha;\alpha\beta} \hat{c}_{\alpha}^{\dagger} \hat{c}_{\beta} \quad (29)$$

describes the contribution to the operator \hat{J}_a due to direct interaction of electrons with electric field, while

$$\hat{J}_a^{(2)} = \frac{iq}{\hbar} \sum_k \sum_{\alpha\beta} (F_{\alpha;\alpha\beta,k}^{-} \hat{c}_{\alpha}^{\dagger} \hat{c}_{\beta} \hat{b}_k + F_{\alpha;\alpha\beta,k}^{+} \hat{c}_{\alpha}^{\dagger} \hat{c}_{\beta} \hat{b}_k^{\dagger}) \quad (30)$$

describes the contribution arising from electron-phonon interaction. The coefficients $F_{a;\alpha\beta,k}^{\pm}$ are given by

$$F_{a;\alpha\beta,k}^{\pm} = \sum_{\alpha'} (g_{\alpha\alpha',k}^{\pm} x_{a;\alpha'\beta} - x_{a;\alpha\alpha'} g_{\alpha'\beta,k}^{\pm}) \quad (31)$$

and satisfy the relation

$$F_{a;\alpha\beta,k}^{\pm} = -F_{a;\beta\alpha,k}^{\mp*} \quad (32)$$

In this work, we are mainly interested in the case of localized electronic states when the matrix elements of the position operator between different states are negligible. This condition can be mathematically expressed as

$$x_{a;\alpha\beta} = \delta_{\alpha\beta} x_{a;\alpha} \quad (33)$$

Therefore, in the case of localized electronic states, $\hat{J}_a^{(1)} = 0$ and consequently $\hat{J}_a = \hat{J}_a^{(2)}$.

Next, we treat electron-phonon interaction as a perturbation and perform the expansion of Eq. (21) with respect to small interaction constants $g_{\alpha\beta,k}^{\pm}$. The evolution operator that appears in Eq. (21) can be expanded in Dyson series as

$$e^{-\frac{i}{\hbar}\hat{H}t} = e^{-\frac{i}{\hbar}\hat{H}_0t} + \frac{1}{i\hbar} \int_0^t dt' e^{-\frac{i}{\hbar}\hat{H}_0(t-t')} \hat{H}_{\text{e-ph}} e^{-\frac{i}{\hbar}\hat{H}_0t'} + \dots \quad (34)$$

Consequently, the expansion of the time-dependent operator $\hat{J}_a(\tau)$ from Eq. (21) reads

$$\hat{J}_a(\tau) = e^{\frac{i}{\hbar}\hat{H}_0\tau} \hat{J}_a e^{-\frac{i}{\hbar}\hat{H}_0\tau} + \left[e^{\frac{i}{\hbar}\hat{H}_0\tau} \hat{J}_a e^{-\frac{i}{\hbar}\hat{H}_0\tau}, \int_0^{\tau} \frac{dt'}{i\hbar} e^{\frac{i}{\hbar}\hat{H}_0t'} \hat{H}_{\text{e-ph}} e^{-\frac{i}{\hbar}\hat{H}_0t'} \right] + \dots \quad (35)$$

Furthermore, the expansion of the first term under trace in Eq. (21) gives

$$\begin{aligned} & e^{-\frac{i}{\hbar}\hat{H}(t-\tau)} \hat{\rho}(0) e^{\frac{i}{\hbar}\hat{H}(t-\tau)} \\ &= \hat{\rho}(0) + \sum_{n=1}^{+\infty} \frac{1}{n!} \left(-\frac{i(t-\tau)}{\hbar} \right)^n [\hat{H}, \dots, [\hat{H}, \hat{\rho}(0)] \dots]_n. \end{aligned} \quad (36)$$

Our aim is to obtain the first nonzero term in the expansion of Eq. (21) in the case of localized electronic states. It is therefore sufficient to take only the first term in the expansion given by Eq. (35) and to isolate the contribution from the expansion given in Eq. (36) which does not contain electron-phonon coupling constants. One can show by direct inspection, using the factorization of the initial density matrix given by Eq. (26), that every summand under the sum on the right hand side of Eq. (36) has only one term which does not contain electron-phonon coupling constants and which is of the type $\frac{1}{n!} \left(-\frac{i(t-\tau)}{\hbar} \right)^n [\hat{H}_e, \dots, [\hat{H}_e, \hat{\rho}_e] \dots]_n \hat{\rho}_{\text{ph,eq}}$. All these

contributions can be resummed so that we finally obtain the zeroth-order term in the expansion given by Eq. (36)

$$e^{-\frac{i}{\hbar}\hat{H}(t-\tau)} \hat{\rho}(0) e^{\frac{i}{\hbar}\hat{H}(t-\tau)} = e^{-\frac{i}{\hbar}\hat{H}_e(t-\tau)} \hat{\rho}(0) e^{\frac{i}{\hbar}\hat{H}_e(t-\tau)} + \dots \quad (37)$$

The first nontrivial term in the expansion of Eq. (21) in the case of localized electronic states is thus given by

$$\begin{aligned} \sigma_{ab}(t,t') &= \frac{nq^2}{m} \delta_{ab} - \frac{i}{\hbar V} \int_0^{t-t'} d\tau \\ &\times \text{Tr}(\hat{\rho}(0) e^{\frac{i}{\hbar}\hat{H}_e(t-\tau)} [\hat{J}_a^{(2),0}(\tau), \hat{J}_b^{(2)}(0)] e^{-\frac{i}{\hbar}\hat{H}_e(t-\tau)}), \end{aligned} \quad (38)$$

where $\hat{J}_a^{(2),0}(\tau) = e^{\frac{i}{\hbar}\hat{H}_0\tau} \hat{J}_a^{(2)} e^{-\frac{i}{\hbar}\hat{H}_0\tau}$. Next, we consider the frequency-time representation of the conductivity tensor which can be defined as

$$\sigma_{ab}(t,\omega) = \int_0^{+\infty} du \sigma_{ab}(t,t-u) e^{i\omega u}. \quad (39)$$

When $\sigma_{ab}(t,t')$ depends only on the difference $t - t'$, Eq. (39) defines the conventional optical conductivity tensor $\sigma_{ab}(\omega)$. The frequency-time representation of the conductivity tensor given in Eq. (38) is

$$\begin{aligned} \sigma_{ab}(t,\omega) &= \frac{inq^2}{m\omega} \delta_{ab} + \frac{1}{\hbar\omega V} \int_0^{+\infty} du e^{i\omega u} \\ &\times \text{Tr}(\hat{\rho}(0) e^{\frac{i}{\hbar}\hat{H}_e(t-u)} [\hat{J}_a^{(2),0}(u), \hat{J}_b^{(2)}(0)] e^{-\frac{i}{\hbar}\hat{H}_e(t-u)}). \end{aligned} \quad (40)$$

In the case when $\sigma_{ab}(t,\omega)$ varies slowly with t on the $1/\omega$ time scale, it can be interpreted as the conventional optical conductivity tensor at time t .

We also note that when the condition of localized electronic states [Eq. (33)] is not satisfied, the dominant term in the \hat{J}_a operator is the $\hat{J}_a^{(1)}$ term. The leading terms in expansions (35) and (36) are then given by first terms in Eqs. (35) and (37), where \hat{J}_a is replaced by $\hat{J}_a^{(1)}$ in Eq. (35). These terms are independent of electron-phonon coupling constants and lead to the following expression for the frequency-time representation of the conductivity tensor:

$$\begin{aligned} \sigma_{ab}(t,\omega) &= \frac{inq^2}{m\omega} \delta_{ab} + \frac{1}{\hbar\omega V} \int_0^{+\infty} du e^{i\omega u} \\ &\times \text{Tr}(\hat{\rho}(0) e^{\frac{i}{\hbar}\hat{H}_e(t-u)} [\hat{J}_a^{(1),0}(u), \hat{J}_b^{(1)}(0)] e^{-\frac{i}{\hbar}\hat{H}_e(t-u)}). \end{aligned} \quad (41)$$

The physical origin of this term is direct absorption of electromagnetic radiation by the electronic subsystem. However, since this term vanishes for a system with localized electronic states, which is of main interest in this work, this term will not be considered in the remainder of the paper. The focus will be on the term from Eq. (40) which arises due to phonon-assisted transitions between states, as will become evident in Sec. III B.

B. Frequency dependence of mobility in low carrier density limit

We will now start from Eq. (40) for the frequency-time representation of conductivity to derive the expression for the optical conductivity that explicitly contains the populations of electronic states (diagonal elements of $\hat{\rho}_e$) and coherences (off-diagonal elements of $\hat{\rho}_e$). By replacing Eq. (30) into the expression for mean value

$\text{Tr}(\hat{\rho}(0) e^{\frac{i}{\hbar}\hat{H}_e(t-u)}[\hat{J}_a^{(2),0}(u), \hat{J}_b^{(2)}]e^{-\frac{i}{\hbar}\hat{H}_e(t-u)})$ and tracing out the phonon degrees of freedom one obtains

$$\begin{aligned} & \text{Tr}(\hat{\rho}(0) e^{\frac{i}{\hbar}\hat{H}_e(t-u)}[\hat{J}_a^{(2),0}(u), \hat{J}_b^{(2)}]e^{-\frac{i}{\hbar}\hat{H}_e(t-u)}) \left(\frac{iq}{\hbar}\right)^{-2} \\ &= \sum_k \sum_{\alpha\beta\gamma\delta} (F_{a;\alpha\beta,k}^- F_{b;\gamma\delta,k}^+ e^{-\frac{i}{\hbar}(\epsilon_\gamma - \epsilon_\delta + \hbar\omega_k)u} - F_{a;\alpha\beta,k}^+ F_{b;\gamma\delta,k}^- e^{-\frac{i}{\hbar}(\epsilon_\gamma - \epsilon_\delta - \hbar\omega_k)u}) e^{\frac{i}{\hbar}(\epsilon_\alpha - \epsilon_\beta + \epsilon_\gamma - \epsilon_\delta)t} \langle \hat{c}_\alpha^\dagger \hat{c}_\beta \hat{c}_\gamma^\dagger \hat{c}_\delta \rangle_e \\ &+ \sum_k \sum_{\alpha\beta\gamma} (F_{a;\alpha\gamma,k}^- F_{b;\gamma\beta,k}^+ e^{-\frac{i}{\hbar}(\epsilon_\gamma - \epsilon_\beta + \hbar\omega_k)u} - F_{b;\alpha\gamma,k}^+ F_{a;\gamma\beta,k}^- e^{-\frac{i}{\hbar}(\epsilon_\alpha - \epsilon_\gamma + \hbar\omega_k)u}) N_k e^{\frac{i}{\hbar}(\epsilon_\alpha - \epsilon_\beta)t} \langle \hat{c}_\alpha^\dagger \hat{c}_\beta \rangle_e \\ &+ \sum_k \sum_{\alpha\beta\gamma} (F_{a;\alpha\gamma,k}^+ F_{b;\gamma\beta,k}^- e^{-\frac{i}{\hbar}(\epsilon_\gamma - \epsilon_\beta - \hbar\omega_k)u} - F_{b;\alpha\gamma,k}^- F_{a;\gamma\beta,k}^+ e^{-\frac{i}{\hbar}(\epsilon_\alpha - \epsilon_\gamma - \hbar\omega_k)u}) (1 + N_k) e^{\frac{i}{\hbar}(\epsilon_\alpha - \epsilon_\beta)t} \langle \hat{c}_\alpha^\dagger \hat{c}_\beta \rangle_e. \end{aligned} \quad (42)$$

Here, N_k is the number of phonons in mode k given by the Bose-Einstein distribution, $\langle \dots \rangle_e$ denotes averaging with respect to $\hat{\rho}_e$, and coefficients $F_{\alpha\beta,k}^\pm$ are given as [by the virtue of the definition of the localized electronic states from Eq. (33)]

$$F_{a;\alpha\beta,k}^\pm = g_{\alpha\beta,k}^\pm (x_{a;\beta} - x_{a;\alpha}). \quad (43)$$

See Eqs. (31) and (32).

In the limit of low carrier densities, only single-particle electronic excitations are relevant. One can therefore restrict the Hilbert space of the system to the space given as a product of single-particle electronic space and the phonon space. In this restricted space, the operators $\hat{c}_\alpha^\dagger \hat{c}_\beta$ and $\hat{c}_\alpha^\dagger \hat{c}_\beta \hat{c}_\gamma^\dagger \hat{c}_\delta$ reduce respectively to $|\alpha\rangle\langle\beta|$ and $\delta_{\beta\gamma}|\alpha\rangle\langle\delta|$, while the Hamiltonian in this restricted space reads

$$\begin{aligned} \hat{H} &= \sum_\alpha \epsilon_\alpha |\alpha\rangle\langle\alpha| + \sum_k \hbar\omega_k \hat{b}_k^\dagger \hat{b}_k \\ &+ \sum_k \sum_{\alpha\alpha'} (g_{\alpha\alpha',k}^- |\alpha\rangle\langle\alpha'| \hat{b}_k + g_{\alpha\alpha',k}^+ |\alpha\rangle\langle\alpha'| \hat{b}_k^\dagger). \end{aligned} \quad (44)$$

The average values of the expressions appearing in Eq. (42) are then given as

$$\langle \hat{c}_\alpha^\dagger \hat{c}_\beta \rangle_e = \text{Tr}_e(\hat{\rho}_e \hat{c}_\alpha^\dagger \hat{c}_\beta) = \langle \beta | \hat{\rho}_e | \alpha \rangle \quad (45)$$

and

$$\langle \hat{c}_\alpha^\dagger \hat{c}_\beta \hat{c}_\gamma^\dagger \hat{c}_\delta \rangle_e = \text{Tr}_e(\hat{\rho}_e \hat{c}_\alpha^\dagger \hat{c}_\beta \hat{c}_\gamma^\dagger \hat{c}_\delta) = \delta_{\beta\gamma} \langle \delta | \hat{\rho}_e | \alpha \rangle. \quad (46)$$

Combining Eqs. (45), (46), (42), and (40), the following equation for the frequency-time representation of the conductivity tensor is obtained:

$$\sigma_{ab}(t, \omega) = i \frac{nq^2}{m\omega} \delta_{ab} - f_{ab}(t, \omega) - f_{ab}(t, -\omega)^*, \quad (47)$$

where $f_{ab}(t, \omega)$ is defined as

$$\begin{aligned} f_{ab}(t, \omega) &= \frac{q^2}{\hbar^2 \omega V} \sum_k \sum_{\alpha\beta\gamma} e^{\frac{i}{\hbar}(\epsilon_\alpha - \epsilon_\beta)t} \langle \beta | \hat{\rho}_e | \alpha \rangle \\ &\times (F_{a;\alpha\gamma,k}^- F_{b;\gamma\beta,k}^+ \mathcal{D}(\epsilon_\beta - \epsilon_\gamma - \hbar\omega_k + \hbar\omega)(1 + N_k) \\ &+ F_{a;\alpha\gamma,k}^+ F_{b;\gamma\beta,k}^- \mathcal{D}(\epsilon_\beta - \epsilon_\gamma + \hbar\omega_k + \hbar\omega)N_k). \end{aligned} \quad (48)$$

Function $\mathcal{D}(\epsilon)$ is given as

$$\mathcal{D}(\epsilon) = \pi \delta(\epsilon) + i \mathcal{P}(1/\epsilon). \quad (49)$$

In the expressions (47) and (48), there are two clear signatures of nonequilibrium: the explicit time dependence and the

presence of off-diagonal elements of $\hat{\rho}_e$ (coherences). Both of these effects would be absent for the system in equilibrium.

Next, we consider the case when the reduced density matrix of the electronic subsystem is an analytic function of the electronic Hamiltonian \hat{H}_e , when we have

$$\langle \beta | \hat{\rho}_e | \alpha \rangle = \delta_{\alpha\beta} r_\alpha, \quad (50)$$

where

$$r_\alpha = \langle \alpha | \hat{\rho}_e | \alpha \rangle \quad (51)$$

is the average occupation of electronic state α . Then in Eq. (48) we remain only with the average occupations of individual electronic states and since the quantity $f_{ab}(t, \omega)$ does not depend explicitly on t , $\sigma_{ab}(t, \omega)$ also does not depend on t and represents the frequency-dependent conductivity tensor. Starting from Eqs. (47) and (48) one can show that under the aforementioned condition the following relation for the real part of the optical conductivity holds:

$$\begin{aligned} \text{Re } \sigma_{ab}(\omega) &= \frac{q^2}{2\hbar\omega V} \sum_{\alpha\beta} (x_{a;\beta} - x_{a;\alpha})(x_{b;\beta} - x_{b;\alpha}) r_\beta \\ &\times [w_{\beta\alpha, \text{ph}}(\epsilon_\beta - \epsilon_\alpha + \hbar\omega) \\ &- w_{\beta\alpha, \text{ph}}(\epsilon_\beta - \epsilon_\alpha - \hbar\omega)], \end{aligned} \quad (52)$$

where the terms $w_{\beta\alpha, \text{ph}}$ are of the form

$$\begin{aligned} w_{\beta\alpha, \text{ph}}(\epsilon_\beta - \epsilon_\alpha) &= \frac{2\pi}{\hbar} \sum_k [|g_{\alpha\beta,k}^-|^2 \delta(\epsilon_\beta - \epsilon_\alpha + \hbar\omega_k) N_k \\ &+ |g_{\alpha\beta,k}^+|^2 \delta(\epsilon_\beta - \epsilon_\alpha - \hbar\omega_k)(1 + N_k)]. \end{aligned} \quad (53)$$

These are identical to the rates that would be obtained by applying Fermi's golden rule to calculate the transition probability from the state β to the state α due to electron-phonon interaction. Equation (52) gives a rather simple expression for the dissipative part of the optical conductivity as it involves the positions of electronic states, their occupations, and Fermi's golden rule transition probabilities. Equations (52) and (53) also offer an intuitive interpretation of elementary processes giving contribution to the dissipative part of the optical conductivity in the lowest nontrivial order of the perturbation expansion. These processes are one-particle transitions $\beta \rightarrow \alpha$ induced by emission (absorption) of one phonon accompanied by emission (absorption) of the quantum of the external electromagnetic field $\hbar\omega$. One should note that within our

lowest-order perturbative approach, one does not take into account multiphonon transitions which may be important in some systems.

From the definition of mobility, one then also obtains for the real part of ac mobility

$$\begin{aligned} \text{Re } \mu_{ab}(\omega) &= \frac{q}{2\hbar\omega} \sum_{\alpha\beta} (x_{a;\beta} - x_{a;\alpha})(x_{b;\beta} - x_{b;\alpha}) \frac{r_\beta}{\sum_\gamma r_\gamma} \\ &\times [w_{\beta\alpha,\text{ph}}(\epsilon_\beta - \epsilon_\alpha + \hbar\omega) \\ &- w_{\beta\alpha,\text{ph}}(\epsilon_\beta - \epsilon_\alpha - \hbar\omega)]. \end{aligned} \quad (54)$$

Equation (54) was derived under the assumption that hopping rates have the mathematical form given by Eq. (53). In Sec. V, the hopping rates given by Eqs. (70) and (66) will be used. Equation (70) can be derived from Eq. (53) under the assumption that electron-phonon coupling elements are proportional to wave function moduli overlap (see Ref. [38]). Equation (66) can then be obtained from Eq. (70) if one assumes that wave function overlaps decay exponentially with distance between states and that phonon density of states (DOS) is such that energy dependence in Eq. (70) disappears. Therefore, both Eqs. (70) and (66) are compatible with the mathematical structure of Eq. (53) and it is appropriate to use them in Eq. (54).

IV. OPTICAL CONDUCTIVITY IN THE PRESENCE OF IMPURITY SCATTERING

In this section, we will show that similar expressions for optical conductivity are obtained if electrons interact with an additional static potential, rather than with phonons. A typical cause of such potential could be the impurities that are present in the material.

Therefore, we consider the Hamiltonian

$$\hat{H} = \hat{H}_0 + \hat{U} = \sum_\alpha \epsilon_\alpha \hat{c}_\alpha^\dagger \hat{c}_\alpha + \sum_{\alpha\beta} A_{\alpha\beta} \hat{c}_\alpha^\dagger \hat{c}_\beta, \quad (55)$$

where \hat{H}_0 is the noninteracting part of the Hamiltonian, while \hat{U} describes the interaction of electrons with static potential. The operator \hat{J}_a can be computed using Eq. (16) and reads

$$\begin{aligned} \hat{J}_a &= \hat{J}_a^{(\text{dir})} + \hat{J}_a^{(\text{imp})} \\ &= \frac{iq}{\hbar} \sum_{\alpha\alpha'} x_{a;\alpha\alpha'} (\epsilon_\alpha - \epsilon_{\alpha'}) \hat{c}_\alpha^\dagger \hat{c}_{\alpha'} + \frac{iq}{\hbar} \sum_{\alpha\beta} \mathcal{A}_{a;\alpha\beta} \hat{c}_\alpha^\dagger \hat{c}_\beta. \end{aligned} \quad (56)$$

The $\hat{J}_a^{(\text{dir})}$ operator is analogous to the operator $\hat{J}_a^{(1)}$ in the case of a system with electron-phonon interaction and describes direct interaction of electrons with perturbing electric field. On the other hand, the $\hat{J}_a^{(\text{imp})}$ operator describes the contribution to \hat{J}_a due to the interaction with the static potential (or, in particular, with impurities). The coefficients $\mathcal{A}_{a;\alpha\beta}$ that appear in Eq. (56) are given as

$$\mathcal{A}_{a;\alpha\beta} = \sum_{\alpha'} (A_{\alpha\alpha'} x_{a;\alpha'\beta} - x_{a;\alpha\alpha'} A_{\alpha'\beta}) \quad (57)$$

and satisfy [compare to Eq. (32)]

$$\mathcal{A}_{a;\beta\alpha} = -\mathcal{A}_{a;\alpha\beta}^* \quad (58)$$

We will treat the interaction with the static potential as a perturbation and we will derive the formula for optical conductivity in the lowest order of the perturbation expansion with respect to small coefficients $A_{\alpha\beta}$. We will assume that electronic states are localized; see Eq. (33). This way, the expression for the operator \hat{J}_a simplifies to

$$\hat{J}_a = \hat{J}_a^{(\text{imp})} = \frac{iq}{\hbar} \sum_{\alpha\beta} A_{\alpha\beta} (x_{a;\beta} - x_{a;\alpha}) \hat{c}_\alpha^\dagger \hat{c}_\beta. \quad (59)$$

The starting point for the perturbation expansion is again Eq. (21). Following a discussion, similar to that conducted in Sec. III, we obtain that the first nonzero term in the expansion of Eq. (21) in the case of localized electronic states is quadratic in quantities $A_{\alpha\beta}$ and that the corresponding expression for the time-frequency representation of the conductivity tensor [Eq. (39)] reads

$$\begin{aligned} \sigma_{ab}(t, \omega) &= \frac{inq^2}{m\omega} \delta_{ab} + \frac{1}{\hbar\omega V} \int_0^{+\infty} dt e^{i\omega t} \\ &\times \text{Tr}(\hat{\rho}(0) e^{\frac{i}{\hbar} \hat{H}_0(t-u)} [\hat{J}_a^{(\text{imp}),0}(u), \hat{J}_b^{(\text{imp})}] e^{-\frac{i}{\hbar} \hat{H}_0(t-u)}). \end{aligned} \quad (60)$$

The notation $\hat{J}_a^{(\text{imp}),0}(t)$ again suggests that the time dependence is governed by the noninteracting Hamiltonian.

In the low density limit, the projection of the Hamiltonian onto the single-particle subspace reads

$$\hat{H}_0 = \sum_\alpha \epsilon_\alpha |\alpha\rangle\langle\alpha| + \sum_{\alpha\beta} A_{\alpha\beta} |\alpha\rangle\langle\beta|, \quad (61)$$

with the average values $\langle \hat{c}_\alpha^\dagger \hat{c}_\beta \rangle = \langle \beta | \hat{\rho}(0) | \alpha \rangle$. Deriving Eq. (60) we obtain the expression for the frequency-time representation of the conductivity tensor which bears formal resemblance to the analogous expression [Eq. (47)] in the case with electron-phonon interaction,

$$\sigma_{ab}(t, \omega) = i \frac{nq^2}{m\omega} \delta_{ab} - f_{ab}(t, \omega) - f_{ab}(t, -\omega)^*, \quad (62)$$

where $f_{ab}(t, \omega)$ is defined as

$$\begin{aligned} f_{ab}(t, \omega) &= \frac{q^2}{\hbar^2\omega V} \sum_{\alpha\beta\gamma} e^{\frac{i}{\hbar}(\epsilon_\alpha - \epsilon_\beta)t} \langle \beta | \hat{\rho}_e | \alpha \rangle A_{\alpha\gamma} (x_{a;\gamma} - x_{a;\alpha}) \\ &\times A_{\gamma\beta} (x_{b;\beta} - x_{b;\gamma}) \mathcal{D}(\epsilon_\beta - \epsilon_\gamma + \hbar\omega). \end{aligned} \quad (63)$$

Again, when the initial density matrix $\hat{\rho}(0)$ is an analytic function of the electronic part of the Hamiltonian \hat{H}_0 , the quantity $f_{ab}(t, \omega)$ defined in Eq. (63) contains only populations of the individual electronic states $r_\alpha = \langle \alpha | \hat{\rho}(0) | \alpha \rangle$ and does not depend explicitly on time. Thus $\sigma_{ab}(t, \omega)$ is the optical conductivity tensor (entirely expressed in terms of populations of electronic states). The final expression for the real part of ac mobility in the presence of interaction with impurities reads

$$\begin{aligned} \text{Re } \mu_{ab}(\omega) &= \frac{q}{2\hbar\omega} \sum_{\alpha\beta} (x_{a;\beta} - x_{a;\alpha})(x_{b;\beta} - x_{b;\alpha}) \frac{r_\beta}{\sum_\gamma r_\gamma} \\ &\times [w_{\beta\alpha,\text{imp}}(\epsilon_\beta - \epsilon_\alpha + \hbar\omega) \\ &- w_{\beta\alpha,\text{imp}}(\epsilon_\beta - \epsilon_\alpha - \hbar\omega)], \end{aligned} \quad (64)$$

where the terms $w_{\beta\alpha,\text{imp}}$ are of the form

$$w_{\beta\alpha,\text{imp}}(\epsilon_\beta - \epsilon_\alpha) = \frac{2\pi}{\hbar} |A_{\alpha\beta}|^2 \delta(\epsilon_\beta - \epsilon_\alpha). \quad (65)$$

We emphasize the formal analogy between Eqs. (54) and (64) for the ac mobility. The form of both equations is the same, regardless of the particular interaction mechanism (electron-phonon interaction or interaction with an additional static potential) which causes transitions between localized states.

V. NUMERICAL RESULTS

A. One-dimensional model with Miller-Abrahams rates and Gaussian density of states

In this section, we apply the derived formulas to a one-dimensional Gaussian disorder model. The assumption of the model is that the states are located on the sites of a one-dimensional lattice with spacing a and that the energies of the states are drawn from a Gaussian distribution with standard deviation σ . The transition rates were assumed to take the Miller-Abrahams form and only the hops between

nearest neighbors were considered. Under these assumptions, the transition rate from the state β to the state γ has the form

$$w_{\beta\gamma} = w_0 e^{-a/a_{\text{loc}}} \exp\left(\frac{\epsilon_\beta - \epsilon_\gamma - |\epsilon_\beta - \epsilon_\gamma|}{2k_B T}\right), \quad (66)$$

where a_{loc} is the localization length which is assumed equal for all sites, T is the temperature, and w_0 is a constant prefactor. Real part of the frequency dependent mobility can under all these assumptions be written in the form

$$\text{Re } \mu_{xx}(\omega) = \sum_{\gamma} \mu_{\gamma,\gamma+1}(\omega), \quad (67)$$

where $\mu_{\gamma,\gamma+1}(\omega)$ is the contribution of the pair of sites $(\gamma, \gamma + 1)$ given as

$$\mu_{\gamma,\gamma+1}(\omega) = \frac{qa^2}{2k_B T} w_0 e^{-a/a_{\text{loc}}} M(x). \quad (68)$$

In the last equation, x is a dimensionless parameter defined as $x = \beta\hbar\omega$ [$\beta = 1/(k_B T)$], while $M(x)$ is the function that reads

$$M(x) = \begin{cases} \frac{r_{\min}}{\sum_{\delta} r_{\delta}} e^{-x_{\gamma,\gamma+1}} \times 2 \frac{\sinh x}{x}, & x < x_{\gamma,\gamma+1}, \\ \frac{r_{\max}}{\sum_{\delta} r_{\delta}} \frac{1}{x} (1 - e^{x_{\gamma,\gamma+1}} e^{-x}) + \frac{r_{\min}}{\sum_{\delta} r_{\delta}} \frac{1}{x} (1 - e^{-x_{\gamma,\gamma+1}} e^{-x}), & x > x_{\gamma,\gamma+1}, \end{cases} \quad (69)$$

where $x_{\gamma,\gamma+1} = \beta|\epsilon_\gamma - \epsilon_{\gamma+1}|$ and r_{\max} (r_{\min}) is the population of the state with larger (smaller) energy among the states γ and $\gamma + 1$.

The frequency range in which this formula can be applied is determined by the condition (5) where τ is the relaxation time towards equilibrium. The relaxation time τ must be larger than the reciprocal value of largest hopping rates $\tau \gtrsim w_0^{-1} e^{a/a_{\text{loc}}}$, so that the relevant frequencies obey the condition $f \gtrsim (2\pi)^{-1} w_0 e^{-a/a_{\text{loc}}}$.

The calculations were performed for a lattice with 10^5 sites, where the following values of the parameters were used: $T = 300$ K, $\sigma = 100$ meV, $a = 1$ nm, $a_{\text{loc}} = 2a/9$, and $w_0 = 1.0 \times 10^{14}$ s $^{-1}$. Two different cases for initial populations of localized states were considered. In case 1, we assume that initial distribution of carriers are nonequilibrium, but still of Maxwell-Boltzmann form with electronic temperatures T_e which can be different than T . Therefore, in this case $r_\gamma = e^{-\beta_e \epsilon_\gamma}$, where $\beta_e = 1/(k_B T_e)$. In case 2, we assume that only the states in some narrow energy window are initially populated, while the other states are not populated. The initial populations are then given as $r_\gamma = 1$ for $\epsilon_{\min} < \epsilon_\gamma < \epsilon_{\max}$, $r_\gamma = 0$ otherwise. The results for different values of the parameter T_e in case 1 and different intervals $(\epsilon_{\min}, \epsilon_{\max})$ in case 2 are shown in Figs. 1 and 2.

As can be immediately seen from expressions in Eqs. (67)–(69), for sufficiently high frequencies f , such that $hf > \max_{\gamma} |\epsilon_\gamma - \epsilon_{\gamma+1}|$, real part of the ac mobility decreases as $\text{Re } \mu_{xx}(f) \sim 1/f$. On the other hand, for sufficiently low frequencies f , such that $hf < \min_{\gamma} |\epsilon_\gamma - \epsilon_{\gamma+1}|$, real part of the mobility tends to a constant value which depends on the particular choice of r_γ .

In case 1 and in the intermediate frequency range real part of the ac mobility reaches its maximum value. The height of this maximum (measured relative to the low-frequency limit of the mobility) decreases with increasing the temperature T_e . The position of the maximum moves towards lower frequencies with increasing the temperature T_e . Namely, the position of the maximum of the mobility spectrum is determined by the positions of the maximum of the function $M(x)$. For all values

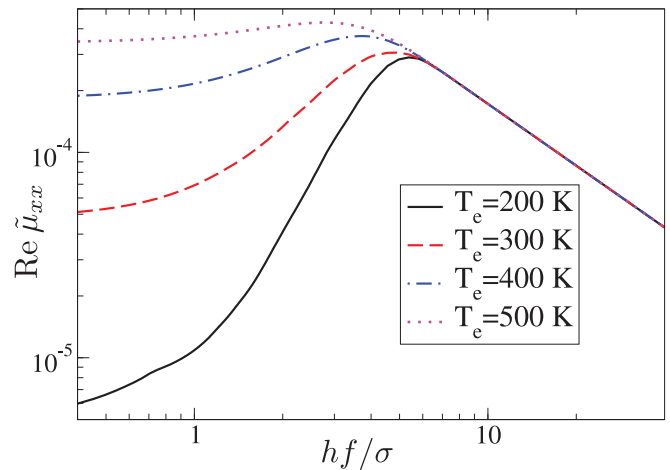


FIG. 1. (Color online) Frequency dependence of real part of the normalized mobility $\tilde{\mu}_{xx} = \mu_{xx}/(qa^2\beta w_0 e^{-a/a_{\text{loc}}}/2)$ for different electronic temperatures T_e in one-dimensional Gaussian disorder model. The nonequilibrium populations of electronic states were assumed as $r_\gamma = e^{-\beta_e \epsilon_\gamma}$.

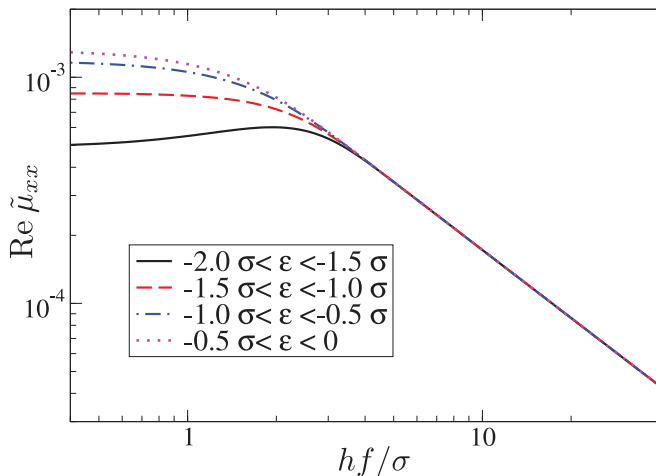


FIG. 2. (Color online) Frequency dependence of real part of the normalized mobility $\tilde{\mu}_{xx} = \mu_{xx}/(qa^2\beta w_0 e^{-a/a_{loc}}/2)$ for different choices of the energy interval $\epsilon \in (\epsilon_{\min}, \epsilon_{\max})$ of the populated states in one-dimensional Gaussian disorder model. The nonequilibrium populations of electronic states were assumed as $r_\gamma = 1$ for $\epsilon_{\min} < \epsilon_\gamma < \epsilon_{\max}$, and $r_\gamma = 0$ otherwise.

of the parameter T_e considered in Fig. 1, it can be shown (by direct inspection) that the function $M(x)$ has its maximum at $x = x_{\gamma, \gamma+1}$. At low temperatures T_e the lowest energy states have the highest values of the factors r_γ and the typical energy difference $|\epsilon_\gamma - \epsilon_{\gamma+1}|$ of the pair of neighboring sites giving significant contribution to the mobility (at least one of the states should have high enough population factor) is fairly high, so that the peak of the contribution $\mu_{\gamma, \gamma+1}$ is at high frequencies. This typical energy difference decreases with increasing the temperature T_e (since higher energy states, which are more numerous, also have appreciable values of population factors), which leads to the shift of the peak position towards lower frequencies. For small enough $|\epsilon_\gamma - \epsilon_{\gamma+1}|$ (compared to $k_B T$), the function $M(x)$, for $x < x_{\gamma, \gamma+1}$, can be approximated by a constant, which leads to flattening of the maximum, as seen at higher electronic temperatures in Fig. 1.

A similar analysis can be used to understand the shapes of the mobility spectra for case 2 shown in Fig. 2. The contribution to the mobility of the pair $(\gamma, \gamma+1)$ reaches its maximum at frequency f_* such that $hf_* > |\epsilon_\gamma - \epsilon_{\gamma+1}|$. When the interval $(\epsilon_{\min}, \epsilon_{\max})$ is in the tail of the Gaussian, the typical energy difference $|\epsilon_\gamma - \epsilon_{\gamma+1}|$ is rather high for the pairs contributing significantly to the mobility, so that the maximum of the mobility spectrum is at high frequencies. Moving the interval towards the center of the Gaussian, the typical energy difference decreases and so does the position of the maximum of the mobility spectrum. For sufficiently small energy difference (compared to $k_B T$), the function $M(x)$ can be well approximated by a constant in the range $x < x_{\gamma, \gamma+1}$ which explains the disappearance of the maximum.

Since the flattening of the maximum in the mobility spectrum appears due to the presence of carriers at higher energies under nonequilibrium conditions, this flattening may be considered as a signature of nonequilibrium effects in the system. It is less pronounced when nonequilibrium distribution is of Maxwell-Boltzmann type with a different electronic

temperature and more pronounced in the case when the carriers are present only at energies in a certain spectral window—a situation where the carrier distribution more strongly differs from the equilibrium one.

B. Model of a disordered conjugated polymer material

Next, we apply the derived formula for frequency dependence of the mobility to a realistic polymer material—strongly disordered poly(3-hexylthiophene) (P3HT) polymer. The positions of electronic states, hopping probabilities between the states, and the energies of states were extracted from our previous calculations reported in Ref. [39]. For completeness, we briefly summarize the methodology employed in these calculations. First, the positions of atoms were obtained from classical molecular dynamics simulations using a simulated annealing procedure. 50 different realizations of the $5 \text{ nm} \times 5 \text{ nm} \times 5 \text{ nm}$ portion of material (that consists of 12024 atoms) were obtained from these simulations and were subsequently used in electronic structure calculations. Charge patching method [40] was used to obtain the single-particle Hamiltonian that approximates well the Hamiltonian that would be obtained from density functional theory in local density approximation. This Hamiltonian was diagonalized using the overlapping fragments method [41]. The transition rates for downhill transitions between the states were then calculated as

$$w_{\alpha\beta} = \alpha^2 S_{\alpha\beta}^2 [N(\epsilon_{\alpha\beta}) + 1] D_{\text{ph}}(\epsilon_{\alpha\beta}) / \epsilon_{\alpha\beta}, \quad (70)$$

where $D_{\text{ph}}(E)$ is the phonon DOS normalized such that $\int_0^\infty D_{\text{ph}}(E) dE = 1$, $\epsilon_{\alpha\beta} = |\epsilon_\alpha - \epsilon_\beta|$, $N(E)$ is the phonon occupation number given by the Bose-Einstein distribution at a temperature T , $S_{\alpha\beta} = \int d^3 \mathbf{r} |\psi_\alpha(\mathbf{r})| \cdot |\psi_\beta(\mathbf{r})|$ is the overlap of the wave function moduli, and α is a constant factor equal to $10^7 \text{ eV s}^{-1/2}$. The phonon energies and the phonon DOS were calculated from the classical force field that was used in molecular dynamics simulations by diagonalizing the corresponding dynamical matrix, as reported in Ref. [42]. Equation (70) gives a good approximation of the transition rates that would be obtained from Eq. (53), as shown in Ref. [38]. The value of the parameter α in Eq. (70) was chosen to provide the best fit of Eqs. (70) to (53).

Frequency dependence of the real part of hole mobility was then calculated using Eqs. (52) and (70) where all data from 50 different realizations of the 12024 atom system were used. The results obtained from the calculation are presented in Fig. 3. We note that the data from electronic structure calculations that were performed are not sufficient to yield convergent results for the mobility. This can be evidenced from the noisy dependence in Fig. 3 and from the fact that the mobility obtained from a smaller number of realizations of the system is different than the one in Fig. 3. Larger number of calculations or the calculations performed on larger systems would be needed to obtain converged value of the mobility. However, such calculations require a huge computational cost and we cannot currently perform them. Nevertheless, from the set of calculations that were performed one can identify the main trends in the frequency dependence of the mobility. As in the simple model discussed in Sec. V A, the real part of the mobility exhibits a peak at a frequency that corresponds to typical transition energies in the system, which is then followed

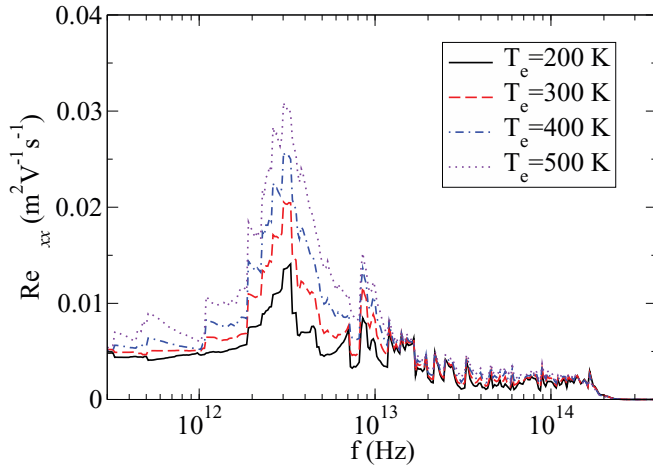


FIG. 3. (Color online) Frequency dependence of real part of hole mobility in disordered P3HT polymer for different electronic temperatures T_e and the lattice temperature $T = 300$ K.

by a decay at higher frequencies. The mobility also increases with an increase in electronic temperature, as expected.

We next compare the results obtained in this work to measurements of high-frequency P3HT hole mobility reported in the literature. These measurements are typically based on time-resolved terahertz spectroscopy [43] and cover the frequencies around 1 THz. At these frequencies our simulations yield the mobilities on the order of (50–100) $\text{cm}^2/(\text{V s})$. In Ref. [44] the mobilities on the order of 10 $\text{cm}^2/(\text{V s})$ were extracted from the fits to measurements. On the other hand, the mobilities on the order of 50 $\text{cm}^2/(\text{V s})$ were obtained in Ref. [45]. Therefore, the simulation yields the same order of magnitude of the terahertz mobility as previously reported in experiments.

VI. DISCUSSION

In this section, we discuss our results in light of other results that exist in the literature and concern optical conductivity in a system with localized states.

Our result for nonequilibrium optical conductivity should, of course, in the special case of equilibrium reduce to the formula valid in equilibrium case. A well-known expression for the real part of optical conductivity in equilibrium that relates it to the mean square displacement of a diffusing carrier reads (see, for example, Ref. [24])

$$\text{Re}\sigma(\omega) = -\frac{q^2\omega^2}{V} \frac{\tanh(\beta\hbar\omega/2)}{\hbar\omega} \text{Re} \int_0^{+\infty} dt e^{i\omega t} \Delta X^2(t), \quad (71)$$

where $\Delta X^2(t) = \langle (\hat{X}(t) - \hat{X}(0))^2 \rangle$, \hat{X} is the sum of position operators of all electrons, and $\langle \dots \rangle = \text{Tr}(e^{-\beta\hat{H}} \dots) / \text{Tr} e^{-\beta\hat{H}}$ is the thermodynamic average at the temperature $T = 1/(\beta k_B)$. While, at first sight, Eq. (71) seems to lead to rather different results for the lowest-order optical conductivity than the one embodied in Eq. (52), a detailed proof can be conducted, showing that the two expressions are identical for the system with localized states in equilibrium. The details of this proof are given in the Appendix.

A somewhat different version of Eq. (71) is often encountered in the literature which contains the $\beta/2$ term instead of the $\frac{\tanh(\beta\hbar\omega/2)}{\hbar\omega}$ term and reads [23,26,27,46]

$$\text{Re}\sigma(\omega) = -\frac{q^2\omega^2\beta}{2V} \text{Re} \int_0^{+\infty} dt e^{i\omega t} \Delta X^2(t). \quad (72)$$

When the condition $\beta\hbar\omega \ll 1$ is satisfied these two expressions are approximately equal. However, at high frequencies these two expressions essentially differ. While Eq. (71) leads to the real part of the conductivity that vanishes at sufficiently high frequencies, Eq. (72) gives a constant real part of the mobility at these frequencies which is not the correct trend. Therefore, Eq. (72) should be applied only if the condition $\beta\hbar\omega \ll 1$ is satisfied.

An expression for optical conductivity in the form similar to the one given in Eq. (52) has also been previously obtained for the case of equilibrium [47,48]. These expressions [Eq. (12) in Ref. [47] and Eq. (3.21) in Ref. [48]] in the limit of low concentration are the special case of Eq. (52) for the case of equilibrium in the limit $\hbar\omega \ll k_B T$. It is very interesting that our main result given by Eq. (52) has the same mathematical form as the expressions for the case of equilibrium. Therefore, we have generalized the result that was known for the case of equilibrium to the case of nonequilibrium systems that satisfy the assumptions of factorization of the density matrix into the electron and the phonon part [Eq. (26)] and weak relaxation at relevant time scales [Eq. (5)].

As we have already pointed out, our results are not expected to be valid at low frequencies, such that the period of perturbation is larger than the carrier relaxation time. For that reason, one can certainly not assume that dc mobility or conductivity is equal to the low frequency limit of our results. There is an additional reason that our results cannot be extended to low frequencies. It has been pointed out in Refs. [47,48] that conductivity at low frequencies cannot be obtained from a formal expansion in powers of electron-phonon interaction strength, which is an approach used in our work.

From the previous discussion, we can conclude that our results reduce to previous results from the literature for the case of equilibrium state. On the other hand, there have been almost no works in the literature with an attempt to obtain similar results for the system out of equilibrium. The exceptions are Refs. [36,37] where Eq. (19) was derived. However, we are not aware of any attempt to obtain a more specific form of nonequilibrium conductivity in a system with localized states and the main contribution of our work is that it covers this so far unexplored area.

VII. CONCLUSION

In conclusion, we have developed an approach for the treatment of nonequilibrium optical conductivity in a system with localized electronic states and weak electron-phonon or electron-impurity interaction. Starting from nonequilibrium generalization of Kubo's formula and performing the expansion of optical conductivity in powers of small electron-phonon interaction parameter, we obtain a relatively simple expression for the optical conductivity of the material. In the special case of incoherent nonequilibrium state the expression contains

only the positions of electronic states, their nonequilibrium populations, and Fermi's golden rule transition probabilities between the states. Interestingly, the same mathematical form of the expression is valid both in the case of electron-phonon and electron-impurity interaction. Our result opens the way to better understanding of the response of nonequilibrium systems to electromagnetic radiation. A typical example where our results can be applied is photoexcited semiconductor where electrons and holes are formed by the optical excitation. If that semiconductor is then probed by low energy (terahertz) excitation, the response will depend on the nonequilibrium distribution of excited carriers. Our final expressions should be able to predict the response of the system to such probes.

The application of the derived formula to two model systems was presented to illustrate the features that one may expect to see in terahertz conductivity spectra.

ACKNOWLEDGMENTS

This work was supported by European Community FP7 Marie Curie Career Integration Grant (ELECTROMAT), Serbian Ministry of Education, Science and Technological Development (Project No. ON171017) and FP7 projects PRACE-3IP and EGI-InSPIRE. V.J. also acknowledges the support by the Fund for Young Talents of the Serbian Ministry of Youth and Sport.

APPENDIX: PROOF OF EQUIVALENCE OF THE LOWEST-ORDER OPTICAL CONDUCTIVITY CALCULATED FROM EQ. (71) AND THE EXPRESSION IN EQ. (52)

The operator $\hat{X}(t) - \hat{X}(0)$ appearing in Eq. (71) can be expressed as [see Eqs. (11) and (16)]

$$q(\hat{X}(t) - \hat{X}(0)) = \int_0^t dt' \hat{J}_x(t'), \quad (\text{A1})$$

so that in the case of localized carriers, when $\hat{J}_x = \hat{J}_x^{(2)}$, the operator $(\hat{X}(t) - \hat{X}(0))^2$ is quadratic in electron-phonon coupling constants. If we are to obtain the conductivity up to quadratic terms in small interaction constants $g_{\alpha\beta,k}^{\pm}$, it is clear that the following factorization of the equilibrium statistical operator should be adopted [compare to the decomposition of the initial density matrix in Eq. (26)]

$$\frac{e^{-\hat{H}/(k_B T)}}{\text{Tr} e^{-\hat{H}/(k_B T)}} \approx \frac{e^{-\hat{H}_e/(k_B T)}}{\text{Tr}_e e^{-\hat{H}_e/(k_B T)}} \frac{e^{-\hat{H}_{ph}/(k_B T)}}{\text{Tr}_{ph} e^{-\hat{H}_{ph}/(k_B T)}}, \quad (\text{A2})$$

and that time dependencies appearing in (71) should be taken with respect to the noninteracting Hamiltonian \hat{H}_0 . The average value $\langle (\hat{X}(t) - \hat{X}(0))^2 \rangle$ is then transformed into

$$\begin{aligned} \langle (\hat{X}(t) - \hat{X}(0))^2 \rangle &= \sum_k \sum_{\alpha\beta\gamma\delta} (x_\beta - x_\alpha)(x_\delta - x_\gamma) \langle \hat{c}_\alpha^\dagger \hat{c}_\beta \hat{c}_\gamma^\dagger \hat{c}_\delta \rangle_e \left(g_{\alpha\beta,k}^- g_{\gamma\delta,k}^+ \frac{e^{\frac{i}{\hbar}(\epsilon_\alpha - \epsilon_\beta - \hbar\omega_k)t} - 1}{\epsilon_\alpha - \epsilon_\beta - \hbar\omega_k} \frac{e^{\frac{i}{\hbar}(\epsilon_\gamma - \epsilon_\delta + \hbar\omega_k)t} - 1}{\epsilon_\gamma - \epsilon_\delta + \hbar\omega_k} (1 + N_k) \right. \\ &\quad \left. + g_{\alpha\beta,k}^+ g_{\gamma\delta,k}^- \frac{e^{\frac{i}{\hbar}(\epsilon_\alpha - \epsilon_\beta + \hbar\omega_k)t} - 1}{\epsilon_\alpha - \epsilon_\beta + \hbar\omega_k} \frac{e^{\frac{i}{\hbar}(\epsilon_\gamma - \epsilon_\delta - \hbar\omega_k)t} - 1}{\epsilon_\gamma - \epsilon_\delta - \hbar\omega_k} N_k \right), \end{aligned} \quad (\text{A3})$$

where $\langle \dots \rangle_e$ denotes averaging with respect to the electronic part of the decomposition (A2). Combining Eqs. (71) and (A3) and in the limit of low carrier densities, when Eqs. (46), (50), and (51) can be used, the following expression for the optical conductivity ($\omega \neq 0$) is obtained:

$$\text{Re} \sigma_{xx}(\omega) = \frac{q^2}{2\hbar\omega V} \tanh\left(\frac{\hbar\omega}{2k_B T}\right) \sum_{\alpha\beta} (x_\beta - x_\alpha)^2 r_\beta [w_{\beta\alpha,ph}(\epsilon_\beta - \epsilon_\alpha - \hbar\omega) + w_{\beta\alpha,ph}(\epsilon_\beta - \epsilon_\alpha + \hbar\omega)], \quad (\text{A4})$$

where the transition probabilities $w_{\beta\alpha,ph}$ are defined in Eq. (53) and the average occupation of electronic state β is $r_\beta = e^{-\epsilon_\beta/(k_B T)}/\text{Tr}_e e^{-\hat{H}_e/(k_B T)}$. In order to prove that the relation (52) (in which we take $r_\beta = e^{-\epsilon_\beta/(k_B T_{ph})}/\text{Tr}_e e^{-\hat{H}_e/(k_B T_{ph})}$) gives the same result for the lowest-order optical conductivity as Eq. (A4) (assuming that $T = T_{ph}$), we note that the transition probabilities satisfy the detailed-balance condition (in the low-density limit and in the presence of external harmonic perturbation)

$$\frac{w_{\beta\alpha,ph}(\epsilon_\beta - \epsilon_\alpha + \hbar\omega)}{w_{\alpha\beta,ph}(\epsilon_\alpha - \epsilon_\beta - \hbar\omega)} = e^{-(\epsilon_\alpha - \epsilon_\beta - \hbar\omega)/(k_B T)} = \frac{r_\alpha}{r_\beta} \frac{1 + \tanh\frac{\hbar\omega}{2k_B T}}{1 - \tanh\frac{\hbar\omega}{2k_B T}}. \quad (\text{A5})$$

Interchanging the dummy electronic indices α, β in the first summand in Eq. (52) we obtain

$$\text{Re} \sigma_{xx}(\omega) = \frac{q^2}{2\hbar\omega V} \sum_{\alpha\beta} (x_\beta - x_\alpha)^2 [-r_\alpha w_{\alpha\beta,ph}(\epsilon_\alpha - \epsilon_\beta - \hbar\omega) + r_\beta w_{\beta\alpha,ph}(\epsilon_\beta - \epsilon_\alpha + \hbar\omega)], \quad (\text{A6})$$

whereas performing the same operation on Eq. (A4) gives

$$\text{Re } \sigma_{xx}(\omega) = \frac{q^2}{2\hbar\omega V} \tanh\left(\frac{\hbar\omega}{2k_B T}\right) \sum_{\alpha\beta} (x_\beta - x_\alpha)^2 [r_\alpha w_{\alpha\beta,\text{ph}}(\epsilon_\alpha - \epsilon_\beta - \hbar\omega) + r_\beta w_{\beta\alpha,\text{ph}}(\epsilon_\beta - \epsilon_\alpha + \hbar\omega)]. \quad (\text{A7})$$

The right-hand sides of Eqs. (A6) and (A7) are equal since, by the condition (A5), single summands under the double sums are mutually equal.

-
- [1] N. F. Mott and E. A. Davis, *Electronic Processes in Non-Crystalline Materials*, 2nd ed. (Clarendon Press, Oxford, 1979).
- [2] B. I. Shklovskii and A. L. Efros, *Electronic Properties of Doped Semiconductors* (Springer, Berlin, 1984).
- [3] H. Böttger and V. V. Bryksin, *Hopping Conduction in Solids* (VCH Publishing, Berlin, 1986).
- [4] *Physics of Organic Semiconductors*, edited by W. Brütting (Wiley, Weinheim, 2005).
- [5] *Introduction to Organic Electronic and Optoelectronic Materials and Devices*, edited by S.-S. Sun and L. R. Dalton (Taylor & Francis, Boca Raton, 2008).
- [6] M. Pope and C. E. Swenberg, *Electronic Processes in Organic Crystals and Polymers* (Oxford University Press, Oxford, 1999).
- [7] M. Schwoerer and H. C. Wolf, *Organic Molecular Solids* (Wiley, Weinheim, 2007).
- [8] T. U. Kampen, *Low Molecular Weight Organic Semiconductors* (Wiley, Weinheim, 2010).
- [9] *Organic Electronics*, edited by H. Klauk (Wiley, Weinheim, 2006).
- [10] *Charge Transport in Disordered Solids with Applications in Electronics*, edited by S. Baranovskii (Wiley, Chichester, England, 2006).
- [11] H. Sirringhaus, P. J. Brown, R. H. Friend, M. M. Nielsen, K. Bechgaard, B. M. W. Langeveld-Voss, A. J. H. Spiering, R. A. J. Janssen, E. W. Meijer, P. Herwig, and D. M. de Leeuw, *Nature (London)* **401**, 685 (1999).
- [12] R. J. Kline, M. D. McGehee, and M. F. Toney, *Nat. Mater.* **5**, 222 (2006).
- [13] J. H. Burroughes, D. D. C. Bradley, A. R. Brown, R. N. Marks, K. Mackay, R. H. Friend, P. L. Burns, and A. B. Holmes, *Nature (London)* **347**, 539 (1990).
- [14] B. K. Yap, R. Xia, M. Campoy-Quiles, P. N. Stavrinou, and D. D. C. Bradley, *Nat. Mater.* **7**, 376 (2008).
- [15] N. S. Sariciftci, D. Braun, C. Zhang, V. I. Srdanov, A. J. Heeger, G. Stucky, and F. Wudl, *Appl. Phys. Lett.* **62**, 585 (1993).
- [16] F. Laquai and D. Hertel, *Appl. Phys. Lett.* **90**, 142109 (2007).
- [17] Y. Kim, S. Cook, S. M. Tuladhar, S. A. Choulis, J. Nelson, J. R. Durrant, D. D. C. Bradley, M. Giles, I. McCulloch, C.-S. Ha, and M. Ree, *Nat. Mater.* **5**, 197 (2006).
- [18] A. Miller and E. Abrahams, *Phys. Rev.* **120**, 745 (1960).
- [19] V. Ambegaokar, B. I. Halperin, and J. S. Langer, *Phys. Rev. B* **4**, 2612 (1971).
- [20] N. S. Sariciftci, L. Smilowitz, A. J. Heeger, and F. Wudl, *Science* **258**, 1474 (1992).
- [21] I.-W. Hwang, D. Moses, and A. J. Heeger, *J. Phys. Chem. C* **112**, 4350 (2008).
- [22] S. R. Cowan, N. Banerji, W. L. Leong, and A. J. Heeger, *Adv. Funct. Mater.* **22**, 1116 (2012).
- [23] H. Scher and M. Lax, *Phys. Rev. B* **7**, 4491 (1973).
- [24] S. Ciuchi, S. Fratini, and D. Mayou, *Phys. Rev. B* **83**, 081202 (2011).
- [25] S. Fratini, S. Ciuchi, and D. Mayou, *Phys. Rev. B* **89**, 235201 (2014).
- [26] F. C. Grozema and L. D. A. Siebeless, *Int. Rev. Phys. Chem.* **27**, 87 (2008).
- [27] H. Němec, P. Kužel, and V. Sundström, *J. Photochem. Photobiol. A: Chem.* **215**, 123 (2010).
- [28] F. Rossi and T. Kuhn, *Rev. Mod. Phys.* **74**, 895 (2002).
- [29] L. V. Keldysh, *Sov. Phys. JETP* **20**, 1018 (1965).
- [30] L. P. Kadanoff and G. Baym, *Quantum Statistical Mechanics* (Benjamin, New York, 1962).
- [31] H. Haug and A.-P. Jauho, *Quantum Kinetics in Transport and Optics of Semiconductors* (Springer, Berlin, 1996).
- [32] J. Rammer, *Quantum Field Theory of Non-Equilibrium States* (Cambridge University Press, Cambridge, UK, 2007).
- [33] G. Mahan, *Many-Particle Physics* (Kluwer Academic, New York, 2000).
- [34] C. Jacoboni, *Theory of Electron Transport in Semiconductors* (Springer, Berlin, 2010).
- [35] P. B. Allen, in *A Standard Model for Ground- and Excited-state Properties*, edited by S. G. Louie and M. L. Cohen (Elsevier Science, Amsterdam, 2006).
- [36] U. Gavish, Y. Imry, and B. Yurke, [arXiv:cond-mat/0404270](https://arxiv.org/abs/cond-mat/0404270).
- [37] U. Gavish, B. Yurke, and Y. Imry, *Phys. Rev. Lett.* **93**, 250601 (2004).
- [38] N. Vukmirović and L.-W. Wang, *Appl. Phys. Lett.* **97**, 043305 (2010).
- [39] N. Vukmirović and L.-W. Wang, *J. Phys. Chem. B* **115**, 1792 (2011).
- [40] N. Vukmirović and L.-W. Wang, *J. Chem. Phys.* **128**, 121102 (2008).
- [41] N. Vukmirović and L.-W. Wang, *J. Chem. Phys.* **134**, 094119 (2011).
- [42] N. Vukmirović and L.-W. Wang, *Nano Lett.* **9**, 3996 (2009).
- [43] R. Ulbricht, E. Hendry, J. Shan, T. F. Heinz, and M. Bonn, *Rev. Mod. Phys.* **83**, 543 (2011).
- [44] X. Ai, M. C. Beard, K. P. Knutsen, S. E. Shaheen, G. Rumbles, and R. J. Ellingson, *J. Phys. Chem. B* **110**, 25462 (2006).
- [45] P. D. Cunningham and L. M. Hayden, *J. Phys. Chem. C* **112**, 7928 (2008).
- [46] N. Vukmirović, C. S. Ponceca, H. Němec, A. Yartsev, and V. Sundström, *J. Phys. Chem. C* **116**, 19665 (2012).
- [47] E. O. Manucharyants and I. P. Zvyagin, *Phys. Status Solidi B* **65**, 665 (1974).
- [48] R. Barrie and P. C. W. Holdsworth, *J. Phys.: Condens. Matter* **1**, 557 (1989).



**VII International School and Conference on Photonics
Belgrade, Serbia, August 26th – 30th 2019**

Vinča Institute of Nuclear Sciences
Mike Petrovića Alasa 12-14, P.O.Box 522, 11351 Belgrade, Serbia
Phone: +381 11 3408 101; Fax: +381 11 8066 425
E-mail: photonica2019@ipb.ac.rs, www.photonica.ac.rs

Dr. Veljko Janković

Institute of Physics Belgrade,
University of Belgrade
Pregrevica 118, 11000 Belgrade
Serbia

Belgrade, March 13th, 2019

Dear Dr. Janković,

On behalf of the Organizing Committee of the International School and Conference on Photonics, we are pleased to invite you to the **PHOTONICA 2019** conference scheduled from **26th** until **30th August 2019** in **Belgrade, Serbia**. This conference will be organized by the Vinča Institute of Nuclear Sciences, Belgrade, Serbia, Optical Society of Serbia and Serbian Academy of Sciences and Arts.

It is our special pleasure to invite you to attend the meeting and present a **progress report lecture (20 min)**. The lecture is expected to contain a review and up-to-date progress in the specific field.

We would be honored if you could accept this invitation and accordingly send us a title of your lecture, to be included in the Conference Announcement. The abstract of the lecture, 1 page in length, should be emailed to us by 1st of June to be published in the Book of Abstracts.

Kindly, as a progress report speaker, the Organizers will cover a half of your conference fee.

Should you have any question please don't hesitate to contact us by e-mail, telephone, mail or fax.

Yours sincerely,

Petra Beličev
(Chair of the Organizing Committee)

phone: +381 11 3408746

fax: +381 11 8066425

cell: +381 63 8323552

e-mail: petrab@vin.bg.ac.rs

photonica2019@ipb.ac.rs

Mechanisms and time scales of free-charge generation in organic photovoltaics: hot and fast or cold and slow

V. Janković^{1,2} and N. Vukmirović²

¹*Institute of Physics, Faculty of Mathematics and Physics, Charles University in Prague,
Ke Karlovu 5, 121 16 Prague 2, Czech Republic*

²*Scientific Computing Laboratory, Center for the Study of Complex Systems,
Institute of Physics Belgrade, University of Belgrade,
Pregrevica 118, 11080 Belgrade, Serbia
e-mail: veljko.jankovic@ipb.ac.rs*

The physical mechanisms and time scales of light-to-charge conversion in photoexcited donor/acceptor organic solar cells have recently been heavily debated. The interpretation of experimental signals stemming from ultrafast spectroscopic experiments suggests that free-charge generation mainly occurs on a subpicosecond time scale following the excitation by virtue of high-energy (“hot”) delocalized interfacial charge transfer (CT) states [1]. On the other hand, there is experimental evidence that free carriers are predominantly generated on time scales ranging from tens to hundreds of picoseconds out of the lowest-energy (“cold”) CT state, which is strongly bound and localized [2, 3].

We study charge separation in a one-dimensional model of an interface between two organic semiconductors, both on ultrashort and on much longer time scales. We obtain that free charges present on a subpicosecond time scale following the photoexcitation are mainly directly optically generated from the ground state thanks to the resonant mixing between states of donor excitons and free charges [4]. However, on the same time scale, we find that the majority of photogenerated charges still remain bound in form of donor or CT excitons [5]. We obtain that their further separation on longer time scales is weakly electric field- and temperature-dependent and is enabled by the synergy between carrier delocalization and moderate disorder [6].

REFERENCES

- [1] G. Grancini et al., *Nat. Mater.* 12, 29 (2013).
- [2] K. Vandewal et al., *Nat. Mater.* 13, 63 (2014).
- [3] A. Grupp et al., *J. Phys. Chem. Lett.* 8, 4858 (2017).
- [4] V. Janković, N. Vukmirović, *Phys. Rev. B* 95, 075308 (2017).
- [5] V. Janković, N. Vukmirović, *J. Phys. Chem. C* 121, 19602 (2017).
- [6] V. Janković, N. Vukmirović, *J. Phys. Chem. C* 122, 10343 (2018).

A Nonequilibrium-Thermodynamics Perspective on Charge Separation in Organic Solar Cells

Veljko Janković and Nenad Vukmirović

Institute of Physics Belgrade, University of Belgrade, Serbia

Abstract. The operation of donor/acceptor (D/A) organic solar cells (OSCs) leans on the separation of the strongly bound charge transfer exciton (CTE) localized at the D/A interface into free charges [1]. Kinetic considerations suggest that CTE separation is facilitated by a combination of charge delocalization and moderate disorder [2], while it is hampered by strong disorder [2] and/or strong interaction with phonons [3]. From the standpoint of equilibrium thermodynamics, the charges in the CTE are thermodynamically free because its large binding energy is generally outweighed by the entropic contribution. While strong disorder and enhanced spatial connectivity eliminate the separation barrier [4], charge delocalization may increase it [5]. Such trends contradict the intuitive trends emerging from kinetic considerations.

We employ nonequilibrium thermodynamics to reconcile the kinetic and thermodynamic perspectives on charge separation in OSCs [6]. Within our one-dimensional model of a D/A interface [2, 3], we compute steady-state populations of interface states, which emerge from a competition between incoherent-light excitation, phonon-induced relaxation, and recombination. We then evaluate the nonequilibrium free-energy profile for charge separation and compare it to its equilibrium counterpart for different disorder strengths and delocalization extents. We find that the difference between the two profiles is maximized (minimized) when the separation efficiency is the largest (smallest). Our nonequilibrium profiles show that better delocalization suppresses the entropic contribution at small distances and enhances it at larger distances, meaning that charge delocalization promotes long-range separation. Despite the reduced dimensionality of our model, which is deleterious to the spatial connectivity of interface states, our nonequilibrium entropic contributions are consistently larger than the equilibrium ones because the former take into account the connectivity by phonon-assisted processes. Overall, we conclude that charge separation in the most efficient OSCs proceeds through a nonequilibrium pathway involving both the strongly bound CTE and higher-energy interface states.

REFERENCES

1. Baessler, H., and Koehler, A., *Phys. Chem. Chem. Phys.* **17**, 28451 (2015).
2. Janković, V., and Vukmirović, N., *J. Phys. Chem. C* **122**, 10343 (2018).
3. Janković, V., and Vukmirović, N., *J. Phys. Chem. C* **124**, 4378 (2020).
4. Hood, S. N., and Kassal, I., *J. Phys. Chem. Lett.* **7**, 4495 (2016).
5. Gluchowski, A., Gray, K. L. G., Hood, S. N., and Kassal, I., *J. Phys. Chem. Lett.* **9**, 1359 (2018).
6. Kaiser, W., Janković, V., Vukmirović, N., and Gagliardi, A., *J. Phys. Chem. Lett.* **12**, 6389 (2021).

Cumulant Expansion in the Holstein model: Spectral Functions and Mobility

Petar Mitrić^a, Veljko Janković^a, Nenad Vukmirović^a and Darko Tanasković^a

^a*Institute of Physics Belgrade, University of Belgrade, Pregrevica 118, 11080 Belgrade, Serbia*

Abstract. The cumulant expansion (CE) method presents an alternative to the usual Dyson equation approach for the calculation of spectral functions and quasiparticle properties of interacting quantum many-particle systems. We examine the range of validity of this method by implementing it in a system described by the simplest electron-phonon model Hamiltonian - the Holstein model [1]. For a benchmark, we use the dynamical mean-field theory (DMFT) [2] which gives, as we have recently shown [3], rather accurate spectral functions in the whole parameter space. The results are also compared to the one-shot and the self-consistent Migdal approximation. While CE is exact in both the weak-coupling and the atomic limit, we find that even in a regime of intermediate coupling in 1D, the CE resolves well both the quasiparticle and the first satellite peak of the spectral function. CE also gives promising results for high temperatures, but it is not exact in the limit $T \rightarrow \infty$, which is proved analytically by analyzing the spectral sum rules.

Charge mobility μ is also calculated, using the bubble approximation of the Kubo formalism. At high temperatures, we demonstrate that it assumes a power law, which is different in the limit of weak coupling $\mu \propto T^{-2}$, and in the case of somewhat stronger coupling $\mu \propto T^{-3/2}$.

REFERENCES

1. Mitrić, P., Janković, V., Vukmirović, N., and Tanasković D., *Phys. Rev. B* **107**, 125165 (2023).
2. Ciuchi, S., de Pasquale, F., Fratini, S., and Feinberg, D., *Phys. Rev. B* **56**, 4494 (1997).
3. Mitrić, P., Janković, V., Vukmirović, N., and Tanasković D., *Phys. Rev. Lett.* **129**, 096401 (2022).

Acknowledgments: The work was supported by the Bulgarian National Science Fund under contract KP-06-N48/5 “Multifunctional composite structures based on ferrites (including magneto electrics) and carbon materials” and by the Bulgarian National Science Fund under contract KP-06-India-2 “Usage of thin $ZnFe_2O_4$ films for various spintronic devices”. This work was also supported by a joint research project between the Bulgarian Academy of Sciences and WBI, Belgium, and by a joint research project between the Bulgarian Academy of Sciences and the Institute of Low Temperature and Structure Research, Polish Academy of Sciences.

S06-CMPSP-107 / Oral presentation

Finite-Temperature Dynamical Properties of the Holstein Model: Hierarchical Equations of Motion Approach

Authors: Nenad Vukmirovic¹; Veljko Jankovic¹

¹ *Institute of Physics Belgrade, University of Belgrade, Serbia*

Presenter: V. Jankovic (veljko.jankovic@ipb.ac.rs)

While ground-state properties of the Holstein model are well understood by now, the evaluation of its finite-temperature spectral properties has received more attention only recently [1, 2]. Here, we develop a hierarchical equations of motion (HEOM) approach to compute real-time single-particle correlation functions and thermodynamic quantities of the Holstein model at finite temperature [3]. We exploit the conservation of the total momentum of the system to formulate the momentum-space HEOM whose dynamical variables explicitly keep track of momentum and energy exchanges between the electron and phonons. Our symmetry-adapted HEOM enable us to overcome the numerical instabilities inherent to the commonly used real-space HEOM. The HEOM results for the electronic spectral function, obtained on chains containing up to ten sites, compare favorably to existing literature. To provide an independent assessment of the HEOM approach and to gain insight into the importance of finite-size effects, we devise a quantum Monte Carlo (QMC) procedure to evaluate finite-temperature single-particle correlation functions in imaginary time and apply it to chains containing up to twenty sites. QMC results reveal that finite-size effects are quite weak, so that the results on 5 to 10 site chains, depending on the parameter regime, are representative of larger systems.

Acknowledgement: The authors acknowledge funding provided by the Institute of Physics Belgrade, through the grant by the Ministry of Education, Science, and Technological Development of the Republic of Serbia.

References

1. J. Bonča, S. A. Trugman, and M. Berciu, *Phys. Rev. B* **100**, 094307 (2019).
2. D. Jansen, J. Bonča, and F. Heidrich-Meisner, *Phys. Rev. B* **102**, 165155 (2020).
3. V. Janković and N. Vukmirović, *Phys. Rev. B* **105**, 054311 (2022).

S06-CMPSP-208 / Poster presentation

Effect of Yttrium Substitution on Structural Properties of nanopowder nickel ferrites: X-Ray and Raman studies

Authors: Stevan Jankov¹; Elvira Toth¹; Maja Stojanovic¹; Sonja Skuban¹; Željka Cvejić¹

¹ *University of Novi Sad, Faculty of Sciences, Department of Physics*

Presenter: S. Jankov (stevan.jankov@df.uns.ac.rs)

Among various ferrites, nanosized nickel ferrite is one of the most frequently employed materials for production of electronic materials due to a set of outstanding physical and chemical properties. Doping with various atoms is a common choice when it comes to the development of new materials with target properties. Rare-earth elements have been frequently used in different research areas in order to improve various physical and chemical properties of materials. Nanocrystalline ferrites with chemical formula $\text{NiFe}_{2-x}\text{Y}_x\text{O}_4$ ($x = 0.20, 0.30$) have been synthesized by the co-precipitation method and further annealed at $750\text{ }^\circ\text{C}$. The details of the synthesis are given in [1]. X-Ray diffraction analysis (XRD) were carried out using Rigaky MiniFlex 600 diffractometer. Raman spectra were collected using a Thermo Scientific DXR Raman Microscope at room temperature with DPSS (Diode Pumped Solid State) laser using $\lambda = 532.2\text{ nm}$ excitation. CCD camera has been used as detector.

Spinel ferrites crystallize in cubic spinel structure belonging to space group $O7h$ ($Fd3m$). The recorded XRD patterns have confirmed the formation of spinel ferrite phase in the samples. No peaks corresponding to any precursor/impurity were recorded in the patterns implying that the samples are single phase. With the substitution of Y^{3+} in NFO, the whole diffraction pattern is shifted towards lower 2θ angle, which is a signature of an increase in lattice parameter of the substituted samples.

Group theory predicts the five Raman active modes, i.e. $A_{1g} + E_g + 3T_{2g}$. The measured spectra have been fitted and it is deconvoluted into individual Lorentzian component in order to determine the peak position. The spectra consists of band around ~ 450 , ~ 560 , ~ 640 , ~ 680 , $\sim 695\text{ cm}^{-1}$. The modes at above 600 cm^{-1} are related to the T-site mode that reflects the local lattice strain effect in the tetrahedral sublattice. The Raman modes below than 600 cm^{-1} corresponds to the O-site mode reflecting the local lattice strain effect in octahedral sublattice.

S06-CMPSP-209 / Poster presentation

Alternating-Basis Quantum Monte Carlo Method for Strongly Correlated Electrons

Authors: Jaksa Vucicevic¹; Veljko Jankovic¹

¹ *Institute of Physics Belgrade, University of Belgrade, Serbia*

Presenter: V. Jankovic (veljko.jankovic@ipb.ac.rs)

Ultracold-atom simulators have provided important insights into charge and spin transport in the two-dimensional Hubbard model [1, 2]. However, theoretical tools to compute quantities directly measured in experiments, such as space- and time-resolved charge/spin densities following a quench of an external density-modulating field, are still scarce. Here, we devise the alternating-basis quantum Monte Carlo (ABQMC) method for interacting electrons on a lattice, which is uniquely suited to compute such quantities. Apart from out-of-equilibrium setups, the formalism is equally applicable in thermal equilibrium described by either canonical or grand-canonical ensemble. The method relies on the Suzuki–Trotter decomposition (STD) and owes flexibility to the representation of the kinetic and interaction terms in the many-body bases in which they are diagonal. We formulate a Monte Carlo update scheme that respects both the momentum and particle-number conservation laws, to restrict the configuration space. The sampling efficiency is further enhanced by ensuring that the ABQMC algorithm manifestly respects several symmetries of the Hubbard model [3, 4]. We find that the method’s performance is heavily plagued by the fermionic sign problem, whose extent is primarily related to the number of time-slices in the STD. Nevertheless, the ABQMC equation of state (density vs. chemical potential curve) computed on square-lattice clusters containing up to 48 sites agrees remarkably well with reference methods. We also discuss how the (real-time) dynamics of the survival probability of pure density-wave-like states on 4x4 clusters depends on the filling and the initial density pattern.

Acknowledgement: The authors acknowledge funding provided by the Institute of Physics Belgrade, through the grant by the Ministry of Education, Science, and Technological Development of the Republic of Serbia, as well as by the Science Fund of the Republic of Serbia, under the Key2SM project (PROMIS program, Grant No. 6066160).

References

1. P. T. Brown et al., *Science* **363**, 379 (2019).
2. M. A. Nichols et al., *Science* **363**, 383 (2019).
3. J. Yu et al., *Phys. Rev. Lett.* **119**, 225302 (2017).
4. H. Zhai et al., *New J. Phys.* **21**, 015003 (2019).

S06-CMPSP-210 / Poster presentation

Magnetic Hyperthermia Potential of Colloidal Zinc-substituted Iron Oxide Nanoparticles and TiO₂@Zinc Ferrite Hybrids

Author: Nataša Jović Orsini¹

Co-authors: Mirjana M. Milić¹; Tijana Marić²; Danijela Danilović¹; Gerardo F. Goya³

The coupling of Frenkel excitons (FEs) and intramolecular vibrations in an organic layer as a part of microcavity has been studied in the paper. Two cases are treated: a) uniaxial layer of point group 4 (optical axis is supposed perpendicular to the layer); b) monoclinic anthracene-like layer with monoclinic axis b perpendicular to the layer. The exciton-phonon coupling produces the vibronic wings with complex spectra which can contain bound exciton-phonon states and many-particle (unbound) bands. Consequently in those regions the absorption lines and the resonance members in dielectric tensor appear. We treat theoretically their effects on the polaritons in the microcavity and illustrate using numerical calculations the peculiarities of the polaritonic spectra in the vibronic wings of Frenkel excitons.

S06-CMPSP-111 / **Oral presentation**

Spectral functions of the Holstein polaron: exact and approximate solutions

Authors: Petar Mitrić¹; Veljko Janković¹; Nenad Vukmirović¹; Darko Tanasković¹

¹ *Institute of Physics Belgrade, University of Belgrade*

Presenter: P. Mitrić (mitricp@ipb.ac.rs)

It is generally accepted that the dynamical mean field theory (DMFT) gives a good solution of the Holstein model [1], but only in dimensions greater than two. Here we show that the DMFT, which becomes exact in the weak coupling and in the atomic limit, provides an excellent numerically cheap approximate solution for the spectral function of the Holstein model in the whole range of parameters even in one dimension. To establish this, we made a detailed comparison with the spectral functions that we obtained using newly developed momentum-space numerically exact hierarchical equations of motion method, which yields electronic correlation functions directly in real time [2]. We crosschecked these conclusions with our path integral quantum Monte Carlo and exact diagonalization results, as well as with the available numerically exact results from the literature [3].

References:

1. S. Ciuchi, F. de Pasquale, S. Fratini, and D. Feinberg, Phys. Rev. B **56**, 4494 (1997).
2. V. Janković and N. Vukmirović, Phys. Rev. B **105**, 054311 (2022).
3. D. Jansen, J. Bonča, and F. Heidrich-Meisner, Phys. Rev. B **102**, 165155 (2020).

Veljko Janković

Institute of Physics Belgrade, University of Belgrade

Incoherent light-induced excitation harvesting in molecular energy-conversion systems

There is a remarkable similarity between physical processes at play in (organic) photovoltaic cells and photosynthetic complexes [1,2]. In both types of systems, ultrafast time-resolved studies suggest that quantum coherences may enhance the excitation-harvesting efficiency by favoring non-equilibrated, "hot", and fast pathways involving delocalized states over equilibrated, "cold", and slow pathways involving localized trap states. Here, we present our recent contributions to the on-going debate on the relevance of these findings for excitation harvesting under incoherent light [3-6]. We develop a (numerically) exact description of excitonic dynamics in a molecular aggregate driven by weak-intensity radiation of arbitrary properties [3]. While the interaction with light is included up to the second order, the excitation-environment coupling is treated up to all orders. The resulting exact expression for the reduced density matrix is then recast as the hierarchy of equations of motion (HEOM) that explicitly and consistently includes the photoexcitation step. We then focus on a model photosynthetic dimer and examine its non-equilibrium steady state arising from the interplay between excitation generation, excitation relaxation, dephasing, trapping at the load, and recombination [4]. While the steady-state coherences in the slow-trapping limit are demonstrated to originate from the excitation-environment entanglement, we unveil an interesting relation between the dynamic coherences observed in ultrafast experiments on unloaded aggregates and the steady-state coherences in the fast-trapping limit. We apply a similar formalism to a microscopic effective Hamiltonian of an organic donor/acceptor heterojunction, where we elucidate the energy- and time-resolved dynamics of charge pairs all the way from their photogeneration to their extraction or recombination. The results indicate that charge separation proceeds via the "cold" pathway on which donor excitons first convert to relaxed charge-transfer excitons and then transform to separated charges [5]. We also analyze these results from the perspective of non-equilibrium thermodynamics. We quantify the difference between the equilibrium and non-equilibrium dependence of the charge-pair free energy on the intrapair separation. Our results reveal that this difference is largest when charge separation efficiency is large, which leads us to conclude that charge separation in efficient organic solar cells proceeds via a "cold" but non-equilibrated pathway [6].

- [1] J.-L. Brédas, E. H. Sargent, G. D. Scholes, *Photovoltaic concepts inspired by coherence effects in photosynthetic systems*, [Nature Materials](#) **16**, 35 (2016).
- [2] A. P. Kirk, D. K. Ferry, *Photosynthesis versus photovoltaics*, [Journal of Computational Electronics](#) **17**, 313 (2018).
- [3] V. Janković, T. Mančal, *Exact description of excitonic dynamics in molecular aggregates weakly driven by light*, [Journal of Chemical Physics](#) **153**, 244122 (2020).
- [4] V. Janković and T. Mančal, *Nonequilibrium steady-state picture of incoherent light-induced*

excitation harvesting, [Journal of Chemical Physics](#) **153**, 244110 (2020).

- [5] V. Janković, N. Vukmirović, *Energy-temporal pathways of free-charge formation at organic bilayers: competition of delocalization, disorder, and polaronic effects*, [Journal of Physical Chemistry C](#) **124**, 4378 (2020).
- [6] W. Kaiser, V. Janković, N. Vukmirović, A. Gagliardi, *Nonequilibrium thermodynamics of charge separation in organic solar cells*, [Journal of Physical Chemistry Letters](#) **12**, 6389 (2021).

Relevance of incoherent light-induced coherences for photosynthetic energy transfer

V. Janković¹

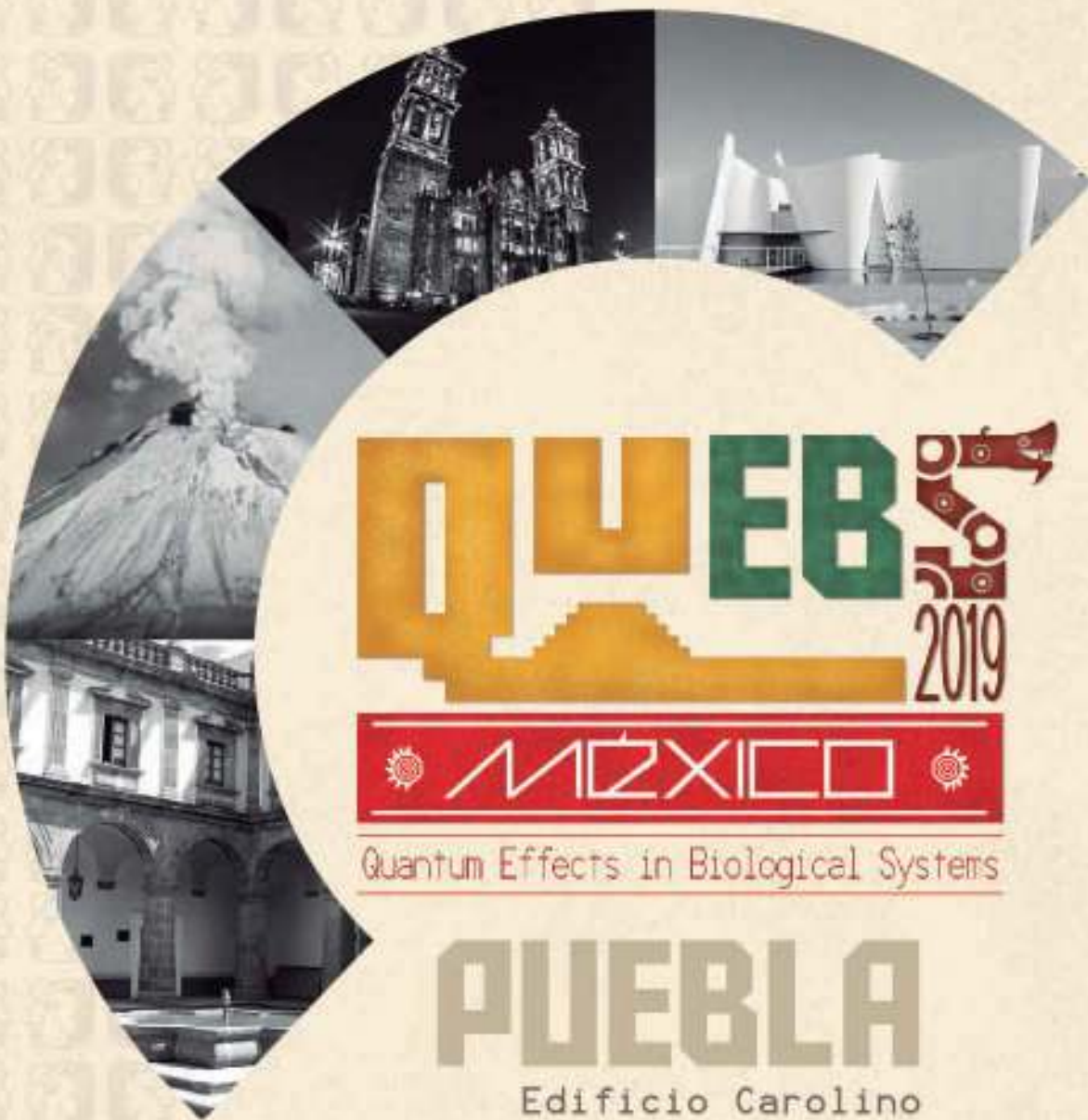
¹*Institute of Physics Belgrade, University of Belgrade, Serbia*
e-mail: veljko.jankovic@ipb.ac.rs

The interpretation of oscillatory features in experimental signals from photosynthetic pigment–protein complexes excited by laser pulses [1] has been motivating vigorous interest in quantum effects in photosynthetic energy transfer (ET) [2]. However, electronic dynamics triggered by natural light, which is stationary and incoherent, is generally substantially different from the one observed in pulsed laser experiments. It has been suggested that the physically correct picture of photosynthetic ET should be in terms of a nonequilibrium steady state (NESS) [3], which is formed when a photosynthetic complex is continuously photoexcited and continuously delivers the excitation energy to the reaction center (RC), in which charge separation takes place.

We study ET in a molecular aggregate that is driven by weak incoherent radiation and coupled to its immediate environment and the RC. We combine a second-order treatment of the photoexcitation with an exact treatment of the excitation–environment coupling and formulate the hierarchy of equations of motion (HEOM) that explicitly takes into account the photoexcitation process [4]. We develop an efficient numerical scheme that respects the continuity equation for the excitation fluxes to compute the NESS of the aggregate [5]. The NESS is most conveniently described in the so-called preferred basis, in which the excitonic density matrix is diagonal. The preferred basis, which is analogous to the set of normal modes of a system of coupled harmonic oscillators, is singled out by the interplay between excitation generation, energy relaxation, dephasing, and excitation delivery to the RC. Having established the proper NESS description, we are in position to critically reassess the involvement of stationary coherences in the photosynthetic ET and claims that stationary coherences may enhance the ET efficiency. Focusing on a model photosynthetic dimer, we examine the properties of the NESS. In the limit of slow delivery to the RC, we find that the NESS is quite similar to the excited-state equilibrium in which the stationary coherences originate from the excitation–environment entanglement. When the excitation delivery is slower than energy relaxation processes, we establish a general relationship between the NESS picture and time-dependent description of an incoherently driven, but unloaded system.

REFERENCES

- [1] G. S. Engel et al., *Nature* **446**, 782–786 (2007).
- [2] J. Cao et al., *Sci. Adv.* **6**, eaaz4888 (2020).
- [3] P. Brumer, *J. Phys. Chem. Lett.* **9**, 2946–2955 (2018).
- [4] V. Janković and T. Mančal, *J. Chem. Phys.* **153**, 244122 (2020).
- [5] V. Janković and T. Mančal, *J. Chem. Phys.* **153**, 244110 (2020).



INSTITUTO DE
CIENCIAS
FÍSICAS



UNIVERSIDAD CATÓLICA del Sacram. Carr.

I-LAMP
Interdisciplinary Laboratories
for Advanced Materials Physics

27 TO 31
OCTOBER

C O N F E R E N C E

BOOK OF ABSTRACTS

chromophores. This study helps predict the properties of the entangled two photon effect in chromophores with different dipolar and quadrupolar character.

[1] H.B. Fei, B. Jost, S. Popescu, B. Saleh, M. Teich, Entanglement Induced Two-Photon Transparency. *Phys. Rev. Lett.* 1997, 78.

[2] Lee, D.I. Goodson III. T. Entangled Photon Absorption in an Organic Porphyrin Dendrimer. *J. Phys. Chem. B. Lett.* 2006, 110, 25582-25585.

[3] Varnavski, O.; Pinsky, B.; Goodson III, T. Entangled Photon Excited Fluorescence in Organic Materials: An Ultrafast Coincidence Detector. *J. Phys. Chem Lett.* 2017, 8, 2, 388-393.

[4] Eshun, A., Cai, Z., Awies, M., Yu, L., Goodson III, T. Investigations of Thienoacene Molecules for Classical and Entangled Two-Photon Absorption. *J. Phys. Chem. A.*, 2018, 122, 8167-8182

Delocalization length in the context of biological exciton transfer processes

Kieran Fox

Charles University

Exciton delocalization in natural light harvesting structures is a well-known phenomenon, recognised as an important factor in photosynthetic excitation energy transfer efficiency. Standard attempts to define delocalization length within the dynamic environment of a protein, and over biological timescales, results in a single real number or an integer range of pigments. We argue that such a notion of delocalization is not particularly informative or characteristic of the potentially complicated connection network of pigments represented by a photosynthetic antenna. Add to this there seems to be some mixing of concepts under the term delocalization due to the ultra-fast methods of measuring it. We aim to disentangle the delocalization relating to transitions between molecules as a result of resonance coupling, from the coherent state caused by laser excitation in spectroscopic experiments. This is done by respecting the uncertainty of delocalization in time, which we show by analysing the structure of the coherent state excited by ultrashort laser pulse. We demonstrate, on a system exhibiting static disorder only, how a generalised notion of delocalization can be introduced. With this is we can give a better representation of the states, including specific pigment contributions to the delocalized states as this can be crucial to the overall function of the system. We revisit past pump-probe measurements of LH1 and LH2 as well as new 2DES spectra to reexamine the concept of delocalization and try to come to grips with what it means in biological excitation energy transfer processes.

A Step Towards a Comprehensive Steady-State Picture of Photosynthetic Solar Energy Conversion

Veljko Janković

Faculty of Mathematics and Physics, Charles University, Prague

The interpretation of oscillating experimental signals observed in ultrafast nonlinear spectroscopies [1] has been motivating vigorous interest in quantum effects in photoinduced biological processes. However, electronic dynamics triggered by natural light, which is stationary and incoherent, is generally substantially different from the one observed in pulsed laser experiments. It has been suggested that the physically correct picture of photosynthetic excitation energy transfer (EET) should be in terms of a steady state [2], which is formed when the photosynthetic antenna is continuously photoexcited and continuously delivers the excitation energy to the reaction center, in which charge separation takes place.

We study EET triggered by a low-intensity photoexcitation of an initially unexcited molecular aggregate, whose molecules interact with their unstructured local environments and which is coupled to the reaction center. We treat the aggregate–environment coupling in a numerically exact manner and extend previous theoretical treatments [3,4] by formulating the hierarchy of equations of motion (HEOM) which explicitly takes into account the photoexcitation process. We investigate the properties of the steady state arising when the aggregate is subjected to a continuous-wave excitation, while photoinduced electronic excitations can either recombine or undergo charge separation from the reaction center. The developed theoretical formalism enables us to approach questions ranging from the influence of the short-time dynamics (which is accessible in pulsed laser experiments) on the steady state to the relevance of steady-state coherences for the EET process.

[1] G. S. Engel et al., *Nature* 446, 782–786 (2007).

[2] P. Brumer, *J. Phys. Chem. Lett.* 9, 2946–2955 (2018).

- [3] L. Valkunas and T. Mančal, *New J. Phys.* 12, 065044 (2010).
[4] A. Chenu, P. Malý, and T. Mančal, *Chem. Phys.* 439, 100–110 (2014).
-

Matrix-product-state-based calculations of exciton-phonon dynamics for light-harvesting complexes

Kevin Kessing
Uni. Göttingen/MIT

Excitonic systems with one to a few dozen sites are an important and commonly studied topic in various contexts, such as quantum optics, molecular spectroscopy or the dynamics of light-harvesting complexes. However, in reality the dynamics are often strongly influenced by their coupling to the environment or internal vibrational modes. Computing such systems with non-negligible and non-perturbative interactions is a challenging problem, and oftentimes simplifications such as the Markov assumption are made to assist in such calculations. In our approach, we investigate the dynamics of excitonic oligomers with such interactions without neglecting the internal dynamics of the bath using a symmetry-adapted state-of-the-art matrix-product-state (MPS) code [1]. By employing this approach together with the analytic transformation of the bath Hamiltonian into discrete sites (TEDOPA) proposed by Martin Plenio et al. [2], we may also model non-Markovian dynamics of exciton systems with strong bath coupling. The insights gained from these analyses help us better understand the phonon-assisted transport effects in photosynthetic complexes such as the purple-photosynthetic-bacterial light-harvesting complex LH2, which exhibits a remarkably efficient energy transfer and notable symmetric structure [3].

1: Time-evolution methods for matrix-product states; Sebastian Paeckel, Thomas Köhler, Andreas Swoboda, Salvatore R. Manmana, Ulrich Schollwöck, and Claudius Hubig; arXiv:1901.05824 [cond-mat.str-el]

2: Exact mapping between system-reservoir quantum models and semi-infinite discrete chains using orthogonal polynomials; Alex W. Chin, Ángel Rivas, Susana F. Huelga, and Martin B. Plenio; *J. Math. Phys.* 51, 092109 (2010); <https://doi.org/10.1063/1.3490188>

3: Optimal fold symmetry of LH2 rings; Liam Cleary, Hang Chen, Chern Chuang, Robert J. Silbey, and Jianshu Cao; *PNAS* 110 (21), 8537-8542 (May 2013); DOI: 10.1073/pnas.1218270110

Pathway Analysis of Protein Electron-Transfer Reactions by Using Ab Initio Electronic Structure Calculations

Hirota Kito-Nishioka
JST-PRESTO and University of Tsukuba

We have developed a novel computational scheme [1] to analyze electron transfer (ET) reactions in protein. Our scheme combines the fragment molecular orbital (FMO) method with an electron tunneling current analysis, which enables an efficient first-principles analysis of ET pathways in huge biomolecules. This poster presents our recent results [2] and discusses the roles of the protein environments in mediating long-distance electron tunneling and quantum interference effects among multiple ET pathways. We also discuss its applicability to a non-Condon theory [3] for analyzing the inelastic electron tunneling mechanism in protein, such as a hypothesis of the vibrational theory of olfaction. We acknowledge support from JST, PRESTO Grant Number JPMJPR17G4.

References: [1] H. Nishioka and K. Ando, *J. Chem. Phys.* 134, 204109 (2011); H. Kito-Nishioka and K. Ando, *J. Chem. Phys.* 145, 114103 (2016)

[2] H. Kito-Nishioka and K. Ando, *J. Phys. Chem. B* 116, 12933 (2012); H. Kito-Nishioka and K. Ando, *Chem. Phys. Lett.* 621, 96 (2015); R. Sato et al. *J. Phys. Chem. B* 122, 6912 (2018)

[3] H. Nishioka et al. *J. Phys. Chem. B* 109, 15621 (2005); H. Nishioka and T. Kakitani, *J. Phys. Chem. B* 112, 9948 (2008)

A Step Towards A Comprehensive Steady-State Picture Of Photosynthetic Solar Energy Conversion

Veljko Janković^{ab} and Tomáš Mančal^a

^a*Faculty of Mathematics and Physics, Charles University, Ke Karlovu 5, CZ–121 16 Prague 2, Czech Republic*

^b*Scientific Computing Laboratory, Center for the Study of Complex Systems, Institute of Physics Belgrade, University of Belgrade, Pregrevica 118, 11080 Belgrade, Republic of Serbia*

Abstract. The interpretation of oscillating experimental signals observed in ultrafast nonlinear spectroscopies [1] has been motivating vigorous interest in quantum effects in photoinduced biological processes. However, electronic dynamics triggered by natural light, which is stationary and incoherent, is generally substantially different from the one observed in pulsed laser experiments. It has been suggested that the physically correct picture of photosynthetic excitation energy transfer (EET) should be in terms of a steady state [2], which is formed when the photosynthetic antenna is continuously photoexcited and continuously delivers the excitation energy to the reaction center, in which charge separation takes place.

We study EET triggered by a low-intensity photoexcitation of an initially unexcited molecular aggregate, which interacts with its environment and is coupled to the reaction center. We treat the aggregate–environment coupling in a numerically exact manner and extend previous theoretical treatments [3, 4] by formulating the hierarchy of equations of motion (HEOM) which explicitly takes into account the photoexcitation process. We investigate the properties of the steady state arising when the aggregate is subjected to a continuous-wave excitation, while the charge separation from the reaction center occurs at a constant rate. The developed theoretical formalism enables us to approach questions ranging from the influence of the short-time dynamics (which is accessible in pulsed laser experiments) on the steady state to the relevance of steady-state coherences for the EET process.

This work has been supported by Charles University Research Centre program No. UNCE/SCI/010 and by the Czech Science Foundation (GAČR) through grant No. 17-22160S.

REFERENCES

1. Engel, G. S., Calhoun, T. R., Read, E. L., Ahn, T.-K., Mančal, T., Cheng, Y.-C., Blankenship, R. E., and Fleming, G. R., *Nature* **446**, 782–786 (2007).
2. Brumer, P., *J. Phys. Chem. Lett.* **9**, 2946–2955 (2018).
3. Valkunas, L., and Mančal, T., *New J. Phys.* **12**, 065044 (2010).
4. Chenu, A., Malý, P., and Mančal, T., *Chem. Phys.* **439**, 100–110 (2014).

Light-To-Charge Conversion In Organic Photovoltaics: Mechanisms And Timescales

Veljko Janković^{ab} and Nenad Vukmirović^b

^aFaculty of Mathematics and Physics, Charles University, Ke Karlovu 5, CZ-121 16 Prague 2, Czech Republic

^bScientific Computing Laboratory, Center for the Study of Complex Systems, Institute of Physics Belgrade, University of Belgrade, Pregrevica 118, 11080 Belgrade, Republic of Serbia

Abstract. Recent years have seen an intense debate on the physical mechanisms and time scales of free-charge generation following photoexcitation of donor/acceptor organic solar cells, which initially produces strongly bound excitons in the donor material. The interpretation of ultrafast spectroscopic signatures suggests that free carriers are predominantly generated on a subpicosecond time scale following the excitation, the key role in this process being played by high-energy (“hot”) delocalized interfacial charge transfer (CT) states [1]. However, other experimental studies indicate that the main precursor towards free charges is the strongly bound and localized (“cold”) CT state, so that free-charge generation occurs on time scales ranging from tens to hundreds of picoseconds [2, 3].

We investigate charge separation in a one-dimensional model of an interface between two organic semiconductors, both on ultrashort and on much longer time scales. We conclude that free carriers present on a subpicosecond time scale following a pulsed photoexcitation are mainly directly optically generated from the ground state thanks to the resonant mixing between states of donor excitons and free charges [4]. However, on the same time scale, we find that the majority of photogenerated charges still remain bound in form of donor or CT excitons [5]. We obtain that their further separation on longer time scales is weakly electric field- and temperature-dependent and is enabled by the synergy between carrier delocalization and moderate disorder [6].

REFERENCES

1. Grancini, G. et al., *Nat. Mater.* **12**, 29–33 (2013).
2. Vandewal, K. et al., *Nat. Mater.* **13**, 63–68 (2014).
3. Grupp, A. et al., *J. Phys. Chem. Lett.* **8**, 4858–4864 (2017).
4. Janković, V., and Vukmirović, N., *Phys. Rev. B* **95**, 075308 (2017).
5. Janković, V., and Vukmirović, N., *J. Phys. Chem. C* **121**, 19602–19618 (2017).
6. Janković, V., and Vukmirović, N., *J. Phys. Chem. C* **122**, 10343–10359 (2018).

Dynamics of Photoexcited Charges in Organic Heterojunctions – Insights from Theory and Simulation

Veljko Janković¹ and Nenad Vukmirović¹,

¹Scientific Computing Laboratory, Center for the Study of Complex Systems, Institute of Physics Belgrade, University of Belgrade, Pregrevica 118, 11080 Belgrade, Serbia, email: nenad.vukmirovic@ipb.ac.rs

Abstract—The process of exciton splitting at heterojunctions of two organic semiconductors in organic photovoltaic devices was investigated. Theoretical model is based on a Hamiltonian taking into account the effects of electronic coupling, interaction of carriers with external electromagnetic field, Coulomb interaction between electrons and holes and carrier-phonon interaction. Exciton dynamics at subpicosecond timescales was investigated within density matrix theory complemented with the dynamics controlled truncation scheme. Our results indicate that the efficiency of charge separation on subpicosecond timescales is low and that the majority of space-separated charges that occur on these timescales are directly optically generated. Next, we investigated charge separation process on longer timescale by considering it as a sequence of phonon-assisted transitions between electron-hole pair states at the interface. We found that donor exciton separation yields larger than 90% can be achieved in agreement with experimentally observed internal quantum efficiencies close to 100% in most efficient organic photovoltaic devices.

I. INTRODUCTION

Significant research attention in the last two decades was devoted to the development of photovoltaic devices based on organic semiconductors which offer the advantage of easy and cheap processing. Nevertheless, understanding of the details of the processes that take place in a solar cell device is still limited. It is well understood that binding between an electron and a hole that are created by an incident photon is sufficiently strong to form a bound electron-hole pair (exciton). For this reason, efficient devices can be obtained only if they are composed of (at least) two semiconductors (donor and acceptor) whose band edge alignment is chosen to energetically allow the dissociation of an exciton into an electron in the acceptor and a hole in the donor. A simple picture of photon-to-charge conversion process suggests that it takes place by photon absorption that creates an exciton, exciton diffusion to an interface between the two materials, exciton separation to charges at opposite sides of an interface, and charge transport from an interface to external contacts [1, 2].

To better understand the mechanism of exciton splitting at the interface, several ultrafast spectroscopy studies that probe the dynamics at subpicosecond timescales have been performed in the last decade [3, 4, 5, 6]. These studies

typically register response signals with subpicosecond decay times, which are often interpreted to originate from ultrafast separation of donor excitons into space-separated charges. Nevertheless, the nature of exciton evolution on these timescales and the mechanism of its possible separation remains unclear.

In this presentation, we will review our recent results on exciton dynamics at photoexcited organic heterojunctions [7-9].

II. METHODS

We model the heterojunction of two organic semiconductors using a microscopic Hamiltonian that takes into account the effects of electronic coupling, interaction of carriers with external electromagnetic field, attractive Coulomb interaction between electrons and holes and interaction of charges with lattice vibrations. We consider a one-dimensional model of a semiconductor in which it is represented using a lattice of sites. Each site provides at least one electron and at least one hole level from which the conduction and valence band of the material are derived. Interaction with phonons is modeled using local Holstein interaction, while electron-hole interaction is modeled in the lowest monopole-monopole approximation with the Ohno interaction potential between the charges.

The parameters of the model – electronic coupling between the sites, site energies, electron-phonon interaction parameters, on-site Coulomb interaction parameter – were chosen to yield values of band gaps, band offsets, bandwidths and exciton binding energies that are representative of typical organic photovoltaic materials.

To model exciton dynamics on ultrafast timescales, we use the density matrix theory along with the dynamics controlled truncation scheme. We consider the case of low excitation field and low carrier densities when it is appropriate to work in the subspace of single electron-hole excitations. The carrier branch of the hierarchy of equations in density matrix approach was truncated by keeping the contributions up to second order in the excitation field. The phonon branch is truncated in such a way to ensure the conservation of particle number and energy [7].

III. RESULTS

Our results indicate that space-separated charges present around 100 fs after the optical excitation, originate mainly from direct optical generation. There is also a certain degree of donor exciton population transfer but it is not the main source of space-separated charges, see Figs. 1(a) and (b). We also find that such a conclusion is insensitive to the values of model parameters since similar behavior is obtained when material parameters were changed within reasonable limits [8].

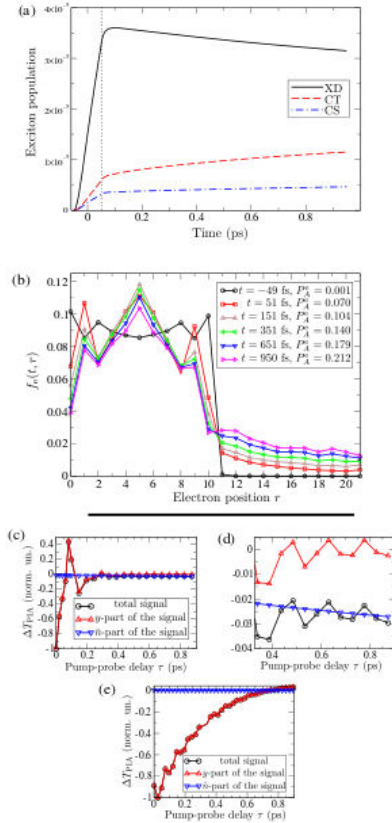


Fig. 1. (a) Dependence of the number of incoherent excitons in donor (XD), charge transfer (CT) and charge separated (CS) states. Optical excitation is centered at photon energy of 1500 meV and lasts from -50 to 50 fs. (b) Time evolution of spatial electron probability distribution. (c) and (d) Simulated photoinduced absorption signal from space separated states after pumping at photon energy of 1500 meV. (e) Simulated PIA signal from donor states after pumping to lowest donor state.

Our analysis indicates that microscopic mechanism responsible for direct optical generation of space-separated charges is resonant mixing between donor states and states of space-separated charges. We find that the efficiency of charge separation at these time scales is quite low, as can be seen for example in Fig. 1(a).

Next, within our theoretical approach we simulate the photoinduced absorption (PIA) signal obtained in ultrafast pump-probe experiments [3]. Our results indicate that for interpretation of PIA signal it is of essential importance to

consider not only the excitonic populations, but also the coherences between the exciton and ground state, as well as the coherences between exciton states. Calculated signals presented in Figs. 1(c)-(e) qualitatively agree with experimental signals obtained in [3]. In the case of excitation well above the lowest donor exciton, PIA signal from space-separated states [labeled as total signal in Figs. 1(c) and (d)] is initially dominated by the contribution of coherences between the exciton and ground state [labeled as y-part of the signal in Figs. 1(c) and (d)], while at longer times the contribution of excitonic populations dominates [labeled as \bar{n} -part of the signal in Fig. 1(d)]. On the other hand, in the case of excitation to the lowest donor exciton, PIA signal completely originates from the contribution of coherences between the exciton and ground state, see Fig. 1(e). Therefore, such a signal does not originate from ultrafast transfer of donor excitons to states of space-separated charges, but rather from relatively slow conversion from coherences to populations of lowest donor state.


Overall, our simulations at subpicosecond timescale do not show that there is ultrafast charge transfer and cannot explain high internal quantum efficiencies observed in best solar cell devices. For this reason, we investigated charge separation process on longer timescale by considering it as a sequence of phonon-assisted transitions between electron-hole pair states at the interface. Our preliminary results indicate that donor exciton separation yields larger than 90% can be achieved in agreement with experimentally observed internal quantum efficiencies close to 100% in most efficient organic photovoltaic devices.

ACKNOWLEDGMENT

We gratefully acknowledge the support by the Ministry of Education, Science and Technological Development of the Republic of Serbia (Project No. ON171017) and the European Commission under H2020 project VI-SEEM, Grant No. 675121, as well as the contribution of the COST Action MP1406.

REFERENCES

- [1] J. L. Bredas, J. E. Norton, J. Cornil, and V. Coropceanu, *Acc. Chem. Res.* vol. 42, pp. 1691-1699 (2009).
- [2] T. M. Clarke and J. R. Durrant, *Chem. Rev.* vol. 110, pp. 6736-6767 (2010).
- [3] G. Grancini, M. Maiuri, D. Fazzi, A. Petrozza, H.-J. Egelhaaf, D. Brida, G. Cerullo, and G. Lanzani, *Nature Mater.* vol. 12, pp. 29-33 (2013).
- [4] A. E. Jaiilaubekov, A. P. Willard, J. R. Tritsch, W.-L. Chan, N. Sai, R. Gearba, L. G. Kaake, K. J. Williams, K. Leung, P. J. Rossky, and X.-Y. Zhu, *Nature Mater.* vol. 12, pp. 66-73 (2013).
- [5] S. Gelinas, A. Rao, A. Kumar, S. L. Smith, A. W. Chin, J. Clark, T. S. van der Poll, G. C. Bazan, and R. H. Friend, *Science* vol. 343, pp. 512-516 (2014).
- [6] A. A. Paraecattil and N. Banerji, *J. Am. Chem. Soc.* 136, pp. 1472-1482 (2014).
- [7] V. Janković and N. Vukmirović, *Phys. Rev. B* vol. 92, p. 235208 (2015).
- [8] V. Janković and N. Vukmirović, *Phys. Rev. B* vol. 95, p. 075308 (2017).
- [9] V. Janković and N. Vukmirović, *J. Phys. Chem. C* vol. 121, pp. 19602-19618 (2017).

START AT	SUBJECT	View All	NUM.	ADD
16:00	<p>Importance of Carrier Delocalization and Disorder for Incoherent Charge Separation at Organic Bilayers</p> <p>Authors : Veljko Jankovic, Nenad Vukmirovic Affiliations : Scientific Computing Laboratory, Center for the Study of Complex Systems, Institute of Physics Belgrade, University of Belgrade, Pregrevica 118, 11080 Belgrade, Serbia; Scientific Computing Laboratory, Center for the Study of Complex Systems, Institute of Physics Belgrade, University of Belgrade, Pregrevica 118, 11080 Belgrade, Serbia</p> <p>Resume : Recent studies [1,2,3] have challenged the view that free-charge generation in all-organic blends predominantly occurs on ultrafast time scales via delocalized hot charge transfer states. However, the mechanisms behind very efficient and weakly electric field-dependent charge separation on longer time scales remain highly debated. We investigate field-dependent charge separation in a one-dimensional lattice model of an all-organic bilayer. Charge separation is considered as a sequence of phonon-assisted transitions among eigenstates of an electron-hole pair supported by the interface. We find that the yield of charge separation starting from the strongly bound charge transfer state is weakly field-dependent and above 50% even at zero electric field. Moderate diagonal static disorder and good charge delocalization increase the yield by strengthening the transitions from the initial state toward long-lived states with increased electron-hole separation, from which further separation proceeds without kinetic obstacles. We also observe almost field-independent (at low to moderate fields) charge separation starting from a donor exciton state, while the yield varies from around 40% (from the lowest-energy donor state) to around 80% (from states energetically well above the lowest-energy donor state). [1] Vandewal et al., Nat. Mater. 13, 63 (2013). [2] Jankovic and Vukmirovic, Phys. Rev. B 95, 075308 (2017). [3] Grupp et al., J. Phys. Chem. Lett. 8, 4858 (2017).</p>		J.12.7	

Origin of Space-separated Charges in Photoexcited Organic Heterojunctions on Subpicosecond Time Scales

Veljko Janković and Nenad Vukmirović

Scientific Computing Laboratory, Centre for the Study of Complex Systems, Institute of Physics Belgrade, University of Belgrade, Pregrevica 118, 11080 Belgrade, Serbia

e-mail: veljko.jankovic@ipb.ac.rs

The promise of economically viable and environmentally friendly conversion of sunlight into electrical energy has driven vigorous and interdisciplinary research on donor/acceptor heterojunction organic photovoltaics. However, the actual mechanism of the emergence of free charges on subpicosecond (<100-fs) time scales following the excitation of a heterojunction remains elusive.

We investigate subpicosecond exciton dynamics in the lattice model of an all-organic heterojunction. Exciton generation by means of a photoexcitation, exciton dissociation, and further charge separation are treated on equal footing and on a fully quantum level using the density matrix formalism combined with the dynamics controlled truncation scheme [1]. Our results indicate that the space-separated charges appearing on <100-fs time scales following the photoexcitation are predominantly directly optically generated [2], in contrast to the usual viewpoint that they originate from ultrafast population transfer from initially generated excitons in the donor material. The space-separated states acquire nonzero oscillator strengths from donor excitons thanks to the strong resonant mixing between these two groups of exciton states. The results of ultrafast pump-probe experiments are commonly interpreted in terms of exciton populations only. Our theoretical insights into the ultrafast pump-probe spectroscopy highlight the importance of coherences, which cannot be disregarded on such short time scales, in the interpretation of pump-probe spectra [2].

REFERENCES

- [1] V. Janković and N. Vukmirović, Phys. Rev. B 92, 235208 (2015).
- [2] V. Janković and N. Vukmirović, Phys. Rev. B 95, 075308 (2017).

Gordon Research Conferences: Participation Certificate**From:** "Gordon Research Conferences" <agrasso@grc.org>**To:** veljko@ipb.ac.rs**Date:** 2016-06-11 07:01

[visit us on the web at http://www.grc.org](http://www.grc.org)

Certificate of Participation

06/11/2016

Veljko Jankovic
Institute of Physics Belgrade
Pregrevica 118
Belgrade, 11080
Serbia

This is a certificate of participation for:

Conference: Electronic Processes in Organic Materials
Dates: 06/05/2016 - 06/10/2016
Location: Renaissance Tuscany Il Ciocco in Lucca (Barga) Italy

This letter certifies your participation as a Poster Presenter at the Gordon Research Conference on Electronic Processes in Organic Materials held 06/05/2016 - 06/10/2016 at Renaissance Tuscany Il Ciocco in Lucca (Barga) Italy.

Presented poster titled: TBD Exciton Formation and Relaxation Dynamics in Photoexcited Organic Semiconductors and Their Heterojunctions: Numerical Study

Nancy Ryan Gray, PhD, President and Chief Executive Officer
Gordon Research Conferences

A handwritten signature in black ink, appearing to read 'Nancy Ryan Gray', is positioned below the typed name.

**Please notify us if you are not the intended recipient of this email.*

Follow GRC: [Facebook](#) | [Twitter](#)

This email message from Gordon Research Conferences is intended only for the individual or entity to which it is addressed. This email may contain confidential or privileged information. If you are not the intended recipient, any disclosure, copying, use, or distribution of the information included in this message and any attachments is prohibited. If you have received this communication in error, please notify us by reply e-mail and immediately and permanently delete this message and any attachments. Thank you.

Gordon Research Seminar 2016

Exciton Formation and Relaxation Dynamics in Photoexcited Organic Semiconductors and Organic Semiconductor Heterojunctions: Numerical Study

Veljko Jankovic and Nenad Vukmirovic

Scientific Computing Laboratory, Institute of Physics Belgrade, University of Belgrade, Pregrevica 118, 11080 Belgrade, Serbia

Recent years have seen vigorous and interdisciplinary research activity in the field of organic photovoltaics with the aim of deeper understanding of ultrafast processes which govern their operation. We have investigated the dynamics of exciton formation and relaxation on a picosecond time scale following a pulsed photoexcitation of a semiconductor [1]. The study is conducted on the two-band semiconductor Hamiltonian, which includes relevant physical effects in the system, employing the density matrix theory combined with the dynamics controlled truncation scheme. We truncate the phonon branch of the resulting hierarchy of equations and propose the form of coupling among single-phonon-assisted and higher-order phonon-assisted density matrices so as to ensure the energy and particle-number conservation in a system without external fields. Time scales relevant for the exciton formation and relaxation processes are determined from numerical investigations performed on a one-dimensional model for the values of model parameters representative of a typical organic semiconductor and organic semiconductor heterojunction. We find that in a neat organic semiconductor the phonon-mediated conversion from coherent to incoherent excitonic populations happens on a 50 fs time scale, followed by the formation of bound excitons on a several-hundred-femtosecond time scale and their subsequent relaxation and equilibration which takes at least several picoseconds. At a heterojunction of two organic semiconductors, we find that the strong (resonant) mixing between interfacial excitonic states and excitonic states in neat materials, as well as proper accounting for interband excitonic coherences, are critical for the accurate description of charge transfer from the donor to the acceptor and subsequent charge separation. Time scales that emerge from our numerical study are consistent with recent experimental reports on the exciton formation and relaxation in conjugated polymer-based materials. We believe that the insights obtained from our study of a typical organic/organic heterojunction may contribute to more profound understanding of fundamental OPV physics.

References

[1] V. Jankovic and N. Vukmirovic, *Phys. Rev. B* **92**, 235208 (2015)

ID 68 - Poster

Nonequilibrium Electrical Transport in Materials with Localized Electronic States

V. Jankovic¹, *N. Vukmirovic¹

¹Institute of Physics Belgrade, Scientific Computing Laboratory, Belgrade, Serbia

A broad range of disordered materials contain electronic states that are spatially well localized. In this work we studied the electrical response of such materials to external terahertz electromagnetic field [1]. We obtained expressions for nonequilibrium terahertz conductivity of a material with localized electronic states and weak electron-phonon or electron-impurity interaction. The expression is valid for any nonequilibrium state of the electronic subsystem prior to the action of external field. It gives nonequilibrium optical conductivity in terms of microscopic material parameters and contains both coherences and populations of the initial electronic subsystem's density matrix. Particularly, in the case of incoherent nonequilibrium state of the electronic subsystem, the optical conductivity is entirely expressed in terms of the positions of electronic states, their nonequilibrium populations, and Fermi's golden rule transition probabilities between the states. The same mathematical form of the expression is valid both in the case of electron-phonon and electron-impurity interaction. Moreover, our result for the nonequilibrium optical conductivity has the same form as the expressions previously obtained for the case of equilibrium. Our results are expected to be valid at sufficiently high frequencies, such that the period of the external field is much smaller than the carrier relaxation time. We apply the derived expressions to two model systems, a simple one-dimensional Gaussian disorder model and the model of a realistic three-dimensional organic polymer material obtained using previously developed multiscale methodology [2]. We note that the simple one-dimensional model captures the essential features of the mobility spectrum of a more realistic system. Furthermore, our simulations of the polymer material yield the same order of magnitude of the terahertz mobility as previously reported in experiments.

[1] V. Janković and N. Vukmirović, Phys. Rev. B 90, 224201 (2014).

[2] N. Vukmirović and L.-W. Wang, Nano Lett. 9, 3996 (2009).

Nonequilibrium High-frequency Conductivity in Materials with Localized Electronic States

Veljko Janković and Nenad Vukmirović

^aScientific Computing Laboratory, Institute of Physics Belgrade, University of Belgrade, Pregrevica 118, 11080 Belgrade, Serbia

Abstract. A broad range of disordered materials contain electronic states that are spatially well localized. These include amorphous inorganic semiconductors, inorganic crystals doped with randomly positioned impurities and organic semiconductors based on conjugated polymers or small molecules. Usual approaches to simulation of ac conductivity of these materials rely on Kubo's formula which expresses the ac conductivity in terms of the mean square displacement of a diffusing carrier. Such approaches therefore assume that carriers are in equilibrium and that they are only slightly perturbed by external alternating electric field. However, in many realistic situations, the carriers are not in equilibrium; a typical example concerns the carriers created by external optical excitation across the band gap of a semiconductor.

In this work we obtain the expression for the optical conductivity in a material with localized electronic states and weak electron-phonon or electron-impurity interaction [1]. The expression is valid for any nonequilibrium state of the electronic subsystem prior to the action of electric field. It gives nonequilibrium optical conductivity in terms of microscopic material parameters and contains both coherences and populations of the initial electronic subsystem's density matrix. Particularly, in the case of incoherent nonequilibrium state of the electronic subsystem, the optical conductivity is entirely expressed in terms of the positions of electronic states, their nonequilibrium populations, and Fermi's golden rule transition probabilities between the states. The same mathematical form of the expression is valid both in the case of electron-phonon and electron-impurity interaction. Moreover, our result for the nonequilibrium optical conductivity has the same form as the expressions previously obtained for the case of equilibrium. The derivation was performed by expanding the general expression for ac conductivity in powers of small electron-phonon or electron-impurity interaction parameter. Our results are expected to be valid at sufficiently high frequencies, such that the period of the electric field is much smaller than the carrier relaxation time. We apply the derived expressions to two model systems, a simple one-dimensional Gaussian disorder model and the model of a realistic three-dimensional organic polymer material obtained using previously developed multiscale methodology [2]. We note that the simple one-dimensional model captures the essential features of the mobility spectrum of a more realistic system. Furthermore, our simulations of the polymer material yield the same order of magnitude of the terahertz mobility as previously reported in experiments.

REFERENCES

1. Janković V., and Vukmirović N., Phys. Rev. B 90, 224201 (2014).
2. Vukmirović N., and Wang L. W., Nano Lett. 9, 3996 (2009).

Nonequilibrium Terahertz Conductivity in Systems with Localized Electronic States

Veljko Janković and Nenad Vukmirović

Scientific Computing Laboratory, Institute of Physics Belgrade, University of Belgrade, Pregrevica 118,
11080 Belgrade, Serbia
veljko.jankovic@ipb.ac.rs

A broad range of disordered materials contain electronic states that are spatially well localized. These include amorphous inorganic semiconductors, inorganic crystals doped with randomly positioned impurities and organic semiconductors based on conjugated polymers or small molecules. Usual approaches to simulation of ac conductivity rely on Kubo's formula which expresses the ac conductivity in terms of the mean square displacement of a diffusing carrier. Such approaches therefore assume that carriers are in equilibrium and that they are only slightly perturbed by external alternating electric field. However, in many realistic situations, the carriers are not in equilibrium; a typical example concerns the carriers created by external optical excitation across the band gap of a semiconductor.

In this work we obtain the expression for the optical conductivity in a material with localized electronic states and weak electron-phonon or electron-impurity interaction [1]. The expression is valid for any nonequilibrium state of the electronic subsystem prior to the action of electric field. Particularly, in the case of incoherent nonequilibrium state of the electronic subsystem, the optical conductivity is entirely expressed in terms of the positions of electronic states, their nonequilibrium populations, and Fermi's golden rule transition probabilities between the states. The same mathematical form of the expression is valid both in the case of electron-phonon and electron-impurity interaction. Moreover, our result for the nonequilibrium optical conductivity has the same form as the expressions previously obtained for the case of equilibrium. The derivation was performed by expanding the general expression for ac conductivity in powers of small electron-phonon or electron-impurity interaction parameter. Our results are expected to be valid at sufficiently high frequencies, such that the period of the electric field is much smaller than the carrier relaxation time. We apply the derived expressions to two model systems, a simple one-dimensional Gaussian disorder model and the model of a realistic three-dimensional organic polymer material obtained using previously developed multiscale methodology [2]. We note that the simple one-dimensional model captures the essential features of the mobility spectrum of a more realistic system. Furthermore, our simulations of the polymer material yield the same order of magnitude of the terahertz mobility as previously reported in experiments.

References

- [1] V. Janković and N. Vukmirović, *Phys. Rev. B* **90**, 224201 (2014).
- [2] N. Vukmirović and L.-W. Wang, *Nano Lett.* **9**, 3996 (2009).

Nonequilibrium terahertz conductivity in materials with localized electronic states

Veljko Janković¹ and Nenad Vukmirović¹

¹*Scientific Computing Laboratory, Institute of Physics Belgrade, University of Belgrade, Pregrevica 118, 11080 Belgrade, Serbia*
email: veljko.jankovic@ipb.ac.rs

A broad range of disordered materials contain electronic states that are spatially well localized. In this work [1] we studied the electrical response of such materials to external terahertz electromagnetic field. We obtained expressions for nonequilibrium terahertz conductivity of a material with localized electronic states and weak electron-phonon or electron-impurity interaction. The expression is valid for any nonequilibrium state of the electronic subsystem prior to the action of external field. It gives nonequilibrium optical conductivity in terms of microscopic material parameters and contains both coherences and populations of the initial electronic subsystem's density matrix. Particularly, in the case of incoherent nonequilibrium state of the electronic subsystem, the optical conductivity is entirely expressed in terms of the positions of electronic states, their nonequilibrium populations, and Fermi's golden rule transition probabilities between the states. The same mathematical form of the expression is valid both in the case of electron-phonon and electron-impurity interaction. Moreover, our result for the nonequilibrium optical conductivity has the same form as the expressions previously obtained for the case of equilibrium. Our results are expected to be valid at sufficiently high frequencies, such that the period of the external field is much smaller than the carrier relaxation time. We apply the derived expressions to two model systems, a simple one-dimensional Gaussian disorder model and the model of a realistic three-dimensional organic polymer material obtained using previously developed multiscale methodology [2]. We note that the simple one-dimensional model captures the essential features of the mobility spectrum of a more realistic system. Furthermore, our simulations of the polymer material yield the same order of magnitude of the terahertz mobility as previously reported in experiments.

REFERENCES

- [1] V. Janković and N. Vukmirović, Phys. Rev. B **90**, 224201 (2014).
- [2] N. Vukmirović and L.-W. Wang, Nano Lett. **9**, 3996 (2009).